WMTC 22

7TH WORLD MARITIME TECHNOLOGY CONFERENCE

PROCEEDINGS

Sponsored by

DNV

MARLOG

DEN DANSKE MARITIME FOND

A/S D/S ORIENT'S FOND

LauritzenFonden

OSK-ShipTech A/S

DanishShipping

A P MOLLER FONDEN

WÄRTSILÄ

DANISH MARITIME FAIR

Ammonia: A Pungent Propulsion

S. Waghmare

Abstract

Due to the IMO's sulfur cap being enforced from 1st January, 2020, the owners were put in a spot, either switch to low sulfur fuel oil and Ultra Low Sulfur Fuel Oil (ULSFO), depending on the region they were in. IMO has announced its vision for 2050. It has a vision to reduce the Carbon Dioxide emission levels 40% by 2030 and 70% by 2050, when compared to the level of 2008. As for its vision for total green-house gas emission reduction, IMO envisions to reduce it to 50% by 2050, when compared to levels of 2008. In this paper we will be concentrating on the possibility of ammonia as an alternative to the fossil fuel derived propulsion. The advantage and disadvantage will be carefully weighted and judged, along with some case studies of the leading shipping companies and experimentation of analyzing an 'ammonia propelled future'.

Keywords: Reverse Fuel Cell; Green Ammonia; EEXI; LCA of Green Ammonia; National Hydrogen Mission

1. Introduction

While the maritime industry was struggling to keep up with the enforcement of IMO 2020 regulations, limiting the Sulfur emissions to 0.5% outside Sulfur Emission Control Areas (SECA) and below 0.1% inside SECA regions, IMO has announced its vision for 2050. It has a vision to reduce the Carbon Dioxide emission levels 40% by 2030 and 70% by 2050, when compared to the level of 2008. As for its vision for total green-house gas emission reduction, IMO envisions to reduce it to 50% by 2050, when compared to levels of 2008. [1]

Hence shifting to low sulfur fuel or even Ultra Low Sulfur Fuel Oil might not be the solution in the long run. We are escaping one trap, just to be trapped into another. For that matter even shifting to carbon-based fuels such as LNG and LPG are not a solution. It is neither economical nor advisable to shift to different fuels every decade or retrofit new equipment such as scrubber towers to meet the ever-rising demands of the industry. It would be foolish to even consider doing so, now that we know what IMO has in store for us. Some of the alternatives to fossil fuels include hydrogen, electricity, fuel cells, ammonia, etc.

In this paper we will be concentrating on the possibility of ammonia as an alternative to the fossil fuel derived propulsion. The advantage and disadvantage will be carefully weighted and judged, along with some case studies of the leading shipping companies and experimentation of analyzing an 'ammonia propelled future'.

2. Impact of IMO 2020 Sulfur Cap on Shipping

As discussed earlier due to the IMO's sulfur cap being enforced from 1st January, 2020, the owners were put in a spot, switch to low sulfur fuel oil and Ultra Low Sulfur Fuel Oil, depending on the region they were in. The second option which was given to them was retrofitting of Scrubber Towers onto the ships. The capital which was required was high plus the time taken for retrofitting these emission reducing towers would be high. If the needs of IMO are evolving every decade, it would be an arduous task to not only install the retrofits but also train the manpower to operate them efficiently and safely.

The use of open loop scrubbers has entered into a controversy with 21 countries banning the discharge of wash water from these scrubbers, Saudi Arabia being the latest one. [2] Many more countries have issued restriction or guidelines regarding the discharge of the wash water from such plants.

3. Impact of Covid-19 on Shipping

For the owners who chose to not retrofit the scrubber towers, the only option left is to change over to low sulfur fuel oil and Ultra Low Sulfur Fuel Oil. This enhanced fuel is highly refined and is bound to cost more, further increasing the cost of shipping. Based on the analysis, the switch to IMO compliant LSFO prices as of 1 January resulted in a nearly two-fold increase in assessed fuel costs across covered routes, equivalent to an average rise in nominal voyage freight rates of 20%, or US$5 per ton, to around US$30 per ton. [3]

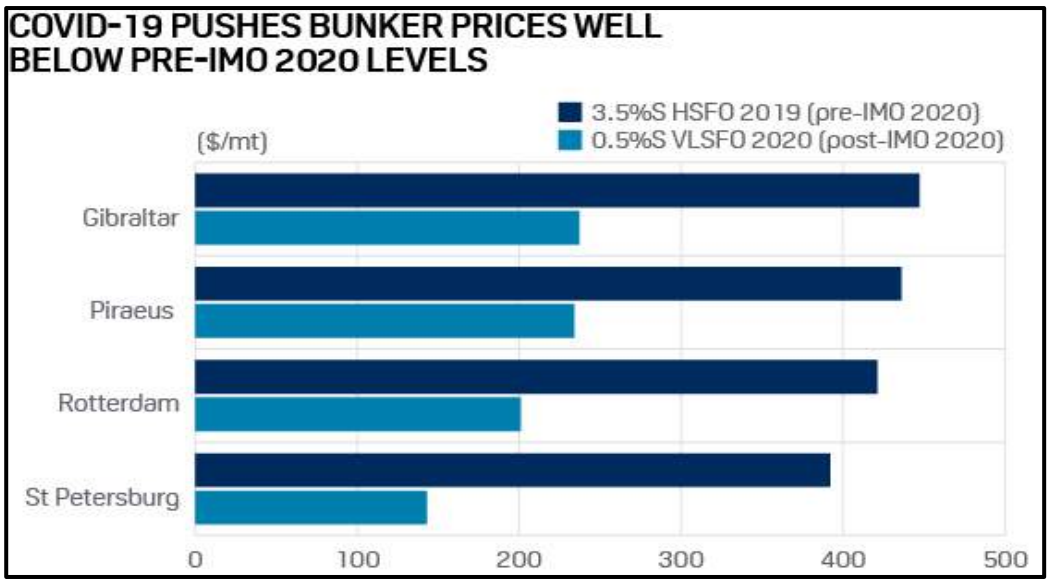

Fig 1. Comparing of Fuel Prices of HFO and VLSFO, pre-COVID and post-COVID respectively [4]

The marine fuel of choice for many ship-owners was 'Very Low Sulfur Fuel Oil' (0.5% sulfur). Its price averaged $201/mt in April on a delivered basis at Rotterdam, half what it was before IMO 2020, despite the main fuel one year ago containing more sulfur. The prevalent marine fuel last year, high sulfur fuel oil (3.5% sulfur), averaged $421/mt in April 2019 at Rotterdam, S&P Global Platts data shows. [4]

The fuel prices were expected to shoot up due to the change-over of fuel but it did not take the projected trajectory but took a steep fall. This can be attributed to the present COVID-19 pandemic, which has shaken even the strongest of economies. Thus, the impact of IMO 2020 is yet to hit the shipping industry and its repercussions are yet to trickle down to the end customer.

4. Alternative in Ammonia

Ammonia's potential as a transport fuel has been demonstrated by NASA in its deployment in rockets. NASA in its paper tited, 'Theoretical Performance Of Liquid Ammonia And Liquid Fluorine As A Rocket Propellant' has highlighted the use of ammonia along with fluorine in its liquid form as a fuel which is very much capable of an expansive thrust. Theoretical values of performance parameters for liquid ammonia and liquid fluorine as a rocket propellant were calculated on the assumption of equilibrium composition during the expansion process for a wide range of fuel-oxidant and expansion ratios [6]. This report was submitted on March 16, 1953 and classified. It was made available only to the public on August 29, 2013.

4.1. Advantages of Liquid Ammonia as a Fuel

Apart from electric propulsion we have two main alternative fuels, hydrogen and ammonia. Ammonia is less dense in energy, when compared to hydrogen. However, in the ease of transportation and storage, the properties of ammonia more than exceed those of hydrogen. Let us look at some of the thermodynamic properties of Ammonia which gives it an upperhand:

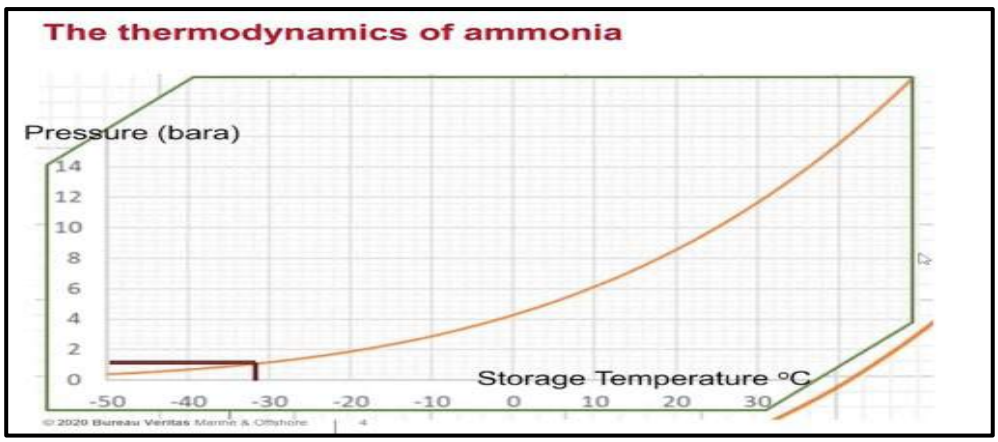

Fig 2. Thermodynamics of Ammonia [6]

- The thermodynamics of ammonia (Fig 2) shows us that Ammonia at atmospheric pressure is liquefied at -33ºC and the same liquefaction point is increased to room temperatures when it is stored under a pressure of 11 bar. [6] Thus it is mildly cryogenic in nature.
- The flammability of ammonia is between 15-28%. The Lower Explosive Limit (LEL) being 15% and Upper Explosive Limit (UEL) being 28% respectively. [7] This makes it harder to ignite and thus reduces the chances of an explosion.
- Ammonia has a molecular formula of NH_3, and it made up by 3 atoms of hydrogen and one atom of nitrogen. As it contains no carbon, the fear of carbon oxide emissions can be safely rested. Thus, the fuel is ready to comply theoretically with the IMO's vision of 2050.
- It is more energy dense than hydrogen and is the most energy dense, zero carbon emission fuel (Fig 2) [8]

4.2. Limitations of Ammonia as A Fuel

- Ammonia is very hard to burn and needs a pilot fuel to burn if used on a Liquid Gas Ignition (LGI) Engine. Thus up to 15% pilot fuel is required to burn it on an LGI engine, eliminating the entire concept of zero-carbon based-emission free fuel.
- It is less energy dense than most of the fossil fuels that are used today. Energy density of ammonia is only 38% of what was obtained from burning of diesel fuels. Thus, for the same power generation we would need thrice the storage capacity. This would have to be done by compromising precious cargo space, thus reducing the cargo carrying capacity.

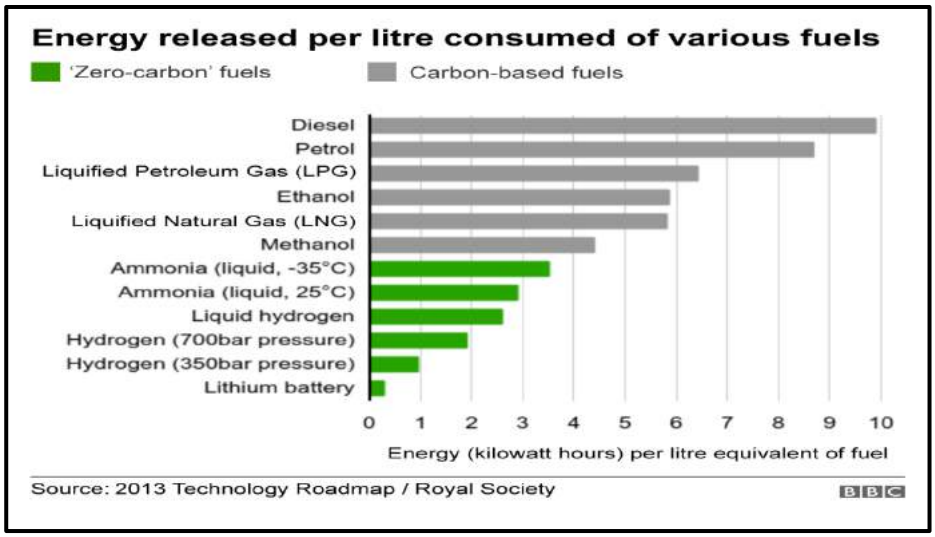

Fig 3. Comparison of Various Fuels with respect to their energy density/litre of equivalent fuel[8]

- The amount of NOx emissions would increase substantially. Thus, to confer with the Tier III regulation of Annex VI, of Marpol, a Selective Catalytic Reduction (SCR) would need to be installed. This would increase the Capital Expenditure (CAPEX) by the owner in terms of installation, maintenance and upskilling of manpower.

5. Reduction of NOx Emissions

NH_3 has been drawing attention recently as a carbon-free alternative fuel. NH_3 is a combustible gas that can be widely used in thermal power generation and industrial furnaces as an alternative to gasoline and light oil. However, it is difficult to burn (high ignition temperature) and generates harmful nitrogen oxides (NOx) during combustion.

5.1. Catalytic Combustion Method

Researchers at the International Research Organization for Advanced Science and Technology (IROAST) in Kumamoto University, Japan focused on a "catalytic combustion method" to solve the NOx emission issue. This method adds substances that promote or suppress chemical reactions during fuel combustion. Recently, they succeeded in developing a new catalyst which improves NH_3 combustibility and suppresses the generation of NOx. The novel catalyst (CuOx/3A2S) is a mullite-type crystal structure $3Al_2O_3 \cdot 2SiO_2$ (3A2S) carrying copper oxide (CuOx). When NH_3 was burned with this catalyst, researchers found that it stayed highly active in the selective production of N_2, meaning that it suppressed NOx formation, and the catalyst itself did not change even at high temperatures. [9]

5.2. Selective Catalytic Reduction

A Selective Catalytic Reduction (SCR) system uses a metallic or ceramic wash-coated catalyzed substrate, or a homogeneously extruded catalyst and a chemical reductant to convert nitrogen oxides to molecular nitrogen and oxygen in oxygen-rich exhaust streams. As exhaust and reductant pass over the SCR catalyst, chemical reactions occur that reduce NOx emissions to nitrogen and water. SCR catalysts can be combined with a particulate filter for combined reductions of both PM and NOx. Open loop SCR systems can reduce NOx emissions by 75 to 90 percent. Closed loop systems on stationary engines can achieve NOx reductions of greater than 95 percent. SCR systems are also effective in reducing HC emissions up to 80 percent and PM emissions 20 to 30 percentage. [10]

6. Case Study

The properties of ammonia have been considered in detail and its merits and its limitations having being addressed, one might begin to wonder about whether this idea of ammonia as an alternative fuel is just limited to the papers or has any of the players of the maritime industry shown serious commitment to the use of ammonia as a fuel.

6.1. Wärtsilä

The technology group Wärtsilä, in close customer cooperation with Knutsen OAS Shipping AS and Repsol, as well as with the Sustainable Energy Catapult Centre, will commence the world's first long term, full-scale, testing of ammonia as a fuel in a marine four-stroke combustion engine. The testing is made possible by a 20 Million NOK grant from the Norwegian Research Council through the DEMO 2000 programme. [11]

Fig 4. Ammonia Engine being testing at Wärtsilä R&D [12]

Meanwhile, Wärtsilä is working on four-stroke engine designs, hoping to reach the stage of field tests as soon as 2022. Fig 4, shows the testing of one such engine at its R&D facility. [12]

6.2. MAN Energy Solutions

Man Energy Solutions is expecting to have a two-stroke ammonia engine ready to deliver by early 2024[12]. The project aims to demonstrate – at full-scale – a large marine engine running on ammonia at MAN Energy Solutions' test facility, Research Centre Copenhagen. The project comprises three main stages [13]:

1. Concept development and initial design of an ammonia engine.
2. Design of an ammonia fuel-supply system.
3. Full-scale testing

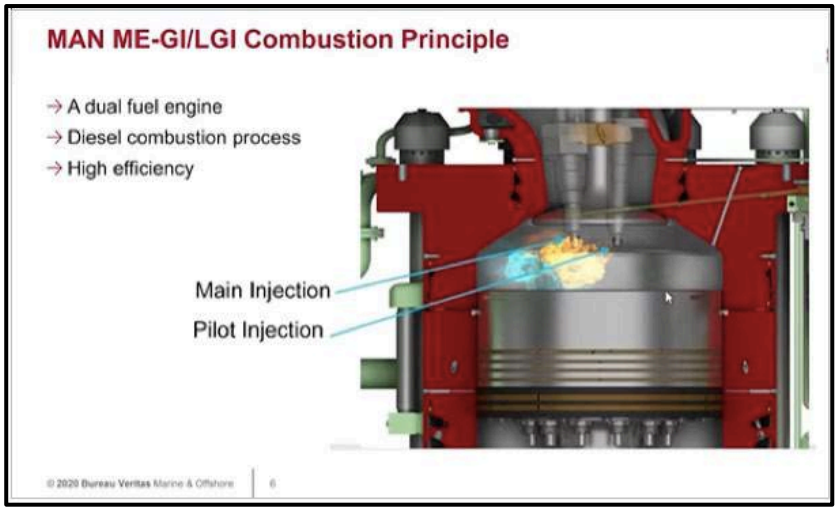

Fig 5. Testing of Ammonia as a fuel by MAN Energy Solutions on their LGI engine [6]

MAN is also looking to burn ammonia in their LGI engines. They have burned LPG and they currently plan to have an evolution of that engine with ammonia as a fuel. The company aims to offer retrofit conversions to allow existing two-stroke engines to use ammonia. [12]

7. Revolution in Manufacturing Process

Traditionally, ammonia is produced from natural gas through steam methane reforming (SMR) process, water-gas shift reaction, and the Haber–Bosch process. The process uses a carbon positive, fossil natural gas, which leads to 2.6 metric tons of life cycle greenhouse gas (GHG) emissions per metric ton of ammonia produced. Ammonia is currently the second most produced chemical in the world. Ammonia production accounts for approximately 2% of worldwide fossil energy use and generates over 420 million tons of CO_2 annually (about 1% of the world's CO_2). [15]

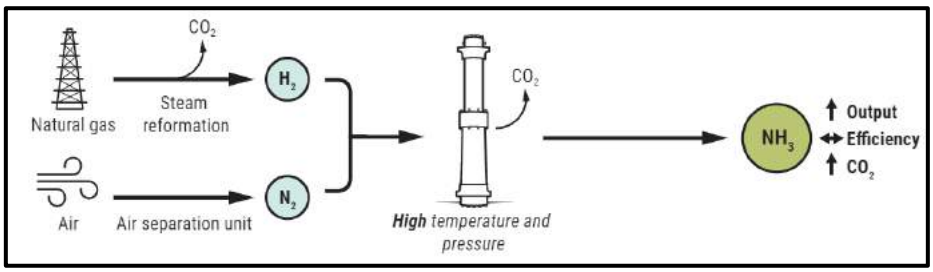

Fig 6. Century old process of manufacturing ammonia [14]

The Haber-Bosch process for the production of ammonia has led to the advent of the Green Revolution, however the process is anything but green. It requires a source of hydrogen gas (H2), which is taken from natural gas or coal in a reaction using pressurized, super-heated steam. Carbon dioxide (CO2) is left behind, accounting for about half the emissions from the overall process. In the second feedstock, N2, is easily separated from air, which is 78% nitrogen. But in order to generate the pressure needed to fuse hydrogen and nitrogen in the reactors, requires more fossil fuels to be burnt, which in turn means more CO2 production. The emissions add up and as a result Ammonia production, in its current form consumes about 2% of the world's energy and generates 1% of its CO2.

7.1. Production of Green Ammonia

The substitution of conventional carbon-based fuel by ammonia will be illogical, if the same production process was to be used to manufacture ammonia. In that case, we would just be taking away carbon dioxide emissions from the shipping industry and give it to the production stage. In this scenario, the emissions generated during the life cycle of the fuel will be the same. Thus, if we were even to think of Ammonia as an alternative to the conventional maritime fuels, there would be a requirement of revolutionizing its production process.

Figure 7, offers us a solution to the above-mentioned problem. Hydrogen which was earlier separated from natural gas at high temperatures and pressures, can now be, separated from water at the cathode during electrolysis. The

energy for electrolysis would come from renewable sources of energy. The proton (hydrogen ions), would pass through a proton-permeable membrane and combine with nitrogen ions at the cathode to form ammonia.

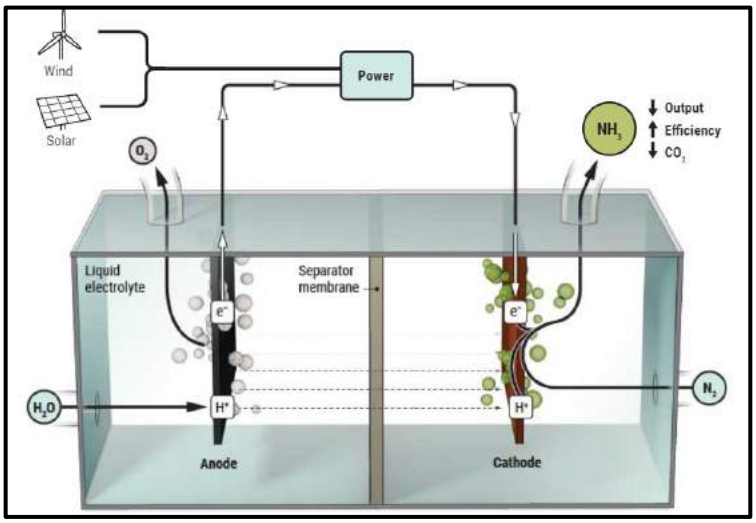

Fig 7. Formation of green ammonia by reverse fuel cell technology [14]

7.2. Commitments Made by Major Stakeholders Towards Green Ammonia

7.2.1 Yara

Leading fertilizer company Yara plans to electrify fully its ammonia plant in Porsgrunn, Norway with the potential to cut 800,000 tons of CO2 per year, equivalent to the emissions from 300,000 passenger cars. Production from the electrified ammonia unit would be some 500,000 tons per year of green ammonia. [16]

7.2.2 Australia

The initial stage of the H2U Eyre Peninsula Gateway Hydrogen Project, the world's largest green ammonia plant, has received a boost from the South Australian government. The project has an initial funding of AUD 240 million (USD173 million). The Australian Government has announced that it will allocate a further AUD37 million (USD26 million) to upgrade the nearby Port Bonython jetty as part of its plan to become an exporter of green energy to world markets.

The H2U plant will run completely on wind and solar power generated in the region to power the electrolyser to split water into hydrogen and oxygen gas. The H2U Eyre Peninsula Gateway Hydrogen Project will accommodate the installation of a 75MW electrolyser near the regional city of Whyalla, capable of producing enough hydrogen to create 40,000 tons of ammonia each year.

The plant will also feature two 16 MW open cycle gas turbines operating 100% on hydrogen at the site to act as a substitute and provide electricity generation to the grid during periods of low wind or solar output. [17]

7.3 India's Vision Towards Production of Green Ammonia

The Indian Prime Minister in his speech at the UNGA 2021, made a commitment of making Indian carbon-neutral by 2070 and cutting India's fuel imports by 2046. This can be done by shifting India's energy requirements to renewable resources. The Indian PM envisions India to emerge as a global hub for Green Hydrogen in the upcoming decade. India is currently among the handful countries that have announced their national plan for hydrogen under the National Hydrogen Mission. The pace at which the national plan is being implemented, it is possible that India will meet its hydrogen targets before the committed time.

The Indian government plans to invite bids for setting up green ammonia projects within six months to reduce import dependence. This initiative is helmed by Union power and new and renewable energy minister Raj Kumar Singh. This move assumes significance given India imports substantive volumes of ammonia each year to produce fertilizers. However, this may achieve some backlash from some political parties owing to the fact that India has only in recent times achieved 100% electrification of all its villages. Another impactful argument would be that this renewable energy could be put to a much better use if it were to power the rural households. Hopefully, we

will be one of the earliest nations to transition to green hydrogen and green ammonia and set up a pathway and roadmap for transition. [18]

8. Life Cycle Assessment (LCA) of Green Ammonia

A true adoption of Green Ammonia as a fuel to replace conventional fuels can only be considered after considering the life cycle analysis of Green Ammonia. An LCA is a cradle-to-grave analysis approach that helps evaluate the environmental impact of a product or process over its entire life, beginning from raw material extraction and extending to final disposal. It considers all life stages of the product or process in order to assess the overall environmental impact. Sometimes an LCA is performed to evaluate the impact of alternative products, but it also can identify areas of major concerns and help to improve processes. LCAs evolved from a method used in the 1960s to reduce the use of raw materials and energy. [18]

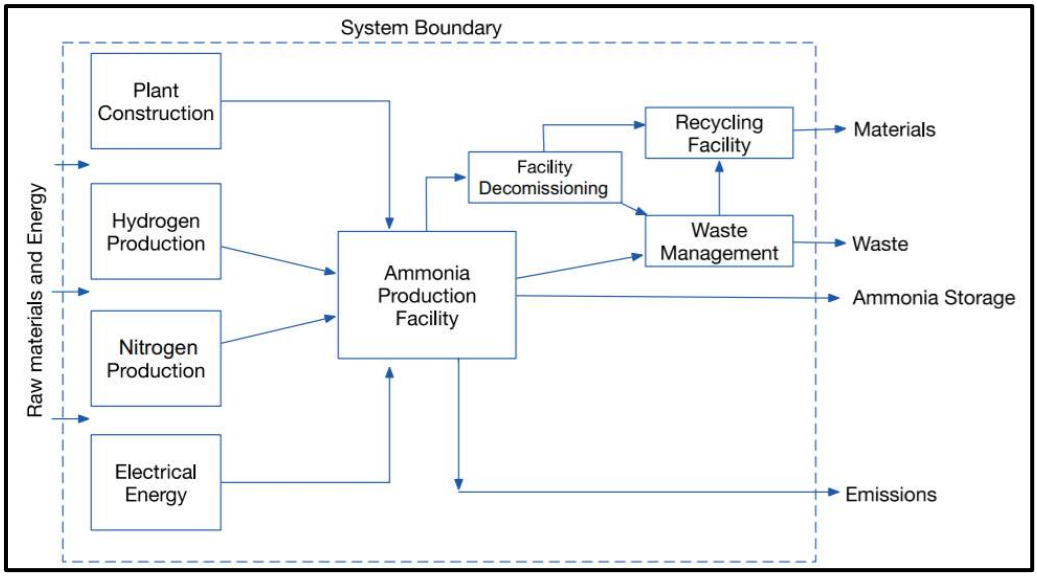

Fig 8. Parameters Considered for LCA of Green Ammonia

As observed in Fig. 8, the LCA includes various paramters such as

- Resources used for the plant construction,
- Emissions caused during the mining of raw materials and its environmental impact,
- Energy demand to keep the ammonia production facility running,
- Estimation of the resources used in decommissioning of the facility,
- Waste produced from the facility and its environmental impact,
- Energy spend on neutralising the waste
- Energy spent in storing ammonia,
- Emissions caused during production (almost zero for green hydrogen)

8.1. Green Ammonia Production and Their Stages

At present there are various forms of harnessing ammonia. Some of them include:

- ***Steam Methane Reforming***: Most efficient and cost-effective process. Adverse impact on environment, uses fossil fuel as feedstock
- ***Underground Coal Gasification:*** Second most commonly used process for hydrogen production.
- ***Biomass Gasification:*** This process provides a reliable and practical alternative and uses one of the fastest-growing renewable technologies
- ***Solar PV-Based Electrolysis:*** Uses photo-voltaic cells to generate electricity and carry out dissociation of water into Hydrogen and Oxygen.
- ***Wind Energy-Based Electrolysis:*** Uses wind turbine to generate electricity and carry out dissociation of water into Hydrogen and Oxygen.

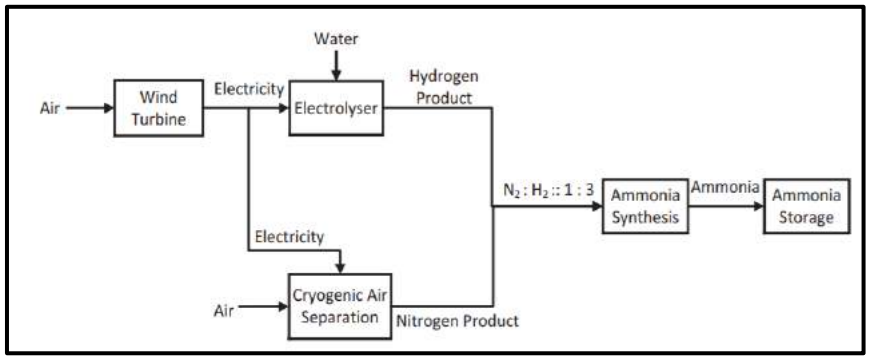

Figure 9. Green Ammonia Production from Wind Turbine

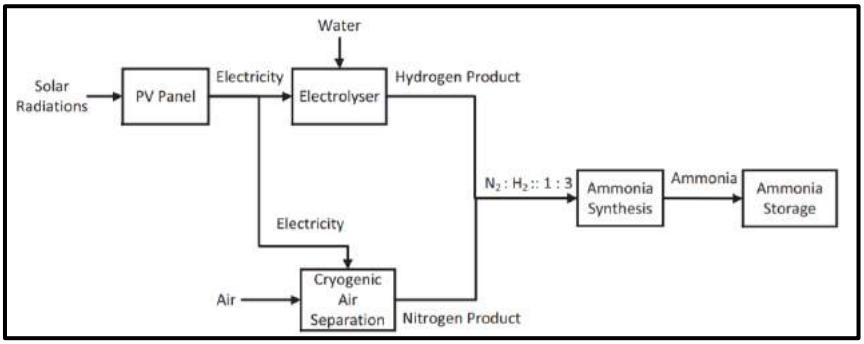

Figure 10. Green Ammonia Production from Photo-Voltaic Cells

Solar PV and Wind Turbine along with other renewable resources are accepted as a practical alternative to fossil fuel based distributed energy systems. Although renewable resources are considered to be environmentally friendly, it may have a large environmental impact owing to panel production and battery use of PV cells and manufacturing of wind turbines. Thus, a Life Cycle Assessment should be carried out to assess the actual environmental impact of the above "green technologies".

The energy demand to produce hydrogen by electrolysis is too high. An approximate 53kWh units of energy are required to produce 1kg of Hydrogen. [20] When compared to production from methane, 0.3138 kWh units are required to produce 1 kg of hydrogen.

Thus, it can be seen that production of ammonia from renewable sources, is a huge energy-demanding process. To meet this energy requirements, the industrial facilities and production would need to be ramped up, leading to perhaps an increased emission, rather than curbing it.

8.2. Impact Categories

Impact Category	Ammonia From Methane	Ammonia From Photovoltaics	Ammonia From Wind	Ammonia From Biomass Downdraft Gasifier
Abiotic depletion (kg Sb-eq)	0.02649	0.00854	0.00340	0.00263
Acidification (kg SO_2-eq)	0.00362	0.00581	0.00220	0.00170
Eutrophication (kg PO_4-eq)	0.00133	0.00376	0.00144	0.00118
Global warming (kg CO_2-eq)	3.03226	1.27745	0.49566	0.37842
Human toxicity (kg 1,4-DB-eq)	0.13893	1.36673	0.59822	0.06318
Freshwater aquatic eco-toxicity (kg 1,4-DB-eq)	0.19229	0.75365	0.31404	0.18374

DB, *dichlorobenzene.*

Table 1. Summary of Category-wise Impact Values for Different Ammonia Production Methods Using CML 2001[21]

The need to have an evaluation tool for the LCA of various production process was found and many methods were devised. Out of them, the data found using CML 2001 will be considered in this paper.

After analyzing data from Table 1, it was found that ammonia production from methane had the greatest global warming potential, highest abiotic depletion due to the extraction process of methane and highest eutrophication potential in which large amount of macro-nutrients are released into the soil.

However, when one looks at the acidification, human toxicity and fresh-water toxicity impact caused by the production of Green Ammonia from PV cells, it is the highest among the peers. This can be credited to the fact that manufacture of PV cells and batteries uses extremely hazardous substances. The low efficiency of PV requires a large number of cells and a large area of use to produce substantial amounts of electrical energy. On the other hand, production of green ammonia by wind energy is the best alternative as it bypasses all the evils of PV cells.

9. Conclusion

The marine industry is cornered and bombarded with regulations from IMO, which in turn wants to bring about revolutionary changes to counter climate changes. It is said that adversity is the mother of all innovations, thus it is now the time to think outside the box or rather expand the box to accommodate the alternative fuels. The fuel is still in its initial stages of testing, with various players testing the fuel capabilities of ammonia in various kinds of engines. Ammonia can be also used as an energy source from fuel cells with the combination of nitrogen and hydrogen release energy which can be used to run a motor. After considering the LCA of green ammonia using PV cells, it was found that the R&D sector of PV cells also need a major boost, as alternatives for the harmful chemical substances used in manufacturing of PV cells is the need of the hour. It is still not a proven technology and is still in its initial stage of testing but since we are backed into a corner, ammonia deserves to be given a shot.

Acknowledgments

This paper would not have been possible without the support of my parents and the guidance offered by my teachers at Tolani Maritime Institute. I would further like to thank two more people, Chief Engineer Pravin Marathe Sir, who accepted me into his workshop 'Torque Techniques' for the duration of 6 months and gave me the pre-requisite knowledge which was required to make this paper possible. Secondly, I would like to thank Chief Engineer Ashish Kumar Sir, Professor at Tolani Maritime Institute, for clearing all my doubts and never dismissing any question as stupid. Lastly, would like thank to Aparajitha Nair for proof reading the paper.

References:

1. Reducing greenhouse gas emissions from ships, International Maritime Organization https://www.imo.org/en/MediaCentre/HotTopics/Pages/Reducing-greenhouse-gas-emissions-from-ships.aspx#:~:text=The%20initial%20GHG%20strategy%20envisages,that%20total%20annual%20GHG%20emissions last assessed on 29/11/2020
2. List of countries that restrict the use of open loop scrubbers, Safety 4 Sea, EMISSIONS | 28/09/20 https://safety4sea.com/list-of-countries-that-restrict-the-use-of-open-loop-scrubbers/ last assessed on 29/11/2020
3. Alexander Karavaytsev and Boris Turkin Article No. 51 , Assessing the impact of IMO 2020 on grains and oilseeds freight costs, [UNCTAD Transport and Trade Facilitation Newsletter N°86 - Second Quarter 2020] https://unctad.org/news/assessing-impact-imo-2020-grains-and-oilseeds-freight-costs#:~:text=Higher%20fuel%20costs%20as%20at%201%20January%E2%80%A6&text=Based%20on%20the%20analysis%2C%20the,around%20US%2430%20per%20ton last assessed on 29/10/2020
4. Britt Russell-Webster, S&B Global, Low bunker fuel prices bittersweet for shipowners as global trade volumes fall, https://www.spglobal.com/platts/en/market-insights/blogs/shipping/052120-low-bunker-fuel-prices-bittersweet-for-shipowners-as-global-trade-volumes-fall last assessed on 29/11/2020
5. Theoretical performance of liquid ammonia and liquid fluorine as a rocket propellant, NTRS - NASA Technical Reports Server https://ntrs.nasa.gov/citations/19930087555 last assessed on 29/11/2020
6. The case of ammonia as a marine fuel, KOKARAKIS JOHN | OPINIONS | 09/04/20 https://safety4sea.com/cm-the-case-of-ammonia-as-a-marine-fuel/ last assessed on 29/11/2020
7. Lower and Upper Explosive Limits for Flammable Gases and Vapors, Goal Zero, Safety http://www.wermac.org/safety/safety_what_is_lel_and_uel.html (last assessed on 29/11/2020)
8. Adrienne Murray, The foul-smelling fuel that could power big ships, Technology of Business reporter, Denmark, Published on 6 November 2020 https://www.bbc.com/news/business-54511743 , last assessed on 29/11/2020
9. New Catalyst Turns Ammonia Into An Innovative Clean Fuel,ScienceBlog.com,

https://scienceblog.com/500593/new-catalyst-turns-ammonia-into-an-innovative-clean-fuel/ last assessed on 30/11/2020
10. Catalytic Converters, Catalytic Converters - SCR System, Meca http://www.meca.org/technology/technology-details?id=5&name=Catalytic%20Converters#:~:text=In%20the%20presence%20of%20the,decreases%20in%20CO%20and%20HC Last assessed on 30/11/2020
11. World's first full scale ammonia engine test - an important step towards carbon free shipping, Wärtsilä Corporation, Trade press release 30 June 2020 https://www.wartsila.com/media/news/30-06-2020-world-s-first-full-scale-ammonia-engine-test---an-important-step-towards-carbon-free-shipping-2737809 , last assessed on 30/11/2020
12. Marine Sector Turns to Ammonia to Decarbonize Shipping, JASON DEIGN MAY 21, 2020 https://www.greentechmedia.com/articles/read/marine-sector-looks-to-ammonia-to-decarbonize-shipping last assessed on 22/11/2020
13. MAN Energy Solutions to Lead Danish Consortium Developing Ammonia-Fuelled Engine for Maritime Sector, MAN Energy Solutions SE https://man-es.com/docs/default-source/press-releases-new/20201021_man_es_pr-aengine-mes_en.pdf last assessed on 30/11/2020
14. Robert F. Service Ammonia—a renewable fuel made from sun, air, and water—could power the globe without carbon, Jul. 12, 2018 https://www.sciencemag.org/news/2018/07/ammonia-renewable-fuel-made-sun-air-and-water-could-power-globe-without-carbon/
15. Xinyu Liu, Amgad Elgowainya and Michael Wanga , Life cycle energy use and greenhouse gas emissions of ammonia production from renewable resources and industrial by-products https://pubs.rsc.org/en/content/articlelanding/2020/gc/d0gc02301a#!divAbstract/
16. Yara planning 500,000 ton/year green ammonia project in Norway, Green Car Congress, https://www.greencarcongress.com/2020/12/20201220-yara.html
17. F&L Asia, World's largest green ammonia plant in South Australia gets boost, November 6, 2020, https://www.fuelsandlubes.com/worlds-largest-green-ammonia-plant-in-south-australia-gets-boost/
18. Utpal Bhaskar, Govt will invite bids for green ammonia projects in 6 months, Updated: 15 Dec 2020, 08:40 AM IST https://www.livemint.com/news/india/-govt-will-invite-bids-for-green-ammonia-projects-in-6-months-11608001104873.html/
19. Curran MA. Life cycle assessment: principles and practice. Report EPA/600/R-06/060. Reston (VA): Scientific Applications International Corporation (SAIC); 2006
20. Spath PL, Mann MK. Life cycle assessment of renewable Hydrogen Production via wind/electrolysis milestone completion report (Vol. NREL/MP-560e35404). Golden (Colorado): National Renewable Energy Laboratory; 2004
21. Vishavdeep Singh, Ibrahim Dincer, Marc A. Rosen; LIFE CYCLE ASSESSMENT OF AMMONIA PRODUCTION METHODS

ROADMAP FOR SUSTAINABLE FUELING OPTIONS IN THE MARITIME SECTOR

Sebastian Franz[1,*], Nicolas Campion[1], Sara Shapiro-Bengtsen[1], Marie Münster[1]

Affiliation:
[1] *Technical University of Denmark, Energy Economics and System Analysis*
[*] *Corresponding Author: semfr@dtu.dk*

ABSTRACT

The maritime industry is at a crossway. Decarbonization of this sector is an essential part of efforts towards climate change mitigation. Especially the long-distance operations are challenging to decarbonize as electrification is not an option there. Therefore, more and more alternative fuels are being considered to decarbonize the shipping industry. There are options such as PtX, biofuels, blue fuel (ammonia), and electro fuels. However, the choice of the fuel for the future requires an in-depth analysis of different costs, sustainability factors, and biomass availability.
This study answers the question of the least cost fueling option given restrictions in greenhouse gas emissions (GHG) and biomass availability.
We use an open-source linear least-cost optimization model, which utilizes data on biomass availability, shipping demand, vessel expenditure, and fuel price to propose fuel transition roadmaps for the maritime industry. The necessary input data are from the MarE-Fuel project and literature. The future fuel mix will be analyzed, including sustainable maritime fuels, which are essential to decarbonize the maritime industry in the long term. The considered fueling options in this model are electrofuels (methanol and ammonia), biofuels (Refined Pyrolysis Oil, LBG), e-biofuel (Bio-emethanol), blue fuel, lower emission fossil fuels (LNG and VLSFO), and classical fossil fuels (HFO). The potential of these new fuels will be critically assessed by including the GHG emissions of the production process of these fuels. This work aims to identify the main issues the industry is facing at present up until 2050 and provides an outlook on challenges and opportunities towards climate mitigation that the maritime industry might be developing in the future.
We find a diversified picture of a decarbonized maritime future. The future fuel mix is expected to be highly dependent on advancing technologies, ramping up fuel-production facilities, biomass availability, and safety advancements. In an ambitious GHG-emission reduction scenario with high biomass availability, one can see a gap between expected fuel demand and feasible fuel supply given the GHG-emission reduction constraints already from 2028 onwards. In a low biomass availability case, this feasibility gap is even more significant. Given the efforts towards NetZero by 2050, this presents enormous challenges for the decarbonization of the maritime industry at present and for the following years to come.

KEY WORDS

Decarbonization, Energy Economics, Maritime Industry, Market-based Measures, Net-Zero-by-2050

INTRODUCTION

The maritime industry is at a crossway. Decarbonization of this sector is an essential part of efforts towards climate change mitigation. Especially the long-distance operations are challenging to decarbonize as electrification is not an option there. Therefore, more and more alternative fuels are being considered to decarbonize the shipping industry. There are options such as Power-to-X (PtX), biofuels, blue fuel (ammonia), and electro fuels(ammonia and methanol). However, the choice of the fuel for the future requires an in-depth analysis of different costs, sustainability factors, and biomass availability. So far, the use of Low-Carbon-Fuels (LCFs) is minimal due to its expensive production cost. Thus, there must be some Market-based measures (MBM) in place that incentivize the use and expansion of LCFs to bring international shipping on the emission reduction pathway, in line with 1.5 ºC (no or low Overshoot (OS)) scenario. The question of the transformational potential of MBMs remains unanswered, as the overall challenges towards climate mitigation in relation to all emissions along the supply chain are not completely clear yet.

Therefore, in this study, we show the challenges towards climate mitigation to get onto an emission reduction pathway in line with 1.5 ºC (Huppmann et al. 2019) (no or low OS). We apply the open-source least-cost optimization model, SEAMAPS, to calculate the future fueling mix in the maritime industry under certain constraints. Our analysis is based on well-to-wake (WTW) emissions, including emissions from the consumption of electricity from the grid and upstream emissions from the construction of plants. In addition, assumptions were made about the speed of ramping up of production facilities.

The novelty of this modeling approach lies in the lifecycle assessment (LCA) perspective and the bottom-up modeling of LCFs production in combination with feasibility constraints in a least-cost optimization framework. Thus, the model can capture the main dynamics between fossil fuels and LCFs to reveal challenges towards climate mitigation in the maritime industry.

METHODS

The SEAPMAPS model used in this study is an open-source optimization model available under: https://github.com/SebastianFra/SEAMAPS

It uses input data previously derived in the MarE-Fuel project (Franz et al. 2021; Campion et al. 2021; Nami et al. 2021; Copenhagen Economics 2021; Sørensen and Laursen 2021). The relevant boundary conditions, assumptions, variables, and parameters are shown in Figure 1. Once all the required input data has been derived and put into a suitable form, the SEAMAPS starts the optimization process. A cost optimization function is used as the objective function.

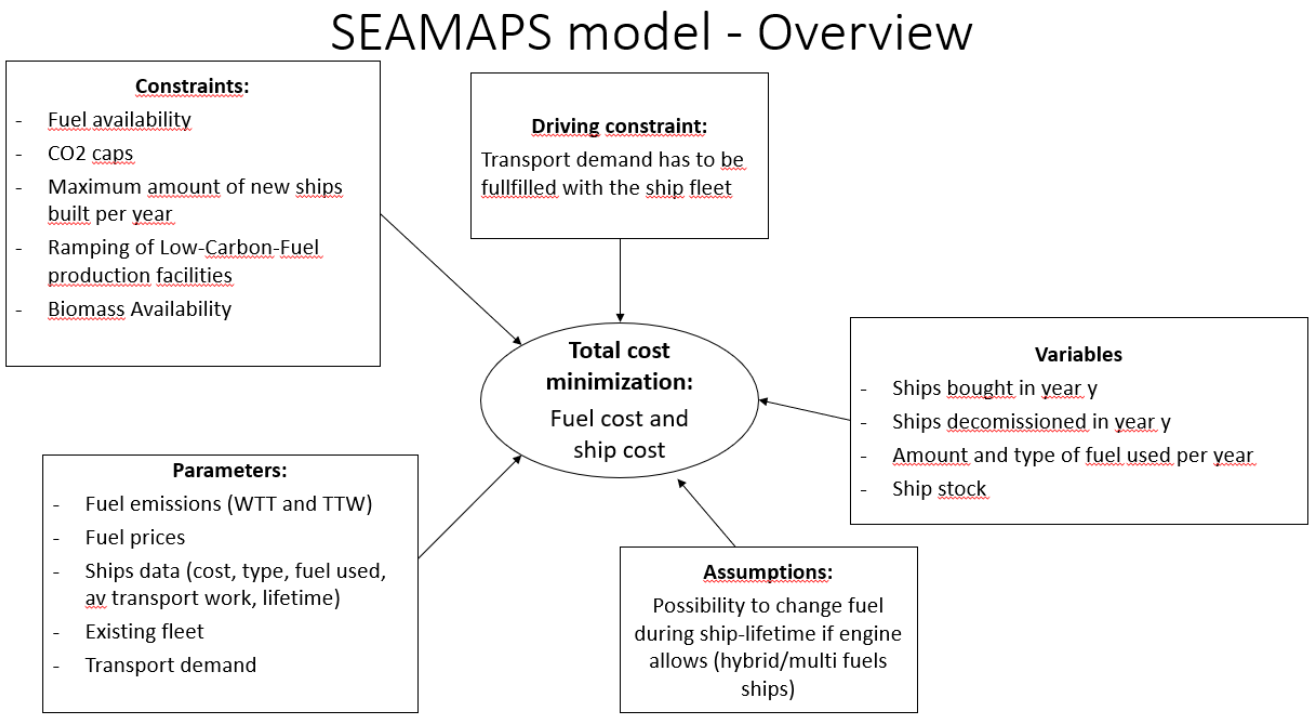

Figure 1: Overview of the Modeling Environment of SEAMAPS

The overall objective is to find the most cost-effective fueling options for the maritime industry. To achieve this, the objective function, which is a cost function, is minimized. The components of the objective function can be divided into two main parts. One part concerns all costs related to the fleet itself, including the investment costs for new vessels and the operation and maintenance costs for the entire fleet. To avoid decommissioning the existing fleet at zero cost, taking an existing vessel out of service before the end of its service life costs half of the original investment. The second cost is limited to fuel costs. The

consumption of each vessel in the fleet is multiplied by the fuel cost (including any fuel taxes). The objective function looks as follows:

$$min_{x,q,z,d^{EF}} \sum_{s,y} SI_s * NewBuildShip_{s,y} + SOM_s * ShipStock_{s,y} + SI_s * Decom_{val} * Decomissioned_{s,y}^{EF} + \sum_{s,f,y} FuelUsed_{f,s,y} * (FC_{f,y} + FT_{f,y}) \quad [1]$$

Where SI_s is the investment expenditure for a new build (average) vessel of type s, SOM_s is the operation and maintenance cost for vessel of type s, $Decom_{val}$ is the decommission value factor for discarding an existing ship (equal to 0.5), $Decomissioned_{s,y}^{EF}$ is the amount of decommissioned ships in y, $FC_{f,y}$ is the fuel cost per fuel type and year, $FT_{f,y}$ is the fuel tax added on top of fuel cost (fuel tax is zero in the base case). $NewBuildShip_{s,y}$ is a variable representing the number of new ships of type s bought in year y. $ShipStock_{s,y}$ is a variable representing the total ship stock of ship of type s at year y (variable). $FuelUsed_{f,s,y}$ is a variable representing the amount of fuel bought per fuel type, ship type and year.

Transport demand

This constraint limits the annual supply in the model scheduled to the IMO exogenous demand forecasts(IMO 2021). This ensures that supply and demand match and that there is no excess demand or supply in the model that could bias the results. It is important to note that IMO demand has a strong influence on the future fuel mix results. This variable may need to be replaced with endogenous demand projections to create a more inherent modeling process. For more details, see (Franz et al. 2021).

Ship stock

This constraint ensures the management of the entire fleet(IMO 2021) used in the model for the ship stock. It states that the vessel stock (number of vessels in the world fleet) is equal to the vessel stock in the previous year plus the newly purchased vessels in the current year minus the "retired vessels" in the current year whose service life has expired minus the decommissioned vessels in the current year. Year 1 vessel inventory includes the existing fleet. For more details, see (Franz et al. 2021).

Ship capacity production

The amount of bought ships of type s in year y cannot exceed the industry ship production capacity(Sørensen and Laursen 2021). The production capacity of ship s in year y is 0 when the engine is not available commercially yet. For more details, see (Franz et al. 2021).

Fuel consumption

The amount of fuel used by ships of type s in year y must be enough to satisfy the transport demand(IMO 2021). The transport demand of the fleet of the ship of type s is equal to the ship stock of that type (the number of ships of type s in the fleet) multiplied by the average transport work. The fuel consumption is calculated using the specific fuel consumption per fuel type and ship. Any fuel can be used to satisfy the demand, meaning that more than one fuel type can be used in the same year if the engine is a dual/multi-fuel engine. For more details, see (Franz et al. 2021).

Fuel availability

For all fuels and all years, the amount of fuel used for the whole shipping fleet cannot exceed the fuel available. This fuel availability is highly dependent on biomass availability for biomass-based fuels. In this study, we show a high and low biomass availability scenario. For more details, see (Franz et al. 2021).

CO2e emissions cap

With this constraint, a global CO_2 emissions cap have to be respected every year. To make the model able to solve, this constraint can be broken at a very high cost. In this study, we used Well-To-Wake(Comer and Osipova 2021) (WTW) fuel emissions including emissions related to electricity purchased from the grid and to building infrastructure and plants. The emissions associated with purchasing electricity from the grid follows the IEA Net Zero in 2050 scenario. As an initial starting value for the global cap, we used data from(Mærsk Mc-Kinney Møller Center for Zero Carbon Shipping 2021). For more details, see (Franz et al. 2021)

Ramping of Production Facilities

With this constraint, the uptake of LCFs is limited. This refers to both yearly uptakes of specific fuels and the global availability of LCFs. In our baseline scenario, we used data from (Energy Agency 2021), say LCF can serve only 81% of global maritime demand in 2050.

RESULTS

Our results show significant feasibility problems with fulfilling our exogenous SSP1-type(van Vuuren et al. 2011; Riahi et al. 2017) demand with the existing fueling options and the availability constraint regarding LCFs. In Figure 2, we can see the future maritime fuel supply mix given the above-described constraints for a high and low biomass availability scenario (for more details, see(Franz et al. 2021)) with a grid-connected electro-fuel production setup (with own production from wind and solar power and the possibility to also use electricity from the grid (around 20% on average)). In the short term, one can see that the global fleet will be fueled by fossil fuels such as VLSFO/HFOsc, LNG, and MDO. From 2030 onwards, we see LCFs such as NH3-blue, NH3-green, Refined-Pyrolysis Oil, and MeOH-ebio coming into the fuel mix. This is due to the strict global GHG emission cap needed to be in line with an emission reduction goal of a 1.5 ºC (no or low OS) scenario.

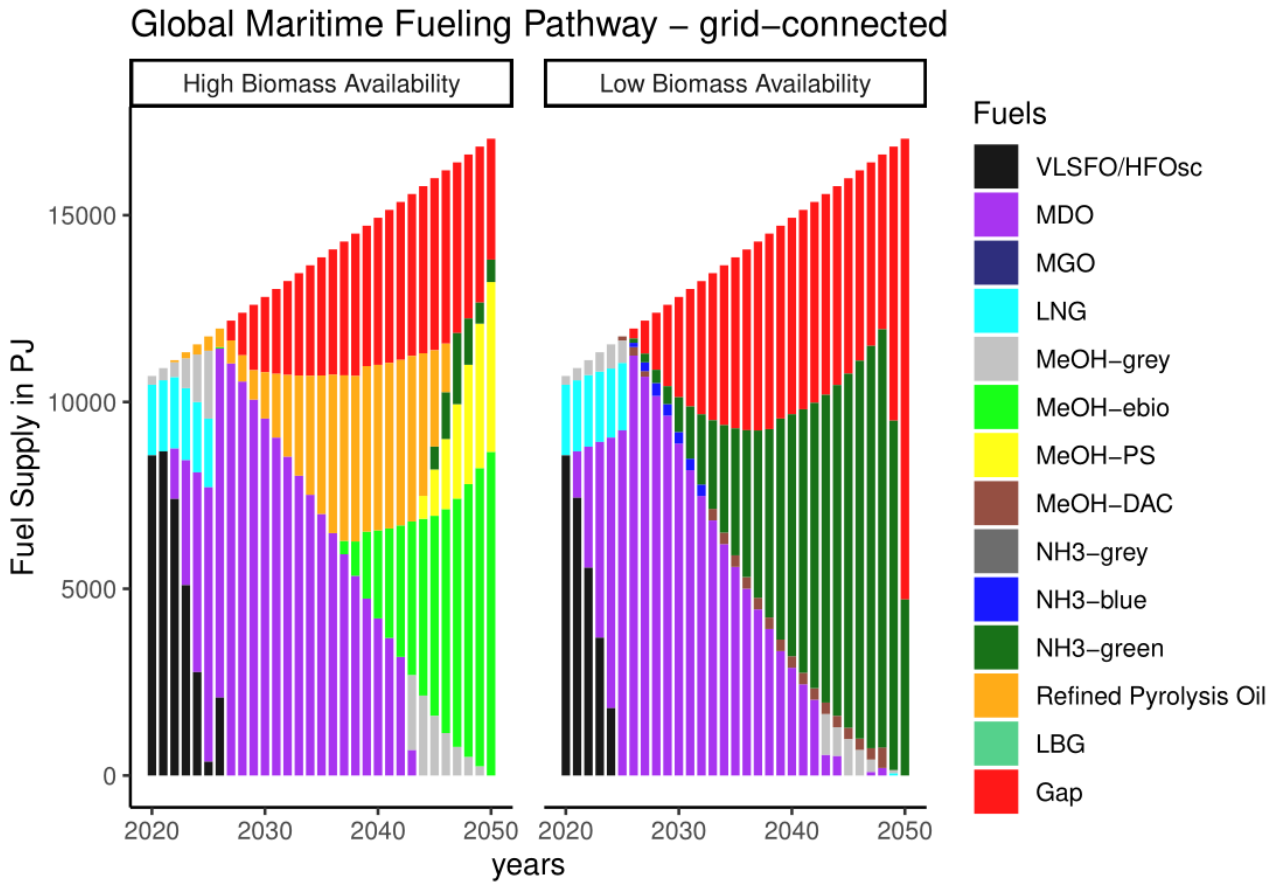

Figure 2: Global Future Maritime Fuel Mix -High Biomass Availability & Low Biomass Availability

Unfortunately, the available LCFs are not enough to fulfill the exogenous demand with the existing fueling options. That is why the model chooses the red fictive fuel "Gap" in both biomass availability scenarios. This "Gap" fuel is characterized by zero-emission and extremely high costs and thus illustrates the only option to fulfill the exogenous demand level constraint at an extremely high cost.

The main difference between the high and low biomass availability cases is the type of LCFs used. In the low biomass availability case, the model uses green ammonia as the primary fuel for the maritime industry. However, in the high biomass availability case, the model uses both Refined-Pyrolysis Oil and MeOH-ebio and methanol using point source biogenic CO_2 (MeOH-PS) as the primary future fuels. Furthermore, the "Gap" fuel usage is higher in the Low Biomass Availability case, illustrating more significant challenges towards climate mitigation in the Low Biomass Availability case (apart from challenges regarding the use of NH3-green due to toxicity and operational problems(Duijm, Markert, and Paulsen 2005)).

When looking at Emission profiles in Figure 2, one can see the transformational potential needed to bring the maritime sector onto emission reduction pathway in line with a 1.5 ºC (no or low OS) scenario.

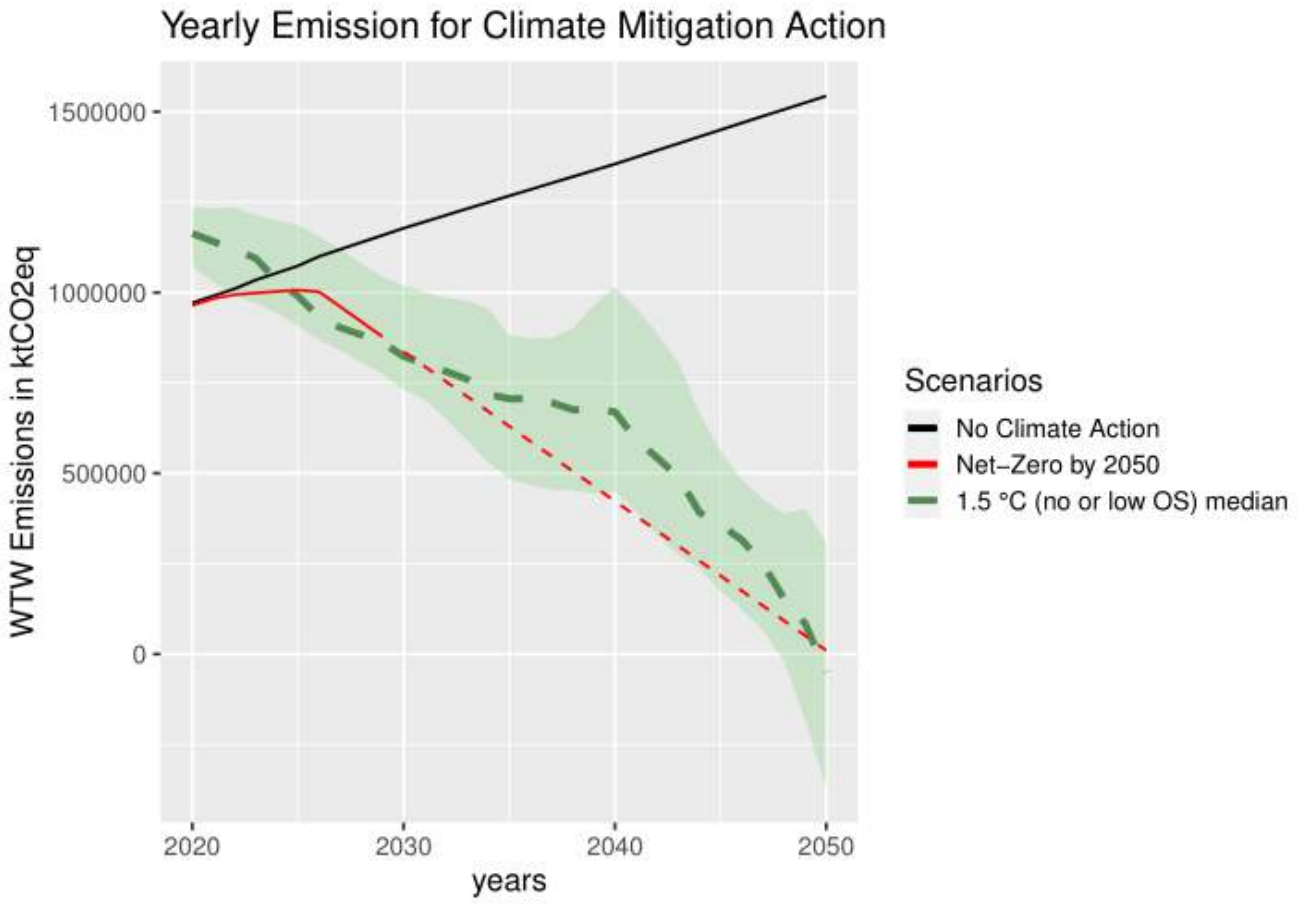

Figure 3: Emission profiles of different climate action efforts

In Figure 3, we show the theoretical WTW + infrastructure emission profiles for a necessary decarbonization pathway to be in line with 1.5 ºC (no or low OS) as well as for a no climate action at all scenario ("No Climate Action"). Furthermore, we show the median, 25^{th,} and 75th quantile of all 1.5 ºC (no or low OS) scenarios provided by (Huppmann et al. 2019) and scaled down to the maritime sector with the WTW emissions from (Mærsk Mc-Kinney Møller Center for Zero Carbon Shipping 2021). One can see that in theory, we can not be within an emission reduction pathway of 1.5 ºC (no or low OS). As the red dashed line indicates, this is not possible due to feasibility problems(see Figure 1 – usage of fictive "Gap" fuel.). In other words: Already from 2028 onwards, the by then-existing fueling options are not sufficient to fulfill the exogenous (SSP1-type(van Vuuren et al. 2011; Riahi et al. 2017)) demand and remain on a 1.5 ºC (no or low OS) emission profile if the e-fuels are not using electricity with zero emissions. This illustrates the enormous transformational potential needed to overcome this feasibility gap in the years to come to decarbonize the maritime industry from an entire lifecycle perspective effectively. IMOs 50% reductions target by 2050 (International Maritime Organization 2018) seems more realistic but not sufficient to stay within Paris Agreement pledges. Thus there is an urgent need to formulate more ambitious reduction targets within the maritime industry to fulfill Paris Agreement pledges.

DISCUSSION & CONCLUSION

As our results show, it is impossible to meet the requirements necessary to lead the maritime sector onto an emission reduction pathway in line with a 1.5 ºC (no or low OS) scenario. This is mainly because of the constraint regarding the availability of LCFs in the future. Therefore, it is essential to significantly lower challenges towards climate mitigation within the maritime industry to massively invest in new fuel production facilities and renewable electricity. This massive ramping of LCFs production would contribute to a cleaner naval sector.

Another technological challenge arises when looking at the availability of biomass. For a low biomass availability case and thus a high usage of green ammonia (see Figure 2), there are safety issues(Duijm, Markert, and Paulsen 2005; Mærsk Mc-Kinney Møller Center for Zero Carbon Shipping 2021) regarding toxicity for humans and marine life and operational feasibility challenges, which have to be solved before usage. On the other hand, a high biomass availability case seems unlikely since other industries (e.g., aviation, petrochemicals) also demand massive ammounts of biomass.

Furthermore, technological progress alone may not be the only option to lower mitigation challenges. Reducing fuel consumption in general, be it with a change in consumers behavior, to ultimately consume less, or the ban of fuel-intensive logistic routines (e.g., "SFTW" – "Steam Fast then Wait" concept") could save a significant amount of GHG

emissions(Zografakis 2021; Jia et al. 2017) and thus make it easier for technological progress to lead the maritime sector onto emission reduction pathway in line with a 1.5 ºC (no or low OS) scenario.

Future research could investigate different Market-Based Measures (MBMs) to incentivize the usage and expansion of LCFs effectively. An overview and comparison of stylized MBM-scenarios following different basic MBM-designs(Psaraftis, Zis, and Lagouvardou 2021) and their impact and transformational potential for a decarbonized maritime sector could be of great value. This analysis would enable us to analyze more realistic scenarios, and help us to build uniform expectations across all stakeholders towards necessary transformation (e.g., needed carbon price or ban of fossil fuels) for the industry to be not just theoretically but effectively decarbonized.

Finally, our analysis shows there are enormous challenges towards climate mitigation within the maritime industry. With technological solutions alone, we find that a decarbonized international shipping industry faces feasibility problems already from 2028 onwards. Therefore, lowering the overall challenges towards climate mitigation by reducing fuel consumption, either by cutting demand or improving efficiencies, is essential for the following years to come. With considerable efforts in technology, policy, and contractual design, a decarbonized maritime industry by 2050 could become a reality.

ACKNOWLEDGEMENTS

This paper is published as part of the MarE-Fuel project funded by the Danish Maritime Fund and the Lauritzen Fund as well as the DeMAR SOSD project funded by the Danish Orient Fund. We thank the partners of the projects for their cooperation and inspiration.

Campion, Nicolas, Martijn Backer, Phil Swisher, and Marie Münster. 2021. “MarE-Fuel: LCOE and Optimal Electricity Supply Strategies for P2X Plants.”
Comer, Brian, and Liudmila Osipova. 2021. “Accounting for Well-to-Wake Carbon Dioxide Equivalent Emissions in Maritime Transportation Climate Policies.”
Copenhagen Economics. 2021. “CO2-Taxes, Fuel Prices and Learning Rates.”
Duijm, Nijs Jan, Frank Markert, and ette Lundtang Paulsen. 2005. “Safety Assessment of Ammonia as a Transport Fuel.”
Energy Agency, International. 2021. “World Energy Outlook 2021.” www.iea.org/weo.
Franz, Sebastian, Nicolas Campion, Sara Shapiro-Bengtsen, Martijn Backer, and Marie Münster. 2021. “MarE-Fuel: ROADMAP for Sustainable Maritime Fuels.”
Huppmann, Daniel, Elmar Kriegler, Volker Krey, Riahi Keywan, Rogelj Joeri, Katherine Calvin, Florian Humpenoeder, et al. 2019. “IAMC 1.5°C Scenario Explorer and Data Hosted by IIASA.” August 8, 2019.
IMO. 2021. “Fourth IMO GHG Study 2020 Full Report.”
International Maritime Organization. 2018. “Initial IMO GHG Strategy.” 2018.
Jia, Haiying, Roar Adland, Vishnu Prakash, and Tristan Smith. 2017. “Energy Efficiency with the Application of Virtual Arrival Policy.” *Transportation Research Part D: Transport and Environment* 54 (July). https://doi.org/10.1016/j.trd.2017.04.037.
Mærsk Mc-Kinney Møller Center for Zero Carbon Shipping. 2021. “We Show the World It Is Possibe - Industry Transiton Strategy.”
Nami, Hossein, Giacomo Butera, Nicolas Campion, Henrik Lund Frandsen, and Peter Vang Hendriksen. 2021. “MarE-Fuel: Energy Efficiencies in Synthesising Green Fuels and Their Expected Cost.”
Psaraftis, Harilaos N., Thalis Zis, and Sotiria Lagouvardou. 2021. “A Comparative Evaluation of Market Based Measures for Shipping Decarbonization.” *Maritime Transport Research* 2: 100019. https://doi.org/10.1016/j.martra.2021.100019.
Riahi, Keywan, Detlef P. van Vuuren, Elmar Kriegler, Jae Edmonds, Brian C. O’Neill, Shinichiro Fujimori, Nico Bauer, et al. 2017. “The Shared Socioeconomic Pathways and Their Energy, Land Use, and Greenhouse Gas Emissions Implications: An Overview.” *Global Environmental Change* 42 (January): 153–68. https://doi.org/10.1016/j.gloenvcha.2016.05.009.
Sørensen, Thorben Anker, and Rene Laursen. 2021. “Total Cost of Ownership (TCO) - Sustainable Marine Fuels.”
Vuuren, Detlef P van, Elke Stehfest, Michel G J den Elzen, Tom Kram, Jasper van Vliet, Sebastiaan Deetman, Morna Isaac, et al. 2011. “RCP2. 6: Exploring the Possibility to Keep Global Mean Temperature Increase below 2 C.” *Climatic Change* 109 (1): 95–116.
Zografakis, Haris. 2021. “The Third Pillar: A Contractual Architecture for Maritime Decarbonisation.”

OPTIMAL ENERGY SYSTEM CONFIGURATION FOR ELECTRO-FUELS PRODUCTION IN DIFFERENT LOCATIONS

Nicolas Campion[1] , Philip R. Swisher[1] , Marie Münster[1]

ABSTRACT

Several stakeholders in the maritime sector have expressed their will to reduce the environmental impact of the shipping industry. The main driver of CO_2 emissions and local pollution is the type of fuel used in the propulsion engines, so "sustainable" fuels are often proposed as an alternative. Among alternative fuels, this study focuses on electro-fuels synthesized from hydrogen and carbon or hydrogen and nitrogen. The hydrogen is produced via water electrolysis with input electricity from solar PV, wind turbines, or the grid. This paper aims to identify which energy system configurations lead to the lowest electro-fuel production costs and where to focus on technology and cost improvements. The first electro-fuels that have been analyzed and reported here are methanol and ammonia. The fuel production system is modeled at the plant level using a mathematical model specifying the source of the electricity, the electrolysis unit, the CO_2 or N_2 sources, and the upgrading facility in the form of methanol or ammonia plant. Furthermore, potential supplementary technologies, such as intermediate storage (e.g., batteries or hydrogen tanks) and a desalination plant, are modeled. To determine optimal system operation and configuration, a least-cost optimization of installed capacities, mass fluxes, energy dispatching, storage management, and sale of by-products is performed. Input data includes state-of-the-art costs and technical constraints of the plant and peripheral systems and hourly wind, solar production profiles, and electricity market prices at specific locations. Results show that a connection to the grid reduces the system cost significantly compared to off-grid operation due to reduced storage and oversizing expenses. In the optimal solution, more than 50% of the electricity consumed comes from the grid, which makes the sustainability of the electro-fuel dependent on the specific grid energy mix. The location of the electro-fuel plant also plays a significant role in the fuel production cost. Here, an area with a large solar potential enables lower costs than an area with high wind potential if the fuel plant can also be connected to the electrical grid. The possibility to sell side products (heat, oxygen, or both) can determine the success of a fuel plant business model.

KEYWORDS

Ammonia; Methanol; Hydrogen; Flexibility; Wind; Solar; Grid

INTRODUCTION

The disastrous socio-environmental effects of anthropogenic Green House Gases (GHGs) emissions is already well documented (IPCC, 2014) and pushes governments and international organization to agree on emissions reduction goals. In the last decades, emissions reduction was mainly focused on the electricity generation sector, but decarbonization of other energy sectors such as transportation is still a major challenge. Electrification of long-range transport like shipping is challenged by the weight of batteries and the resulting loss of cargo capacity. Due to the limited availability of biomass, other energy carriers such as electro-fuels synthesized from renewable hydrogen produced via water electrolysis are often considered. However, the production cost is still very high, primarily due to the electricity cost and, to a lower extent, the CAPEX of the electrolyzer (McDonagh *et al.*, 2018). Many studies have been conducted to estimate electro-fuel production costs and identify key reduction potentials. Some focus on plant level techno-economics and they usually propose optimized process design to reduce the production cost but do not consider in detail the origin of power supply and plant integration within the surrounding energy system (Pérez-Fortes *et al.*, 2016; Hasan and Dincer, 2020; Zhang and Desideri, 2020). Other studies are made at the country level using large energy system models, including other energy sectors (heat, transport, chemicals) to identify cost reduction potential at the country system level (Blanco *et al.*, 2018; Ikäheimo *et al.*, 2018). This paper addresses an intermediate level

[1] Department of Technology, Management and Economics, Danmarks Tekniske Universitet, Copenhague, Denmark

between detailed process modeling and country-level analysis, focusing on integrating a single fuel plant in the surrounding energy system. This study aims to understand the dynamics of electro-fuel production at the plant level and identify cost reduction potentials regarding local power supply strategies and fuel plant sizing. The fuels considered are ammonia and methanol produced via CO_2 hydrogenation. Different representative weather profiles are tested, and the possibility of combining local renewable production and grid electricity is investigated.

METHOD

This section presents the method used to design the optimal electro-fuel plant depending on the production site. The study focuses on minimizing the fuel production cost in a current/near future context (2021-2025).

System Description

The study focuses on a localized fuel plant composed of a desalination plant, an alkaline electrolyzer, intermediate storage systems (hydrogen tanks or batteries), methanol or ammonia reactor, and carbon/nitrogen source. Three options are investigated for power supply: islanded (off-grid), fully connected (only using the grid), or semi-islanded (a mix of both). When grid electricity is used, it is purchased hourly at market price plus grid fees. If the electricity is produced off-grid, the fuel plant producer owns the local renewable facilities. In that case, only investment and operation costs are supported by the fuel plant. In the semi-islanded case, the fuel producer can choose when to use electricity from the grid or its own renewable production.

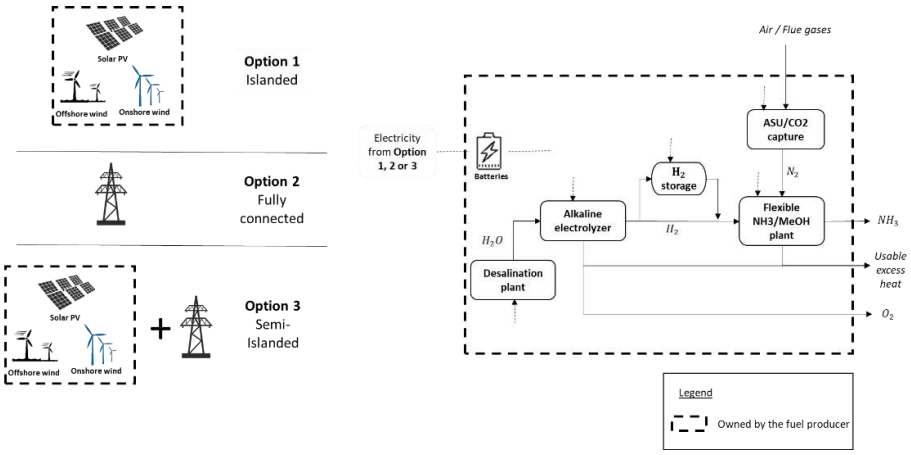

Figure 1: Fuel Production System Description

Three different sites with remarkable renewable potentials are tested. The first one is in North Chile and has a very high solar potential but poor wind. The second is in Denmark South West Cost with high wind potential but low solar resources. The third is in South Australia, with high wind and solar potential. The selected sites are near the sea, assuming that fuel producers prefer coastline for easy access to water and facilitated fuel transportation.

Table 1: Capacity factors year 2019 per site and per technology (%)*

	Site 1 (Solar +)	Site 2 (Wind +)	Site 3 (Solar/Wind)
Wind onshore	11.1	40.2	35.8
Wind offshore	10.2	43.6	33.5
Solar PV fixed	23.3	12.2	20
Solar PV 1 axis tracking	30.3	15.3	24.6

* See section INPUT DATA for detailed technology assumptions

Mathematical Modeling

The system is modeled using linear programming. Given the input data and system constraints, invested capacities and hourly operation of the plant are optimized minimizing the fuel production cost.

The objective function minimizes the total system cost by optimizing the hourly mass and energy fluxes of the different fuel plant components $F_{c,t}$ and the invested capacities IC_c:

$$Min_{F_{c,t},IC_c} \sum_{c,t}(\mathrm{Pr}_{c,t} + VOM_c)F_{c,t} + \sum_c(Inv_c * CRF_c + FOM_c)IC_c \quad [1]$$

$Pr_{c,t}$ is the hourly price of the output from component c at time t. The price is negative when the output product is sold to the market. FOM_c and VOM_c are respectively the fixed and variable operation and maintenance cost of the component c. $Inv_c * af_c$ is the CAPEX of component c times the Capital Recovery Factor, CRF, of component c. The discount rate used is 8%.

The driving constraint is the minimal amount of fuel that has to be produced per year, which is set to 2.5 TWh_{fuel} per year, representing 484 ktonnes of ammonia per year and 452 ktonnes of methanol per year. This production capacity is comparable to standard fossil methanol and ammonia plants in operation today (Burridge, 2009; Methanol Institute, 2021; Statista, 2021). Thus, the presented results give an idea of the infrastructure size needed to substitute a standard fossil plant with its "green" counterpart. Other constraints are related to the minimal/maximal load of the different components and mass/energy balances: power balance, heat balance, chemical reactions, and storage management.

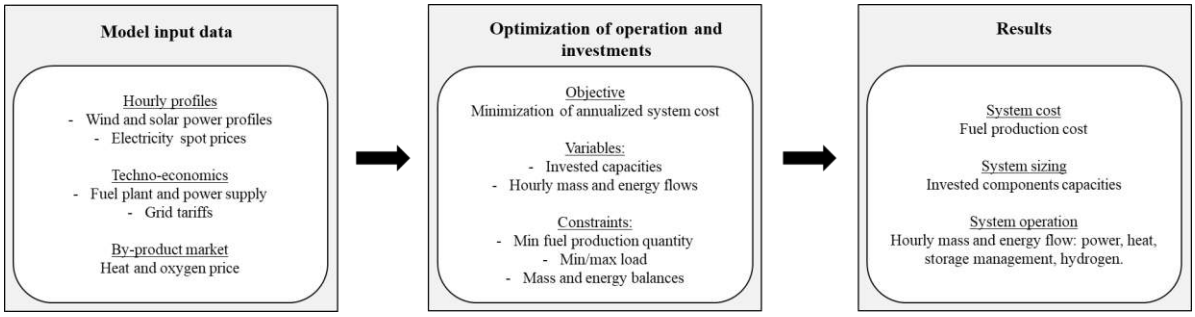

Figure 2: Graphical Description of the Method

INPUT DATA

Data fed into the optimization model are techno-economic features of the fuel plant components, hourly renewable power production, hourly electricity market prices (2019), and by-product selling price (heat/oxygen). Data are valid for the near-term future (2020-2025). The fuel plant is assumed to be closed for maintenance 10% of the year (in summer). Techno-economic input data used in the model are summarized in Tables 2 and 3.

Fuel Plant Components

Desalination Plant

To simplify the comparison between the 3 sites, the desalination plant is always used, disregarding the local freshwater availability. The technology used is a reverse osmosis plant. We assume that the purity of desalted water is sufficient to be used in the alkaline electrolyzer. The plant CAPEX is 1128.5 $€_{2019}$/(m³ of desalinated water/day), m³ /day being the capacity of the desalination plant. The operation cost (without electricity) is 0.27 $€_{2019}$/m³ of desalinated water. Electricity consumed is 4 kWhe/m³ of purified water (Kettani and Bandelier, 2020). Water requirements are driven by the electrolysis reaction, which consumes 1.35 L/Nm³ of hydrogen, so 15 kg_{H2}/kg_{H2O} (Bellotti *et al.*, 2017). Water consumption includes losses and auxiliaries consumption.

Alkaline Electrolyzer

Due to its limited cost, large-scale development potential, and high Technology Readiness Level (TRL), the type of electrolyzer selected for this study is an alkaline electrolyzer (AEC). IEA (2019) stated that current AEC electrolyzer efficiency lies between 63 and 70% LHV. For this study, we considered an efficiency of 66% including utilities representing an electrical consumption of 51 kWh_e/ kg_{H_2} also consistent with data from IRENA (2020). Similarly to other studies (Hank *et al.*, 2018; Armijo and Philibert, 2020; Mallapragada *et al.*, 2020), we consider an electrolyzer 100% flexible. Usable excess heat from the electrolysis reaction has been estimated to be 14% of total energy input, so around 7 kWh_{th}/ kg_{H_2} (Danish Energy Agency and Energinet, 2020c). The stack lifetime has been reported between 55kh and 120kh by Buttler and Spliethoff (2018), so between 7 and 15 years, assuming 8000h of operations per year. In the model, the stack is changed every 10 years, and the whole system has a 25 years lifetime. Buttler and Spliethoff (2018) report an investment expenditure between 800 and 1500 €2019/kW (including auxiliaries), but other sources indicated costs down to 500 €2019/kW (IEA, 2019b; Danish Energy Agency and Energinet, 2020c; IRENA, 2020). As an average, a CAPEX of 830 €/kW is used in the model. Fixed operation and maintenance cost is taken at 2% of investment expenditure which is the minimum value proposed by Buttler and Spliethoff (2018) (between 2-3%).

Methanol Reactor and Carbon Capture Unit

The selected production route for methanol is based on pure CO_2 hydrogenation. As Direct Air Capture technology is still in its early stage of development, the carbon is assumed to originate from a point source. The carbon capture technology is an amine-based retrofitted to a 500 MW_{th} biomass-fired CHP (capture capacity around 164 t_{CO2}/hour). The electrical consumption

of the carbon capture plant is estimated to be 0.13 kWhe/kg of CO_2 captured. Specific investments are reported to 2700 €/($kg_{CO_2Output}$/h) with a fixed cost of 81 €/(kg_{CO2}/y) and a variable cost of 0.0025 €/kg_{CO2} captured (Danish Energy Agency, 2020). The CO_2 price is null, meaning that the biomass-fired plant does not sell the CO_2 or pay to get rid of it. The costs of the biomass plant itself are supported by another entity having other purposes than fuel production.
The methanol plant techno-econometrics are based on a large-scale (440 kt_{MeOH}/y) heat integrated process model developed by Pérez-Fortes *et al.* (2016). In the original study, 0.68 kWh_{th}/kg_{MeOH} of excess heat is still available after plant heat integration (excluding the electrolyzer). The plant consumes 0.316 kW_e/kg_{MeOH} of electricity to power compressors, pumps and utilities. Pérez-Fortes *et al (*2016) calculated that the methanol plant consumes 1.46 kg_{CO2}/kg_{MeOH} and produces 5.03 kg_{MeOH}/kg_{H2}. The plant CAPEX is estimated to be 4168 €/(kg $_{MeOH}$/h) and variable costs to 0.027 €/kg_{MeOH} (obtained after excluding the cost of raw materials such as hydrogen). The fixed plant costs, or manufacturing costs, were calculated to 618 €/(kg_{MeOH}/h)/y using Turton *et al.* (2012) method with 5 plant operators (estimate from Pérez-Fortes *et al (*2016)). Like Hank *et al.* (2018), the methanol plant is flexible down to 40% load with the ability to ramp up and down within an hour, which assumes a significant technical improvement in the coming years. Lifetime is assumed to be 25 years (Nguyen and Clausen, 2019) which may be optimistic given that flexible operation could impact plant lifetime but has not been quantified yet.

Ammonia Plant and Air Separation Unit
The ammonia is synthesized through the Haber-Bosch process using hydrogen and nitrogen captured from the air with an Air Separation Unit (ASU type cryogenic distillation unit). Blanco *et al.* (2018) reported a conversion efficiency of 93.5%, so 5.29 kilo of ammonia is produced per kilo of hydrogen. Similar to Armijo and Philibert (2020), the ammonia plant can operate flexibly. The minimal operating load is 40%, as suggested by (IEA, 2019a). Using an Aspen model, excess heat is estimated to be 1 kWh_{th} /kg_{NH3} without heat integration with the electrolyzer. Electrical consumption of the plant, including the ASU, is estimated to be 0.64 kWh_{el}/kg_{NH3} (Morgan, 2013). Plant lifetime is 25 years (Zhang *et al.*, 2020).

Hydrogen Tanks and Batteries
If needed, hydrogen tanks and batteries can be used to keep the minimal level of fuel production and avoid complete shutdowns. The hydrogen storage system is a pressurized tank and a compressor pressurizing the hydrogen from 20 bars to 800 bars. For convenience, only one tank and one compressor (more or less large) are modeled. Compressor consumption is calculated to be 3 kWh/kgH2 with a 75% isentropic and 98% mechanical efficiency. 12% of the hydrogen is lost during the compression. Compressor investment expenditure is 9092 $€_{2019}$/(kg_{H2}/h) and fixed O&M 182 $€_{2019}$/(kg_{H2}/h)/y. CAPEX for a 450-800 bars hydrogen tank is 982 $€_{2019}$/$kg_{H2stored,}$ and maintenance and insurance account for 2% of investment (Hank *et al.*, 2018; Danish Energy Agency and Energinet, 2020a).
The battery park modeled uses a stationary high-temperature NMC lithium-ion technology. The round-trip efficiency is 91%, including the conversion AC/DC, technical lifetime is 20 years, and the assumed maximal discharge is 80% (Danish Energy Agency and Energinet, 2020a). The speed of charge and discharge is not considered, which may give optimistic results. Based on IRENA (2017), investment expenditure is 362 $€_{2019}$/$kWh_{capacity}$. The maintenance cost is fixed to 5.1 $€_{2019}$/$kWh_{capacity}$/y (Ikäheimo *et al.*, 2018).

Table 2: Fuel plant technical metrics

	Input/Output (in/out)	Production rate [kg_{out}/kg_{in}]	Usable excess heat [kWh_{th} / kg_{out}]	Minimal load [% of capacity[2]]	Electrical consumption [kWh_{el} / kg_{out}]
Desalination plant	- /H_2O	-	0	0	0.004
AEC electrolyzer	H_2O/H_2	0.07	7.07	0	51
CO_2 capture PS	MeOH/ CO_2[1]	1.46	0	0	0.13
MeOH CCU plant	H_2/MeOH	5.03	0.68	40	0.316
NH_3 plant + ASU	H_2/NH_3	5.29	1	40	0.64
H_2 tank	H_{2in}/H_{2out}	-	0	3	3[3]
Battery Li-Ion	kWh_{in}/kWh_{out}	-	0	20	0.09[4]

[1] Input expressed in this way for modeling convenience
[2] Check table 3 for the capacity units.
[3] 3 kWh/kg of hydrogen compressed. In addition, 12% of hydrogen is lost in the compression process.
[4] 0.04 kWh losses per kWh charged (4%) and 0.05 kWh losses per kWh discharged (5%). Total round trip efficiency of 91%.

Renewable Power Supply
Solar PV
The model was given two photovoltaic generation options, fixed-axis PV and single-axis tracking PV. The annual and hourly generation inputs came from renewables.ninja platform (Pfenninger and Staffell, 2016), which uses the SARAH (Surface Solar Radiation Data Set - Heliosat) dataset to generate the hourly capacity factor of PV power plants. A 90% inverter efficiency has been assumed at an optimum tilt angle for electricity production taken from the Global Solar Atlas (World Bank, 2020). CapEx

and OpEx were taken from the DEA technology catalog (Danish Energy Agency and Energinet, 2020b). The resulting data inputs can be seen in Tables 1 and 3.

Wind

The onshore wind turbine selected for this study has a rotor diameter of 142m, a hub height of 100m, and a power rating of 3.15 MW, which is a turbine that is optimized for high capacity factor rather than optimized solely for LCOE. While this turbine is more expensive per MW than a more traditional onshore turbine, the increased capacity factor was optimal as it reduced the overall cost of the system in the islanded mode. Meanwhile, the offshore wind turbine used in this study has a rotor diameter of 164m, a hub height of 150m, and a power capacity of 9.5 MW. Annual and hourly generation data for these wind turbines were found using DTU Wind's CorRes model (Koivisto *et al.*, 2019), which uses Merra-2 reanalysis (weather data), wind turbine technical specifications (power curve, hub height, wind farm topology), and PyWake to calculate accurate generation data for each wind turbine in each location, including wake losses. The wake loss calculation assumed a 200 MW wind farm and seven rotor diameters of space separating each turbine.

The resulting capacity factors can be seen in Table 1, and economic metrics are summarized in Table 3.

Table 3: Fuel plant and renewable power supply economic metrics

	Unit output	CAPEX [€$_{2019}$/Capacity[1]]	Fixed cost [€$_{2019}$/Capacity[1]/y]	Variable cost [€$_{2019}$/Unit$_{out}$]	Lifetime [Years]
Desalination plant	kg$_{H2O}$	26	0[2]	0.0003	20
AEC electrolyzer	kg$_{H2}$	55371[3]	1107	0	25[3]
CO2 capture PS	kg$_{CO2}$	2700	81	0.0025	20
MeOH CCU plant	kg$_{MeOH}$	4168	618	0.027	25
NH3 plant + ASU	kg$_{NH3}$	4285	601	0	25
Solar PV fixed	MWh	553	9.1	0	35
Solar PV 1 axis	MWh	647	11.2	0	35
Wind onshore	MWh	1759	14.6	0.0016	27
Wind offshore	MWh	2266	41.8	0.0031	27
H2 tanks	kg$_{H2stored}$	982	19.6	0	25
Batteries	MWh	362	5.1	0	20

[1] Capacity expressed in Unit output/h expected for H2 tanks (Capacity = kg H2) and batteries (Capacity = MWh)
[2] Included on the variable cost
[3] Assuming a stack replacement every 10 years. Auxiliaries are not replaced until the end of life.

Grid Electricity

In the fully connected and semi-islanded cases, the fuel plant can buy electricity from the grid. Fuel production cost then depends on grid tariffs and market spot price (when the electricity market is liberalized).

In this paper, grid tariffs are defined as the costs added to the electricity spot price. The same grid tariffs have been applied to the 3 different sites to focus on weather profile type comparison. Based on the Danish TSO Energinet's (2019) analysis on electricity tariffs applied to electrolysis systems, the grid fees are set to 16.65 €/MWh, including 10.74 for transmission, 5.37 for distribution 0.54 for taxes.

Electricity spot prices are real data from 2019, which is the same year as solar and wind profile, to keep any potential correlation between weather profile and electricity price. Prices are taken from Coordinador Eléctrico National (Site1, Solar+, Arica, North Chile), Nordpool (Site 2, Wind+, DK1, Denmark), and AEMO (Site 3, Solar/Wind, Ceduna, South Australia). In South Australia, a few hours per year, the spot market price reaches exceptionally high (9070 €/MWh) or low (-555 €/MWh) electricity prices. Most hours are also more expensive in South Australia than North Chile or Denmark. North Chile and Denmark have relatively similar electricity prices, except that Chile has no negative prices. For modeling convenience, the few hours with negative prices are set to 0 €/MWh.

RESULTS AND DISCUSSION

Least-cost Sizing of the Fuel Production System

Islanded Configuration

At first, the system is set up as an islanded fuel production, meaning that no grid connection is available. That configuration could be preferred in remote areas or if using the grid leads to high CO2 emissions.

The system sizing leading to the lowest methanol production cost is presented in table 4. Similar results are obtained for ammonia production.

Table 4: Least-cost plant sizing in the Islanded configuration (2.5 TWh_{fuel})*

	Capacity	Site 1 (Solar +)	Site 2 (Wind +)	Site 3 (Wind/Solar)
AEC electrolyzer	kg_{H2}/h	29	19	21
CO2 capture PS	kg_{CO2}/h	95	106	100
MeOH CCU plant	kg_{MeOH}/h	65	73	69
Solar PV 1 axis	MW	2272	1196	1532
Wind onshore	MW	0	1309	877
H2 tanks	$Tonne_{H2}$	158	214	149
Batteries	MWh	474	152	135

* No investment in wind offshore and solar PV with fixed support

In Site 1, with high solar resources, the cheapest power supply option is a Solar PV plant with one-axis tracking. This technology is more expensive than fixed Solar PV but is worthier from a system point of view due to its higher capacity factor. In an Islanded solar-powered configuration, large electrolyzer and storage systems (both tank and batteries) have to be installed to keep a minimal level of fuel production during the night and provide an excess of hydrogen to fill the storage during the day. Batteries are used to store electricity at day and used at night to run the electrolyzer once the hydrogen storage is empty.
In Site 2, with essentially large wind resources, both solar PV with 1 axis tracking and onshore wind power are used in the cheapest power supply mix. It is still worth investing in solar PV in sites with low solar resources due to its low cost and complementarity with the wind power profile. Indeed, increasing the plant full load hours reduces the size of the electrolyzer required to keep a minimal production load and fulfill the annual fuel demand. Compared to sites 1 and 3, larger hydrogen storage is needed due to the wind power availability profile. While solar power has a regular daily production cycle, wind power production can remain low for longer periods. Offshore wind power is not used due to its high costs. Investing in offshore wind can be relevant when onshore power is not available due to limited space or social acceptance.
When both solar and wind resources are available (Site 3), the cheapest solution invests in both solar PV and wind power for the same reasons as Site 2 (Wind +). The storage size is also significantly reduced due to more hours with available power.

Fully Connected Configuration
In this configuration, all the electricity used by the electrolyzer originates from the grid. The three selected sites have a liberalized electricity market, meaning that electricity prices are variable and depend on the match between supply and demand. In all sites, a fixed grid tariff of 16.65 €/MWh is added to the electricity spot price.

Table 5: Least-cost plant sizing in the Fully Connected configuration (2.5 TWh_{fuel})

	Capacity	Site 1 (Solar +)	Site 2 (Wind +)	Site 3 (Wind/Solar)
AEC electrolyzer	kg_{H2}/h	12	11	13
MeOH CCU plant	kg_{MeOH}/h	58	58	61
Electrical grid	MW	614	610	699
H2 tanks	$Tonne_{H2}$	0	0	30
Batteries	MWh	0	0	16

In Site 1 and 2, the cheapest option does not use intermediate storage systems. Operating the plant flexibly is enough to benefit from the electricity price change: the plant operates at minimal load when the prices are high and maximal load when the prices are low. In the last site, batteries are used to limit the cost penalty involved by the few hours of the year where the market price spikes (up to 9070 €/MWh). The system is designed assuming perfect foresight (prices are known in advance), meaning that an actual plant scenario may include more storage to ensure the system robustness. Therefore, the prices obtained from this method must be seen as a lower cost boundary.
The electrolyzer and fuel plant sizes are much smaller compared to the islanded case due to the larger amount of full load operation hours. Compared to the islanded case in Site 1, 2.5 times less electrolyzer capacity is installed because there are no storage needs.

Semi-Islanded configuration
An option could also be to combine local power production and still have access to the grid if the price is low or if the renewable power is too low to keep a minimal level of fuel production.

Table 6: Least-cost plant sizing in the Semi-Islanded configuration (2.5 TWh_{fuel})*

	Capacity	Site 1 (Solar +)	Site 2 (Wind +)	Site 3 (Wind/Solar)
AEC electrolyzer	kg_{H2}/h	12	11	14
MeOH CCU plant	kg_{MeOH}/h	58	58	61
Electrical grid	MW	617	610	744
Solar PV 1 axis	MW	836	0	1072
Wind onshore	MW	0	0	20
H2 tanks	$Tonne_{H2}$	0	0	30

* No investments in batteries, wind offshore, and solar PV with fixed support

In the site with high solar resources, when both grid and local production are available, the cheapest option uses both solar PV with one axis tracking and grid electricity. The plant size is similar to the fully connected case, meaning that fuel producers benefit from both cheap renewable production and limit the plant oversizing. Usually, the fuel plant produces at full load using solar power during the day and operates at minimal load using grid electricity during the night.
In Site 2, the cheapest option does not include any local renewable power production. It means that, as a fuel producer, investing in onshore wind power is economically less attractive than getting powered by the grid. This result is valid under the assumption that grid connection costs are not supported by the fuel producer, which may not be the case in an actual project. The result is also dependent on the specific wind, solar, and electricity price profiles used in the model (year 2019). So optimal design may change in the future with a change of dynamics of grid price or weather profile.
In Site 3, even if the wind potential is large, it is cheaper to invest only in solar PV (with tracking) and use grid electricity during the night. Hydrogen tanks are used to cover the grid peak prices.

Table 7: Share of total yearly electricity production per source in the semi-islanded case (%)

	Site 1 (Solar +)	Site 2 (Wind +)	Site 3 (Wind/Solar)
Electrical grid	58	100	55
Solar PV 1 axis	42	0	44
Wind onshore	0	0	1

It can be seen in Table 7 that in the least-cost option, more than 50% of the power originates from the grid. Therefore, the fuel's carbon footprint depends directly on the grid electricity origin. Given the difficulty to track the grid-related emissions, using this configuration to produce fuel may be challenging to label the fuel produced as "green".

Cost analysis

Comparison of the power supply configuration

Figure 3 presents the cost breakdown and final methanol production cost depending on the renewable potential and the power supply configuration. The costs presented include the annualized investments, the operation and maintenance cost (fixed and variable), and the cost of electricity.

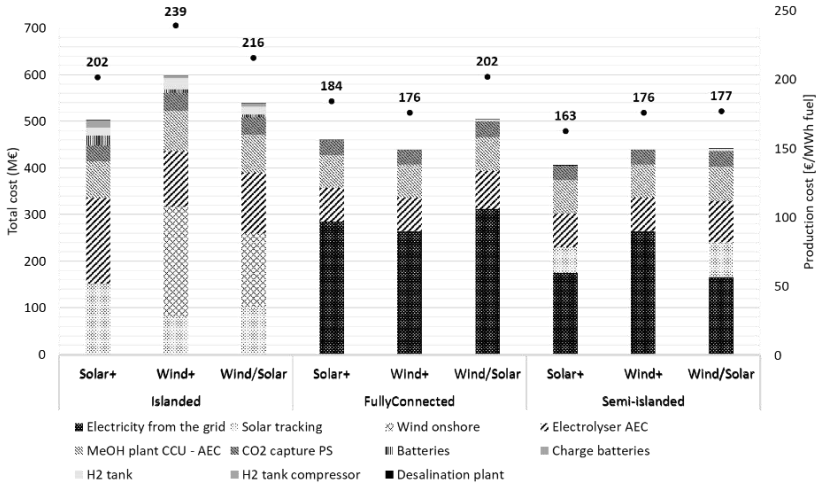

Figure 3: Methanol production cost depending on the configuration (2.5 TWh_{fuel})

In all cases, producing the fuel in an islanded configuration leads to higher production costs due to large storage systems investments but mostly to oversized power supply and electrolyzer. When using electricity from the grid, the size of the electrolyzer needed is reduced by half, reducing the investment expenditure significantly. The cost of electricity then represents the higher share of expenses. Combining grid-electricity and local power production (semi-islanded) reduces fuel production costs considerably. Usually, low-cost solar power is used in priority, but when solar power is unavailable, the fuel plant lowers its production load to the minimum and gets powered by the grid rather than using storage systems and an oversized electrolyzer/power supply. If the wind resource is significant but electricity prices relatively low, using the grid alone is the cheapest option. A site with high solar potential gives the lowest fuel production cost if a tracking system is used and if the storage cost is relatively low.

Comparison Ammonia versus Methanol

The ammonia production process consumes a larger amount of electricity and hydrogen to produce the same fuel energy content, so more power and electrolyzer capacity are needed compared to methanol production. However, if the fuel plant costs are similar between methanol and ammonia, the carbon capture system adds a penalty, making methanol 8% more expensive than ammonia (in the Semi-Islanded configuration). In addition, the carbon source availability can limit the large-scale development of methanol production, while nitrogen from the air is available in large quantities at a relatively low cost.

Cost Reduction Potentials

By-Product Sale: Heat and Oxygen

If the infrastructures and markets are available near the fuel production plant, selling oxygen, heat, or both is possible. The oxygen produced via electrolysis has very high purity, making it suitable for all applications, from blast furnaces to medical use. The selling price of gaseous oxygen reported in the literature ranges from 27 to 150 €/t_{O2} (Hannula, 2015; Zhang *et al.*, 2020). Like Atsonios *et al* (2016), a value of 87.4 €/t_{O2} is used in the model.

The excess heat of the electrolysis and fuel plant process has a relatively low temperature and can be used in a local district heating or cooling network. The Danish district heating organization reported an annual average price of 23€/MWh_{th} with a variation between 20€/MWh_{th} in summer and 26€/MWh_{th} in winter (Dansk Fjernvarme, 2021). 23 €/MWh_{th} is used for the calculations.

Model results show that selling by-products can significantly reduce costs, especially for oxygen. Selling heat and oxygen can reduce the production cost by up to 24% for ammonia production. Selling heat and oxygen alone could reduce ammonia production costs by 7 and 17%, respectively. Selling heat and oxygen alone reduces methanol costs by 5 and 15%.

Plant flexibility

Figure 5 shows the influence of plant flexibility on the final fuel production cost. The base case defined in the previous section is a plant flexible down to 40% load. The base case is compared to an extra flexible plant with a minimal load of 10% capacity and a non-flexible plant always running at full capacity.

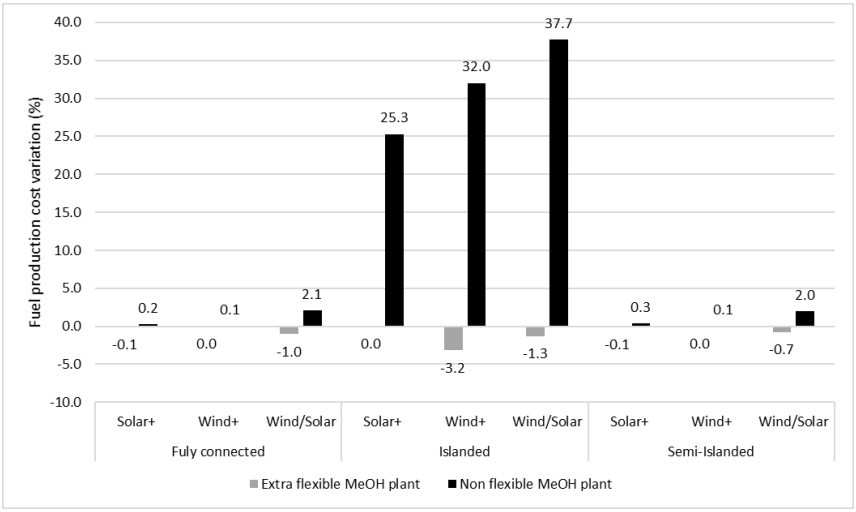

Figure 5: Fuel production cost variation depending on the fuel plant flexibility

Results show that in an off-grid setup, a non-flexible fuel plant adds a considerable cost penalty (up to a 37 % cost increase). However, additional flexibility does not reduce the cost significantly because to produce the minimal yearly demand, the plant owner still needs to invest in a storage system and oversize the system. When the plant has access to the grid, the flexibility does not significantly impact the production cost either. Indeed, the cheapest option limits the expensive investments (into

electrolyzer and fuel plant capacity) and maximizes the plant full load hours, meaning that the plant operates at a lower load as little as possible. Flexibility has a more significant influence on cost if the grid electricity prices have a large cost amplitude like in site 3 (Wind/Solar) with some price peaks over the year. However, higher renewable penetration in the electricity grid may increase the amplitude of price variation and push investment into flexible plant assets.

CONCLUSIONS

We developed a model to identify the least-cost system design in a different configuration. The fuel production is driven by an annual demand of 2.5 TWh of fuel, a typical size for existing fossil methanol or ammonia plant. We study 3 possible configurations to power the fuel plant: with local renewable power supply (Islanded), using electricity exclusively from the grid (Fully Connected), or a mix of both (Semi-Islanded). 3 sites with typical weather profiles have been included in the study: one site with very high solar potential, one site with high wind potential, and one with high wind and solar potential. The study considered the possibility of including the sale of side-products in the plant business model. The conclusions are valid given the data and profiles presented in the article.
The primary outcomes are:

- The fuels with the lowest cost are produced in areas with high solar potential using solar PV with one-axis tracking.
- When producing off-grid, the installed capacities need to be significantly oversized to fulfill the minimal demand and fill large intermediate storage systems. A non-flexible plant operation can add 25 to 35% of extra costs. If wind resource is available and even if the solar potential is limited, combining onshore wind with solar PV 1-axis tracking gives the lowest production cost. Offshore wind is not invested if onshore power is available.
- For the 3 sites, given the tariffs used, powering the system with electricity from the grid is cheaper than running the plant off-grid due to smaller invested capacities. A flexible fuel plant does not significantly affect the fuel production cost except if the electricity price has a large variation amplitude and/or punctual very high peak prices.
- When solar resources are available, the cheapest powering option is to combine local solar PV 1-axis tracking (off-grid) with electricity from the grid. In that case, the system benefits from cheap solar electricity and backup grid power, avoiding system oversizing and large intermediate storage. More than 50% of the electricity then originates from the grid, which can make the sustainability of the fuel questionable.
- Using the assumption presented in this paper, producing ammonia is 8% cheaper than producing methanol via CO2 hydrogenation.
- Selling heat and oxygen can reduce the production cost by up to 24%. Selling heat and oxygen alone could reduce costs by 7 and 17%, respectively.
- In the cheapest case and selling both heat and oxygen, ammonia can be produced at 115 €/MWh (593 €/t) and methanol at 130 €/MWh (717 €/t). As a comparison, the Very Low Sulphur Oil (VLSFO) price was around 40 €/MWh in 2021 (high price range).

ACKNOWLEDGEMENTS

This paper is published as part of the MarE-fuel project funded by the Danish Maritime Fund and the Lauritzen Fund. We thank the partners of the project for their cooperation and inspiration.

REFERENCES

AEMO (no date) *Electricity market Australia*. Available at: https://www.aemo.com.au/.
Armijo, J. and Philibert, C. (2020) 'Flexible production of green hydrogen and ammonia from variable solar and wind energy: Case study of Chile and Argentina', *International Journal of Hydrogen Energy*, 45(3), pp. 1541–1558. doi: 10.1016/j.ijhydene.2019.11.028.
Atsonios, K., Panopoulos, K. D. and Kakaras, E. (2016) 'Investigation of technical and economic aspects for methanol production through CO2 hydrogenation', *International Journal of Hydrogen Energy*. Elsevier Ltd, 41(4), pp. 2202–2214. doi: 10.1016/j.ijhydene.2015.12.074.
Bellotti, D. *et al.* (2017) 'Feasibility study of methanol production plant from hydrogen and captured carbon dioxide', *Journal of CO2 Utilization*. Elsevier, 21(May), pp. 132–138. doi: 10.1016/j.jcou.2017.07.001.
Blanco, H. *et al.* (2018) 'Potential for hydrogen and Power-to-Liquid in a low-carbon EU energy system using cost optimization', *Applied Energy*. Elsevier, 232(October), pp. 617–639. doi: 10.1016/j.apenergy.2018.09.216.
Burridge, E. (2009) *European chemical profile: Methanol*, *ICIS*. Available at: https://www.icis.com/explore/resources/news/2009/11/16/9263011/european-chemical-profile-methanol/ (Accessed: 31 May 2021).
Buttler, A. and Spliethoff, H. (2018) 'Current status of water electrolysis for energy storage, grid balancing and sector coupling via power-to-gas and power-to-liquids: A review', *Renewable and Sustainable Energy Reviews*, 82(September 2017), pp. 2440–2454. doi: 10.1016/j.rser.2017.09.003.
Danish Energy Agency (2020) *Technology Data for Industrial Process Heat and Carbon Capture | Energistyrelsen*.

Danish Energy Agency and Energinet (2020a) *Technology data Energy Storage*.
Danish Energy Agency and Energinet (2020b) *Technology data for generation of electricity and district heating*.
Danish Energy Agency and Energinet (2020c) *Technology Data for Renewable Fuels*.
Dansk Fjernvarme (2021) *Power-To-X and district heating*.
Energinet (2019) *PTX in Denmark before 2030*.
Hank, C. *et al.* (2018) 'Economics & carbon dioxide avoidance cost of methanol production based on renewable hydrogen and recycled carbon dioxide-power-to-methanol', *Sustainable Energy and Fuels*. Royal Society of Chemistry, 2(6), pp. 1244–1261. doi: 10.1039/c8se00032h.
Hannula, I. (2015)' Co-production of synthetic fuels and district heat from biomass residues, carbon dioxide and electricity: Performance and cost analysis', *Biomass and Bioenergy*. Elsevier Ltd, 74, pp. 26–46. doi: 10.1016/j.biombioe.2015.01.006.
Hasan, A. and Dincer, I. (2020) 'ScienceDirect An ocean thermal energy conversion based system for district cooling , ammonia and power production', *International Journal of Hydrogen Energy*. Elsevier Ltd, 45(32), pp. 15878–15887. doi: 10.1016/j.ijhydene.2020.03.173.
IEA (2019a) *The future of hydrogen.*, *IEA report*. doi: 10.1016/S1464-2859(12)70027-5.
IEA (2019b) 'The Future of Hydrogen for G20. Seizing today's opportunities', *Report prepared by the IEA for the G20, Japan*, (June).
Ikäheimo, J. *et al.* (2018) 'Power-to-ammonia in future North European 100 % renewable power and heat system', *International Journal of Hydrogen Energy*, 43(36), pp. 17295–17308. doi: 10.1016/j.ijhydene.2018.06.121.
IPCC (2014) *Climate Change 2014: Synthesis Report Contribution of Working Groups I, II and III to the Fifth Assessment Report of the Intergovernmental Panel on Climate Change*.
IRENA (2017) *Electricity storage and renewables: Costs and markets to 2030*, *Electricity-storage-and-renewables-costs-and-markets*. Available at: http://irena.org/publications/2017/Oct/Electricity-storage-and-renewables-costs-and-markets%0Ahttps://www.irena.org/-/media/Files/IRENA/Agency/Publication/2017/Oct/IRENA_Electricity_Storage_Costs_2017.pdf.
IRENA (2020) *Green Hydrogen cost reduction*.
Kettani, M. and Bandelier, P. (2020) 'Techno-economic assessment of solar energy coupling with large-scale desalination plant: The case of Morocco', *Desalination*. Elsevier, 494(June), p. 114627. doi: 10.1016/j.desal.2020.114627.
Koivisto, M. *et al.* (2019) 'Using time series simulation tools for assessing the effects of variable renewable energy generation on power and energy systems', *Wiley Interdisciplinary Reviews: Energy and Environment*, 8(3), pp. 1–15. doi: 10.1002/wene.329.
Mallapragada, D. S. *et al.* (2020) 'Can Industrial-Scale Solar Hydrogen Supplied from Commodity Technologies Be Cost Competitive by 2030?', *Cell Reports Physical Science*, 1(9). doi: 10.1016/j.xcrp.2020.100174.
McDonagh, S. *et al.* (2018) 'Modelling of a power-to-gas system to predict the levelised cost of energy of an advanced renewable gaseous transport fuel', *Applied Energy*. Elsevier, 215(February 2018), pp. 444–456. doi: 10.1016/j.apenergy.2018.02.019.
Methanol Institute (2021) *Renewable Methanol*. Available at: https://www.methanol.org/renewable/ (Accessed: 31 May 2021).
Morgan, E. R. (2013) 'Techno-Economic Feasibility Study of Ammonia Plants Powered by Offshore Wind', *University of Massachusetts - Amherst, PhD Dissertations*, p. 432. doi: https://doi.org/10.7275/11kt-3f59.
Nguyen, T. Van and Clausen, L. R. (2019) 'Techno-economic analysis of polygeneration systems based on catalytic hydropyrolysis for the production of bio-oil and fuels', *Energy Conversion and Management*. Elsevier, 184(January), pp. 539–558. doi: 10.1016/j.enconman.2019.01.070.
Nordpool (no date) *Electricity market North Europe*. Available at: https://www.nordpoolgroup.com/.
Pérez-Fortes, M. *et al.* (2016) 'Methanol synthesis using captured CO2 as raw material: Techno-economic and environmental assessment', *Applied Energy*. Elsevier Ltd, 161, pp. 718–732. doi: 10.1016/j.apenergy.2015.07.067.
Pfenninger, S. and Staffell, I. (2016) 'Long-term patterns of European PV output using 30 years of validated hourly reanalysis and satellite data', *Energy*. Elsevier Ltd, 114, pp. 1251–1265. doi: 10.1016/j.energy.2016.08.060.
Statista (2021) *Ammonia plant production capacity in the United States in 2019, by facility*. Available at: https://www.statista.com/statistics/1266392/ammonia-plant-capacities-united-states/ .
Turton, R. *et al.* (2012) *Analysis, synthesis and design of chemical processes*. 4th edn. Prentice Hall: Prentice Hall international series in the physical and chemical engineering sciences.
World Bank (no date) *Global Solar Atlas*. Available at: https://globalsolaratlas.info/map.
Zhang, H. *et al.* (2020) 'Techno-economic comparison of green ammonia production processes', *Applied Energy*. Elsevier, 259(November), p. 114135. doi: 10.1016/j.apenergy.2019.114135.
Zhang, H. and Desideri, U. (2020) 'Techno-economic optimization of power-to-methanol with co-electrolysis of CO2 and H2O in solid-oxide electrolyzers', *Energy*. Elsevier Ltd, 199, p. 117498. doi: 10.1016/j.energy.2020.117498.

BREAK DOWN OF COST FOR DIFFERENT ROUTES TO GREEN AMMONIA

Hossein Nami*[1], Peter V. Hendriksen[1] and Henrik L. Frandsen[1]

ABSTRACT

"Green" ammonia to be used as an energy storage medium and directly as a marine fuel has attracted significant attention recently. Ammonia is among the chemicals with a growing demand worldwide. From a climate perspective, this is a challenge since commercial ammonia production is very energy-intensive, responsible for about 1% of global greenhouse gas emissions, and produces 2.07 ton CO_2 per ton of ammonia. Green ammonia can be produced by using conventional ammonia synthesis, however with the hydrogen produced from water electrolysis rather than using steam methane reforming. The remaining components of the conventional route are an air separation unit to supply nitrogen and a Haber-Bosch loop (HBL) to synthesise the ammonia. Although, green ammonia production from renewables is not a new technology, cost reduction in renewable electricity, and progressed technical readiness of electrolyzers have opened new opportunities. The increased cost of green ammonia compared to fossil-derived "grey" ammonia is, however, still a matter of concern for maritime transportation. In this work, the thermodynamics of green ammonia production are studied and the economic feasibility is evaluated to suggest the most cost-effective solution. The production cost is modeled using both low- and high-temperature electrolyzers (AEC and SOEC, respectively) operating with renewable electricity input only and assumed to be closely coupled with a HBL. It is shown that by applying SOEC with a HBL there is a possibility of heat integration and waste heat recovery from the HBL leading to economic advantages. On the other hand, AEC is a mature technology and has today a lower CAPEX than SOEC. Consequently, two different routes; one based on AEC and one on SOEC, are described. A techno-economic analysis is carried out to identify the most cost-effective system and show the share of each of the major components on the required CAPEX. Currently, although SOEC performs efficiently compared with AEC, employing this technology to produce green ammonia is not economically advantageous. However, it is shown that ammonia costs will likely be lower using the SOEC route as compared to the one using AEC considering the cost reductions expected from upscaling of the electrolysis production.

KEYWORDS

Green ammonia, Green hydrogen, SOEC, AEC, Haber-Bosch

INTRODUCTION

Maritime industry releases around 940 million tCO_2 annually, which is about 2.5% of global greenhouse gas (GHG) emissions [1]. These emissions are estimated to increase if an appropriate alternative fuel is not put in place swiftly. Green ammonia has attracted a huge amount of attention as an alternative fuel to reduce the emissions associated with maritime transport. Currently, world ammonia production is around 180 million metric tons [2] and due to a long history of ammonia usage in agriculture, a vast ammonia infrastructure already exists. When compared with hydrogen, ammonia has a higher energy density and can be stored in liquid form at a much less energy-intensive condition (-33 ˚C). A wide spectrum of studies has focused on alternative fuels for the shipping industry. In Ref. [3] authors have concluded that MeOH and ethanol are not appropriate alternative fuels for shipping. The following literature review summarizes some of the most recently published research works.

McKinaly et al. [4] considered hydrogen, methanol and ammonia as the main candidates to deliver zero-emission shipping to identify the main engineering challenges for utilizing these fuels in the ships. They showed that a reduction of fuel storage quantities makes alternative fuels significantly more viable. An overview of emerging and state-of-the-art technologies for decarbonizing shipping via ammonia as an alternative fuel is presented in Ref. [5]. Hansson et al. [6] assessed the prospects for ammonia as an alternative fuel for the maritime industry compared with other marine fuels. They stated that ammonia can be considered as an interesting future marine fuel option, but many issues remain to be solved before large-scale introduction. Ammonia, hydrogen and methanol are selected as the alternative fuels for a pathway to climate-neutral shipping by Brahim et al. [7]. It is found that methane leakage is crucial for future alternative fuels. Cardoso et al. [8] revealed that the estimated payback period for a small-scale green ammonia production system based on biomass gasification in mainland Portugal is around 4.6 years. Gomez et al. [9] found that feeding hydrogen

from water electrolysis and nitrogen from cryogenic air separation unit is the potentially most viable pathway to produce green ammonia. The payback period was estimated to be 4–6 years for this pathway.

In the present work, green ammonia synthesis based on water electrolysis driven by renewable electricity is assessed economically. The proposed system is the combination of an electrolyzer to produce green hydrogen, a cryogenic air separation unit (ASU) to deliver nitrogen and a Haber-Bosch loop (HBL) to synthesize ammonia. Alkaline electrolyzers (AEC) as the most developed low-temperature type of electrolyzer and solid oxide electrolyzers (SOEC) as a newly developed high-temperature technology are compared as the possible routes to green hydrogen. The main reason behind combining SOEC with HBL is to benefit from heat integration between the two. Both systems are modeled at the component level. Anticipated future development of the capital expenditure (CAPEX) of electrolysis technologies is taken into account.

SYSTEM DESCRIPTION AND ASSUMPTIONS

Figure 1 illustrates a schematic diagram of a green ammonia producing system. As can be seen, it is assumed that wind electricity runs both electrolyzer and ASU. Then, produced hydrogen and nitrogen are fed to the HBL for ammonia synthesis. The only difference between AEC-and SOEC-based systems is that a heat integration between the electrolyzer and HBL exists in the SOEC-based system (not shown in the figure).

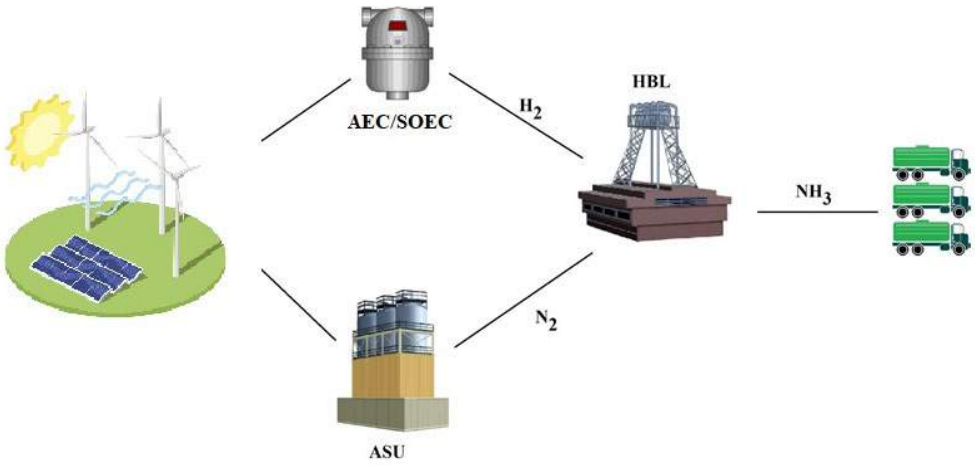

Figure 1: Illustration of green ammonia production route

Assumptions

The following key assumptions are made to simplify the entire system modeling:

- AEC operating temperature and pressure are 80 ˚C and 30 bar, respectively.
- SOEC operating temperature and pressure are 750 ˚C and 1.1 bar, respectively.
- HBL reactor operating temperature and pressure are 550 ˚C and 250 bar, respectively.
- Power consumption by the ASU is 0.108 MWh/tN_2 delivering nitrogen at 8 bar [10].
- H_2:N_2 molar ratio in HBL feeding stream is 3:1.
- Heat losses from the components and pipelines and pressure drop across the pipelines are negligible [11].
- Employed compressors and pumps have isentropic efficiency.
- Employed heat exchangers have maximum effectiveness of 90%.
- The lower heating value of hydrogen and ammonia is assumed to be 120 and 18.6 MJ/kg, respectively.
- Enhancement in the electrolyzer future electrochemical performance is neglected.
- The entire system is operating 7884 hours per year.
- System economic life is 25 years.
- SOEC and AEC stack replacement time is 5 and 10 years, respectively.
- The annual interest rate is assumed to be 8%.
- The average € to $ exchange rate constant is assumed to be 1.12.
- SOEC operates at the thermoneutral point and AEC operates at a current density of 0.5 A/cm^2.

METHODOLOGY

Thermodynamic modeling

Each main component is considered as a separate control volume and then mass and energy balance equations are applied as follows:

$$\sum \dot{m}_i = \sum \dot{m}_e \quad [1]$$

$$\sum \dot{m}_i h_i + \dot{Q}_{cv} = \sum \dot{m}_e h_e + \dot{W}_{cv} \quad [2]$$

here, $\dot{m}$, h, $\dot{Q}$ and $\dot{W}$ represent mass flow rate, specific enthalpy, heat transfer and mechanical power, respectively. Also, subscripts *i*, *e* and *cv* stand for inlet, outlet and control volume, respectively.
After applying the energy conservation equation and calculating the required power to run the electrolyzer and the entire system, the thermodynamic efficiency of the employed electrolyzer and the entire system are defined as follows:

$$\eta_{electrolyzer} = \frac{\dot{m}_{H2} LHV_{H2}}{\dot{W}_{electrolyzer}} \quad [3]$$

$$\eta_{total} = \frac{\dot{m}_{NH3} LHV_{NH3}}{\dot{W}_{total}} \quad [4]$$

here, $\dot{m}_{H2}$ and $\dot{m}_{NH3}$ are the mass flow rate of produced hydrogen and ammonia, respectively. $\dot{W}$ is also consumed renewable electricity.

Techno-economic assessment

Electrolyzer CAPEX are estimated for today as well as in the future. This and the cost of renewable electricity are the main parameters to determine the cost of green ammonia. To estimate the current and currently projected CAPEX of electrolysis technologies different papers and technical reports were reviewed [12]–[20].
In this study, the methodology for assessing direct, fixed and general manufacturing costs is adopted from Ref. [21].

Table 1 lists the cost of the main components employed in the AEC- and SOEC-based systems. Changes in CAPEX for the Haber-Bosch loop (HBL), the air separation unit (ASU) and heat exchangers over time are neglected (the 2020 numbers are used for all cases).

Table 1: CAPEX of the main components employed in the green ammonia producing systems

Parameter	Value (unit)
SOEC [12]–[20]	2020: 2770 (€/kW) 2030: 1140 (€/kW) 2050: 400 (€/kW)
SOEC stack replacement cost	2020: 18.5% CAPEX 2030: 12.5% CAPEX 2050: 8.5% CAPEX
AEC [12]–[20]	2020: 840 (€/kW) 2030: 700 (€/kW) 2050: 300 (€/kW)
AEC stack replacement cost	2020: 48% CAPEX 2030: 46% CAPEX 2050: 42% CAPEX
Heat exchanger [22]	$110\ (\frac{A_{HEX}}{0.093})^{0.78}$ (€) A_{HEX} is in m^2
HBL [23]	3 (M€/(tNH_3/h))
ASU [23]	1.45 (M€/(tN_2/h))

Net present value (NPV) method is selected to calculate the current value of each cash flow at the end of n^{th} time period, as follows:

$$NPV = \sum_{n=0}^{BL} \frac{Y_n}{(1+i)^n} \quad [5]$$

here Y_n, is the net cash flow at the end of n^{th} time period.

The capital recovery factor (CRF) is also defined hereunder to include the cost of a loan for the duration of the entire economic life of the system:

$$CRF = \frac{i(1+i)^m}{(1+i)^m - 1} \quad [6]$$

here, m is the system economic life and i is the annual interest rate.

RESULTS

Figure 2 illustrates the efficiencies calculated for each subsection of the plant for both AEC- and SOEC-based systems. Overall, the SOEC-based system performs 28 % more efficiently than the AEC-based one. This is the case, as the efficiency in the hydrogen generation is higher in the SOEC case as some waste heat from the HBL can be utilized in the hydrogen synthesis. Also, the alkaline unit at the operation point produces some waste heat. The employed HBL in the SOEC-based system has on the other hand a slightly lower efficiency compared with that in the AEC-based system. This is mainly due to the compression power needed to increase the pressure of the hydrogen to the reactor pressure. The hydrogen supplied via SOEC and AEC is at atmospheric and 30 bar pressure, respectively, and hence a compression step is required in the HBL for the case of hydrogen from the SOEC. However, the employed electrolyzer is the unit that dictates the overall efficiency of the entire system. The employed electrolyzer is responsible for 90 and 96% of the entire electricity consumption within the SOEC- and AEC-based system. So, the majority of the consumed power refers to this unit. Then, the electrical efficiency of the SOEC-based system is higher than that of the AEC-based system. Obtained efficiencies for AEC- and SOEC-based systems are 54 and 69%, respectively.

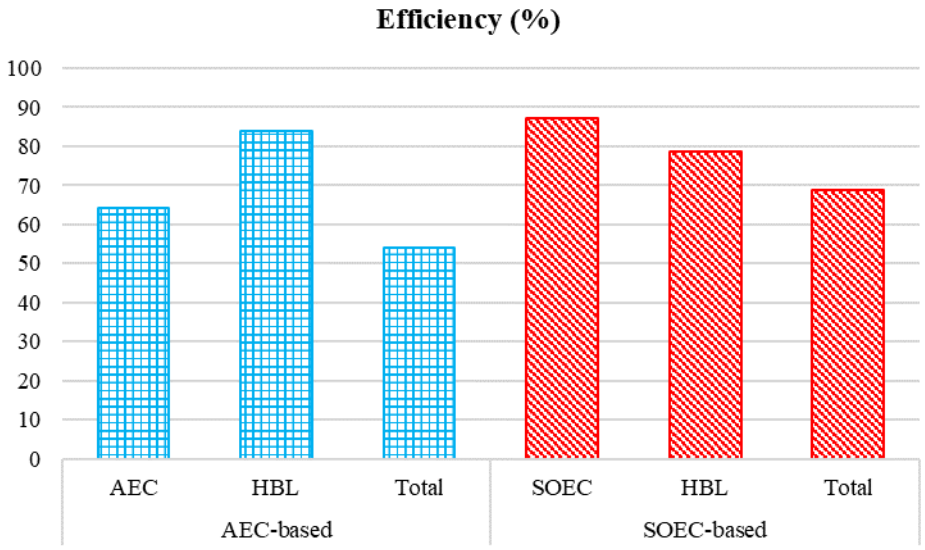

Figure 2: Efficiencies calculated for AEC- and SOEC-based green ammonia producing systems

In the economic assessment, cost of electricity is assumed to be 30 €/MWh. Also, it is assumed that the payment associated with electricity consumption occurs in the middle of each year. Besides, purchased equipment and stack replacement costs are assumed to be CAPEX. Furthermore, annually paid cash flows i.e. maintenance cost, manufacturing cost and costs associated with electricity consumption are presented as OPEX.

Figure 3 shows the estimated CAPEX values for both AEC- and SOEC-based systems by 2020, 2030 and 2050. Referring to this figure, currently, the required CAPEX to establish a SOEC-based green ammonia producing system is much higher than that of AEC-based system. This is because SOEC is currently rather expensive compared with AEC, due to the low production volumes. However, as the figure shows, in long term, the required CAPEX for the SOEC-based system is expected to become comparable with AEC-based system due to an anticipated reduction in the cost of SOEC, due to manufacturing upscaling.

The CAPEX values are based on the projections in Table 1 which reflect the expected increase of the production capacity over the years. However, if the green transition is realized faster than initially anticipated in this projection the production capacity and cost reductions could appear accordingly faster.
The OPEX for the entire AEC- and SOEC-based systems is shown in figure 4 for years 2020, 2030 and 2050. As the figure shows, the estimated OPEX for the SOEC-based system will be lower in the long term. This is mainly due to an expected decrease in maintenance and manufacturing costs. It is worth mentioning that for higher values of cost of electricity, the OPEX values for the SOEC-based system will be much lower than those for the AEC-based system due to the higher efficiency.
The manufacturing cost and maintenance cost are based on the methods outlined in Ref. [24] for chemical plants, which might not transfer directly to electrolysis technologies, and might be on the high side. With the assumed cost of electricity, the estimated OPEX of green ammonia produced via SOEC-based system is only 14 and 18% lower than that of AEC-based system by 2030 and 2050, respectively.

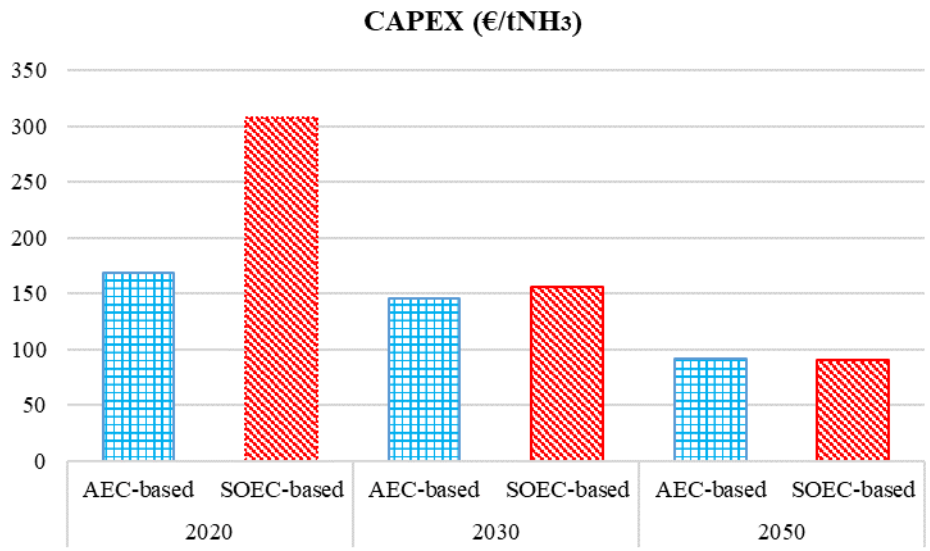

Figure 3: Required CAPEX for the entire system by 2020, 2030 and 2050

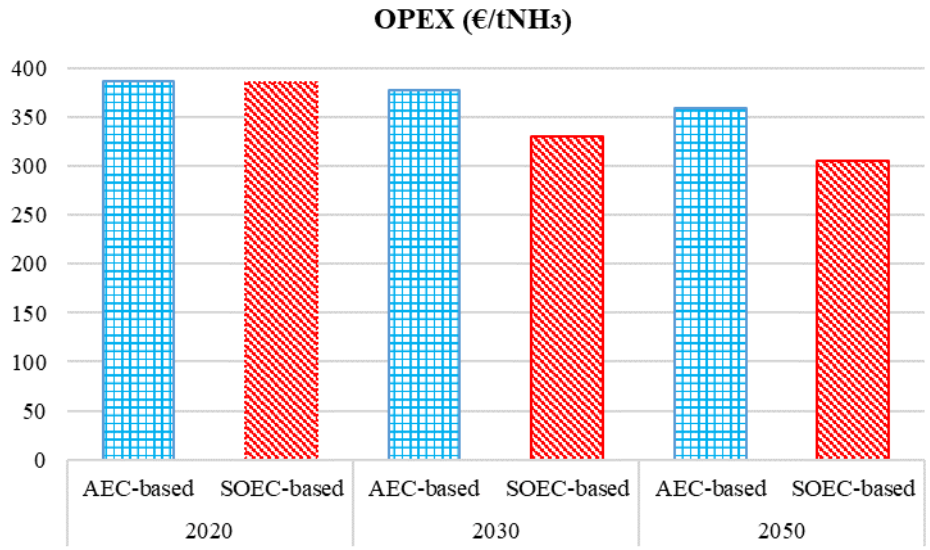

Figure 4: Required OPEX for the entire system by 2020, 2030 and 2050

CONCLUSIONS

Currently, employing AEC to produce electrolytic hydrogen required for green ammonia production is economically attractive to using SOEC. This is while SOEC performs more efficiently compared with AEC and utilizes less electricity. The efficiency of AEC- and SOEC-based green ammonia producing systems are found to be 54 and 69%, respectively.

Currently, the CAPEX share in the cost of green ammonia produced via SOEC-based system is comparable with the OPEX. Nevertheless, SOEC technology is expected to experience a stronger cost reduction than AEC mainly due to mass production and technology development which results in a considerable reduction in the share of CAPEX in cost of green ammonia. Therefore, utilizing SOEC as a green hydrogen route in green ammonia production seems attractive after 2030 for the assumptions applied here. By 2050, cost of green ammonia produced via AEC-based system is around 14% higher than that of SOEC-based system.

ACKNOWLEDGEMENTS

Support from the Danish Maritime fund within the project; *MarE-fuel; sustainable maritime fuels* is thankfully acknowledged.

REFERENCES

[1] T. W. P. Smith *et al.*, "Third IMO GHG Study 2014," *Int. Marit. Organ.*, p. 327, 2014.
[2] ALFA LAVAL, HAFNIA, HALDOR TOPSOE, VESTAS, and SIEMENS GAMESA, "Ammonfuel-an industrial view of ammonia as a marine fuel," *Hafnia*, no. August, pp. 1–59, 2020.
[3] C. Deniz and B. Zincir, "Environmental and economical assessment of alternative marine fuels," *J. Clean. Prod.*, vol. 113, no. X, pp. 438–449, 2016.
[4] C. J. McKinlay, S. R. Turnock, and D. A. Hudson, "Route to zero emission shipping: Hydrogen, ammonia or methanol?," *Int. J. Hydrogen Energy*, vol. 46, no. 55, pp. 28282–28297, 2021.
[5] T. Ayvali, S. C. Edman Tsang, and T. Van Vrijaldenhoven, "The position of ammonia in decarbonising maritime industry: An overview and perspectives: Part I," *Johnson Matthey Technol. Rev.*, vol. 65, no. 2, pp. 275–290, 2021.
[6] J. Hansson, S. Brynolf, E. Fridell, and M. Lehtveer, "The potential role of ammonia as marine fuel-based on energy systems modeling and multi-criteria decision analysis," *Sustain.*, vol. 12, no. 8, p. 3265, Apr. 2020.
[7] T. ben Brahim, F. Wiese, and M. Münster, "Pathways to climate-neutral shipping: A Danish case study," *Energy*, vol. 188, p. 116009, 2019.
[8] J. S. Cardoso, V. Silva, J. A. M. Chavando, D. Eusébio, M. J. Hall, and M. Costa, "Small-Scale Biomass Gasification for Green Ammonia Production in Portugal: A Techno-Economic Study," *Energy & Fuels*, vol. 35, no. 17, pp. 13847–13862, Sep. 2021.
[9] J. R. Gomez, J. Baca, and F. Garzon, "Techno-economic analysis and life cycle assessment for electrochemical ammonia production using proton conducting membrane," *Int. J. Hydrogen Energy*, vol. 45, no. 1, pp. 721–737, 2020.
[10] E. R. Morgan, "Techno-Economic Feasibility Study of Ammonia Plants Powered by Offshore Wind," University of Massachusetts Amherst, 2013.
[11] H. Nami, F. Ranjbar, M. Yari, and S. Saeidi, "Thermodynamic analysis of a modified oxy-fuel cycle, high steam content Graz cycle with a dual-pressure heat recovery steam generator," *Int. J. Exergy*, vol. 21, no. 3, 2016.
[12] A. Dubois, S. Ricote, and R. J. Braun, "Benchmarking the expected stack manufacturing cost of next generation, intermediate-temperature protonic ceramic fuel cells with solid oxide fuel cell technology," *J. Power Sources*, vol. 369, pp. 65–77, 2017.
[13] IRENA, *Green hydrogen cost reduction*. 2020.
[14] T. Data and R. Fuels, "Technology Data for Renewable Fuels," pp. 1–259.
[15] M. Götz *et al.*, "Renewable Power-to-Gas: A technological and economic review," *Renew. Energy*, vol. 85, pp. 1371–1390, 2016.
[16] "IEA (2019), The Future of Hydrogen, IEA, Paris https://www.iea.org/reports/the-future-of-hydrogen."
[17] G. Glenk and S. Reichelstein, "Economics of converting renewable power to hydrogen," *Nat. Energy*, vol. 4, no. 3, pp. 216–222, 2019.
[18] ICCT, "Assessment of Hydrogen Production Costs from Electrolysis: United States and Europe," *Int. Counc. Clean Transp.*, pp. 1–73, 2020.
[19] H. Böhm, A. Zauner, D. C. Rosenfeld, and R. Tichler, "Projecting cost development for future large-scale power-to-gas implementations by scaling effects," *Appl. Energy*, vol. 264, no. February, p. 114780, 2020.
[20] J. S. G. Mýrdal, C. Hendriksen , Peter Vang; Graves, and E. R. Jensen, Søren Højgaard; Nielsen, "Predicting the price of Solid Oxide Electrolysers (SOECs)," no. October, pp. 1–7, 2016.
[21] R. Turton, R. C. Bailie, W. B. Whiting, and J. A. Shaeiwitz, *Analysis, synthesis and design of chemical processes*, 4th ed. Prentice Hall: Prentice Hall international series in the physical and chemical engineering sciences, 2012.
[22] H. Nami, S. M. S. M. S. S. Mahmoudi, and A. Nemati, "Exergy, economic and environmental impact assessment and optimization of a novel cogeneration system including a gas turbine, a supercritical CO2 and an organic Rankine cycle (GT-HRSG/SCO2)," *Appl. Therm. Eng.*, vol. 110, pp. 1315–1330, Jan. 2017.
[23] J. Ikäheimo, J. Kiviluoma, R. Weiss, and H. Holttinen, "Power-to-ammonia in future North European 100 % renewable power and heat system," *Int. J. Hydrogen Energy*, vol. 43, no. 36, pp. 17295–17308, Sep. 2018.

[24] R. Turton *et al.*, *Analysis, synthesis and design of chemical processes*, 4th ed. Prentice Hall: Prentice Hall international series in the physical and chemical engineering sciences, 2012.

IMPLICATIONS OF THE EMISSION-RELATED POLICY ENVIRONMENT ON EXISTING CONTAINERSHIPS

M. Schroer[1], G. Panagakos[1], M. Bruhn Barfod[1]

ABSTRACT

Global warming and, correspondingly, reducing CO_2 emissions is one of the most challenging tasks the world faces today. The maritime industry contributed to 2.89% of the global anthropogenic CO_2 emissions. To decrease this share, the International Maritime Organization (IMO) defined, among others, the goal to reduce the carbon intensity of international shipping by 40% until 2030. In this context, the short-term measures recently adopted, in the form of a technical standard (Energy Efficiency Existing Ship Index, EEXI) and a rating scheme based on an operational indicator (Carbon Intensity Indicator, CII), mark a crucial step to achieving the mentioned goal. In addition, the EU Commission has recently introduced the FuelEU Maritime Initiative limiting the annual greenhouse gas (GHG) intensity of a ship's energy use incorporating a reduction occurring in a five-year rhythm between 2025 and 2050. The paper investigates the practical options availed to existing containerships of different sizes and technological vintages for meeting the specific EEXI, CII, and GHG intensity reduction requirements imposed by the regulations. The investigation will be based on the actual technical and operational profiles of six sample ships and will consider a set of possible compliance options including, but not limited to, engine power limitation, waste heat recovery system, variable frequency drives, and virtual arrival. The data used originates from noon reports of existing containerships provided by a European industry leader. The ship-specific CO_2 emission reduction potentials required for the impact assessment result from either literature or actual data-based calculations. Financial data is used for investigating the economic impact of the reduction requirements. Conclusions drawn include an operational advantage that pre-EEDI ships enjoy when applying engine power limitation (EPL) for EEXI compliance, the occurrence of payback periods exceeding ship lifetimes, and an estimate of the effect that onshore power supply can have on complying with the FuelEU Maritime Initiative.

KEY WORDS

Container shipping; Decarbonization; Maritime policy; IMO regulation; Fit for 55; Carbon intensity; Fuel standards.

INTRODUCTION

Since the Paris Agreement of 2015, decarbonization of shipping became the top priority of the International Maritime Organization (IMO). The organization introduced its goals in the Initial IMO GHG strategy published in 2018. IMO's primary goal for 2050 is a 50% reduction of the greenhouse gas (GHG) emissions of international shipping compared to the 2008 level. Three categories of measures of different timeline are envisaged for meeting this goal:

- Short-term measures (finalized and agreed between 2018 and 2023)
- Mid-term measures (finalized and agreed between 2023 and 2030)
- Long-term measures (finalized and agreed beyond 2030).

Accordingly, the 76th Marine Environmental Protection Committee (MEPC76) adopted the IMO short-term measures in June 2021, comprising of a technical standard expressed by the Energy Efficiency Existing Ships Index (EEXI), and a rating scheme built around the operational Carbon Intensity Indicator (CII).

Besides IMO's global efforts, regional authorities also add regulations to the environmental regulatory portfolio. In July 2021, the European Commission (EC) proposed its "Fit for 55" package consisting of the FuelEU Maritime Initiative and the inclusion of shipping in Europe's Emission Trading Scheme (ETS).

[1] Department of Technology, Management and Economy, Technical University of Denmark, Denmark

On the whole, the maritime community faces an ever-changing and increasingly complex emission-related regulatory environment imposing new challenges to the old ones. Addressing these challenges requires (a) technical and operational knowledge on emission mitigation solutions, especially regarding the solutions' ship-specific reduction potentials, and (b) a techno-economic impact assessment of complying with the regulations.

This is precisely the aim of this paper, which focuses on container shipping. It first introduces the current environmental regulatory portfolio, conducts a literature review on emission mitigation solutions and impact assessments, and explains the evidence-based approach used for analyzing the regulation implications. Based on this, the paper calculates ship-specific emission reduction potentials for the chosen set of mitigation solutions and sample ships. It combines these with the corresponding financial implications to assess the techno-economic consequences of compliance. The paper closes with a discussion of the results and a summary of its conclusions.

REGULATIONS

The first IMO regulatory measures on carbon emissions were introduced in 2011 and concerned the Energy Efficiency Design Index (EEDI) and the Ship Energy Efficiency Management Plan (SEEMP). The EEDI comprises a technical index for newbuilds, and the SEEMP secures ongoing energy efficiency management of existing ships.

Before launching the second generation of measures, both global and regional authorities established reporting schemes to collect the necessary environmental and operational data. The European Union (EU) initiated the so-called EU Monitoring, Reporting, and Verification (EU MRV) system that covers all shipping operations to, from, or within the EU. The IMO also operates a monitoring scheme examining global shipping operations, namely the IMO Data Collection System (DCS). Both systems differ in not only geographical scope but also the applied carbon intensity indicator. The EU MRV is based on the Energy Efficiency Operational Index (EEOI), depicting a ship's CO_2 emissions divided by its transport work. The IMO DCS uses the Annual Efficiency Ratio (AER) instead, also dividing CO_2 emissions by transport work but defining transport work differently. Whereas the EEOI considers the actual cargo carried during a ship's voyage, the AER looks at a ship's deadweight tonnage. (Panagakos et al 2019)

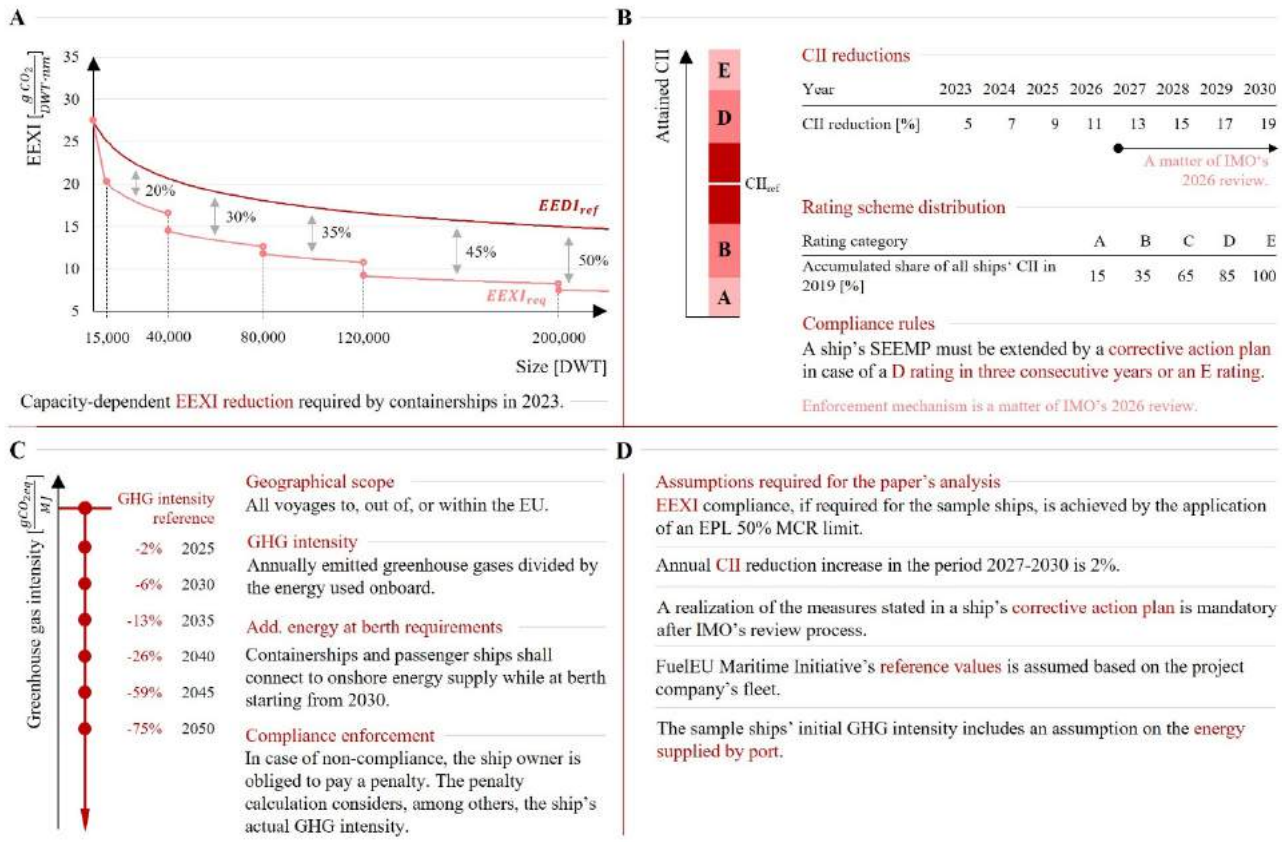

Figure 1: Emission-related regulatory environment. (A) EEXI reductions applicable for containerships. (B) CII-based rating scheme. (C) General information on the FuelEU Maritime Initiative. (D) Policy-related assumptions required for the paper's analysis.

The latest developments were the adoption of the IMO short-term measures and the EC proposal on its "Fit for 55" package. IMO's EEXI introduces a technical index for existing ships and stipulates a one-off reduction requirement in 2023. The EEXI's ship-specific reduction requirement is derived by applying a ship type and size-dependent reduction factor to the already known EEDI reference line (Figure 1(A)). (MEPC 2021)

The CII rating scheme (Figure 1(B)) comprises an annual evaluation of a ship's operational performance. For this, it compares a ship's annual carbon intensity (for example, its AER) with a CII reference line. Depending on the distance between them, the vessel is rated in one of five categories (A to E), where the C zone's mid-value equals the reference value. A ship's rating determines its compliance with the regulation. Currently, a D rating for three consecutive years or an E rating enforces the inclusion of a corrective action plan in the ship's SEEMP. In this context, the paper assumes that a realization of the corrective action plan will be mandatory after IMO's review before 2026. Further, the CII incorporates annual reductions applied to the reference line over its duration. Starting with a 5% reduction in 2023, it will constantly increase by 2% per year. For now, IMO did not define the cutbacks between 2027 and 2030 as they are part of IMO's review process, but the paper assumes maintenance of the annual 2% decline for this period. (MEPC 2021)

Not yet adopted but proposed as part of EC's "Fit for 55" package is the FuelEU Maritime Initiative, which aims at promoting the uptake of alternative fuels. Like the EU MRV scheme, the Initiative covers all shipping operations to, from, or within the EU. The alternative fuel uptake shall be achieved by comparing the annual GHG intensity of a ship's energy use against a reference value based on the 2020 EU MRV data. The reduction requirement increases every 5 years, starting with 2% in 2025 and ending with 75% in 2050. New in environmental regulations, the Initiative considers life-cycle assessments (LCA) of all applicable alternative fuels, adding Well-to-Tank (WtT) emissions to the usual Tank-to-Wake (TtW) ones. (EC 2021) Being at an early stage, the FuelEU Initiative proposal does not define the actual 2020 reference value.

LITERATURE REVIEW

Shipping decarbonization is a popular subject of academia. Numerous literature sources research either emission mitigation solutions or regulation impacts. Literature on emission mitigation solutions approaches the topic in two different ways: (a) by literature reviews on solution groups or specific solutions (Bouman et al 2017; Mallouppas and Yfantis 2021; Serra and Fancello 2020; Singh and Pedersen 2016), or (b) by case studies usually covering one ship type and solution (Guan et al 2015; Henriksson and Vierto 2016; Kocak and Durmusoglu 2018).

Sources on regulation impacts are also diverse. Some impact assessments mainly focus on least developed countries (LDCs) and small island developing states (SIDS) as requested by IMO (e.g., Psaraftis and Zis 2021). Other IMO-focused sources research the regulations' contribution to the IMO targets (Comer et al 2018; Halim et al 2018), and few sources look at the ship or fleet-level effects (Zis et al 2020; Zis and Psaraftis 2021). Besides IMO regulations, research on the FuelEU Maritime Initiative is rare. One of the only available sources, Hughes (2021), discusses the Initiative's potential advantages and disadvantages. The source highlights the proposal's reduced scope, stating that only 15% of global shipping emissions are covered. The reduced scope is an issue that Panagakos et al (2019) also reported in the context of the EU MRV.

Very few sources use an evidence-based approach combining possible solutions with imposed requirements, and none investigates the impacts of the FuelEU Maritime Initiative. Therefore, the paper's novelty and relevance are threefold: (a) it uses an evidence-based research approach for revealing regulation impacts, (b) it introduces calculation methods for uncovering ship-specific reduction potentials of a number of emission mitigation solutions, and (c) it covers not only IMO's short-term measures but also the FuelEU Maritime Initiative.

EVIDENCE-BASED APPROACH

Contrary to usual research in the field, this paper uses an evidence-based approach to assess the implications of IMO's short-term measures and the FuelEU Maritime Initiative. For this, it works with a selection of sample containerships combined with a selection of emission mitigation solutions, from now on called "compliance options".

Sample ships and data

The analysis investigates the regulation impacts on six different sample containerships. It uses actual operational noon report data for a full report year, either 2018 or 2019, and technical data defining the ship status. The data originates from a leading European shipowner.

A typical fleet composition was the key driver in the selection of sample ships. Additionally, the selection also considered potential factors influencing ship compliance with the regulations.

As a result, three sample ship groups (A, B, and C) formed the foundation for the analysis, each containing two sample ships differing in only one characteristic. Group A includes 10,500 TEU containerships of different ages. Group B consists of 8,500 TEU containerships with varying management status. Lastly, Group C is made of two differently aged but smaller (2,500 TEU) ships. Hence, the researched potential influencing factors are age, management status, and size.

Compliance options

The paper considers six compliance options to meet the reduction requirements imposed by the regulations, namely:

- Engine power limitation (EPL)
- Turbocharger cut-out (TCCO)
- Waste heat recovery systems (WHRS)
- Auxiliary engine economizers (AEE)
- Variable frequency drives (VFD)
- Virtual arrival (VA).

The selection of the options considered industry interests mirrored by the project company.

Engine power limitation is a technical option widely supported by the IMO, especially for EEXI compliance. EPL denotes a mechanical or electrical fuel intake blockage activated above a certain power limit of the main engine. This limit ultimately results in lower speeds and, thus, a reduction of CO_2 emissions. EPL's limit can only be exceeded in urgent cases, which have to be documented. (IMO 2020; Rutherford et al 2020)

The turbocharger is one of the system components affected when a ship operates below its optimal conditions due to, for example, EPL or speed reduction. While a propulsion system usually distributes exhaust gas energy between several turbochargers, all working under optimal conditions, a decrease of the main engine power results in less available energy that might not be sufficient for all installed turbochargers anymore. Cutting out one or more turbochargers concentrates the reduced energy on fewer turbocharger units and increases the efficiency of the system. EPL limits under 50% MCR usually come with a TCCO as standard. (Guan et al 2015)

Waste heat recovery systems, too, utilize the main engine's exhaust gas energy, particularly its heat energy. Installed in the exhaust gas system, the WHRSs convert heat into mechanical or electrical energy and feed it back into the ship's energy system. The heat sources for waste heat recovery can be categorized in high (above 649 °C), medium (232-649 °C), and low-temperature ones (below 232 °C). The current retrofit solution for existing ships recovers waste heat from the exhaust gas (200-500 °C). WHRSs' reduction potential given in Table 1 focuses on solutions feasible for maritime applications. (Singh and Pedersen 2016)

Not only the main engine but also auxiliary engines lose energy through their exhaust gases. Again, applying a waste heat recovery system here called auxiliary engine economizer can reduce the ship's energy loss. (Henriksson and Vierto 2016)

A ship's auxiliary systems are another target for emission reduction, addressed by variable frequency drives. The onboard systems consist of multiple electrical actuators such as pumps or fans. In most cases, these actuators can only work at full load, although this might not be required. VFDs can reduce the resulting energy loss by allowing adjustable actuator speeds. A VFD installed in the turbo generator condenser pumps relies on the initial installation of WHRS. (Kocak and Durmusoglu 2018)

Unlike the above technical options, virtual arrival is an operational solution. VA can reduce a ship's average speed during a voyage without lengthening the voyage time by decreasing the anchorage time through improved ship-port communication. (Poulsen and Sampson 2019)

Estimation of reduction potential

The analysis combines the reduction potential found in the literature for the abovementioned compliance options with estimates based on ship-specific data. For two of these options (EPL and VA), the reduction potential is estimated by a method using the available operational data of the sample ships. For the remaining four options (TCCO, WHRS, AEE, and VFD), the study applies directly the literature values.

At ship level, it is assumed that EPL will influence only the voyages where the average main engine power is above the EPL limit. For these voyages, the effect will be lower speeds and reduced GHG emissions, accompanied by longer transit times. Ship-specific statistical data is used to estimate the effect of a lower main engine power on the through-water speed and the required prolongation of the sailing time. In combination with the new main engine power, the altered time leads to an estimate of the emissions generated again based on statistical information connecting the daily fuel consumption with the power of the main engine.

VA's reduction potential also originates from a data-based calculation. Although the sailed distance of a VA-improved leg remains the same, the sailing time increases by the leg's previous anchorage time. This allows the calculation of the decreased sailing speed and, resultantly, VA's reduction potential.
Table 1 shows the resulting ship-specific emission reduction potentials for each compliance option.

Table 1: Calculated option and ship-specific as well as literature-based reduction potentials.

	Calculated CO_2 reduction potential [%]						Red. potential in literature	Influenced variable	Source
	A1	A2	B1	B2	C1	C2			
EPL [60% MCR]	-	-	-	-	-	9.76	- 0.0 to 18.4%	CO_2 emissions (total)	(Rutherford et al 2020)
EPL [50% MCR]	EEXI	EEXI	EEXI	EEXI	EEXI	15.13	- 0.0 to 18.4%	CO_2 emissions (total)	(Rutherford et al 2020)
EPL [40% MCR]	4.82	2.13	0.67	3.35	5.68	21.07	- 0.0 to 18.4%	CO_2 emissions (total)	(Rutherford et al 2020)
TCCO	1.04	a.i.	a.i.	a.i.	1.25	0.10	- 2%	CO_2 emissions (total)	(Guan et al 2015)
WHRS	9.28	a.i.	9.91	10.42	10.23	9.83	+ 0.5 to 25.5%	Energy efficiency (main engine)	(Singh and Pedersen 2016)
AEE	1.30	a.i.	0.90	0.69	0.88	0.84	- 16 to 22%	Fuel cons. (aux. eng. in port)	(Henriksson and Vierto 2016)
VFD (excl. WHRS)	a.i.	n.a.	0.64	0.53	3.11	2.43	- 355 t/yr.	Fuel cons. (total)	Project company
VFD (incl. WHRS)	0.24	0.67	0.93	0.77	3.75	2.92	- 355 t/yr.	Fuel cons. (total)	Project company
VA	n.a.	n.a.	0.07	0.20	0.12	n.a.	- 7 to 19%	Fuel cons. (main engine)	(Jia et al 2017)

EEXI, installed for EEXI compliance; a.i., already installed onboard; n.a., not applicable

COMPLIANCE WITH IMO'S SHORT-TERM MEASURES

Compliance with IMO's short-term measures is two-sided. The first restriction that shipowners must meet is the EEXI. Out of the six sample ships, only one ship (C2) will be compliant as is. The remaining five ships are obliged to reduce their EEXI values (required reductions range between 7.50% and 27.25%). It is assumed that applying a 50% MCR EPL limit equal to 37% EEXI reduction is sufficient for this purpose (Kock et al 2021).

The second restriction to be met is the CII. As this is not a one-off requirement but an annual rating of a ship performance, compliance results from the sample ships' position against the reference line for the entire period. At the same time, the compliance rules (D for three consecutive years or E) set the limit for the attained CII value of a ship and result in CII reduction requirements for each sample ship until 2030. The paper assumes a minimum action strategy followed by the ship owners allowing the ships to be rated D for three consecutive years before taking action and only act to reach the highest possible CII for a C rating the year after.

Table 2: Sample ship's location within the CII rating scheme

	CO_2 reduction required in 2023 to reach the upper bound of …		CO_2 reduction required in 2030 to reach the upper bound of …	
	C	D	C	D
A1	in C	-	8.90%	in D
A2	in C	-	9.26%	in D
B1	in C	-	6.70%	in D
B2	in C	-	12.85%	3.08%
C1	1.74%	in D	16.22%	6.83%
C2	in C	-	12.56%	2.75%

Table 2 presents the required reductions of the sample ships to reach the upper bound of zones C and D in 2023 and 2030 (if outside these zones). EEXI compliance is already accounted for in these figures.

Ship C1, the older one in group C, underperforms compared to the other sample ships. It is already rated D in the first year of measure enforcement and will be rated E in 2030 if no mitigation actions are taken. The same rating in 2030 will be exhibited by two other ships (B2, C2).

Table 3: Literature-based financial data for the researched compliance options

	Investment cost [€*]	**Maintenance cost** [€/year]	**Source**	**Comments**
EPL	50,400**	-	(GloMEEP 2016)	Based on the lowest value within the range for engine de-rating
TCCO	50,400	-	(GloMEEP 2016)	Based on the lowest value within the range for engine de-rating
WHRS	7,980,000	25,200	(Gundersen et al 2016; Shu et al 2013)	For high-efficiency WHRS plant
AEE	89,500	8,400	(Gundersen et al 2016; Henriksson and Vierto 2016)	Based on an Aalborg XS TC7A by Alfa Laval
VFD	33,600***	4,200	(Gundersen et al 2016; Kocak and Durmusoglu 2018)	Investment costs for VFDs applied to seawater cooling systems
VA	8,400	4,200	(Gundersen et al 2016)	Based on values for voyage execution and corresponding software solutions

* When required, a conversion factor of 0.84 €/US$ has been used.
** Investment costs are only necessary for a new application.
*** Investment costs per system application.

Combining the EEXI and CII reduction requirements with the reduction potential of the mitigation options examined and the corresponding financial data (Table 3) reveals the combination of options that each ship must implement to remain compliant. A minimum investment approach was followed for the selection process, which was based on a greedy algorithm of the so-called knapsack problem considering the cost-effectiveness of the available options.

Table 4: Ship-specific necessary compliance combinations

	Total req. CO_2 reduction* [%]	**Necessary compliance combinations**	**Resulting CO_2 reduction [%]**	**Payback period [year]**
A1	6.65	EPL [40% MCR] & TCCO, AEE	7.16	< 1
A2	4.78	Not possible at all	max. 2.80	-
B1	6.70	WHRS & VFD	10.21	10
B2	6.40	WHRS & VFD	10.67	8
C1	16.22	WHRS & VFD, EPL [40% MCR] & TCCO	17.80	11
C2	6.08	EPL [60% MCR]	9.76	< 1

* Required reduction in AER values on top of the reduction induced by implementing the EPL [50% MCR] option as required by EEXI-related restrictions.

The combinations necessary for each ship also define the implications of IMO's short-term measures. From a technical perspective, Ship A2, the older one in group A, cannot fulfill the requirements at all by applying the chosen compliance options, whereas the other sample ships can comply with the measures. This contrasts expectations, since Ship A2 faces the lowest reduction requirements. The reason lies to the fact that the ship is already equipped with most of the examined mitigation options. This is an initial indicator for the limits of IMO's short-term measures, underlining that the less disruptive mitigation solutions, such as those examined here, can only improve a ship's carbon intensity to a certain extent.

On the contrary, the ship facing the highest reduction requirements, C1, can comply with the measures but must implement numerous compliance options, including WHRS. The latter exhibits large reduction potentials ranging between 9.28% to 10.42% while demanding the highest investment costs. Consequently, the technical practicability lacks financial feasibility illustrated by a payback period of 11 years that results in a recovery of invested capital only at the age of 37, exceeding by far the usual lifetime of a ship (Table 4). The same applies for the other two sample ships (B1, B2), requiring a WHRS installation and depicting payback periods of 10 and 8 years respectively. The effects are twofold: (a) waste heat recovery systems are inescapable if facing high reduction requirements, and (b) compliance imposes financial and technical challenges, potentially resulting in a renewal of a good part of the world fleet.

COMPLIANCE WITH THE FUELEU MARITIME INITIATIVE

The FuelEU Maritime Initiative includes a provision on supplying onshore electrical energy to a ship at berth, also called 'cold ironing.' Although the introduction of alternative fuels, which constitutes the primary goal of this Initiative, is not reflected in the present study, the available data allows for an estimate of the potential that cold ironing exhibits in complying with the Initiative.

The GHG intensity reduction induced by cold ironing results from assuming that all energy formerly provided by auxiliary engines at berth in European ports now originates on shore. In this geographical context, only three ships (A1, B2, and C2) will be affected by the regulation. For these ships, the berth energy adds up to 2.17% (B2), 2.67% (A1), and 2.86% (C2) of the total energy consumed over their report period and resembles the GHG intensity reduction that can be expected from cold ironing.

On the assumption that the sample ships are positioned around the Initiative's reference value in 2020, the stipulated 2% reduction for 2025 in the GHG intensity of the energy consumed will be met merely by applying the cold ironing solution as early as in 2025. However, this will not be sufficient for covering the 6% reduction requirement for 2030. The more than 3% differential will have to be met by the introduction of alternative fuels.

It is worth mentioning that although the technical and operational solutions examined in this study as compliance options for the IMO short-term measures are expected to have only minor, if any, effect on the GHG intensity of a ship's energy consumption, the opposite is not true. The alternative fuels including cold ironing of the FuelEU Initiative are expected to have a considerable effect on the ship's EEXI and CII, rendering the solutions examined above unnecessary as means of regulatory compliance. This should not undermine though the importance of energy efficiency in operating a vessel, particularly when considering the much higher prices of alternative fuels in comparison to those of the traditional ones.

DISCUSSION

The achieved results raise a number of issues worth discussing. The first one concerns the implications of EPL on sailing time. In most cases, the imposition of EPL, either as a means of EEXI compliance or otherwise, results in an increase in a vessel's sailing time in order to produce the same transport work. The calculations uncovered that this increase is much more visible in younger ships (A1: 73.43 hours/year) than in older ones (A2: 5.93 hours/year, C1: 25.29 hours/year). The difference relates to the main engine load profiles of the ships. A power limit is expected to have repercussions that are more substantial on an engine operating at high MCR regions than otherwise, as more voyages will be affected in the former case. Pre-EEDI ships like A2 are normally equipped with larger main engines resulting in lower average main engine loads (A2: 31.79%, C1: 38.08%) than their post-EEDI counterparts (A1: 43.63%, C2: 71,06%) that have smaller engines. Although not in the context of EEXI, it is found that Ship C2 has to apply a 60% MCR EPL limit to be CII compliant, resulting in additional 488.76 hours per year. It is certain that this will have serious implications on the employment of this ship.

A second issue relates to the investment minimization opportunities that the CII regulation provides because of the possibility of operating a ship labelled D for three consecutive years prior to taking corrective actions. The aggregate CII reduction requirements of a specific vessel within a period are determined by two critical factors, the timing of non-compliance and the number of non-compliance incidents during this period of analysis. In general, a strategy leading to the earliest possible non-compliance without increasing the total number of non-compliance incidents in the period is preferable as it exploits the increasing stringency of the reduction requirements with time. The application of this strategy on Ship C1 by voluntarily applying mitigation options before 2023, leads to a drop in the total reduction requirements in the period 2023-2030 by 6.20% (before: 16.22% / after: 10.02%).

Whereas the FuelEU Maritime Initiative allows pooling (fleet-level) compliance, IMO's short-term measures impose compliance by each and every single ship of certain types and sizes. Faber et al (2021) has recently claimed that pooling compliance would also be beneficial in the context of IMO's measures. The results of this paper support this finding. If the six sample ships of the study are viewed as a fleet, a fleet-level compliance can be achieved when the aggregate emission reduction is equal to the sum of the absolute reductions occurred when every single ship in the fleet is compliant on its own. This pooling arrangement offers the possibility of applying all feasible compliance options on young ships (A1, C2)

while decreasing the EPL limit of the other ships by an additional 10%. This solution achieves the same emission reduction in 2030 but with a total investment cost that is 32% lower when compared to the ship-level compliance option presented in the previous sections. This result renders fleet-level compliance a considerable add-on to the IMO's short-term measures.

Cold ironing has a limited but not negligible effect on compliance with the FuelEU Initiative. The use of alternative fuels will not only be necessary for meeting the Initiative's targets but will prove an indispensable ally in reaching the IMO's ambitions in terms of both carbon intensity and absolute GHG emissions.

CONCLUSIONS

This research focused on the implications of current emission-related regulations, particularly IMO short-term measures and the FuelEU Maritime Initiative. It studied implications of the regulations on six sample containerships and considered the application of a set of technical and operational compliance options. The paper results lead to the following conclusions:

- Engine power limitation proves to be a cost-effective and easy to install option, but it can severely affect a ship's operational schedule.
- The suggested way of complying with EEXI, through EPL, rewards pre-EEDI ships as they experience lower sailing time increases than their post-EEDI counterparts.
- The technology and design vintages of a ship affect its reduction potential. A ship's age might additionally influence financial decisions on compliance options considering the long payback periods revealed.
- Fleet-level compliance, as introduced by the FuelEU Maritime Initiative, appears to be a considerable addition to IMO's short-term measures. It can potentially reduce the financial burdens that current compliance impose on shipowners.
- The contribution of cold ironing on reducing the GHG intensity of the energy consumed by the three of the six sample ships affected by the FuelEU Maritime Initiative ranges between 2% and 3%. Although non-negligible, the use of alternative fuels is imperative not only for meeting the Initiative's targets, but also for contributing to reaching the IMO's ambitions in terms of both carbon intensity and absolute GHG emissions.

ACKNOWLEDGEMENTS

The authors thank the Danish Maritime Fund for funding the NICE project and the project company for providing data.

REFERENCES

BOUMAN, E. A., E. LINDSTAD, et al. "State-of-the-art technologies, measures, and potential for reducing GHG emissions from shipping – A review." *Transportation Research Part D: Transport and Environment*, **52** (2017): 408–421.

COMER, B., C. CHEN, et al. "Relating short-term measures to IMO ' s minimum 2050 emissions reduction target. Appendix to paper MEPC 73/INF.27 presented to IMO Marine Environment Protection Committee." *International Council on Clean Transportation*, *13* (2018): 7.

EUROPEAN COMMISSION. *Regulation of the Euoprean Parliament and of the Council on the use of renewable and low-carbon fuels in maritime transport and amending Directive 2009/16/EC* (COM(2021) 562) (2021). Article COM(2021) 562.

FABER, J., J. KIRÁLY, et al. *Fleet-level compliance with the CII Regulation* (2021), A CE Delft report produced on behalf of Danish Shipping.

GLOMEEP. *Engine de-rating* (2016). URL https://glomeep.imo.org/technology/engine-de-rating/ (accessed 12 April 2021)

GUAN, C., G. THEOTOKATOS, et al. "Analysis of two stroke marine diesel engine operation including turbocharger cut-out by using a zero-dimensional model." *Energies*, **8**:6 (2015): 5738–5764.

GUNDERSEN, H., M. S. EIDE, et al. *Project report - EE Appraisal Tool for IMO* (2016).

HALIM, R. A., L. KIRSTEIN, et al. "Decarbonization pathways for international maritime transport: A model-based policy impact assessment." *Sustainability (Switzerland)*, **10**:7 (2018).

HENRIKSSON, D., and R. N. VIERTO. *Exhaust gas economizer on auxiliary engines* [Chalmers University of Technology] (2016).

HUGHES, E. *FuelEU Maritime – Avoiding Unintended Consequences* (Issue May) (2021), A report produced on behalf of the European Community Shipowners' Associations and the International Chamber of Shipping.

INTERNATIONAL MARITIME ORGANISATION. *Draft guidelines associated with draft amendments to MARPOL Annex VI to incorporate the goal-based efficiency improvement measure utilizing Energy Efficiency Existing Ship Index (EEXI)* (ISWG-GHG 7/2/7) (2020). Article ISWG-GHG 7/2/7.

JIA, H., R. ADLAND, et al. "Energy efficiency with the application of Virtual Arrival policy." *Transportation Research Part D: Transport and Environment*, **54**:July 2011 (2017): 50–60.

KOCAK, G., and Y. DURMUSOGLU. "Energy efficiency analysis of a ship's central cooling system using variable

speed pump." *Journal of Marine Engineering and Technology*, **17**:1 (2018): 43–51.
KOCK, F., J. WIENKE, et al. *Energy Efficiency Existing Index* (2021). A presentation on behalf of DNV GL. https://www.dnv.com/maritime/webinars-and-videos/on-demand-webinars/EEXI-what-you-need-to-know.html (accessed 7 May 2021).
MALLOUPPAS, G., and E. A. YFANTIS. "Decarbonization in Shipping industry: A review of research, technology development, and innovation proposals." *Journal of Marine Science and Engineering*, **9**:4 (2021).
MARINE ENVIRONMENTAL PROTECTION COMMITTEE. *Consideration and adoption of amendments to mandatory instruments - Draft amendments to MARPOL Annex VI* (MEPC 76/3) (2021). Article MEPC 76/3.
PANAGAKOS, G., T. de S. PESSÔA, et al. "Monitoring the carbon footprint of dry bulk shipping in the EU: An early assessment of the MRV regulation." *Sustainability (Switzerland)*, (2019).
POULSEN, R. T., and H. SAMPSON. "'Swinging on the anchor': The difficulties in achieving greenhouse gas abatement in shipping via virtual arrival." *Transportation Research Part D: Transport and Environment*, **73**:July (2019): 230–244.
PSARAFTIS, H. N., and T. ZIS. "Impact assessment of a mandatory operational goal-based short-term measure to reduce GHG emissions from ships: the LDC/SIDS case study." *International Environmental Agreements: Politics, Law and Economics*, *0123456789* (2021).
RUTHERFORD, D., X. MAO, et al. "Limiting engine power to reduce CO2 emissions from existing ships." In *ICCT Working Paper 2020-01* (2020).
SERRA, P., and G. FANCELLO. "Towards the IMO's GHG goals: A critical overview of the perspectives and challenges of the main options for decarbonizing international shipping." *Sustainability (Switzerland)*, **12**:8 (2020).
SHU, G., Y. LIANG, et al. "A review of waste heat recovery on two-stroke IC engine aboard ships." *Renewable and Sustainable Energy Reviews*, **19** (2013): 385–401.
SINGH, D. V., and E. PEDERSEN. "A review of waste heat recovery technologies for maritime applications." *Energy Conversion and Management*, **111**:X (2016): 315–328.
ZIS, T. P. V., H. N. PSARAFTIS, et al. "Decarbonizing maritime transport: A Ro-Pax case study." *Research in Transportation Business and Management*, **37**:September (2020).
ZIS, T. P. V., and H. N. PSARAFTIS. "Impacts of short-term measures to decarbonize maritime transport on perishable cargoes." *Maritime Economics & Logistics*, *0123456789* (2021).

OPERATIONAL CYCLES IN MARITIME TRANSPORT: LESSONS LEARNED FROM ROAD TRANSPORT

A. Godet[1], J. T. Saber, J. N. Nurup, G. Panagakos[1], M. B. Barfod[1]

ABSTRACT

In recent years, international shipping has received considerable attention with regard to reducing its greenhouse gas (GHG) emissions. While efficient ships are key, benchmarking the energy efficiency of ships is not straightforward. Technical indicators, such as the EEDI (Energy Efficiency Design Index), reflect a ship's efficiency in ideal conditions (calm sea, no wind, fully laden, design speed). In contrast, operational indicators, such as the EEOI (Energy Efficiency Operational Index), are affected by factors either completely out of the operator's control (weather conditions, etc.) or partially controllable due to market conditions (volume of cargo, speed, etc.). In its way towards decarbonization, the maritime industry needs a realistic benchmarking tool for ship energy efficiency that considers both technical and operational aspects. The automotive industry has been using driving cycles for decades to test and assess the efficiency of vehicles in terms of air pollutants, and more recently, GHG emissions. This concept does not exist in maritime transport, at least not in formal policy-making. This work investigates the possibility of applying the concept of operational cycles in the maritime industry based on experiences acquired from the automotive driving cycles. More specifically, we will: (i) present the motivations for developing operational cycles for ships, (ii) provide an overview of the methods and uses of the driving cycles in road transport, and (iii) suggest an initial procedure for developing these cycles in maritime transport, including the data needed. A literature review identifies the development and use of the driving cycles, the methodologies applied worldwide, and the benefits and limitations of the different types of driving cycles. We also identify the few applications of operational cycles in the maritime industry. The lessons learned from the automotive industry form the foundation for discussing the possibility of applying this concept in the maritime sector, considering the differences between the two industries. We identify the necessary data, and we discuss further development work along with the potential use of these cycles as a tool for enhancing policy-making and ultimately improving the design of efficient ships.

KEY WORDS

Operational cycle; Automotive industry; Maritime transport; Decarbonization; Benchmarking; Maritime policy.

INTRODUCTION

In recent years, international shipping has received considerable attention with regard to reducing its greenhouse gas (GHG) emissions. While efficient ships are key, benchmarking the energy efficiency of ships is not straightforward. Technical indicators, such as the Energy Efficiency Design Index (EEDI), reflect a ship's efficiency in ideal conditions (calm sea, no wind, fully laden, design speed), which is not representative of actual sailing conditions (Lindstad et al 2019; Panagakos et al 2019). In contrast, operational indicators, such as the Energy Efficiency Operational Index (EEOI), are affected by factors either completely out of the operator's control (weather conditions, etc.) or partially controllable due to market conditions (volume of cargo, speed, etc.). In its way towards decarbonization, the maritime industry needs a realistic benchmarking tool for ship energy efficiency that considers both technical and operational aspects. The automotive industry has been using driving cycles for decades to test and assess the efficiency of vehicles in terms of air pollutants, and more recently, GHG emissions. This concept does not exist in maritime transport, at least not in formal policy-making.

A driving cycle is a time series of vehicle speeds developed to represent typical driving patterns (Achour and Olabi 2016). Regulators use the cycles to normalize the test procedures for assessing the fuel consumption of vehicles and related pollutant emissions. In the early 1970s, the European Union (E.U.), the United States (U.S.), and Japan started developing the first driving cycles for legislation and labeling (Gieseke and Gerbrandy 2017;

[1] Department of Technology, Management and Economics, Technical University of Denmark, 2800 Kongens Lyngby, Denmark

U.S. Environmental Protection Agency 2020). A driving cycle intends to reproduce, in a test facility, the real-world operating conditions of a vehicle for a given geographical area and period. Nevertheless, the standard driving cycles have historically struggled to represent actual driving conditions (Joumard et al 2000). A driving cycle consists of four main modes: acceleration, deceleration, stop, and running (André 1996).

This work investigates the possibility of applying the concept of operational cycles in the maritime industry based on experiences acquired from the automotive driving cycles. More specifically, the work will: (i) present the motivations for developing operational cycles for ships, (ii) provide an overview of the methods and uses of the driving cycles in road transport, and (iii) suggest an initial procedure for developing these cycles in maritime transport, including the data needed.

METHODS

Fostered by 50 years of development of the driving cycles, the automotive industry serves as the basis for our analysis. We reviewed the literature to identify the further developments of the driving cycles, the methodologies applied worldwide, and the benefits and limitations of the different types of driving cycles. The review is limited to English literature, including scientific articles, technical reports, and regulatory directives.

Additionally, we searched for applications of operational cycles in the maritime industry using the following search string: *("Operational profile" OR "Driving cycle" OR "Operational cycle") AND ("Ship" OR "Maritime") AND "Emission" AND NOT "Energy management*." We found 66 articles, among which we identified only four articles relevant to the study.

DEVELOPMENT OF DRIVING CYCLES IN THE AUTOMOTIVE INDUSTRY

Overview of the Standard Driving Cycles

We present in the following subsection standard driving cycles developed worldwide since 1970. While academia and the industry proposed numerous cycles over time, we selected cycles adopted by countries or regions for their regulation.

European Union: ECE-15 to NEDC. The E.U. developed its first driving cycle for light-duty vehicles (LDV), called ECE-15, describing urban driving (speed under 50 km/h), in 1970 for regulation on emission standards (Gieseke and Gerbrandy 2017). In 1990, the E.U. introduced the Extra Urban Driving Cycle (EUDC) for higher speed patterns, such as on highways. In 1997, the E.U. combined four ECE-15 cycles and a EUDC into the New European Driving Cycle (NEDC). As shown in Figure 1, the NEDC uses a cold start procedure: the test starts simultaneously as the engine (Gieseke and Gerbrandy 2017).

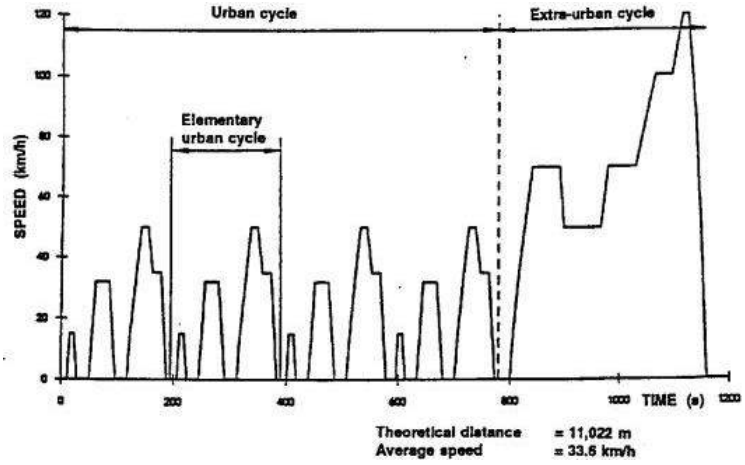

Figure 1: The NEDC combines urban and extra-urban driving cycles (United Nations 2013)

United States: FTP. In 1972, the U.S. developed its first Federal Test Procedure (FTP) for LDVs to describe urban driving. The procedure consisted of a cold phase followed by a stabilized phase (U.S. Environmental Protection Agency 2021). In 1975, the FTP-75 added a hot phase, identical to the cold phase from the FTP-72, as shown in Figure 2. In 1996, the U.S. adopted the Supplemental Federal Test Procedures (SFTP) with two

additional cycles: the US06 cycle describes high-speed conditions and accelerations, and the SC03 cycle reflects the use of air conditioning on engine load and emissions (U.S. Environmental Protection Agency 2021).

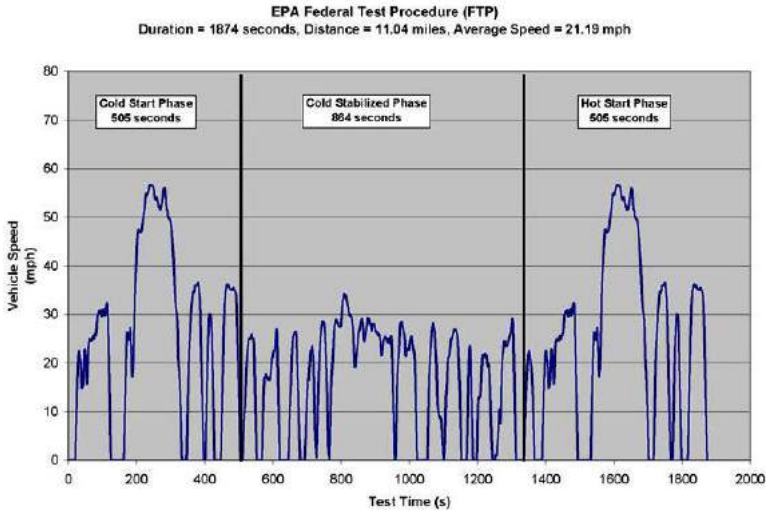

Figure 2: The FTP-75 and its three phases (U.S. Environmental Protection Agency 2020)

Japan: JC08. In 1973, Japan introduced its first driving cycle, called the Japanese 10 Mode, for emission certification of LDVs for urban driving conditions. The cycle starts with a 15 minutes warm-up. In 1991, Japan developed the 10-15 mode driving cycle, adding higher speed (up to 70 km/h) to the 10-mode cycle. The JC08 cycle replaced the 10-15 mode in 2005 (MLIT n.d.). It accurately represents congested city traffic by including idling periods and alternating acceleration and deceleration (Tutuianu et al 2015). Besides, the JC08 differentiates from the previous cycle by adding a cold cycle to represent real-world driving better.

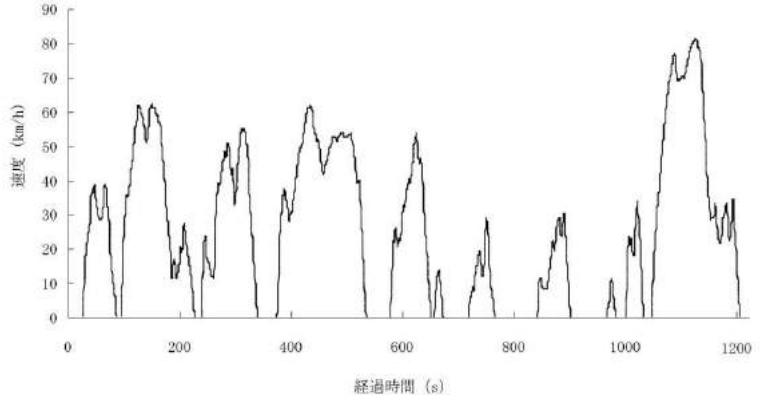

Figure 3: JC08 cycle. X-axis is time (s) and Y-axis is speed (km/h) (MLIT n.d.)

WLTC: Worldwide. The Working Party on Pollution and Energy from the United Nations Economic Commission for Europe (UNECE) developed the Worldwide harmonized Light vehicles Test Procedure (WLTP) and the Worldwide harmonized Light vehicles Test Cycles (WLTC). The WLTP and WLTC form a basis for the emission regulations of LDVs within regional type approval and certification procedures. The WLTC aims at developing a globally harmonized and applicable cycle representative of real-world vehicle performance in terms of emissions and energy consumption (European Commission 2018). A harmonized cycle allows more efficient development of and adaption to technical progress and knowledge sharing between the authorities, which is interesting for the regulators (Riemersma 2015). As shown in Figure 4, the WLTC consists of several driving cycles for vehicles with different power-to-mass ratios (PMR), which measures the actual engine's performance. The E.U. moved from NEDC to the WLTC in 2017 for type approval testing of emission and fuel consumption from LDVs, and revised the emission standards legislation (European Commission 2018). Table 1 provides an overview of the standard driving cycles developed worldwide since 1970.

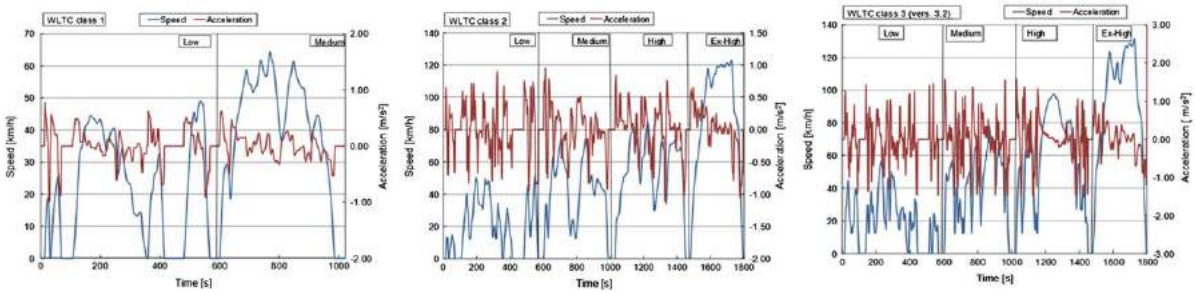

Figure 4: WLTC (Class 1: PMR < 22 kW/ton; Class 2: 22 kW/ton < PMR < 34 kW/ton; Class 3: PMR > 34 kW/ton) (Tutuianu et al 2015)

Table 1: Standard driving cycles for light-duty vehicles (European Commission 2018; Gieseke and Gerbrandy 2017; Riemersma 2015; Tutuianu et al 2015)

Region	Effective from	Cycle name	Average speed incl. stops [km/h]	Max speed [km/h]	Maximum acceleration [m/s^2]	Idle time [s]	Duration [s]	Distance [km]	Cold/ Hot start
EU	1970	ECE-15	18.4	50	1.04	57	195	4.0	Hot
EU	1990	EUDC	62.6	120	0.83	39	400	7.0	Hot
EU	1997	NEDC	33.4	120	1.04	267	1180	10.9	Cold
U.S.	1972	FTP-72	31.5	91	1.83	253	1400	12.1	Cold
U.S.	1975	FTP-75	34.1	91	1.83	362	1877	17.8	Hot & Cold
U.S.	1996	SFTP (US06)	77.9	129	4.64	41	596	12.8	Hot
U.S.	1996	SFTP (SC03)	34.8	88	N/A	N/A	596	5.8	Hot
U.S.	2008	FTP (20F)	31.0	91	1.83	253	1400	12.1	Cold
Japan	1973	10 mode	17.7	40	N/A	N/A	1350	6.6	Hot
Japan	1991	10-15 mode	22.7	70	N/A	N/A	660	4.2	Hot
Japan	2005	JC08	24.4	81	N/A	N/A	1204	8.2	Hot & Cold
Global	2017 (in EU)	WLTC	53.3	131	1.58	226	1800	23.2	Cold

VECTO. The driving cycles previously presented concern LDVs. The European Commission has developed a different methodology for certifying heavy-duty vehicles (HDVs) with regard to CO_2 emissions. The methodology is known as the Vehicle Energy Consumption Calculation Tool (VECTO) (Zacharof and Fontaras 2016). The VECTO approach consists of four elements: 1) specific component test procedures for the main fuel efficiency components (engine, transmission, torque components, axle, air drag, and tires); 2) standardized pre-processing tools to account for auxiliaries like cooling fans, steering pumps, the electrical system, pneumatic systems, and the air-conditioning systems; 3) the simulation VECTO tool itself; and 4) the implementation of the above methods. VECTO calculates CO_2 emissions based on test cycles. These cycles define the speed the driver is supposed to reach or to which traffic dictates. Since HDVs serve different missions, ten test cycles exist to test HDVs through simulation: long haul, regional delivery, urban delivery, construction, and municipal utility for trucks; Citybus heavy Urban, Citybus Urban, Citybus suburban, Interurban bus, and Coach for buses.

Limitations of Standard Driving Cycles

While the NEDC is simple to drive and easy to repeat, it does not represent real-world emissions (Gieseke and Gerbrandy 2017; Pelkmans and Debal 2006; Tsiakmakis et al 2017). For example, tests with Portable Emissions Measurement Systems showed that diesel cars exceed the NOx emissions measured with the NEDC by more than 200% (Degraeuwe and Weiss 2017). While the JC08 reflects actual driving behaviors in congested traffic situations in a city, it does not describe other driving conditions and road types. The FTP covers a broader range of driving conditions without covering all driving cases. While driving cycles underestimate real-world emissions, the WLTC estimates are the closest to real-world emissions (Chindamo and Gadola 2018). A more realistic driving cycle should account for higher acceleration and deceleration values (Chindamo and Gadola 2018).

Additionally, limitations include the simplification of describing actual driving through a target speed, the variety of operations resulting in diverse driving conditions, and the absence of external parameters, such as the road and traffic conditions (Pettersson et al 2018). Addressing these limitations would ensure a fair comparison between different vehicle concepts in a simulated environment. Pettersson et al. (2019) proposed the idea of operational cycles for heavy-duty vehicles to cope with these limitations by including the following parameters: the mission, the traffic, the road conditions, and the weather. The mission reflects the need a vehicle meets, which can be the transportation of goods or people. The traffic explains the impact of various elements, such as other vehicles and traffic lights. The road conditions describe the time constant infrastructure and the road's physical properties. The weather describes physical surroundings, excluding the road, as a function of the position, which is not suited for long missions (Pettersson et al 2019).

Even if the WLTP presents limitations, it responded to a global incentive for one harmonized cycle and addressed drawbacks from previous cycles. We chose the WLTP as a model for the maritime industry due to its international nature, essential for the shipping industry, and its foundation on actual operational data, which appears more accurate and feasible to reproduce within the maritime sector.

WLTP methodology

The WLTP developed the test cycle and the test procedure as separate workstreams. While the cycle should represent average real-world vehicle operation, the procedure should comprise a method to determine emissions and energy consumption levels in a repeatable, reproducible, cost-efficient, and practical manner (Riemersma 2015). We describe the methodology used for developing the WTLP in the following paragraphs. Figure 5 summarizes the procedure.

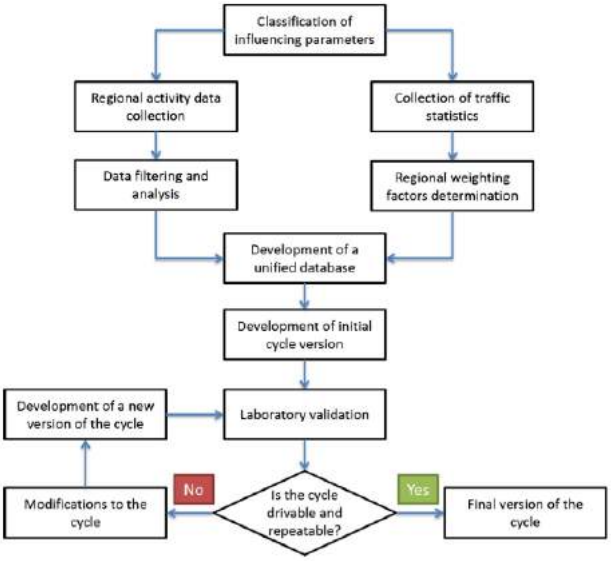

Figure 5: Flow diagram of WLTC development (Tutuianu et al 2015)

Real-world data from five regions (Europe, India, Japan, Korea, and the U.S.) for different road types (rural, urban, motorway) and driving conditions (peak, off-peak, weekend) served as the basis to build the WLTC (Tutuianu et al 2015). The influencing parameters include driving behavior data (speed and acceleration profiles) and traffic statistics for LDVs. The analysis of the most critical parameters led to two observations: 1) activity data for each region is necessary to derive the driving behaviors for each road category (urban, rural, and motorway); 2) regional weighting factors determined by traffic statistics allow to merge all the regional activity databases into one database (Tutuianu et al 2015).

Real-world traffic data, including vehicle's speed and acceleration and engine speed at a frequency of at least 1 Hz, were collected for 441 vehicles equipped with onboard data acquisition systems. The participating countries used different data collection methods. Japan, Korea, and India used instructed drivers (hired vehicles and drivers with a predefined route). Europe used customer data, i.e., data from vehicles with drivers, without instruction on how to drive the car. The U.S. submitted both customer data and instructed drivers using the chase car method, which uses an instrumented vehicle that follows a target vehicle in the traffic stream and mimics its behavior. While instructed drivers allow for planning the data collection to represent the targeted region, they do not describe actual driving behavior. Allowing data collection with both approaches is more comprehensive and reduces the effect of the most extreme driving behaviors (Tutuianu et al 2015).

The definition of idling periods and short trips allowed the creation of databases for each region and each part of the cycle (urban, rural, and motorway). A short trip occurs when the vehicle is between two idling periods and consists of three driving modes: acceleration, deceleration, and cruise. Idle periods occur when the vehicle speed is lower than 5 km/h. A set of elimination criteria on phase duration and acceleration ranges was applied to improve statistical representativeness and the feasibility of the laboratory tests, such as the maximum duration of the WLTC, which is 1800 seconds (Tutuianu et al 2015).

Regional weighting factors compensate for various driving behaviors in different areas (Tutuianu et al 2015). A global harmonized cycle requires developing speed classes instead of road categories to deal with varying speed limits globally. Therefore, Low (L), Medium (M), High (H), and Extra-high (Ex-H) replaced the urban, rural, and motorway categories. The short trips of the cycle are selected from the unified database to ensure representativeness of the speed and acceleration distributions. The selection is accomplished through a χ^2 test that measures the level of discrepancy between the samples (Corder and Foreman 2011; Tutuianu et al 2015). The first version of the WLTC resulted in the combination of short trips with the smallest χ^2. Laboratories from all participating regions tested the first WLTC to investigate whether the cycle was driveable and repeatable. The test results led to several modifications (Tutuianu et al 2015): 1) limit the maximum acceleration phases to the 95th percentiles for the cumulative frequency distribution for each speed phase; 2) set the maximum deceleration to 5.31km/h/s, which is appropriate to avoid wheel lock and shortage of brake power; 3) smooth small fluctuations in the speed profiles to improve the cycle's driveability; 4) redesign the Ex-H speed phase by combining different segments of existing short trips; 5) select the new combination with the smallest χ^2 value for the final WLTC; 6) adapt the cycle into three classes according to the vehicle's PMR.

FROM THE AUTOMOTIVE INDUSTRY TO THE MARITIME INDUSTRY

The International Maritime Organization (IMO) established emission reduction goals for 2030 and 2050, with technical and operational measures to reach the targets (IMO 2018). Indicators track the efficiency of these measures on a ship level. Currently, the EEDI is the only mandatory indicator and it measures a ship's efficiency under specific conditions (loading conditions, speed, and sea conditions). While operational indicators, such as the Carbon Intensity Indicator (CII), can better reflect actual efficiency, they are affected by external factors (sea and market conditions, port organization, etc.). It is essential to combine technical and operational aspects to reflect real-life emissions from a ship. While driving cycles in the automotive industry present some drawbacks, as mentioned in the previous section, the wide use of driving cycles for regulation and setting standards prove to be an efficient tool for benchmarking. Developing similar procedures in maritime could help benchmark the energy efficiency of ships. Besides, as ships can be optimized to improve their EEDI for specific conditions, an operational cycle including various operating conditions could prevent ships from performing poorly when not sailing to their design conditions. In summary, our motivation to develop operational cycles for the maritime industry is to create a benchmarking tool that better reflects real-life operations.

Cases from the literature

The benchmark of ship emissions does not currently rely on operational cycles. Norbakyah et al. (2015) tested an operational profile on Plug-in Hybrid Electric Recreational Boats (PHERB) for a specific route in Malaysia. A profile was created by monitoring a PHERB with a GPS to obtain speed-time data from 20 runs on a regular route of the Kuala Terengganu river. After calculating the mean values of the explanatory variables (average speed, acceleration, deceleration, driving period, idling time, cruise time, acceleration time, deceleration time), the most representative profile was selected as the voyage with the lowest percentage difference from the mean values (refer to Figure 6). The same authors applied the methodology to the Seberang Takir and Kampung Laut rivers, located in Malaysia (Atiq et al 2015; Norbakyah et al 2015; Salisa et al 2015). To our knowledge, the mentioned studies are the only ones to use the term 'driving cycle' for a maritime vessel.

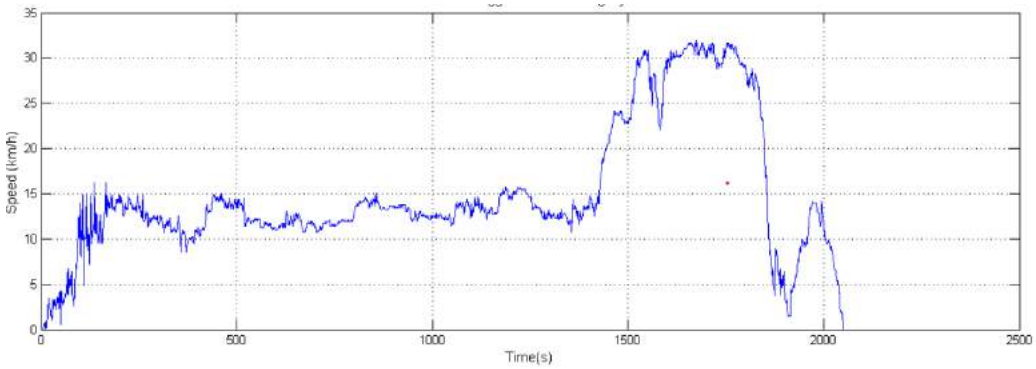

Figure 6: The Kuala Terengganu river profile (Norbakyah et al 2015)

A ship's fuel consumption depends on its operations. When a ship sails at a low speed, it reduces the fuel consumption per cargo transported, assuming that no other ship fills the gap in the market (Trivyza et al 2016). A study on an Aframax tanker ship identified four operation modes: ballast, laden, port loading, and port unloading (Trivyza et al 2016). While driving cycles use absolute time and speed, Figure 7 shows speed profiles as a percentage of the time derived from a voyage from the Persian Gulf to North America. Based on two speed distributions (ballast, laden), Trivyza et al. (2016) defined three operational profiles: a base case, a lower speed case (1 knot lower than the base case), and a higher speed case (1 knot higher than the base case).

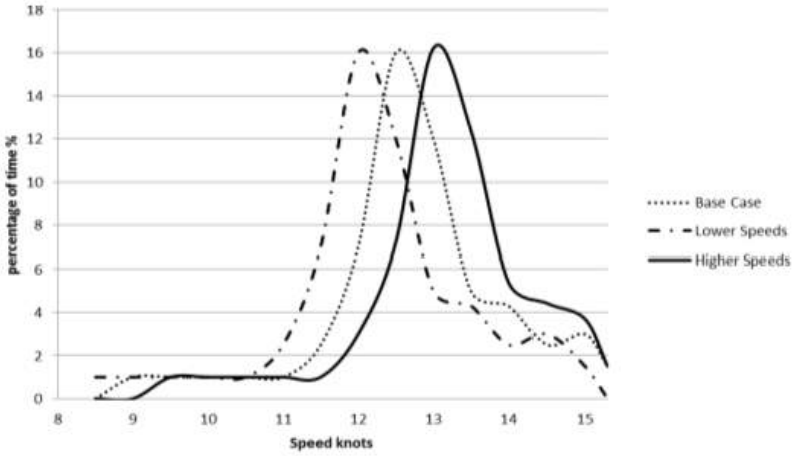

Figure 7: Three different operational profiles (Trivyza et al 2016)

Another study focuses on a cruise ship operating daily in the Baltic Sea (Baldi et al 2018). Data derived from a monitoring system logging data from the engines every 60 seconds revealed that the cruise ship was seagoing 59% of the time, maneuvering 7% of the time, and at port 34% of the time. Baldi et al. (2018) developed an operational profile, shown in Figure 8, to maximize energy efficiency and reduce fuel consumption.

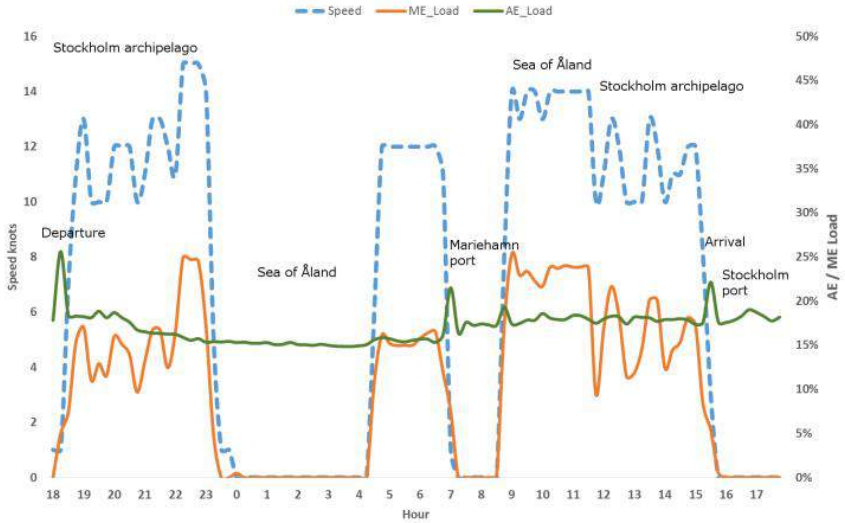

Figure 8: The operational profile of a cruise ship (Baldi et al 2018)

Lessons Learned from the Automotive Industry

This section discusses methodological advantages and issues from the automotive industry, which are relevant to further developing operational cycles in the maritime sector. While specific driving cycles can test LDVs, HDVs, tested using VECTO, need different benchmarking baselines according to their missions. Ship operations differ significantly depending on the ship type and size. Therefore, operational cycles for different size ranges of any given segment, such as containerships, will prove to be more relevant. Nevertheless, we need to balance the level of detail for a typical operational cycle with the risk of becoming too specific and inappropriate for benchmarking.

The European Commission examined four options for HDV CO_2 certification: engine test, chassis dynamometer test, on-road test, component test, and vehicle simulation (Magagna et al 2018). They concluded that vehicle simulation based on driving cycles was the best way to benchmark emissions from HDVs. In the maritime industry, the engine test can quickly assess CO_2 emissions. However, the engine test only measures CO_2 emissions per kWh rather than per km and ignores other parameters, such as the hull form. While the chassis dynamometer test is not feasible for ships, towing tanks test the model of a ship during its design. The tests suggest the ship's behavior in realistic conditions. Nevertheless, results produced from towing tank tests correspond to specific loading conditions, speed, and sea state, making the hull optimization dependent on these conditions.

Furthermore, sea trials equate to on-road tests and calculate the ship's total fuel consumption. Sea trials supplement towing tank results. However, sea trials are performed only for calm sea and fully laden conditions. Simulation can estimate a ship's fuel consumption and is cost-efficient, flexible, and reproducible. However, there might be a gap between the simulation results and the real-world emissions, and if this gap grows too large, the test might lose credibility. Similar to the automotive industry, benchmarking in maritime transport can be performed by simulation guided through standard operational cycles and supported by engine and towing tank results.

An Initial Procedure to Develop Operational Cycles for the Maritime Sector

This section proposes a methodology to develop operational cycles for ships inspired by WLTP. The methodology accounts for the differences between the automotive and shipping industries. While WLTP uses the term 'Short trip' to describe a trip between two idling periods, we refer to a sea passage between two port stays with the term 'Leg.' An 'idling period' describes a port stay. We present in the following section a preliminary procedure, illustrated in Figure 9, to develop an operational cycle that is representative of sailing conditions around the world. We discuss the similarities and deviations from the WLTP approach to fit the maritime context.

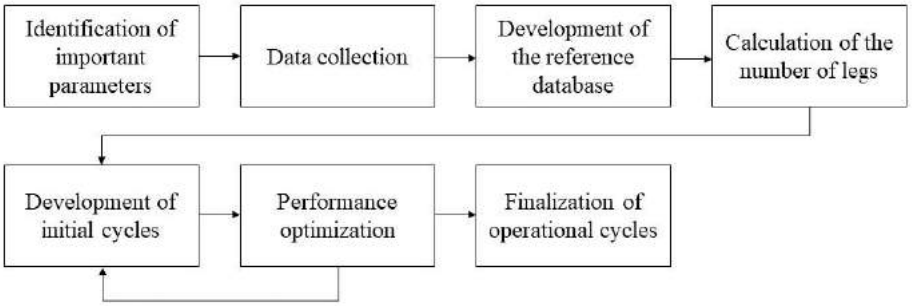

Figure 9: Procedure to develop operational cycles for the maritime industry

Identification of important parameters. The WLTP uses speed and acceleration as selection criteria to find the most representative driving cycle. In shipping, most of the acceleration and deceleration happens when a vessel leaves and approaches ports. As ships tend to sail at a constant speed, we suggest not including acceleration as an essential parameter. Instead, we consider other factors: speed, revolutions per minute (RPM), and draught are the main determinants of a ship's fuel consumption (Bialystocki and Konovessis 2016; Işıklı et al 2020). We suggest including the draft to reflect on loading conditions and the speed, which is the primary determinant of fuel consumption, to develop operational cycles.

Data collection. Data from several vessels worldwide is crucial to represent the global context. Each segment (container ships, bulk carriers, etc.) should have its profiles, reflecting typical operations. According to the IMO bin classification, we can divide vessels into size groups to improve the accuracy of the operational cycles (Faber et al 2020). Operating data can derive from noon reports or onboard monitoring systems. The crew produces noon reports daily with standardized data, such as draft and speed, to assess a ship's performance. Nevertheless, the

frequency of noon reports, usually 24 hours, is significantly lower than the 10-seconds intervals of WLTC. Therefore, higher-frequency data, such as Automatic Identification System (AIS) data, should be preferred.

Development of reference database. Like the WLTC approach, the leg database consists of all the sea reports, while the idling database includes the port stays.

Calculations for the number of legs. We want to calculate the number of legs required to generate the operational cycles. Following the WLTC approach, we split the legs into three speed categories (low, medium, and high speed), containing the same number of legs. Therefore, the threshold values are dynamic and depend on the size group. The number of legs for each speed category depends on the phase duration. The WLTC duration is 600 seconds for each speed category, for a total duration of 1800 seconds. This duration is not suitable for maritime operations. Firstly, ships accelerate and decelerate significantly less than cars, likely resulting in a steady-state for 1800 seconds. Secondly, if we use noon reports, the data frequency requires a longer cycle duration. Consequently, we suggest one month for each speed category, for a total of three months. We calculate the total number of legs required for each speed category to reach one month using the following formula:

$$N_{Leg,i} = \frac{P_i - \overline{I_\iota}}{\overline{Leg} + \overline{I_\iota}} \quad [1]$$

where P_i is the phase duration, $\overline{Leg}$ is the average leg duration, and $\overline{I_\iota}$ is the average idling duration (Tutuianu et al 2015). Since the cycle starts and ends with a leg, there is one less idling period than the number of legs.

Development of initial cycles. We discuss two methods for selecting the most representative combination of legs. The WLTC approach uses the χ^2-method to test all possible combinations of legs and idling periods and chooses the lowest χ^2 value as the operational cycle. Unfortunately, the computational time for this approach is high and might be a limiting factor. We can decrease the number of legs in the database by excluding all the legs that deviate by more than one standard deviation from the mean. Inspired by the Kuala Terengganu river profile, the second method is to sum the normalized absolute difference from the mean and use the sum of these differences over all variables to find the most representative legs. We can use the absolute difference from the mean idling duration to find the most representative idling periods. Finally, we can combine the best performing legs and idling periods in a randomized order to generate the operational cycle.

Performance optimization and finalization of operational cycles. The cycle's optimization highly depends on the results for the initial cycles and will be the object of further work. For example, we could optimize the performance by modifying the influencing parameters, including the RPM or the cycle's duration. We can also compare the results from noon reports or AIS data. We will address these questions in further work.

CONCLUSION

Motivated by the need to track decarbonization in the shipping industry, we looked at driving cycles in the automotive industry over the decades. We investigated the standard driving cycles, their advantages, and their limitations. We focused more specifically on the WLTP, the harmonized global driving cycle already applied by the E.U. We detailed the methodology to develop the WLTP. Then, we discussed the application of operational cycles in the maritime industry, considering the differences between the automotive and maritime industries. The literature revealed three cases of operational profiles for ships without concrete generalized results. To our knowledge, the idea of using operational cycles to benchmark ship efficiency is new in the literature. We proposed a procedure to develop such cycles for ships. Further work will consist of applying this procedure and creating these cycles for different ship sizes and types, addressing challenges specific to maritime transportation, such as weather and sea conditions, market conditions and current regulations in terms of energy efficiency.

ACKNOWLEDGEMENTS

The work presented in this paper results from the master thesis of Jacob Normann Nurup and Jonas Thoustrup Saber, "Applying data analysis to define operational profiles for container ships" (2021).

REFERENCES

ACHOUR, H., and A. G. OLABI. "Driving cycle developments and their impacts on energy consumption of transportation." *Journal of Cleaner Production*, **112** (2016): 1778–1788.

ANDRÉ, M. "Driving Cycles Development: Characterization of the Methods." *International Spring Fuels & Lubricants Meeting*, (1996).

ATIQ, W. H., J. S. NORBAKYAH, et al. "ST river driving cycle characterization." *ARPN Journal of Engineering*

and Applied Sciences, **10**:18 (2015): 8511–8515.
BALDI, F., F. AHLGREN, et al. "Energy and Exergy Analysis of a Cruise Ship." *Energies*, **11**:10 (2018): 2508.
BIALYSTOCKI, N., and D. KONOVESSIS. "On the estimation of ship's fuel consumption and speed curve: A statistical approach." *Journal of Ocean Engineering and Science*, **1** (2016): 157–166.
CHINDAMO, D., and M. GADOLA. "What is the Most Representative Standard Driving Cycle to Estimate Diesel Emissions of a Light Commercial Vehicle?" *IFAC-PapersOnLine*, **51**:5 (2018): 73–78.
CORDER, G. W., and D. I. FOREMAN. *Nonparametric Statistics for Non-Statisticians: A Step-by-Step Approach* (2011). John Wiley & Sons, Inc.
DEGRAEUWE, B., and M. WEISS. "Does the New European Driving Cycle (NEDC) really fail to capture the NOX emissions of diesel cars in Europe?" *Environmental Pollution*, **222** (2017): 234–241.
EUROPEAN COMMISSION. *COMMISSION REGULATION (EU) 2018/1832* (2018).
FABER, J., S. HANAYAM, et al. "Fourth IMO Greenhouse Gas Study 2020." In *International Maritime Organization (IMO)* (2020).
GIESEKE, J., and G.-J. GERBRANDY. *Report on the inquiry into emission measurements in the automotive sector (2016/2215(INI))* (2017).
IMO. "Initial IMO Strategy on reduction of GHG emissions from ships." *MEPC.304(72)*, (2018).
IŞIKLI, E., N. AYDIN, et al. "Estimating fuel consumption in maritime transport." *Journal of Cleaner Production*, **275** (2020): 124142.
JOUMARD, R., M. ANDRÉ, et al. "Influence of driving cycles on unit emissions from passenger cars." *Atmospheric Environment*, **34**:27 (2000): 4621–4628.
LINDSTAD, E., H. BORGEN, et al. "The Need to Amend IMO's EEDI to Include a Threshold for Performance in Waves (Realistic Sea Conditions) to Achieve the Desired GHG Reductions." *Sustainability*, **11**:3668 (2019).
MAGAGNA, D., L. MARGHERITINI, et al. "Workshop on identification of future emerging technologies in the ocean energy sector - 27th March 2018, Ispra, Italy." In D. Magagna & L. Margheritini (Eds.), *EUR 29315 EN* (Issue March) (2018).
MLIT. *Appendix 42 Measurement method of light and medium-sized vehicle exhaust gas - JC08 mode method* (n.d.).
NORBAKYAH, J. S., W. H. ATIQ, et al. "Power requirements for PHERB powertrain." *IOP Conference Series: Materials Science and Engineering*, **100** (2015): 012035.
PANAGAKOS, G., T. de S. PESSÔA, et al. "Monitoring the carbon footprint of dry bulk shipping in the EU: An early assessment of the MRV regulation." *Sustainability (Switzerland)*, **11**:18 (2019).
PELKMANS, L., and P. DEBAL. "Comparison of on-road emissions with emissions measured on chassis dynamometer test cycles." *Transportation Research Part D*, **11**:4 (2006): 233–241.
PETTERSSON, P., S. BERGLUND, et al. "A proposal for an operating cycle description format for road transport missions." *European Transport Research Review*, **10**:31 (2018).
PETTERSSON, P., P. JOHANNESSON, et al. "A statistical operating cycle description for prediction of road vehicles' energy consumption." *Transportation Research Part D: Transport and Environment*, **73** (2019): 205–229.
RIEMERSMA, I. *Technical Report on the development of a World-wide Worldwide harmonised Light duty driving Test Procedure (WLTP)* (Issue Informal document no. GRPE-72-02) (2015).
SALISA, A. R., W. H. ATIQ, et al. "Development of a KL river driving cycle for PHERB powertrain." *Jurnal Teknologi*, **76**:8 (2015): 101–106.
TRIVYZA, N. L., A. RENTIZELAS, et al. "The influence of ship operational profile in the sustainability of ship energy systems." *International Conference of Maritime Safety and Operations 2016*, (2016).
TSIAKMAKIS, S., G. FONTARAS, et al. "From NEDC to WLTP: effect on the type-approval CO2 emissions of light-duty vehicles." In *EUR 28724 EN* (2017).
TUTUIANU, M., P. BONNEL, et al. "Development of the World-wide harmonized Light duty Test Cycle (WLTC) and a possible pathway for its introduction in the European legislation." *Transportation Research Part D*, **40** (2015): 61–75.
U.S. ENVIRONMENTAL PROTECTION AGENCY. *EPA Federal Test Procedure (FTP)* (2020).
U.S. ENVIRONMENTAL PROTECTION AGENCY. *Protection of Environment, Part 86: Control of Emissions from New and In-use Highway Vehicles and Engines* (2021).
UNITED NATIONS. *E/ECE/324/Rev.2/Add.100/Rev.3 Agreement Concerning the Adoption of Uniform Technical Prescriptions for Wheeled Vehicles, Equipment and Parts which can be fitted and/or be used on Wheeled Vehicles and the Conditions for Reciprocal Recognition of Approvals* (2013).
ZACHAROF, N.-G., and G. FONTARAS. *Report on VECTO Technology Simulation Capabilities and Future Outlook* (EUR 28272 EN) (2016). Article EUR 28272 EN.

DECARBONIZE GLOBAL SHIPPING: LESSONS LEARNED FROM COVID-19 PANDEMIC RESPONSE

Lamin Jawara[1]

ABSTRACT

The COVID-19 pandemic, just like climate change, poses one of the greatest challenges to the existence of human life. By measuring and characterizing the spread of the coronavirus and how the world is able to mitigate the spread of the virus could give important insights into how we can potentially deal with global warming and the consequences of carbonization. Using the coronavirus pandemic as an analogy to global climate change, we can conceptualize, measure, communicate and advance theories that can increase our understanding of the risk posed by climate change. Such analogy could also help us identify similarities in structure, quantifying and explaining the highs and lows, and the triggers around such nodes and eventually led to the formation of hypotheses for a wider understanding of future global environmental challenges. The central idea in this study as posited by Gentner is that a relational structure exists between the current covid-19 pandemic and the potential pandemic risks posed by climate change. Using the Structure-mapping theory, the covid-19 pandemic (A) will be referred to as the base and climate change pandemic (B) will be referred to as the target, which allows us to map from A to B creating the analogy. An analogy is created when a relational predicate is mapped from base to target with or without consideration of an object attribute. In order to develop an analogy using covid-19 (A) as the base of the derived knowledge, synthesization of time series on the available covid-19 responses is required. The rational predicates used will be major events and responses from the World Health Organization and selected countries. International shipping is governed by both domestic and international laws. Regime development and enforcement in the maritime environment is similar to the global health sector. Many studies have documented the relationship between infectious diseases and maritime transport but correlation on how the two sectors deal with global concerns is limited or non-existent. Both sectors rely heavily on national authorities for domestic implementation and enforcement through port state control inspections and flag state responsibilities.

KEY WORDS

Analogy; Anthropogenic; Covid-19; Decarbonization; GHG; Maritime; Pandemic.

INTRODUCTION

Climate change poses one of the greatest challenges to the existence of human life. The main driver for this change is human interference with the climate system through emission of greenhouse gas into the atmosphere. The main greenhouse gases include carbon dioxide, methane and nitrogen dioxide. Anthropogenic greenhouse gas emissions have increased largely with economic and population growth as the main driving force (Ipcc, 2014). Shipping, being the backbone of global economic development and trade, is the principal carrier of world trade of up to 90% by volume and a major contributor to anthropogenic greenhouse gas emission (IMO, 2015). From 2012 to 2018, greenhouse gas (GHG) emissions from shipping

[1]Doctorate student in Maritime Affairs, World Maritime University
Correspondence: World Maritime University, 211, 18 Malmo, Sweden
Email: w1903510@wmu.se

have increased from 977 million tonnes to 1,076 tonnes, an increase of 9.6% due to increased international maritime trade (IMO, 2020). The contribution of shipping to global anthropogenic GHG emissions has increased from 2.76% in 2012 to 2.89% in 2018, making it a major contributor to anthropogenic GHG emissions (IMO, 2020). In the absence of mitigation measures and based on existing economic and energy models, emission from shipping is projected to increase from 90% in 2018 to 90-130% in 2050 using 2008 as the baseline year.

Anthropogenic greenhouse gas emissions from international shipping are on the increase with instances of decline related to reduced economic activities. Operational solutions proposed are also related to reducing or slowing down economic activities of shipping through speed reduction measures. According to data compiled by four difference international scientific bodies; Japanese Meteorological Agency, NASA GISS, the National Oceanic and Atmospheric Administration (NOAA) National Climatic Data Center and the Met Office Hadley Centre in the United Kingdom, the earth's temperature is on the rise and with current mitigation measures global temperature rise is expected to reach 2.7 degrees by the end of this century (UNEP, 2021). Questions are posed: Would this be the beginning of a pandemic? How would the world respond to such a pandemic? What would be the likely contribution of shipping? Would the lessons learned from Covid-19 pandemic response be valuable in such a situation?

However, since all the sign of climate change including flooding, droughts, wildfires, hurricanes, heat waves, seawater rise are already seen around the world at various times and diverse places resulting to thousands of fatalities or displacement and economic lost measured in trillions (UNEP. 2021), could we assume that the climate change pandemic had already began and that the world is not recognizing the beginning because of time-scale masking?

By measuring and characterizing the spread of the coronavirus and how the world is able to deal with it could give important insights into how we can potentially deal with the consequences of climate change. Climate change is characterized by global warming with sea level rise, severe or inclement weather including floods, droughts, wildfires, hurricanes and heatwaves (UNEP, 2021). The central question in this paper is at what level would global warming be regarded as a pandemic, assuming mitigation measures are unable to cap greenhouse gas emission as it continues to rise; in such a scenario what would constitute the contribution from international shipping towards mitigation of potential global pandemic? The objective of this paper is to analyze this scenario and investigate if lessons learned from the Covid-19 pandemic could be applicable to a climate change pandemic triggered by global warming and what role international shipping is likely to play.

The aim of this paper is to deal foremost with the global picture of climate change not only from the perspective of international shipping but from the broad perspective of how the world is dealing with the issue and to relate the consequences to the current covid-19 pandemic. This work is expected to address the problem of the subject matter and lay the groundwork for research into the contribution of global shipping towards a carbon-free and a greener world.

METHOD

The first two steps in the methodology used in this research paper is data collected from available and relevant literature on climate change and covid-19 pandemic and development of a time series to the response of the international community in both cases. The third step is analogical development for correlation of covid-19 and potential climate change pandemic based on data available in literature. Data is collected from the United Nations, its agencies and other international organizations as well as intergovernmental bodies including World Health Organization (WHO), Intergovernmental Panel on Climate Change (IPCC), World Meteorological Organization (WMO), National Aeronautical and Space Administration (NASA) among others.

Analogy and underlying theories

Using the coronavirus pandemic as an analogy to global climate change, we can conceptualize, measure, communicate and advance theories that can increase our understanding of the risk posed by climate change. Such analogies could also help us identify similarities in structure, quantifying and explaining the highs and lows and the triggers around such nodes and

eventually led to the formation of hypotheses for a wider understanding of future global environmental challenges. The central idea in this study is that a relational structure exists between the current covid-19 pandemic and the potential pandemic risks posed by climate change. Using the Structure-mapping theory, the covid-19 pandemic (A) will be referred to as the base and climate change (B) will be referred to as the target, which allows us to map from A to B creating the analogy. "An analogy is a comparison in which relational predicates, but few or no object attributes, can be mapped from base to target" (Gentner, 1983). According to Gentner (1983), showing that the two issues are different, since covid-19 is a health issue and climate change an environmental issue does not weaken the analogy. The important thing to consider is that both have high fatality with serious economic losses, collectively referred to as pandemic and both have global dimensions which can better be managed through international efforts.

Analogy has found applications in a number of disciplines from a variety of perspectives; research on the subject includes natural sciences, cognitive science, education, linguistics, mathematics, philosophy, psychology, and other social sciences (Guarini et al, 2009). Analogy is widely used in education to assess understanding of a particular subject matter and its usage in the school systems (Ugur, 1995; Gokhan, 2012). Gokhan et al (2012) discovered that analogical related teaching has a significantly positive effect on the understanding of the subject matter but no effect on attitude towards the subject under investigation.

Time series characterization of Covid-19 pandemic and Climate Change Responses

Development of time series is important to the overall understanding of how the world was able to respond to the challenges pertaining to Covid-19. Qualitative data from the WHO was used to develop a time series (figure 1). This time-series has given insights into how mitigation measures were taken at every stage of the pandemic. The response timeline now becomes the basis of the derived knowledge as it details lessons learned in dealing with the COVID-19 pandemic. This time-series shall now be referred to as the based knowledge (A).

Therefore, in order to develop an analogy using (A) as the base of the derived knowledge, synthesization of time series on the available timeline compiled by WHO is adopted. Based on the detailed nature of the timeline, not all details could be considered for this paper. Therefore, selected events are considered and adopted as in figure 1. The selected events are the rational predicates adopted for this study.

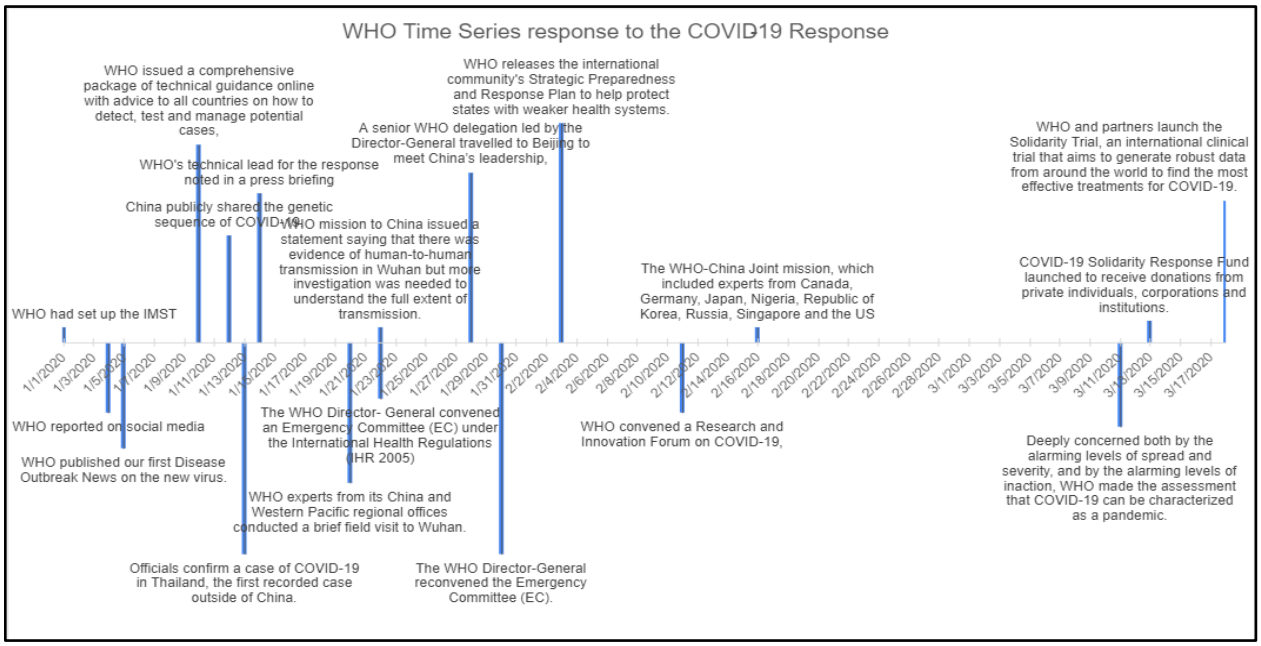

Figure 1: WHO Time Series to the Covid-19 Response

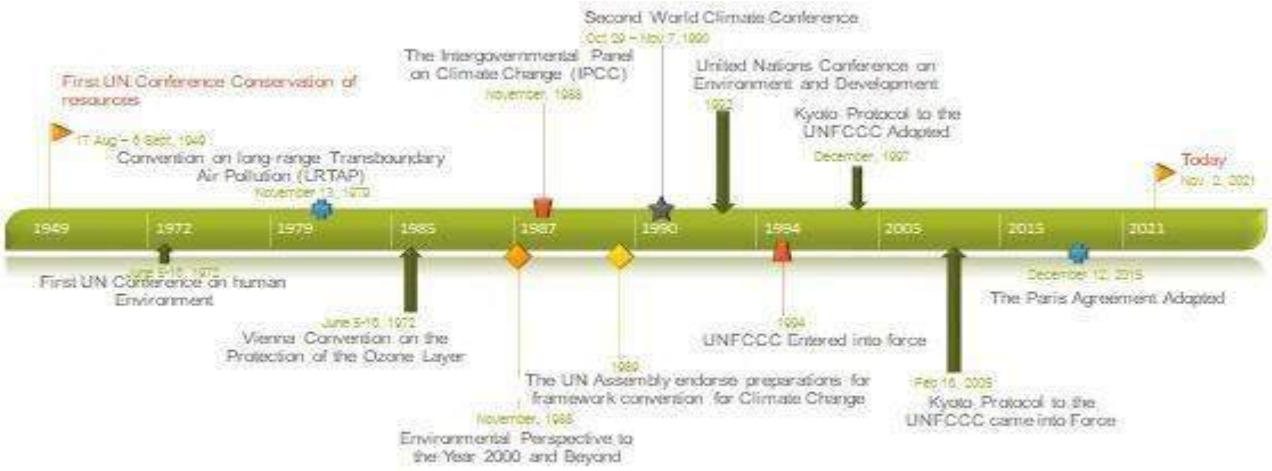

Figure 2: Climate disaster response timeline

Climate change was first recognized in the late 19th century after the development of instruments for measurements of temperature and carbon dioxide. However, global efforts leading to climate actions did not begin until 1949, when the first UN conference on the conservation and utilization of resources was convened to address the social and economic impact on the depletion of natural resources following several decades of inaction by the international community.

LITERATURE REVIEW

Greenhouse Gas Emissions from Shipping is on the Increase

Despite mitigation measures, global annual anthropogenic greenhouse gas emissions continue to increase at an unprecedented rate of 2.2% per annum from 2000 to 2010 compared to 1.3% from 1970 to 2000 (IPCC, 2014). Similar trend exists in shipping though the sector recorded some gains with reduction from 2.8% in 2007 and 2.2% in 2012, but this was mainly attributed to reduced economic activities of international shipping as a result of depressions in market conditions after 2008 (Psaraftis, H. N., & Lagouvardou, S., 2019; IPCC, 2014).

The customary approach to reducing GHG from maritime transport has been through three main measures; technological/ technical measures, logistic based/ operational measures and market-based measures (MBM) (IMO, 2020). Technical measures include efficient engines, optimal ship hull designs, alternate fuels, exhaust gas cleaning technologies, heat recovery systems. Operational measures include speed optimization, weather routing, fleet management and others. MBM include Emission Trading Systems (ETS) and levy on bunker fuel (Psaraftis, H. N., & Lagouvardou, S., 2019).

The target set by IMO to cut shipping emission by at least 50% by 2050 is not close to be achieved under the current IMO strategy. In 2018, the sector was responsible for 937 million tonnes of CO_2 emission which is only 0.3% lower than a decade before (IMO, 2020). As a result, new and novel research into possible solutions to cap the greenhouse gas emissions from shipping as the industry's contribution to avoid global anthropogenic emissions from interfering with the climate system.

IMO's Strategy on the Reduction of Greenhouse Gas from International Shipping

In 2018, after several years of negotiations, the IMO adopted an initial strategy for the reduction of greenhouse gas from shipping with a vision to reach zero emissions by the end of the century. Although the initial strategy was a significant step

towards decarbonizing the shipping sector, the path to achieving zero carbon by the end of the century remains uncertain. However, IMO has introduced two mandatory resolutions to the MARPOL Annex VI; one technical measure on Energy Efficiency Design Index (EEDI) and one operational measure on Ships' Energy Efficiency Management Plan (SEEMP) that is mandatory to ships irrespective of flag and enforced through Port State control (Chircop, 2019; Zhang, 2014).

In light of current trends in economic growth and increased international trade, technical and operational measures alone will not be adequate to reduce greenhouse gas from shipping; a view that is also shared by the International Parcel Tankers Association (IPTA), Cyprus, Denmark, the Marshall Islands and Nigeria (IMO, 2009; IMO, 2020). In a paper sponsored by Cyprus, Denmark, the Marshall Islands, Nigeria and the International Parcel Tankers Association (IPTA) on the establishment of a greenhouse fund for the reduction of emission from shipping and was considered by the Conference of Parties (COP) had called for a comprehensive package for the reduction of greenhouse gas emission from shipping that will include the development of market-based measures by IMO that will complement the technical and operational measures (IMO, 2009). This effort could not be successful without a concerted approach from the international community. The collaborative actions learnt during the peak of the pandemic will play a significant role in the implementation of any mitigation measure towards a potential climate pandemic.

Resilience of International Shipping in an In-pandemic Era

International shipping continues to be resilient amidst challenges from the Covid-19 pandemic keep disruptions to maritime services and supply chain to a minimum. UNCTAD (2020) reviewed that "Business continuity plans and emergency-response mechanisms have never been as vital as in the case of covid-19 crises". Although the crisis had led to a drop in port calls for many vessel types (UNCTAD, 2020) , clearly the general impact of the pandemic on global economy and maritime trade was lightened because of the resilience of the sector.

The maritime sector is governed by both domestic and international laws. Regime development and enforcement in the maritime environment is similar to the global health sector. However, the global health sector has had a fairly stable and consistent implementation regime. Many studies have documented the relationship between infectious diseases and maritime transport (Ruria, 2009). Correlation on how the two sectors deal with global concerns is limited or absent even though the two sectors work together with several commonalities as in the case of the current novel coronavirus disease 2019 (Ghebreyesus & Lim, 2020). Both sectors heavily rely on national authorities for domestic implementation and enforcement through port state control inspections and flag state responsibilities.

DISCUSSIONS

Temperature Anomaly and its Implications on International Shipping

Data from the Intergovernmental Panel on Climate Change (IPCC), (2021) on surface temperature anomaly (figure 3a) which is also consistent with data compiled by NASA Earth Observatory (figure 1) from four different research institutions has shown that the earth's surface temperature is increasing at unprecedented rates. This temperature anomaly resulting from climate change has the tendency to result in extreme weather events. Extreme weather events are defined as a "natural occurrence over a certain time period and space with unusual characteristics in terms of magnitude, location, timing, and/or extent" (WMO, 2021). When such events occur without early warning, they usually lead to detrimental consequences usually leading to high death tolls and economic damage. Ships plying international routes are designed to resist such weather but with the temperature anomaly on the rise leading to more extreme climate events, there is tendency for ships to be redesigned to withstand such extreme weather conditions.

Sea-level rise resulting from climate change has a tendency to affect port infrastructure and potential disruption to port service and overall supply chain (Christodoulou et al, 2018) With the present temperature anomaly trend, storm surges and flash floods are expected to increase in frequency with increased disruptions in port operations. Part of the container stocking

areas of the port of The Gambia is covered by sea during high tide, resulting in loss of container terminal areas. Many of the European ports have been designed to be resilient against not only high tide during spring tide but heightened storm surge such as the ports of Amsterdam, Rotterdam and London while Belgium and port of Hamburg have storm surge protection plans (Christodoulou et al, 2018).

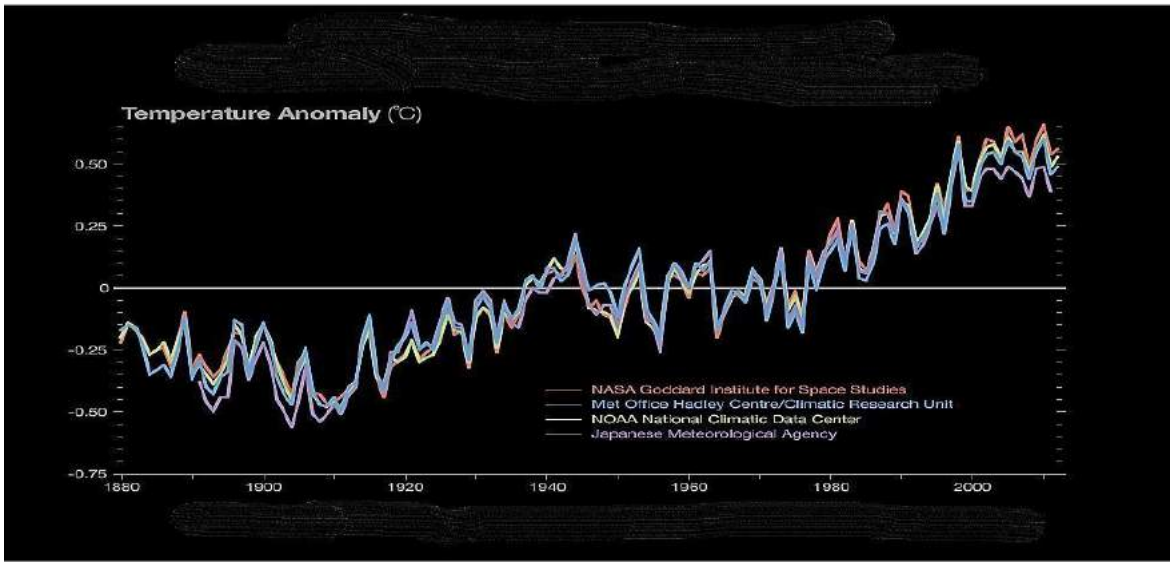

Figure 3: Temperature anomaly (Source: NASA Earth Observatory)

Average global greenhouse gas concentrations have generally been on the rise since 1900 with carbon dioxide concentrations reaching 407.8 ppm in 2018 which is 147% of pre-industrial levels of 1750. Similar trends are seen in concentrations of methane and Nitrous oxide (figure 4c) both of which have increased 259% and 123% of pre-industrial levels respectively. These are indicators that call for urgent actions from a policy and implementation standpoint.

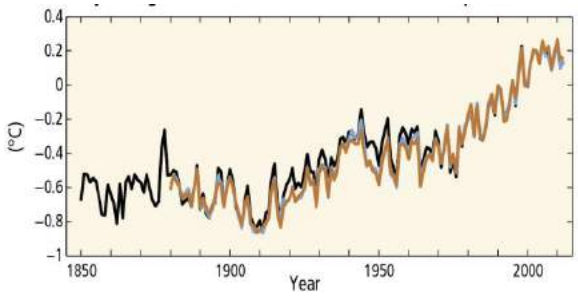

Figure 4(a): Globally averaged combined land and ocean surface temperature anomaly

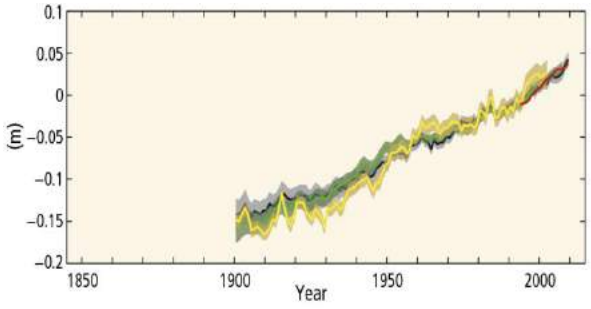

Figure 4(b): Globally averaged greenhouse gas concentrations

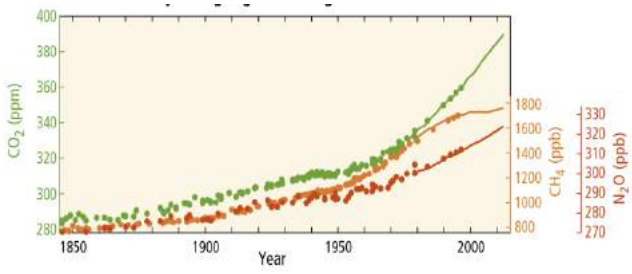

Figure 4(c): Globally averaged greenhouse gas concentrations

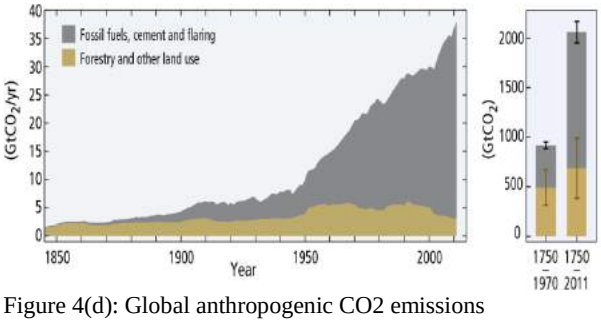

Figure 4(d): Global anthropogenic CO2 emissions

Figure 4: Climate change indicators (Source: IPCC, 2014)

Temperature Anomaly Projections and the Future of International Shipping

Various temperature anomaly projects from 23 different models (figure 4) have all shown that surface temperature will continue to rise. Higher temperatures will give rise to more extreme weather events and sea water levels will continue to rise. With more stormy weather conditions and stronger currents, these have obvious implications for international shipping. This begs the question: does this mean that future ships have to be designed to climate change class to be able to resist even stronger storms, extreme winds and stronger currents? The answer to the above is obvious as glaciers continue to melt and add to the world's ocean resulting in not only sea level rise but stronger currents that require higher energy output to overcome the added sea resistance. This has the potential to disrupt supply chains through increased turnaround time and increased freight cost.

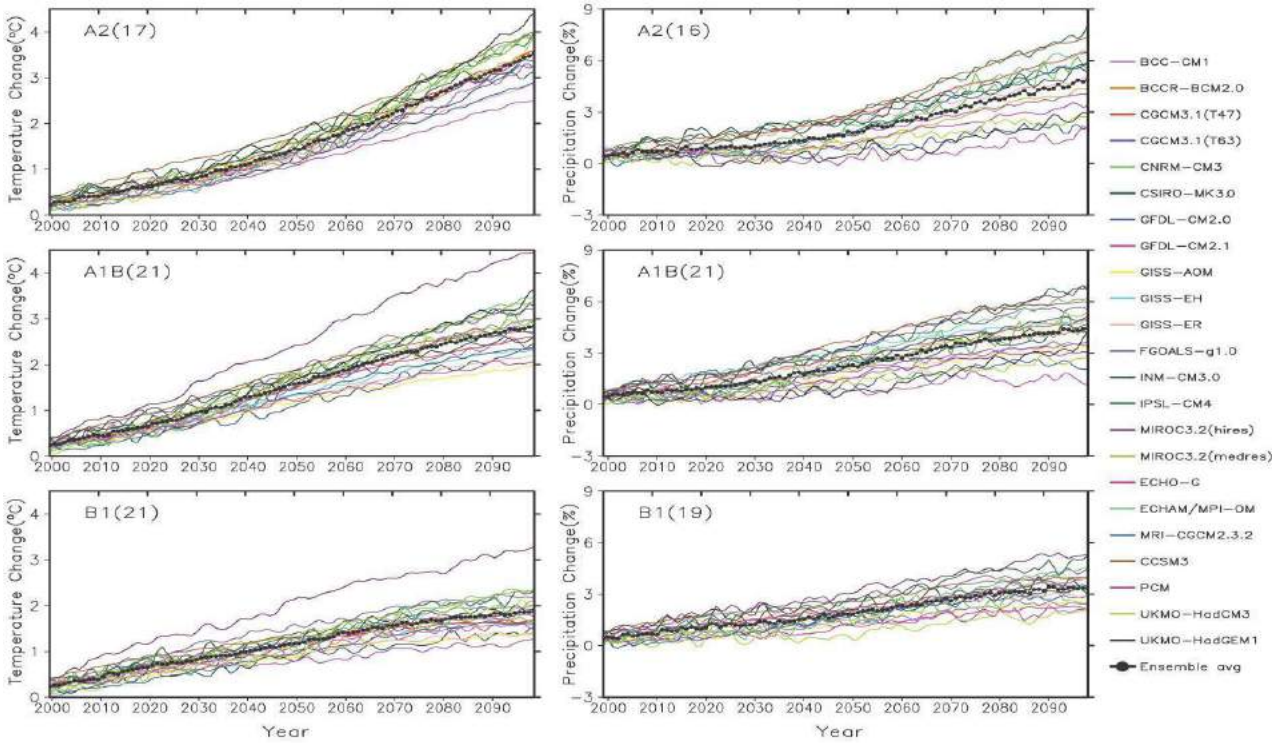

Figure 5: Temperature anomaly projections (Source: IPCC)

WHO Covid-19 Response and What Lessons to Learn for Climate Change

While the impact of Covid-19 is worldwide, the Americas and Europe has been hit more than any other region. These two regions have had a death toll in excess of 3.7 million as at 29th October 2021 representing over 74% of the global death toll. After the virus was detected and officially reported on the 31th of December 2019, the World Health Organization (WHO) had set up an Incident Management Support Team (IMST) prior to the first reported death on the 4th of January 2020 was reported. One of the reasons for this proactive decision was because the scientific community has had a convergent view on the potential impact of the virus. As at 26th January 2021, WHO headquarters had conducted 134 media briefings and 41 member states information sessions and media briefings. On the 16th of January, 2020, the WHO regional offices in the Americas issued recommendations for infection prevention, control measures and international travels through its first epidemiological alert. This had helped curb the early spread of the disease through restrictions in international travel and general awareness. Though there was general inertia on the part of the states in terms of travel restrictions and border control, the WHO had not slowed down on its process of mitigation through providing guidance to states.

On the other hand, information on the potential impact of climate change was reported in the late ninth century but with divergent views on the issue. There is evidence that many of the policy makers do not really understand the implications of the climate change policies and higher level of knowledge of climate change, particularly of its causes, did not lead to

changes in concern towards climate change, attitudes towards measures to fight it and attributions of responsibility (Lázaro et al, 2007).

It is evident that climate change has serious consequences on the environment and the lives of the people but response on climate actions is slow and enforcement is also limited. According to Lee et al (2015) educational attainment is the strongest predictor of understanding anthropogenic causes of climate change. Temperature anomaly projections have shown that increased consequences of climate disasters are inevitable unless drastic actions are taken to turn this around. Several models have been proposed over the years and all seem to give similar results (Figure 4). This calls for urgent action from a policy and implementation perspective.

The WHO had declared covid-19 a public health emergency of international concern on the 31st December 2019 and followed by its declaration as a pandemic on the 11th of March 2020 at a press conference held in Geneva. By 15th March the Center for Disease Control (CDC) had advised the public to avoid mass gatherings of 50 or more people. This was followed by several countries imposing mass gatherings, travel restrictions and lockdowns.

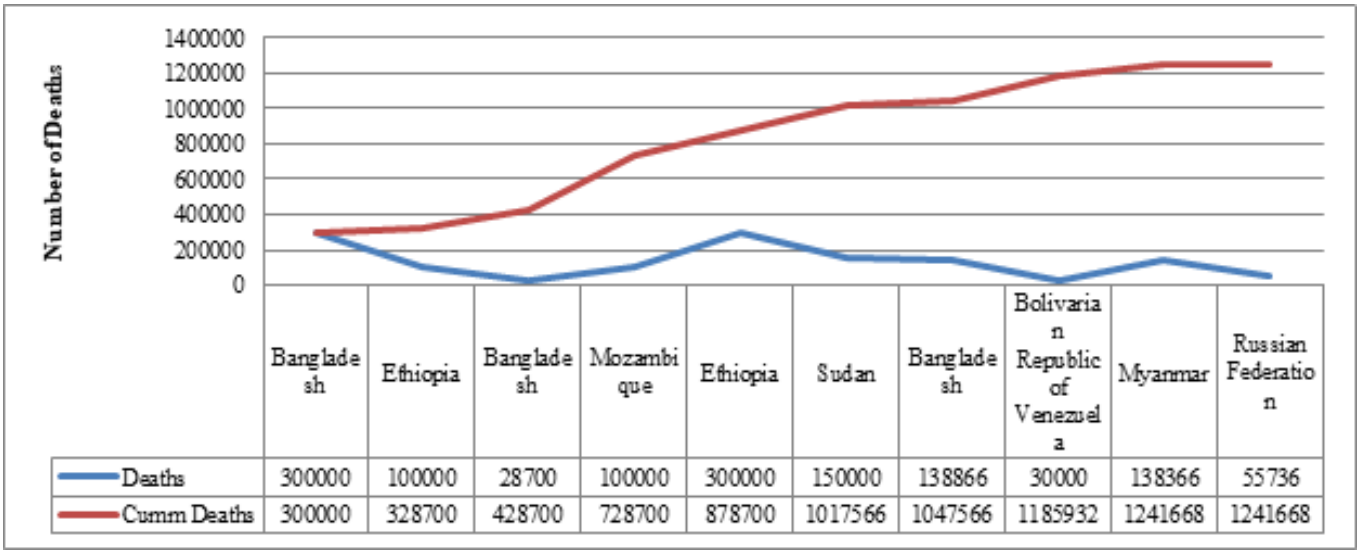

	Bangladesh	Ethiopia	Bangladesh	Mozambique	Ethiopia	Sudan	Bangladesh	Bolivarian Republic of Venezuela	Myanmar	Russian Federation
Deaths	300000	100000	28700	100000	300000	150000	138866	30000	138366	55736
Cumm Deaths	300000	328700	428700	728700	878700	1017566	1047566	1185932	1241668	1241668

Figure 5: Top ten countries with the highest Climate change disaster death toll.

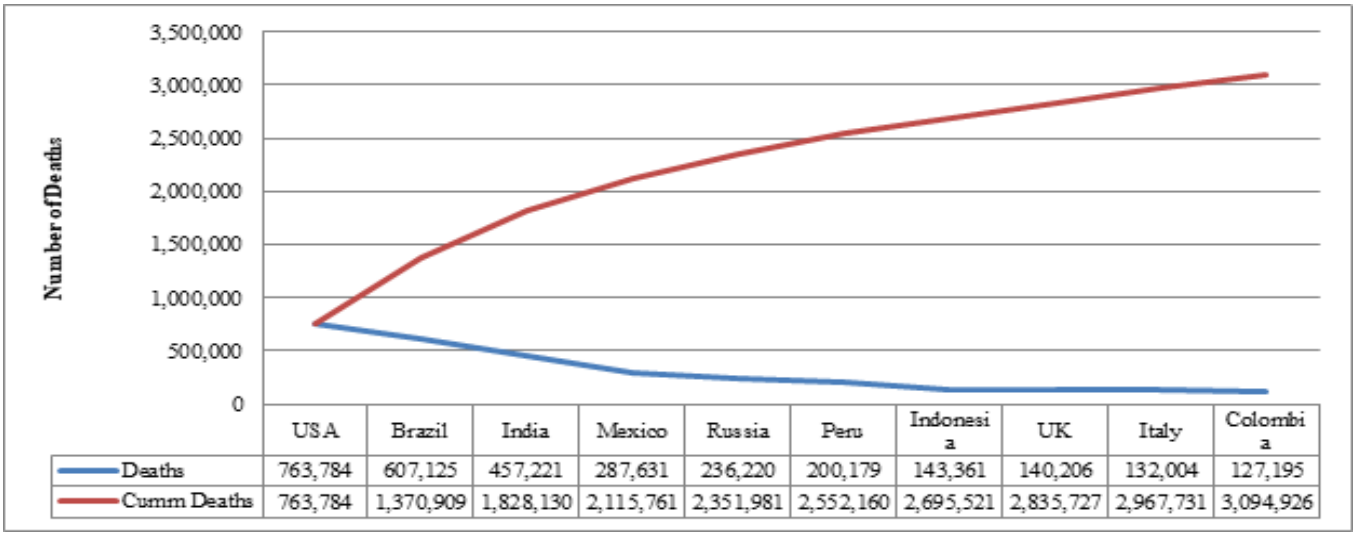

	USA	Brazil	India	Mexico	Russia	Peru	Indonesia	UK	Italy	Colombia
Deaths	763,784	607,125	457,221	287,631	236,220	200,179	143,361	140,206	132,004	127,195
Cumm Deaths	763,784	1,370,909	1,828,130	2,115,761	2,351,981	2,552,160	2,695,521	2,835,727	2,967,731	3,094,926

Figure 6: Top ten countries with the highest death toll

Data from the WMO (2021) on the top ten countries affected by the climate change pandemic from 1970 to 2019 (figure 6) shows developing countries as the most affected by climate disaster. The data has shown that 91% of all deaths occur in developing countries primarily as a result of lack of technological support for early warning systems. Bangladesh alone has registered three different climate disasters within the top ten highest recorded disasters which resulted in over 467,000 deaths.

Data acquired from the WHO on the top ten affected countries by covid-19 (figure 7) show that over 60% of the deaths occur in developed countries despite several actions taken by those countries. USA and Brazil recorded the highest with a combined death toll of over 1,370,000.

CONCLUSIONS

The Coronavirus disease 2019 had caused the death of about 1.7 million and over 16 million infections resulting in its declaration by the WHO as a global pandemic. The declaration of the disease as a global pandemic had resulted in several countries taking actions by imposing travel restrictions and lockdowns in cities most affected by the disease. Key lessons to learn from these actions are that Covid-19 has been characterized by cause and effect relationships where responses are triggered by an event. Recognizing such triggers in the context of climate pandemic situations may prevent potential heightened disasters.

Climate change pandemic and coronavirus pandemic are both Transboundary and pose a serious challenge to human existence. Initial stage in both cases is characterized by less frequent events, a stage that is characterized by inertia in response. This response style is usually necessitated by the need to observe the events as they unfold for understanding of the trend and the opportunity to select the most appropriate response strategy. However, key lessons to be learned from such inertia are the economic and social cost of ignoring the initial warnings.

Based on analysis of data presented from the various sources cited (IPCC, 2014; WMO, 2020; UNEP, 2021) the earth's surface temperature is increasing and this will only lead to more frequent occurrences of natural climate disasters with increased mortality. Developments in technology will continue to save life through early warning but because of the pace the developing countries are closing the technology gap, it is likely that mortality as a result of climate disaster will continue to increase in the developing countries.

Maritime sector's ability to ensure business continuity to keep supply chains active during a pandemic era requires further investigation with a view of sustaining such business continuity in the event of a potential climate disaster. Transportation, especially shipping being one of the cornerstones of international trade and commerce, continues to perform its role thereby preventing potential supply chain disruptions.

Global response to climate disaster events did not occur until 1949 though evidence was available since the mid nineteenth century, an indication that awareness on the pandemic scale of the issue was not recognized. though one could argue the lack of a global unified body at the time to pursue such efforts. Climate change has obvious implications for shipping in terms of design, operations and overall economic impact. Ship machinery and hull design is highly dependent on ambient temperature and sea conditions. Increased precipitation has the ability to not only lead to sea level rise but could also increase the water flow into seas through rivers thereby reducing ship speed in the process with potential interruptions to global supply chain. Higher temperatures have a tendency to increase wind energy culminating in even stronger storms. These indicators are a wakeup call for urgent climate action.

ACKNOWLEDGEMENT

I thank my supervisors, Professor Ronan LONG (WMU-Sasakawa Global Ocean Institute) for his support and Dr. Tafsir Johansson (WMU-Sasakawa Global Ocean Institute) for his comments on the manuscript and for providing useful reference materials.

REFERENCES

Christodoulou, A et al. (2018). Sea-level rise in ports: a wider focus on impact. https://doi.org/10.1057/s41278-018-0114-z

Gentner, D. (1983). Structure-Mapping: A Theoretical Framework for Analogy. Cognitive Science, 7(2), 155-170. https://10.1207/s15516709cog0702_3

Ghebreyesus, T. A., & Lim, K. (2020). A Joint Statement On the Response to the COVID 19 Outbreak

IMO. (2009). *PREVENTION OF AIR POLLUTION FROM SHIPS, An International Fund for Greenhouse Gas emissions from ships, Submitted by Cyprus, Denmark, the Marshall Islands, Nigeria and the International Parcel Tankers Association (IPTA). Marine Environment Protection Committee (MEPC), 60th Session(Agenda Item 4). IMO.*

Guarini, M. et al (2009). Resources for research on analogy: A multi-disciplinary guide. *Informal Logic*, *29*(2), 84. https://10.22329/il.v29i2.1225

IMO. (2015). Third IMO greenhouse gas study 2014. ().International Maritime Organization (IMO), London, UK. http://www.manchester.ac.uk/escholar/uk-ac-man-scw:266097

IMO. (2020). Fourth IMO Greenhouse Gas Study 2020. International Maritime Organization (IMO), London, UK.

IPCC. (2014). Climate change 2014: Mitigation of climate change. contribution of working group III to the fifth assessment report of the intergovernmental panel on climate change. Cambridge University Press.

Patwardhan, A. (2007). Disaster prevention, preparedness and management and linkages with climate change adaptation characteristics and impact of climate extremes in india view project maritime history of india and national maritime heritage complex view project

Ugur, G., Dilber, R., Senpolat, Y., & Duzgun, B. (1995). *July 2 0 0 8 , xx-xx treagust*. Dilber and Düzgün.

UNCTAD. (2020). *Review of maritime transport.* (). New York, United States:

UNEP. (2021). Emissions gap report 2021: The heat is on – A world of climate promises not yet delivered. . (). Nairobi:

Suleyman, A. (2016). Analysis of analogy use in secondary education science textbooks in turkey. *Educational Research and Reviews, 11*(19), 1841-1851. https://10.5897/ERR2016.2984

Ruria, I. (2009). INFECTIOUS DISEASES AND MARITIME LAW

World Meteorological Organization. (2021). WMO atlas of mortality and economic losses from weather, climate and water extremes (1970–2019). (). Switzerland: World Meteorological Organization

(WMO). https://library.wmo.int/doc_num.php?explnum_id=10769

WMO. (2020). Weather-related disasters increase over past 50 years, causing more damage but fewer deaths. https://public.wmo.int/en/media/press-release/weather-related-disasters-increase-over-past-50-years-causing-more-damage-fewer

The Prediction of Sea State Parameters by Deep Learning Techniques using Ship Motion Data

Malte Mittendorf[1,*], Ulrik D. Nielsen[1,2] and Harry B. Bingham[1]

ABSTRACT

The reliable and accurate determination of prevalent sea state conditions during a vessel's passage is of high scientific and practical importance not only due to crew and cargo safety, but also due to increasing energy efficiency demands. The present paper deals with the prediction of integral sea state parameters using 5-minute time series samples of wave-induced ship motions and builds upon deep neural networks. The study is based on synthetic motion histories of heave, pitch and roll of a container vessel generated from transfer functions and a parametric wave spectrum. The multi-dimensional search space of the four free variables: significant wave height, zero-upcrossing period, relative wave direction and advance speed, is discretized by Latin Hypercube Sampling. In order to comply with the assumption of moderate wave steepness, an empirical wave breaking constraint is incorporated into the spectral simulation procedure. Both a residual network and a multichannel convolutional LSTM (Long Short Term Memory) network are employed and compared to a state of the art architecture. In the frequency domain, a multilayer perceptron is used for comparison and trained on features obtained from cross-spectral analysis. The results of the simulation-based study show sufficient accuracy and generalization for all models in both time and frequency domain. Lastly, limitations of the present study are pointed out and it stressed that the applicability of the presented methodology to real in-situ measurement data is an important part of future work.

KEY WORDS

Ship Operation; Sea State Estimation; Ship Safety; Machine Learning; Spectral Simulation

INTRODUCTION

The number of containers lost at sea due to large accelerations rose significantly over the last couple of years, which is mainly attributed to environmental impact in severe weather conditions, BIMCO (2021). Real-time monitoring of the predominant sea state is essential for safe and intelligent ship navigation, in order to mitigate maritime accidents, such as container losses, and enhance the energy efficiency of ship operation at the same time.

The acquisition of accurate sea state data is challenging and traditionally performed using satellite data, wave rider buoys or wave radars. However, all of these methods come with their own limitations and uncertainties. Therefore, the herein presented work exploits the *wave buoy analogy*, an overview of which is given by Nielsen (2018). The wave buoy analogy considers ship motions in the frequency domain and establishes an inverse mapping from response (cross) spectral densities to encountered directional wave spectrum using transfer functions. The model-based mathematical framework is non-trivial and has consequently been subject to many research efforts over the last decades. Iseki and Ohtsu (2000), Tannuri et al. (2001) as well as Nielsen (2006) describe Bayesian approaches for obtaining the directional wave spectrum using complex-valued transfer functions and cross response spectra. Whereas, Pascoal and Guedes Soares (2009) present a Kalman Filter approach directly in the time domain. Nielsen (2017) provides a summary of methods for ship-based sea state estimation using motion recordings. It is important to distinguish between parametric and non-parametric approaches: The latter provides the full directional spectrum, whereas the parametric approach yields input values to parametric wave energy density spectra and/or spreading functions. Obviously, the applicability and accuracy of the presented estimation methods inherently depend on accurate transfer functions, which are not always available for the entirety of operational conditions, and in some cases the transfer functions are

[1] DTU Mechanical Engineering, Technical University of Denmark, Kgs. Lyngby, Denmark
[2] NTNU AMOS Centre for Autonomous Marine Operations and Systems, Trondheim, Norway
[*] Corresponding author: Malte Mittendorf (mamit@mek.dtu.dk)

simply not known to the ship operator due to a lack of detailed hull information. Additionally, the mentioned procedures rely on assumptions of linearity and stationarity of 30-60 minutes time sequences; however, these are not always valid in reality – in high sea states in particular. This motivates a data-driven machine learning (ML) based study. Machine learning techniques are widely applied in ship hydrodynamics as surrogate models, i.e. approximate results of computationally expensive calculation methods by regression models. In the field of ship-based sea state estimation, ML is also increasingly applied, like in the work of Åvist and Pyörre (2013), in which non-parametric regression methods, i.e. MARS (Multivariate Adaptive Regression Splines) and a random forest regressor, were applied for the prediction of significant wave height and encountered direction. Tu et al. (2018) propose a stacked ensemble sea state classifier and provide a detailed preprocessing approach including features from both time and frequency domains. Cheng et al. (2019) develop a deep learning classification end-to-end learning approach via a multichannel convolutional network for sea state estimation using the Beaufort scale for non-forward speed cases (i.e. dynamic positioning). Liu et al. (2019) provide a study for the prediction of pitch motion time series using wave elevation data derived from CFD (Computational Fluid Dynamics) simulations. For this reason, they employ a recurrent deep neural network as a surrogate of the pitch transfer function. Düz et al. (2019) present a real-time multivariate time series regression approach of sea state parameters applying several deep neural network architectures on 2.5-minute motion samples of a frigate-type ship. The displayed results show sufficient accuracy for the prediction of relative wave direction, significant wave height and peak period under forward speed conditions. One distinct feature of their work is the application of transfer learning: Firstly, the model is trained on synthetic data derived from time domain potential flow simulations and then re-trained on in-service measurement data. Scholcz and Mak (2020) extended this work and presented a methodology for non-parametric wave spectrum estimation using wave radar data and a convolutional encoder-decoder network with sufficient prediction accuracy.

The main novelty of this paper is the application of deep neural networks on simulated time series data in an end-to-end-learning fashion for real-time sea state estimation and, comparison to a corresponding frequency domain approach. The heave, pitch and roll time series are simulated for a Post-Panamax container vessel for a multitude of different operational conditions. The core of the machine learning task is defined in the time domain and the high dimensionality of the motion time series necessitates a deep learning approach as these are capable of handling high dimensional data. Furthermore, the models are defined as multi-output regressors since it is thought that they will infer physical relationships and interdependencies of the target variables when predicting them simultaneously. Lastly, a benchmark model is trained on frequency domain features similar to the work of Åvist and Pyörre (2013). The comparison between the time and frequency domain approaches in terms of accuracy and computational effort is one of the novelties of the present work.

In the following section of this paper, the applied methodology will be provided including the time series simulations, the studied neural networks, and their training set-up. In section 3, the main findings and results are displayed and discussed. In the final section 4, several opportunities of future work and limitations of the present work are pointed out.

METHODS

Time Series Simulation

The seakeeping attitude of a ship, also referred to as sea worthiness, plays a pivotal role both in ship design and operation. Ship motions in irregular waves are random in both time and space and are considered as an *ergodic* process, St. Denis and Pierson (1953). Thus, an irregular seaway is defined by the superposition of multiple regular wave components with relatively small wave steepness. In a statistical sense and under sensible assumptions, the process is completely characterized by a power spectral density function $S(\omega)$. For seakeeping analyses, the International Towing Tank Conference (ITTC) recommends the use of the two-parameter Bretschneider spectrum, cf. Eq. 1.

$$\mathrm{S}(\omega)=\frac{a}{\omega^5}\cdot exp\left(\frac{-b}{\omega^4}\right) \text{ with } a=\frac{H_s^2}{4\pi}\left(\frac{2\pi}{T_z}\right)^4 \text{ and } b=\frac{1}{\pi}\left(\frac{2\pi}{T_z}\right)^4 \quad [1]$$

The Bretschneider spectrum is a function of the intrinsic wave frequency ω, significant wave height H_s, and zero upcrossing period T_z. The spectrum is valid for unlimited fetch, deep water as well as no swell conditions, i.e. for fully developed seas (Bretschneider, 1959). From Eq. 1, one can infer that the Bretschneider spectrum is unidirectional, despite the fact that irregular waves are, in reality, short crested. However, as a demarcation, only long-crested and unimodal sea states are taken into account in the present paper. The spectral density function can be directly related to several sea state parameters, using spectral moments m_n, cf. Eq. 2.

$$m_n=\int_0^\infty \omega^n S(\omega)d\omega \quad [2]$$

It is noted that in Eq. 2, n refers to the order of the spectral moment. The significant wave height H_s, which is defined as the mean of the highest third of all waves, is determined by the zeroth order spectral moment as can be seen in Eq. 3.

$$H_s=4\sqrt{m_0} \quad [3]$$

An approximation of the mean zero-upcrossing period is given in Eq. 4 according to Jensen (2001). However, the actual zero-upcrossing period T_Z is defined uniquely in the time domain.

$$\overline{T_Z} = 2\pi \sqrt{\frac{m_0}{m_2}} \quad [4]$$

Further assumptions consider the seaway as stationary, without any additional environmental influences (e.g. sea current) and with small amplitude waves in deep water conditions. In order to comply with the assumption of moderate wave steepness, a wave breaking condition is incorporated into the time series simulation procedure. According to the DNV-GL guidelines for wave loads (2018), the maximum wave steepness S_S in irregular waves is defined as follows.

$$S_S = \begin{cases} \frac{1}{10} & for\ T_z \leq 6s \\ \frac{1}{15} & for\ T_z \geq 12s \end{cases} \text{ with } S_S = \frac{2\pi}{g}\frac{H_s}{T_z^2} \quad [5]$$

The values in between the given thresholds in Eq. 5 are linearly interpolated and g is the gravitational acceleration. The sea state characteristics $\{H_S, T_Z\}$ are variables of the data generation process and also the targets of the machine-learning procedure. The range of validity for H_S is defined as [0.5, 10.0]m and T_Z will be distributed in the range of [3.5,9.6]s. As can be seen, the present study considers low to more severe sea states and the advantage of a study on simulated data is that data quality and distribution are dictated and thus subject to less uncertainty than measurement data.

The wave-induced response of a ship includes all rigid body motions, which are defined by Newton's second law. In comparison to wave rider buoys, the response of a ship is of higher complexity due to its distinct shape, the low pass filtering effect, i.e. the ship does not respond to high wave frequencies, and the forward speed introducing the Doppler shift. We adopt a right-handed, body-fixed coordinate system, where the x-axis coincides with the forward direction and the origin is placed at the center of gravity. The ship responses are defined in the encounter frequency domain ω_e as we consider forward speed. The so-called Doppler shift is defined in the following Eq. 6.

$$\omega_e = \omega - \frac{\omega^2 U}{g} cos\,\beta \quad [6]$$

The ship's forward speed is denoted as U in [m/s] and the relative heading between ship and wave propagation β takes the value of $\beta=0$ deg. in following seas and $\beta=180$ deg. in head seas. The Doppler shift leads in following waves to long waves overtaking and to short waves *being* overtaken by the ship. This ambiguity may lead to a drop-off in accuracy of the ML models in this particular regime of relative wave directions.

The ship responses are obtained via the complex-valued transfer functions $\Phi_{R,i}$, which are determined by the linear system itself, since they are the ratio of the response and the excitation for all degrees of freedom (DOF). Transfer functions are dependent on the hull geometry, loading conditions and the ship's advance speed as well as the predominant wave heading. In the present work, heave, pitch and roll motions are considered, as these are most susceptible to wave induced excitations. The case study is a 6600 TEU Post-Panamax container vessel and its essential main particulars are listed in Tab. 1.

Table 1: Main particulars of the Post-Panamax container vessel.

Dimension	Unit	Magnitude
L_{PP}	[m]	332
B_m	[m]	42.8
T_d	[m]	12.2
C_B	[-]	0.65

In this work, we assume a constant draft ($T=13$m) as well as zero trim and heel throughout the study. For the calculation of the transfer functions, a linear 5-DOF strip theory solver implemented in I-Ship (Pedersen, 2000) was employed. The software makes use of the formulation proposed by Salvesen et al. (1970) and damping and added mass are approximated by the Frank close fit method, Frank and Salvesen (1970). The hull geometry of the container vessel is discretized into 31 strips and each strip contains up to 20 panels. The calculations are performed for 100 wave frequencies ω in the range of $[0.001, 4.0]$rad/s. In addition, the wave heading β is discretized into 36 headings for $[0, 350]$deg. Three forward speeds $U \in \{12,18,22\}kts$ are considered in the present work. It is noted that linear interpolation is only performed for the relative wave direction, but not for the forward speed due to the coarse speed discretization of the database.

The reaction of the ship is proportional to the encountered wave height under linear assumptions. Hence, the simulation of a linear response $u_i(t)$ may be determined by the sum of the individual responses to harmonic wave components.

$$u_i(t) = \sum_{k=1}^{N} \Phi_{R,i} \sqrt{2\,S(\omega) d\omega}\ e^{i\omega_e t + \theta_k} \quad [7]$$

The random phase shift θ_k in Eq. 7 takes values in the range $[0,2\pi]$rad ensuring stochastic behavior. The frequency bands $d\omega$ are *non-equidistant*, in fact, their width is randomly distributed, in order to avoid repetition of individual sequences. The spectral

density function $S(\omega)$ is adopted from Eq. 1. A more detailed theoretical background on ship motions in irregular waves can be found in Faltinsen (1990) and in Price and Bishop (1974).

Latin Hypercube Sampling (LHS), which was proposed by McKay et al. (1979), discretizes the resulting four dimensional search space Ω of H_S, T_Z, β and U. LHS carries out a stratified sample procedure for each free variable and considers their entire definition range by a number of sample points at a uniform distance. It is stressed that the definition range of U is not continuous, but discrete as opposed to the remaining three variables. In this case, 30,000 initial parameter combinations are employed and the training dataset comprises ca. 18,000 samples due to the incorporated wave breaking constraint. For the time series simulation, Eqs. 1, 5, 6 and 7 are applied and the chosen sample frequency is 5Hz and the sample length is defined as 300s. In Fig. 1, time series realizations of heave, pitch and roll motions are depicted for a given sea state in bow oblique waves.

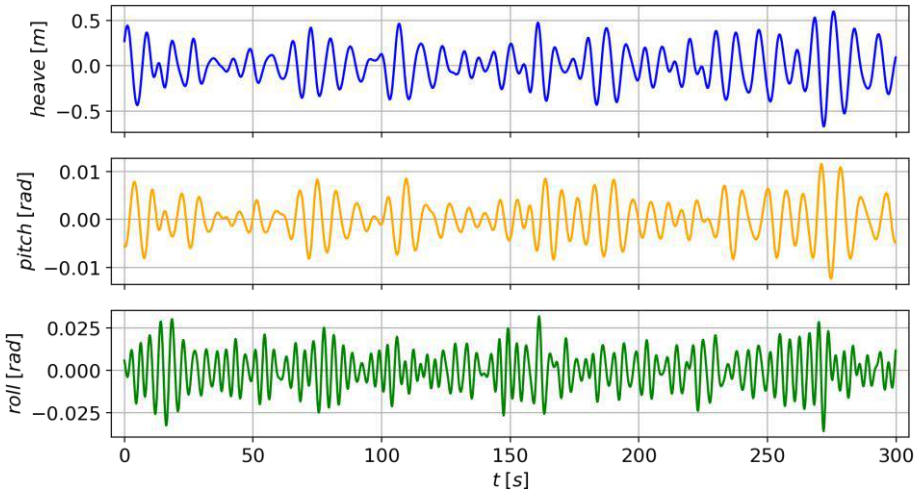

Figure 1: Realizations for *β=150deg, U=18kts, H_S=3m* and *T_Z = 8s*.

For generating a corresponding dataset in the frequency domain, the sample length was increased to 1800s to ensure a satisfactory frequency representation, as described in Nielsen (2018). The 3x3 matrix of cross-spectral densities were determined using the Welch algorithm, Welch (1967). For computing the cross spectra, the Hanning window was applied and the length of each segment equals 512. The phase information is obviously directly available in the time domain for predicting the relative wave direction β. In the frequency domain, on the other side, cross spectral analysis, i.e. the cross-correlation of two time series, is used as a predictor for β. In case of the diagonals, the zeroth, first, second and fourth order spectral moments were extracted from the response spectra using Eq. 2. The third order spectral moment was disregarded due to its tendency to diverge. From the off-diagonal elements, i.e. the complex valued cross spectra, the peak frequency and peak value of both real and imaginary part were included in the feature space. It is noted that this is only performed for one side of the off-diagonals, as they are complex conjugate symmetric. Moreover, it is part of the study to analyze, whether the obtained frequency features are capable predictors for integral sea state parameters. In Fig. 2, the pitch-heave cross spectrum is shown for the same conditions as in Fig. 1.

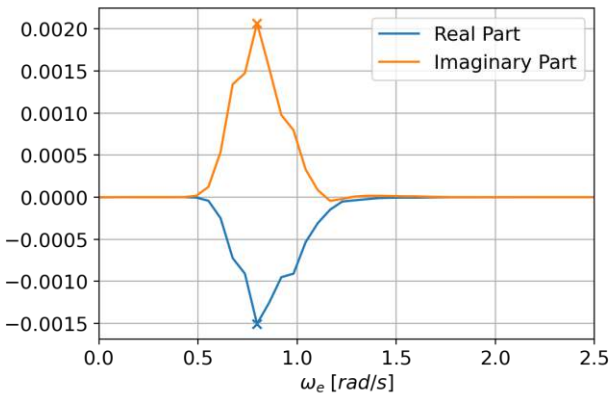

Figure 2: Pitch-heave cross spectrum for the same conditions in Fig. 1 and the peak values are indicated.

Ultimately, the feature vector in the frequency domain has a length of 24 and the input matrix in the time domain has the shape 1500x3 indicating the increased computational effort of the time domain approach. Before feeding the data into the neural networks both the time series data, frequency features and the targets, i.e. the integral sea state parameters are normalized, i.e. scaled according to their global extrema, since neural networks are not scale invariant. For the assessment of the achieved generalization capability of the models, a validation dataset is required. This set is unseen by the models and generated using the same methodology as described above, but different parameter combinations and makes up 1,872 data points. The model architectures as well as their setup is presented in the following subsection.

Deep Learning for Sea State Estimation

Artificial neural networks are inspired by the governing principles of mammalian brains and their dendrites; cf. Goodfellow et al. (2016). They are utilized as universal function estimators, since the combination of affine functions, i.e. matrix operations, and non-linearities, i.e. activation functions, lead to the *universal approximation theorem*. A traditional neural network has three layers: An input and output layer as well as a hidden layer and can consequently be seen as a *composite function.* Recently, deep neural networks (DNN) – neural networks with more than one hidden layer – have emerged in the machine-learning field achieving significant performance in a vast range of tasks, from image classification to multivariate time series regression. Much of this success of is credited to special layer types, such as convolutional layers, but the presentation of the related theoretical backgrounds is beyond the scope of this paper. For detailed information, see Goodfellow et al. (2016).
In the herein presented work, the focus is solely on Deep Learning (DL) architectures due to their capability of coping with high dimensional tensors and their ability of implicit feature construction, i.e. generating meaningful data themselves. Other advantages of deep architectures over traditional machine and statistical learning algorithms include better scalability and increased generalization capability by transfer learning. The multilayer perceptron (MLP) is the simplest deep architecture; however, MLP or fully connected layers are not applicable for time series or sequential data, since they treat each time step independently, i.e. have *no spatial invariance*, Ismail Fawaz et al. (2019). Thus, multivariate time series regression requires advanced architectures and layer types, which are introduced at a later stage.

The caveats of deep neural networks are on one hand the high computational cost of their training process and on the other hand the tendency of overfitting (on small datasets) due to their large amount of trainable parameters. Furthermore, very deep architectures might lead to the vanishing/exploding gradient problem especially in case of a recurrent neural network. Solutions to this problem are (1) simpler activation functions, such as the Rectified Linear Unit (*ReLU=max(0,x)*) and (2) certain advanced architectures, such as the LSTM (Long short-term memory) (Hochreiter and Schmidhuber (1997)) or residual networks (He et al. (2015)). *ReLU* not only decreases the chance of vanishing gradients, but also speeds up the training process, since it is faster to differentiate than other activations, such as the sigmoid or hyperbolic tangent functions. For these reasons, the application of *ReLU* as the activation function is considered as best practice. In the presented methodology, for every hidden layer batch normalization and *ReLU* activation is applied. Batch normalization converts the output of the hidden layer into a standard format before applying the activation. In doing so, the distribution of the output of the previous layer is reset, in order to facilitate the processing by the following layer, Ioffe and Szegedy (2015). It leads to more robust neural networks making the need for hyperparameter optimization less important.

The training process of neural networks is formulated as a gradient-based optimization problem: The loss function is defined during backpropagation and minimized by, e.g. a stochastic gradient decent algorithm. Herein, the *Adam* optimizer proposed by Kingma and Ba (2015), is applied as a learning algorithm, which works with the exponential moving average of the gradient and scales the learning rate according to the squared gradient. The applied loss function is the mean squared error (MSE), which is relatively responsive to outliers and noise, cf. Eq. 8.

$$\mathrm{MSE}=\frac{1}{N}\sum_{i=1}^{N}\left(y_i-\hat{y}_i\right)^2 \qquad [8]$$

It is noted that *N* is the length of the dataset and hat indicates the model predictions. The loss function in case of a multi-output regression model is calculated as the sum of losses for all elements of the output vector. As opposed to the work of Düz et al. (2019), the activation of the output layer (with a width of 3) is a linear function instead of the hyperbolic tangent. The individual architectures are described in detail in the following part.

Multichannel convolutional Long Short Term Memory

The proposed multichannel convolutional LSTM (MCLSTM) architecture is characterized by its three branches and resembles the models proposed in Cheng et al. (2019) and the MLSTM in Düz et al. (2019). Firstly, the recurrent path features a bidirectional LSTM layer with a width of 16 and a dropout probability of 0.25. For minimizing the risk of overfitting, dropout regularization is applied omitting certain neurons randomly during training, which increases generalization. LSTMs were proposed by Hochreiter and Schmidhuber (1997) and are able to memorize information and patterns from sequential data. The LSTM cell contains a hidden state c_t and has three different gates controlling the flow of information/data in the cell by the means of weight matrices. The flow of data and the individual gates are indicated in Fig. 2.

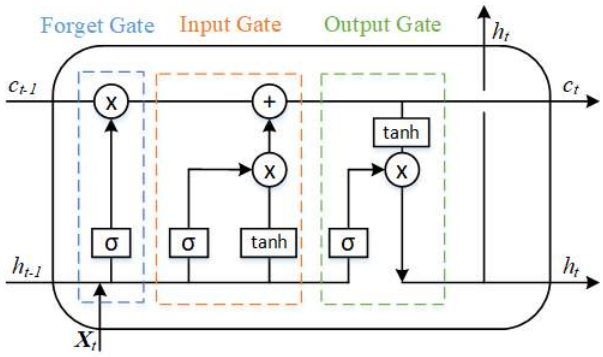

Figure 3: LSTM cell according to Hochreiter and Schmidhuber (1997).

Each arrow carries a vector, from gate to gate and the multiplication sign represents pointwise multiplication, while the boxes containing activation functions (sigmoid & hyperbolic tangent) are trainable weight matrices. The parameter matrices are connected recursively having not only a connection with itself, but to the three gates. For mathematical intricacies, the interested reader is referred to the paper of Hochreiter and Schmidhuber (1997). In essence, each of the different recurrent gates enable memory units of LSTM networks to receive and store long-term information from sequential (time series) data. Moreover, a bidirectional LSTM connects two hidden layers of opposite directions to the same output, in doing so the output layer gets information from past and future states at the same time. It is thought that a bidirectional processing of the motion time series improves prediction accuracy, but in turn, the trainable parameters, i.e. model complexity, increase as well.
The remaining two paths of the MCLSTM are convolutional networks, which are inspired by the visual cortex of the brain and have been predominantly used in image recognition. These architectures utilize spatial shared weights followed by a pooling or subsampling procedure. Formally, a convolution takes a multidimensional array as input and modifies it by the kernel - another multidimensional array - whose parameters are adapted according to the learning algorithm. For more detailed information consult the work of Krizhevsky et al. (2012). The first convolutional branch works directly on the multivariate time series and comprises three convolutional layers followed by a global average pooling layer. The filters have a size of 64, 32 and 16, respectively. Whereas the kernel sizes are 5, 4 and 3. The third branch of the MCLSTM is also a convolutional one with the same structure as the second branch, but it applies the Fast Fourier Transform (FFT) to the output of the first convolutional layer accounting for patterns in the frequency domain. The activated outputs of the three branches are concatenated and passed through two fully connected layers with 100 and 50 neurons. It is noted that dropout regularizes the penultimate hidden layer with the probability of 0.2. The parallel architecture leads to an increased number of weights and thus model complexity.

Residual Network
Residuals networks have been proposed by He et al. (2015) from Microsoft Research and feature a block-wise architecture. The concept of the ResNet draws inspiration from the pyramidal cells of the cerebral cortex and its skip connections. The skip connections or identity mappings are, in fact, a solution to the vanishing/exploding gradient problem and allow the training of very deep models with increased abilities. A residual network is made of multiple residual blocks as shown in Fig. 4.

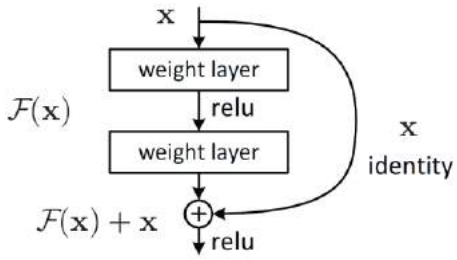

Figure 4: Fundamental idea behind the Residual Network, He et al. (2015).

The herein applied model comprises three blocks and a block's internal structure consists of three convolutional layers of constant filter size, but with 8, 4 and 2 kernels, respectively. Lastly, the output of the block is the sum of the last layer's activations and the input matrix activated by *ReLU*, cf. Fig. 4. The blocks have feature maps of size 32, 64 and 64, respectively. The final part of the model contains an average pooling layer and a fully connected layer with a width of 50 neurons.

Sliding Puzzle Network
The sliding puzzle network (SPN) is the herein used benchmark architecture in the time domain and adopted from Düz et al. (2019). The architecture is built out of two convolutional layers and the first convolutional layer only works in the time

direction, whereas the second one merges the six resulting branches (or channels) into one. However, the output of the first convolutional layer is run through a squeeze and excite block, which is a *content aware* mechanism and ranks each channel adaptively by, e.g. adding a parameter to each channel. The mathematical intricacies of it are described in greater detail in Mak and Düz (2019). Furthermore, the minimum, maximum and mean of the activations from the different patches are extracted in three pooling (subsampling) layers removing the spatial dependency. These features are then concatenated and passed on to a fully connected layer with 30 neurons. It is stressed that the hidden and the output layer(s) are activated using the hyperbolic tangent function. Additionally, the SPN is trained using the full 5-minute samples and not on random subsamples, like in the work of Düz et al. (2019).

Multilayer Perceptron

The benchmark neural network in the frequency domain is a straightforward multilayer perceptron architecture and features four hidden layers with 250, 150,100 and 50 neurons, respectively. The chosen approach in the frequency domain is considered as computationally very efficient due to the low dimensionality of the feature space and the used MLP model with moderate complexity. As stated above, the MLP is not applicable for time series regression, as it treats each time step independently.

Training Setup

All calculations were performed using DTU's HPC infrastructure on a GPU node equipped with two Nvidia® Volta-100 GPUs, each with 16GB of memory and the CPUs were multiple Intel® Xeon® Gold 6126 with 2.60 GHz. Moreover, the utilized programming language is Python 3.6 and the deep learning framework is TensorFlow 2.6 (Abadi et al., 2015). For GPU parallelization of the computations CUDA/CuDNN were used. Furthermore, shuffled 5-fold cross validation (similar to Düz et al. (2019)) was applied and the maximum number of epochs is set to 200. Due to the bias-variance-tradeoff, an early stopping callback was implemented into the training setup and as soon as a convergence criterion (25 epochs without improvement of the test loss) was reached the training process is terminated. Another callback for the reduction of the learning rate was defined as soon as a loss plateau appeared and it was triggered after 10 epochs without improved test loss. The third callback is the so-called model checkpoint saving the models parameters with the smallest test loss, so that the model with the highest generalization capability is saved before overfitting occurs with an increasing number of epochs. The learning rate can be seen as the step size of the optimization procedure and is set to $\alpha=10^{-3}$. Even though, a systematic hyperparameter optimization was not conducted, the essential parameters were modified, such as the loss function, learning rate and batch size.

RESULTS

In this section, the obtained results are presented and discussed. For the sake of brevity, only essential results are shown and initially the training and test loss as well as the model convergence behavior of the time domain models are analyzed in view of Fig. 5.

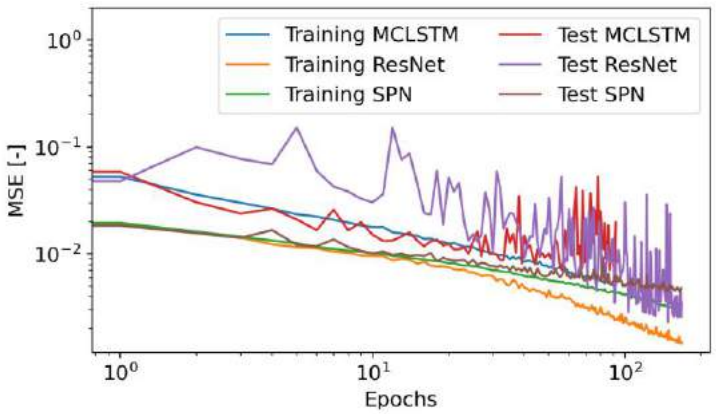

Figure 5: Losses of training and 5-fold cross validation presented for the number of epochs. Note that both axes are in logarithmic scale and that the data applies exclusively to time domain analysis.

It is evident that the use of 5-fold cross validation leads to a volatile test loss compared to the respective training loss resulting from the fact that the test set is a randomly partitioned subsample for each epoch. The loss curves of the MLP are not considered in Fig. 5, as it is trained on a different dataset generated in the frequency domain. It can be observed that the implementation of the early stopping callback has an influence on model convergence, because the maximum number of epochs is not reached by any model. Subsequently, this callback leads to a significant decrease in computational cost comparing the herein required epochs to the corresponding number in Düz et al. (2019). The errors of the ResNet yield the lowest respective values, which is

an indication of superior performance. The applied performance metrics are the root mean squared error and mean absolute error, which are calculated by the square root of Eq. 8 and using Eq. 9, respectively.

$$\mathrm{MAE}=\frac{1}{N}\sum_{i=1}^{N}|y_i-\hat{y}_i| \quad [9]$$

The root mean squared error pays more attention to outliers and the mean absolute error quantifies the error magnitude regardless of its sign. In addition, both metrics have the same unit as the original targets. The performance of all models on the validation data is summarized in Table 2 using both defined metrics.

Table 2: Out-of-sample performance of all models applied to the validation dataset. Note that the MLP used frequency domain features.

Metric	Target	MCLSTM	ResNet	SPN	MLP
RMSE	H_S	0.731	**0.482**	0.566	0.390
	T_Z	0.599	**0.352**	0.473	0.337
	β	22.07	**7.965**	15.52	47.15
MAE	H_S	0.564	**0.339**	0.412	0.270
	T_Z	0.429	**0.261**	0.337	0.234
	β	12.25	**4.738**	8.446	19.78

As can be inferred from Table 2, the ResNet performs, indeed, superior on multivariate time series and its results are thus emphasized by bold font. in addition, the sliding puzzle network shows satisfactory out-of-sample predictive power. The relatively inaccurate and noisy results of the MCLSTM result from three possible reasons: (1) The FFT branch is subject to considerable uncertainty due to the unclear frequency representation using just 5-minute samples. Secondly, (2) the model has a large amount of trainable parameters due to the three branches leading to overfitting and decreased generalization. Lastly, (3) the MCLSTM utilizes dropout regularization adding variance to the predictions. In the following Fig. 6, the predictions of the ResNet are presented for the actual validation samples by transparent dots and the identity line is given as well.

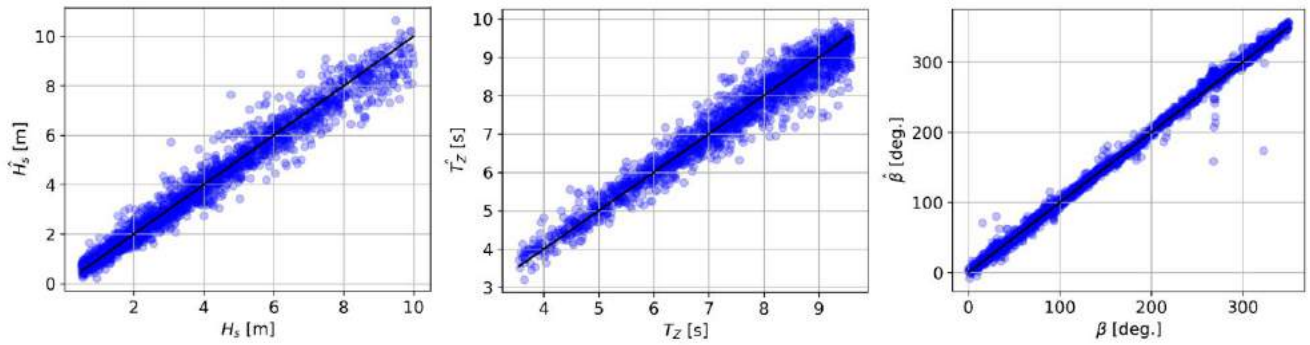

Figure 6: Model predictions of ResNet architecture indicated by hat for 1872 samples of the validation dataset.

In view of Fig. 6, it is stated that the ResNet shows satisfactory accuracy on the unseen validation dataset as the predictions match the true samples closely. Thus, the observations in Table 2 are confirmed. Furthermore, the tendency of the residual variance to increase with target variables T_Z is evident, which is an indication of heteroscedasticity. This results from the fact, that with increasing period, longer time series are actually necessary to capture the prevailing mean. Ultimately, this observation reveals a clear disadvantage to working on short motion sequences. Moreover, minor discrepancies in case of the relative wave direction are visible in following and especially in beam waves (90 and 270 deg.). Lastly, the proposed ResNet achieves comparable performance to that reported in Düz et al. (2019) using simulated data from a potential flow solver.

The results of the MLP are included in Table 2, but it is stressed that the results are not directly comparable due to the use of two different domains (and datasets). As anticipated, the prediction accuracy for H_S and T_Z exceeds the performance of the time domain models, because the required 30-minute samples for the frequency representation contain more information than only 1/6 of it (in the time domain). The out-of-sample predictions of the MLP are presented in Fig. 7.

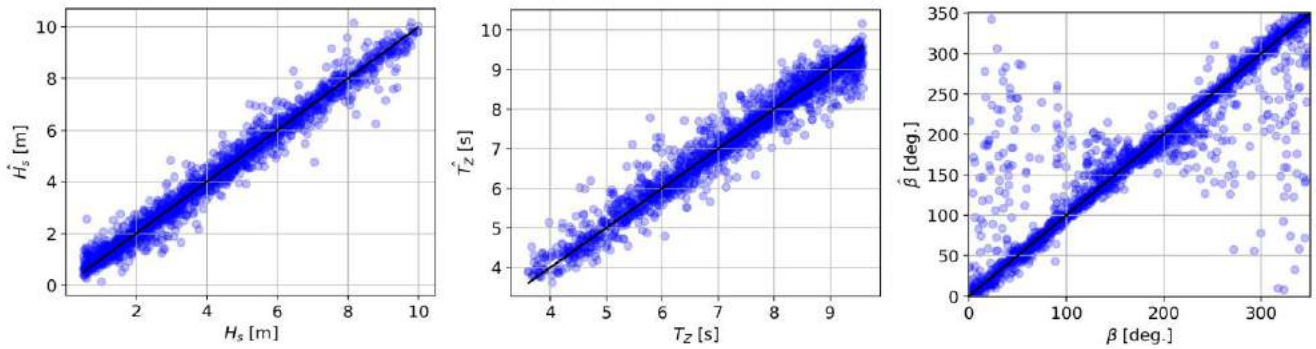

Figure 7: Model predictions of frequency domain approach using the MLP for the validation dataset.

As opposed to Fig. 6, there is less heteroscedasticity in Fig. 7 in case of the residuals of the zero upcrossing period resulting from the information of 30-minute samples. Nevertheless, the accuracy of the relative wave direction is considered as insufficient, which is mainly due to inaccurate estimates in following and oblique sea cases. This indicates that the features from the off diagonal elements of the cross spectral densities were not expressive enough. However, the performance of the frequency domain method stands out in terms of both accuracy and computational efficiency. Ultimately, the frequency domain approach exhibits great potential for future work.

Discussion

With the increase of necessary sample length, the assumption of time invariance is subject to growing uncertainty, especially under forward speed conditions, Iseki and Nielsen (2015). Therefore, the comparison of time, frequency and time-frequency ML approaches as well as a sensitivity study of the required sample length and frequency discretization will be important aspects in the future. Moreover, machine learning methods are capable of establishing a *non-linear* mapping from experienced motions and prevalent sea state parameters. However, the herein used simulated time series data itself is subject to the assumption of linearity. In reality, the ship undergoes non-linear phenomena, in severe sea states in particular, such as hull flexure, wave breaking and viscous roll damping or even flow separation. Additionally, the consideration of unimodal and unidirectional waves further simplifies the presented approach. For this reason, it is expected that corresponding machine learning results on real measurement data will exhibit more variance or rather uncertainty. Therefore, the application of the proposed models is essential for extending the work. Lastly, deep learning methods require large amounts of data, however, the Bayesian model-based methods, by e.g. Nielsen (2006), are not dependent on data availability alone and are both data- *and* physics-driven. For this reason, the study of a hybrid-approach merging ML and model-based approaches seems worthwhile.

CONCLUSIONS

The present paper dealt with a pattern recognition task using multi-output regression models. The prediction of sea state parameters using ship motion histories derived by spectral calculations was presented. Latin Hypercube Sampling generated a plethora of different sea states for the generation of time series recordings using the parametric Bretschneider spectrum and a database of motion transfer functions for a large container vessel. Moreover, the applied methodology included a wave steepness constraint and the results of several deep learning architectures showed sufficient results even for challenging conditions, such as following and beam seas. In addition, the change in forward speed did not have a considerable effect on accuracy. The paper had its focus on the multivariate time series regression, however, the time domain approach revealed limitations especially considering the computational cost for taking longer time series into account. Conversely, the frequency domain approach using the MLP showed great potential, but more advanced features from the cross spectra are necessary for the sufficient prediction of the relative wave direction. Lastly, a data-driven estimation approach for integral sea state parameters was proposed and it was possible to reproduce similar results from state of the art publications.

The major drawback of neural networks is their *opaqueness* making the post processing and drawing of conclusions complex. Hence, sensitivity and ablation studies, i.e. leaving some inputs out and studying their effect on the models performance, are necessary for more elaborate conclusions on feature importance. The herein presented work relies solely on implicit feature construction by convolutional encoder parts; however, it might be worthwhile to combine this with handcrafted features, like in Tu et al. (2018), and apply both features from time and frequency domain. Cheng et al. (2020) for example applied deep learning models on spectrograms of ship motions for sea state estimation. Furthermore, the application of the trained models to real in-service measurement data using a transfer learning approach, like in Düz et al. (2019), shows great potential. However, the direct approach on real data will be challenging due to considerable uncertainties regarding loading conditions, sensor noise and non-linear multimodal sea states. Lastly, a non-parametric approach like Scholcz and Mak (2020) is an important aspect for future work predicting the entire directional spectrum using motion measurement data.

ACKNOWLEDGEMENTS

The helpful suggestions given by Daniel Schmode (Wärtsilä Voyage) are gratefully acknowledged. The financial support from The Danish Maritime Fund (Projekt 2019-043), Orients Fond and Department of Mechanical Engineering (DTU) is highly appreciated. The second author has received funding by the Research Council of Norway through the Centres of Excellence scheme, project number 223254 AMOS.

REFERENCES

ABADI, M., et al. *TensorFlow: Large-scale machine learning on heterogeneous systems.* 2015, Software available from tensorflow.org.

ÅVIST, P. and J. PYÖRRE "Modeling the Impact of Significant Wave Height and Wave Vector using an On-board Attitude Sensor Network." *Proc. of the 12th Int. Conf. on Computer and IT Applications in the Maritime Industries,* Cortona, 2013.

BIMCO "IMO Agrees on new Measures to Detect and Report Containers lost at Sea." [Accessed on: 5th November 2021] https://www.bimco.org/news/safety/20210518-imo-agrees-on-new-measures-to-detect-and-report-containers-lost-at-sea

BRETSCHNEIDER, C.L. *"Wave variability and wave spectra for wind-generated gravity waves",* Technical Memorandum No. 118, Beach Erosion Board, U.S. Army Corps of Engineers, Washington, DC, USA, 1959.

CHENG, X., G. LI, R. SKULSTAD, S. CHEN, H.P. HILDRE and H. ZHANG "Modeling and Analysis of Motion Data from Dynamically Positioned Vessels for Sea State Estimation." *Proc. of 2019 Int. Conf. on Robotics and Automation (ICRA).* IEEE, 2019, pp. 6644–6650.

CHENG, X., G. LI, R. SKULSTAD; H. ZHANG and S. CHEN "SpectralSeaNet: Spectrogram and Convolutional Network-based Sea State Estimation." *IECON 2020 The 46th Annual Conference of the IEEE Industrial Electronics Society*, 2020.

DNV-GL *Class Guideline: Wave loads (DNVGL-CG-0130).* Edition January 2018.

DÜZ, B., B. MAK, R. HAGEMAN and N. GRASSO "Real Time Estimation of Local Wave Characteristics From Ship Motions Using Artificial Neural Networks." *Proc. 14th Int. Symp. Practical Design of Ships and Other Floating Structures (PRADS'19),* Yokohama, Japan, 2019.

FALTINSEN, O.M. *Sea loads on ships and offshore structures.* Cambridge: Cambridge University Press, 1990.

FRANK, W. and N. SALVESEN "The Frank Close-Fit Ship-Motion Computer Program." *NSRDC Report* No. 3289, 1970.

GOODFELLOW, I., Y. BENGIO and A. COURVILLE *Deep Learning.* Cambridge: The MIT Press, 2016.

HE, K., X. ZHANG, S. REN and J. SUN "Deep Residual Learning for Image Recognition." *2016 IEEE Conference on Computer Vision and Pattern Recognition (CVPR)*, 2016, pp. 770-778.

HOCHREITER, S., and J. SCHMIDHUBER "Long short-term memory." *Neural Comput.* **9**:8, (1997): 1735–1780.

IOFFE, S. and C. SZEGEDY "Batch Normalization: Accelerating Deep Network Training by Reducing Internal Covariate Shift". *arXiv:1502.03167,* 2015.

ISEKI, T. and K. OHTSU "Bayesian estimation of directional wave spectra based on ship motions." *Control Eng. Practice* **8**, (2000): 215-219.

ISEKI, T. and U.D. NIELSEN "Study on Short-term Variability of Ship Responses in Waves." *J. of Japan Institute of Navigation* **132**, (2015): 51-57.

ISMAIL FAWAZ, H., G. FORESTIER, J. WEBER, et al. "Deep learning for time series classification: A review." *Data Mining and Knowledge Discovery* **33**, (2019): 917–963.

JENSEN, J.J. *Load and Global Response of Ships*. Vol. 4 of *Elsevier Ocean Engineering Book Series*, Amsterdam: Elsevier, 2001.

KINGMA, D.P. and J. BA "Adam: a method for stochastic optimization." *Proc. of 3rd Int. Conf. on Learning Representations (ICLR '15),* San Diego, 2015.

KRIZHEVSKY, A., I. SUTSKEVER and G.E. HINTON "ImageNet Classification with Deep Convolutional Neural Networks." *NIPS* (2012): 1106-1114.

LIU, Y., Q. ZHENG, W. DUAN and L. HUANG, "Improving deterministic pitch motions estimation using bivariate sequential wave input." *IOP Conf. Ser.: Mater. Sci. Eng.* **688** 033017, 2019.

MAK, B. and B. DÜZ "Ship as a Wave Buoy – Estimating Relative Wave Direction from In-Service Ship Motion

Measurements using Machine Learning." *Proc. 38th Int. Conf. on Ocean, Offshore & Arctic Engineering OMAE 2019*, Glasgow, Scotland, 2019.

McKAY, M.D., R.J. BECKMAN and W.J. CONOVER "A comparison of three methods for selecting values of input variables in the analysis of output from a computer code." *Technometrics*, **21**:2 (1979): 239-245.

NIELSEN, U.D. "Estimation of on-site directional wave spectra from measured ship responses." *Mar.Struct.***19**:1 (2006): 33–69.

NIELSEN, U.D. "A concise account of techniques available for shipboard sea state estimation." *Ocean Eng.* **129** (2017): 352 – 362.

NIELSEN, U.D. *Sea state estimation based on measurements of wave-induced ship responses.* Dr. Techn. thesis, DTU Mechanical Engineering, Kgs. Lyngby, Denmark, 2018.

PASCOAL R. and C. GUEDES SOARES, "Kalman filtering of vessel motions for ocean wave directional spectrum estimation." *Ocean Eng.* **36**:6-7, (2009): 477–488.

PEDERSEN, T. *Wave load prediction-a design tool.* Department of Naval Architecture and Ocean Engineering, Technical University of Denmark, 2000.

PRICE, W. C. and R.E.D. BISHOP *Probabilistic theory of ship dynamics.* London: Chapman and Hall, 1974.

SALVESEN, N., E.O. TUCK and O.M. FALTINSEN *Ship Motions and Sea Loads*, Trans. SNAME, **78**, (1970): 250-287.

SCHOLCZ, T.P. and B. MAK "Ship as a Wave Buoy – Estimating Full Directional Wave Spectra from in-service Ship Motion Measurements using Deep Learning." *Proc. of 39th Int. Conf. on Ocean, Offshore & Arctic Engineering (OMAE 2020)*, 2020, Fort Lauderdale, USA.

ST. DENIS, M. and W.J. PIERSON *On the motion of ships in confused seas.* SNAME Transactions, 1953.

TANNURI, E.A., J.V. SPARANO, A.N. SIMOS and J.J.D. CRUZ "Estimating directional wave spectrum based on stationary ship motion measurements." *Applied Ocean Res.* **25**, (2003): 243-261.

TU, F., S. SAM GE, Y. SANG CHOO and C. CHIEH HANG "Sea state identification based on vessel motion response learning via multi-layer classifiers." *Ocean Eng.* **147** (2018): 318–332.

WELCH, P. "The use of fast Fourier transform for the estimation of power spectra: a method based ontime averaging over short, modified periodograms." *IEEE Transactions on audio and electroacoustics* **15**, (1967): 70–73.

ADDED RESISTANCE IN OBLIQUE WAVES ON A CONTAINER SHIP USING CFD

H. Mikkelsen[1], Y. Shao[1] and J. H. Walther[1,2]

ABSTRACT

The importance of CFD is increasing in marine hydrodynamics in studying seakeeping and added resistance of ships. While extensive numerical studies have been reported for various ships in head seas in the literature, much fewer CFD studies are found for oblique waves, which in practice is very important in, for instance, estimating required power and maneuverability of ships in realistic sea states. In this paper, the added resistance and motion responses for the KCS container ship in regular waves are studied and validated systematically for two wave headings and six wavelengths using CFD. The ship is free to heave, pitch, and roll. User-defined implementations in the commercial CFD code are made to effectively constrain the surge and yaw. Results of the CFD model are compared with up to three sets of experimental data sets, Potential Flow (PF) and existing CFD results from the literature. In general, the present CFD results show significantly better agreement with the experiments than previously published CFD results. The present study shows that CFD simulations can accurately predict motion responses and added resistance in oblique regular waves. With these results, designers of ship hulls can get an insight of where to focus the optimization work in the pursuit of fuel-efficient vessels.

KEY WORDS

CFD; Added resistance in waves; Oblique waves; Design; Seakeeping.

INTRODUCTION

For the last decades most commercial ship hulls have been designed and optimized for sailing fully loaded with full speed in calm water. Traditionally, the effects of wind and waves have been included by adding a sea margin of 15 percent (Molland et al., 2011) to the required engine power. Over the last 10 years, this single design point approach has started to change by including more draughts and speeds into the design matrix (Psaraftis and Kontovas, 2014). This has narrowed the gap between the conditions ships are design for and the conditions the ships will operate in. However, almost all ship hulls are still designed using a combination of experience, towing tank tests and Computational Fluid Dynamics (CFD), mostly in calm water. The next natural step is to include the influence of interaction with waves into the ship hull design phase. Since almost no ships are constantly sailing in calm water, optimizing the ship hull to realistic sea states in the future has significant potential to reduce fuel costs and emissions. Seakeeping tests of motion responses and added resistance in towing tanks can be expensive, time demanding and dependent on the availability of the tanks. If numerical approaches are verified and validated to become trustworthy, they could be used with confidence in the design phase of new ship hulls. Since numerical simulations only require an available computer and not a large manufactured wooden ship model or a free towing tank slot, ship designers can easily test the seakeeping capabilities of tens or hundreds of ship hulls in the design phase. The use of numerical approaches also makes it possible to study the full-scale ships (Jasak et al., 2018;

[1] Technical University of Denmark, Department of Mechanical Engineering, Nils Koppels Allé, Building 404, 2700 Kgs. Lyngby, Denmark.
[2] Swiss Federal Institute of Technology Zurich, Computational Science & Engineering Laboratory, Clausiusstrasse 33, CH-8092 Switzerland

Niklas and Pruszko, 2019; Mikkelsen and Walther, 2020) and thereby avoid scale effects. The knowledge of a ship's seakeeping properties is also important from both a comfort and safety point of view. Most often, the comfort limit is reached before the motion limit for safety, especially for passenger ships. For non-passenger ships, comfort limits related to ship motions in waves are not as strict. For these ships, the safety can sometimes be the limiting factor, e.g., for container ships, where containers can fall into the sea, if motions become too large. However, the added resistance in waves is important for all ships, since it increases fuel consumption and potentially limits the ship speed.

One of the first studies of added resistance in waves is by Storm-Tejsen et al. (1973), who conducted added resistance experiments of the series 60 ships. Fujii and Takahashi (1975) compared experiments and strip theory simulations on the S175 container ship. Most seakeeping and added resistance research have been focusing on head sea waves. Added resistance in head sea waves using CFD, has been studied intensively by e.g., Sadat-Hosseini et al. (2013), who numerically studied the KRISO Very Large Crude 2 Carrier (KVLCC2). Kim et al. (2017) have also studied the KVLCC2 using both CFD and 3D potential flow theory. Park et al. (2016) studied the added resistance of a tanker in head sea waves at different drafts using the Salvesen-Tuck-Faltinsen (STF) strip theory (Salvesen et al., 1970) and a B-spline based time-domain Rankine panel method (Kim et al., 2011). Simonsen et al. (2013) and Wu et al. (2020) studied the added resistance of the KRISO Container Ship (KCS) in head sea waves both experimentally and using CFD.

Fewer validation studies have been conducted in oblique waves. Studying the ship-wave interaction in oblique waves is important in order to quantify the added power and maneuverability in a realistic sea, where the waves are seldomly uni-directional. A study by Sadat-Hosseini et al. (2015) presented experiments, potential flow, and CFD computations for added resistance for variable headings and wave lengths for the KCS. However, CFD simulations were only conducted for one wavelength. They found that the potential-flow method captures the heave and pitch motions well. However, surge, roll, and added resistance were not well predicted for most cases. In general, the accuracy of the CFD simulations was better. The reason why CFD simulations were only conducted for one wavelength, is that only one wave length was studied at the Tokyo 2015 CFD workshop (Hino et al., 2020). The Tokyo 2015 CFD workshop had a test case, where participants submitted CFD results of motion responses and added resistance for five headings and a single wavelength. Only two participants presented their CFD simulations. The first was Iowa Institute of Hydraulic Research (IIHR) using the CFD code CFDShip-Iowa Sadat-Hosseini et al. (2015). The second was University of Zagreb (UZ) using Naval Hydro Pack (Vukcevic and Jasak, 2016). Both participants showed fair prediction of the motion responses, but the discrepancy of added resistance between the CFD simulations and experiments were up to 100 %.

Considering the increasing popularity of CFD modelling in ship hydrodynamics and its potential capacity to model a more complex phenomenon that an ordinary PF approach cannot handle, e.g., water entry and exit, local wave breaking, viscosities, etc., there is a strong need for dedicated verification and validation studies for ships in waves with various heading and wavelengths.

The aim of the present study is to conduct validation studies of CFD simulations of motions responses and added resistance in oblique waves. The present study conducts CFD simulations of the KCS in two headings and six

wavelengths. The validation is done by comparing the CFD results with experiments from IIHR (Sadat-Hosseini et al., 2015; Sanada et al., 2021) and FORCE Technology (Simonsen et al., 2013).

METHODOLOGY

The present Unsteady Reynolds Averaged Navier-Stokes (URANS) CFD simulations are performed with the commercial CFD-code STAR-CCM+ v.2020.1 from Siemens (2020). STAR-CCM+ discretizes the governing equations using an unstructured finite-volume method. The code is widely used in the marine industry and is well known for its capabilities within marine applications. The CFD model has previously been validated for calm water resistance calculations in both model and full-scale (Mikkelsen et al., 2019; Mikkelsen and Walther, 2020).

KCS and Towing Tank Test

The studied ship is the Kriso Container Ship (KCS). The main particulars of the KCS can be seen in Table 1. The KCS is chosen since both experimental data and the hull geometry is publicly available. The studied wave conditions are shown in Table 2. The present study uses the same ship-fixed coordinate system used by IIHR (Sadat-Hosseini et al., 2015; Sanada et al., 2021) and is seen in Fig. 1. The towing tank tests at IIHR are conducted in a $40\text{m} \times 20\text{m} \times 3\text{m}$ wave basin (Sadat-Hosseini et al., 2015). Unless otherwise mentioned, this same model scale described in Table 1 will be used in all analyses in this paper. The towing tank tests in head sea by FORCE Technology are conducted with a longer ship model with $L_{pp} = 4.37$ m and a $240\text{m} \times 12\text{m} \times 5.5\text{m}$ wave basin.

Table 1: Main particulars

	Symbol	Value
Length between perpendiculars	L_{pp}	2.7 m
Beam	B	0.378 m
Draft	T	0.1268 m
Longitudinal radius of gyration	k_{xx}	$0.39B$
Transverse radius of gyration	k_{yy}	$0.25\ L_{pp}$

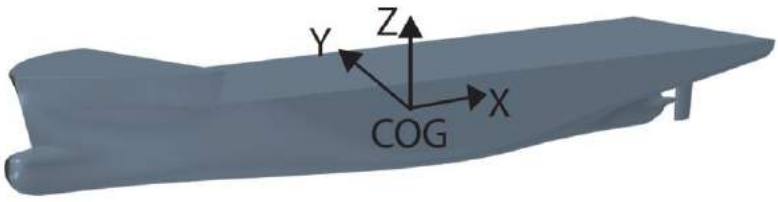

Figure 1. KCS ship geometry and coordinate system.

Table 2: Simulated wave conditions

Wave heading	Wave lengths [-]
Head sea	$\lambda/L = (0.5, 0.75, 1.00, 1.25, 1.50, 2.00)$
Bow sea	$\lambda/L = (0.5, 0.75, 1.00, 1.25, 1.50, 2.00)$

Computational Domain and Wave Generation

The shape of the CFD domain is a rectangular box. The top of the domain is set to a pressure outlet in order to allow the air flow to evolve freely. All vertical sides are velocity inlets. When all vertical sides are velocity inlets and not pressure outlets, the heading of the ship can be allowed to change in future maneuvering simulations. The modelled water depth in the CFD model is 3m, which is the same as that in the model tests. Since the longest wavelength considered in our study is 5.4m, it is not expected that the water depth has any important effects on the seakeeping and added resistance of the ship. Therefore, the bottom of the domain is treated as a velocity inlet.

The total computational domain contains two parts, namely the forcing zone (or relaxation zone) and the solution zone, see Fig. 2 for an illustration. The forcing zone at the outer layer of the computational domain is used to generate the incident regular waves. A smooth-transition function in the form of $cos^2(x)$ is applied within the forcing zone, so that the flow solution is enforced to be the same as the prescribed incident waves at the outer boundaries (the 4 vertical boundaries), while the forcing becomes zero at the end of the forcing zone, i.e. close to the boundary of the solution zoom. The forcing zone also acts as a wave absorbing zone due to the relaxation of the solution towards the targeted incident wave solution at the outer boundaries. In this paper, Stokes fifth-order waves are used as input waves, which are available from the built-in wave module in STAR-CCM+. The steepness of the incident wave is 1.7% in order to match the experimental data provided in (Sadat-Hosseini et al., 2015) and (Sanada et al., 2021).

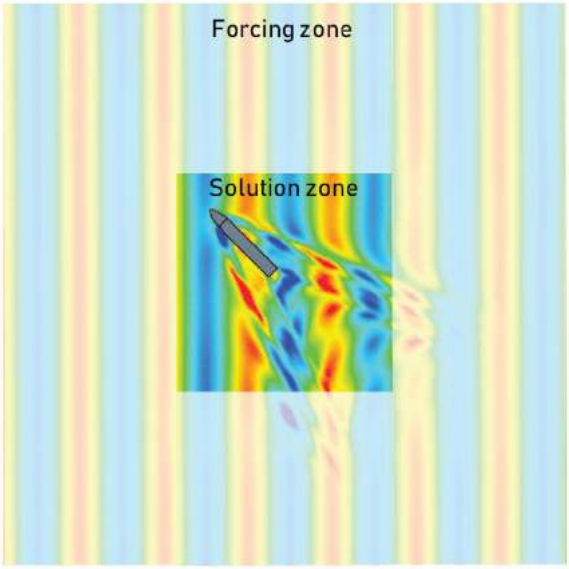

Figure 2. Forcing zone, solution zone and wave elevation for bow quartering sea and $\lambda/L_{pp} = 1$.

The width of the forcing zone is equal to two times the wavelength of the incident wave. The influence of the forcing zone width has been studies in detail. It is found that a forcing zone width of two incident wavelengths is a good compromise between numerical diffusion, wave reflection and computational cost. A forcing zone width of only one incident wavelength caused significant reflection (not shown). The inner volume, where no forcing is applied, is denoted the solution zone. The size of the solution zone is slightly different for each heading because the combination of generated steady Kelvin wave pattern and unsteady diffraction and radiation waves is different for each heading. However, the size of the solution zone is the same for all wavelengths for a given heading. A

size of the solution zone of approximately $3L_{pp} \times 3L_{pp}$ is chosen, so it is enough not to influence the added resistance and seakeeping.

Motions

In the IIHR experiments (Sadat-Hosseini et al., 2015; Sanada et al., 2021), the ship is fixed in z-rotation (yaw) and y-translation (sway). A spring-mass system is used in the experiments in the x-direction (surge), as described by Sadat-Hosseini et al. (2015). However, the surge motions are small (less than $1\%\ L_{pp}$) and for the Tokyo CFD workshop (Hino et al., 2020), which the experiments are made for, it was recommended to constrain the surge in the numerical studies. Therefore, the aim is to make a CFD model, where only the ship is free in z-translation (heave), *y*-rotation (pitch) and *x*-rotation (roll).

In the CFD model, the heave, pitch, and roll motions of the vessel are solved using the Dynamic Fluid Body Interaction (DFBI) Multi Body solver in STAR-CCM+ cf. (Ohmori, 1998; Siemens, 2020) and is applied as a rigid translation and rotation of the overset domain mesh. The DFBI Multi Body solver is chosen for its stability and accuracy. Sway is constrained accurately by the motion solver in STAR-CCM+. However, the DFBI solver in STAR-CCM+ version 2020.1 is found to produce an unacceptable drift in the constrained yaw. Besides the drift, it is found that constraining the yaw motion by the built-in motion module in STAR-CCM+ makes the roll response non-physical. Therefore, the surge and yaw motions are constrained using implementations by the authors. The surge motion is constrained by applying a concentrated *x*-force at each time step in the center of mass equal to the integrated shear and pressure forces acting on the hull with opposite sign. With this implementation, the speed of the ship never deviates more than 0.1% from the target ship speed. Since the integrated *x*-force is calculated each time step, the implementation allows the ship speed to be non-constant in future studies of, for instance, maneuvering simulations in waves and self-propulsion simulations in waves. The yaw motion is constrained by applying a concentrated z-moment and a torsional spring around the z-axis of the ship. The magnitude of the applied concentrated z-moment is equal to the integrated z-moment of the ship with opposite sign. The torsional spring constant is set to $20\mathrm{kNm/deg}$ in order to ensure a small yaw angle and a natural yaw frequency far from the natural frequencies of the motions and incident waves. The magnitude of the concentrated z-moment is approximately 50 times larger than the *z*-moment from the torsional spring. With this implementation, the simulated yaw angle never exceeds 0.01 deg and it is found not to influence the other motions.

Post-Processing of the Results

The main output from the simulations are time histories of heave (*Z*), pitch (θ), roll (φ) and total resistance (R). The resistance is the integrated shear stress and pressure on the hull in the *x*-direction. An example of a resistance time history is shown in Fig. 3. From an instant, where the solution $(s(t))$ has periodically steady outputs, an integer number of encounter periods T_e are fitted to a 4-term Fourier series:

$$s(t) = a_0 + a_1 \cos(\omega_1 t) + b_1 \sin(\omega_1 t) + \cdots + a_4 \cos(\omega_4 t) + b_4 \sin(\omega_4 t) \quad [1]$$

where $\omega_k = 2\pi\ f_e\ k$, and f_e is the encounter frequency.

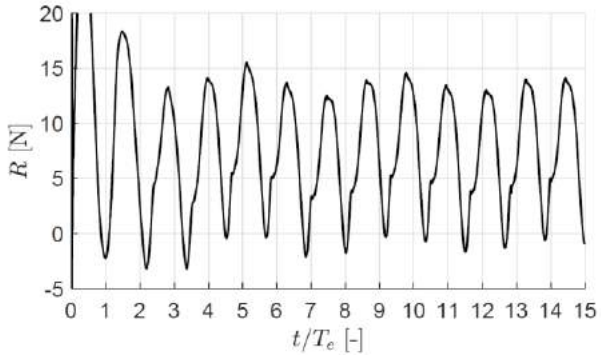

Figure 3. Time history of the measured resistance (R) at bow quartering sea and $\lambda/L_{pp} = 1$ as function of the time non-dimensionalized by with the encounter period (T_e).

Each fit is visually inspected to ensure that the fit is representable of the time history and that the fitting window does not start before the time history has stabilized. For the time history shown in Fig. 3, the fit only uses the time history for $t/T_e = 9 - 15$. Based on the Fourier coefficients from these fits, the amplitudes (A_k) for heave, pitch, roll, and resistance are calculated using:

$$A_k = \sqrt{a_k^2 + b_k^2} \quad [2]$$

where k is the Fourier term.

The same procedure is used in the Tokyo workshop (Hino et al., 2020) allowing for direct comparison. The present study only focuses on the added resistance and the first amplitude of heave (Z_1), pitch (θ_1), roll (ϕ_1). The added resistance (σ_{aw}) is defined as

$$\sigma_{aw} = \frac{R_0 - R_{CW}}{\frac{\rho g A^2 B^2}{L_{pp}}} \quad [3]$$

where R_0 is the zero-th amplitude (mean) resistance using Equation 1 and R_{CW} is the calm water resistance.

For the validation, the amplitudes are non-dimensionalized with the incident wave amplitude that actually reaches the ship and not the target wave amplitude, which is specified at the domain boundaries. The added resistance will also be calculated using the actual wave amplitude.

RESULTS AND DISCUSSION

The present CFD model is validated for each of the two studied headings in the following two subsections. The present CFD results are compared with up to three sets of Experimental Fluid Dynamics (EFD) data. For all headings, two set of experimental data are from IIHR by Sadat-Hosseini et al. (2015) and Sanada et al. (2021). The study by Sanada et al. (2021) also presents a calculated standard deviation for the $\lambda/L_{pp} = 1$ waves. These standard deviations are included as error bars in Fig. 4 and 5. In head sea, the results from FORCE Technology by Simonsen et al. (2013) are also included in the comparison as (FORCE). Furthermore, the present CFD results are compared with potential flow (PF) results by Sadat-Hosseini et al. (2015) who used the 3D PF code FATIMA (Bunnik, 1999). At the Tokyo CFD workshop in 2015, only two participants submitted their CFD results for the

case with motion responses and added resistance in oblique waves. The first participant is IIHR using the CFD code CFDShip-Iowa (Sadat-Hosseini et al. 2015). The second participant is University of Zagreb (UZ) using Naval Hydro Pack (Vukcevic and Jasak, 2016). Translatory and rotational motion responses are non-dimensionalized by the actual wave amplitude (A) and wave steepness (kA) respectively, where $k = \frac{2\pi}{\lambda}$. The added resistance is calculated using Equation 3.

Head sea

The comparison of the present CFD results, previously reported CFD and PF results, and three sets of experimental data for head sea can be seen in Fig. 4. For this heading, the agreement between the three experimental data sets is good. Both the present CFD, UZ CFD and PF motions responses agree very well with the experiments. In general, the present CFD results show slightly better agreement in motion responses than the PF results, especially for the longer waves. The encounter frequency of the $\lambda/L_{pp} = 1.25$ wave is very close to the natural heave and pitch frequencies causing resonance. The CFD by IIHR and the PF results overestimates the added resistance near the resonance area by approximately 45%. However, the added resistance estimated by the present CFD model is within the standard deviation of the experiments by Sanada et al. (2021).

Bow quartering sea

Fig. 4 shows the comparison of the present CFD results, previously reported CFD and PF results, and two sets of experimental data for bow quartering sea. The heave responses shown in Fig. 5a, predicted by both the present CFD and PF agree very well with the experiments. The largest deviation is observed for the longest wave. However, the deviation is still smaller than the difference between the two sets of experiments. For the pitch response, shown in Fig. 5b, both the present CFD and PF agree well with the experiments for the two shortest waves. For the longer waves, both the PF and the present CFD results approach an asymptotic limit. The PF agrees excellently with the pitch found in the EFD by Sadat-Hosseini et al. (2015) for all wavelengths and approaches an asymptotic value very similar to the value found by the experiments by Sadat-Hosseini et al. (2015) at $\lambda/L_{pp} = 2.0$. The present CFD approaches a value similar to the value found in the experiments by Sanada et al. (2021) at $\lambda/L_{pp} = 2.0$. The CFD by UZ predicts the heave and pitch responses well, whereas the CFD by IIHR overestimates the heave and pitch responses by approximately 10%. The roll responses found in the experiments are much larger than any of the numerical methods as seen in Fig. 5c. The roll responses predicted by the PF and all three CFD approaches agree well with each other, but not with the experiments. Even the smallest encounter frequency of the studied waves in bow quartering sea is 0.72 Hz. This is more than double the natural roll period (0.33 Hz) with forward speed. It is not clear why the experimental roll responses are about one order of magnitude higher than numerical results. This needs more dedicated experimental studies in the future and is out of the scope of the present study. When the wavelength is increased, the encounter frequency is decreasing for the bow quartering sea. Therefore, it is expected that the roll responses should only increase slowly while the wavelength is getting larger, and the encounter frequency becomes closer to the natural roll frequency. This is the behavior of all the numerical results in Fig. 5c. In general, both the PF and the present CFD overestimates the added resistance at the shorter waves and underestimates the added resistance at the longer waves as seen in Fig. 5d.

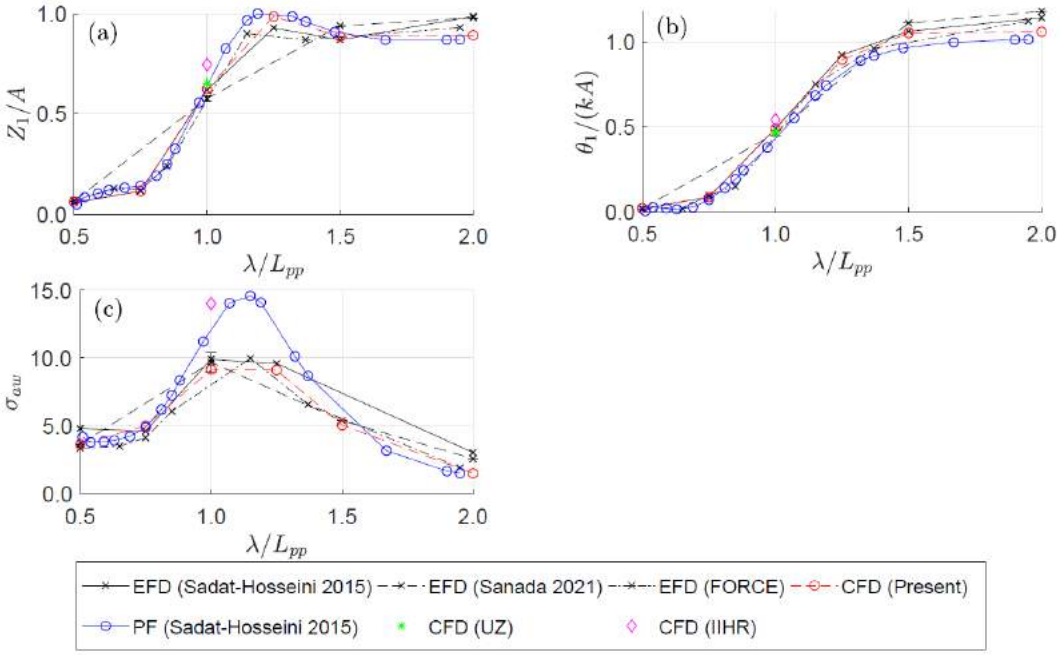

Figure 4. Comparison of results for head sea as a function of non-dimensional wavelength (λ/L_{pp}). (a) Heave, 1st amplitude (Z_1); (b) Pitch, 1st amplitude (θ_1); (c) Added resistance (σ_{aw}).

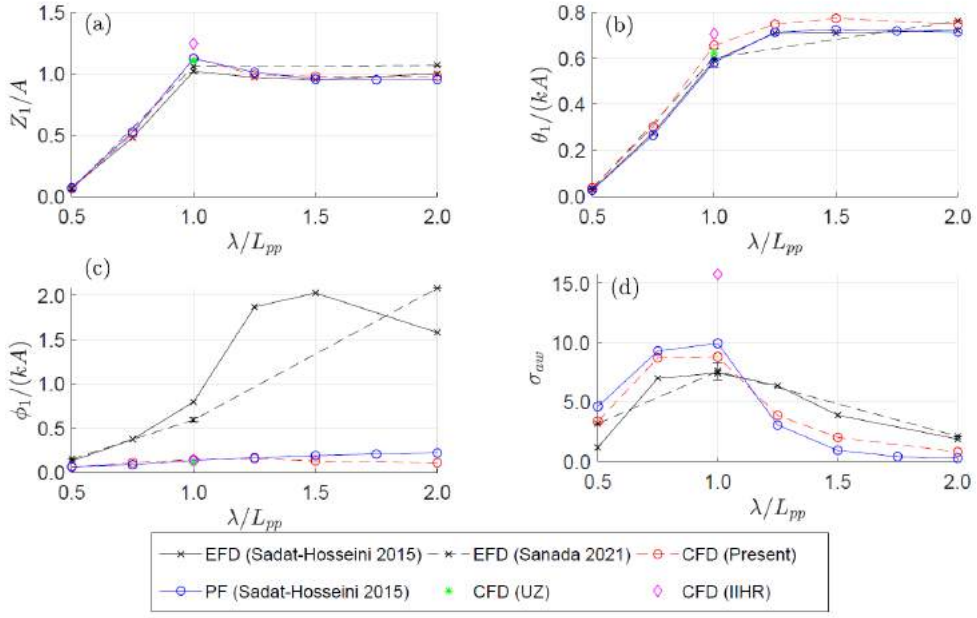

Figure 5. Comparison of results for bow quartering sea as a function of non-dimensional wavelength (λ/L_{pp}). (a) Heave, 1st amplitude (Z_1); (b) Pitch, 1st amplitude (θ_1); (c) Added resistance (σ_{aw}).

However, the added resistance from the present CFD is closer to the experiments for all wavelengths than the PF results. For the $\lambda/L_{pp} = 1.0$ wave, the CFD by IIHR overestimates the added resistance by approximately 100%, whereas the present CFD overestimates the added resistance by approximately 18%. The standard deviation of the experimental added resistance by Sanada et al. (2021) is 10.7% at this wave.

CONCLUSION

This study presents a validation of seakeeping responses and added resistance of the KCS container ship in regular oblique waves by using CFD. The surge and yaw motions are constrained by user-implementations in the commercial software, which consist of additions of springs and concentrated forces/moment to cancel the fluid forces and moments. For each test case, the added resistance as well as the heave, pitch, and roll response are compared with previously reported potential flow and CFD results and up to three sets of experimental data. Due to the loss of incident wave amplitude caused by numerical diffusion, the motion and added resistance results are non-dimensionalized based on the actual incident wave amplitude obtained from separate runs in an empty wave tank, where similar spatial and temporal discretization is used.

In most cases the discrepancy between the experiments and the present CFD results are within the uncertainty of the experiments. In general, both the previously reported potential flow calculations and present CFD simulations predict the motion responses well. However, the added resistance predicted by the present CFD model is in better agreement with the experiments, than the previously reported potential flow results. Furthermore, the present CFD results in general show significantly better agreement with the experiments than previously published CFD results. The tendencies in the results of the present CFD model matches very well the expected behavior regarding the natural motion frequencies of the ship. The study has shown that CFD simulations accurately can predict motion responses and added resistance in oblique regular waves.

ACKNOWLEDGEMENT

The research is supported by the Danish Maritime Fund under grant 2018-11, whose support is greatly appreciated.

REFERENCES

Bunnik, T. H. J. (1999). “Seakeeping calculations for ships, taking into account the non-linear steady waves”. PhD thesis, Delft University of Technology.

Fujii, H. and Takahashi, T. (1975). “Experimental study on the resistance increase of a large full ship in regular oblique waves", Numerical ship hydrodynamics: An assessment of the Tokyo 2015 workshop. Springer-Verlag.

Jasak, H., Vukčević, V., Gatin, I., and Lalović, I. (2018). “CFD validation and grid sensitivity studies of full scale ship self propulsion”. Int. J. Nav. Archit. Ocean Eng., 11(1):33–43.

Kim, Y., Kim, K.-H., Kim, J.-H., Kim, T., Seo, M.-G., and Kim, Y. (2011). “Time-domain analysis of nonlinear motion responses and structural loads on ships and offshore structures: development of WISH programs”. Int. J. Nav. Archit. Ocean Eng., 3(1):37–52.

Kim, M., Hizir, O., Turan, O., and Incecik, A. (2017). “Numerical studies on added resistance and motions of KVLCC2 in head seas for various ship speeds”. Ocean Engng., 140(May):466–476.

Mikkelsen, H., Steffensen, M. L., Ciortan, C., and Walther, J. H. (2019). “Ship scale validation of CFD model of self-propelled ship”. In MARINE 2019 Computational Methods in Marine Engineering VIII, pages 718–729.

Mikkelsen, H. and Walther, J. H. (2020). “Effect of roughness in full-scale validation of a CFD model of self-propelled ships”. Appl. Ocean Research, 99:1–14.

Molland, A., Turnock, S., and Hudson, D. (2011). “Ship resistance and propulsion”. Cambridge University Press.

Niklas, K. and Pruszko, H. (2019). “Full-scale CFD simulations for the determination of ship resistance as a rational, alternative method to towing tank experiments”. Ocean Engng., 190:1–13.

Ohmori, T. (1998). “Finite-volume simulation of flows about a ship in maneuvering motion”. J. Mar. Sci. Tech., 3(2):82–93.

Park, D. M., Kim, Y., Seo, M. G., and Lee, J. (2016). “Study on added resistance of a tanker in head waves at different drafts”. Ocean Engng., 111:569–581.

Psaraftis, H. N. and Kontovas, C. A. (2014). “Ship speed optimization: Concepts, models and combined speed-routing scenarios”. Transp. Res. Part C Emerg. Technol., 44:52–69.

Sadat-Hosseini, H., Wu, P. C., Carrica, P. M., Kim, H., Toda, Y., and Stern, F. (2013). “CFD verification and validation of added resistance and motions of KVLCC2 with fixed and free surge in short and long head waves”. Ocean Engng., 59:240–273.

Sadat-Hosseini, H., Toxopeus, S., Kim, D. H., Sanada, Y., Stocker, M., Otzen, J. F., Toda, Y., and Stern, F. (2015). “Experiments and computations for KCS added resistance for variable heading”. In 5th World Maritime Technology Conference, pages 1–15.

Salvesen, N., Tuck, E., and Faltinsen, O. (1970). “Ship motions and sea loads”. Trans. - Soc. Nav. Archit. Mar. Eng., 78:250–287.

Sanada, Y., Simonsen, C., Otzen, J., Sadat-Hosseini, H., Toda, Y., and Stern, F. (2021). “Experimental data for KCS added resistance and ONRT free running course keeping/speed loss in head and oblique waves”, volume 94. Springer-Verlag.

Siemens (2020). STAR-CCM+ user guide, version 2020.1.

Simonsen, C. D., Otzen, J. F., Joncquez, S., and Stern, F. (2013). ”EFD and CFD for KCS heaving and pitching in regular head waves”. J. Mar. Sci. Tech., 18:435–459.

Storm-Tejsen, J., Yeh, H. Y. H., and Moran, D. D. (1973). “Added resistance in waves”. Trans. - Soc. Nav. Archit. Mar. Eng., 81:250–279.

Vukčević, V. and Jasak, H. (2016). “Validation and verification of decomposition model based on embedded free surface method for oblique wave seakeeping simulations”. In Tokyo 2015: A Workshop on CFD in Ship Hydrodynamics, pages 495–502.

Wu, P.-C., Hossain, M. A., Kawakami, N., Tamaki, K., Kyaw, H. A., Matsumoto, A., and Toda, Y. (2020). “EFD and CFD study of forces, ship motions, and flow field for KRISO container chip model in waves”. J. Ship. Res., 64(1):61–80.

Towards hydrodynamic modelling of ship-to-ship LNG bunkering in waves with focus on gap resonance

Y. F. Ding[1], J. H. Walther [1, 2] and Y. L. Shao[1]

ABSTRACT

Ship-to-ship bunkering of liquid fuel, e.g., LNG, outside the port can be a flexible and cost-efficient solution without having to upgrade the infrastructures at the port. The occurrence of fluid resonance in the narrow gap between side-by-side receiving vessel and bunkering vessel under wave actions may greatly influence the dynamic responses of the vessels through hydrodynamic interaction. The proximity of marine structures can generate drastic wave elevation in the narrow gap, which may reduce the operational time window of the bunkering and even risk the safety of the crew. In this paper, the fluid resonance inside the gap between two non-identical ship cross-sections in side-by-side configuration is studied under various wave conditions. The bunkering scenario that a larger cross-section on the upstream is fixed while a small cross-section free to heave in the downstream is considered as more realistic. A numerical wave tank is set up based on the commercial CFD package STAR-CCM+. The unsteady Reynolds averaged Navier-Stokes turbulence model is required to consider viscous dissipation. The volume of fluid method is applied to capture the position of the free surface, and regular waves are generated and absorbed using forcing zones at upstream and downstream boundaries, respectively. The overset meshing technique is employed near the downstream section to enable the heave motion. The heave response of the downstream section and its effect on the linear and nonlinear harmonics of wave elevation and resonant frequency inside the gap are investigated and compared with the fixed-sections scenario. It can be concluded that the heave motion reduces the gap resonance to a large extent by modulating the frequency of wave elevation inside the gap, thus avoiding the occurrence of second-order excitation.

KEY WORDS

Gap resonance; Ship-to-ship LNG bunkering; Harmonic analysis; Free heave motion; STAR-CCM+.

INTRODUCTION

Recently, ship-to-ship bunkering has become a more efficient and safe way to fuel the LNG-fueled vessels outside the port. During the bunkering operations, fluid resonance inside the gap between the side-by-side receiving vessel and bunkering vessel may elevate the water surface within the gap to a large extent and influence the dynamic responses of the vessels due to hydrodynamic interaction. One of the relevant and important phenomena is referred to as piston-mode gap resonance in the literature, which is a key hydrodynamic issue that needs a thorough and deep understanding of the underlying physics. Large wave elevation due to the gap resonance may also lead to wave impacts on the soft hoses which are typically used to transfer liquid LNG between the two vessels.

Physical experiment is a direct approach to explore this problem (Kristiansen and Faltinsen 2008, 2010; Faltinsen, et al. 2011; Tan, et al. 2014). Saitoh et al. (2006) conducted laboratory experiments to understand the characteristics of fluid resonance in the gap between two fixed barges exposed to waves. Perić and Swan (2015) used experiments to characterize both the amplitude and nature of the excitation within the gap. Experiments were also carried out by Ning et al. (2018) to investigate the wave response in the gap between two barges of different draughts in incident waves.

Early numerical studies towards fluid resonance in a confined region with the presence of a free surface started with the theoretical investigation based on the linear potential-flow theory (Miao, et al. 2000; Iwata, et al. 2007; Zhu, et al. 2008).

[1] Department of Mechanical Engineering, Technical University of Denmark, 2800 Kgs. Lyngby, Denmark
[2] Computational Science and Engineering Laboratory, ETH Zürich, CH-8092 Zürich, Switzerland

Molin (2001) considered rectangular moonpools of large horizontal dimensions and determined the natural modes for the oscillation of the inner free surfaces in both two and three dimensions. Improved potential-flow methods with viscous corrections were applied to avoid non-physically large wave elevation within the gap at the resonance (Tan, et al. 2014; Ning, et al. 2015a, 2015b; Zhao, et al. 2018; Tan, et al. 2019). Based on both the viscous-flow model and the potential-flow model with the introduction of artificial damping term, Lu et al. (2011) presented two-dimensional (2D) numerical results of the wave loads on multiple floating bodies in close proximity and their dependences on the wave frequency, gap width, body draft, body breadth, and the number of bodies. However, they pointed out that the artificial damping has to be calibrated by model tests or Computational Fluid Dynamics (CFD) simulations in order to achieve better prediction, which may lose its advantage and limit the application of the potential-flow models to a large extent.

With the development of the capacity of modern computers to run large-scale computations, CFD methods based on Navier-Stokes equations have become a popular alternative to deal with the gap resonance problem (Lu, et al. 2010; Chua, et al. 2018; Jiang and Bai 2020). Moradi et al. (2016) reported that the water depth, body draft, and the ratio between water depth and body draft are the key factors that influence the resonant responses. It was also found that the potential-flow models not only overpredict the resonant wave heights but also fail to predict the variation trends of the resonant wave height as function of water depth. In the work of Jiang et al. (2019), piston-mode wave resonance between a ship section and a bottom-mounted terminal was studied, where it is also confirmed that the effects of fluid viscosity and the vorticity increase significantly with the increase of incident wave amplitudes. Some numerical investigations were also carried out by Gao et al. (2019, 2020a, 2020b) to simulate transient resonant motions of the free surface inside a narrow gap under various configurations and wave conditions.

As we can see from the previous studies, the focuses of most existing studies are on the fixed structures (Sun, et al. 2010; Moradi, et al. 2015; Gao, et al. 2019, 2020a, 2020b; Jiang, et al. 2021a, 2021b). In practice, floating marine structures are free to move in certain directions although they may be constrained in other degrees of freedom. To date, only few studies considered the floating structure with certain degrees of freedom of motion (Li and Zhang 2016; Li 2019; Lu, et al. 2020). These studies simulated the coupled motions of two structures and applied the potential-flow models, while the relevance to practical ship-to-ship bunkering operations is not clear. Gao et al. (2021) studied the influence of the free-heave motion of an upstream box on the gap resonance under wave actions while the downstream box remains fixed. However, in practical ship-to-ship bunkering operations, the two vessels are typically very different in size, and, naturally, the small bunkering vessel will be situated behind the larger receiving vessel thus avoiding violent relative motion between them. Therefore, the present work focuses on the gap resonance formed by two non-identical square cross-sections under wave actions. The larger upstream section remains fixed and the smaller downstream section is free to heave.

The remainder of this paper is organized as follows: the mathematical formulation of the numerical model, the applied numerical schemes and solvers are introduced, followed by the establishment of the 2D numerical wave flume. After that, two validation studies are presented, including two fixed barges and a single barge free to heave. Finally, numerical results for two non-identical barges, i.e., a fixed upstream barge and a downstream barge free to heave, are presented.

NUMERICAL MODEL

The Unsteady Reynolds Averaged Navier-Stokes (URANS) turbulence model is applied to consider viscous dissipation and the Volume of Fluid (VOF) implementation is selected to capture the free surface. The motion of the heaving section is realized by employing the overset meshing technique. For more implementations on the scheme and solver regarding the numerical model, interested readers are referred to the book by Ferziger et al. (2002) or the STAR-CCM+ user guide.

Governing Equations

The VOF multiphase model in STAR-CCM+ is applied to predict the distribution and the movement of the interface between the air and water phases, in which mass conservation equation and momentum equation can be expressed as:

$$\frac{d}{dt}\int_V \rho dV + \int_S \rho(\boldsymbol{v}-\boldsymbol{v}_g)\cdot\boldsymbol{n}dS = 0 \quad [1]$$

$$\frac{d}{dt}\int_V \rho u_i dV + \int_S \rho u_i(\boldsymbol{v}-\boldsymbol{v}_g)\cdot\boldsymbol{n}dS = \int_S (\tau_{ij}\boldsymbol{i}_j - p\boldsymbol{i}_i)\cdot\boldsymbol{n}dS + \int_V \rho\boldsymbol{g}\boldsymbol{i}_i dV \quad [2]$$

where V is the control volume bounded by the closed surface S; $\boldsymbol{v}$ and $\boldsymbol{v}_g$ are the velocity vectors of the fluid with the Cartesian components u_i and of the grid, respectively; $\boldsymbol{n}$ is the unit vector normal to S and pointing outwards; t represents the time; p is the pressure and ρ is the fluid density; $\boldsymbol{i}_i$ and $\boldsymbol{i}_j$ are the unit vectors in direction x_i and x_j, respectively; $\boldsymbol{g}$ is the gravity vector; τ_{ij} are the components of the viscous stress tensor.

The volume fraction in this method is defined as:

$$\alpha = \begin{cases} 0, & \text{in air} \\ 0 < \alpha < 1, & \text{at the surface} \\ 1, & \text{in water} \end{cases} \quad [3]$$

Then the spatial variation of any fluid property f (e.g., the density ρ, and the dynamic viscosity μ) can be represented as a weight of α:

$$f = \alpha f_{water} + (1-\alpha) f_{air} \quad [4]$$

in which, the subscript "water" and "air" denote the property of the corresponding phase, respectively.

The governing equation of volume fraction is:

$$\frac{d}{dt}\int_V \alpha dV + \int_S \alpha(\boldsymbol{v} - \boldsymbol{v}_g)\cdot \boldsymbol{n} dS = 0 \quad [5]$$

Here, α is the volume fraction of water. In this study, $\alpha = 0.5$ is adopted to capture the interface between the two phases.

Body and Mesh Motions

The Dynamic Fluid Body Interaction (DFBI) module in STAR-CCM+ is employed to simulate the motion response of the ship section exposed to incident regular waves. In this work, only translatory motion in heave will be considered and solved based on Newton's second law.

The overset meshing technique is coupled with the DFBI module to update the mesh position around the heaving section. Meshes in the overset region move rigidly with the motion of the section, where the solution is coupled with the flow domain (the background region) by linearly interpolating donor-cell values to provide data for acceptor cells.

Boundary Conditions and Numerical Implementations

The wave is generated by prescribing the volume fractions and the velocities according to Fenton's 5th-order Stokes theory at both the inlet and outlet boundaries ($x = -L/2$ and $x = L/2$). Here L denotes the total length of the numerical wave flume. To minimize the undesired wave reflection for long-duration simulations, wave forcing is applied at the inlet and outlet boundaries to enforce the solution of the Navier-Stokes equations towards the prescribed nonlinear wave solution (Kim, et al. 2012). The no-slip boundary condition is imposed on the fixed section and the seabed, and the overset mesh is prescribed on the surfaces of the overset region that moves with the heaving section. The top boundary of the domain is defined as a pressure outlet by prescribing the hydrostatic pressure and the volume fractions of both phases (see Figure 1). The simulations are run in a quasi-2D manner with only one layer of cells in the transverse direction and symmetry boundary conditions are applied on the side-walls of the wave flume. Numerical simulations start from the still-water state with predefined initial conditions of the velocity and hydrostatic pressure of the incident wave.

The governing equations 1, 2 and 5 are solved for each cell based on the finite volume method, with all integrals approximated by the midpoint rule. The VOF method is used to account for the two fluid phases with the setup of angle factor in the High Resolution Interface Capturing scheme (HRIC) to eliminate wiggles on the free surface (Muzaferija and Perić 1999). The standard low-Re k-ε turbulence model with all-y+ wall treatment is applied to prevent excessive growth of turbulent viscosity in the free-surface zone (Perić 2018). The interpolation of variables from cell centre to face centre and numerical differentiation are performed using linear functions (second-order accuracy). The applied time-integration scheme is also of second order. The resulting coupled system of equations is then linearized and solved by the iterative implicit unsteady segregated solver in STAR-CCM+, using a multigrid method. Eight outer iterations are performed in each time step, which consists of solving the governing equations for the velocity components, the pressure-correction equation (using the SIMPLE method), and the transport equations for the volume fraction of water, as well as the turbulent kinetic energy k and the turbulent dissipation rate ε. In addition, the time step is adaptive to satisfy the Courant-Friedrichs-Lewy (CFL) condition on the free surface, that is, $\Delta t \leq C_r \Delta x / v_r$. Here, Δx and v_r are the mesh size and relative velocity of the fluid to the mesh, respectively. To guarantee the accuracy and stability of the results, the maximum convective Courant number C_r on the free surface is set to around 0.1 in all simulations.

NUMERICAL WAVE FLUME

The 2D numerical wave flume is established, which is shown in Figure 1. The height of the wave flume is three times the height H_1 of the larger section and its length is around 9λ, where λ is the incident wavelength. To achieve quasi-2D simulations, only one grid cell is applied along the width of the flume, whose size is set as $W = 0.08H_1$. The origin of the Cartesian coordinate system is set on the still wave line (SWL) and at the middle of the wave flume, with wave propagating along the x-axis and elevating along the z-axis. Two non-identical square sections are located at the centre of the wave flume with a water depth of $h = H_1$ and a gap width of $B_g = 0.1B_1$. The larger upstream section (hereafter denoted as section A) is fixed, which has the height H_1 and breadth B_1 and a draft of $d_1 = 0.5H_1$. The smaller downstream section (hereafter section B) is free to heave with the side width of $H_2 = B_2 = 0.6H_1(B_1)$ and the draft of $d_2 = 0.3H_1$.

To the best of the authors' knowledge, no model-test data for non-identical sections are available in the literature, thus we will use the two identical sections which have been experimentally studied by Saitoh et al. (2006) to validate our setup in the numerical model. For simplicity, the system with two identical fixed boxes will be referred as "*fixed system*" later in this paper, and the other non-identical system studied here with a freely-heaving section is named "*heave system*".

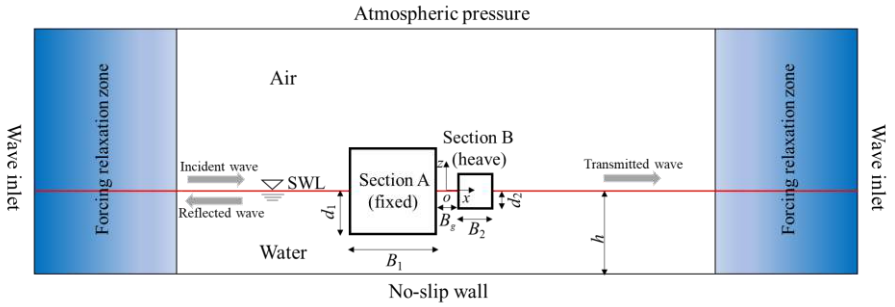

Figure 1: Sketch of the 2D numerical wave flume with two non-identical sections in the middle.

Two Stokes waves (hereafter called wave A and wave B) with equal wave height $H_0 = 0.048H_1$ but different wavelengths $\lambda_A = 4.044B_1$ and $\lambda_B = 9.92B_1$ are considered as incident waves in the numerical analysis. The frequency of wave A corresponds to the natural frequency of the liquid in the gap (the resonant frequency) of the *fixed system*, while the frequency of wave B is half this resonant frequency. Two relaxation zones, whose lengths are twice the wavelengths of the incident regular waves, are applied at the inlet and outlet boundaries respectively to absorb the reflected and transmitted waves.

Trimmed mesh is adopted in the entire domain and a typical mesh configuration is displayed in Figure 2, with finer resolution near the free surface and inside the narrow gap. Near the free surface, the amount of meshes along the vertical z direction is 20 per wave height for all the studied cases and the mesh size along the horizontal x direction is designed to keep a constant aspect ratio $\Delta x/\Delta z = 8$, which was determined based on careful tests to produce high-quality incident waves (details not shown here). The meshes are also refined close to the sections in both phases to better resolve the flow due to the motion of section B and the flow separation around the sharp corners of both sections. The same mesh refinement is supposed to be employed in the overset region with adequate prism layers at the interface to achieve the data interpolation between cells.

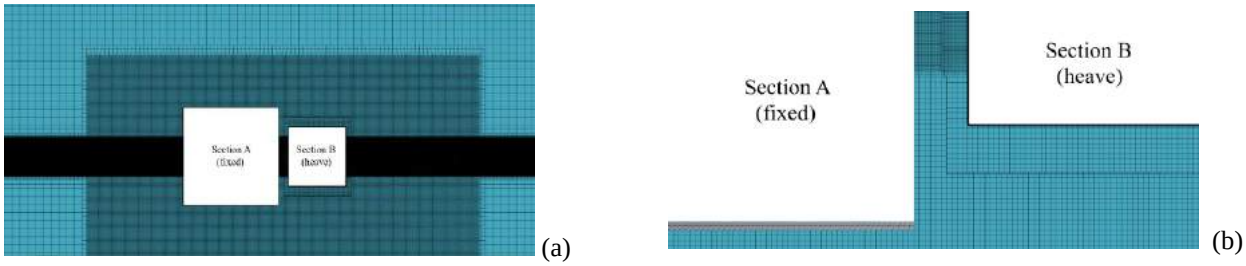

(a) (b)

Figure 2: Mesh configuration in the computational domain: (a) around the sections; (b) close to the gap.

VALIDATION

The present numerical model will be validated by two cases: (I) a *fixed system* with two identical sections and 5 different gap widths; (II) a single section free to heave in waves with 9 different wavenumbers. In the first case, the numerical results of free-surface elevation in the narrow gap obtained by using the computational setup described in the previous section will be compared with the existing experimental data (Saitoh et al. 2006). In the second case, the heave motion of the floating section will be compared with the experimental measurement by Rodríguez and Spinneken (2016).

Free Surface Amplification (Case I)

The simulated non-dimensional wave height amplifications in the gap of various widths B_g for the *fixed system* with incident wave height $H_0 = 0.048H_1$ and non-dimensional water depth $kh = 2.476$ are presented in Figure 3. Here k and h are the wavenumber and water depth, respectively. It has to be noted that the draft of both sections is $d/H_1 = 0.31$ in this validation study. H_g represents the free surface elevation within the gap and B_g is the gap width. It can be seen that the present results correspond well with the experimental data except for a small underestimation for the gap with a width of $0.06B_1$.

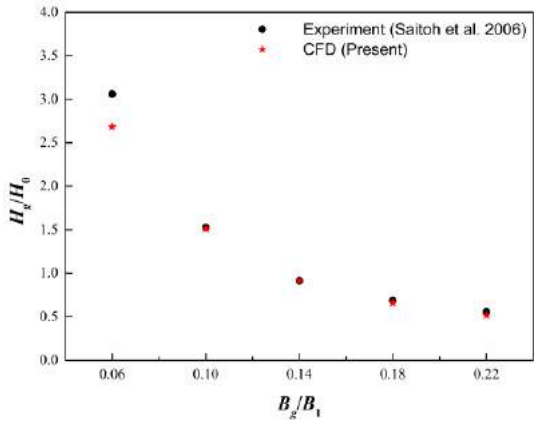

Figure 3: Amplifications of wave elevation (H_g/H_0) in the gap of various widths B_g for the *fixed system*.

Heave Amplitude (Case II)

Rodríguez and Spinneken (2016) carried out physical experiments in a 2D wave flume to investigate the free heave motion of a single rectangular box under regular waves. The wave tank is 63 m long, 2.79 m wide, and has a water depth of 1.25 m. A rectangular box is located at $x = 29$ m while the incident wave is generated from $x = 0$ m. A gap width of 0.015 m is set between the box surface and the side boundaries of the tank to approximate 2D flow condition. The box has a breadth of 0.5 m and a draft of 0.25 m. Stokes waves with the steepness $kA_0 = 0.05$ and different wavenumbers k are considered to validate the present numerical model. Here A_0 denotes the incident wave amplitude. The numerical wave flume adopted (not shown here) is similar to that in Figure 1 except for a different water depth and that a single box in the middle of the wave flume is studied in this validation case. The length of the wave tank is not exactly the same as that in the experiment due to the application of the forcing zones at both the inlet and outlet boundaries. Figure 4 shows the normalized heave motion amplitude of the floating box versus the non-dimensional wavenumber. It is observed that the numerical results correspond well with the experimental data except for some underestimation near the resonance.

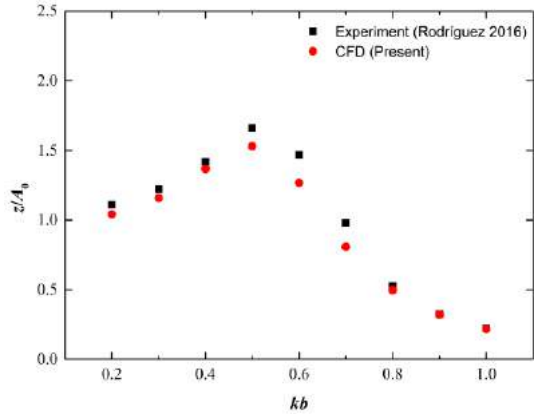

Figure 4: Non-dimensional heave amplitudes (z/A_0) of a free-heaving box under incoming Stokes waves.

RESULTS AND ANALYSIS

To study the effect of the heave motion of downstream section B on the gap resonance, the free surface elevation in the narrow gap is monitored for the *heave system* under the action of incident waves with different wavelengths. Then the Fast Fourier Transform (FFT) method is applied to obtain the harmonics of the responses. Next, the time series of the heave displacement of section B is measured, and its relationship with the vertical force acting on section B is discussed. The harmonic analysis is subsequently carried out for the heave displacement and the results are discussed. Finally, the

flow field of wave A (wave frequency equals to gap-resonant frequency) is demonstrated in the vicinity of the gap to understand the physics of this phenomenon.

Free Surface Elevations

Overall Amplifications

The non-dimensional time histories of free surface elevation inside the gap for the *heave system* exposed to two Stokes waves (wave A and wave B) are shown in Figure 5. The corresponding results for the *fixed system* and the incident-wave elevation are also included for comparison. It is observed that the wave elevations in the gap for the *heave system* under both waves are smaller than those for the *fixed system*, and are also smaller than the incident wave amplitudes. Large wave amplitude appears in the gap for the *fixed system* when the wave frequency coincides with the natural frequency of the water bulk within the gap, which demonstrates the occurrence of the gap resonance and the corresponding Response Amplitude Operator (RAO), namely the ratio of amplitude of free surface elevation in the narrow gap to the height of the incident wave, can reach up to 4.6. For incident wave B, the elevation decreases to around 1.5 times the incident wave height for the *fixed system*. It should be noted that the second-order component presents as a result of nonlinear wave-wave and wave-structure interactions in wave case B (wave frequency equals to half-resonant frequency). When the incident wave frequency is close to half the resonant frequency, the second-order wave loads can stimulate the resonant gap response. The wave elevations in the narrow gap for the *heave system* do not show similar trends as those for the *fixed system*. The heave motion of section B absorbs the energy in the gap and modulates the resonant frequency to some extent.

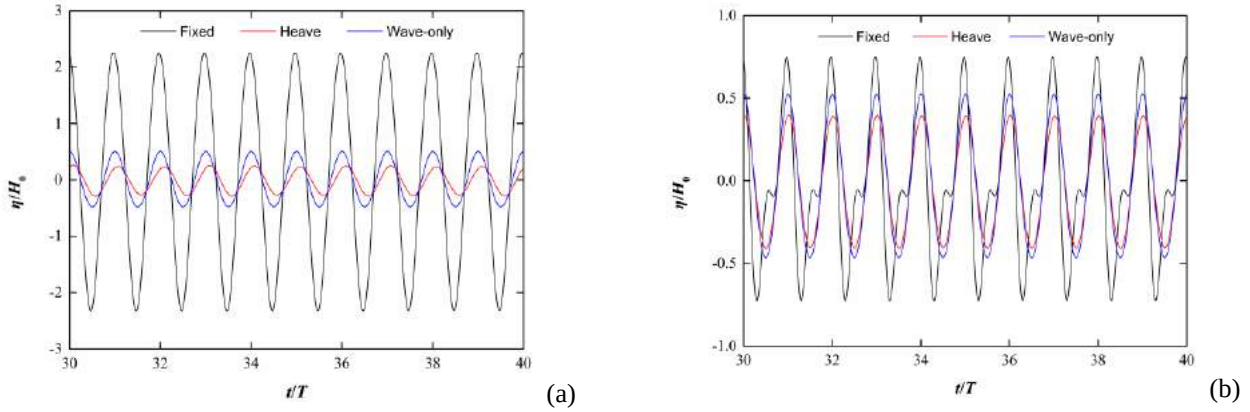

Figure 5: Time history of the free surface elevation in the gap (η/H_0) for the *fixed system* and *heave system* under different incident wavelengths: (a) Stokes wave A (resonance); (b) Stokes wave B (half-resonance).

Harmonic Analysis

Harmonic analysis is performed to understand the contribution of each frequency component. Figure 6 presents the first three orders of normalized amplitudes of the free-surface elevation in the gap for both the *fixed system* and *heave system* under different incident waves, and the amplitudes of the harmonics are listed in Table 1. It can be seen that the first-harmonic component of wave elevation in the gap is excited in the *fixed system* at the resonance, while the first-harmonic component for the *heave system* remains smaller than the incident wave amplitude. A rather small second-harmonic component can be observed for the *heave system*. When the incident wave frequency is half the resonant frequency, the second-harmonic component is excited in the *fixed system*, and its amplitude can take up 42.4% of the first-harmonic component while the first-harmonic component drops back to a bit larger than that of the incident wave, which is consistent with the conclusion in the previous time-domain result. The second-harmonic component of wave elevation is not stimulated by the incident wave for the *heave system*. This is due to the existence of heave motion of section B, which modulates the frequency of the free surface variation inside the gap and averts the occurrence of second-order excitation.

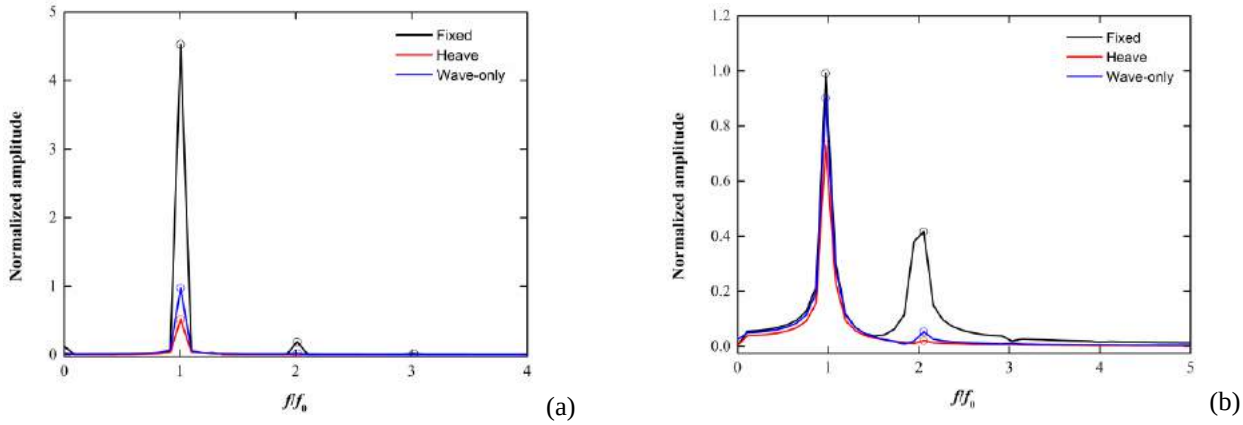

Figure 6: Normalized amplitude of the free surface elevation in the narrow gap for the *fixed system* and *heave system* under different incident wavelengths: (a) Stokes wave A (resonance); (b) Stokes wave B (half-resonance).

Table 1: Normalized harmonic components of wave elevation amplifications in the gap under different incident wavelengths

	$H_g^{(i)}/H_0$ ($H_g^{(i)}/H_g^{(1)}$)					
λ/h	i = 1		i = 2		i = 3	
	Fixed	Heave	Fixed	Heave	Fixed	Heave
4.044 (wave A)	4.53	0.258	0.19 (4.19%)	0.005 (1.94%)	0.02 (0.44%)	0.001 (0.39%)
	Fixed	Heave	Fixed	Heave	Fixed	Heave
9.920 (wave B)	0.991	0.731	0.42 (42.4%)	0.021 (2.87%)	0.03 (3.03%)	0.007 (0.96%)

Heave Displacements

Overall Displacements

The heave displacements of section B excited by the incident waves are monitored and analyzed to investigate the relationship between the heave motion and the gap resonance (see Figure 7). The non-dimensional vertical forces acting on section B are also displayed in the figure, where $A_0 = H_0/2$ denotes the incident wave amplitude. It is obvious that the heave displacement under the action of wave B is larger than that under wave A, while the vertical force is smaller. This is due to the fact that wave B is longer than wave A. A longer wave experiences less diffraction due to the presence of the upstream section, and thus more energy can be transmitted to the downstream to excite the motion of section B.

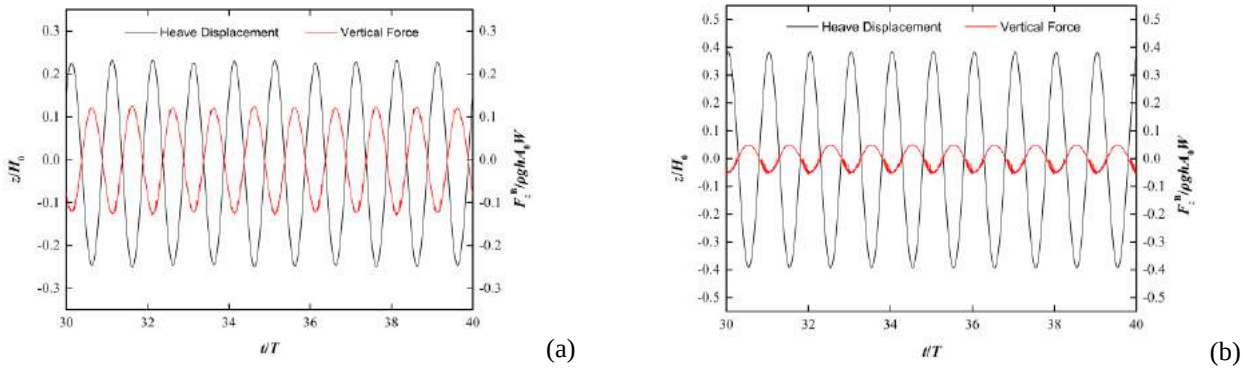

Figure 7: Time history of the heave displacement and the normalized vertical force of section B under different incident wavelengths: (a) Stokes wave A (resonance); (b) Stokes wave B (half-resonance).

Harmonic Analysis

The FFT method is also applied to the heave displacements of section B and the normalized amplitudes of first-, second- and third-harmonics are summarized in Table 2. It is noted that each harmonic of heave displacement is larger under wave B, which also indicates that more energy is transmitted from upstream to excite the heave motion. To link the harmonic components of the free-surface elevation in the gap with those of the heave displacement, the energy transmission alleviates the second-harmonic responses of the wave elevation within the gap for the incident wave B. In

general, the predicted motions of section B which is situated in the sheltered area of section A, are seen to be small. Intuitively, this is also a preferred ship-to-ship configuration in a practical bunkering operation.

Table 2: Normalized harmonic components of the heave displacements of section B under different incident wavelengths

	$Z^{(i)}/H_0$ ($Z^{(i)}/Z^{(1)}$)		
λ/h	$i = 1$	$i = 2$	$i = 3$
4.044 (wave A)	0.474	0.006 (1.29%)	0.002 (0.42%)
9.920 (wave B)	0.710	0.017 (2.25%)	0.004 (0.56%)

Flow Field Patterns

Additionally, the flow field near the sections for the *heave system* under the incident wave A is investigated to understand the viscous effect involved in the gap resonance. As illustrated in Figure 8, there is stronger vortex shedding at the upstream corners of the large fixed section. Obvious flow separation can be observed in the vicinity of the gap due to the violent piston-type motion of the fluid in the gap. However, the vorticity is much smaller than that for the *fixed system* with two identical sections owing to the sheltering from the upstream large section (details not shown here). Since the downstream section is allowed to move, it may have absorbed some of the energy from the fluid in the gap, which also appears to lead to a smaller liquid response in the gap. By examining the results of gap responses at resonances in Table 1, it seems that the heave motion has exhausted most of the energy accumulated by gap resonance.

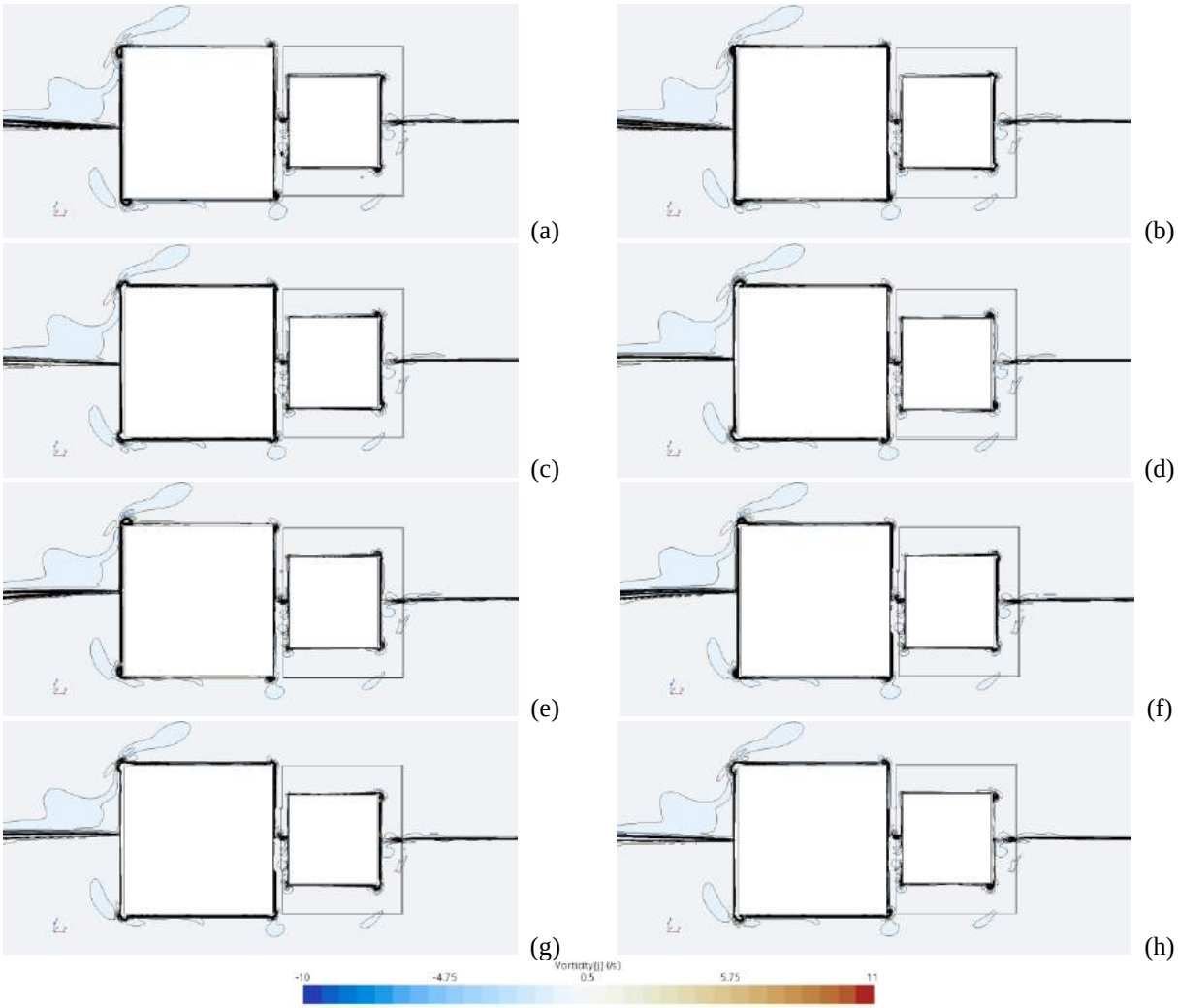

Figure 8: Vorticity contours near the sections during one period of heave motion in the narrow gap under the incident wave A: (a) 0*T*/8; (b) 1*T*/8; (c) 2*T*/8; (d) 3*T*/8; (e) 4*T*/8; (f) 5*T*/8; (g) 6*T*/8; (h) 7*T*/8.

CONCLUSIONS

A 2D numerical wave flume is established based on the URANS turbulence model and the VOF method to study the effect of the heave motion on the gap resonance between two non-identical rectangular cross-sections under different incident Stokes waves. The present work considers a more realistic scenario that a bunkering vessel, typically of smaller size, will hide behind a larger receiving vessel. The studied 2D cases are relevant for vessels under beam sea conditions. The free surface elevations inside the gap are compared between cases where the downstream section is either fixed or free to respond in heave. Harmonic components are analyzed to illuminate the frequency relation that incurs high-order resonance. The heave displacements are obtained and their harmonic components are also investigated to study the effect on the gap resonance. Some conclusions are drawn as follows:

(1) The first harmonics of the free surface elevation decrease with the wavelength for the *fixed system*, and large second harmonics are excited when the incident wave frequency is close to half the resonant frequency. The wave elevation in the gap for the *heave system* does not show a similar trend as that for the *fixed system*, which is due to the existence of the heave motion of the downstream section, thus leading to a modulation of free surface variation in the narrow gap and avoiding the second-order excitation.
(2) The heave motion under the action of a wave with a larger wavelength is more violent than that with a smaller wavelength. The vertical force acts like a resistance on the heaving section. Small force excited by the longer wave takes more energy from the water inside the gap and reduces the fluid response in the gap.
(3) As observed from the flow separation near both cross-sections, the sheltering effect achieved by hiding the small floating section behind the large fixed section can reduce the free surface elevation in the narrow gap and decrease the heave displacement to a large extent, which is a more preferred configuration for the bunkering operation at sea.

However, the bunkering operation can also be conducted in shallow water areas where Stokes wave theories are less applicable. Large free surface nonlinearity may also affect the gap response in the narrow gap. This part of the work is not included in the paper but will be presented during the conference.

ACKNOWLEDGEMENTS

This research was financially supported by China Scholarship Council (CSC No.202006060050) and performed using computational resources sponsored by Technical University of Denmark.

REFERENCES

CHUA, K. H., TAYLOR, R. E., and CHOO, Y. S. "Hydrodynamic interaction of side-by-side floating bodies part I: Development of CFD-based numerical analysis framework and modified potential flow model." *Ocean Engineering*, **166** (2018): 404-415.
FALTINSEN, O. M., FIROOZKOOHI, R., and TIMOKHA, A. N. "Steady-state liquid sloshing in a rectangular tank with a slat-type screen in the middle: Quasilinear modal analysis and experiments." *Physics of Fluids*, **23**:4 (2011): 042101.
FERZIGER, J. H., PERIĆ, M. *Computational methods for fluid dynamics*. Vol. 3. Berlin: springer, 2002.
GAO, J. L., et al. "Topographic effects on wave resonance in the narrow gap between fixed box and vertical wall." *Ocean Engineering*, **180** (2019): 97-107.
GAO, J. L., et al. "Numerical investigations of wave loads on fixed box in front of vertical wall with a narrow gap under wave actions." *Ocean Engineering*, **206** (2020): 107323.
GAO, J. L., et al. "Numerical investigations of gap resonance excited by focused transient wave groups." *Ocean Engineering*, **212** (2020): 107628.
GAO, J. L., et al. "Effects of free heave motion on wave resonance inside a narrow gap between two boxes under wave actions." *Ocean Engineering*, **224** (2021): 108753.
IWATA, H., SAITOH, T., and MIAO, G. P. "Fluid resonance in narrow gaps of very large floating structure composed of rectangular modules." *Proceedings of the fourth international conference on asian and pacific coasts*, Nanjing, China. 2007.
JIANG, S. C., BAI, W., and TANG, G. Q. "Numerical investigation of piston-modal wave resonance in the narrow gap formed by a box in front of a wall." *Physics of Fluids*, **31**:5 (2019): 052105.
JIANG, S. C., and BAI, W. "Coupling analysis for sway motion box with internal liquid sloshing under wave actions." *Physics of Fluids*, **32**:7 (2020): 072106.
JIANG, S. C., GU, Q., and CONG, P. W. "Fluid resonance in the narrow gap of a box-wall system under cnoidal wave action." *Ocean Engineering*, **238** (2021): 109774.
JIANG, S. C., BAI, W., and YAN, B. "Higher-order harmonic induced wave resonance for two side-by-side boxes in close proximity." *Physics of Fluids*, **33**:10 (2021): 102113.
KIM, J., O'SULLIVAN, J., and READ, A. "Ringing analysis of a vertical cylinder by euler overlay method." *International Conference on Offshore Mechanics and Arctic Engineering*. Vol. 44915. American Society of Mechanical Engineers, 2012.

KRISTIANSEN, T. and FALTINSEN, O. M. "Application of a vortex tracking method to the piston-like behaviour in a semi-entrained vertical gap." *Applied Ocean Research*, **30**:1 (2008): 1-16.
KRISTIANSEN, T. and FALTINSEN, O. M. "A two-dimensional numerical and experimental study of resonant coupled ship and piston-mode motion." *Applied Ocean Research*, **32**:2 (2010): 158-176.
LI, Y. J. and ZHANG, C. W. "Analysis of wave resonance in gap between two heaving barges." *Ocean Engineering*, **117** (2016): 210-220.
LI, Y. J. "Fully nonlinear analysis of second-order gap resonance between two floating barges." *Engineering Analysis with Boundary Elements*, **106** (2019): 1-19.
LU, L., et al. "Numerical investigation of fluid resonance in two narrow gaps of three identical rectangular structures." *Applied Ocean Research*, **32**:2 (2010): 177-190.
LU, L., et al. "Modelling of multi-bodies in close proximity under water waves—Fluid forces on floating bodies." *Ocean Engineering*, **38**:13 (2011): 1403-1416.
LU, L., et al. "Two-dimensional numerical study of gap resonance coupling with motions of floating body moored close to a bottom-mounted wall." *Physics of Fluids*, **32**:9 (2020): 092101.
MIAO, G. P. "Influence of gaps between multiple floating bodies on wave forces." *China Ocean Engineering*, **4** (2000): 407-422.
MOLIN, B. "On the piston and sloshing modes in moonpools." *Journal of Fluid Mechanics*, **430** (2001): 27-50.
MORADI, N., ZHOU, T. M., and CHENG, L. "Two-dimensional numerical study on the effect of water depth on resonance behaviour of the fluid trapped between two side-by-side bodies." *Applied Ocean Research*, **58** (2016): 218-231.
MUZAFERIJA, S. and PERIĆ, M. "Computation of Free Surface Flows using Interface Tracking and Interface Capturing Methods,'Chap. 2." *Mahrenholtz, O. and Markewicz, M., Nonlinear Water Wave Interaction, Comput. Mech. Publications* (1999).
NING, D. Z., et al. "Numerical study of resonance induced by wave action on multiple rectangular boxes with narrow gaps." *Acta Oceanologica Sinica*, **34**:5 (2015): 92-102.
NING, D. Z., et al. "Hydrodynamic difference of rectangular-box systems with and without narrow gaps." *Journal of Engineering Mechanics*, **141**:8 (2015): 04015023.
NING, D. Z., et al. "Experimental and numerical study on wave response at the gap between two barges of different draughts." *Applied Ocean Research*, **77** (2018): 14-25.
PERIĆ, M., and SWAN, C. "An experimental study of the wave excitation in the gap between two closely spaced bodies, with implications for LNG offloading." *Applied Ocean Research*, **51** (2015): 320-330.
PERIĆ, M. "Best practices for wave flow simulations." *The Naval Architect International Journal of the Royal Institute of Naval Architects* (2018).
RODRÍGUEZ, M. and SPINNEKEN, J. "A laboratory study on the loading and motion of a heaving box." Journal of Fluids and Structures, **64** (2016): 107-126.
SAITOH, T., MIAO, G. P., and ISHIDA, H. "Theoretical analysis on appearance condition of fluid resonance in a narrow gap between two modules of very large floating structure." *Proceedings of the 3rd Asia-Pacific Workshop on Marine Hydrodynamics*. China Ocean Press, 2006.
SUN, L., TAYLOR R. E., and TAYLOR, P. H. "First-and second-order analysis of resonant waves between adjacent barges." *Journal of Fluids and Structures*, **26**:6 (2010): 954-978.
TAN, L. et al. "Dissipative effects of resonant waves in confined space formed by floating box in front of vertical wall." *The Eleventh ISOPE Pacific/Asia Offshore Mechanics Symposium*. OnePetro, 2014.
TAN, L., et al. "A viscous damping model for piston mode resonance." *Journal of Fluid Mechanics*, **871** (2019): 510-533.
ZHAO, W. H., et al. "Estimation of gap resonance relevant to side-by-side offloading." *Ocean Engineering*, **153** (2018): 1-9.
ZHU, H. R., ZHU, R. C., and MIAO, G. P. "A time domain investigation on the hydrodynamic resonance phenomena of 3-D multiple floating structures." *Journal of Hydrodynamics*, **20**:5 (2008): 611-616.

A COMPUTATIONALLY EFFICIENT PROCEDURE FOR TUNING OF SHIP TRANSFER FUNCTIONS

Raphaël E. G. Mounet [1 2], Ulrik D. Nielsen [1 2], Astrid H. Brodtkorb [2]

ABSTRACT

The analysis of wave-ship interactions is highly relevant for the safety – as well as the energy efficiency – of the maritime operations. One application is the onboard estimation of the ship's responses in incoming seaways, which requires regular and accurate updates of the vessel's seakeeping model, accounting for possible changes in the operational conditions. This paper presents a simple approach for fast estimation of the wave-to-motion transfer functions of vessels. Prior information of the wave spectrum, characterizing the sea state, and ship motion measurements, i.e. time series sequences from onboard sensors, are supposed to be available. Semi-empirical closed-form expressions derived for a box-shaped vessel define Parameterized Response Amplitude Operators (P-RAOs) for the heave and pitch motions. The five input parameters, namely the ship speed, length, breadth, draught and block coefficient, are regarded as optimization variables. An optimization problem is established to minimize the spectral discrepancy between, on one hand, the *measured responses, and, on the other hand, the theoretical responses computed with the wave spectrum and P-RAOs. Numerical simulations of measured motions in a predefined long-crested sea state are carried out in the frequency domain for two different ships, a small research vessel and a container ship, using a set of RAOs obtained by a commercial potential flow code. The simulated measurements are considered as the ground truth. Tuning of the P-RAOs is carried out, and the results show a fairly good agreement between the tuned P-RAOs and the true RAOs over a wide portion of the frequency range. Moreover, the normalized error between the true and estimated response spectra is significantly decreased after tuning the P-RAOs.*

KEY WORDS

Measured ship motions; Parameterized Response Amplitude Operators; Wave spectrum; Transfer function tuning; Seakeeping model; Closed-form expressions.

INTRODUCTION

The information extracted from a vessel's response during operations at sea is essential for ensuring the safety of the ship, crew and cargo, as well as to evaluate the energy efficiency of the operations. Historically, the theory of the linear response of a marine vessel sailing in ocean waves was to a large extent inherited from the theory of linear superposition, which at first was conceptualized in electronics and communication (Rice 1944; Lee 1960). St. Denis and Pierson (1953) resolved many of the problems inherent to the application of the principle of superposition to marine systems, including the fact that a vessel is typically moving with non-zero speed within the seaway. Modelling the behavior of vessels in moderate seas for analysis of wave-ship interactions, the so-called *seakeeping* problem, relies typically on accurate complex-valued linear transfer functions (TRFs) which describe the relation in the frequency domain between the energy spectra of the first-order wave-induced ship motions and the wave spectrum. In the literature, the amplitude of the TRFs is commonly related to the *Response Amplitude Operator* (RAO). The RAOs are estimated from the knowledge of the ship geometry, and additionally depend on the loading conditions and forward speed. They are functions of the wave direction and the encountered wave frequency. They can be computed by solving the equations of motions for the ship, on the basis of potential flow theory. Some numerical methods to estimate the transfer functions make use of hydrodynamic models (radiation-diffraction codes) based on 3D panel code or strip theory (e.g. Salvesen, Tuck and Faltinsen 1970). These methods can have varying degrees of accuracy and computational costs, depending on the methodology of calculation. In the reality of ship operations, there is a significant degree of uncertainty in the experienced operational conditions, including the uncertain knowledge of the ship speed and loading conditions. For these reasons, it is quite unpractical to directly use precomputed linear transfer functions for the purpose of real-time estimation (or prediction) of the wave-induced responses of vessels during their operations at sea. Research has been conducted to solve this issue, employing various *system identification* techniques to estimate the important parameters (center of gravity, inertia terms, etc.) upon which the hydrodynamic vessel model is determined, e.g. Han (2021). Studies have also been conducted on estimating the hydrodynamic coefficients - i.e. added mass, damping, stiffness coefficients, and wave excitation forces - based on relevant vessel data, estimates of the directional

[1] DTU Mechanical Engineering, Technical University of Denmark, DK-2800 Kgs. Lyngby, Denmark
[2] Centre for Autonomous Marine Operations and Systems, NTNU AMOS, NO-7052 Trondheim, Norway

wave spectrum, and measurements of the wave-induced response (Yuan *et al.* 2016; Kaasen *et al.* 2020; Skandali *et al.* 2020).
Jensen *et al.* (2004) developed closed-form solutions for the RAOs for the vertical motions, roll, relative motions and vertical wave induced bending moment. The derived closed-form expressions (CFEs) for the heave and pitch RAOs simplify the geometry of the hull to that of a box-shaped vessel. This is an advantage for onboard applications, as the simplified vessel model requires only a limited number of parameters. However, the simplifications can introduce many errors in the estimation of the RAOs, depending on the geometry of the vessel and the sea state. This motivates the need to tune the CFEs before use in a seakeeping analysis. Nielsen *et al*. (2021) proposed an optimization algorithm for direct tuning of RAOs, using these CFEs, in addition to vessel response measurements and ERA5 2D wave spectra. The main inconvenience was that the algorithm is only able to tune RAOs at the observed wave directions and frequencies. The present paper proposes an alternative computationally efficient tuning method, considering the CFEs as *parameterized RAOs* (P-RAOs). The input parameters of the P-RAOs are optimized to better match the vessel's seakeeping behavior in given operational conditions. In other words, one tries to identify an (hydrodynamic-) equivalent box experiencing the same motions as the actual ship.

THEORY

Fundamental Assumptions and Definitions for the Seakeeping Study

A floating vessel at sea is excited by wave loads, in addition to loads from wind and sea current which are disregarded in the present study. The wave loads are related to the environmental parameters describing the sea state, including significant wave height H_s, wave spectral peak period T_p, mean wave direction μ, and others. The wave process is assumed to be stationary, ergodic and Gaussian over the observation period. This enables to perform a linear steady-state approach in the frequency domain. The wave-induced vessel motions can be estimated by using linear transfer functions and a wave spectrum.

Long-crested waves are assumed, meaning that the wave system is uniquely described by a 1-D wave spectrum $E(\omega_0)$, where ω_0 is the (intrinsic) wave frequency. The wave direction β is defined relatively to the ship heading, as shown in Figure 1, and it follows that $\beta = 0°$ is a following sea, $\beta = 180°$ is head sea, and $\beta = 90°$ or $270°$ is beam sea.

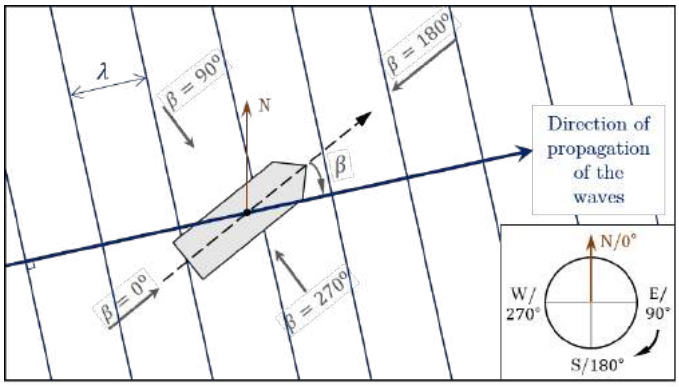

Figure 1: Definition of the heading angles.

For an advancing vessel, the waves are encountered at a frequency that is different from the (intrinsic) wave frequency, due to the Doppler Effect. Typically, the frequency is increased in head waves and decreased in following waves. The so-called *encounter frequency* is calculated by Equation (1), which is found in e.g. Nielsen (2010):

$$\omega_e = \omega_0 - \omega_0^2 \frac{U}{g} \cos(\beta) \quad [1]$$

where U is the ship forward speed.

The transition of the wave spectrum from the intrinsic wave frequency domain to the encounter frequency domain is essentially a transformation of the frequency coordinate system such that the wave energy is preserved. The encountered wave spectrum for long-crested waves may be written (Lewis 1989) as in Equation (2):

$$E_e(\omega_e; \beta, U) = E(\omega_0) \frac{g}{|g - 2\omega_0 U \cos\beta|} \quad [2]$$

Computation of Linear Wave-To-Motion Transfer Functions for Monohull Ships

The linear wave-to-motion transfer functions are denoted Φ_R for a given response R. Those are complex-valued functions of the wave frequency and direction. They depend on the geometry of the vessel and the operational conditions, especially the ship speed. In the present paper, the amplitude of the transfer function is referred to as the *Response Amplitude Operator*

(RAO). There exist many methods to estimate the RAOs of vessels; in particular, strip theory or panel element codes relying on potential flow theory can be used. Alternatively, *closed-form expressions* (CFEs) for the RAOs have been found for monohull ships, and are given in Jensen *et al.* (2004). For the vertical ship motions, namely heave (w) and pitch (θ), the equations of motion (EoMs) are solved analytically for a homogeneously loaded box-shaped vessel using linear strip theory. The coupling terms between heave and pitch are neglected. The required information for the procedure is restricted to the main dimensions of the box – length L, breadth B, draught T, block coefficient C_B – together with the forward speed U and relative wave heading β. The simplified EoMs in regular waves with amplitude a are given in Equations (3) and (4):

$$2\frac{kT}{\omega^2}\,\ddot{w} + \frac{A^2}{kBC_B\delta^3\omega}\dot{w} + w = aF\cos(\omega_e t) \quad [3]$$

$$2\frac{kT}{\omega^2}\,\ddot{\theta} + \frac{A^2}{kBC_B\delta^3\omega}\dot{\theta} + \theta = aG\sin(\omega_e t) \quad [4]$$

where $k = \omega^2/g$ is the wave number, and differentiation with respect to time t is denoted with a dot. Parameters A and δ are related to the sectional hydrodynamic damping and Doppler shift, respectively, while F and G are the forcing functions; all four can be approximated using the aforementioned input information, see Jensen *et al.* (2004) for more details. Note that the closed-form expressions for pitch motion always predict zero amplitude in beam seas ($\beta = 90°$ or $270°$), because of the bow-stern symmetry of the box-shaped vessel.

Estimation of Response Spectra in Long-crested Waves

The so-called *response spectrum* for the individual rigid-body motion component R can be estimated theoretically by filtering the wave energy spectrum with the appropriate motion transfer function. In long-crested waves, this is achieved by multiplying each ordinate of the encountered wave spectrum $E_e(\omega_e;U)$ by the RAO at the corresponding encounter frequency (Lewis 1989):

$$\hat{S}_{RR}(\omega_e) \overset{\text{def}}{=} \Phi_R(\omega_e,\beta;U)\cdot\overline{\Phi_R(\omega_e,\beta;U)}\cdot E_e(\omega_e;\beta,U) = |\Phi_R(\omega_e,\beta;U)|^2\cdot E_e(\omega_e;\beta,U) \quad [5]$$

where the overbar indicates the complex conjugate.

Strictly speaking, Equation (5) is only valid in head or bow seas, that is $90° \le \beta \le 270°$. In quartering or following seas, i.e. $\beta \le 90°$ or $\beta \ge 270°$, the transformation between encounter and wave frequency is not a unique mapping, meaning that a given encounter frequency can be mapped into up to three wave frequencies, located in three different regions of the frequency domain. Thus, the encountered response spectrum is formed by summation of contributions from these three regions:

$$\hat{S}_{RR}(\omega_e) = |\Phi_R^I(\omega_e,\beta;U)|^2\cdot E_e^I(\omega_e;\beta,U) + |\Phi_R^{II}(\omega_e,\beta;U)|^2\cdot E_e^{II}(\omega_e;\beta,U) + |\Phi_R^{III}(\omega_e,\beta;U)|^2\cdot E_e^{III}(\omega_e;\beta,U) \quad [6]$$

where, for example, $E_e^I(\omega_e;\beta,U)$ is the contribution to the wave encounter spectrum from Region I, and $|\Phi_R^I(\omega_e,\beta;U)|^2$ is the RAO associated with the wave frequencies of Region I (Lewis 1989). Similar can be said about $E_e^{II}(\omega_e;\beta,U)$ and $E_e^{III}(\omega_e;\beta,U)$ as the contributions from Regions II and III, respectively.

Error Measure of Response Spectrum Estimate

In order to quantify the level of error ϵ_R in the spectrum estimate for a given response R, a difference metric between the true (or measured) response spectrum $S_{RR}(\omega_e)$ and an estimate $\hat{S}_{RR}(\omega_e)$ can be obtained as the normalized "area-deficit" encased between the two spectra:

$$\epsilon_R \overset{\text{def}}{=} \frac{\int_0^\infty |S_{RR}(\omega_e) - \hat{S}_{RR}(\omega_e)|\,d\omega_e}{m_{0,R}} \quad [7]$$

where $m_{0,R} = \int_0^\infty S_{RR}(\omega_e)\,d\omega_e$ is the zeroth order spectral moment of the response spectrum.

METHODOLOGY

General overview of the procedure

The closed-form expressions (Jensen *et al.* 2004), already introduced in the "Theory" section, are considered as *Parameterized Response Amplitude Operators* (P-RAOs), taking five input parameters: the ship's forward speed U, length L, breadth B, draught T, and block coefficient C_B. Obviously, these are also functions of the relative wave heading and wave frequency. Three inputs are needed to tune the P-RAOs: a wave spectrum, the measured response spectra for the heave and pitch motions, and an initial guess of the input parameters for the P-RAOs. For the first guess, the P-RAOs are computed for the actual (physical) values of the aforementioned quantities, namely the logged speed-through-water and the ship's main particulars. It must be noted that both the wave spectrum and the measured response spectra are considered as the ground truth. The consideration of uncertainties in these quantities is out of the scope of the paper and left for future work.

Implementation of the RAO-tuning procedure

The RAO-tuning method solves an optimization problem that can be formulated as in Equation (8):

$$\begin{aligned} &\text{minimize } f(\boldsymbol{\alpha}) \\ &\text{subject to } \alpha_i \geq 0, \text{for each } i \in \{1,2,\dots,4\}, \\ &\text{and } 0.4 \leq \alpha_5 \leq 1 \end{aligned} \quad [8]$$

The set of tuning parameters is composed of five quantities, which form the variables of optimization:

$$\boldsymbol{\alpha} = [\alpha_1, \alpha_2, \alpha_3, \alpha_4, \alpha_5] \propto [U, L, B, T, C_B] \quad [9]$$

where the symbol "$\propto$" indicates the physical quantities to which the tuning parameters relate in the P-RAOs. The reason for the imposed bounds on the tuning parameters in Equation (8) is that the values of the physical quantities must be positive and that the block coefficient must not exceed one. The cost function $f(\boldsymbol{\alpha})$ is computed as shown in Equation (10):

$$f(\boldsymbol{\alpha}) = \int_0^\infty \left[\left(\frac{|S_{zz}(\omega_e) - \hat{S}_{zz}(\omega_e;\boldsymbol{\alpha},\beta,U)|}{m_{0,z}} \right)^2 + \left(\frac{|S_{\theta\theta}(\omega_e) - \hat{S}_{\theta\theta}(\omega_e;\boldsymbol{\alpha},\beta,U)|}{m_{0,\theta}} \right)^2 \right] d\omega_e \quad [10]$$

It expresses the squared error between the true response spectrum $S_{RR}(\omega_e)$ and the theoretical response spectrum $\hat{S}_{RR}(\omega_e;\boldsymbol{\alpha},\beta,U)$, which is calculated using the tuning parameters in connection with the P-RAOs, as described in Equation (11):

$$\hat{S}_{RR}(\omega_e;\boldsymbol{\alpha},\beta,U) = \left|\widehat{\Phi}_{R,\mathrm{P-RAO}}(\omega_e;\boldsymbol{\alpha},\beta)\right|^2 \cdot E_e(\omega_e;\beta,U) \quad [11]$$

where it is emphasized that the Doppler shift presented in Equations (1) and (2) must be calculated with the logged physical speed U, which will differ from tuning parameter α_1 after optimization.

The errors for the heave and pitch spectra are summed in the cost function, so that both responses take part into the tuning process. Normalization of the error is needed before summation in order to give equal weight to heave and pitch. The zeroth order moment of the measured response spectrum is used for the normalizing factor in Equation (10).

The range of encountered frequencies ω_e is chosen as $[0,2\pi]$ rad/s, with a spacing of $\pi/100$ rad/s in the discretization, corresponding to 200 frequency components, which is supposed to be sufficient to perform the numerical integrations in Equation (10). The Trust-Region Constrained algorithm developed by Byrd *et al.* (1999) is exploited to solve the optimization problem, noticing that an implementation in Python 3 is available in the optimisation library of SciPy, under the function `minimize` with the method `'trust-constr'`.

Scenarios of simulation for the case study

A simulation study is performed with two vessels: the NTNU-owned research vessel Gunnerus (denoted "RV") and a larger S175 container ship (denoted "S175"). Their main particulars are given in Table 1.

Table 1: Main particulars of the two studied vessels.

	RV	S175	
Length between perpendiculars, L_{pp}	28.9	175.0	[m]
Breadth middle, B	9.6	25.4	[m]
Draught, T	2.63	9.4	[m]
Displacement, Δ	418.06	24589.00	[t]
Block coefficient, C_B	0.559	0.570	[-]

The wave-induced motions of these two vessels are simulated in the frequency domain for one predefined sea state characterized by $H_s = 2$ m and $T_p = 10$ s. The (generalised) JONSWAP spectrum (Hasselmann *et al.*, 1973) is assumed with a peak shape parameter $\gamma = 1$, and the corresponding wave spectrum is plotted in Figure 2.

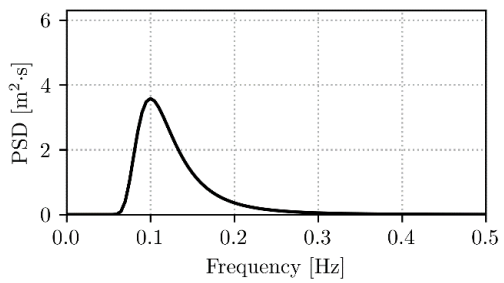

Figure 2: 1-D wave spectrum used for the case study. PSD stands for power spectral density.

Realism of the study is introduced by working with a set of theoretical RAOs purely used for generating the simulated wave-induced responses. To serve this purpose, the "ground true" heave and pitch RAOs of the vessels are obtained from the hydrodynamic code ShipX. It is emphasized that the tuning algorithm applies only on the P-RAOs, and not on the "true" ShipX RAOs. In this regard, the methodology for the simulations resembles the work of Mounet *et al.* (2022). The (true) RAOs of the two vessels are plotted in Figure 3 for various headings and zero forward speed. Although not represented here, the RAOs for the same vessels at forward speeds $U = 5$ and 10 knots are also available. As expected, the two vessels behave as low-pass filters with respect to the encountered waves. Overall, it is noted that S175 has a lower cut-off frequency than Gunnerus, which is explained by the larger dimensions of the former.

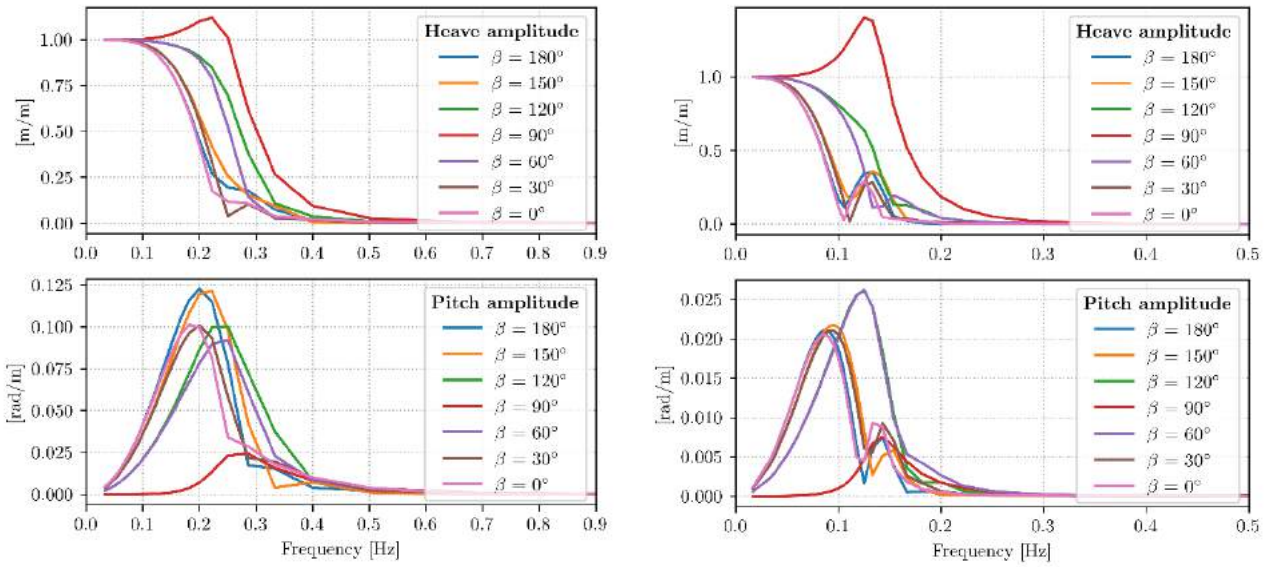

(a) RV (b) S175

Figure 3: Heave and pitch amplitude of the transfer functions at zero forward speed for the two ships selected for the case study. Note the different vertical and horizontal scales in the subplots.

In total, twenty-one scenarios are analysed for each of the two vessels, as listed in Table 2. Three different vessel speeds are considered, including cases with zero forward speed, and for each of them, simulations are carried out for seven relative wave headings covering head, bow quartering, beam, stern quartering, and following seas, which allows for a detailed sensitivity study. Due to the port-starboard symmetry of the vessels, there is no need to study the relative wave headings in the range $[180°, 360°]$.

Table 2: Scenarios of simulation, in terms of forward speed and relative wave heading.

Scenario number	U [knots]	β [deg]
A1, A2,…, A7	0	[180, 150, 120, 90, 60, 30, 0]
B1, B2,…, B7	5	[180, 150, 120, 90, 60, 30, 0]
C1, C2,…, C7	10	[180, 150, 120, 90, 60, 30, 0]

The initial guess $\boldsymbol{\alpha^0}$ for the optimization variable $\boldsymbol{\alpha}$ has values taken:

- For U: from the particular scenario in Table 2.
- For $L, B, T,$ and C_B: from the ship's main particulars provided in Table 1.

RESULTS AND DISCUSSIONS

On average, it takes approximately 13-15 seconds to run the optimization procedure for one ship for one simulation scenario on the available laptop (CPU Intel(R) Core(TM) i7-10510U CPU @ 1.80 GHz, 16 GB memory). The computations are thus relatively fast.

The results of the tuning procedure are shown in Figure 4 for a few arbitrarily selected scenarios (A1, B3, and C5) for the two ships. The tuned P-RAOs are compared to the original P-RAOs and to the ShipX RAOs. Overall, it is seen that the tuned P-RAOs agree significantly better with the ShipX RAOs, than the original P-RAOs. The latter have a clear tendency to underestimate the amplitude, as a systematic error (bias) towards higher frequencies. This is quite successfully corrected by the tuning procedure in most cases. An important observation is that tuning the P-RAOs preserves their physical shape. However, for scenario C5, as well as scenarios C6 and C7 (results not shown here), the tuned P-RAOs present some oscillations of the heave and pitch amplitudes at higher frequencies, which do not correctly represent the true vessel

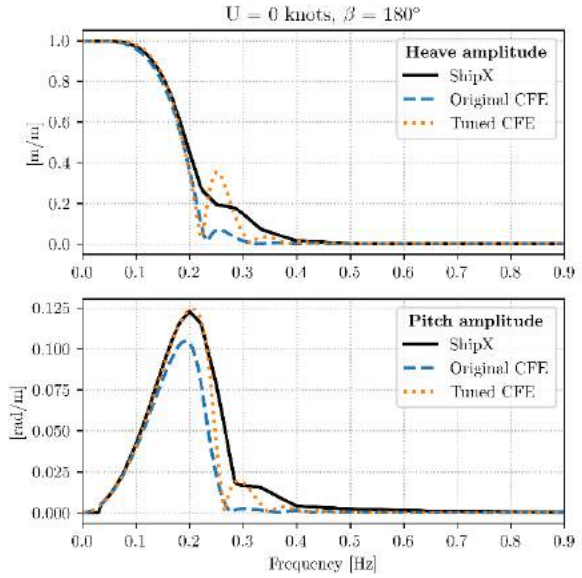

(a) RV, scenario A1

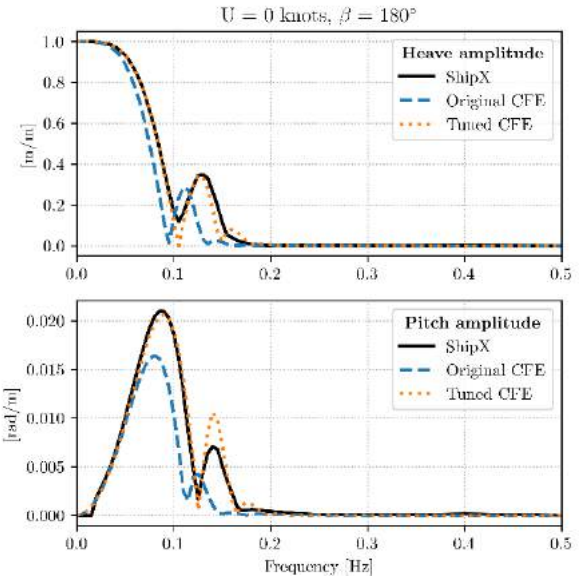

(b) S175, scenario A1

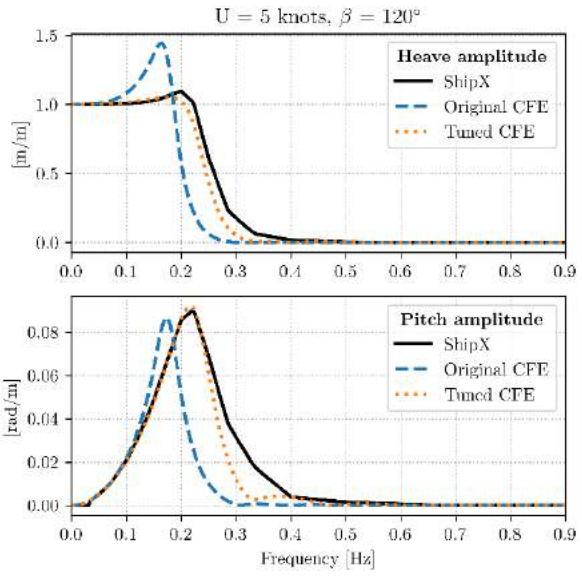

(c) RV, scenario B3

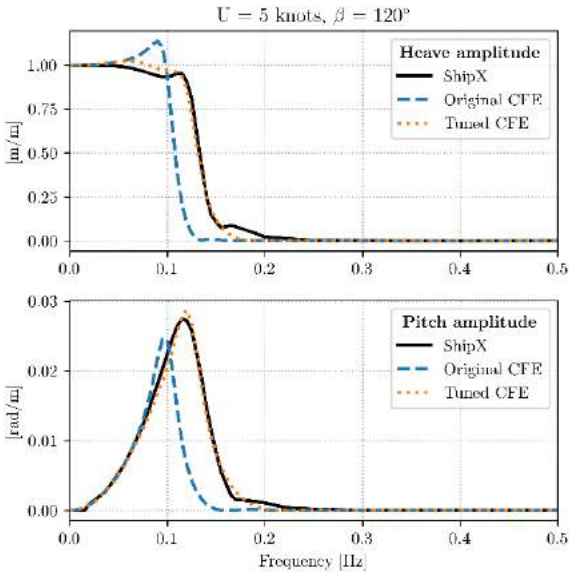

(d) S175, scenario B3

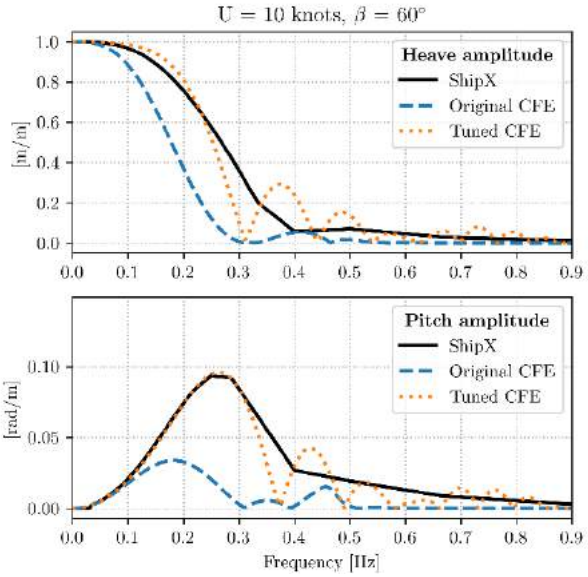

(e) RV, scenario C5

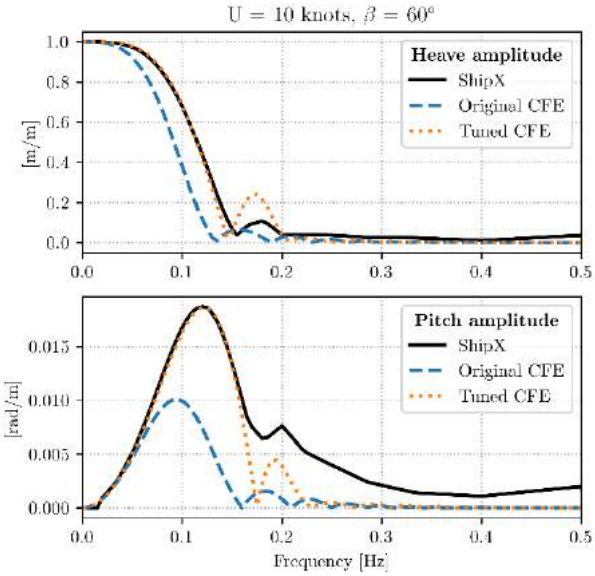

(f) S175, scenario C5

Figure 4: Some selected tuning results from the numerical simulations, at three different ship speeds and wave headings, for the two studied ships (RV and S175). Note the different horizontal and vertical scales in the subplots.

behavior. This affects RV even more than S175. Those scenarios correspond to stern quartering to following seas with a speed of 10 knots. Therefore, it is hypothesized that the oscillatory behavior is due to the handling of the Doppler shift in the closed-form expressions. The observed oscillations do not affect the theoretically computed response spectrum, because they happen at frequencies where the encountered wave spectrum has little energy. Nevertheless, extreme caution should be used when employing the tuned transfer functions to predict the response spectra in future sea states, because those might have energy at frequencies where the oscillations appear.

The theoretical response spectra – both before and after the RAO-tuning – are plotted in Figure 5 in the encounter frequency domain, for the same scenarios as in Figure 4, and the true response spectrum is represented as well for comparison. It is seen that in all the presented cases, there is a good agreement between the true spectrum and the estimated spectrum after tuning. The original P-RAOs did not enable such a good match. Consequently, the tuned P-RAOs represent an improvement with regards to a seakeeping analysis focused on the estimation of ship motion responses. Note, for scenario C5, the true response spectrum of RV in pitch has a quite distorted shape, with a discontinuity at a frequency $f_e = 0.155$ Hz. This is due to how the Doppler shift is handled in frequency-domain simulations. Such a discontinuity would not be observed if one had generated a set of time series realizations of the motion response and computed the associated average spectrum. More insights into this technical issue can be found in Nielsen (2017). Nonetheless, it is interesting to notice that the tuning procedure is also able to correct – to some extent – the RAOs at unobserved frequencies, that is at frequencies where there is zero measured response energy. This is visible for scenario C5 for RV, for instance, where the tuned P-RAOs have also been successfully corrected at frequencies over 0.155 Hz, up to 0.25 Hz and 0.30Hz in pitch and heave, respectively.

The tuning effect at unobserved wave headings was also investigated, by computing the full set of P-RAOs using the optimized tuning parameters $\boldsymbol{\alpha}^*$ for a given scenario. Contour lines of the error between the true ShipX RAOs and the P-RAOs are shown in a polar diagram in Figure 6, i.e. as a function of frequency and heading, for scenario B3 with the two ships. The error was normalized by the maximum amplitude of the ShipX transfer functions, and the dotted line represents the direction of tuning. In the presented scenario, it is remarkable that tuning reduces the error – compared to the original P-RAOs – not only in the vicinity of the tuning direction, but also in a wider portion of the angular domain. This must be contrasted by the fact that the tuning parameters are not optimal for all headings, and a closer look at the values of the optimized tuning parameters (not presented here) shows that they vary quite drastically between scenarios. Therefore, $\boldsymbol{\alpha}^*$ must rather be considered as a function of the logged ship speed and heading. This should be kept in mind when developing an extension of the proposed methodology in short-crested seas, which is left for future work.

The normalized error between the theoretical response spectrum in heave and pitch – before as well as after tuning – and the true spectrum is computed for all scenarios as per Equation (7), and shown in Figure 7. In almost all scenarios, there is a much better agreement between the true spectrum and the theoretical spectrum obtained via the use of the tuned P-RAOs, compared to the original P-RAOs. Nonetheless, for scenarios in beam sea conditions, namely A4, B4 and C4, tuning does not improve the results in pitch. This is due to the fact that pitch energy vanishes in beam seas in the formulation of the P-RAOs, as previously mentioned in the 'Theory' section. A way to mitigate this issue could be to force some pitch amplitude in the beam sea cases by using, say, $\beta = 95°$, but keeping all weight on heave in the tuning process in the particular cases. Anyway, the fact that the tuned pitch P-RAO remains zero in beam seas is a minor concern for practical applications, simply because the measured pitch variance is significantly lower (actually, more than 95% lower) at a heading of $\beta = 90°$, compared to the neighboring heading ($\beta = 120°$). On the other hand, the tuning in heave for the corresponding scenarios is successful. Besides the special case of beam sea, the tuning results are in general similarly good for both responses (heave and pitch), which indicates that the normalization in the cost function of Equation (10) is made appropriately to tune both responses with equal weight.

CONCLUSIONS

This paper presented a simple method to tune in an efficient way the closed-form expressions, developed by Jensen *et al.* (2004), for the response amplitude operators in heave and pitch motions of monohull ships. Those semi-empirical expressions are regarded as parameterized formulas, for which the input parameters are optimized so that the theoretically estimated motions closely match the measured ones. The optimization is carried out in a combined manner for the heave and pitch responses.

The procedure was tested via numerical simulations of motion responses in long-crested waves, for two ships of very different dimensions. In total, 42 scenarios were analyzed for various ship speeds and relative wave headings. In all cases, the error between the estimated and true response spectra is greatly reduced by tuning for both heave and pitch. Moreover, the tuned P-RAOs agree well with the true RAOs that were used for the simulations of vessel responses. In fact, the agreement is fairly reasonable over an extended portion of the frequency domain, even at frequencies where zero energy is found in the response spectra. The use of the optimized tuning parameters for RAO estimation at unobserved headings is touched upon, but it is argued that better results can be found by defining heading-dependent tuning parameters.

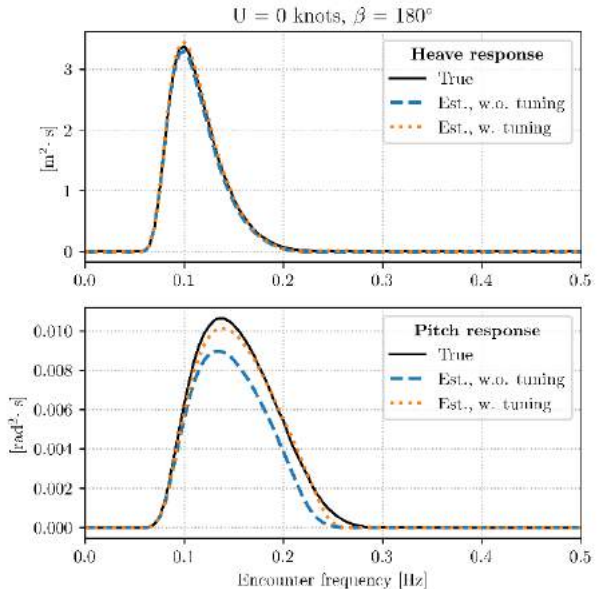

(a) RV, scenario A1

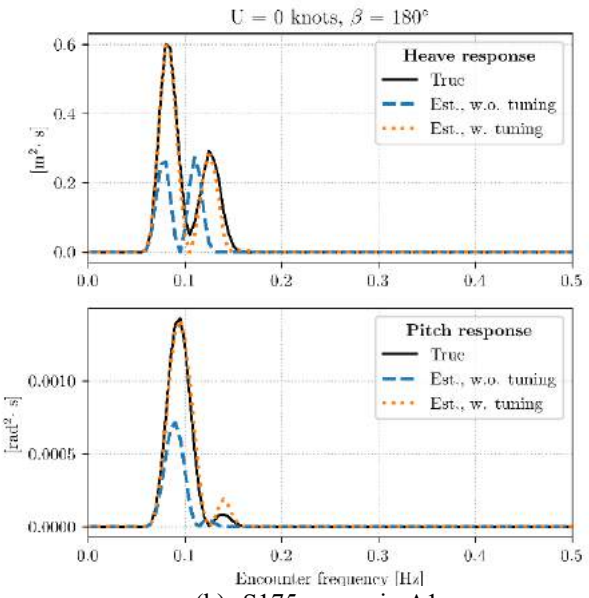

(b) S175, scenario A1

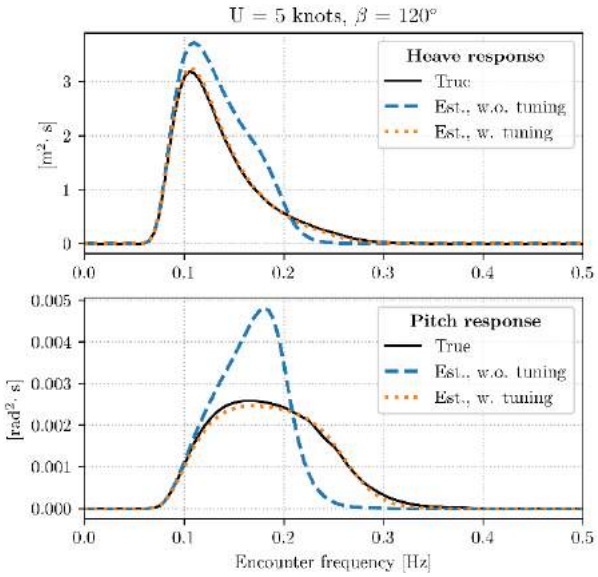

(c) RV, scenario B3

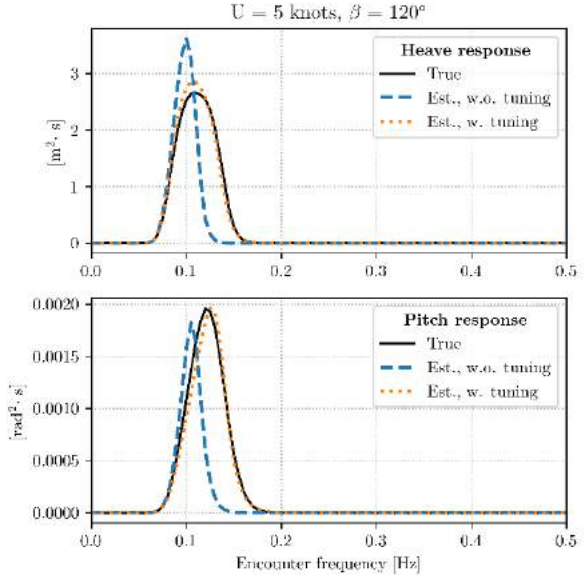

(d) S175, scenario B3

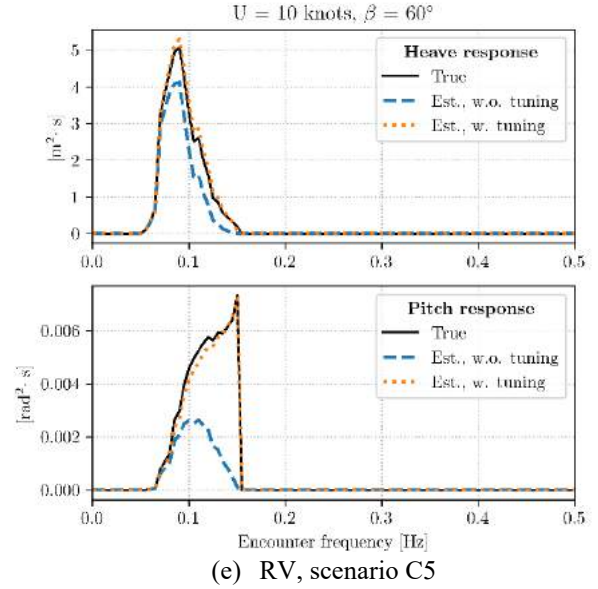

(e) RV, scenario C5

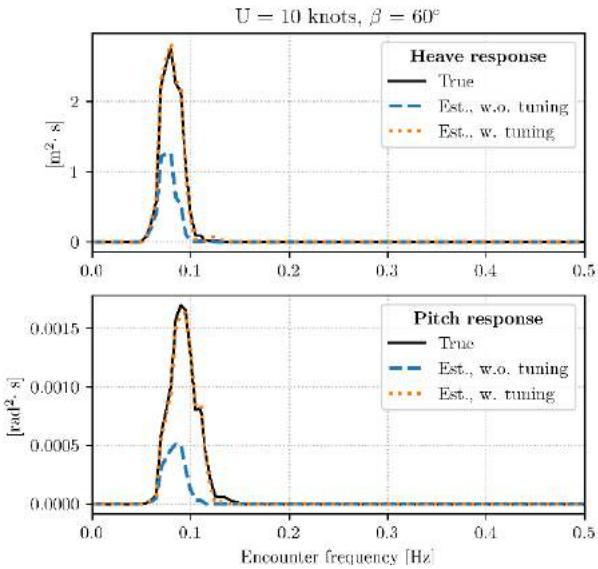

(f) S175, scenario C5

Figure 5: Estimated and true response spectra in heave and pitch at three different ship speeds and wave headings, for the two studied ships (RV and S175). Note the different vertical scales in the subplots.

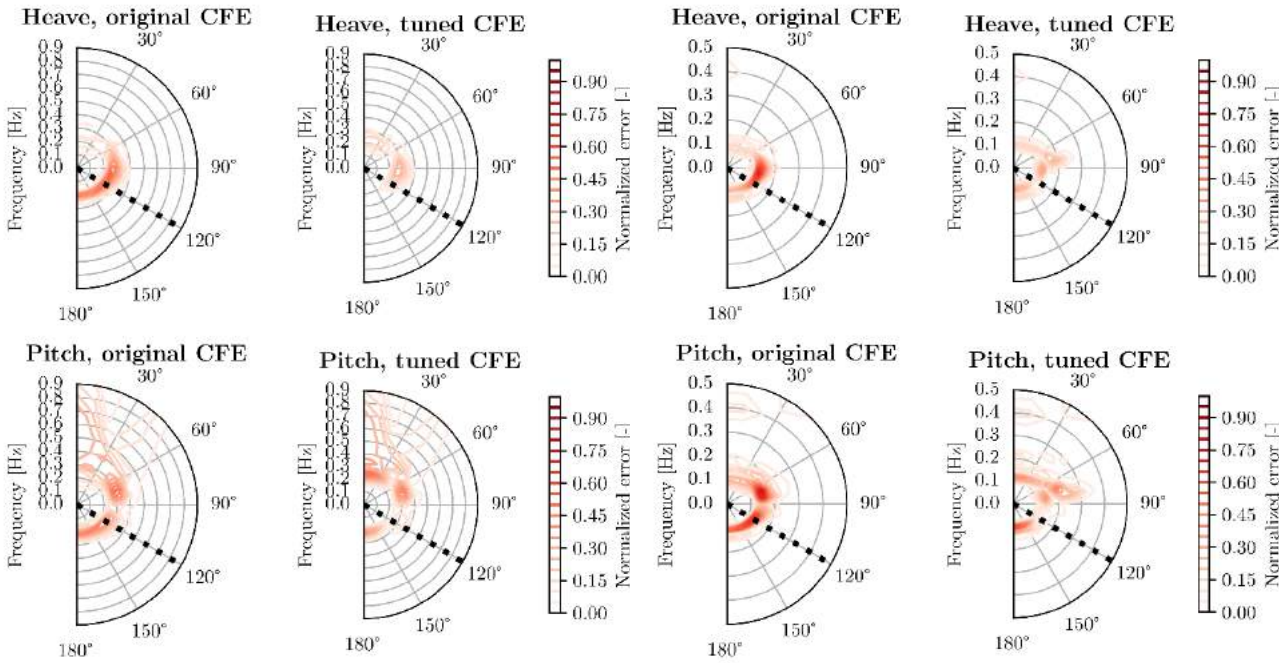

(a) RV, scenario B3 (b) S175, scenario B3

Figure 6: Normalized error of the full set of original and tuned P-RAOs with respect to the ShipX RAOs, defined as: error $= \left|\hat{\Phi}_{R,\mathrm{P-RAO}} - \Phi_{R,\mathrm{ShipX}}\right| / \max_{\omega,\beta}(\Phi_{R,\mathrm{ShipX}})$. The dotted line indicates the direction of tuning.

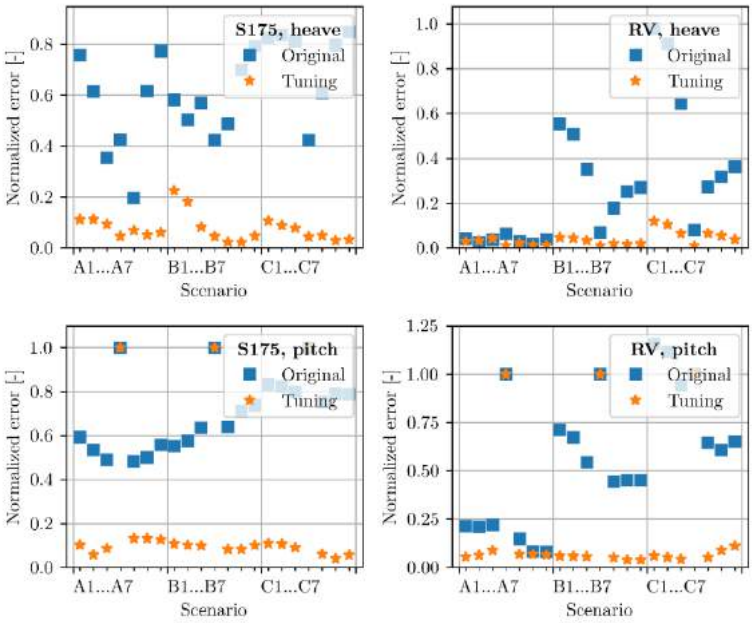

Figure 7: Overview of the normalized error between true and estimated response spectra in heave and pitch, for the two studied ships. 'Original' means that the original P-RAOs are used, while 'Tuning' uses the tuned P-RAOs. Note the different vertical scales in the subplots.

In future works, the procedure will be adapted to deal with scenarios in short-crested waves. Moreover, other responses could be included in the process, such as the roll motion or the wave-induced bending moment amidships. The ability to accurately predict, ahead of time, the response spectra based on tuned P-RAOs and sea state estimates could then be studied, in connection with real-life scenarios where in-service data collected onboard vessels are used. In this endeavor, quantification of the tuning uncertainties will require special attention.

ACKNOWLEDGEMENTS

The work has been supported by the Research Council of Norway through the Centres of Excellence funding scheme, project number 223254 AMOS. Moreover, the financial support from The Danish Maritime Fund, case numbers 2017-101 and 2020-074, is greatly acknowledged.

REFERENCES

BYRD, R. H., M. E. HRIBAR, and JORGE NOCEDAL. "An Interior Point Algorithm for Large-Scale Nonlinear Programming." Siam Journal on Optimization 9:4 (1999): 877–900, doi:10.1137/S1052623497325107.

HASSELMANN, K., et al. "Measurements of wind-wave growth and swell decay during the Joint North Sea Wave Project (JONSWAP)." Ergaenzungsheft zur Deutschen Hydrographischen Zeitschrift, Reihe A, Hamburg, Germany, 1973.

HAN, X. "Onboard Tuning and Uncertainty Estimation of Vessel Seakeeping Model Parameters." Vol. 2021:356 of Doctoral thesis at NTNU, Norwegian University of Science and Technology, Faculty of Engineering, Department and Marine Technology, Trondheim, 2021.

JENSEN, J. J., A. E. MANSOUR, and A. S. OLSEN. "Estimation of Ship Motions Using Closed-Form Expressions." *Ocean Engineering*, 31:1 (2004): 61–85, doi:10.1016/S0029-8018(03)00108-2.

KAASEN, K. E., K. BERGET, H. LIE, and R. BJØRKLI. "Automatic Tuning of Vessel Models Offshore: A Feasibility Study Using High-Precision Data from Model Test." Offshore Technology Conference. OnePetro, 2020.

LEWIS, E. V. "Principles of Naval Architecture: Motions in Waves and Controllability." *Principles of Naval Architecture*. Volume III. Second Revision, the Society of Naval Architects and Marine Engineers, 1989, pp. 429 s.

LEE, Y. W. "Statistical Theory of Communication." John Wiley and Sons, New York, 1960.

MOUNET, R. E. G., U. D. NIELSEN, and A. H. BRODTKORB. "Simultaneous sea state estimation and transfer function tuning using a network of dynamically positioned ships." *Submitted to Marine Structures* (2022).

NIELSEN, U. D. "Ship Operations – Engineering Analyses and Guidance." *Lecture notes*, Technical University of Denmark, 2010.

NIELSEN, U. D. "Transformation of a wave energy spectrum from encounter to absolute domain when observing from an advancing ship." *Applied Ocean Research*, 69 (2017): 160-172, doi: 10.1016/j.apor.2017.10.011.

NIELSEN, U. D., R. E. G. MOUNET, and A. H. BRODTKORB. "Tuning of transfer functions for analysis of wave-ship interactions." *Marine Structures*, 79 (2021): 103029, doi:10.1016/j.marstruc.2021.103029.

SALVESEN, N., E. O. TUCK, and O. M. FALTINSEN. "Ship Motions and Sea Loads." Vol. 75, 1970, pp. 30 s.

SKANDALI, D., E. LOURENS, and R. H. M. OGINK. "Calibration of response amplitude operators based on measurements of vessel motions and directional wave spectra." *Marine Structures*, 72 (2020): 102774, doi:10.1016/j.marstruc.2020.102774.

St. DENIS, M., and Jr. PIERSON. "On motions of ships in confused seas". Society of Naval Architects and Marine Engineers – Papers 2, 1953.

RICE, S. O. "Mathematical analysis of random noise." *Bell System Technical Journal*, 23:3 (1944): 282–332, doi:10.1002/j.1538-7305.1944.tb00874.x

YUAN, Y., G. FU, and W. ZHANG. "Extended and unscented Kalman filters for parameter estimation of a hydrodynamic model of vessel." 35th Chinese Control Conference (CCC). IEEE, 2016.

World Maritime Technology Conference (WMTC), Denmark, Copenhagen, 26-28 April 2022

Improvements in the Computation of Added Wave Resistance Using Classical Strip Theory

Mostafa Amini-Afshar* and Harry B. Bingham

Technical University of Denmark, Department of Mechanical Engineering
Section for Fluid Mechanics, Coastal and Maritime Engineering
*maaf@mek.dtu.dk, hbb@mek.dtu.dk

1 Abstract

In this paper we present two methodologies for calculation of wave added resistance inside the classical strip theory [1]. The first method is principally an implementation of Maruo's far-field equation [2] using the Kochin function. For the second method we used a new version of the original formulation by Salvesen in [3]. The results for several ship geometries are compared with the measurements and other reference solutions. Through this, we demonstrate how strip theory can be employed more effectively for fast and accurate computation of the wave added resistance.

2 Introduction

Fast and reliable calculation of added wave resistance plays a vital role in performance monitoring of ships. This in turn facilitates a more logical decision making process in terms of proper maintenance, repair and routing plans. At the present time shipping companies which are involved in performance monitoring generally employ empirical methods and formulations. Examples of these methods include the Kreitner relation [4], STAwaveII [5], and the recently developed method by [6] which is based on model test data. These empirical approaches are preferred by the industry since they provide a quick way of calculating the added resistance for a wide range of operational data (wave conditions, forward speed, etc.), based only on simple geometric vessel parameters. At the Technical University of Denmark we are working on an alternative method based on a large database of *pre-calculated* added resistance curves for a vast collection of hull geometries representative of the world's existing fleet. Knowing only the bulk geometrical properties of a vessel, and the actual operational condition, this database can provide a framework for fast calculation of the added wave resistance through a simple interpolation scheme. These pre-calculated values are all based on the classical strip theory of [1], which in contrast to empirical methods, takes a much more realistic account of the vessel motion, wave directionality and wave frequency. For the purpose of enriching this added-resistance database, we have developed some enhanced approaches for calculation of the added resistance within strip theory. For this conference, we aim to present and disseminate the results of the these improved methodologies.

3 Theory

The methods which are employed in this paper for computation of the added resistance, are developed using an open-source implementation of the well-known Salvesen-Tuck-Faltinsen (STF) strip theory [1]. This implementation is based on the low-order Boundary Element Method and the zero-speed Green function. Further details can be found in [7]. This strip-theory solver provides two-dimensional (2D) disturbance velocity potentials (radiation and scattering), which are used to compute the added resistance based on following two methods.

3.1 Maruo's Method and the Kochin Function

According to Maruo [2], the wave added resistance R_w can be calculated from

$$R_w = \frac{\rho}{4\pi}\left\{-\int_{-\infty}^{\bar{k}_1} + \int_{\bar{k}_2}^{\bar{k}_3} + \int_{\bar{k}_4}^{\infty}\right\} \frac{\bar{\kappa}\left(m - K\cos\beta\right)}{\sqrt{\bar{\kappa}^2 - m^2}} \left|H(m)\right|^2 dm. \tag{3.1}$$

In the context of strip theory, the Kochin function $H(m)$ can be defined by

$$H_k(m) = \int_L e^{\mathrm{i}xm}\left[\int_{C_x} e^{\nu z} e^{\mathrm{i}\nu y}\left\{\left(\mathrm{i}\nu N_y + \nu N_z\right)\psi_k - \left(\frac{\partial \psi_k}{\partial N}\right)\right\} dl\right] dx, \tag{3.2}$$

for the 2D radiation potentials ψ_k in mode k, and by

$$H_s(m) = \int_L e^{\mathrm{i}xm}\left[\int_{C_x} e^{Kz} e^{\mathrm{i}Ky}\left\{\left(\mathrm{i}KN_y + KN_z\right)\psi_s - \left(\frac{\partial \psi_s}{\partial N}\right)\right\} dl\right] dx, \tag{3.3}$$

for the 2D velocity potential due to the wave scattering ψ_s. Here $\nu = \omega^2/g$, $\bar{\kappa}(m) = \left(\omega + mU\right)^2/g$, $K = 2\pi/\lambda$ with λ the incident wavelength, and N_y, N_z are the 2D sectional normal vectors to the hull section C_x in the y and z direction respectively. ω is the encounter frequency, g is acceleration due to the gravity, and ρ the fluid density. In addition, the derivative normal to the 2D sections is denoted as $\partial/\partial N$. To obtain the Kochin function for each frequency two integrals should be computed. One is over each 2D section C_x, and the other is along the ship length L. Finally we compute the added resistance by evaluating three line integrals from (3.1), where the integration limits $\bar{k}_i$, $i = 1, 4$, are functions of the Froude number and the reduced frequency $\tau = U\omega/g$. Further details regarding this methodology and its numerical implementation can be found in [8].

3.2 Improved Salvesen's Method

In the next method, we have considered the well-know Salvesen's formulation in [3]. The original exact equation which Salvesen used for deriving his approximate formulation inside the strip theory can be expressed as follows

$$\begin{aligned} R_w = \frac{\rho A g K \cos\beta}{2\omega_0}\Re\left\{\int_L e^{\mathrm{i}Kx\cos\beta}\left[\int_{C_x}\left(\psi_B\frac{\partial}{\partial N} - \frac{\partial \psi_B}{\partial N}\right)e^{Kz}e^{\mathrm{i}Ky\sin\beta}dl\right]dx\right\} \\ + \frac{1}{4}\rho\Re\left\{\int_L\int_{C_x}\left(\psi_B\frac{\partial}{\partial N} - \frac{\partial \psi_B}{\partial N}\right)\frac{\partial \psi_B^*}{\partial x}dldx\right\}, \end{aligned} \tag{3.4}$$

in which ω_0 is the wave frequency and A is the amplitude of the incident wave. ψ_B is the total disturbance velocity potential including the radiation and the scattering waves. The conjugate and the real part of the complex variables are denoted by $*$ and $\Re$. Salvesen introduces two approximations to (3.4). First he neglects the second integral (the so-called weak-scatterer assumption), and next he invokes the following long-wave assumptions

$$e^{Kz} \approx e^{-Ksd}, \tag{3.5}$$

$$e^{\mathrm{i}Ky\sin\beta} \approx e^{\mathrm{i}K\left(\pm\frac{1}{2}b\right)s\sin\beta}, \tag{3.6}$$

to evaluate the first integral in (3.4). Here the sectional coefficient $s = s_0/bd$ is defined for a 2D section with total area s_0, sectional beam b and sectional draft d. His final approximate formulation for the wave added resistance is then expressed in terms of a line integral along the ship length, with the integrands comprised of the sectional 2D hydrodynamic coefficients (added mass and damping), and geometrical properties. In a recent paper [9] we have shown that the accuracy is considerably improved if none of the above-mentioned approximations are invoked in evaluating the add resistance from (3.4). For this improved version of Salvesen's method, the disturbance velocity potentials ψ_k and ψ_s over each 2D section, and their derivatives along the ship hull should be computed. See [9] for further details.

4 Results

Three ship geometries are considered here for the *direct* computation of wave added resistance using the above-mentioned methods. The modified Wigley hull in [10], the KVLCC2, and the RIOS bulk carrier from [11]. The results are compared with measurements and other reference solutions in Figure 1. The added resistance based on the original approximate formulation by Salvesen is denoted by Salvesen (App.), and those which are obtained using the improved method from Sec. 3.2 are labeled Salvesen (New). The results based on Maruo's far-field method from Sec. 3.1 are denoted by STF-Maruo. The results using the *Enhanced Unified Theory (EUT)* are according to [10]. The experimental data for the modified Wigley hull has been obtained also from the same reference. For the KVLCC2 the measurements and the CFD calculations are all from the results of the SHOPERA project in [12, 13]. The measurements for the RIOS bulk carrier are also due to [14, 15].

As mentioned in the Introduction, our main objective is to build a large database of pre-calculated added-resistance curves using the methods presented in Sec. 3.1 and Sec. 3.2. The desired added resistance can then be obtained quickly through an interpolation inside this database, knowing just the bulk geometrical properties of the vessel and the operational data. In particular, this method uses linear interpolation in the five-dimensional parameter space of $F, \beta, \omega\sqrt{L/g}, B/L, T/L$, where $F = U/\sqrt{gL}$ is the Froude number, β the incident wave heading angle, ω the wave frequency, and L, B, T the ship length, beam, and draft. In Figure 2 we present some preliminary results based on this *indirect* procedure for computation of wave added resistance. The computations are denoted by DTU Design Tool. These results are for the container ship DTC, the KVLCC2, and also a bulk carrier from [16]. The MARINTEK measurements and NTUA computations are all from [16]. Note that NTUA results are based on 3D Boundary Element Method, and the far-field Kochin function together with a semi-empirical equation for the short waves.

5 Conclusions

In this paper we have disseminated the results of our recent progress in developing methodologies for fast and reliable computation of wave added resistance using classical strip theory. Two methods have been developed. In the improved Salvesen's method, we have avoided both the weak-scatterer and the long-wave assumptions, and treated the original equation (3.4) in its exact form in terms of the sectional velocity potentials. We have also implemented Maruo's method, without invoking the above-mentioned approximations. As can be seen from Figure 1 the presented methods compare much better with the reference solutions than the widely used approximate Salvesen method. This is specifically true for the case of zero-speed drift forces. These improved methods can be employed for creating a large database of added resistance curves. Since strip theory requires less computational effort than 3D methods, this database can be created in the order of hours for a wide range of reference geometries and operational conditions. Interpolation inside this database then gives the added-resistance curves in a matter of seconds. In Figure 2 we have also shown the reliability and accuracy of this interpolation method.

Acknowledgment

This research has been funded by the ShippingLab project[1], and its financial support is highly appreciated.

[1] `https://shippinglab.dk/`

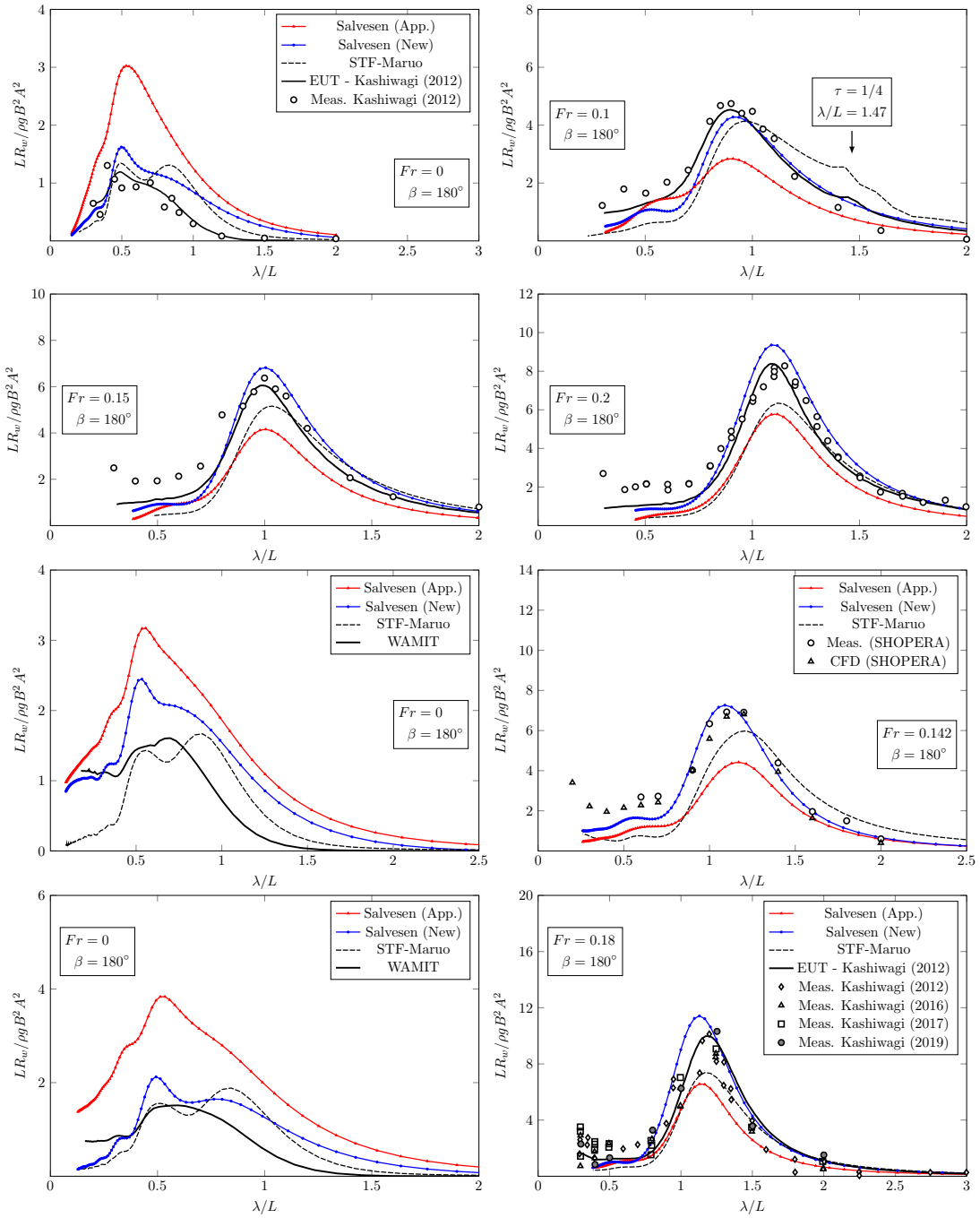

Figure 1: *Direct* calculations of the added wave resistance based on the methods presented in Sec. 3.1, and Sec. 3.2. Modified Wigley hull (1st and 2nd row), the KVLCC2 (3rd row), the RIOS bulk carrier (4th row). Note that all plots at the left side are for the zero-speed drift force.

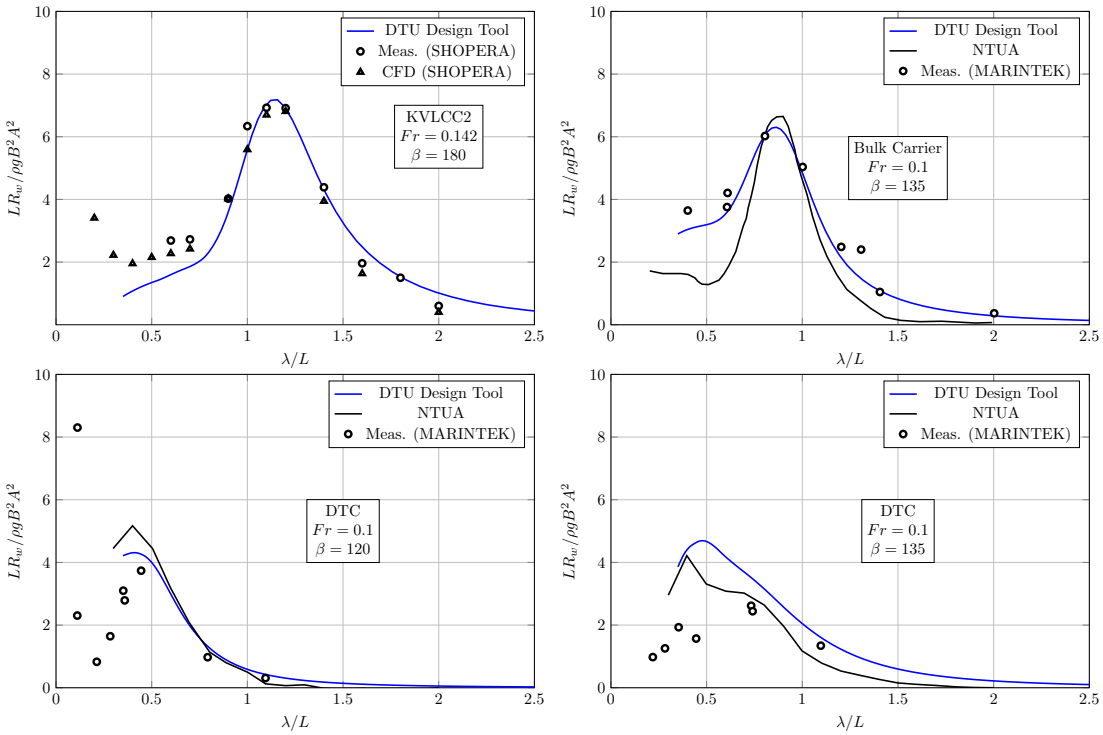

Figure 2: Example results for added resistance based on the *indirect* procedure.

References

[1] N. Salvesen, E. O. Tuck, and O. Faltinsen, *Ship motions and sea loads.* Annual Meeting of the Society of Naval Architecture and Marine Engineers (SNAME), New York, November 12-13, 1970.

[2] H. Maruo, "Resistance in waves," *Research on Seakeeping Qualities of Ships in Japan, The Society of Naval Architects of Japan*, vol. 8, pp. 67–102, 1963.

[3] N. Salvesen, "Added resistance of ships in waves," *Journal of Hydronautics*, vol. 12, no. 1, pp. 24–34, 1978.

[4] J. Kreitner, "Heave, pitch and resistance of ships in a seaway," *Transactions of the Royal Institute of Naval Architects,'London*, vol. 87, 1939.

[5] ITTC, "Procedures and guidelines: Prediction of power increase in irregular waves from model test," in *International Towing Tank Conference (ITTC 2014)*, 2014.

[6] S. Liu and A. Papanikolaou, "Regression analysis of experimental data for added resistance in waves of arbitrary heading and development of a semi-empirical formula," *J. Ocean Eng.*, vol. 206, 2021.

[7] H. B. Bingham and M. Amini-Afshar, "DTU_StripTheorySolver," 2020. `https://gitlab.gbar.dtu.dk/oceanwave3d/DTU_StripTheorySolver.git`.

[8] M. Amini-Afshar and H. B. Bingham, "Added resistance using Salvesen–Tuck–Faltinsen strip theory and the Kochin function," *Applied Ocean Research*, vol. 106, p. 102481, 2021.

[9] M. Amini-Afshar, "Salvesen's Method for Added Resistance Revisited," *Journal of Offshore Mechanics and Arctic Engineering*, vol. 143, no. 5, p. 051902, 2021.

[10] M. Kashiwagi, T. Ikeda, T. Sasakawa, *et al.*, "Effects of forward speed of a ship on added resistance in waves," *International Journal of Offshore and Polar Engineering*, vol. 20, no. 3, pp. 196–203, 2010.

[11] H. Iwashita, M. Kashiwagi, Y. Ito, and Y. Seki, "Calculations of ship seakeeping in low-speed/low-frequency range by frequency-domain Rankine panel methods," *Journal of the Japan Society of Naval Architects and Ocean Engineers*, vol. 24, pp. 129–146, 2016, (In Japanese).

[12] A. Papanikolaou, G. Zaraphonitis, E. Bitner-Gregersen, V. Shigunov, O. El Moctar, C. G. Soares, D. Reddy, and F. Sprenger, "Energy efficient safe ship operation (SHOPERA)," *Transportation Research Procedia*, vol. 14, pp. 820–829, 2016.

[13] V. Shigunov, O. el Moctar, A. Papanikolaou, R. Potthoff, and S. Liu, "International benchmark study on numerical simulation methods for prediction of manoeuvrability of ships in waves," *Ocean Engineering*, vol. 165, pp. 365 – 385, 2018.

[14] H. Iwashita and M. Kashiwagi, "An innovative EFD for studying ship seakeeping," *Proceedings of 33rd IWWWFB (Guidel-Plages, France)*, pp. 85–88, 2018.

[15] M. Kashiwagi, H. Iwashita, S. Miura, and M. Hinatsu, "Study on added resistance with measured unsteady pressure distribution on ship-hull surface," *Proceedings of 34th IWWWFB (Noah's on the Beach, Newcastle, NSW, Australia)*, pp. 81–84, 2019.

[16] S. Liu and A. Papanikolaou, "Prediction of the added resistance of ships in oblique seas," in *The 26th International Ocean and Polar Engineering Conference*, OnePetro, 2016.

SCRUBBERS ON HIGH SEAS TO RULE THIS DECADE

Manogaran Vijayakumar[1] and Kappuvaveetil Gauthamgopinath[2]

ABSTRACT

The aim of MARPOL convention is to prevent pollution of the marine environment. It seeks to control airborne emissions from the ships with some limitations. The convention prescribed the Sulphur content in fuel oils used on board ships not to exceed 0.5% m/m on and after 1 January 2020. These contemplate the shipping companies to switch over to use other compliant fuels or install Exhaust Gas Cleaning System (EGCS) / Scrubbers. EGCS/Scrubbers clean the exhaust gas released in order to discharge a minimum amount of So_x. To evaluate the selected EGCS/Scrubbers technology from ship owners and charterer's point of view, the proposed analysis in this paper indicates the success of scrubbers than 0.5% VLSFO, in which the amount that vessels with the EGCS/Scrubbers units installed can earn for a voyage. At the outset fuel cost plays a vital role which is always an exponential function, in this part EGCS/Scrubbers take more attractive investment appraisals than other alternative compliant fuels throughout this decade.

KEYWORDS

MARPOL convention; EGCS / Scrubbers; 0.5% VLSFO; 3.5% HSFO

INTRODUCTION

The IMO has efficiency requirements as part of Annex VI of MARPOL to reduce CO_2 emissions from the shipping industry, and they adopted the "IMO strategy on reduction of Green House Gas (GHG) emissions from ships" in 2018. They've agreed on the following objectives: - Carbon intensity of international shipping to decline: reduce CO_2 emissions per transport work, on average across international shipping, by at least 40% by 2030, with efforts to reach 70% by 2050, compared to 2008; and GHG emissions from international shipping to peak and decline, with total annual GHG emissions reduced by at least 50% by 2050, with efforts to phase them out, in line with the Parley for the Oceans (Knudsen, 2021). In the year ahead, a strategy review will take place.

EU Regulations (All voyages to, from and between EU ports) in 2013, the Commission set out a strategy towards reducing GHG emissions from the shipping industry.

- Monitoring, Reporting, and Verification of CO_2 emissions from large ships using EU ports are the three steps in the strategy. This step has now been implemented and is known as the EU MRV.
- Goals for reducing greenhouse gas emissions in the maritime transportation sector.
- In the medium to long term, additional measures, including market-based measures. The European Union recently approved the inclusion of shipping in its emissions trading scheme.

The requirements are similar to those of the International Maritime Organization (IMO), but the EU regulations include cargo information, and data submitted to them will be made public. 2018 was the first year of reporting.

According to the European Environment Agency's greenhouse gas emissions data, emissions account for 3.7 % of total EU CO_2 emissions. This annual report is based on data from 2018 emissions reported by companies until September 2019 under the EU Regulation on CO_2 emissions from maritime transport monitoring, reporting, and verification (MRV). The data and report are published each year to provide a better understanding of the monitored fleet's characteristics, CO_2 emissions, and energy efficiency.

EGCS / Scrubbers are used on some ships to reduce air pollution. Flag states accept this as an alternative method of meeting the Sulphur

limit. According to the European Environment Agency's greenhouse gas emissions data, emissions account for 3.7 % of total EU CO_2 emissions. This annual report is based on data from 2018 emissions reported by companies until September 2019 under the EU Regulation on CO_2 emissions from maritime transport monitoring, reporting, and verification (MRV). The data and report are published each year to provide a better understanding of the monitored fleet's characteristics, CO_2 emissions, and energy efficiency.

Some ships reduce air pollution by incorporating EGCS / Scrubbers. Flag States accept this as an alternative method of meeting the Sulphur limit requirement. These scrubbers are intended to remove Sulphur oxides from the exhaust gases of the ship's engines and boilers. As a result, a ship equipped with a scrubber can use heavy fuel oil (3.5 %) because the Sulphur oxide emissions will be reduced to a level equivalent to the required fuel oil Sulphur limit (0.5 %).

As a result, the article discusses VLSFO's challenges, future fuel options, the edges taken over by the EGCS / Scrubbers.

SULPHUR CAP- 2020

Sulphur Oxides (Sox) are produced during the combustion of Sulphur-containing fuel. The main concern with Sox emissions is when they are emitted close to land, where they have a direct impact on human health and the environment; they cause lung and heart diseases, as well as acid rain, which has a significant impact on the health of forests, farmland, and freshwater. Shipping accounts for approximately 9% of global SO emissions. The International Maritime Organization (IMO) has imposed a Sulphur limit on marine fuel oils. The legislation also allows a vessel to burn high Sulphur fuels if Sox emissions are removed from the exhaust and result in the same concentration of Sox emissions as burning low Sulphur fuels, such as if a vessel installs an EGCS / Scrubbers. As of January 1st, 2020, the IMO adopted a global Sulphur cap limiting all vessel exhaust emissions to a maximum 0.5 % Sulphur content, requiring ships to either burn 0.5 % Sulphur fuel or use alternative technology to reduce emissions to an equivalent level. This requirement is in addition to the 0.1 % Sulphur limit in the North American, US Caribbean, North Sea, and Baltic Emission Control Areas (ECA), In addition to the IMO legislation, local limits are enforcing in Hong Kong, European Union Ports, China, South Korea, Malaysia and California. The Californian regulations differ slightly from ECA requirements, as they require vessels to use MDO/MGO. The Sulphur cap in China's designated 'inland' ECA (navigable waters of the Yangtze River, and the Xijiang River main lines) was further tighten to 0.1%S on 1st January 2020 for sea-going vessels. We expect in time more ecas will appear around the world – Mediterranean, Caribbean, Japan, and Norway are possible in the near future (Knudsen, 2021)..

Sulphur Oxides (Sox) are formed by combustion of fuel containing Sulphur. The major concern for Sox emissions are when they emitted close to land where they have a direct impact on human health and the environment; they cause lung and heart diseases, and acid rain, which in turn has a huge impact on the health of forests, farmland and freshwater. Shipping accounts for around 9% of the global sox emissions. The International Maritime Organization (IMO) has set a limit on the Sulphur content of marine fuel oils. The legislation also allows for a vessel to burn high Sulphur fuels if sox emissions are removed from the exhaust and result in the same concentration of sox emissions as burning low Sulphur fuels, for example if a vessel installs an EGCS / Scrubbers.

0.5%VLSFO AND ITS CHALLENGES

After started using 0.5%VLSFO continuously, the shipping fraternity faced the key issues which can damage the marine diesel engines due to cat fines, excessive sludging, compatibility issues, asphaltene, high wax appearance temperatures (cloud point) and fuel stability. 0.5%VLSFO is incompatible even with same type of fuel from same refiner but bunkered in different locations. The new low Sulphur fuel hasn't stopped the issues of fuel instability and contamination which are of primary concern for ship owners, ship managers and operators. The problem is that VLSFO does not really exist as one fuel. It is a range of chemicals that are so wide, variable and volatile that it is staggering that it is even labelled as one type of fuel (Mahajan, 2021).

UNSTABLE AND VOLATILE FUEL

0.5%VLSFO was discovered to be not just one fuel but new blends forming thousands of unique permutations. Various blends of 0.5%VLSFO have been found to be highly variable, easily contaminated and very unstable. These blends were also very volatile, changing critical properties within the space of days and weeks, rather than the usual months when the oil is stored.

METALLIC SAND IN THE ENGINE

0.5%VLSFO is the residual part left at the end of the refining process, and is produced using a chemical process called catalytic cracking. To make this cracking process more effective at lower temperatures, hard particles of Aluminum (Al) and Silicon (Si) are added to the oil. They resemble a metallic form of sand.

COMBUSTION QUALITY OF FUEL IN THE ENGINE

0.5%VLSFO poses a particular risk. It takes much longer between the time the fuel enters the chamber of an engine to when it ignites. This causes a massive shock wave (known as a 'diesel knock'). Swedish ship reinsurers, one of the thirteen big ship insurers in the world), highlighted that ignition problems occurred with 0.5%VLSFO when the CCAI was between 850 and 890.

WAX DEPOSITS

Solidifying 0.5%VLSFO in colder temperatures poses a major risk of engine failure in colder temperatures.

One of the most visible issues with 0.5%VLSFO is what the industry describes as 'wax deposits.' Chemicals known as Aromatic and Paraffinic compounds are mixed in different ways to make 0.5%VLSFO. This turns flowing ship oil into a sticky putty. This putty is unusable in ships and clogs up all aspects of a ship's pipelines and machinery.

THE VISCOSITY PROBLEM

Oil needs to maintain a certain viscosity to be safe given the way that ship engines have been designed.

Viscosity is measured as a centistoke (CST). Industry reports from March 2020 show viscosity plummeting to dangerously low levels (indicating a high degree of running fluids).

.

EXHAUST GAS CLEANING SYSTEMS / SCRUBBERS WITH 3.5% HSFO

The IMO guidance covers aspects of the fuel oil purchase all the way up to loading the purchased fuel oil on board. The requirements for fuels used in marine diesel engines and boilers are specified in an International Standardization Organization (ISO 8217). ISO has released a new standard: ISO/PAS 23263:2019 Petroleum products - Fuels (class F) - Considerations for fuel suppliers and users regarding marine fuel quality in light of the implementation of a Sulphur limit of 0.5 % in 2020 (Li et al., 2020).

To achieve the same level of emission reduction, Regulation 4 of MARPOL Annex VI allows Administrations (flag States) to approve "equivalents" - any fitting, material, appliance, or apparatus to be installed in a ship or other procedures, alternative fuel oils, or compliance methods used as an alternative to that required" - that enables the same emission control standards to be met Flag States have accepted and approved EGCS / Scrubbers**,** as meeting the requirements for Sulphur oxide reduction (Green book, 2021).

The same regulation on Equivalents contains an important requirement, which states in paragraph 4 that "the Administration of a Party that allows the use of an equivalent shall Endeavor not to impair or damage its environment, human health, property, or resources, or those of other States." The International Maritime Organization (IMO) has established stringent criteria for the discharge of wash water from any EGCS / Scrubbers residues produced by the EGCS/Scrubber unit, which is typically in a closed-loop configuration, should be delivered ashore to appropriate reception facilities. Such residues should not be discharged into the sea or burned on board.

Open- loop scrubbers add water to the exhaust gas which turns Sulphur oxides (Sox) to sulphates/sulphuric acid. Open-loop scrubbers return wash water to the sea. The wash water must meet strict criteria, so that discharge wash water should have a pH of no less than 6.5. There are also strict limits on discharge of Polycyclic Aromatic Hydrocarbons (PAHs) and nitrates (Lack & Corbett, 2012).

PRINCIPLE OF EGCS / SCRUBBERS SYSTEM

Exhaust gas streams pass through an alkaline scrubbing material inside the scrubber, which neutralizes the acidic nature of the exhaust gases and removes any particulate matter.

The scrubbing material is then collected with the wash water, which can either be stored or disposed of as effluent right away. The system's cleaned exhaust is discharged into the atmosphere. The scrubbing material is selected so that specific impurities such as Sox or NOx can be removed through chemical reactions.

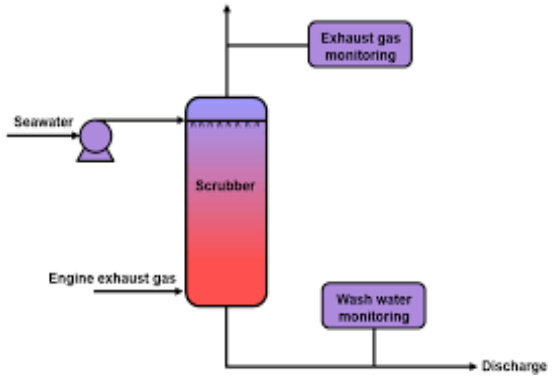

Marine scrubbers use lime or caustic soda to desulphurize water, resulting in Sulphur-based salts that can be easily discharged because they do not pose a threat to the environment. Because of their alkaline nature, scrubbers can use sea water, fresh water with added calcium/sodium sorbents, or hydrated lime pellets as a scrubbing medium (Paulsrud, 2015).

Inside the scrubbers, packed beds of gas-pollutant removal reagents (such as limestone) are used to increase the contact time between the scrubbing material and the gas. The vertical flow of water inside the scrubbers is slowed by these packed beds, which intensifies the exhaust gas cooling and acidic water neutralization process. Scrubbers are designed to maximize the abs reactions involved:

$$SO_2\ (gas) + H_2O + \tfrac{1}{2}O_2 \rightarrow SO_4^{2-} + 2H+\ (Sulphate\ ion + Hydrogen\ ion).$$

$$HCO_3^- + H^+ \rightarrow CO_2 + H_2O\ (Carbon\text{-}di\text{-}oxide + Water).$$

Salient features of using EGCS / Scrubbers system includes;

- It has very few moving parts, the design is simple and easy to install on board.
- Apart from de-fouling and operational checks, the system requires very less maintenance
- This system does not require storage for waste materials

INVESTMENT WORTHY FOR EGCS / SCRUBBERS SYSTEM

- Total Engine Power---------- 53,000KW
- Sulphur content---------- 3.5%
- Fuel oil consumption per day---------- 35MT/day
- Estimated HFO per year---------- 12,775 MT/annum
- Fuel price 3.5% HSFO (as on mid Nov 2021) ----------460USD/MT
- Fuel price 0.5% VLSFO (as on mid Nov 2021) ----------630USD/MT
- EGCS / Scrubbers Component cost ---------- 3,500,000USD
- EGCS / Scrubbers Installation cost ----------1,000,000USD
- EGCS / Scrubbers Total investment cost ---------- 4,500,000USD
- Estimated 3.5% HSFO cost per year (as on mid Nov 2021) ---------- 5,876,500USD
- Estimated 0.5%VLSFO cost per year (as on mid Nov 2021) ---------- 8,048,250USD
- Estimated rate spread between 3.5%HSFO and 0.5%VLSFO per year -------- 2,171,750USD

Estimated payback period for the EGCS / Scrubbers system total investment will be less than 2.1 years

This calculation is an approximate estimation, various factors influencing the fuel consumption, fuel cost, load, current, routing etc., has to be taken into account for detailed estimation.

FUTURE FUEL AND ITS TRANSITION PERIOD

The work of classification and standardization societies like DNV GL helps to ensure systems are brought up to scratch and held to a higher standard. It is with LNG, LPG, Methanol, ammonia, hydrogen, and lithium-ion battery. May be by 2050 we will have found a way to include decarbonized source of fuel within the maritime sector. That would be transformational (McKinnon, 2011).

CONCLUSION

By using exhaust gas cleaning system-scrubbers, ship operators, owners, managers, front liners ship staffs can operate marine diesel engines without worry about costly engine failures, lay-up or any off-hire caused by contamination, fuel instability and its associated problems with the low Sulphur fuel, also scarcity and availability of the future fuels. In far, future fuels like lithium-ion batteries, methanol, ammonia, hydrogen may be the complementary to EGCS /Scrubbers but still cannot be compensated in terms of monetary beneficial.

REFERENCES

1. Green book, environmental sustainability and Seaspan action Rev: 27-oct 2021.
2. Knudsen, D.B. 2021. Is the Shipping industry still Sulfuring?-A study of compliance factors from the IMO 2020 sulfur cap.
3. Lack, D., Corbett, J. 2012. Black carbon from ships: a review of the effects of ship speed, fuel quality and exhaust gas scrubbing. *Atmospheric Chemistry and Physics*, 12(9), 3985-4000.
4. Li, K., Wu, M., Gu, X., Yuen, K., Xiao, Y. 2020. Determinants of ship operators' options for compliance with IMO 2020. *Transportation Research Part D: Transport and Environment*, 86,102459.
5. Mahajan, K. 2021. COVID-19, IMO 2020 and decarbonization challenges create entry barriers for new entrants. *Tribology & Lubrication Technology*, 77(3), 20-22.
6. Paulsrud, H.M. 2015. A Practical Guide to Wärtsilä Scrubber Systems. *Marine Engineering*, 50(3), 315-317.

EFFECT OF THE IMO GLOBAL SULFUR CAP ON SO_X AND CO_2 EMISSIONS OF THE WORLD'S BULK CARRIER FLEET

Maria C. Iosifidi[1], Georgios Charvalos[1], Georgios N. Rossopoulos[1], Christos I. Papadopoulos[1]

ABSTRACT

This work addresses the problem of quantifying air pollution due to marine traffic, emphasizing on SO_X and CO_2 emissions from the world's bulk carrier fleet. To reduce the SO_x emissions from marine vessels, IMO implemented a global sulphur limit, widely known as the Global Sulfur Cap, which has been put into effect since January 1st 2020. The most commonly accepted methods to comply with the Global Sulfur Cap are (a) the use of low-sulfur fuels and (b) the installation of exhaust gas after-treatment systems. The main objective of this work is to quantify the effect of Global Sulfur Cap enforcement on a global scale. The proposed methodology includes calculation of emissions on a virtual global fleet bearing statistical characteristics equivalent to that of the actual world's fleet. Four different scenarios have been investigated: (i) ships do not take any measure to comply with the IMO regulations, simulating the pre- Global Sulfur Cap period, (ii) all ships install an exhaust gas treatment system, (iii) all ships operate with low sulfur fuel oil and (iv) 10% of the world's fleet uses exhaust gas treatment systems, while the rest of the fleet operates with low sulfur fuel oil. Having found the location and route of each ship and having calculated the emissions' mass per hour, based on the ship's real-time speed and draft, spatial heat maps of the pollutants for the world's bulk carrier fleet have been generated for given points in time. An additional case study has been performed, comparing results for four (4) selected dates, namely March 12, March 17, March 22 and May 24 2020. The series of performed simulations have demonstrated a significant decrease in SO_X emissions due to the enforcement of the regulations; their effectiveness can be quantified either globally or focusing on specific sensitive areas, such as the Baltic and North sea, the Mediterranean sea and the North American eca zones. More specifically, installation of exhaust gas treatment systems shows potential to further decrease SO_X emissions with a relatively small increase of CO_2. Overall the pollutants remain relatively unchanged over the first consecutive dates studied and the last date, an increase in emissions is observed, mainly attributed to the COVID-19 situation, and the corresponding effects on the shipping transport sector.

KEYWORDS

Global Sulfur Cap; Scrubbers; Low sulfur fuel; Bulk carrier fleet; Emission heat-map; Regulation effectiveness; Shipping.

[1] School of Naval Architecture and Marine Engineering, National Technical University of Athens, Zografos, Greece

INTRODUCTION

Until January 2020, the most typical marine fuel had been heavy fuel oil, derived as a residue from crude oil distillation. During the combustion of heavy fuel oil, sulfur, contained in the fuel, is burnt and sulfur oxides are formed. The sulfur is mainly oxidized to SO_2; however, there is also a conversion fraction into SO_3, which is in a range of 2.6-6.7% (Andreasen 2010):

$$S + O_2 \rightarrow SO_2 \quad [1]$$

$$2SO_2 + O_2 \rightarrow 2SO_3 \quad [2]$$

Sulfur oxides are known to be harmful to human health, causing respiratory symptoms and lung disease. In the atmosphere, SO_X can lead to acid rain, which can harm crops, forests, and aquatic species, and contributes to the acidification of the oceans (World Bank Group 1999). Limiting SO_X emissions from ships improves air quality, and protects the environment. In regard to this, IMO regulations to reduce sulfur oxides emissions from ships first came into force in 2005, under Annex VI of the International Convention for the Prevention of Pollution from Ships. This Annex introduced a worldwide limit on the sulfur content of marine fuels and the Sulfur Emission Control Areas (SECAS) where the sulfur limit is stricter. As of 2011, there are six existing ECAs: the Baltic Sea area, the North Sea area, the North American area, the sea areas located off the Atlantic coasts of the United States and Canada, and the sea area located off the coasts of the Hawaiian Islands. From 1 January 2015, the limit for sulfur in fuel oil used on ships operating inside designated ECAs is reduced to 0.1 percent, and from 1 January 2020, the limit outside designated ECAs is reduced to 0.50 percent m/m (mass by mass). There are also several regional and local regulations concerning the sulfur oxides emissions (ABS 2017). The prominent ways for the marine industry to be compliant with the above regulations are two. The primary compliance option is to use low sulfur fuel. There is a wide variety of low-sulfur fuels, including low-sulfur distillate oil, 'hybrid' fuel oil, liquefied natural gas (LNG), liquefied petroleum gas (LPG), biofuels, dimethyl ether, ethane, and methanol. The secondary compliance option is to use an exhaust gas treatment system, such as a scrubber, to desulfurize the exhaust gas and reduce SO_X emissions to a level equivalent to the required fuel sulfur content.

Having set a brief background upon which the study was made, the primary goal of the present work is the calculation of the SO_X emissions worldwide with a view to the mapping of the emissions. A secondary aim of the study is the calculation of carbon dioxide CO_2 emissions, without, however, including the emissions caused by the fuel production and transferring. The main greenhouse gas is another matter of great concern at this moment. It is considered valuable to quantify the differences in the SO_X and CO_2 emissions between the two compliance options and their map distribution both worldwide and in sensitive areas.

PROBLEM DESCRIPTION - METHODOLOGY

Fleet Description

The subject fleet used for this case study consisted of 10,777 bulk carriers. The data available for further processing for this fleet are shown in the following table:

Table 1: Collected Data for Bulk Carrier Equivalent Fleet

Category	Given data
General Characteristics	Name
	IMO Number
	Ship type
	Deadweight [t]
Dimensions	Length over all [m]
	Length between perpendiculars [m]
	Breadth moulded [m]
	Depth moulded [m]
Shipbuilding characteristics	Shipbuilder
	Ship design
	Yard number
	Date of build

Main Engine characteristics	Engine builder
	Engine design
	Engine model
Auxiliary Engine characteristics	Auxiliary engine builder
	Auxiliary engine model

The data presented in Table 1 were thoroughly processed to exclude instances that contain misstated and inconsistent values or have any sort of data gaps. The first step of the data processing was sorting the vessels by date of build. We made the assumption that the vessels built before January 2005 will not invest in such an expensive and time demanding installation as the exhaust gas cleaning system, thus not contributing to the comparison between the two compliance methods and therefore these vessels were excluded from the analysis. Hence, the resulting fleet consisted of 8,382 vessels. The subject fleet is considered to be a satisfactory representation of the currently active global bulk carrier fleet and the calculated emissions depict the most significant percentage of the total SO_X and CO_2 emitted globally from bulk carriers.

Web Extraction of Fleet Real-Time Data

A major factor for the process of calculating and mapping ship emissions is the current location of each vessel. In order to create a map of the emissions, it is imperative to connect each source of emissions with a location. Furthermore, the location of each vessel affects the SO_X emissions, as there are different limitations of sulfur content in the fuel oil by the regulations for some areas around the world, such as the Emission Control Areas. This necessity led to the development of an algorithm that records data from websites that use Automatic Identification System (AIS) technology. For the extraction of the required data, the MMSI number is used. The MMSI number is a Maritime Mobile Service Identity, namely a series of nine digits which are sent in digital form over a radio frequency channel in order to uniquely identify ship stations, ship earth stations, coast stations, coast earth stations, and group calls. The MMSI is not a unique number throughout a vessel's life, as it may change when the vessel changes owner or flag. However, two or more vessels cannot have the same MMSI at the same time. Each vessel's data extracted from the internet are presented in the below table.

Table 2: Additional Data Extracted for Actual Bulk Carrier Fleet

Extracted data	Description
Latitude	The values range from -90 to 90deg, and the negative values indicate that the vessel is in the southern hemisphere. Most vessels are sailing between -55 and 75 deg.
Longitude	The values range from -180 (western) to 180 degrees for the eastern hemisphere.
Status of the vessel	The status suggests whether the vessel is underway or anchored.
Speed	The current operational speed of the vessel in knots
Course	The current operational course of the vessel, ranging from 0 to 360 degrees. The zero value states that the vessel is heading to the north and the values increase clockwise.
Location	The area, sea, or gulf in which the vessel is located.
Port/Destination	The port, if the vessel is berthed in a port, otherwise the destination of the vessel.
ETA	Estimated time and date (UTC) of arrival at the destination port.
Draft	The current operational draft of the vessel in meters.
Date	The date and the time that the AIS data were received.

The position, the speed, and the course of the vessel are data that have automatic input in the AIS system. The real time speed which is extracted incorporates in the analysis the impact of higher priced low sulfur fuel on ship speed at the time extracted. However, the voyage information, such as the destination and the draft are inserted manually by the crew. It becomes clear that the manually inserted data do not have the same validity. Another fact that is important to mention is that the data reflect the time that they were transmitted and not the time that the program ran. It can, thus, be seen that the data of each vessel corresponds to a different moment which may vary from a minute to a month before the running of the program. Nevertheless, within the framework of the present study, it is considered that the data of the whole fleet reflect approximately the same moment in time which coincides with the time that the data collection software was executed.

Description of the base fleet calculation tool

Another critical factor is the main propulsion engine of a vessel. Since this information is not readily available per vessel for the entire fleet, an algorithm has been used to select an appropriate main engine in the course of a preliminary design analysis, based on the basic principles of resistance and propulsion of a ship. This algorithm has been developed in the Division of Marine Engineering of the School of Naval Architecture and Marine Engineering of National Technical University of Athens (Charvalos et al, 2020). The tool receives as input the deadweight of the subject fleet and creates a virtual fleet. Based on the deadweight and semi-empirical equations the program calculates the service speed, the operational speed, the length between perpendiculars, the depth, and the breadth. The calculated operational speed as well as the three dimensions are used only when the real input values are invalid. The valid values presented in table 3 were selected after processing the input list in order to exclude the invalid outliers and replace them with reasonably calculated values, utilizing empirical equations.

Table 3: Valid Input Data Values for Statistically Equivalent Bulk Carrier Fleet

Data	Valid values
Operational speed V [kn]	$0 \leq V \leq$ Service speed
Length BP [m]	$90 \leq LBP \leq 370$
Depth [m]	$11 \leq D \leq 35$
Breadth [m]	$14 \leq B \leq 70$

In order to acquire the complete vessel geometry, the maximum draft, the displacement, the dimensionless coefficients CB, CM, CP, CWP, and the longitudinal center of buoyancy are calculated. They are all calculated using semi-empirical equations and the calculated dimensions from the previous step. Based on the calculated geometry, the wetted surface is calculated as well as the total resistance of the vessel. After the selection of a propeller diameter, so that the propeller is fully immersed, and the semi-empirical calculation of all the necessary factors, the program grid_b.F95 (Politis 2011) runs, which calculates the optimised propeller pitch and runs for a fouled hull. The pair of power and RPM, for the fouled hull resulting from the grid_b is the major factor for proper propulsion engine selection. For the requested pair of power - rpm, the program searches for an engine through a catalog which includes data for eighteen engines, built by a known manufacturer. These engines are considered to cover the sizes of the fleet. The catalog includes the four points of the engines' layout diagram L1, L2, L3, L4, and the program constructs the diagram. The selected engine is the first engine found with the requested pair of power - rpm to be inside the layout diagram. The Maximum Continuous Rating of the engine, the MCR point, is selected to be equal to the calculated power for the fouled hull. To this point, it has to be mentioned that the propeller is considered to have 4 blades. In case that no engine is found, the propeller blades are considered to be five and the process is repeated. If again no engine is found, then the particular vessel is excluded from the study. The last and most important part of the tool, which is used for the emissions calculations, is the one that estimates the operational power of the vessel. The resistance is calculated for the operational draft and the grid_b runs again. In addition, the operational power of the vessel is calculated using the propeller law in order to correspond to the operational speed as well. The value of the operational draft is the one extracted from the web. In case that this value is invalid, which means that it is below the propeller diameter or higher than the maximum draft, the operational draft takes a calculated value from the tool.

The first addition to the base tool towards the emissions calculation concerns the position of the vessel. The position of the vessel affects the emissions in two ways. The first one refers to the engine consumption. The temperature of the intake air and the cooling water has a slight effect on the engine consumption, but cumulatively it has quite an effect on the fleet emissions. The engine consumption rises as the air and the seawater temperature rises. For this reason, the earth was considered to be divided into three areas, the warm, the cold, and the mid area. Initially, the position of the vessel is considered to be in a cold area. Then, it is checked if the latitude is above -30 and below 30 degrees. In that case, the vessel is in a warm area. Otherwise, if it is above -60 and below 60 degrees, it is considered to be in the mid area. If the latitude of the vessel does not have a value, due to a data gap, the area is randomly selected. The other effect which the position of the vessel has on the emissions concerns the Emission Control Areas. The sulfur limit in the ECAs, as set out in the regulations, is stricter than outside the ECAs. Therefore, whether the vessel is in an ECA or not affects the emissions deeply. The polygons of the ECAs were found on the International Maritime Organisation webpage (IMO 2019). The position of the vessel is considered as a point with the latitude as the x-coordinate and the longitude as the y-coordinate. If the point is inside one of the polygons, the vessel is in an ECA. In the case of a data gap, the vessel is considered to be outside an ECA by definition. It is considered more likely the vessel to be outside the ECAs and since the data gaps are not many, this definition is not thought to negatively affect the accuracy of the results.

Description of selected scenarios

For the particular study four different scenarios were considered in order to define the two fundamental parameters which directly affect the emissions, the fuel type consumed by the vessel main engine, and whether the vessel is fitted with an exhaust gas cleaning system or not. As far as the vessels fitted with scrubbers are concerned, most of the scrubber manufacturers adjust the water flow in the tower to reach the sulfur limit with the minimum electric consumption. This is the reason why, for this study, the sulfur content of the fuel burnt in each vessel is considered to be the same as the sulfur limit defined by the regulations.

"No Sulfur Cap" Scenario. The first scenario (CS1) relates to the condition before 2020. For this scenario, it is considered that the sulfur content of the fuel used globally is a maximum of 3.5% m/m and 0.1% m/m inside ECAs. It is, therefore, decided that no vessel has a scrubber installed. The fuel that the vessels use inside the ECAs is Marine Diesel/Gas Oil and outside the ECAs Heavy Fuel Oil. The Marine Diesel Oil is selected for this scenario instead of another low sulfur fuel, due to its higher availability before 2020. It is considered that this scenario represents quite accurately the reality before 2020.

"Scrubber - All vessels" Scenario. The second scenario (CS2) refers to the current situation that the Sulfur Cap regulation has come into effect. The compliance method for all the vessels is chosen to be the exhaust gas cleaning system. As the water flow in the scrubber can fluctuate in order to succeed the desired sulfur limit, inside and outside ECAs, burning Heavy Fuel Oil with a maximum sulfur content of 3.5% m/m, it is considered that all the vessels burn solely Heavy Fuel Oil. In this case, the fuel used affects only the CO2 emissions and not the SOX, as the SOX emissions are considered to be the equivalent of burning fuel with 0.5% m/m content outside the ECAs and 0.1% m/m inside. This fuel is solely selected for this scenario because it is the most economic option.

"No scrubber - All vessels" Scenario. The third scenario (CS3) refers as well to the Sulfur Cap regulation. This time, the compliance method is chosen to be the use of alternative low sulfur fuel oils. Thus, it is considered that no vessel has installed an exhaust gas cleaning system. The fuel considered to be burnt is low sulfur heavy fuel oil (LSHFO) globally and ultra-low sulfur fuel oil inside the ECAs. Both fuels are selected residual instead of distillates due to the higher availability and reduced price.

"Scrubber - 10% of the fleet" Scenario. The last scenario (CS4) is an attempt at an accurate representation of the actual present conditions. Based on literature estimations (Argus 2019), it is considered that about 10% of the vessels have chosen the scrubbers as a compliance method with the regulations. Moreover, it is more likely for the larger vessels to have installed a scrubber, due to the larger fuel oil consumption and therefore higher operational costs of expensive fuels. Consequently, for this scenario, according to these assumptions, a 15% probability value is selected for the Very Large Bulk Carriers (VLBC) to have scrubbers installed, a 10% probability value for the Capesize vessels, and a 5% probability value for the smaller ships. The rest of the vessels are considered to burn low sulfur fuel oils. Initially, it is considered that no vessel has a scrubber installed and the scrubber installation probability is defined as a random real number between 0.0 and 100.0. If the vessel belongs to the VLBC class and if the random number is less than or equal to 15.0, it is considered that this vessel has installed a scrubber. Otherwise, if the vessel belongs to the Capesize class and the random number is less than or equal to 10.0, it is considered that this vessel has installed a scrubber. For the vessels that belong to the other classes, it is considered to have scrubber only if the random number is less than or equal to 5.0. In this way, we achieved an approximate percentage of the 10% of the fleet installing scrubber, incorporating the higher likelihood for a larger vessel to proceed with the installation. For the vessels that the procedure resulted in having scrubbers installed, the fuel is selected to be Heavy Fuel Oil regardless of whether the vessel is inside an ECA, similar to the scrubber scenario. For the rest of the vessels, the fuel burnt is selected to be low-sulfur heavy fuel oil outside the ECAs and ultra-low sulfur fuel oil inside the ECAs, similar to the third scenario.

At this point, it is important to mention that for each fuel oil, three parameters are defined which affect the emissions. The first one is the Lower Calorific Value (LCV), which affects the specific fuel oil consumption of the engine. The second parameter is the sulfur content of the fuel and the third parameter the CO2 emission factor. In table 4 the characteristics of each fuel are presented:

Table 4: Fuel Related Parameters for Each Scenario

Fuel	*Heavy Fuel Oil*	*Low Sulfur Heavy Fuel Oil*	*Marine Diesel Oil*	*Ultra-Low Sulfur Fuel Oil*
LCV kJ/kg	39550	39550	42700	39550
S Content % m/m	3.5	0.5	0.1	0.1
CO2 emission factor	3.114	3.114	3.206	3.114

Specific Fuel Oil Consumption estimation

The Specific Fuel Oil Consumption of each engine is calculated as per the engines' project guide. The SFOC is a unique curve for each engine depending on each engine's load, namely the operational power to the MCR power. The manufacturer provides for each engine a SFOC curve for a specific MCR to L1 ratio. According to the above, a table was made, which consists of the values of SFOC for specific MCR to L1 values and specific engine loads. The values of MCR to L1 ratio were selected to range from 100% to 80% or 85%, depending on the information provided by the manufacturer for each engine with step 5%, while the load was selected to range from 100% to 10% with step 5%. These numbers are considered to result in a good SFOC estimation. The table is inserted into the program and with linear interpolation, the operational SFOC of each engine is calculated. This resulting operational SFOC corresponds to standard conditions and fuel which are:

- Ambient air pressure of 1,000 mbar
- Ambient air temperature of 25 °C
- Scavenge air coolant temperature of 25 °C
- Fuel LCV of 42700 kJ/kg

The SFOC must be corrected for the real conditions and the specific fuel based on the selected scenario. The air pressure in the engine room is considered to be at 1 bar, and therefore there is no need for correction. The first correction concerns the temperature of the air and the coolant. The coolant is considered to be the seawater and therefore the temperature of the seawater and the air in the engine room are affected by the position of the vessel. These parameters for the warm, mid and cold area zones, are selected according to table 5:

Table 5: Seawater and E/R Air Temperature at Different Zones

Area	E/R air temperature °C	Seawater temperature °C
Cold	20-30	5-15
Mid	30-40	15-25
Warm	40-50	25-35

The exact value of the temperature is selected randomly from the above intervals. According to the manufacturer, the operational SFOC corrected to correspond to real conditions is calculated as in the following formula:

$$SFOC_{cor1} = \frac{SFOC}{(1-0.6\%)^{\left(\frac{T_{SEA}-25}{10}\right)} \cdot (1-0.2\%)^{\left(\frac{T_{AIR}-25}{10}\right)}} \quad [3]$$

The second correction of the SFOC concerns the fuel. According to the manufacturer, per 1% rise of the specific fuel LCV, the SFOC falls 1% and therefore the corrected SFOC is calculated as follows:

$$SFOC_{cor2} = \frac{SFOC \cdot 42700}{LCV} \quad [4]$$

There is one last additional correction to be made. This one refers to the scrubber installation. Due to the additional back pressure added to the exhaust gas outlet because of the existence of the scrubber unit, the SFOC rises slightly in the case that the vessel has installed a scrubber. According to the engine manufacturer, 1 gr/kWh should be added to the SFOC value in case of a scrubber (MAN B&W 2017).

SOX and CO2 emissions

Since the SFOC is calculated, the fuel oil consumption of the vessels is the result of the multiplication of the SFOC with the operational power of the engine, which is already calculated by the base tool and adjusted to the required real-time speed and draft of the vessel. The CO_2 emissions are the result of the fuel oil consumption multiplied by the CO_2 emission factor. As mentioned above, the CO_2 emission factor is a specific fuel characteristic. As far as the SO_X emissions are concerned, a simplified description of the oxidation of the sulfur contained in the fuel is outlined in the following reactions:

$$S + \tfrac{1}{2}O_2 \rightarrow SO, \quad \Delta H_{298^\circ} = 6\ kJ/mol \quad [5]$$

$$SO + \tfrac{1}{2}O_2 \rightarrow SO_2, \quad \Delta H_{298^\circ} = -297\ kJ/mol \quad [6]$$

$$SO_2 + \frac{1}{2} O_2 \rightarrow SO_3, \quad \Delta H_{298^\circ} = -396\ kJ/mol \quad [7]$$

$$SO_3 + H_2O \rightarrow H_2SO_4, \quad \Delta H_{298^\circ} = -814\ kJ/mol \quad [8]$$

To which degree the sulfur is oxidised into H_2SO_4 depends on thermodynamics and reaction kinetics. Here, the simplifying assumption is made, that the SO is fully converted into SO_2 and there is no conversion of SO_3 to H_2SO_4. Moreover, it is considered that 5% of the SO2 is converted into SO_3. According to the literature (Andreasen 2010), these assumptions are considered to be close to reality. The atomic weight of the sulfur is 32.065 g/mol and the atomic weight of the oxygen is 15.999 g/mol. Thus, the atomic weight of the SO_2 is 64.063 g/mol. This means that mass m of sulfur produces 1.998·m mass of SO_2. From this mass, approximately 5% (0.0999·m) is converted into SO_3, and, therefore, the remaining mass of SO_2 is 1.8981·m. The atomic weight of the SO_3 is 80.062 g/mol and so the 0.1·m mass of SO_2 produces 0.125·m SO_3. The total mass of SO_X produced by m mass of sulfur is, thus, 2.023·m. The mass of sulfur is calculated by the fuel oil consumption multiplied with the sulfur content of the fuel burnt. With the summation of all the vessels' main engine emissions, the process of the main engine emissions calculation for the fleet is completed. The illustration of the pollutants followed with the production of heatmaps.

Experimental results - Case studies

SOX emissions

The case study simulation results regarding SO_X emissions demonstrated significant SO_X emission reduction similar in all three scenaria. The calculated numerical values of SO_X emissions in tn/h for the four selected dates are presented in Table 6 and are compared in Figure 3, while Figures 1 & 2 present the SO_X emission heatmaps on a global scale.

Table 6: SO_X Emission Comparison

SOX emissions (tn/h)	2020-03-12		2020-03-17		2020-03-22		2020-05-24	
Area	**World**	**Med Sea**	**World**	**Med Sea**	**World**	**Med Sea**	**World**	**Med Sea**
No Sulfur Cap	342.83	22.83	344.98	22.70	352.96	20.81	361.76	16.03
Scrubber - All vessels	50.10	3.33	50.43	3.30	51.38	3.01	53.14	2.39
No scrubber - All vessels	49.67	3.32	50.30	3.29	50.84	3.01	52.64	2.35
Scrubber - 10% of the fleet	49.74	3.31	50.17	3.28	50.99	3.00	52.37	2.34

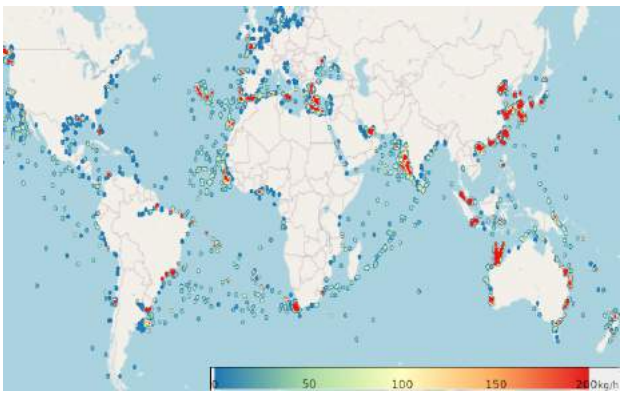

Figure 1: 2020-03-17-SOx Emissions World-CS1

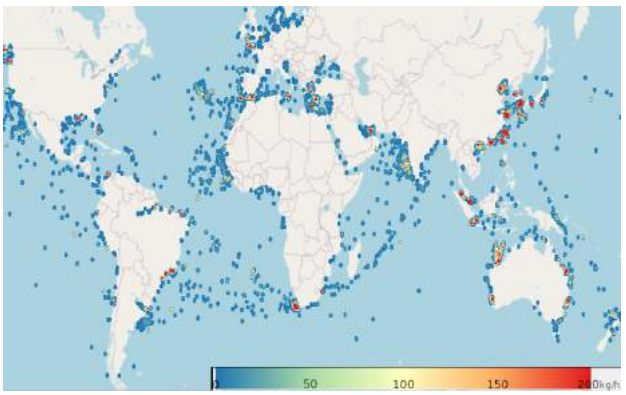

Figure 2: 2020-03-17-SOx Emissions World-CS2

The most noticeable conclusion to which the comparison of the four scenarios leads, is the sharp decrease of the SOX emissions due to the enforcement of the regulations, which is estimated to be about 85%. Another fact that can be observed is that the compliance method of the scrubbers (scenario 2) shows a slight rise in the emissions compared to the method of low-sulfur fuel oil. The scrubber results in larger SFOC because of the additional back-pressure, which is the reason why this slight rise exists and is calculated at about 0.7%. The values of the last scenario should be higher than the low-sulfur fuel oil scenario (scenario 3) and lower than the scrubber scenario (scenario 2) for all the dates, but there are negligible fluctuations that could be explained by the random operating profile chosen for the vessels. The comparison of the different dates demonstrates a slight increase in March which can also be considered as negligible, as the values remain unchanged. This increase could also be explained by the randomly selected profiles of the vessels. The thing that stands out, however, is the rise of the emissions and the difference in the position of the vessels in May. This date is considered to be affected by the world quarantine and lockdown due to the pandemic outbreak in the spring

of 2020, which means that the data extracted from the Internet could be wrong. Therefore, this date should be excluded from the conclusion referring to the emissions change in time.

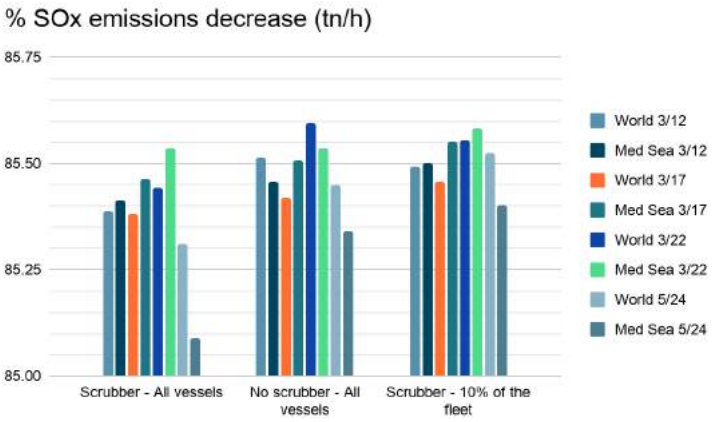

Figure 3: SO_X Emission Decrease Comparison for Four Selected Dates

Another conclusion is that the Mediterranean Sea suffers from a relatively large percentage of SO_X emissions in all four dates, approximately 6% of the world's emissions. It is a frequent passage for the vessels and it is not as open as an ocean. Therefore, the vessels have courses proximate to the shore and to one another. However, in the Mediterranean sea, this percentage of the vessels is not sufficient to follow the global trends. The numbers of the first three dates show an unexpected slight decrease, which is considered to be because of the vessel's percentage. Nonetheless, this is an indication that the emissions remain almost stable in time.

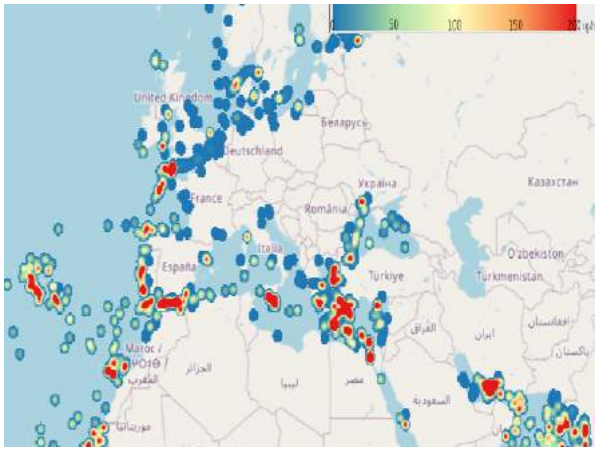

Figure 4: 2020-03-22-SOx Emissions EU-CS1

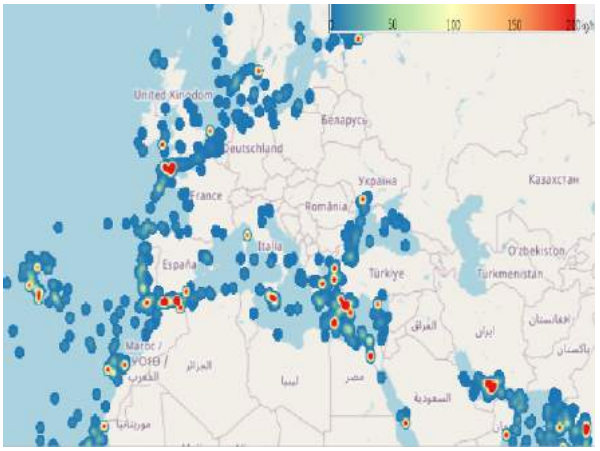

Figure 5: 2020-03-22-SOx Emissions EU-CS2

CO2 emissions

The case study simulation results regarding CO_2 emissions demonstrated a slight CO_2 emission increase similar in all three scenaria. The calculated numerical values of CO_2 emissions in tn/h for the four selected dates are presented in Table 7 and are compared in Figure 8, while Figures 6 & 7 present the CO_2 emission heatmaps on a global scale.

Table 7: CO_2 Emission Comparison

CO2 emissions (tn/h)	2020-03-12		2020-03-17		2020-03-22		2020-05-24	
Area	**World**	**Med Sea**	**World**	**Med Sea**	**World**	**Med Sea**	**World**	**Med Sea**
No Sulfur Cap	16021	1088	16166	1048	16566	969	17201	797
Scrubber - All vessels	16241	1098	16393	1058	16728	972	17481	816
No scrubber - All vessels	16106	1095	16350	1057	16553	974	17315	804
Scrubber - 10% of the fleet	16125	1092	16312	1053	16602	972	17241	800

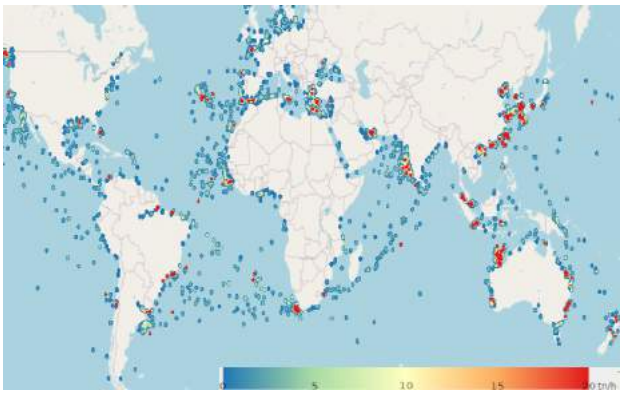

Figure 6: 2020-03-17-CO_2 Emissions World-CS1

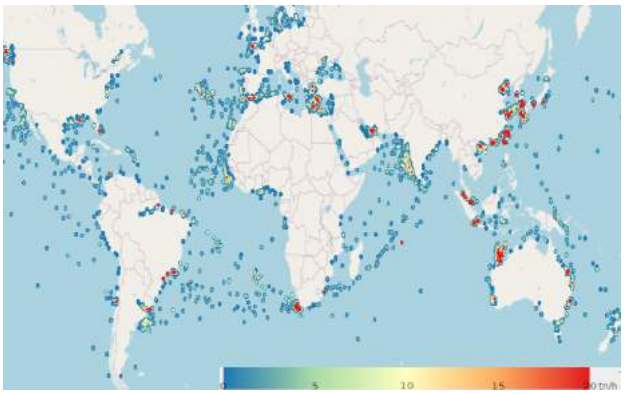

Figure 7: 2020-03-17-CO_2 Emissions World-CS2

As far as the CO2 emissions worldwide are concerned, unlike the SO_X emissions, there is no substantial change in the numbers. However, it is quite clear that the emissions in the second scenario with the scrubbers are higher, which is because of the higher SFOC. The values of the second scenario are almost 1.2% higher than the first one. Moreover, the third scenario with the low sulfur fuel oil has also slightly higher values than the first scenario, about 0.5%. This can be explained due to the higher CO_2 emission factor of the fuel burnt in the third scenario. Similarly, with the SO_X emissions, the slight increase in the numbers of all scenarios in March is considered to be negligible and explained by the randomly calculated values.

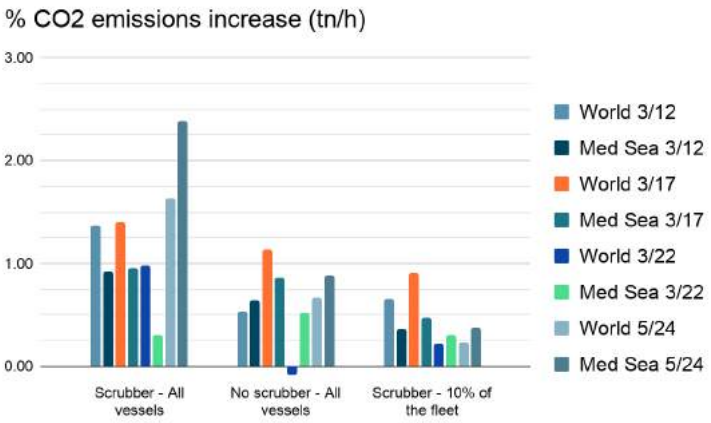

Figure 8: CO_2 Emission Increase Comparison for Four Selected Dates

Correspondingly to the world CO_2 emissions, the numbers in Europe maintain the same level. Besides, the increase in the values of the second and the third scenario in comparison with the first is obvious and it is due to the increase of SFOC and CO_2 emission factor, respectively. In contrast to the world results, the pollution in the Mediterranean Sea, as far as the carbon dioxide is concerned, seems to have a slight decrease in March. This decrease agrees also with the drop of the SO_X emissions in Europe. The origins of this slight drop are believed to be in the local corresponding vessels' percentage. Similar to the SO_X emissions, the CO_2 emissions in the Mediterranean Sea are also a considerable percentage of the world's emissions, in particular 6%.

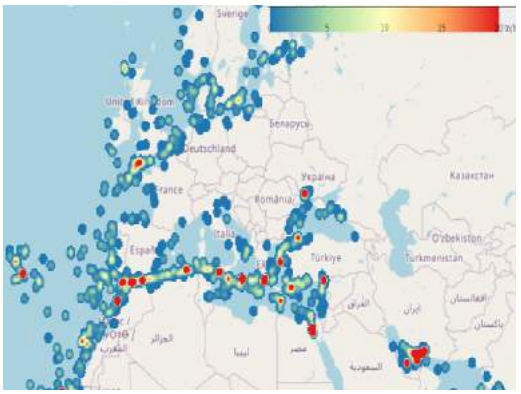

Figure 9: 2020-05-24-CO_2 Emissions EU-CS1

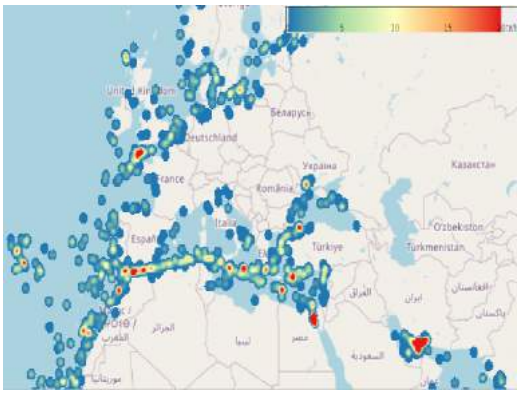

Figure 10: 2020-05-24-CO_2 Emissions EU-CS2

Conclusions

In the present study, a methodology has been developed to evaluate the SO_X and CO_2 emissions of the Bulk Carrier world fleet. First, the regulatory framework has been presented, which limits the sulfur content in fuels to 0.5% worldwide and 0.1% in ECAs, followed by a comparison of the most widely applied compliance methods, namely the use of low sulfur fuel oil and the installation of scrubber technologies onboard the ship. The main scope of this study was the illustration of the emissions of a large fleet on the world map. The fleet consisted of 8,382 bulk carriers and for this depiction, four scenarios were defined, namely, (a) "No Sulfur Cap" Scenario, (b) "Scrubber - All vessels" Scenario, (c) "No scrubber - All vessels" Scenario, and (d) "Scrubber - 10% of the fleet" Scenario.

For a specific point in time, the location, the operational speed, and draft of each vessel were extracted from online databases and using an in house developed application, the SFOC and finally, the SO_X and CO_2 emissions for each scenario were calculated. The heatmaps of the emissions were chosen to depict the dates 12, 17, 22 March, and 24 May 2020. Based on the results of the present study, the following conclusions have been drawn:

- The SO_X emissions demonstrated a sharp decrease due to the enforced regulations, accounting for approximately 85%, while the CO_2 emissions showed a slight increase.
- In the case that all vessels use scrubbers as a compliant method, the SO_X and the CO_2 emissions were moderately higher than the ones in the case with low sulfur fuel oil, because the scrubber system slightly increases the fuel oil consumption.
- The SO_X and CO_2 emissions and their map distribution remained almost stable throughout March.
- The Mediterranean Sea received about 6% of the world's emissions

All things considered, the impact of the sulfur limitation regulations is substantial and thoroughly positive. Since the CO_2 emissions are of this magnitude, the strategy adopted from IMO on reducing CO_2 emissions seems quite apt. Lastly, it is clear that the Mediterranean Sea receives a respectable amount of emissions, and the proposal for an ECA across the Mediterranean is also considered quite beneficial to this area.

Acknowledgements

The research work was supported by the Hellenic Foundation for Research and Innovation (H.F.R.I.) under the "First Call for H.F.R.I. Research Projects to support Faculty members and Researchers and the procurement of high-cost research equipment grant" (Project Number: 61509100).

References

ANDREASEN, A. and S. MAYER, "Modelling of the oxidation of fuel sulfur in low speed two-stroke Diesel engines", PAPER NO. 39, CIMAC Congress (2010)
WORLD BANK GROUP, "Pollution Prevention and Abatement Handbook" (1999)
ABS, "Exhaust Gas Scrubber Systems Advisory", Status and Guidance (2017)
CHARVALOS, G. "Investigation of tribological properties of mechanical systems of merchant vessels", Diploma Thesis, School of Naval Architecture and Marine Engineering, NTUA (2020)
POLITIS, G. "GRID_b.F95" (2011)
IMO, "Emission Control Areas (ECAs) designated under MARPOL Annex VI", https://www.imo.org/en/OurWork/Environment/Pages/Emission-Control-Areas-(ECAs)-designated-under-regulation-13-of-MARPOL-Annex-VI-(NOx-emission-control).aspx (2019)
ARGUS, "Scrubber installations focus on large vessels" (2019)
MAN B&W Two-stroke Marine Engines, "Emission Project Guide for Marpol Annex VI Regulations", 8th Edition (2017)

GRAPHENE OXIDE, A GAME CHANGER IN THE MERCHANT MARINE DESALINATION

Kumar Sambhav[1] and Shubham K Verma[2]

ABSTRACT

This paper aims to unravel the potential of Graphene oxide in the desalination and/or filtration of the abundantly available sea water on board merchant marine vessels. The paper uses a quantitative approach to prove how efficient, the proposed design is. The said innovation will replace the way, the fresh water generators work on board. Currently marine vessels are known to use distillation to fulfill the fresh water requirements in the seas. The existing process present on board the merchant ships is extremely slow and also found to be highly inefficient. By using strategically doped Graphene oxide membranes and the hydrophilic properties of Graphene oxide, the process is made efficient and fast.
Since merchant marine industry is a cost driven industry, aspects covering operational costs and crew training are well taken care of. Setting up of the said technology is also made highly cost efficient by using simple and economical design elements.

INTRODUCTION

Scarcity of potable water is growing at an alarming rate even at present when more than one-fifth of the global population lack access to clean drinking water. In 2015 water scarcity was listed by the World Economic Forum as the largest global risk in terms of potential impact over the next decade. Of all the water that is available to us, 97% is saline therefore low cost and low environmental impact desalination techniques hold the key for resolving this issue. Over the last two decades there has been huge development in seawater desalination and in particular, reverse osmosis technology, however there are several disadvantages of using reverse osmosis for getting drinkable water. First is the set-up cost of the plant which can be an impractical possibility for a lot of developing nations. Second is the membrane that needs to be treated with care and last but not the least the yield amount is very low in smaller systems and the amount of waste water is very high. A typical system will only be able to reuse about five to fifteen percent of the water that is going to be pumped in. Thus leaving up to 85% waste water. In light of this looming crisis the promise of Graphene based desalination is very reassuring. A sieve made out of Graphene has already been successfully tested for filtering out salts while allowing water. Graphene's flat honeycomb pattern gives it many amazing characteristics. It is one of the strongest, lightest, most conductive and transparent materials. The single layers of carbon atoms provide the basis for many other materials. Graphene oxide (GO) is an oxidized Graphene derivative, which is less expensive and easier to produce as compared to Graphene.
Graphene cannot be used as a separation membrane being hydrophobic and impermeable to water. The more hydrophilic GO serves as a basis for nano membranes impermeable to impurities, salts, or bacteria but permeable to water.
It is interesting to note that the maximum distance between carbon atoms at the two opposite ends of a single hexagon in graphene mesh is about 0.28 for nanometers whereas the size of a water molecule is about 0.275 nanometers so the gap is just right enough to send the water molecules through. For reference the size of sodium chloride molecule is about 0.564 nanometers that means it is twice as big as the gap and hence it is filtered out.

[1] Indian Maritime University, Kolkata Campus
[2] Indian Maritime University, Kolkata Campus

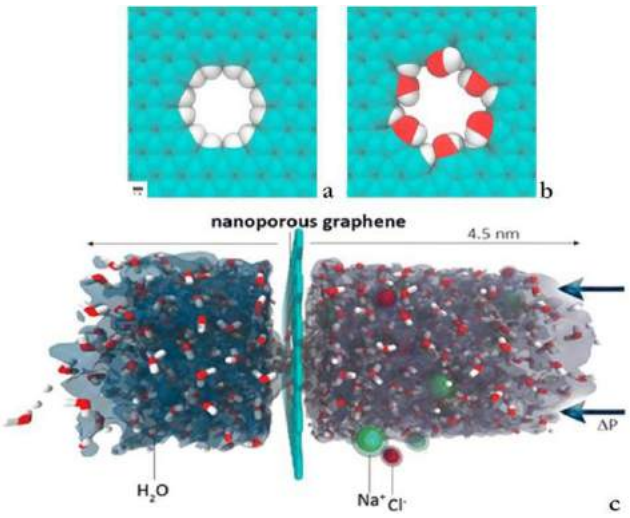

Figure 1:
Model of (a) hydrogenated graphene pores, (b) hydroxylated graphene pores, and (c) complete computational system of reference

Despite the seemingly straightforward application of using graphene as a filter scientists initially struggled to use it as such the reason for that is graphene weakened and expanded when immersed in water this allowed more than just water molecules to pass through the graphene mesh but now manchester-based graphene research group developed these graphene membranes with chemical coating to avoid the swelling of the membrane.
When exposed to water the pore size in the membrane can be precisely controlled which can save common salts out of salty water and make it safe to drink. Molecular dynamics simulations have predicted that nanoporous Graphene, due to its extraordinary water flow rate (up to 66 L.cm −2 .day −1 .MPa −1) and high (>99%) salt rejection, may be one of the most desirable materials for water desalination.

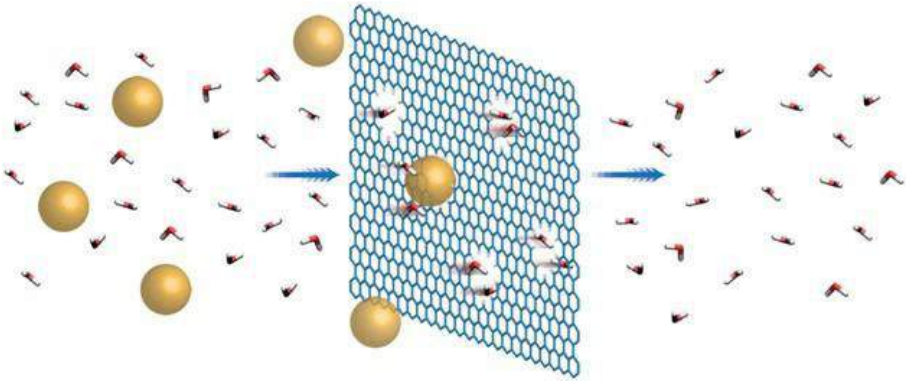

Figure 2:
A graphene membrane with subnanometer pores as an RO membrane. In this process, the salt water (left), subjected to a high pressure, is divided into two parts: water molecules (red and white) passing through the membrane (right) and salt ions (golden spheres) that are blocked.

DEMERITS OF THE EXISTING SYSTEM

The existing technology which is present on board Merchant marine vessels is based on the principle of vacuum distillation and has several shortcomings in the course of time such as loss of vacuum ,cracking of the body, mechanical seal issues resulting in loss of proper pressure build up hence resulting in low production of fresh water. The major challenge in designing this filtration system was to unlearn the existing practices and re engineer it from scratch, keeping in mind the properties of Graphene Oxide membrane.

DESIGN ELEMENTS OF THE PROPOSED SYSTEM

The casing of the filtration system is made up of High Density Polyethylene (HDPE) because of its alkaline and acidic resistance which will be a bane while operating in seawater.

The proposed design encompasses 3 stage filtration utilizing 2 Activated Carbon Chambers and finally one Graphene Oxide membrane at the center. Electrical pumps are used to pull the water to the center through the housing case.

Activated Carbon is a highly porous material providing a large surface area which traps contaminants when they pass next to its surface. The water passes through the activated carbon which acts as a primary filter and with minimal operation costs it can be maintained easily, which in turn reduces the efforts of Graphene Oxide. In this stage, Chlorine, sediments, organic compounds, taste and odor are eliminated. The Graphene Oxide membrane can thus efficiently filter out Sodium Chloride.

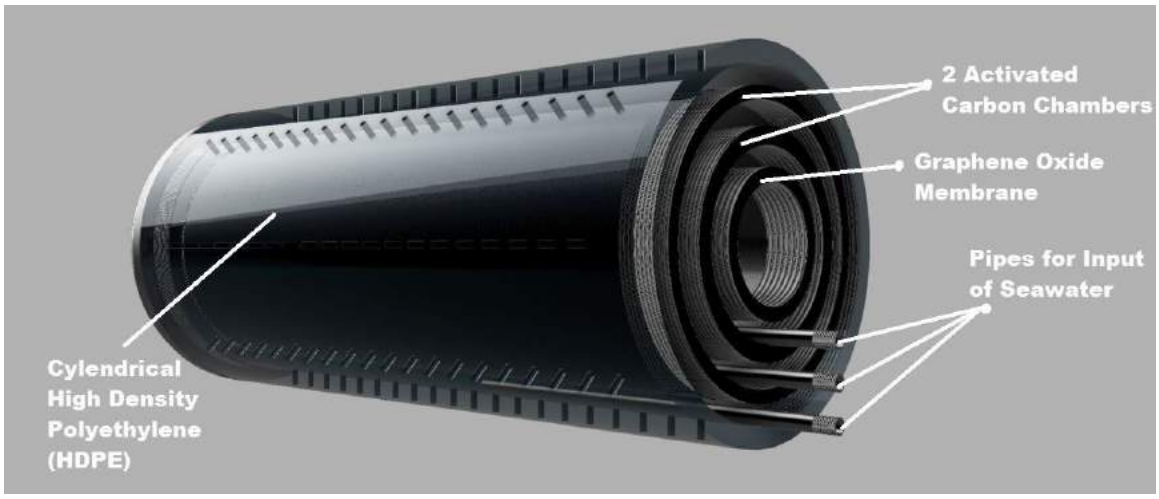

Figure 3

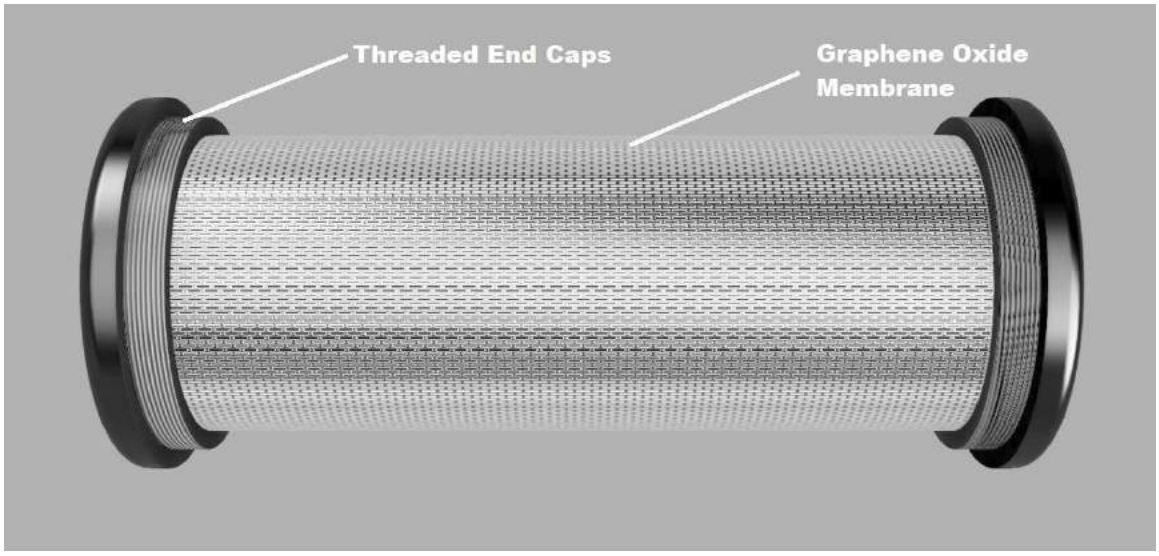

Figure 4

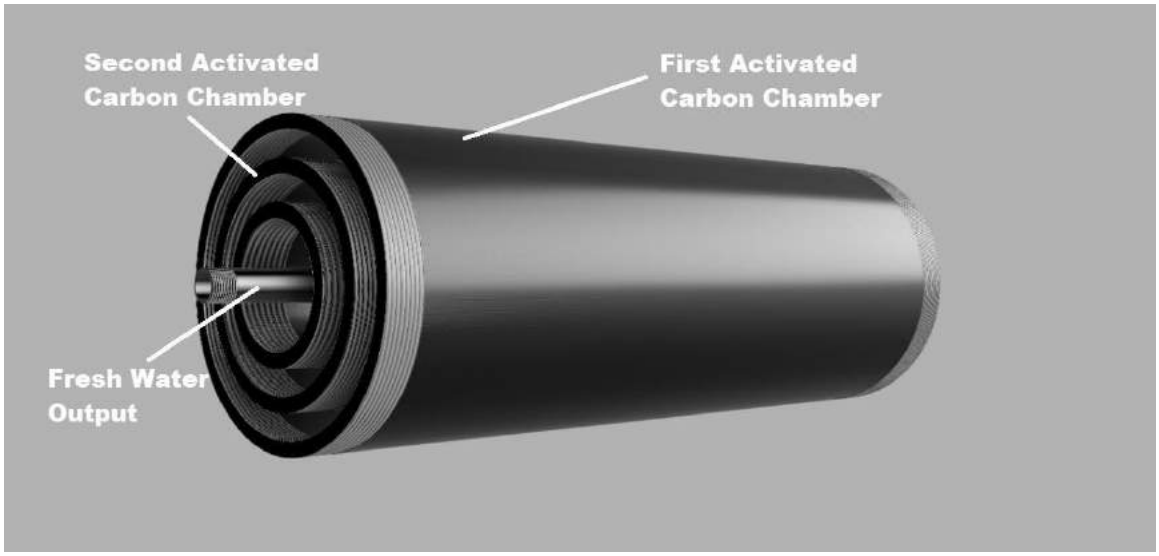

Figure 5

CHALLENGES FACED

Graphene is known to swell in water which will in turn affect the hydrodynamics of the design. To overcome this, the Graphene oxide layer can be sandwiched between 2 layers of Epoxy Resin on either side to restrict this expansion.

SALIENT FEATURES

Cylindrical HDPE threaded meshes allow each compartment to be accessed for maintenance,
Threaded end caps screw onto the meshes thereby sealing the unit and eliminating any possibility of leaks between the chambers.
The adapted methodology ensures maintenance of sea density, vital for sea life.
Has a cost effective and a versatile design for universal implementation.

ADVANTAGES

1. Graphene-based membranes possess several fascinating advantages over conventional membranes. First, their raw material is graphite, that is an inexpensive material that affords low membrane fabrication costs.
2. GO nanosheets can be produced on a large scale at a very low cost via chemical oxidation and the ultrasonic exfoliation of graphite. This method promises the cost-efficient and industrially applicable fabrication of stacked membranes. Finally, 2D graphene offers not only extraordinary chemical and thermal stabilities but also superior flexibility and solution processibility.
3. The nano-level defects and channels in GO films play a key role in molecules rejection. Theoretically, the interlayer spacing of GO sheets is ∼0.8 nm in a dry environment. Even though, it will be enlarged to ∼1.3 nm in an aqueous environment, it still can resist most of particles with different diameters and allow pure water molecules to pass through.52 Therefore, GO membranes are able to deal with all sorts of water contaminants.
4. The 2D channels enable the permeation of water while rejecting undesired solutes. In addition, the presence of oxygen-containing functional groups, such as Carboxyl groups, on the GO nanosheets enables functioning and thus enables related charge-based interactions with water pollutants.Such promising features make multilayer GO structure an ideal candidate for the production of advanced ionic and molecular sieving membranes for desalination.

CONCLUSION

Because of with its excellent hydrophilicity, pores structure and nanosized flakes Graphene Oxide sheets are an ideal candidate for membrane based water purification and separation processes. For the merchant shipping industry it's role becomes even more vital because of the economic factor. The simple design makes it easy for maintenance and also the crew doesn't need any extra skill set to carry out its operation which reduces training costs. The proposed design can also be

implemented on the already available purification systems on board by replacing and altering some parts, a little more designing on this aspect and the proposed design has the potential to get worldwide acceptance.

REFERENCES

1. Boretti, A., Al-Zubaidy, S., Vaclavikova, M. et al. Outlook for graphene-based desalination membranes. npj Clean Water 1, 5 (2018). https://doi.org/10.1038/s41545-018-0004-z

2. Homaeigohar, S., Elbahri, M. Graphene membranes for water desalination. NPG Asia Mater 9, e427 (2017). https://doi.org/10.1038/am.2017.135

3. J. Lyu , X. Wen , U. Kumar , Y. You , V. Chen and R. K. Joshi , RSC Adv., 2018, 8 , 23130 —23151

4. Fig 1 - Boretti, A., Al-Zubaidy, S., Vaclavikova, M. et al. Outlook for graphene-based desalination membranes. npj Clean Water 1, 5 (2018). https://doi.org/10.1038/s41545-018-0004-z

5. Fig 2 - Homaeigohar, S., Elbahri, M. Graphene membranes for water desalination. NPG Asia Mater 9, e427 (2017). https://doi.org/10.1038/am.2017.135

MARITIME TRANSPORT OF CO_2 IN LIQUID OR SOLID FORM – A QUALITATIVE COMPARISON

Henrik O. Madsen, PhD[1]

ABSTRACT

Capture and permanent storage of CO_2 is an important element in scenarios for minimizing global warming to 1.5 degrees Celsius by 2100. Many storage solutions will include maritime transport of CO_2, and CO_2 can therefore become a significant future cargo. When transporting gasses on board ships the intuitive thought is that this must be in compressed or liquid form. LNG, LPG and other gasses are transported by ship in dedicated cargo tanks under optimized temperature and pressure conditions. For maritime transport of CO_2 the option to transport the cargo in solid form – better known as dry ice – at ambient pressure and minus 80 degrees Celsius, however, also exists. The paper makes a mainly qualitative comparison of transport in liquid versus solid form for a transport chain from a land-based CO_2 capture plant to a permanent storage site. The paper concludes that both ways of transporting CO_2 have merit and can be the preferred solution depending on the specific situation.

KEY WORDS

CCS; CO_2; Dry Ice; Phase Diagram; Gas Tanker; Containerization; Sublimation.

INTRODUCTION

To reach the 1.5 degrees target of the Paris Convention there is general consensus that Carbon Capture and Storage (CCS) must play a role. The IPCC (IPPC 2006) has for decades advocated this point, and in its recent scenario towards 2050 also the IEA includes 5.7 billion tons yearly CO_2 emissions reduction through CCS (IEA 2021). Utilization of CO_2 plays a smaller role in this IEA scenario, but it is still important for a number of industries like those producing synthetic fuels for shipping through Power-to-X technologies.

Storage of CO_2 captured from power production using biogenic sources can lead to net carbon removal, which is important both in the short and long term. Direct air capture with CO_2 storage undergoes a lot of research and small-scale demonstrators. The cost of direct air capture is, however, still prohibitive for large scale installations. It competes in a sense with afforestation, which is a much lower cost alternative. The concentration of CO_2 in the atmosphere is about one permille of the CO_2 concentration in the exhaust pipe from a power plant, and CCS from industrial facilities and power plants will take first priority.

To develop a CCS value chain all of CO_2 capture, CO_2 transport, and permanent CO_2 storage must have sustainable solutions. This paper deals with the CO_2 transport and compares transport options in solid and liquid modes, but it first offers some observations on capture and permanent storage.

Many different technologies have been proposed for the CO_2 capture part. Chemical absorption technologies based on amines have been successfully operated for decades and are mature and proven technologies. The CO_2 capture plant on the offshore gas platform Sleipner West has as an example captured 1 million tons of CO_2 every year for 25 years. Other technologies

[1] HOM Consult, Vedbæk, Denmark

based on adsorption, membrane separation, cryogenic separation, and electro-chemical separation are being developed, qualified and demonstrated, some also in large scale.

Existing CCS projects have storage solutions, which can be roughly divided into three categories - onshore or offshore:

- geological structures with an impermeable overlying cap, which prevents stored CO_2 from escaping into the atmosphere; the Northern Lights (Northern Lights 2021) concept is an example
- depleted oil and gas fields and associated aquifers; project Greensand (Greensand 2021) is an example
- reactive rock formations offering fast mineralization; Carbfix is an example (Carbfix 2022). CO_2 is mixed with water at a ratio of about 1:25 and is pumped down into a network of shallow wells. Here the CO_2 reacts with basalt rock and a complete mineralization takes place in about 2 years.

We should, however, expect that other and radically different storage solutions will be proposed in the coming years. One such novel and radically different concept for permanent CO_2 storage in deep seabed sediments through CO_2 hydrate formation is presented in another conference paper, (Madsen and Moltke 2022).

The transport and storage elements in the value chain are very important for the overall cost. Thousands of kilometers of pipelines are available in the US for CO_2 transport to an onshore storage site. This is the main reason why CCS is growing faster in the US than in Europe, where onshore storage is in effect prohibited for the time being. Iceland is a country which has ideal conditions for storage through mineralization in its young basalt base rock. Japan also has many areas with tuff formed from volcanic ash and rock containing calcium and magnesium ideal for fast mineralization like in Iceland.

ROLE OF SHIP TRANSPORT IN CO_2 TRANSPORT CHAIN

A ship transport leg is present in several of the transport chains under consideration and development. In the Northern Lights concept gas carrier ship newbuildings have already been contracted for transport of captured CO_2 from the cement factory in Brevik in Southern Norway to a CO_2 gathering site near Bergen in Western Norway, from where it will be sent by pipeline to an offshore storage site and injected for permanent storage. Greensands is based on ship transport to the depleted Nini offshore field, where the CO_2 is pumped from the ship into the reservoir. Ships with Dynamic Positioning capabilities are being offered for the first test phase of this project. For storage in Iceland dedicated newbuild gas carrier specifications have been prepared and shipyard prices gathered.

All of the above transport chains for CO_2 from the capture site are based on transporting CO_2 in liquid form. The CO_2 phase diagram in figure 1 shows the pressure and temperature conditions for the three different phases, gas, liquid and solid, and a fourth supercritical fluid phase also exists as shown in the upper right corner.

Three different pressure/temperature combinations for the ship transport leg in a CO_2 tanker are shown with each of them having advantages. The 7 bar/minus 50 degrees Celsius case is studied by several ship owners like Evergas (Evergas 2022). It saves steel in the cargo tanks and intermediate storage tanks on land, and it increases the density of the liquid CO_2. The 20 bar/minus 20 degrees Celsius case is the basis for the Northern Lights concept, and the 40 bar/10 degrees Celsius case has recently been proposed by Knutsen NYK Carbon Carriers (Knutsen NYK 2022) in combination with on board storage in stacks of standard offshore pipelines in each cargo hold. The latter solution may yield itself better to a ship conversion than the first two pressure/temperature combinations, where a newbuilding is probably inevitable.

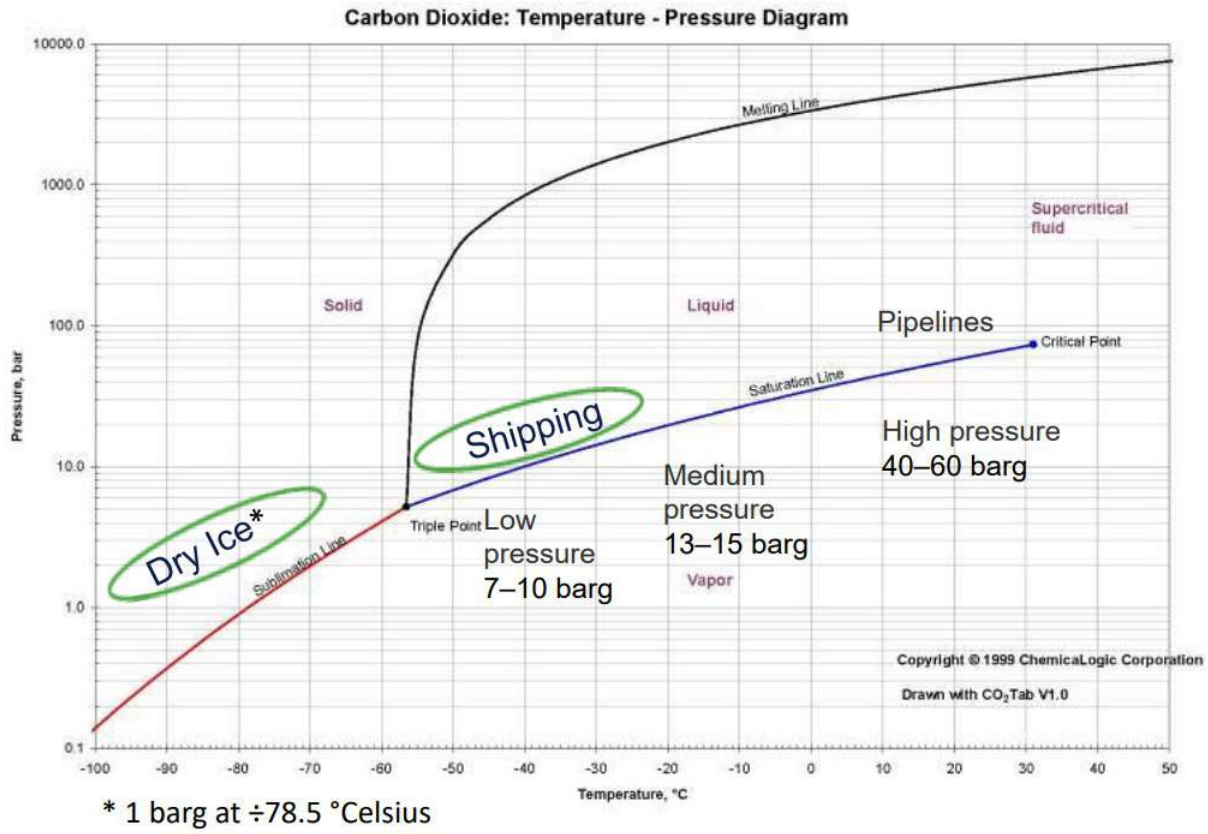

Figure 1. CO_2 phase diagram with shipping alternatives

We now describe the commonly proposed transport value chain involving a ship transport leg. The CO_2 is available from the capture plant in liquid form (LCO_2) in an intermediate storage tank. From here the LCO_2 is transported to a port facility and stored in a second intermediate storage tank. When the capture site is not located by the ocean and with its own loading pier, a transport by pipeline can be possible for short distances, but otherwise transport in ISO tank containers by truck and barge is used. The gas carrier then picks up the LCO_2, which is pumped from the intermediate storage tank to the ship cargo tanks. The gas carrier may perform a "milk route" operation collecting LCO_2 from different locations before it travels to the storage site or the gathering point for pipeline transport to the storage site. Depending on the storage method the need for a third intermediate storage tank may arise. Before the pipeline transport to the storage formation, the liquid CO_2 is heated to ambient temperature and pressurized to about 100 barg where it takes supercritical liquid form and is pumped into the pipeline.

INNOVATIVE CONCEPT OF CO_2 TRANSPORT IN DRY ICE FORM

The innovative concept of this paper is to transport the CO_2 in solid form as dry ice. At ambient pressure of 1 barg CO_2 exists as dry ice at temperatures below the normal sublimation temperature of minus 78.5 degrees Celsius.

In order to utilize only proven technology, we assume that the CO_2 from the capture plant has been liquefied through compression and cooling. In a pure electrical solution, the energy consumption for liquefaction ranges between 120 and 180 kWh/ton CO_2 depending on the efficiency of the compressor and the availability of cooling water.

It is standard technology to form dry ice from LCO_2. The LCO_2 is depressurized, and an adiabatic process takes place where a little less than 50% of the LCO_2 becomes dry ice and the remaining becomes CO_2 gas. The cold gas part is then recirculated to the liquefaction unit and mixed with the CO_2 gas from the capture plant. The additional cost related to production of dry

ice is therefore a CAPEX cost for the dry ice machines, and an additional OPEX energy cost similar to the OPEX cost of liquefaction.

An off the shelf dry ice machine producing 750 kg dry ice pellets per hour costs in the order of EUR 150.000. Machines producing higher density dry ice blocks are a little more expensive. This cost is very close to the cost of an ISO tank container truck. The operating cost of a dry ice machine is negligible. A capture plant with a capacity of 100.000 tons per year or 300 tons per day will thus require some 15 standard dry ice machines in an efficient lay-out to minimize the required land space. Larger and higher capacity dry ice machines can, however, be tailormade to reduce the required land space.

The dry ice transportation to the port can be done in insulated 20 feet standard containers by truck or barge. A new container costs about USD 5.000. A 25 cm thick internal PIR (Polyisocyanurate, density 30-40 kg/m^3) insulation known from the construction industry is inexpensive and will reduce sublimation to 0.2% per day, which is acceptable. Other insulation materials may reduce the sublimation even further.

The insulated containers are filled with the dry ice. Depending on the compaction of the dry ice the density is around 1.2-1.4 t/m^3. The available space in the container means that there is volume left for about 25 tons of dry ice, and 25-30 tons is also the normal load capacity of the container. At the loading port the containers are stored on the quay without the need for separate storage facilities.

The ship transport of the dry ice filled containers can be by standard MPV's, bulk carriers, open hatch bulk carriers or container vessels. It is advantageous if the ship has its own cargo gear to be able to load containers also at smaller facilities e.g. belonging to a "milk route".

The ship finally delivers the containers at the area for permanent storage. At the Carbfix terminal in Iceland the solid CO_2 can be mixed with water and stored without any complicating factors. If CO_2 is to be sent to an offshore storage site by pipeline, it is necessary to re-gasify and compress the dry ice back into liquid form. An intermediate storage tank, maybe in the form of rags of connected standard offshore pipelines, can be one solution. The dry ice is loaded into the pipeline, and it will over a short period sublimate and pressure will build up and liquids form, which allows for an easy transfer to the pumping station.

COST COMPARISON OF THE TWO TRANSPORT CHAINS

It is difficult to generalize under which conditions the dry ice alternative can have the lowest transport chain cost. The cost reductions compared to the LCO_2 transport chain include:

- No need for intermediate LCO_2 storage tanks at the capture site and ship loading or discharge port.
- Use of less expensive standard 20 feet containers rather than ISO tank containers. The standard 20 feet pressure containers will also be available in much larger numbers than the ISO tank containers.
- Use of a ship with lower day rate. A ship able to carry 1.000 containers – 25.000 tons of dry ice – can be chartered at USD 8-10.000 per day, while a specialized CO_2 gas carrier with the same cargo capacity will probably have a charter rate of USD 35-50.000 per day. Existing ships can be used.
- There is no risk of operational problems from CO_2 hydrate formation during pumping of LCO_2.
- The requirements for the purity of the CO_2 are lower.

Additional cost and other considerations for the dry ice alternative include:

- There is an additional cost for liquefaction depending on the price of electricity
- There is an additional land space requirement at the capture plant
- There is an additional capital cost for the dry ice machines
- There is a time penalty with handling dry ice in 20 feet containers rather than pumping liquid CO_2 in bulk.
- In case of transport by pipeline to an offshore storage site, it is necessary to have an intermediate tank at the discharge site.

CONCLUSION

In conclusion, no barriers have been identified, which will prevent the dry ice transport chain to be developed. The dry ice transport chain only utilizes well known and off the shelf technologies. A further quantitative comparison is necessary to identify conditions, where the dry ice transport chain can compete with a liquid transport chain. In many cases specific site or geography parameters will influence the comparison. A first intuitive conclusion is that the LCO_2 option has lower cost and other benefits for large capture plants and pipeline transport from large hubs to offshore storage sites, and these cases will probably be developed first. In the longer term, we will see many CCS projects in the order of 100-200.000 tons of CO_2 captured per year at inland facilities. For such projects the dry ice transport chain may become attractive.

REFERENCES

IPCC, “Special Report on Carbon Dioxide Capture and Storage”, Chapter 6 Ocean Storage, 2006.
IEA, https://www.iea.org/reports/about-ccus , 2021
Northern Lights, https://norlights.com/news/how-does-co2-storage-work/ , 2021
Project Greensand, https://www.projectgreensand.com/ , 2021
Carbfix, “We turn CO_2 into stone,” www.carbfix.com , 2022
MADSEN, H.O. and MOLTKE, I.: ”CO_2 sequestration in deep sea sediment formations - decarbonICE project”, in proceedings WMTC2022, 2022.
ARORA, A. “CO_2 Carriers Design,”, in proceedings WMTC2022, 2022
Knutsen NYK Carbon Carriers, https://www.kn-cc.com/ , 2022.

Demonstration of Precise Point Positioning (PPP) Accuracy at North Sea

Patrick Henkel[1], Philipp Bohlig[1], Ulrich Mittmann[1], Michael Heinrich[1], Andreas Sperl[1], Robert Rydlinger[2] and Joakim Lundman [2]

ABSTRACT

The accurate knowledge of a vessel's position, velocity, attitude and turn rate is essential for an accurate prediction of the position and a safe navigation. The need for an accurate and reliable position becomes especially important in frequently used waterways or in general at bad weather conditions.
The objective of this paper is to demonstrate the performance of the newest Multi-frequency, Multi-GNSS Precise Point Positioning (PPP) system at a pilot boat at the North Sea. We are using a Kalman filter that jointly estimates the vessel's position, velocity, tropospheric zenith delay, ionospheric slant delays and carrier phase ambiguities. We have tested our ANavS Multi-Sensor RTK/ PPP module on a pilot boat near Gothenburg in the North Sea and used the RTK solution as ground truth. The measurement results show that a positioning accuracy of a few decimeters is achievable without the need of corrections from a reference station.

KEY WORDS

Navigation; Positioning; PPP; RTK; Sensor Fusion.

INTRODUCTION

Standard Global Navigation Satellite System (GNSS) receivers provide position information with an accuracy in the order of 1 m under good satellite visibility conditions. This is not enough for many maritime applications: For example, the navigation in frequently used waterways and/ or in bad weather conditions requires a higher accuracy.
In this case, Real-Time Kinematic (RTK) positioning is an attractive choice. It uses the carrier phase measurements besides the conventional pseudorange measurements, resolves the integer ambiguities of the (periodic) carrier phases, and uses corrections from a reference station to suppress atmospheric delays and residual satellite position and clock offset errors to improve the accuracy.
However, RTK positioning has also some limitations: First, there is a need for a reference station within at most 50 km from the RTK receiver to suppress the atmospheric delays sufficiently. Second, there is a need for a communication link, e.g. a mobile communication or any other radio communication link for the transmission of corrections. Both points are often not fulfilled in remote locations and at open sea. Another disadvantage of RTK is that the corrections are quite costly for everyday users on a global basis.
Precise Point Positioning (PPP) (Zumberge et al. 1997) is an attractive alternative to RTK that overcomes the disadvantages of RTK: PPP is an absolute positioning technique where the user does no longer need any measurements from a reference station. High-accuracy satellite position, clock offset, phase and code bias corrections are used instead of range corrections to improve the accuracy of the measurements. These corrections will be broadcasted directly by the Galileo satellites as High Accuracy Service (HAS) in the near future. This service will be for free. The only disadvantage of PPP is its relatively convergence time and its slightly lower accuracy. Both points arise from the large number of unknowns, i.e. the PPP user needs to estimate the

[1] ANavS GmbH, Gotthardstraße 40, 80686 Munich, Germany
[2] RISE – Research Institutes of Sweden, Gibraltargatan 35, 41279 Gothenburg, Sweden

tropospheric and ionospheric delays as additional state parameters and also has to apply models for various additional errors including phase wind-up, phase centre offsets and site displacement effects.

METHODOLOGY

In this section, we start with a detailed mathematical description of the raw carrier phase and pseudorange measurements of a GNSS receiver. Subsequently, we describe the main processing steps for determining the PPP solution: This includes the application of the satellite position, clock offset and bias corrections, the computation of satellite-satellite single differences to eliminate receiver clock and bias errors, and the use of a Kalman filter for parameter estimation.

Measurement models

The carrier phase measurement of satellite k at user u on frequency m and signal type s is modeled according to (Teunissen and Montenbruck 2017) as:

$$\begin{aligned}\lambda_m \varphi^k_{u,m,s}(t_n) = {} & \|\vec{x}_u(t_n) - \vec{x}^k(t_n - \Delta t^k_n)\| + c\left(\delta t_u(t_n) - \delta t^k_{\mathrm{IF}}(t_n - \Delta t_n)\right) \\ & + m_{\mathrm{T}}\left(\theta^k_u(t_n)\right) \cdot T_{z,u}(t_n) - \frac{f_1^2}{f_m^2} I^k_{u,1}(t_n) + \lambda_m N^k_{u,m,s} + \beta_{u,m,s} - \beta^k_{m,s} \\ & + \lambda_m \Delta\varphi^k_{\mathrm{PW,u,m}}(t_n) + (\vec{e}^k_u)^{\mathrm{T}}\left(\Delta\vec{x}_{\mathrm{PCO},u,m} + \Delta\vec{x}_{\mathrm{PCV},u,m} - \Delta\vec{x}^k_{\mathrm{PCO},m} - \Delta\vec{x}^k_{\mathrm{PCV},m}\right) \\ & + \lambda_m \Delta\varphi^k_{\mathrm{MP},u,m,s}(t_n) + \varepsilon^k_{u,m,s}(t_n)\end{aligned} \quad [1]$$

with the receiver position $\vec{x}_u$, the satellite position $\vec{x}^k$, the signal propagation time Δt^k_n from the satellite to the receiver, the speed of light c, the receiver clock offset δt_u, the satellite clock offset δt^k_{IF} (referring to the ionosphere-free combination), the tropospheric mapping function m_{T} being dependent on the satellite elevation θ^k_u, the tropospheric zenith delay $T_{z,u}$, the squared carrier frequency f_m^2, the slant ionospheric delay $I^k_{u,1}$ on the first frequency, the wavelength λ_m, the integer ambiguity $N^k_{u,m,s}$, the receiver phase bias $\beta_{u,m,s}$, the satellite phase bias $\beta^k_{m,s}$, the phase wind-up correction $\Delta\varphi^k_{\mathrm{PW,u,m}}$, the normalized satellite-receiver direction vector $\vec{e}^k_u$, the receiver Phase Centre Offset (PCO) $\Delta\vec{x}_{\mathrm{PCO},u,m}$, the receiver Phase Centre Variation (PCV) $\Delta\vec{x}_{\mathrm{PCV},u,m}$, the satellite PCO $\Delta\vec{x}^k_{\mathrm{PCO},m}$, the satellite PCV $\Delta\vec{x}^k_{\mathrm{PCV},m}$, the phase multipath error $\Delta\varphi^k_{\mathrm{MP},u,m,s}$, and the phase measurement noise $\varepsilon^k_{u,m,s}$.
The pseudorange measurement is modeled accordingly (Teunissen and Montenbruck 2017):

$$\begin{aligned}\rho^k_{u,m,s}(t_n) = {} & \|\vec{x}_u(t_n) - \vec{x}^k(t_n - \Delta t_n)\| + c\left(\delta t_u(t_n) - \delta t^k_{\mathrm{IF}}(t_n - \Delta t_n)\right) \\ & + m_T\left(\theta^k_u(t_n)\right) \cdot T_{z,u}(t_n) + \frac{f_1^2}{f_m^2} I^k_{u,1}(t_n) + b_{u,m,s} - b^k_{m,s} \\ & + (\vec{e}^k_u)^{\mathrm{T}}\left(\Delta\vec{x}_{\mathrm{PCO},u,m} + \Delta\vec{x}_{\mathrm{PCV},u,m} - \Delta\vec{x}^k_{\mathrm{PCO},m} - \Delta\vec{x}^k_{\mathrm{PCV},m}\right) \\ & + \Delta\rho^k_{\mathrm{MP},u,m,s}(t_n) + \eta^k_{u,m,s}(t_n)\end{aligned} \quad [2]$$

with the receiver code bias $b_{u,m,s}$, the satellite code bias $b^k_{m,s}$, the pseudorange multipath error $\Delta\rho^k_{\mathrm{MP},u,m,s}$ and the measurement noise $\eta^k_{u,m,s}$.

Precise Point Positioning (PPP)

The user corrects the raw carrier phase measurement for the broadcast position and clock corrections, for the high-precision satellite position, clock offset and phase bias corrections (being highlighted in color in [3]), for the relativistic corrections $\delta\hat{t}^k_{\mathrm{rel}}$, for the phase wind-up, PCOs and PCVs:

$$\begin{aligned}\lambda_m \tilde{\varphi}^k_{u,m,s}(t_n) = {} & \lambda_m \varphi^k_{u,m,s}(t_n) + \left(\vec{e}^k_u(t_n)\right)^{\mathrm{T}}\left(\hat{\vec{x}}^{k,\mathrm{BC}}_{\mathrm{ECEF}} + R^{\mathrm{ECEF}}_{\mathrm{SCS}}\Delta\hat{\vec{x}}^k_{\mathrm{SCS}}\right) \\ & + c\delta\hat{t}^{k,\mathrm{BC}}_{\mathrm{IF}} + c\Delta\delta\hat{t}^k_{\mathrm{IF}} + c\delta\hat{t}^k_{\mathrm{rel}} + \hat{\beta}^k_{m,s} - \lambda_m \Delta\varphi^k_{\mathrm{PW,u,m}}(t_n) \\ & - (\vec{e}^k_u)^{\mathrm{T}}\left(\Delta\vec{x}_{\mathrm{PCO},u,m} + \Delta\vec{x}_{\mathrm{PCV},u,m} - \Delta\vec{x}^k_{\mathrm{PCO},m} - \Delta\vec{x}^k_{\mathrm{PCV},m}\right) \\ = {} & \left(\vec{e}^k_u(t_n)\right)^{\mathrm{T}}\vec{x}_u(t_n) + c\delta t_u(t_n) + m_{\mathrm{T}}\left(\theta^k_u(t_n)\right) \cdot T_{z,u}(t_n) - \frac{f_1^2}{f_m^2} I^k_{u,1}(t_n) \\ & + \lambda_m N^k_{u,m,s} + \beta_{u,m,s} + \lambda_m \Delta\varphi^k_{\mathrm{MP},u,m,s}(t_n) + \varepsilon^k_{u,m,s}(t_n),\end{aligned} \quad [3]$$

whereas the second identity is obtained by replacing $\lambda_m \varphi^k_{u,m,s}$ by its detailed model of [1].
The pseudorange measurements are corrected accordingly as:

$$
\begin{aligned}
\tilde{\rho}^{k}_{u,m,s}(t_n) \;&= \rho^{k}_{u,m,s}(t_n) + \left(\vec{e}^{\,k}_{u}(t_n)\right)^{\mathrm{T}}\left(\hat{\vec{x}}^{k,\mathrm{BC}}_{\mathrm{ECEF}} + R^{\mathrm{ECEF}}_{\mathrm{SCS}}\Delta\hat{\vec{x}}^{k}_{\mathrm{SCS}}\right) \\
&\quad + c\delta\hat{t}^{k,\mathrm{BC}}_{\mathrm{IF}} + c\Delta\delta\hat{t}^{k}_{\mathrm{IF}} + c\delta\hat{t}^{k}_{\mathrm{rel}} + b^{k}_{m,s} \\
&\quad - (\vec{e}^{\,k}_{u})^{\mathrm{T}}\left(\Delta\vec{x}_{\mathrm{PCO},u,m} + \Delta\vec{x}_{\mathrm{PCV},u,m} - \Delta\vec{x}^{k}_{\mathrm{PCO},m} - \Delta\vec{x}^{k}_{\mathrm{PCV},m}\right) \\
&= \left(\vec{e}^{\,k}_{u}(t_n)\right)^{\mathrm{T}}\vec{x}_u(t_n) + c\delta t_u(t_n) + m_{\mathrm{T}}\left(\theta^{k}_{u}(t_n)\right)\cdot T_{z,u}(t_n) + \frac{f_1^2}{f_m^2} I^{k}_{u,1}(t_n) \\
&\quad + b_{u,m,s} + \Delta\rho^{k}_{\mathrm{MP},u,m,s}(t_n) + \eta^{k}_{u,m,s}(t_n)
\end{aligned}
\qquad [4]
$$

Subsequently, we perform satellite-satellite single differences of the corrected carrier phase and pseudorange measurements to eliminate the receiver clock offset, phase and code biases.
The remaining estimable unknowns are stacked in the state vector:

$$
x_n = \left(\vec{x}^{\mathrm{T}}_{u}(t_n), \vec{v}^{\mathrm{T}}_{u}(t_n), T_{z,u}(t_n), I^{1l}_{u,1}(t_n), \ldots, I^{Kl}_{u,1}(t_n), N^{1l}_{u,1,s}, \ldots, N^{Kl}_{u,1,s}, \ldots, N^{1l}_{u,M,s}, \ldots, N^{Kl}_{u,M,s}\right)^{\mathrm{T}} \qquad [5]
$$

whereas the receiver velocity $\vec{v}_u$ is the time-derivatives of the position $\vec{x}_u$. The velocity is included in the list of estimated state parameters to reduce the uncertainty of the movement, i.e. the process noise needs to include only the acceleration and higher order terms. We use a Kalman filter for the state estimation as described e.g. in (Brown and Hwang 2006). The Kalman filter consists of two steps in each epoch: a state prediction step and a state update step. The latter one uses the corrected measurements of Eq. (3) and (4) to improve the state prediction. As the determination of the corrected measurements requires a knowledge of the (unknown) receiver position $\vec{x}_u$ for determining $\vec{e}^{\,k}_{u} = (\vec{x}_u - \vec{x}^{\,k})/\|\vec{x}_u - \vec{x}^{\,k}\|$, the state update is performed iteratively at each epoch. This includes the re-calculation of the corrected measurements based in Eq. (3) and (4) and the re-determination of the updated state parameters.

Real-Time Kinematics (RTK)

RTK positioning provides centimeter-level positioning accuracy and, thereby, is ideally suited for validation of PPP (Alissa et al. 2021). RTK positioning is characterized by using double difference measurements and by resolving the integer ambiguities related to the periodicity of the carrier phase measurements.
Double difference measurements are performed by first differencing the measurements between the user and a reference station for each satellite, and by subsequently differencing the obtained single difference measurements of each satellite with respect to a common reference satellite. This double differencing eliminates the receiver and satellite clock offsets, code and phase biases. Moreover, it strongly suppresses the satellite position and atmospheric delays if the receivers are sufficiently close to each other. Thereby, the RTK user receiver only needs to estimate the receiver's position (relative to a surveyed reference station of know position) and the carrier phase integer ambiguities. This is typically done by a Kalman filter as described by (Brown and Hwang 2006). The float ambiguity estimates are subsequently fixed to integer numbers e.g. with the well-known Least-Squares Ambiguity Decorrelation Adjustment (LAMBDA) method of (Teunissen 1995), and the position is adjusted accordingly (Teunissen 1995).

MEASUREMENT RESULTS

We have used the ANavS Multi-Sensor (MS) RTK/ PPP module (maritime version) as shown in Figure 1. It includes 3 GNSS receivers for RTK/ PPP positioning and 3D attitude determination, an inertial sensor, the ANavS tightly coupled RTK/ PPP engine, and various interfaces (LTE, WiFi, Ethernet). The RTK corrections were provided by Landmäteriet (SWEPOS) and the PPP corrections were provided by NAVCAST. More specifically, NAVCAST provides precise position, clock offset, code and phase bias corrections for all GPS and Galileo satellites.

Figure 1: ANavS Multi-Sensor (MS) RTK/ PPP Module – maritime version.

Figure 2 shows the test track of the vessel around Gothenburg as determined by the ANavS MS RTK/ PPP module. The track included also some bridge passages and various turns.

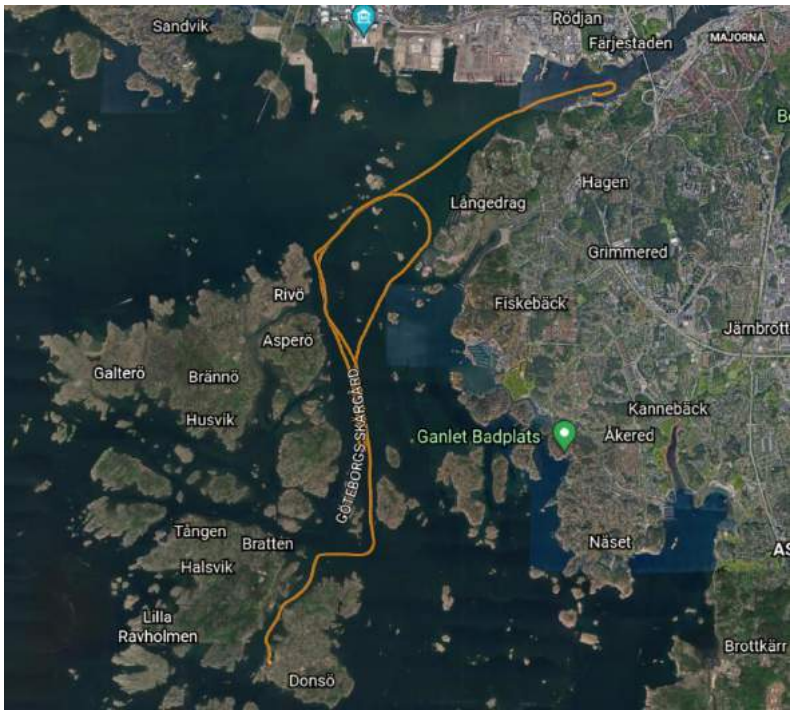

Figure 2: Track of vessel as determined by ANavS PPP solution.

Figure 3 shows the convergence of the PPP solution over time. More specifically, the position offset between the PPP and ambiguity-fixed RTK solution is shown as the latter one is considered as ground truth with centimeter-level accuracy.
The relatively long convergence time of ~30 minutes is typical for PPP solutions and arises from the large number of unknown parameters (position, velocity, receiver clock offset, tropospheric zenith delay, ionospheric slant delays, and ambiguities). After convergence, an accuracy of ~20 cm is achieved and kept during the whole test drive shown in Figure 2. The residual error of ~20 cm arises from imperfect PPP corrections and residual modeling errors.

Figure 4 shows a histogram of the horizontal positioning errors as obtained during the first 100 minutes of the convergence process. Thereby, the histogram includes both the errors during the initialization/ convergence (> 30 cm) as well as the errors after convergence. The latter one corresponds to the peak in the histogram between 20 and 30 minutes.

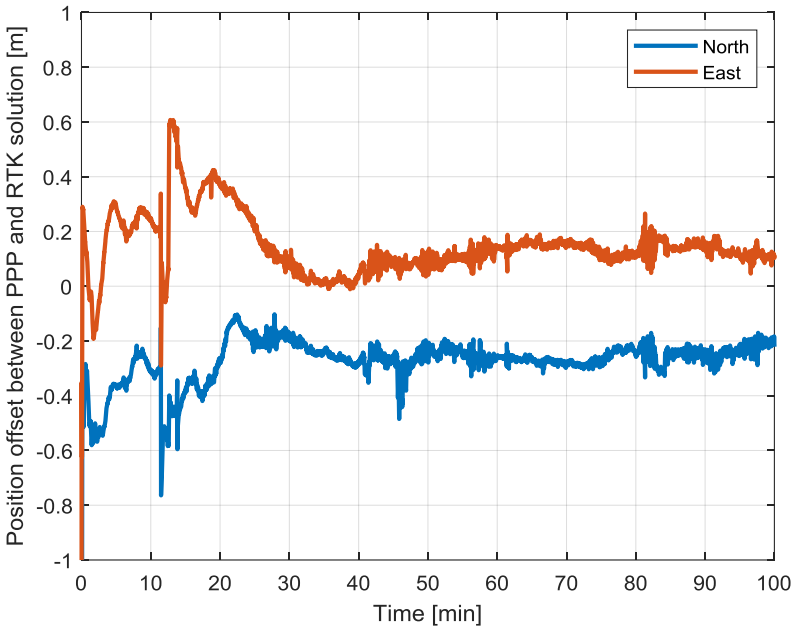

Figure 3: Convergence behavior of PPP solution.

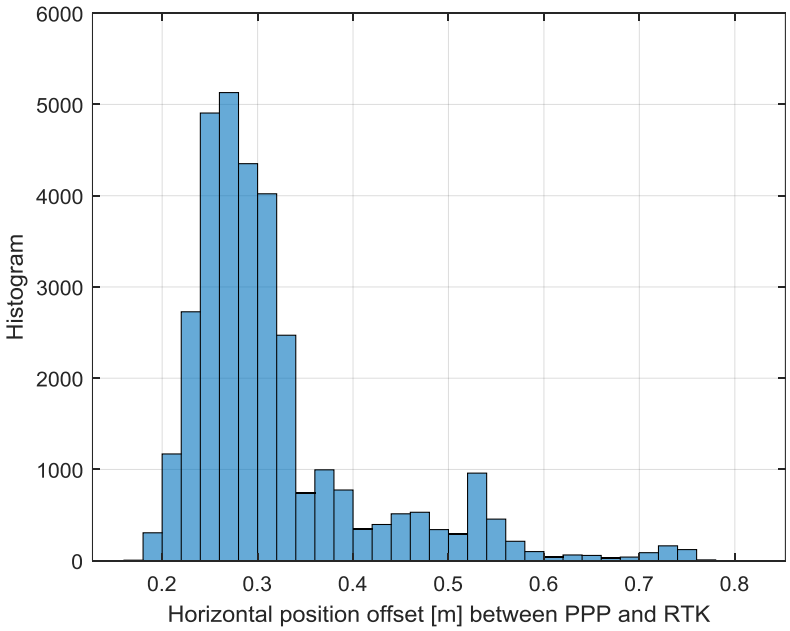

Figure 4: Accuracy Analysis of PPP solution using RTK as reference.

DISCUSSION AND CONCLUSIONS

Navigation in frequently used waterways and/ or at bad weather conditions requires an accurate position solution. In this paper, we have compared the Precise Point Positioning (PPP) and Real-Time Kinematics (RTK) solutions on a vessel in the North Sea near Gothenburg, Sweden. We observed that both solutions agreed within 30 cm over the 2-hour vessel drive. We used the ANavS Multi-Sensor RTK/ PPP module and NAVCAST corrections for this demonstration. The RTK solution served as ground truth.

There are various reasons for the offset between RTK and PPP: For RTK, a reliable integer ambiguity fixing can be obtained within a few epochs, which then leads to a stable solution with an accuracy of a few centimeters. For PPP, there is a need to estimate much more parameters, i.e. ionospheric slant delays and a tropospheric zenith delay have to be estimated besides the position and ambiguities. This larger number of unknowns typically leads to a lower accuracy and less stable solution. There is also a need to apply additional corrections for PPP, i.e. high-accuracy position, clock offset, phase and code bias corrections have to be used for each satellite. Moreover, site displacement corrections (e.g. Earth tides), antenna phase centre offsets and variations have to be considered as well. Any errors in these corrections reduce the position accuracy. The lumped sum of all residual range errors has to be much smaller than one wavelength to enable an integer ambiguity fixing. As this requirement is often not fulfilled, a partial integer ambiguity fixing or even only a float solution can be achieved.
The complementary properties of RTK and PPP make a combination of both positioning techniques very attractive: RTK positioning has a much shorter convergence time and achieves best performance close to reference stations, i.e. it can be used in harbors and their surroundings up to 20 km. RTK positioning can also be used to initialize the PPP solution instantaneously. Thereby, the long convergence times of a PPP "cold-start" can be prevented. The PPP solution can then be used offshore without the need of a mobile communication link for RTK corrections. Once the vessel returns to the coastal area and has again access to RTK corrections, there is simply a hand-over from PPP to RTK.

ACKNOWLEDGEMENTS

The authors would like to thank the European Global Navigation Satellite Systems Agency (GSA) for a grant to the H2020-SPACE-EGNSS-2019-2020 project "**Prepare Ships**" with Grant Agreement Number 870239 that supported this work.

REFERENCES

ALISSA, S., M. HAKANSSON, P. HENKEL, U. MITTMANN, J. HÜFFMEIER and R. RYDLINGER. "Low Bandwidth Network-RTK Correction Dissemination for High Accuracy Maritime Navigation." *TRANSNAV – the International Journal on Marine Navigation and Safety of Sea Transportation*, **15**:1 (2021): 171-179.

BROWN, R.G. and P.Y.C. HWANG. "Introduction to Random Signals and Applied Kalman Filtering with Matlab Exercises." Wiley and Sons, (2021).

HEINRICH, M., A. SPERL, U. MITTMANN and P. HENKEL. "Reliable Multi-GNSS Real-Time Kinematic Positioning." *IEEE Proceedings of 60th ELMAR Symposium,* (2018): 103-108.

TEUNISSEN, P.J.G., and O. MONTENBRUCK. "Handbook of Global Navigation Satellite Systems." Springer, (2017).

TEUNISSEN, P. "The Least-Squares Ambiguity Decorrelation Adjustment: A Method for Fast GPS Integer Ambiguity Estimation." *Journal of Geodesy,* **70** (1995): 65-82.

ZUMBERGE, J.F., M.B. HEFLIN, D.C. JEFFERSON, M.M. WATKINS, and F.H. WEBB. "Precise point positioning for the efficient and robust analysis of GPS data from large networks." *Journal of Geophysical Research*, **102**(B3) (1997): 5005-5017.

ANALYSIS AND RESEARCH ON THE RESPONSE OF SPRINGING AND WHIPPING OF VERY LARGE ORE CARRIER

XUANKAI WANG

ABSTRACT

In recent years, there is a trend of ship increasing in size which has attracted lots of attention, and more and more very large ore carriers have appeared in the world. As the main dimensions of very large ore carriers continue to increase, in order to maximize the profits, the use of high-strength steel in the construction of ships is also increasing, which results in the increase of rigidity of very large ore vessels.As a result, the natural frequency of the first-order global vibration is approaches the encounter wave frequency, and "springing" may occur. When the ship is sailing in the medium and high waves, at a relatively high speed, wave impact on the hull may occur due to the large ship motion relative to the waves. A "whipping" phenomenon will be produced due to the slamming load,Springing and whipping effects have an influence on the fatigue strength the hull structure. In this thesis, the characteristics of load response due to springing and whipping of a 400,000-ton ore ship is analyzed by a numerical calculation method, and the structural fatigue strength impact under the springing response is assessed. Select the sea conditions prone to springing and whipping responses, and analyze the stress monitoring data of the actual ship. The specific research contents of this thesis are as follows:

(1)The dry matrix analysis of the hull girder of the target ship is carried out using the migration matrix method and the finite element method, respectively, to obtain the global vibration mode and natural frequency of the ship. It is found that the two methods have little difference when calculating the low-order natural frequency. The modal calculation results of the migration matrix method can be used to calculate the springing and whipping loads.

(2)Based on the three-dimensional hydroelastic theory, the wave load calculation codes Compass-WALCS-BASIC, Compass-WALCS-LE, Compass-WALCS-NE are used to calculate the springing and whipping load of the target ship, and to study and analyze the springing load of the ship response characteristics that indicate the phenomena of springing and whipping cannot be ignored.

(3)An assessment of fatigue strength of the ship is performed according to the CCS rules, and the impact of the springing response on the target ship's fatigue strength is investigated,and find that the springing response has a certain degree of contribution to the target ship's fatigue damage.

KEY WORDS

Very large ore carrier;Springing ;Whipping ;Fatigue damage

0 INTRODUCTION

Nowadays, ultra-large ships use more high-strength steel, which makes the structural rigidity of the hull smaller and the natural frequency is small. The natural frequency of a ship with a larger main dimension is approximately close to the frequency of wave encounters when sailing in ocean waves, which makes the hull structure occur. Elastic vibration response, which has a very adverse effect on the fatigue strength of the super large ship hull.

When a super large ship sails in high sea conditions and at high speed, it will be impacted by waves, and the hull will "flutter" due to the instantaneous slamming load. Flutter not only affects the ultimate strength of the hull structure, but also affects the fatigue strength of the hull structure.

This paper takes the 400,000-ton ultra-large ore ship as the target ship type. First, the hull girder of the target ship is subjected to dry modal analysis using the migration matrix method and the finite element method, and the calculation results of the two methods are compared and analyzed. Then, based on the three-dimensional hydroelasticity theory, The wave load calculation software Compass-WALCS-BASIC, Compass-WALCS-LE, Compass-WALCS-NE is used to calculate the elastic vibration and flutter load of the target ship, and then the elastic vibration and flutter stress response of the target ship through the beam theory method Solved. Finally, the spectrum analysis method is used to calculate the fatigue damage of the target ship, and the contribution to the fatigue damage of the hull structure considering the effect of elastic vibration is obtained.

1 Target ship modal analysis

1.1 Transfer matrix method

When solving the structural modal of the target ship by using the migration matrix method, the hull can be divided into 20 sections.

1.2 Three-dimensional finite element method

The finite element model is shown in Figure1

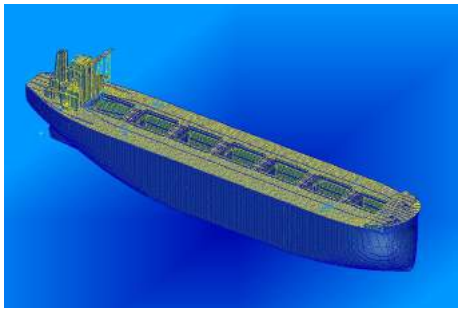

Figure 1 Finite element model of the target ship

1.3 Analysis of calculation results

The dry mode of the target ship is calculated by the three-dimensional finite element method. Due to space limitations, only the next-order vertical vibration mode diagram under ballast conditions is listed here, as shown in Figure 2

Figure2 First-order vertical vibration mode diagram (ballast)

The total mode diagram of the hull girder of the migration matrix method is shown in the figure. Here, only the mode diagram of the next-order vertical vibration under the ballast condition is listed, as shown in Figure 3

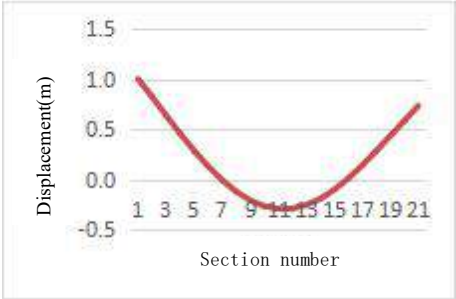

Figure 3 First-order vertical (ballast)

1.4 Comparative analysis of results

The natural frequency calculation results of the migration matrix method and the three-dimensional finite element method are shown in Table 1.

Table 1 The calculation results of the natural frequency of the target ship

	Ballast （HZ）			Fully loaded（HZ）		
	migration matrix	FEM	Relative error	migration matrix	FEM	Relative error
1st vertical	0.59	0.57	0.0351	0.49	0.48	0.0208
1st horizontal	0.96	0.89	0.0787	0.74	0.67	0.1045
1st twist	0.87	0.83	0.0481	0.62	0.57	0.0877
2nd vertical	1.43	1.15	0.2435	1.17	1.08	0.0833
2nd horizontal	2.14	1.58	0.3544	1.59	1.4	0.1357
2nd twist	2.25	1.68	0.3393	1.52	1.38	0.1014
3rd vertical	2.82	1.90	0.4842	2.03	1.52	0.3355
3rd horizontal	3.88	2.71	0.4317	2.47	1.73	0.4277
3rd twist	3.41	2.32	0.4698	2.71	1.79	0.5139

It can be seen from the above table that the natural frequency results of 1st vertical, 1st horizontal,2nd vertical,2nd horizontal, and 1st twist are in good agreement with the natural frequency results of the three-dimensional finite element method. The error of the result of state vibration is relatively large. The reason is that the transfer matrix method is not suitable for calculating high-order vibration modes, and large errors will occur.

2 Elastic vibration load and stress response analysis

The elastic vibration calculation analysis mainly adopts the linear frequency domain hydroelastic spectrum analysis method to calculate.

The wave load forecasting software Compass-WALCS [1]is selected to calculate the target ship's elastic vibration load.

Compass-WALCS-BASIC is based on the rigidity theory, and Compass-WALCS-LE is based on the three-dimensional hydroelastic theory[2]. The calculation results of the two are compared and analyzed.

2.1 Calculation of preliminary preparation

The North Atlantic sea state is selected as the sea state for calculating the target ship's bounce load. Based on the requirements of CCS specification [3], the frequency range is 0-2.5 rad/s, the frequency interval is 0.05 rsd/s, the wave direction is 0-180° , and the wave direction With an interval of 30° , the maximum speed is selected for the calculation speed, the calculated water depth is infinite water depth, and the calculation modes are the first three-order vertical vibration and the first two-order horizontal vibration. This paper selects two typical loading conditions of ballast and full load for research and analysis.

This paper uses Patran finite element software to mesh the wet surface of the hull. The number of grids on the wet surface in Figure 4 is about 10,000, and the number of grids on the wet surface in Figure 5 is about 3,000. The hydrodynamic model of the wet surface grid on the target ship is shown in the figure:

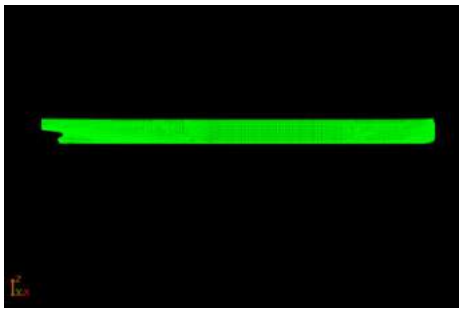

Figure 4 Hydrodynamic grid (LE)

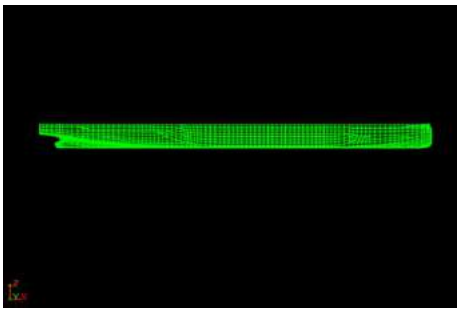

Figure 5 Hydrodynamic grid (BASIC)

2.2 Calculation of elastic vibration load

Due to space limitations, the vertical wave bending moment with a wave angle of 0° when fully loaded is listed here. Figure6 is the vertical wave bending moment in an elastomeric ship, and Figure 7 is the vertical wave in an elastomeric ship. Wave bending moment.

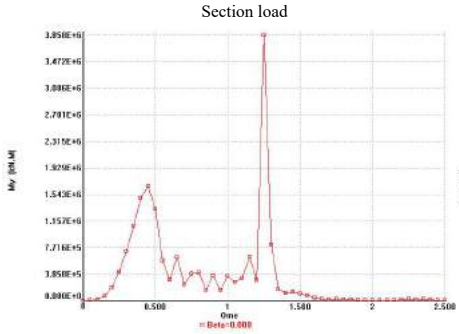

Figure 6 Vertical bending moment (full load, β=0°)

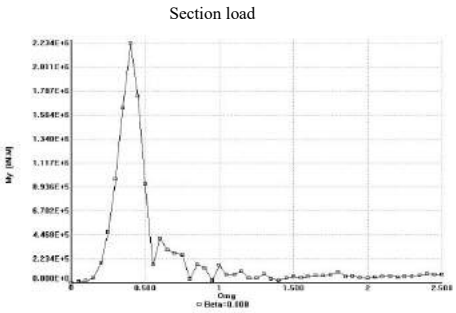

Figure 7 Vertical bending moment (full load, β=0°)

The calculation results show that the vertical wave bending moment diagram and the horizontal wave bending moment diagram in the elastic hull ship will have a second peak, which is the peak of the elastic vibration response, which is similar to that in the rigid hull ship. The vertical wave bending moment is different.

2.3 Elastic vibration stress calculation

In the two loading conditions of full load and ballast, the midship section is selected as the stress analysis section for the typical section. Choose 4 points in the profile as the reference points for the solution. The selected areas of the four points are near the inner keel of the outer bottom, near the junction of the inner bottom and the inclined inner shell, near the side waterline, and near the deck opening, as shown in the figure. Shown in Figure 8.

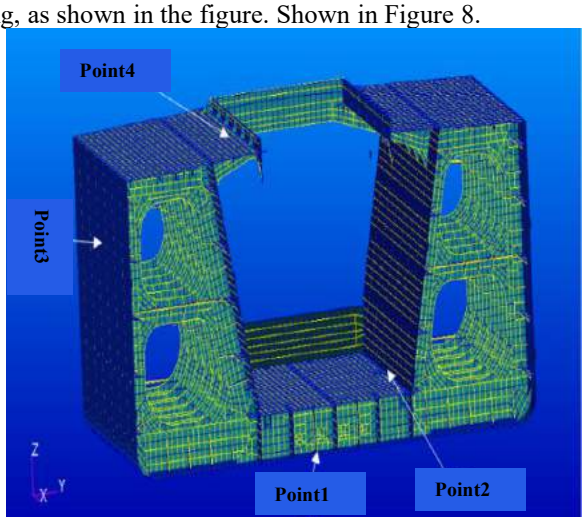

Figure 8 Schematic diagram of calculation points

The beam theory is used to calculate the elastic vibration stress response. Due to space limitations, only the stress transfer function of the calculation point where the wave angle is 0° under full load and ballast is listed here, as shown in Figure 9 to Figure 12

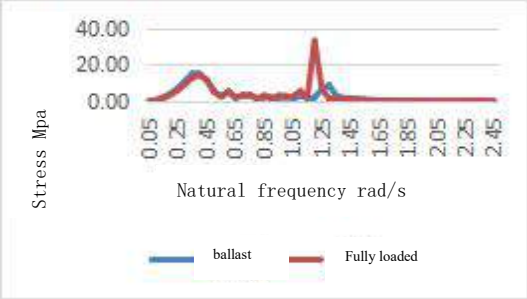

Figure 9 Stress transfer function (0°, point 1)

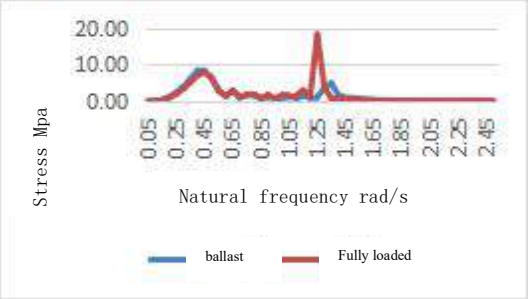

Figure 10 Stress transfer function (0°, point 2)

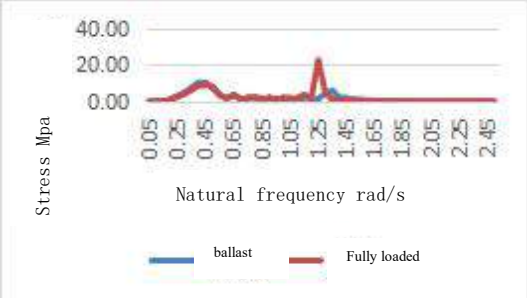

Figure 11 Stress transfer function (0°,point 3)

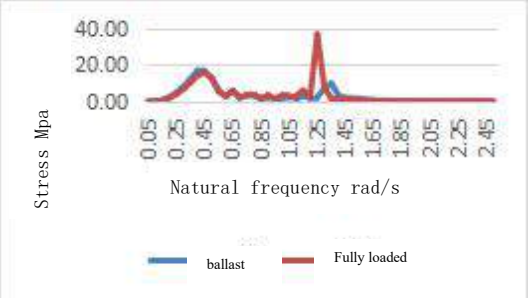

Figure 12 Stress transfer function (0°, point 4)

The calculation shows that the elastic vibration stress response obviously occurs in the high frequency part, and the elastic vibration response stress frequency at full load is lower than the elastic vibration response frequency at the time of ballasting. The response stress in the fully loaded state is always greater than the response stress in the ballast state.

The response stress when the wave direction angle is 30° is greater than the response stress when the wave direction angle is 60°, and the response stress when the wave direction angle is 60° is greater than the response stress when the wave direction angle is 0°. The contact surface between the hull and the wave is larger, which produces a greater wave load. In the non-high frequency area, the stress curves of ballast and full load have a certain consistency.

3 Calculation of ship flutter load and stress response

To analyze the flutter load of the target ship, the non-linear load prediction method of CCS is mainly used to calculate the flutter load of the target ship, and the modal analysis result of the migration matrix method is used to predict the flutter load.

According to the CCS Guidelines for Direct Calculation and Evaluation of Hull Structure Wave-Induced Vibration and Slamming Flutter, the working conditions for calculating flutter load are selected, that is, for ships in an infinite navigation zone, the slamming flutter fatigue load calculation working conditions and slamming flutter limit can be used Non-linear time-domain slamming flutter calculation and evaluation are performed on the simplified conditions specified by the load calculation conditions. This paper selects the North Atlantic Ocean to calculate the sea conditions, and calculates the speed according to the specifications. The flutter load is calculated for the two loading conditions of ballast and full load respectively.

3.1 Flutter load calculation results

Due to space limitations, only β =0°, T=4.5s, =5m regular wave and β =0°, T=4.5s,=1.5m irregular wave calculation results are listed here, as shown in Figure 13-14shown

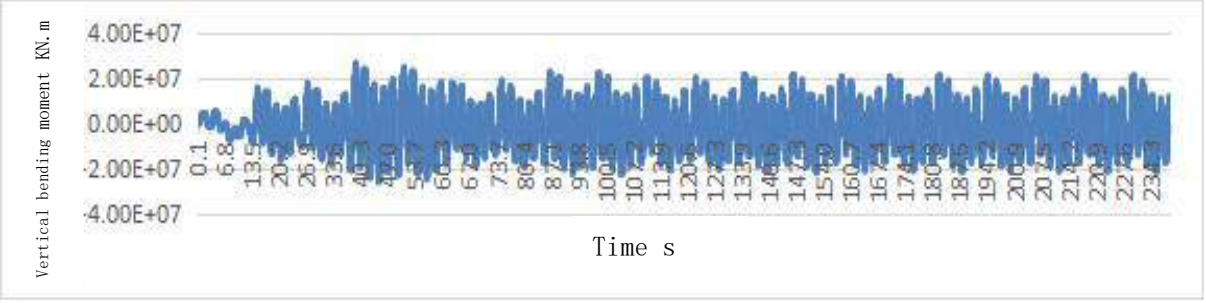

Figure13 Regular wave calculation results (β =0° , T=4.5s, =5m)

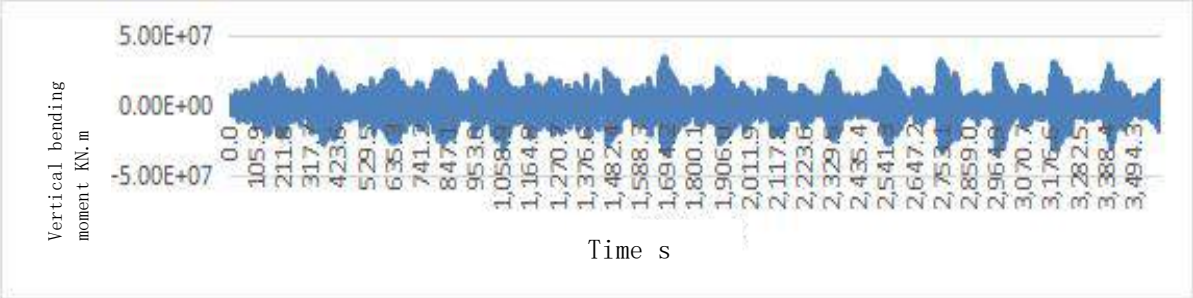

Figure 14 Irregular wave calculation results (β =0° , T=4.5s, =1.5m)

The calculation results show that as the wave height increases, the vertical wave bending moment also increases. The flutter load change trend is more consistent under different wave height periods.

When the wave height is small, the vertical bending moment is small, and there is no obvious slamming flutter phenomenon. As the wave height gradually increases, the vertical bending moment also becomes larger. At this time, the appearance of slamming flutter load can be clearly seen . Under the same wave height and different periods, the slamming flutter of the midship section is different. Through comparison, it is found that the slamming flutter with the same wave height and smaller period is more obvious. The flutter load of the midship section under the same wave height and the same period and different wave angles is different. The basic trend is that the vertical bending moment is larger when the wave angle is 0° . When the wave height is larger, the flutter response is more obvious.

3.2 Flutter stress response calculation

In the following, taking the wave height of 5.5m, the period of 10.5s, the calculated speed of 14.5kn and the wave height of 8.5m, the period of 10.5s, and the calculated speed of 10.875kn as an example, the two working conditions of the ballast situation will be calculated to calculate the typical position under this sea condition. (See Figure 8 for the schematic diagram of the calculation points) of the flutter response stress time history curve, here only the stress time history curve at β =0° , V=10.875. Point 1， as shown in Figure 15

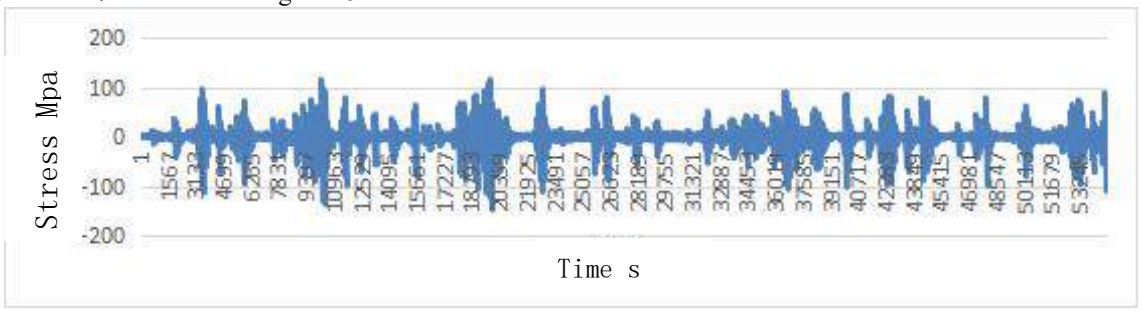

Figure 15 Stress time history curve (β =0° , V=10.875. Point 1)

The calculation results show that the flutter response stress values at points 1 and 4 are greater than the stress values at points 2 and 3 in both low sea state and high sea state, which is consistent with the elastic vibration response stress law. The flutter response stress at the same location and different wave direction angles is different. When the wave direction angle is 0° , the flutter response stress at each point is greater than the response stress when the wave direction angles are 30° and 60° . The flutter response is more obvious under high sea conditions, and the flutter response stress is greater than that under low sea conditions. Therefore, it is necessary to consider the impact of flutter response on the ship during ship design and operation.

4 The influence of elastic vibration effect on the fatigue strength of a very large ore carrier

4.1 Fatigue damage calculation of very large ore carrier

The loading conditions for the fatigue assessment of ore carriers are generally full load and ballast. With reference to the introduction of IACS Rec.34, the North Atlantic wave scatter diagram is finally selected, and the P-M spectrum is used as the wave power spectral density function. The wave direction angles are taken as full wave directions with an interval of 30°, and the probability of occurrence of each wave direction angle is the same.

4.2 Analysis of calculation results

The stress transfer function under ballast and full load obtained by using the beam theory method is solved by fatigue spectrum analysis taking into account the elastic vibration response. At the same time, the fatigue damage of the rigid body is calculated under the ignoring of the elastic vibration response, so as to obtain the contribution of the elastic vibration to the fatigue damage according to the CCS code. The solution results are summarized in Table 2 to Table 3.

Table 2 Fatigue damage of beam theory method (ballast)

		0°	30°	60°	90°	120°	150°	180°	Total damage	Contribution degree
POINT1	Don't consider springing	0.028	0.157	0.062	0.009	0.035	0.007	0.016	0.315	0.262
	Consider springing	0.097	0.178	0.062	0.007	0.032	0.006	0.016	0.397	
POINT2	Don't consider springing	0.001	0.022	0.011	0.002	0.006	0.001	0.003	0.045	0.255
	Consider springing	0.015	0.027	0.008	0.000	0.004	0.001	0.002	0.057	
POINT3	Don't consider springing	0.008	0.039	0.019	0.003	0.011	0.002	0.005	0.088	0.289
	Consider springing	0.029	0.053	0.017	0.001	0.008	0.001	0.005	0.113	
POINT4	Don't consider springing	0.013	0.240	0.085	0.013	0.047	0.009	0.023	0.431	0.274
	Consider springing	0.133	0.244	0.086	0.011	0.045	0.008	0.022	0.549	

Table 3 Fatigue damage of beam theory method (full load)

		0°	30°	60°	90°	120°	150°	180°	Total damage	Contribution degree
POINT1	Don't consider springing	0.086	0.134	0.051	0.001	0.031	0.019	0.015	0.338	0.358
	Consider springing	0.097	0.224	0.076	0.001	0.028	0.018	0.014	0.459	
POINT2	Don't consider springing	0.009	0.020	0.009	0.000	0.005	0.003	0.003	0.049	0.281
	Consider springing	0.014	0.032	0.009	0.000	0.003	0.002	0.002	0.063	
POINT3	Don't consider springing	0.018	0.042	0.016	0.000	0.009	0.006	0.005	0.096	0.330
	Consider springing	0.028	0.064	0.020	0.000	0.007	0.005	0.004	0.128	
POINT4	Don't consider springing	0.120	0.184	0.070	0.002	0.042	0.027	0.020	0.464	0.370
	Consider springing	0.133	0.310	0.107	0.002	0.039	0.025	0.020	0.636	

It can be seen from Table 2 and Table 3:
(1) The fatigue damage caused by the head wave and the bow wave is larger than the fatigue damage caused by other wave directions, so it accounts for the main part of the total fatigue damage. The reason is analyzed and found in the head wave and the bow wave. The stress response of is also larger than the stress response of other waves.

(2) The impact of elastic vibration on the fatigue damage of the target ship is not small. The fatigue damage caused by ballast is about 25%-29%, and the fatigue damage caused by full load is about 29%-37%. The fatigue damage produced is slightly larger than that of ballast, so no matter under full load or ballast, the fatigue damage caused by elastic vibration response cannot be ignored.

5 CONCLUSION

Very large ore ships have obvious bounce vibrations in the vertical and horizontal directions, and the frequency of bounce response is low. Therefore, when the ship is sailing, it is easy to be affected by waves and produce high frequency response, which affects the fatigue strength of the hull. ; When the ship is sailing, the wave direction angle is different, and the elastic vibration response is also different. Generally, the elastic vibration response under the bow wave is greater than the elastic vibration response under the heading wave; when the same position and the same wave direction angle, the elastic vibration stress response under full load is greater than Stress response under ballast.

The vertical bending moment of the midship section under regular waves and irregular waves changes with the change of wave height. The larger the wave height, the greater the vertical bending moment and the more obvious the phenomenon of slamming flutter. The vertical wave bending moments under the same wave height and different periods are also different. The smaller the period, the greater the value of the vertical wave bending moment, the more obvious the slamming and flutter phenomenon.

The fatigue damage of the target ship is calculated and solved with and without elastic vibration, and finally the contribution of the elastic response to the fatigue damage of the target ship is obtained. It is found that the contribution of the elastic vibration response to the fatigue damage of the target ship at full load is greater than that of the target ship. The contribution of ballasting is different from the fatigue damage caused by different positions and different waves, and the contribution of fatigue damage is also different. The fatigue damage during head-on waves accounts for a larger proportion of the total damage.

REFERENCES

【1】三维水弹性力学分析软件 WALCS 理论手册。
【2】李辉.船舶波浪载荷的三维水弹性分析方法研究[D].哈尔滨工程大学,2009
【3】CCS,船体结构波激振动和砰击颤振直接计算评估指南。2018 年 11 月.
【4】吴小平。大型集装箱船弹振和颤振研究。2012 年 1 月.
【5】Drummen I, Moan T,Storhaug G,et al. Experimental and full scale investigation of the importance of fatigue damage due to wave-induced vibration stress in a container vessel[C] .2006.
【6】Storhaug, Gaute. The measured contribution of whipping and springing on the fatigue and extreme loading of container vessels[J]. International Journal of Naval Architecture and Ocean Engineering, 2014, 6(4):1096---1110.

A numerical study on the noise characteristics according to cavitation number using Delft twist11 hydrofoil

Hong-Sik Hwang[1], Jun-Hui Cho[2], Soon-Hyun Lee[3], Kwang-Jun Paik[4]

ABSTRACT

Underwater radiated noise (URN) is greatly increasing due to increase in commercial shipping, sonar activities, and climate change. As a result, marine life is having difficulty communicating, and marine ecosystem disturbances are occurring. The noise from the cavitation of propellers is affecting URN. Cavitation is a phenomenon in which rapid changes of pressure in a liquid lead to the formation of small vapor-filled cavities in places where the pressure is relatively low. This phenomenon results in poor efficiency of the propeller or turbine of a ship and noise, vibration, and erosion. For these reasons, this study examines the URN of sheet and cloud cavitation. A numerical analysis was done using a Delft Twist11 hydrofoil. The URN resulting from cloud cavitation and sheet cavitation was compared with the numerical results of previous studies. The results showed that URN normally increases due to pressure fluctuations when cavitation occurs. URN increased more significantly in conditions of cloud cavitation than cavitation inception. It is also shown that a frequency begins to occur after the occurrence of the cloud cavitation, and the frequency grew as the cavitation fully developed.

KEY WORDS

Delft Twist11 hydrofoil; URN (Underwater Radiated Noise); Sheet cavitation; Cloud cavitation; RANS; DES; LES; Vibration, FW-H, Shnerr-Sauer model.

INTRODUCTION

Cavitation is a phenomenon in which a rapid pressure changes in a liquid condition result in the formation of a small vapor cavity where the pressure is relatively low. The cavitation caused by a propeller rotating causes erosion of the propeller, vibration, and noise. This reduces the efficiency of the propeller and turbine, and the noise produced by the cavitation greatly affects the communication of marine life. Various organizations and committees are making efforts to resolve problems related to Underwater Radiated Noise (URN), including IMO, MEPC, MSFD, and NORSOK. In addition, guidelines were developed to regulate URN emitted by ships in the North Sea (SONIC, 2012), and the European Union established Quiet MED to address noise problems in the Mediterranean region.

The effects of noise from the propellers of ships are considerable. Therefore, studies on cavitation occurring from the propulsion of ships are needed. Foeth et al.(2006) did an experimental study on the cavitation features and frequency of hydrofoils. The experiment was conducted at the cavitation tunnel of Delft University of Technology, and detailed research was conducted on cavitation features over time using PIV according to the flow rate and cavitation number. Hoekstra et al.(2011) compared and analyzed the results simulated by various institutions based on the results of the experiment by Foeth et al.(2006). A variety of turbulence models and mass transfer models were used.

Bensow(2011) conducted a numerical study on the cavitation features and frequency of a Delft Twist11 hydrofoil and compared the results for different turbulence models. RANS, DES, and LES models were used as turbulence models, and the LES models obtained the results most similar to those of the experiments. Asnaghi(2015) carried out a cavitation analysis using the LES model. 2D and 3D hydrofoils and a cavitating propeller were used, and the cavitation was examined. Vaz et al. (2017) conducted a cavitation analysis with RANS, RANS including an eddy-viscosity “Reboud” correction, and DDES Scale-Resolving-Simulation models.

Lidtke et al.(2016) compared the results of frequency and noise from the cavitation of a Delft Twist11 hydrofoil using different cavitation models. The turbulence model was the DDES model, and the cavitation model was compared with the results obtained using the Schnerr-Sauer model and a hybrid Lagrangian-Eulerian cavitation model based on the Schnerr-Sauer model.

[1] Affiliation
[2]Affiliation

This study analyzed the noise and vibration characteristics based on the cavitation characteristics of a Delft Twist11 hydrofoil. The noise characteristics produced by cavitation were predicted using the Schnerr-Sauer model by analyzing the cavitation features and frequency. RANS, DES, and LES models were used as turbulence models, and simulations were performed with three time steps to obtain accurate results. A study was conducted to predict the sound pressure level (SPL) from cavitation using a direct method. In addition, SPLs were compared according to the cavitation number to identify the correlation between the noise and cavitation.

Materials

The shape of the hydrofoil used in the cavitation simulation has a NACA0009 profile with a chord length C of 150 mm and span length S of 300 mm. The hydrofoil's angle of attack at both ends is -2°, the angle of attack at the mid span is 9°, and it has a symmetrical shape. The domain used for the numerical simulation is 9C in the streamwise direction. The distances from the inlet to the leading edge of the foil and from the trailing edge to the outlet are each 4C. The centerline is symmetrical in the direction of the span, and there is a distance of C up and down in the Z direction. For the boundary conditions of the domain, the top, bottom, and sides are set as walls. The velocity is 6.97 m/s, and the cavitation number is 1.07 from the experimental paper by Foeth (2008).
The commercial CFD software Star-CCM+ 13.06 was used. The governing equation and turbulence model were RANS (SST k-ω), DES (SST k-ω), and LES models. The Eulerian Multiphase model was used to simulate the formation of cavitation due to the pressure drop in the fluid. Also, the cavitation model was the Schnerr-Sauer model. To measure URN, a direct method was used to directly predict the measured pressure at a point.
The number of grids was about 3.9 million (all isotropic elements) with y+≤1 at the walls. A fixed pressure of 29 kPa was applied to generate cavitation, and the simulation was calculated in wetted flow conditions until the simulation showed convergence. A numerical discretization technique of second-order accuracy was applied for time and space, and simulations were performed with time intervals of 2.5×10^{-5}

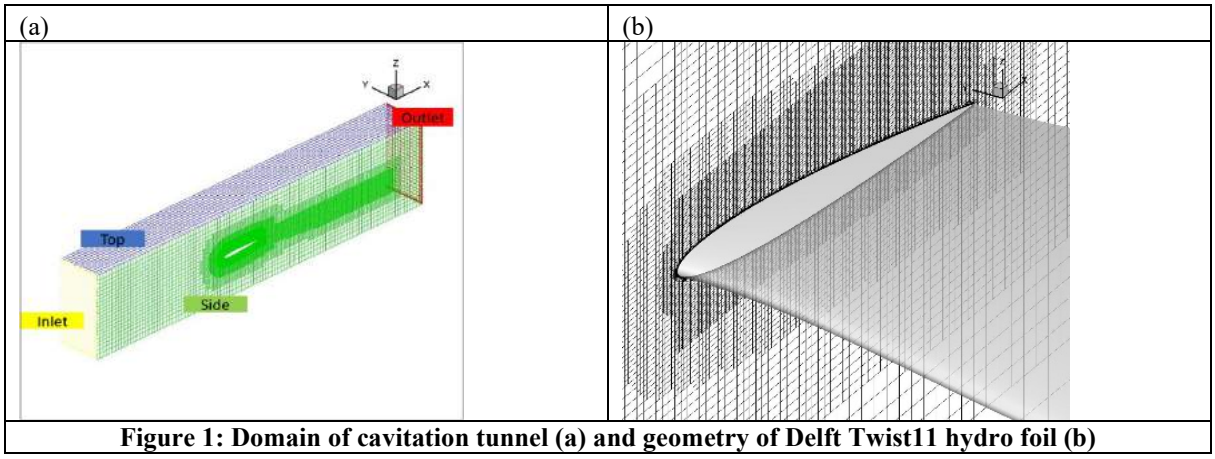

Figure 1: Domain of cavitation tunnel (a) and geometry of Delft Twist11 hydro foil (b)

Wetted flow

Table 1 and Figure 2 show the results of the experiment and the simulation results for each turbulence model according to the number of grids in a wetted flow where cavitation does not occur. The time step was 2.5×10^{-4}. The RANS model, DES model, and LES model were simulated, and the RANS model showed a 3% lift force error rate, regardless of the number of grids. The result of the number of grids was not changed, and it is thought that the reason is that sufficient grids had been added to check the lift coefficient. The reliability for performing the simulation in the cavitating flow was verified.
In the case of the DES model, the error rate increased as the number of grids increased, but it was determined that there was no problem in terms of the Grid Convergence Index (GCI) because it showed convergence as the number of grids increased (table 3). The LES model also showed a tendency for the lift coefficient to converge as the number of grids increased, and the error rate converged to around 3.5%. Since all three models converged in the medium grid condition, the analysis was carried out under the medium grid condition in the subsequent analysis. When comparing by turbulence models, the RANS, LES, and DES models in the wetted flow state showed high accuracy in that order.

Table 1: Lift coefficient in wetted flow according to the number of grids and turbulence models

Wetted flow		RANS		DES		LES	
Grid	EXP	C_L	Error rate [%]	C_L	Error rate [%]	C_L	Error rate [%]

Coarse (1.9M)	0.456	0.4440	2.63	0.4440	2.63	0.4328	5.08
Medium (4.0M)		0.4424	2.98	0.4321	5.24	0.4425	2.96
Fine (5.5M)		0.4423	3.00	0.4320	5.26	0.4425	2.96

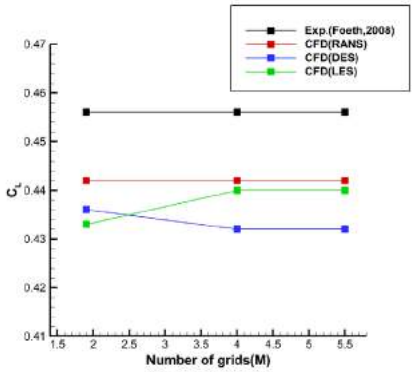

Figure 2: Lift coefficient according to the number of grids

Table 2: Lift coefficient at wetted flow according to the time steps and turbulence models

Wetted flow		RANS		DES		LES	
Time step	EXP	C_L	Error rate [%]	C_L	Error rate [%]	C_L	Error rate [%]
2.5×10^{-4}	0.456	0.4424	2.98	0.4321	5.24	0.4425	2.96
5.0×10^{-5}		0.4428	2.89	0.4329	5.06	0.4434	2.76
2.5×10^{-5}		0.4428	2.89	0.4336	4.91	0.4463	2.12

In addition, the simulation results of the wetted flow according to the time step are shown for the time step verification. The simulation results are shown in Table 2, and the three turbulence models could be seen to increase their accuracy with a lower time step. Also, the lower the time step, the greater the accuracy of the LES model was, and the accuracy was increased in the order of LES, RANS, and DES models.

Cavitating flow

In the case of cavitation flow, the lift coefficient is shown according to time step in Table 3 for each turbulence model, and Figure 3 shows the lift coefficient over time for each turbulence model. For stability in the process of simulation, a pressure drop was carried out after convergence in the wetted flow state and simulating the cavitating flow. In the case of the RANS model, there was a tendency to converge and not to fluctuate periodically after the occurrence of the cavitation, indicating that the lift coefficient also resulted in a large error. For the DES model, the results were more accurate than the RANS model, and it was also noted that the lift coefficient fluctuated periodically over time. For LES models, the accuracy was the highest compared to other models.

When comparing the lift coefficient for each model according to the time step, we could see that the smaller the time step, the lower the lift coefficient was compared to the experimental results, and the error was larger. However, the smaller the time step, the more constant the lift coefficient values are, so this cannot be regarded as similar to the experimental value when the time step is large, nor is the simulation result incorrect. By analyzing the frequency shown in the section 3.2.2., the reliability of the analytical results could be obtained.

Table 3: Lift coefficient in cavitating flow according to the time steps and turbulence models

Cavitating flow		RANS		DES		LES	
Time step	EXP	C_L	Error rate [%]	C_L	Error rate [%]	C_L	Error rate [%]
2.5×10^{-4}	0.510	0.4095	19.71	0.4535	11.08	0.4737	7.12
5.0×10^{-5}		0.4093	19.75	0.4370	14.31	0.4427	13.20
2.5×10^{-5}		0.4079	20.02	0.4366	14.39	0.4410	13.53

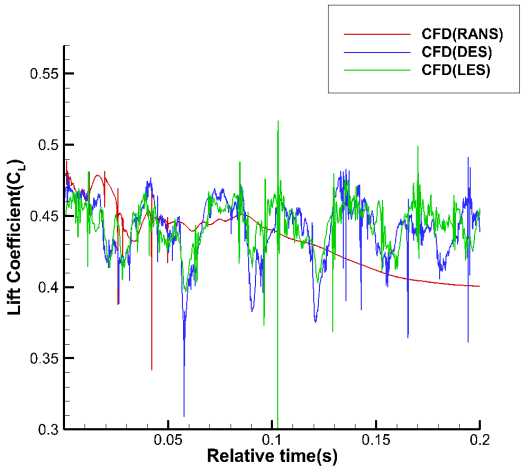

Figure 3: Lift coefficient according to turbulence model with a narrow time interval

Table 4 shows that the smaller the time step in the DES and LES models is, the greater the accuracy of the shedding frequency. Based on the results Table 3, the simulation was done with timestep = $2.5x10^{-5}$. In the case of the RANS model, the cavitation developed stably, and not only near the wall. Thus, it was difficult to identify the frequency, and only a representative value could be put in Table 4. In the case of the DES and LES models, the frequency increased due to lower time steps, and similar results were obtained.

Table 4: Shedding frequency according to the time steps and turbulence models and another numerical study

Cavitating flow	Frequency [Hz]							
Time step	EXP	Present			Bensow (LES)	LR (DES)	TUHH (RANS)	MARIN (RANS_corr)
		RANS	DES	LES				
2.5×10^{-4}			24.37	24.78				
5.0×10^{-5}	32.55	15.81	29.24	30.00	34	35	38.79	38
2.5×10^{-5}			32.00	33.32				

For comparison of the results of Foeth(2006), cavitation features are presented in Figure 4 in a time sequence. From the left, the results of the experiment are RANS, DES, and LES. The time sequence is shown from top to bottom, and after sheet cavitation, cloud cavitation and contraction are repeated. First of all, the results of the RANS model show that sheet cavitation is created, but there is no cloud cavitation. Also, as mentioned in Section 3.2.2 earlier, cavitation developed stably, so periodicity was not visible, and it could not simulate the characteristics of cavitation that developed periodically.

Secondly, we ca see that the cavitation shape of the DES model is similar to the results of the experiment. Periodic development and contraction of sheet cavitation and cloud cavitation were identified. However, the Q-criterion confirmed that it did not appear on the surface of the hydrofoil, which showed stable flow near the wall due to the characteristics of the DES model, which was interpreted as a RANS model near the wall.

Finally, the LES model showed a cavity shape similar to the experimental results. The development and contraction of periodic cavitation, like in the DES model, could be seen. Also, we were able to check the free movement of sheet cavitation compared to the DES model. This can be seen as a result of the model's characteristic of performing eddy simulation in the entire domain, whereas the DES model uses the RANS (SST k-w) model near the wall to generate stable sheet cavitation.

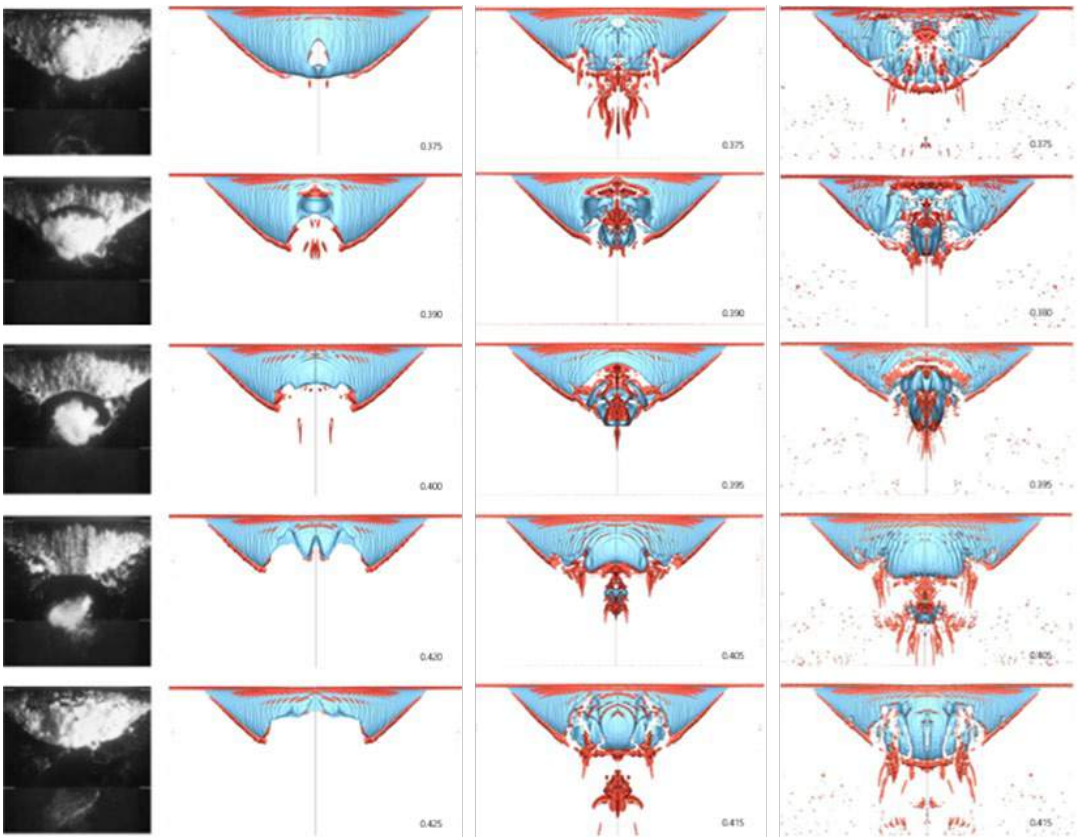

Figure 4: Comparison of RANS (left), DES (middle) and LES (right); iso-surfaces show the volume fraction α=0.5 and Q-criterion

Next, the -Cp curve of the mean time in cavitating flow was compared according to the span direction section, and the results are shown in Figure 5. From the top, y/S=0.3, 0.4, and 0.5 are shown. The black symbol shows the experiments results, red is RANS, blue is DES, and green is LES. Figure 6 shows the mean time value of the volume fraction at y/S=0.5.

First of all, Figure 5 and Figure 6 show that sheet cavitation is developed in the case of the RANS model, but it is less created in the direction of code length compared to other models. Also, errors occur compared experiment results as it progresses in the direction of code. In the case of the DES model, Figure 6 shows the development of sheet cavitation and cloud cavitation. It can also be seen that sheet cavitation is strongly developed. Thus, similar results were obtained to those in Figure 5.

The model of LES was also able to show the development of cavitation and the results of Figure 6. The DES model showed that sheet cavitation was smaller than those of Figure 6. As mentioned in Section 3.2.3, this is a result of the characteristics of the DES model, and it is judged that the LES model is also a model that interprets large eddies directly.

$C_p = \frac{p - p_v}{0.5\rho U^2}$	[1]

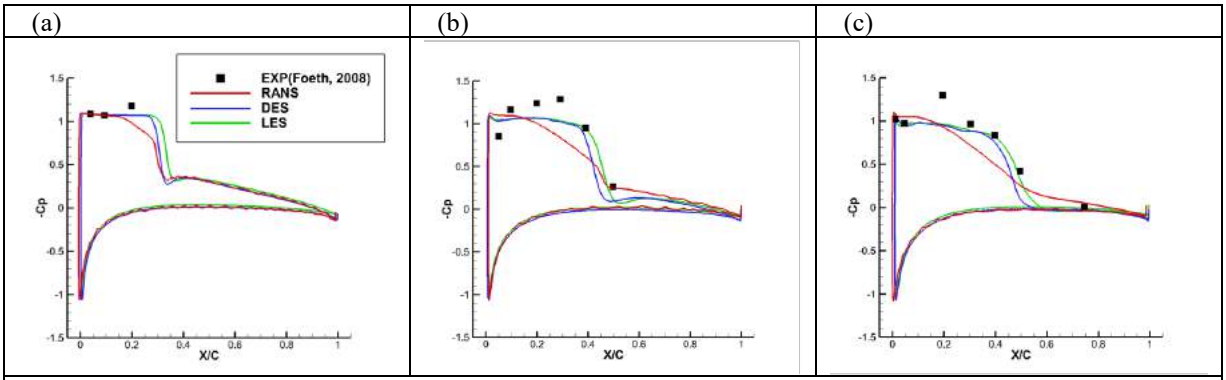

Figure 5: Mean Cp curve of cavitating flow at y/S=0.3 (a), 0.4 (b), 0.5 (c) according to turbulence models

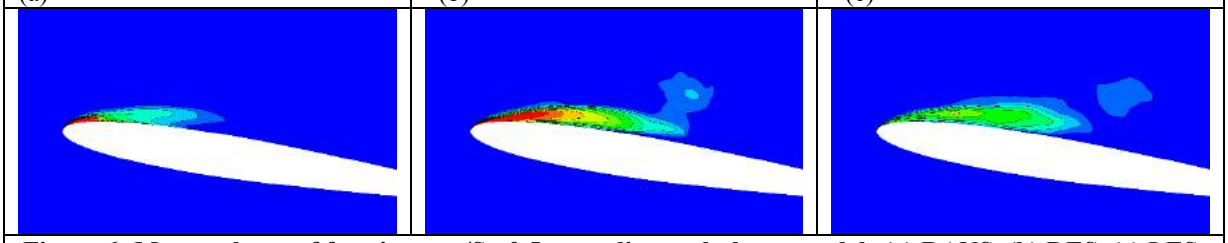

Figure 6: Mean volume of fraction at y/S= 0.5 according turbulence models (a) RANS, (b) DES, (c) LES.

SPL was measured using the frequency and PSD(Power Spectral Density), as mentioned in Section 3.2.2. The point at which the pressure was measured is indicated by coordinates Table 5 and in Figure 7. First, the measured sound pressure at the points was expressed as SPL_1, which was expressed as the reference SPL on a 1-m distance basis. The expression for SPL is shown below, where p is the measured pressure, p_0 is the reference pressure, and r is the distance to the measured position.

$SPL_1 = 20\,log_{10}(\frac{p}{p_0})$	[2]
$SPL = SPL_1 + 20\,log_{10}(r)$	[3]

Table 5: Location of probe to monitor pressure at top wall

Probe	X [m]	Y [m]	Z [m]
1	0.038	0.150	0.150
2	0.001	0.150	0.150
3	-0.013	0.150	0.150
4	-0.028	0.150	0.150
5	-0.043	0.150	0.150
6	-0.066	0.150	0.150

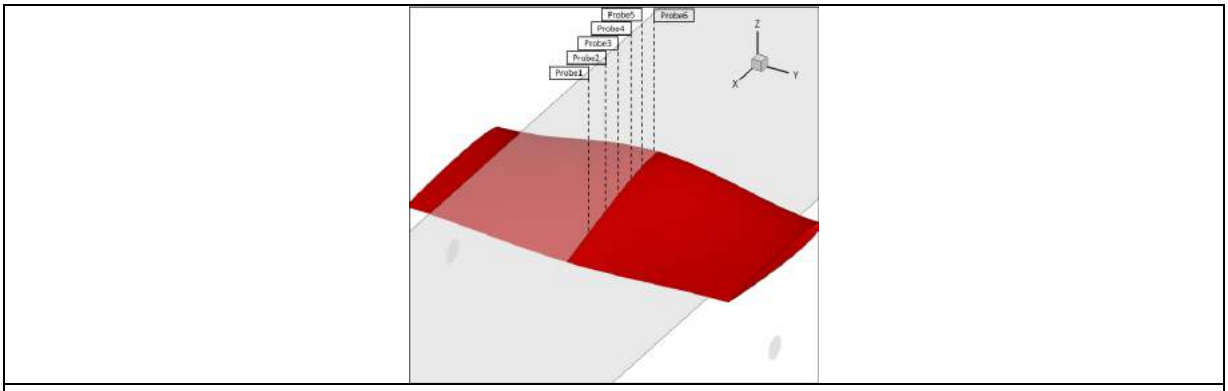

Figure 7: Geometry of Delft Twist11 hydrofoil and location of probes 1 to 6

SPL according to the distance is shown in Table 5 and Figure 8. The results were compared with Lidtke's(2016) numerical analysis paper, and the numerical method was confirmed to have used RANS. The results of the reference paper can be seen to be similar to those of the RANS model in this study, thereby verifying the results of this study. For DES and LES models, the results are more than 10 dB higher than the RANS model's SPL. Considering the accuracy of the DES and LES model's results, it was determined that the SPL of the DES and LES models was correct. In addition, in distance generally indicates a decrease in SPL, but the difference in distance was not significant.

Table 5: The results of SPL of wall pressure

SPL [dB]	LE/c	Lidtke (RANS)	RANS	DES	LES
Probe 1	1.25	152.30	155.07	164.46	167.02
Probe 2	1.12	153.00	155.30	165.03	167.63
Probe 3	1.08	153.20	155.41	165.19	167.81
Probe 4	1.05	153.38	155.54	165.23	167.81
Probe 5	1.02	153.43	155.62	165.24	167.85
Probe 6	1.00	153.50	155.66	165.23	168.28

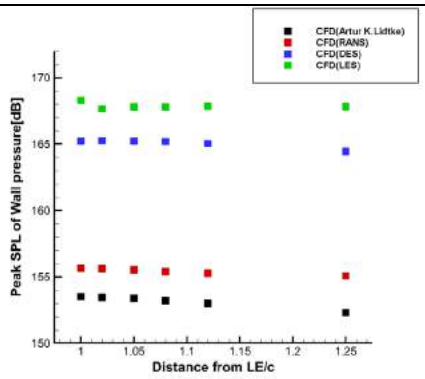

Figure 8: SPL of wall pressure with distance from LE/c according to turbulence models.

In addition, the above results are presented in Figure 9 and Table 6 according to the time step and the turbulence model. the results were from Probe 6, which is closest to the leading edge, and the results from the time step were compared with the LES model. As mentioned earlier, the results for each model were highest in the order of the LES, DES, and RANS models. Frequency also shows that the LES and DES models are most similar to the experimental paper by Foeth(2008). As mentioned in Section 3.2.2 for the results of other LES models in the time step, the lower the time step, the more similar the frequency is to the experimental results. SPL increases when the time step is lower.

(a) (b)

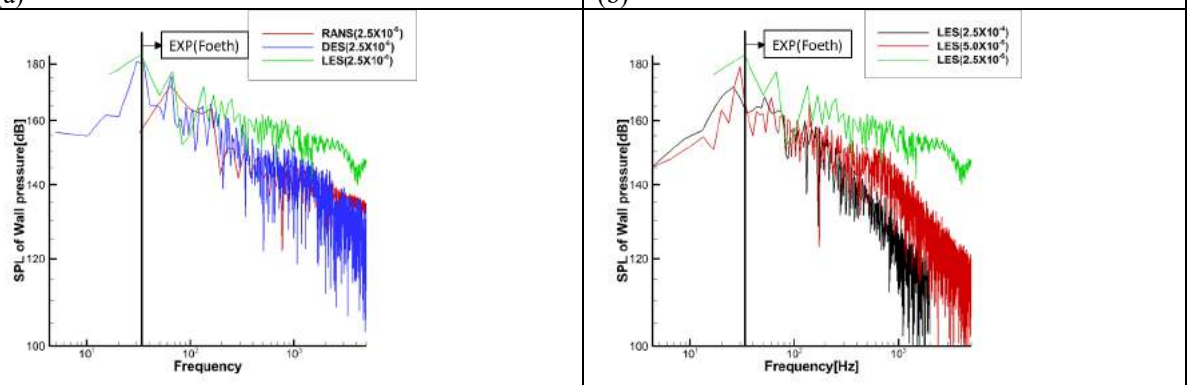

Figure 9: SPL of wall pressure using LES model according to time steps (a) and turbulence model (b)

Table 6: SPL_1 and SPL of wall pressure using LES model according to time steps and turbulence model at probe 6

	Time step	SPL_1 [dB]	SPL [dB]
LES	$2.5X10^{-4}$	171.74	155.26
	$5.0X10^{-5}$	179.10	162.62
	$2.5X10^{-5}$	184.76	168.28
RANS	$2.5X10^{-5}$	172.14	155.66
DES		181.71	165.23
LES		184.76	168.28

Next, SPL with or without cavitation is shown in Figure 10 and Table 7 for each model. The conditions of wetted flow are atmospheric pressure conditions, and the cavitating flow is the same as the experimental conditions. Results from the cavitating flow indicate that the LES model's result was the highest, as mentioned earlier, the DES model had similar results to the LES, and the RANS model result was 10 dB below the other two models.

In the case of wetted flow, the LES model was also the largest. However, the DES model was significantly smaller than the LES model and was similar to the RANS model, unlike for the cavitating flow. This is because of the RANS and DES models' characteristics. Unlike LES models that use eddy simulation, as mentioned in Section 3.2.2, these models use the RANS (SST k-ω) model near the wall to achieve more stable results. Therefore, the SPL of the RANS model is lower with or without cavitation, and the DES model obtains stable results near the wall.

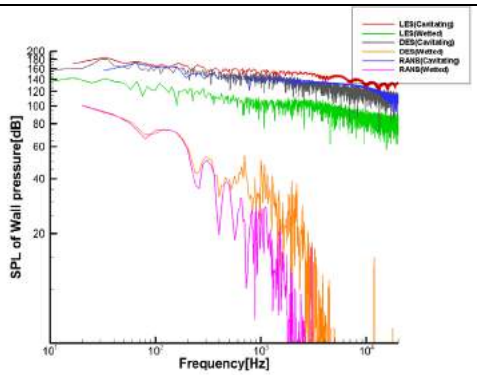

Figure 10: Comparison LES, DES, and RANS models; SPL of wall pressure according to cavitating flow and wetted flow.

Table 7: Comparison difference of SPL_1 and SPL according to cavitating flow and wetted flow

Probe 1	Flow	SPL_1 [dB]	SPL [dB]
LES	Cavitating	184.76	168.28
	Wetted	142.97	126.49
DES	Cavitating	181.71	165.23
	Wetted	100.8	84.32
RANS	Cavitating	172.14	155.66
	Wetted	100.9	84.42

Finally, the SPL was predicted and compared according to the cavitation number. The cavitation number conditions for the simulation were carried out with a total of six conditions, including atmospheric pressure conditions, experimental conditions, cavitation inception, and cavitation development conditions. The conditions are shown in Figure 11 and Table 8. The cavitation numbers of 3.1 and 3.0 are cavitation inception conditions, and the cavitation numbers of 2.5 and 2.0 are set for the cavitation development conditions.

(a) (b)

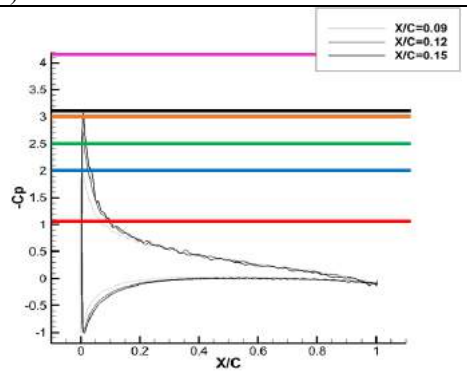

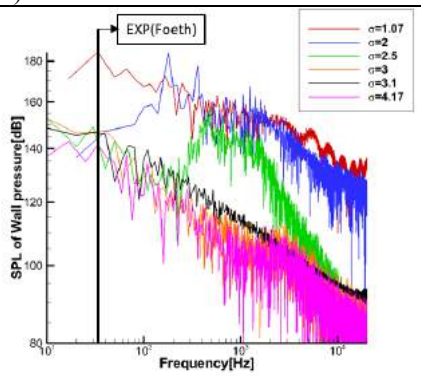

Figure 11: Condition of simulation according to cavitation number (a), and SPL-frequency graph of wall pressure according to cavitation number

The results are shown in Table 8 and on the right side of Figure 11. Overall, SPL increases when the cavitation number is smaller, the cavitation inception section increases by about 6 to 10 dB compared to the wetted flow, and the frequency cannot be shown. When the cavitation number is 2.5, the SPL is approximately 4 dB higher than the cavitation inception condition, and high frequency is created. In addition, the cavity volume was expressed according to the time series to confirm the frequency occurrence, which is shown in Figure 12. From the cavitation number of 2.5, we were able to check the fluctuation of cavitation.

Subsequently, when the cavitation number was 2.0, the SPL increased significantly, similar to the experimental condition when the cavitation number is 1.07. The frequency was also confirmed to be constant at about 120 Hz. The fluctuation of the overall cavity volume shows that the frequency decreases as the cavitation number decreases, and the cavity volume can be seen to increase as the cavitation number decreases.

cavitation numbers of 3.1 and 3.0 are cavitation inception conditions, and the cavitation numbers of 2.5 and 2.0 are set for the cavitation development conditions.

Table 8: SPL_1, SPL, and cavitation volume according to cavitation number

	Cavitation number σ	SPL_1 [dB]	SPL [dB]	Cavitation volume (m^3)
LES	4.17	142.97	126.49	0.00
	3.1	148.57	132.09	1.11E-10
	3.0	152.75	136.27	7.37E-10
	2.5	156.76	140.28	1.30E-8
	2.0	184.39	167.91	1.99E-7
	1.07	184.76	168.28	9.36E-6

(a) (b)

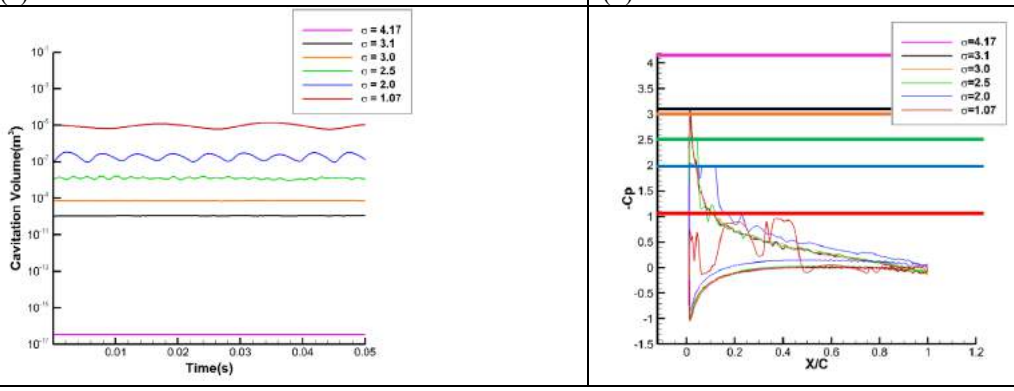

Figure 12: Cavitation-volume/time graph according to cavitation number (a), Cp curve according to cavitation number at an instantaneous time (b).

Finally, by comparing the cavitation features according to the cavitation number, the relationship between cavitation and noise was identified. The shape according to cavitation number is shown in Figure 13, and the Cp curve is shown in Figure 12. When the cavitation number is 4.17, cavitation does not occur, and when the cavitation number is 3.0 and 3.1, which are the cavitation inception conditions, there is very small cavitation in the leading edge. When the cavitation number is 2.5, we were able to see cavitation at the leading edge, and we confirmed that it was vibrating finely. The cavitation number of 2.0 indicates that cloud cavitation occurs, and as we have seen in Table 8, the SPL increases significantly in these conditions. Therefore, the reason for the significant increase in SPL is related to the development of cloud cavitation. The cavitation number of 1.07 confirmed that cavitation is fully developed.

(a) σ=4.17	(b) σ=3.1	(c) σ=3.0
(d) σ=2.5	(e) σ=2.0	(f) σ=1.07

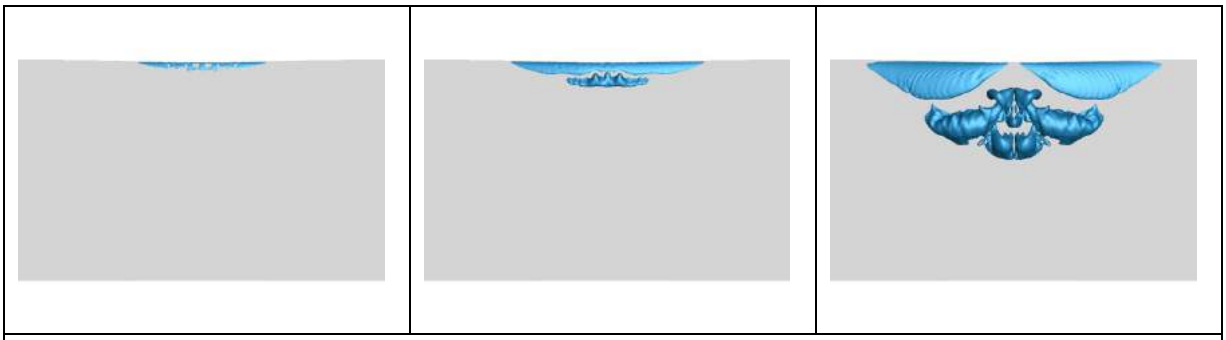

Figure 13: Cavitation features according to cavitation number. From (a) to (f), the cavitation number(σ) is 4.17-1.07 (experiment condition)

CONCLUSIONS

In this study, cavitation simulation was performed using a Delft Twist11 hydrofoil. Several numerical studies have been carried out using Foeth's (2006, 2008) experimental results. This study was conducted according to various turbulence models and time steps to analyze the correlation between cavitation and noise. The accuracy of the results was best in the order of LES, DES, and RANS models, and the lower the time step overall, the more similar the experimental results were. In the case of the RANS models, the periodic movement of the cavitation was not predicted, and accordingly, the noise produced by the cavitation was not predicted. Cavitation was created once after the pressure drop, but the cavitation no longer developed after shrinkage, as in Figure 5. Thus, the accuracy of the frequency was reduced, and the result was that the SPL was low without the creation of the cloud cavitation. Lidtke et al(2016). predicted SPL using the RANS model, and using the RANS model of this study, we could see that it was similar to the predicted SPL.

In the case of the DES model, the accuracy in predicting cavitation and noise was high, and for sheet cavitation near the wall, stable cavitation features were confirmed like in the RANS model. However, away from the wall, periodic cloud cavitation was formed, like in the experiment results and the LES model. This is due to the use of the RANS (k-w) model on the wall and the other parts following the characteristics of the LES model, which is a characteristic of the DES model. Therefore, SPL was similar to the RANS model in stable wetted flow where no cavitation occurred. In cavitating flow, where pressure fluctuation occurred due to periodic cavitation, it was similar to RANS model near the wall and similar to the LES model in other areas of cloud cavitation. In addition, the SPL was similar to the LES model because of the occurrence of a cloud cavitation that affected noise.

For LES models, cavitation features were similar to DES models. The development and contraction of cavitation were well illustrated, and the Q-criterion, which indicates the degree of turbulence, was also well shown along the cavitation features. In addition, a similar frequency was obtained from Foeth's (2008) experiment results. The SPL appeared similar to the DES model with similar cavitation geometry and frequency. However, the SPL results in the wetted flow state were different from the DES model.

Using the above results, we were able to obtain the correlation between cavitation and SPL by simulating it according to the cavitation number. We could see that noise increased as cavitation occurred, especially with the occurrence of cloud cavitation, which resulted in a significant increase in SPL.

Future research will simulate the noise generated by the Tip Vortex Cavitation (TVC) using a NACA16-020 because TVC occupies a large amount of noise generated by cavitation. After conducting a study on the correlation of noise according to the case of cavitation, we will conduct a study to predict noise from propellers of ships by simulating propellers.

ACKNOWLEDGEMENTS

This research was funded and conducted under 「the Competency Development Program for Industry Specialists」 of the Korean Ministry of Trade, Industry and Energy (MOTIE), operated by Korean Institute for Advancement of Technology (KIAT). (No. P0012646, HRD program for Global Advanced Engineer Education Program for Future Ocean Structures)

REFERENCES

Abolfazl Asnaghi, "Developing Computational Methods for Detailed Assessment of Cavitation on Marine Propellers" the degree of licentiate of engineering, Department of shipping and marine technology, Chalemers university of technology, Göteborg, Sweden, 2015.

Artur K. Lidtke, Stehen R. Turnock, Victor F. Humphrey., "Multi-Scale Modeling of Cavitation-Induced Pressure Around the Delft Twist11 Hydrofoil" 31st Symposium on Naval Hydrodynamics Monterey, CA, USA. 2016.

Bensow R.E., “Simulation of the unsteady cavitation on the Delft Twist11 foil using RANS, DES and LES” Second International Symposium on Marine Propulsors. Hamburg, Germany. 2011.
Foeth, E.J., C.W.H. van Doorne, T. van Terwisga. B. Wieneke., “The structure of unsteady cavitation. Part I: Observation of an attached cavity on a three-dimensional hydrofoil” 6th International Symposium on Cavitation, Wageningen, The Netherlands. 2006.
Foeth, E.J., C.W.H. van Doorne, T. van Terwisga. B. Wieneke., “The structure of three-dimensional sheet cavitation” PhD Thesis, TU Delft. 2008.
Guilherme Vaz; Thomas Lloyd and Arun Gnanasundaram “Improved Modeling of sheet cavitation dynamics on Delft Twist11 Hydrofoil” 7th International Conference on Computational Methods in Marine Engineering. 2017.
M Hoekstra, Tom van Terwisga, E.J.Foeth “smp’11 Workshop -Case 1: DelftFoil” Second Intermational Symposium on Mairne Propulsors. 2011.

A STUDY ON SHIP PERFORMANCE USING A RANS SOLVER: COMPARISON OF REQUIREMENT POWER PREDICTION METHODS IN IRREGULAR WAVES

Soon-Hyun Lee[1*], **Jun-Hui Cho**[1], **Gu-Hyun Kim**[1], **Kwang-Jun Paik**[1]

ABSTRACT

A series of numerical studies have been conducted to suggest the reasons and methods for considering self-propulsion performance that changes according to wave conditions using KVLCC2. By comparing the propulsive factors according to the wave conditions, the change of self-propulsion performance was found. It showed that the propulsion efficiency decreased similarly to the tendency of the added resistance that increases in regular waves and the required power increased according to the wave height. In advance, power prediction in the irregular waves was done using a spectral method as an indirect method, which was used to derive the increase in variables in a target sea state with a quadratic transfer function and wave spectrum. In this study, the 4 spectral methods were considered depending on the parameters used and can be divided into the methods (SA, TNM, QNM) that use the assumed self-propulsion factors and a proposed method that considers the changes of factors in wave conditions. As a result, when considering the change of self-propulsion factors in the sea state where the wave height increases, the power was estimated to be relatively low. This indicates that as the wave height increases, the linear relationship between the variables and the wave height decreases. This paper suggests the necessity that considers the effect of waves on self-propulsion for estimating the realistic power of ships.

KEY WORDS

Reynolds averaged Navier-Stokes (RANS), Regular wave, Self-propulsion test, Propulsive coefficient, KVLCC2, Added resistance, Delivered horserpower (DHP), Virtual disk, Irregular wave

INTRODUCTION

One of the methods to reduce CO2 emission is reducing the operating speed of a ship, which leads to a reduction of engine capacity. The MEPC (Marine Environment Protection Committee) pointed out that, the engine capacity of the ship must satisfy the minimum speed to advance in heavy sea conditions. Res.MEPC.232 (65) underline the 2013 Interim guidelines which estimates the minimum power, minimum navigational speed of a ship, and heavy sea conditions. A formalized process is still being discussed, and efforts are ongoing to determine the performance in heavy sea conditions (MEPC.1/Circ.850/Rev.3, 2021). Even if heavy sea conditions are determined, much research is still needed for model tests and numerical simulations of a ship in a state similar to a real sea environment. In real sea conditions, the direction, wave height, and wavelength of the waves are not constant. In addition, significant wavelength and wave height generated by differences in the marine environment vary depending on the route of the ship and are represented by the wave spectrum of the sea.

Generally, there have been many studies on ship performance in regular wave conditions. As an advanced study of regular wave condition, research on the required power of ships in an irregular wave corresponding to the real sea states are being steadily conducted. To consider the irregular wave condition, power estimation can be divided into a direct method and an indirect method. The direct method is to measure the resistance and propulsion performance acting on a ship by making the

[1] Department of Naval Architecture and Ocean Engineering, Inha University, Incheon, Republic of Korea

irregular wave directly. On the other hand, the indirect methods calculate the increased power through the empirical formulas. One of the representative indirect methods is a spectral method that calculates the power in the irregular waves using the superposition of waves and transfer function derived from regular wave results.

The spectral method was proposed by Maruo (1957). It was suggested that the resistance is proportional to the square of the wave height. In addition, the propulsion performance in irregular waves can be estimated by linearly superimposing the results of regular waves. This method was applied to an experiment by Gerritsma et al. (1960) with two wave spectra, and it was confirmed that the required power was 2-3 times that in calm water. Using a DART EUROPE container ship, the required power in the actual seaway was estimated by Aerssen and Vanslys (1972) and compared with the case of using the spectral method by Jinkine and Ferdinande (1974). It was confirmed that the required power can be underestimated when the indirect method is used. Pérez Arribas (2007) estimated the increase in resistance of an S175 hull in irregular waves using the ITTC standard spectrum corresponding to sea state 4 and compared it with the results of the momentum energy method and pressure integration method. Both methods showed that the increase in resistance was underestimated because it is difficult to capture the property of added resistance in the short wavelength region.

Tsujimoto et al. (2009, 2019) systematically studied the increase in power and the decrease in speed in real sea conditions according to the Beaufort number for a container and tanker. In addition, by using marine environment data, the increase in added resistance was predicted, and the increase in power was compared with the full-scale data to validate the performance of the prediction method. Yu et al. (2019) compared the increase in resistance measured by a model test with the KVLCC2 in irregular waves and showed a tendency for the spectral method to measure the resistance excessively. Although Yu et al. (2019) showed the spectral method can overestimate the resistance, Jinkine and Ferdinanade (1974) showed that the increase in resistance derived by the spectral method was underestimated when compared to the full-scale data. The difference between the above results can occur depending on the type of ship and the variables used in the spectral method. The prediction process can be even more complex in real sea conditions when considering the fouling of ships and the decrease in manoeuvrability in the heavy sea. Therefore, to this day, it is still being researched to predict the increase of power in real sea conditions, and continuous review is necessary through sufficient experiments and numerical analysis results.

The first purpose of this study is to observe the changes in propulsive factors based on the self-propulsion test results simulated by CFD. The reliability of the CFD calculation was evaluated through a series of verification processes. Changes in the propulsive factors were illustrated by wavelength and wave steepness, and the causes of the factors were tried to be scrutinized.

The second objective of this study is comparing the minimum required power in irregular waves according to the estimated methods (Indirect methods). The first method is a SA (Simplified Assessment) guideline proposed by Res.MEPC.232 (65). As the second and third methods, the ITTC recommended procedure 7.5-02-07-02.2, TNM (Thrust and Revolution Method) and QNM (Torque and Revolution Method) are also applied and compared. Meanwhile, the previous three methods estimate the DHP (Delivered Horsepower) by assuming self-propulsion factors in wave conditions or through empirical formulas. As a result of this study, the change of DHP was suggested as a transfer function to use the spectral method. By using the DHP obtained through the self-propulsion test in the regular waves as the transfer function, the influence of the self-propulsion factors that change in the waves is included.

Objective vessel and coordinate system

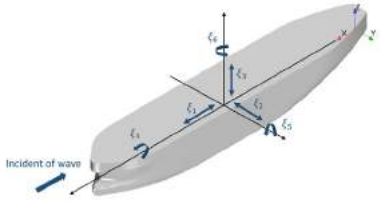

Figure 1: Coordinate system of ship

The KVLCC2 hull, which is 300,000 tons of crude oil tanker and a general form of modern commercial tankers, has been studied. This hull has a large bulbous bow and is a low-speed full ship with a long parallel mid-body. The main particulars of KVLCC2 and target propeller KP458 are denoted in Table 1. Three scales ratios are considered, and a scale ratio of 100 was used for most calculations. The purpose of using the three scales is to validate the resistance performance in calm water and

wave conditions (Scale ratio=100), the self-propulsion in calm water (Scale ratio=58), and the self-propulsion performance in waves (Scale ratio=177.8).

The coordinate system used for the calculation is shown in Fig. 1. The x-axis is positive from the stern to the bow, the y-axis is the positive direction to the port side, and the z-axis is the opposite direction of gravity. The origin of the coordinate system set as the stern and the free surface was realized at the point where the z-axis is 0. Also, the Wave travels in the negative x-direction.

Table 1. Main particulars of KVLCC2 & KP458

	Full-scale	EFD model & CFD model	CFD model	
Scale ratio	1	177.8	100	58
Length between perpendiculars, L_{PP} (m)	320.000	1.800	3.200	5.517
Breadth, B_{WL} (m)	58.000	0.326	0.580	1.000
Draft, d (m)	20.8	0.117	0.208	0.359
Wetted surface area (with rudder), S_w (m^2)	27,467	0.869	2.747	8.165
Displacement, ∇ (m^3)	312,622	0.056	0.313	1.602
Vertical centre of gravity, KG (m)	18.6	0.105	0.186	0.321
Longitudinal center of buoyancy (%L_{PP})		3.48		
Block coefficient, C_B		0.8098		
Radius of gyration		K_{xx}=0.4B_{WL}, K_{tt} & K_{zz}=0.25L_{PP}		
		KP458		
Diameter, D_P (m)	9.860	0.055	0.098	0.170
Pitch ratio, P/D_P (0.7R_P)		0.7212		
Thickness ratio, t/c (0.7R_P)		0.0667		
Chord ratio, c/D_P (0.7R_P)		0.2338		
Number of blades		4		
Hub ratio		0.155		

Numerical setup & Convergence test

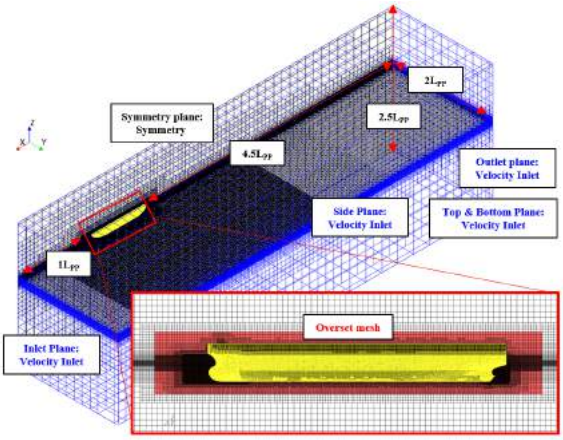

Figure 2: Mesh distribution and Boundary conditions of the domain

The CFD computations are conducted with commercial RANS (Reynolds Averaged Navier-Stokes) solver STAR-CCM+ 15.06 version, which can generate unstructured grids relatively simply and shows high stability in calculations. As the governing equations, incompressible N-S (Navier-Stokes) equation and the continuity equations are implemented with Realizable K-Epsilon turbulence model. The VOF wave model has been selected to simulate the free surface and the regular waves with an HRIC (High-Resolution Interface Capturing) scheme. The ship motion is 2DOF (Degree of Freedom), free with heave and pitch motion with fixed surge motion. To cover the various wavelength, a DFBI model is used with an overset mesh that can deal with the grid deformation.

Since the simulation is transient, the simulations were conducted as an implicit unsteady model with a first-order temporal scheme. As the time-step, a time corresponding to 1/350 of the encounter wave period according to equation (1) was chosen. Furthermore, as the number of inner iterations, 10 inner iteration was adopted for converged computation. The convective courant number set lower than 1.0 and wall Y+ was around 60 in the bow shoulder part.

$$\omega_e = \omega - k \times V \quad [1]$$

For the self-propulsion test, the virtual disk, body for the propeller method, was applied. In particular, this method does not need to rotate the propeller with a very small-time step (Generally, the propeller model is required to rotate about 2 degrees in one time step to obtain accurate thrust and torque). Furthermore, there is no grid distribution for the shape of the propeller, it is convenient to apply, and the computation time is greatly reduced. A detailed description and verification of the virtual disk can be found in the previous study of this paper (Lee, et al 2021)

Two grid systems were used to evaluate resistance and self-propulsion performance. Firstly, the grid used in the resistance computation is shown in Figure 2. The distance from the hull to the inflow boundary was $1L_{PP}$, which is intended to minimize wave dissipation. $2L_{PP}$ was applied to the side to observe wave propagation, and it had a length of $4.5L_{PP}$ including grid damping area in the downstream area of the hull to prevent wave reflection. On the other hand, in the case of the self-propulsion test, the full domain was generated by completely symmetrical half-width domains, and the domain was reduced by $0.5L_{PP}$ in the inflow and outflow planes.

In this study, since the test wave conditions are varied, the grid system was also modified according to the wavelength and wave height. In detail, about 90-150 cells are used for the wavelength, and 16-24 cells are located at the wave height. Additionally, as shown in Figure 2, a square fine grid was applied to the bow and stern to simulate the flow of the wave flowing into the bow and the wake of the stern.

To confirm the convergence, the resistance coefficient of the calm water was compared under the condition of 15.5 knots, the design speed of KVLCC2. The coefficient values are dependent on three different timesteps and grids as shown in Table 2. To determine the convergence, the GCI (Grid Convergence Index) values proposed by Celik et al. (2008) were compared. Through the resistance computation, it was observed that as the time step becomes smaller and the grid becomes finer, it converges to one value. The GCI value by the time step was 0.005%, and the value by the grid was 0.121%, indicating that the convergence of the calculation is sufficient. Based on the test, T3G3, a converged condition, was used for resistance and self-propulsion computation of calm water. The grid around the hull was fixed according to the condition of T3G3 for calculation in wave condition, and only the grid of the free surface was changed according to the wave condition.

Table 2. Comparison of the resistance coefficient and motions in the calm water (*Fr*= 0.142)

Variables	Case no.	Base size (× L_{PP})	Number of grids	Time step (s)	$C_{TM}\times10^3$	Grid Convergence Index (GCI) (%)
Time step	T1G1	0.028	909,292	0.1	5.116	0.005
	T2G1	0.028	909,292	0.01	4.795	
	T3G1	0.028	909,292	0.005	4.787	
Grid fineness	T3G1	0.028	909,292	0.005	4.787	0.121
	T3G2	0.020	1,639,139	0.005	4.783	
	T3G3	0.014	2,072,500	0.005	4.766	

Validation & Verification

To verify the performance of resistance on hull and motion response, the model test results and CFD results of WAVIS2 were compared in Table 3 according to the shipping speed. In the case of resistance coefficient, the difference between EFD is less than 5%, but in the case of motion, the error rate is large. Considering that the absolute values are very small, it seems the motions also have a similar tendency depending on the speed of the ship.

The propulsive factors at *Fr*=0.142 are compared according to the scale ratio (58, 100, 177.8) as shown in Table 4. The case with scale ratio=100 was mainly used in this study, which is possible to compare with the resistance results (Kim et al. 2010) in *Fr*=0.092. Meanwhile, there are the experiment self-propulsion test results with two different scales. The 58 scales (Kim et al. 2001) performed by KRISO and the IUTT (Inha University Towing Tank) scale of 177.8 were considered. To validate the CFD results, it was tried to consider the results of both scales.

Table 3. Comparison of the resistance coefficient, sinkage, and trim in the calm water (Scale ratio: 100)

	Ship speed	$C_{TM}\times10^3$	$\sigma\times10^2$ (m)	τ (deg)
Kim et al. (2010) EFD	*Fr*= 0.092	5.161	-0.1300	0.0243
	Fr= 0.142	4.872	-0.3136	0.0968
Kim et al. (2010) CFD	*Fr*=0.092	4.886 (5.3%)	-0.1307 (-0.5%)	0.0566 (-133.4%)
	Fr=0.142	4.767 (2.2%)	-0.3135 (0.0%)	0.1304 (-34.7%)
Present	*Fr*=0.092	5.152 (0.2%)	-0.1198 (23.1%)	0.0591 (-143.6%)
	Fr=0.142	4.766 (2.2%)	-0.3190 (-1.7%)	0.1347 (-41.1%)

Firstly, when the virtual disk was applied, a similar trend is observed when comparing the case of using the propeller model. Although the propeller model comes out more similar to the experiment in terms of POW (Propeller Open Water) efficiency, it is judged that the virtual disk shows sufficiently similar performance. As the next step, when comparing the results of 58 and 177.8 scales using virtual disk, it was observed that the thrust deduction factor and the wake fraction factor increase as the scale decreases. The size of the boundary layer increases as the scale decreases. The thickened boundary layer on the small scale means that the speed of inflow into the propeller is slowed, resulting in a relatively large wake fraction factor. In terms of thrust deduction factor, the pressure distribution in the stern during propeller rotation was similar regardless of the scale. Therefore, it is thought that the thrust deduction factor appears large at the low scale where the initial pressure was large. Although it was pointed out that the propulsive factors are changed in different scale ratios, it seems acceptable enough to represent the propulsion performance.

Table 4. Comparison of the self-propulsion factors

Case	Kim et al. (2001), EFD	Virtual Disk, CFD	Propeller Model, CFD	Virtual Disk, CFD	Inha University, EFD	Virtual Disk, CFD	Virtual Disk, CFD
Fr	0.142						0.092
Scale	58	58	100	100	177.8	177.8	100
t	0.190	0.194	0.205	0.198	0.239	0.225	0.224
w_{TM}	0.443	0.425	0.420	0.456	0.428	0.488	0.476
w_{TS}	0.305	0.323	0.315	0.326	0.330	0.340	0.343
η_R	1.005	1.022	1.080	1.022	1.042	1.034	1.024
η_H	1.165	1.191	1.161	1.190	1.135	1.175	1.181
η_O	0.620	0.549	0.559	0.548	0.541	0.558	0.557
η_D	0.726	0.669	0.701	0.666	0.640	0.677	0.674

(a) (b)

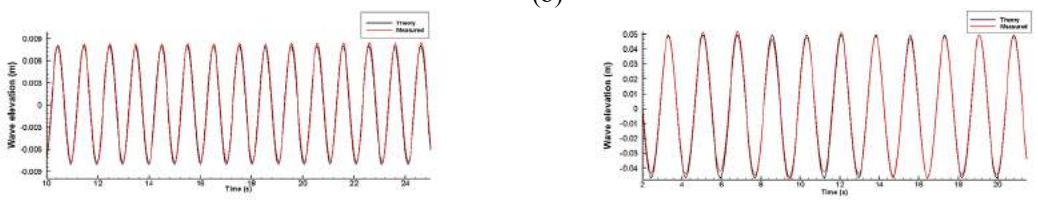

Figure 3: Comparison of generated wave elevation, (a) λ/L_{PP} =0.5, H/λ =0.01, (b) λ/L_{PP} =1.5, H/λ=0.02

As following conditions, two different ship operation speed was tested. Considering the speed at which the ship slows down in real seaway, the *Fr*=0.092 (10knots) is the target speed in this study. Also, *Fr*=0.037 (4knots) was chosen to study the MPP condition which represents the adverse weather that can cause manoeuvrability problems within minimum propulsion power. On the other hand, propulsive factors showed similar values except for the wake fraction factor in low ship speed. It is judged that a larger low-speed region of the stern part is distributed due to the lowered operating speed.

A series of verifying procedure conducted to validate the performance of the ship in waves. The added resistance and self-propulsion performance were tested for various wave conditions from long to short wavelength region, and the analysis conditions are shown in Table 5. The case marked with IUTT Exp. represents the condition that is comparable to the IUTT experiment (Lee et al., 2021). In the condition of Fr=0.092, the effect of the wave steepness was also considered.

Table 5. The cases of resistance and self-propulsion test

Ship speed	Fr=0.142 (15.5knots)	Ship speed	Fr=0.092 (10knots)	Ship speed	Fr=0.037 (4knots)
Wave steepness, H/λ	0.01	Wave steepness, H/λ	0.01, 0.02	Wave steepness, H/λ	0.01
Test wavelength, λ/L_{PP}					
Resistance	Self-Propulsion	Resistance	Self-Propulsion	Resistance	Self-Propulsion
Calm water (IUTT Exp.)	Calm water (IUTT Exp.)	Calm water (IUTT Exp.)	Calm water (IUTT Exp.)	Calm water (IUTT Exp.)	Calm water
0.5 (IUTT Exp.)	-	0.3 (IUTT Exp.)	-	0.3 (IUTT Exp.)	-
0.7 (IUTT Exp.)	-	0.5 (IUTT Exp.)	0.5 (Exp.)	0.5 (IUTT Exp.)	0.5
0.9 (IUTT Exp.)	-	0.7 (IUTT Exp.)	0.7	0.7 (IUTT Exp.)	0.7
1.0 (IUTT Exp.)	-	0.9 (IUTT Exp.)	0.9 (Exp.)	0.8	0.8
1.1 (IUTT Exp.)	-	1.0 (IUTT Exp.)	1.0 (Exp.)	0.9 (IUTT Exp.)	0.9
1.3	-	1.1 (IUTT Exp.)	1.1	1.0 (IUTT Exp.)	1.0
1.5	-	1.3	1.3	1.1 (IUTT Exp.)	1.1
-	-	1.5	1.5	1.3	1.3
-	-	2.0	-	1.5	1.5
-	-	-	-	2.0	-

As a preliminary process, the verification of the waves generated in the computation domain was performed. The generated wave conditions were selected as the short-wave condition (λ/L_{PP} =0.5, H/λ =0.01) and the long-wave condition (λ/L_{PP} =1.5, H/λ =0.02). The wave measurement point was set at the FP point where the wave enters the vessel. As shown in Figure 5, the generated waves are well-matched with the theoretical wave.

In terms of the influence of the wave acting on the hull, the added resistance coefficient and motion RAOs (Response Amplitude Operator) were compared with experiment and empirical formula. The Osaka University (OU) and Seoul National University (SNU) experimental results are adopted at the design speed, Fr=0.142 (Larsson et al., 2013, Park et al., 2016). The results under the low-speed conditions of Fr=0.092 and 0.037 were compared with the IUTT experiment.

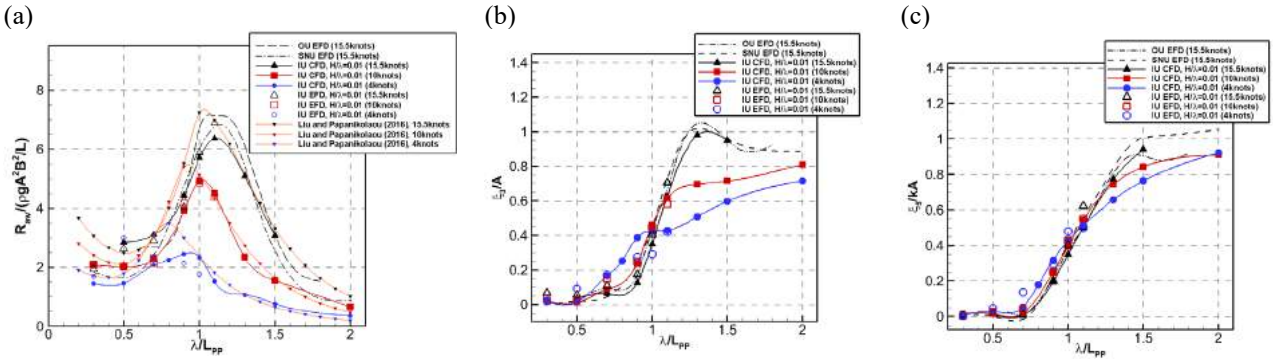

Figure 4: Comparison of (a) added resistance coefficient, (b) Heave coefficient, (c) Pitch coefficient

At first, the results of the CFD at the design speed show reliable trends in resistance and motion RAO compared with the experiments as shown in Figure 4. In general, the present results well evaluate the performance of the added resistance of ship in the wave. At Fr=0.092 present CFD shows the tendency of the added resistance and heave motion to decrease according to the operation speed, which is also found in EFD results. When the shipping speed decreases, the peak of the added resistance coefficient is shifted to the shorter wavelength region, which shows that the encounter wave period is

changed, and the resonance frequency moves to the shorter wavelength region. In order to indirectly confirm the following results, the added resistance values predicted using the empirical formula proposed by Liu and Papanikolaou (2016) are also compared in Figure 4 (a). The theoretical results also show a decrease in the resistance coefficient and a shift in the peak wavelength. On the other hand, the results at Fr=0.037 (4 knots) show slightly different trends in all three of the EFD, CFD, and empirical formulas. It illustrates the difficulty of interpreting the short wavelength region with a very low speed.

Table 6. Comparison of DHP according to wave conditions

Operation speed: Fr=0.092 (10 knots)								
	IUTT EFD	CFD	IUTT EFD	CFD	IUTT EFD	CFD	IUTT EFD	CFD
H/λ	Calm water		0.02		0.02		0.01	
λ/L_{PP}	Calm water		0.5		0.9		1.0	
EHP (kW)	4,203	4,180	7,465	7,143	28,149	22,629	11,528	11,515
DHP (kW)	6,721	6,354	13,228	12,307	58,025	54,294	23,632	22,425

Finally, it was reviewed the self-propulsion performance in the waves. For performance evaluation, same as calm water condition, ITTC 1978 performance prediction method was used. For the application of the method, thrust and resistance values for each number of propeller revolutions are required. In this study, all these values are determined by time-series average values. For the stability of the computation, the ship moved forward without propeller rotation while the encountered wave passed for 10 cycles. After the wave stabilized, thrust, torque, and resistance for 3 cycles at one rotational speed were used. Two rotation rates per one condition were used to estimate the self-propulsion point. The predicted values are compared with the IUTT EFD result as shown in Table 6. The CFD predicted value can represent the increasing trend of power according to the wave conditions, just like EFD, and the quantitative error is less than 10%, so fair agreement to represent the self-propulsive performance. Meanwhile, it was observed that the amounts of EHP (Effective Horsepower) and DHP increasing in waves compared to the calm water conditions. Here, changes in EHP exhibit the added resistance, and changes in DHP represent changes in propulsion efficiency. It can be thought that, due to the above effect, the power required in the wave with high wave height is significantly increased compared to that of calm water.

Comparison of the propulsive factors according to wave conditions

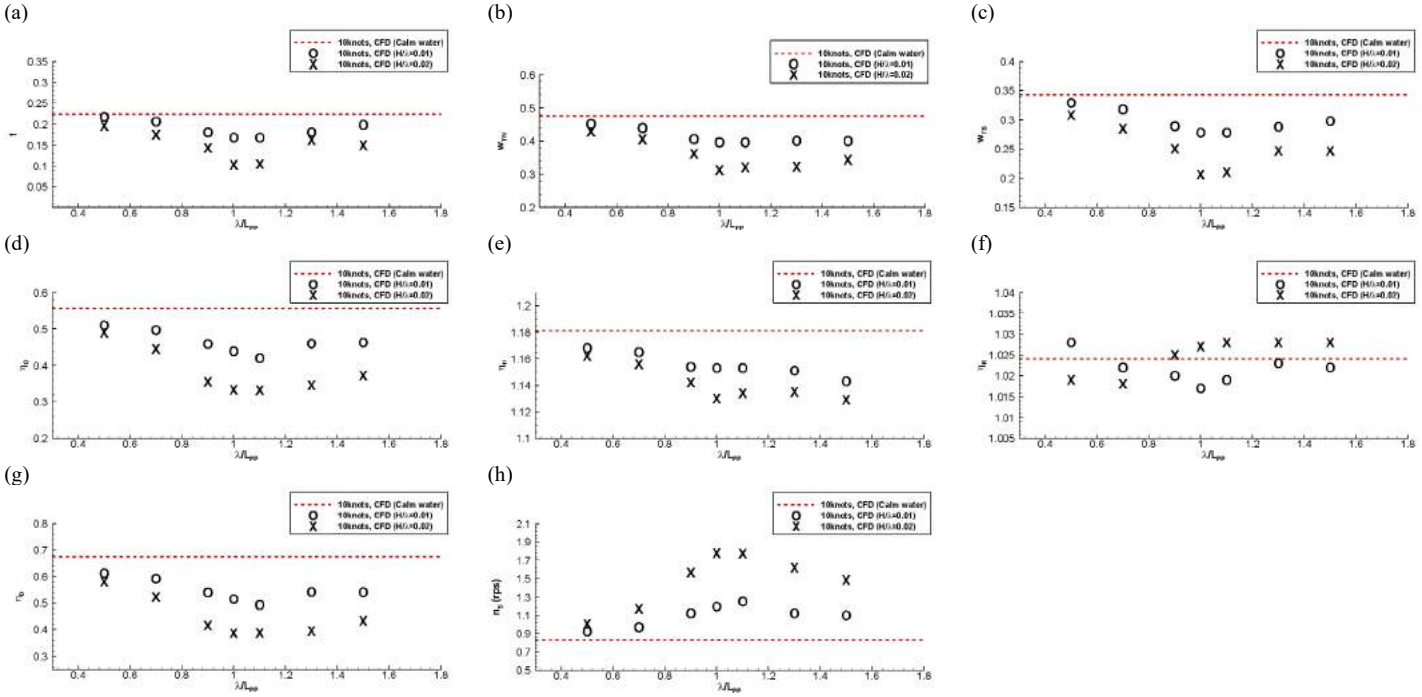

Figure 5: Comparison of the propulsive factors according to wavelength and wave steepness,
(a) Thrust deduction factor, (b) Wake fraction factor in model scale, (c) Wake fraction factor in full scale,
(d) Propeller Open Water efficiency, (e) Hull efficiency, (f) Relative rotational efficiency,
(g) Quasi-propulsive efficiency, (h) Propeller revolution in full scale

In wave condition, the propeller rotation rate increase compared to calm water due to the increase of resistance, and thus the self-propulsion point is changed. In this study, changed in propulsive factors in waves were identified through a series of processes. Based on the ITTC 1978 performance prediction method, the self-propulsion point in wave condition was determined. At first, towing force in calm water condition was calculated. Next, the self-propulsion computations are conducted in waves for two propeller rotations. Assuming that the ship resistance, thrust, and torque change linearly through two revolutions, find the point where the difference between thrust and resistance equals the towing force. Based on the determined point, the self-propulsion factors are determined using the thrust identity method (ITTC, 2014). This study tried to observe the change of wavelength and wave steepness for propulsive factors in Fr=0.092.

As shown in Figure 5, the predicted propulsive factors change according to the wave conditions. At first, the thrust deduction factors and wake fraction factors similarly decrease depending on the wave condition, which is a similar way to the increase in added resistance. The cause for the decrease in the thrust deduction factor is that the effect of the propeller rotation on the ship is reduced in waves. In the calm water, the pressure at the bottom of the ship is lowered as a whole when the propeller rotates, and it causes that the pressure to recovery too slow. On the other hand, when the propeller does not rotate in the wave, the pressure change occurs quickly. When the propeller rotates, it is observed that the change in the average pressure during the wave is relatively small. In addition, the pressure changes due to the hub vortex acting on the rudder are reduced by the movement of the ship in the wave. It is judged that the thrust deduction factor decreases during the wave because the change in the pressure distribution in the wave is relatively low. The decrease in the wake fraction factor is due to an increase in the average flow velocity entering the propeller plane in the wave. Shin et al. (2020) showed that the propeller inflow velocity varies according to the encounter frequency of the ship and that the axial velocity increases.

As with the two factors that have been changed, the efficiency of the ship also depends on the wave conditions. In Figure 5 (d), the propeller open water efficiency decreases in waves, and the decrease rate is the largest in the resonance frequency region. Although it slightly increases in the long-wavelength region, it still shows low efficiency. This is considered to be due to the increase of the overall flow velocity in the wave and the greater the influence of the particle velocity as the wave increases. Eom et al. (2021) indicated that the particle velocity due to the wave can influence the propeller performance. Next, in the case of hull efficiency, it gradually decreases as the wave height increases. It is judged to cause a remarkable change in the performance of the ship because the change of shape of the bow and stern, which vertically does not have a constant shape, increases as the wave height increases. In a similar concept, Yang et al. (2018) have studied in the short waves that the shape above the still water level can affect the added resistance of the ship. On the other hand, it shows that the change in relative rotational efficiency is insignificant regardless of the wave. Finally, the change in quasi-propulsive efficiency, which is the product of three efficiency values (η_O, η_R, and η_H), appears similar to the trend of POW efficiency. Through this, it shows that the propulsion efficiency descends according to the wave conditions, and it can be confirmed that the change is greatest in the resonance condition and the condition of high wave height. Corresponding to this, the propeller revolution in the wave rises, and the shape of the increase is similar to the distribution of the added resistance coefficient, and the higher the wave height, the larger it becomes.

Spectral method

The spectral method was proposed by Maruo (1957) based on the theory that the effects of regular waves can be linearly superimposed. Through linear superposition, it is possible to estimate the forces (resistance, thrust, and torque) and the motion response change in irregular waves. In this method, the assumption that the variables are proportional to the square of the wave height is used for superposition, which is represented as a quadratic transfer function. And the wave spectrum is required to consider the sea state. Since the spectral method does not need to directly perform experiments or computation in irregular waves, it is possible to consider irregular wave conditions in a simple.

In the process of estimating power in the irregular waves, the spectral method derives the amount of change in the variable used, and the method is divided according to the subsequent process. In this study, the four methods were considered: SA using added resistance [Res.MEPC.232 (65)], TNM, and QNM using trust and torque (ITTC recommended procedure and guideline 7.5-02-07-02.2), and the change of DHP, which is the method proposed in this paper. Methods are divided into SA, TNM, and QNM methods using force (resistance, thrust, and torque) linearity for the wave height, and the case of using DHP values in regular waves. In the case of using the force as the transfer function, it is obtained through conservative values or empirical formulas when selecting self-propulsion factors that change in waves. On the other hand, in this study, the spectral method was performed under the assumption that the value of DHP obtained through self-propulsion computation in waves is proportional to the square of the wave height to consider the self-propulsion factor that changes in wave conditions.

$$\delta P_{D,Irregular} = 2\int_0^{\infty} \frac{\delta P_D(\omega)}{\zeta_a^2} S_{\zeta\zeta}(\omega)\, d\omega \qquad [2]$$

This procedure first makes a transfer function based on the computation results in a regular wave [$\delta P_D(\omega)$]. The obtained transfer function is multiplied with the wave spectrum to obtain the amount of change of the DHP in irregular waves ($\delta P_{D,Irregular}$), as shown in equation (2), and by adding it to the DHP in calm water, the DHP in irregular waves is calculated. In this study, as the irregular wave conditions, it was used that a peak parameter of 3.3 in the JONSWAP (Joint North Sea Wave Project) spectrum with 3 to 8 BN (Beaufort Number).

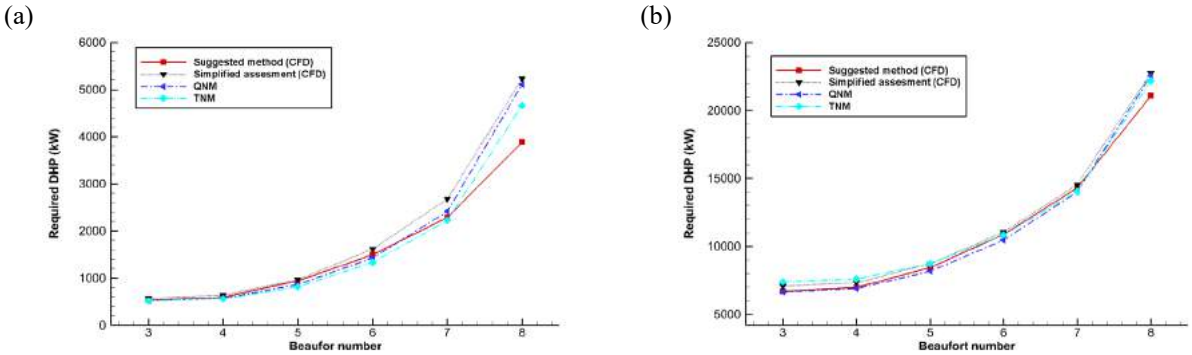

Figure 6: Estimated delivered horsepower according to Beaufort number with (a) 4 knots (*Fr*=0.037), (b) 10 knots (*Fr*=0.092)

Based on the methods described above, the DHP obtained according to the BN was compared, as shown in Figure 6. Both ship speeds show similar results regardless of the methods up to BN=5, which has a low wave height. From BN=6, the difference between methods increases, and the largest difference is shown at BN=8. Overall, the results of TNM, QNM, and SA (CFD) for both ship speeds were estimated to have higher DHP compared to the suggested method. The difference increased as the wave height increased, which is thought to be due to the greater influence of the self-propulsive factors that change in waves as the wave height increases.

Conclusions

In this study, changes in the self-propulsion performance of ships in the wave were studied through CFD calculation for a KVLCC2 in regular waves. In addition, the required power in irregular waves was estimated through the four spectral methods using CFD results in the regular wave. It was confirmed how the change of the self-propulsion factors in waves can affect the power estimation method in irregular waves.

By comparing the self-propulsion factors, the propulsion performance was compared according to the wave conditions. The self-propulsion points were changed depending on the added resistance, and the propeller rotation rate increased to get more thrust. The efficiency of the ship fell compared to the calm water condition, and there were changes in propulsive factors. The effect of the rotation of the propeller appeared less than that of calm water in waves, which causes the thrust deduction factor to tend to decrease. The reduction rate in the thrust deduction factor becomes the greatest at the point where the wave height is increased. The wake fraction factors also show a larger reduction under the condition of high wave height. This seems to be due to ship motions and particle velocity of waves, which leads to the increase in the axial velocity of inflow into the propeller plane. A further study will be conducted to obtain sufficient evidence for this.

The hull efficiency and POW efficiency decreased according to the wave conditions, and it is thought that the shape of the hull and the particle velocity of the wave had an effect, respectively. Comprehensively, the propulsive efficiency fell in the waves, and the required power increased. While the obtained DHP was largely due to the regular wave condition with a high wave height, it suggests the decline in the efficiency and the rise in the power in the wave. Therefore, to estimate more realistic required power, the change of self-propulsion factors should be considered.

The spectral method, the minimum required power in irregular waves according to BN was not different in all methods due to the wave height was not high until BN=5. However, after that, the difference becomes bigger from BN=6. When the force acting on the ship is used as the transfer function (TNM, QNM, and SA), the required power is estimated to be relatively high. When the required power among the regular waves was used as the transfer function, the estimated power was low. It is

judged as a difference that occurs due to the force acting on the ship and the number of rotations of the propeller is not linearly proportional. The above results show that the power can be estimated relatively large when using the assumption that the force and the propeller revolution have a linear relationship. Through this, it is suggested that the selection of an engine with excessive capacity may cause environmental problems if the self-propeller factor in waves is not considered.

Through this study, it was confirmed that the performance of a ship changes in waves. Since an indirect method was used here, we will perform the resistance calculation in an irregular wave directly through experiments and a numerical analysis.

ACKNOWLEDGEMENTS

This research was supported by the 'Development of Autonomous Ship Technology(20200615)' funded by the Ministry of Oceans and Fisheries(MOF, Korea).

REFERENCES

Aertssen, G., and M. F. Van Sluys. “Service Performance and Seakeeping Trials on a Large Containership.” *Royal Institution of Naval Architects Transactions*, vol. 114, 1972.

Celik, Ismail, et al. “Procedure of Estimation and Reporting of Uncertainty Due to Discretization in CFD Applications.” J. *Fluids Eng*., vol. 130, 2008, p. 78001, doi:10.1115/1.2960953.

Eom, Myeong Jin, et al. “A Study on the Propeller Open Water Performance Due to Immersion Depth and Regular Wave.” *Ocean Engineering*, vol. 219, no. January 2020, Elsevier Ltd, 2021, p. 108265, doi:10.1016/j.oceaneng.2020.108265.

Gerritsma, J., et al. “Propulsion in Regular and Irregular Waves1.” *International Shipbuilding Progress*, vol. 8, no. 82, 1960, pp. 235–47, doi:10.3233/isp-1961-88201.

ITTC “Resistance Uncertainty Analysis, Example for Resistance Test.” *ITTC – Recomm. Proced. 7.5-02-02-02*, 2002.

ITTC “Prediction of Power Increase in Irregular Waves from Model Test.” *ITTC – Recomm. Proced. 7.5-02-07-02.2*, 2014.

ITTC “1978 ITTC Performance Prediction Method.” *ITTC-Rcomm. Proced. 7.5-02-03-01.4*, 2018.

Jinkine, V., and V. Ferdinande. “A Method for Predicting the Added Resistance of Fast Cargo Ships in Head Waves.” *International Shipbuilding Progress*, vol. 21, IOS Press, 1974, pp. 149–67, doi:10.3233/ISP-1974-2123801.

Kim, W. J., et al. “Measurement of Flows around Modern Commercial Ship Models.” *Experiments in Fluids*, vol. 31, no. 5, 2001, pp. 567–78, doi:10.1007/s003480100332.

Kim, K. S., Park, I. R., Kim, J., Van, S. H. “Numerical Study for Characterization of Resistance Performance and Shape Coefficient according to the Scale Ratio Change of the Similarity Model Ship.” *Proceeding of the Korea Association of Ocean Science and Technology Societies*, 2010, June.

Larsson, L., et al. “Numerical Ship Hydrodynamics: An assessment of the Gothenburg 2010 Workshop.” Springer, 2013, Dordrecht. http://dx.doi.org/10.1007/978-94-007-7189-5

Lee, Soon Hyun, et al. “A Study on Ship Performance in Waves Using a RANS Solver, Part 1: Comparison of Power Prediction Methods in Regular Waves.” *Ocean Engineering*, vol. 227, no. March, Elsevier Ltd, 2021, p. 108900, doi:10.1016/j.oceaneng.2021.108900.

Liu, Shukui, and Apostolos Papanikolaou. “Fast Approach to the Estimation of the Added Resistance of Ships in Head Waves.” *Ocean Engineering*, vol. 112, Elsevier, 2016, pp. 211–25, doi:10.1016/j.oceaneng.2015.12.022.

Maruo, Hajime. “The Excess Resistance of a Ship in Rough Seas.” *International Shipbuilding Progress*, vol. 4, no. 35,1957, pp. 337–45, doi:10.3233/isp-1957-43501.

MEPC 1/Circ.850/Rev.3 “GUIDELINES FOR DETERMINING MINIMUM PROPULSION POWER TO MAINTAIN THE MANOEUVRABILITY OF SHIPS IN ADVERSE CONDITIONS” 2021.

MEPC 71/INF.28 “Draft revised guidelines for determining minimum propulsion power to maintain the manoeuvrability of ships in adverse conditions” 2017.

Park, Dong Min, et al. “Study on Added Resistance of a Tanker in Head Waves at Different Drafts.” *Ocean Engineering*, vol. 111, Elsevier, 2016, pp. 569–81, doi:10.1016/j.oceaneng.2015.11.026.

Pérez Arribas, F. “Some Methods to Obtain the Added Resistance of a Ship Advancing in Waves.” *Ocean Engineering*, vol. 34, no. 7, 2007, pp. 946–55, doi:10.1016/j.oceaneng.2006.06.002.

Res.MEPC.232 (65), “Interim guidelines for determining minimum propulsion power to maintain the manoeuvrability of ships in adverse conditions.” *MEPC 65, 22*., 2013.

Shin, Hyun Woo, et al. “A Numerical Investigation on the Nominal Wake of KVLCC2 Model Ship in Regular Head Waves.” *International Journal of Naval Architecture and Ocean Engineering*, vol. 12, Elsevier Ltd, 2020, pp. 270–82, doi:10.1016/j.ijnaoe.2020.01.001.

Tsujimoto, Masaru, et al. “On a Calculation of Decrease of Ship Speed in Actual Seas.” *Journal of the Japan Society of Naval Architects and Ocean Engineers*, vol. 9, no. 0, 2009, pp. 79–85, doi:10.2534/jjasnaoe.9.79.

Tsujimoto, Masaru, and Hideo Orihara. “Performance Prediction of Full-Scale Ship and Analysis by Means of on-Board Monitoring (Part 1 Ship Performance Prediction in Actual Seas).” *Journal of Marine Science and Technology (Japan*), vol. 24, no. 1, Springer Japan, 2019, pp. 16–33, doi:10.1007/s00773-017-0523-1.

Yang, Kyung Kyu, et al. “Enhancement of Asymptotic Formula for Added Resistance of Ships in Short Waves.” *Ocean Engineering,* vol. 148, no. November 2017, Elsevier Ltd, 2018, pp. 211–22, doi:10.1016/j.oceaneng.2017.11.010.

Yu, Jin-Won, et al. “Experimental Study on the Added Resistance of KVLCC2 in Irregular Waves.” The 29th International Ocean and Polar Engineering Conference, *International Society of Offshore and Polar Engineers*, 2019.

LASER-BASED NON-DESTRUCTIVE 3D SCANNING OF MARINE COATINGS

Christian Rosenberg Petersen[1], Narayanan Rajagopalan[2], Niels Møller Israelsen[1], Rasmus Eilkær Hansen[1], Christos Markos[1], Claus E. Weinell[2], Søren Kiil[2], and Ole Bang[1].

ABSTRACT

Optical coherence tomography (OCT) is presented as a field-applicable, non-contact, and non-destructive imaging technique for performing sub-surface inspection of marine coatings. The method is based on broadband mid-infrared supercontinuum laser light to significantly increase the imaging depth and resolution. The OCT system was able to image sub-surface structures, such as cracks and defects, as well as detect substrate corrosion through 369 μm of highly scattering marine coating. The system was also put into the field to show its applicability in an industrial marine environment. OCT imaging therefore has the potential to provide information about the sub-surface coating and substrate environment on marine structures and vessels, which is difficult to achieve using traditional methods.

KEY WORDS

NDT; non-destructive; non-contact; coatings; corrosion; defect; inspection; maintenance; OCT; supercontinuum; laser;

INTRODUCTION

Non-destructive testing (NDT) is an important part of assuring the performance and lifetime of protective coatings both in development, production, and in the field. To assess the quality of a coating, it is important to measure the thickness and detect any internal defects or delamination from the substrate. One technique, which has so far been largely missed by the NDT community, is optical coherence tomography (OCT). OCT is a reflection modality method originally developed for medical imaging based on the interference of light reflected/scattered from different depths of a sample, and because it is based on low intensity laser light it can reach microscopic resolution, is non-destructive, and does not require a contact medium. The challenge of OCT is that light is gradually lost when propagating through a sample due to scattering and absorption, so the penetration depth is very limited. Compared to a more widespread NDT technology like high frequency ultrasound, OCT does not penetrate as far (usually less than 1 mm), and is very sensitive to the particle size. On the other hand, ultrasound cannot resolve any details of the first few hundred microns from the surface, so in that case OCT can be complementary to existing ultrasound NDT.

One way to improve the penetration of OCT is to employ longer wavelengths of light, which results in reduced scattering. When moving towards longer wavelengths, physics unfortunately dictate that the spatial resolution is proportionally reduced. However, the depth resolution in OCT depends not only on the wavelength of light, but also the bandwidth of the light source (i.e. the span/spectrum of different wavelengths combined). Luckily, there is type of broadband laser that can extend far into the infrared: Supercontinuum (SC) lasers [1,2]. SC refers to the process whereby a relatively narrowband but high intensity laser pulse is gradually broadened in a nonlinear optical medium, such as an optical fiber. Using this technology, researchers have demonstrated various applications within spectroscopy and imaging, including OCT. There has been few reports of OCT being applied for inspection of coatings, primarily for cultural heritage preservation, but also for automotive and industrial coatings [3–10]. Marine coatings in particular make use of functional additives, which are highly scattering to visible and near-infrared light, and so there is a need for developing OCT systems based on longer wavelength mid-infrared light to improve the penetration depth. We recently demonstrated such a system for non-destructive, near real-time inspection of highly scattering samples, such as ceramics and polymers, as well as complex structures including the internal circuitry of a credit card chip [11]. In this paper we present the results of a recently finished project by the name SHIP-COAT (Sub-surface, High-resolution Inspection of Paints and Coatings using nOn-destructive lAser Tomography). In the project, OCT was evaluated as a NDT technique for inspecting marine coatings, including monitoring the curing process and detecting cracks and defects in

[1] DTU Fotonik, Department of Photonics Engineering, Technical University of Denmark, 2800 Kgs. Lyngby, Denmark.
[2] DTU Kemiteknik, Department of Chemical Engineering, Technical University of Denmark, 2800 Kgs. Lyngby, Denmark.

coatings exposed to extreme environments [12]. Towards the end, a transportable mid-infrared OCT system based on a robotic-arm was taken to a boat wharf in Copenhagen to demonstrate that the technology can be applied in the field.

METHODS

Optical Coherence Tomography

The MIR OCT system is based on a custom-built MIR supercontinuum (SC) laser, a free-space Michelson interferometer, and a specialized detection system that converts the mid-infrared light to near-infrared light, to allow for faster and more sensitive detectors to be used [13]. The mid-infrared SC laser is filtered such that the spectrum covers from 3.2-4.8 μm in wavelength, and about 20 mW of power is illuminating the sample. The broad spectrum of the SC laser results in an axial (depth) imaging resolution of about 6 μm, and the scanning lens used provides a lateral resolution of about 15 μm [14]. Images are created by scanning the laser-beam across a sample using galvanometric scanning mirrors with a variable integration time that allow for scanning with up to kHz line rates. A 3-5 mm scan with 1000 points takes between 0.3-3 seconds to capture depending on integration time. For more highly scattering coatings, a longer integration time is generally needed. The resulting 2D cross-section image is called a B-scan, and by also scanning the beam in the orthogonal direction a 3D volume or C-scan is made. A schematic of the system is shown in Figure 1.

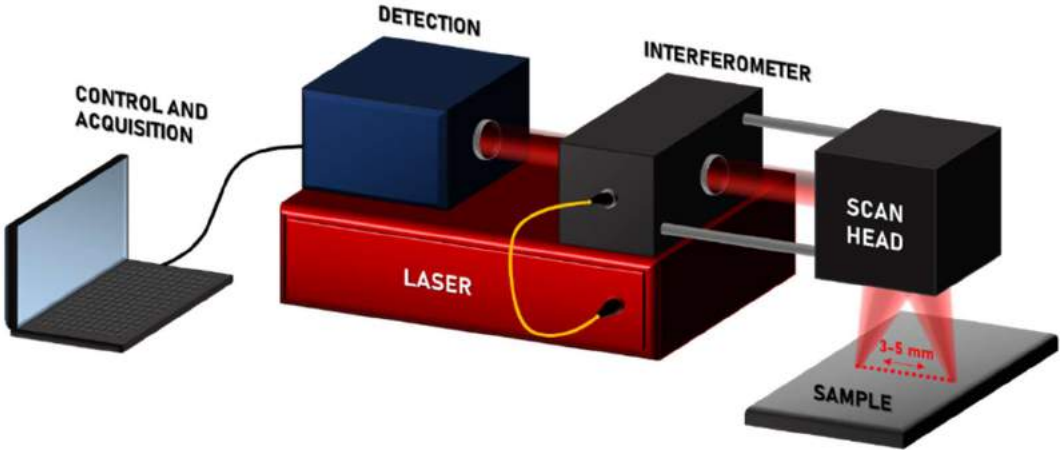

Figure 1. Schematic illustration of the MIR OCT system.

Sample preparation

High-pressure, high-temperature coating.
The coating was formulated using a DEN 438 epoxy novolac resin base with a functionality (f) of 3.6 and an m-xylylene diamine (MXDA) curing agent. The sample substrate was sandblasted carbon (mild) steel with dimensions 5 mm x 70 mm x 120 mm. Using a paintbrush of width 25 mm and aiming for a total dry film thickness (DFT) of 150 ± 25 μm, the coating was applied in two layers. The cured sample (Figure 2(a)) was subsequently immersed in salt water and exposed to a high pressure and high temperature (HPHT) environment, one of the extreme downhole application conditions of the oil and gas industry (for more information about the sample preparation and HPHT test see [15]). HPHT exposure of the coating led to three distinct zones with different degrees of coating degradation, as seen in Figure 2(b). In the region near the edge of the seawater level, a discrete red-colored deposition indicates the presence of iron oxide. From inspection of the sample using an optical microscope (Figure 2(c)), this region, in particular, had an abundance of cracks, and from preliminary inspection using OCT, this region showed the most subsurface features. Consequently, this zone was chosen for further inspection using OCT.

Commercial pigmented coatings.
Two commercial marine coatings were tested: (1) A blue-pigmented, self-polishing anti-fouling (AF) hull coating based on cuprous oxide (Cu2O) with a low self-polishing rate, and (2) a white-pigmented, high gloss (HG), alkyd enamel that is flexible and resistant to saltwater and other contaminants. The coatings were applied to line-polished aluminum substrates by a paintbrush and left to dry in a fumehood for min. 12 hours. For the corrosion detection measurements, a partially corroded aluminum substrate was used.

RESULTS

High-pressure, high-temperature coating

Figure 2(d) and 2(e) show a comparison between microscope images and OCT images of the coating surface near the iron oxide line. It is clear that OCT provides a significantly different contrast. The microscope images clearly show the iron oxide line and crystalline-like appearance of the salt water exposed region, whereas OCT highlights the finer surface structure and various defects, such as cracks and pits. Several cracks are clearly seen at points P1, P2, and P4, while the iron oxide line at P3 is barely distinguishable. Figure 2(f) show OCT B-scans revealing the subsurface structure of the coating. The top image shows a B-scan of an unexposed sample, revealing the high degree of roughness of the substrate compared to the relatively smooth surface. The only noticeable feature is a single point close to the surface indicated by a white arrow, which could be a small defect in the coating or simply part of the substrate. At P1 the presence of a crack can be seen from the feature appearing in the middle of the coating layer accompanied by a gap in the coating surface. The crack at P2 is seen more clearly because it runs parallel to the scan direction. At the iron oxide line P3 the only noticeable feature is a point of heightened substrate level accompanied by a small hole at the surface. Lastly, in P4 a group of three cracks meet and forms a complex structure below the surface, which is only partially captured by the B-scan. These images demonstrate how OCT can be used for monitoring the formation of subsurface cracks and defects due to exposure.

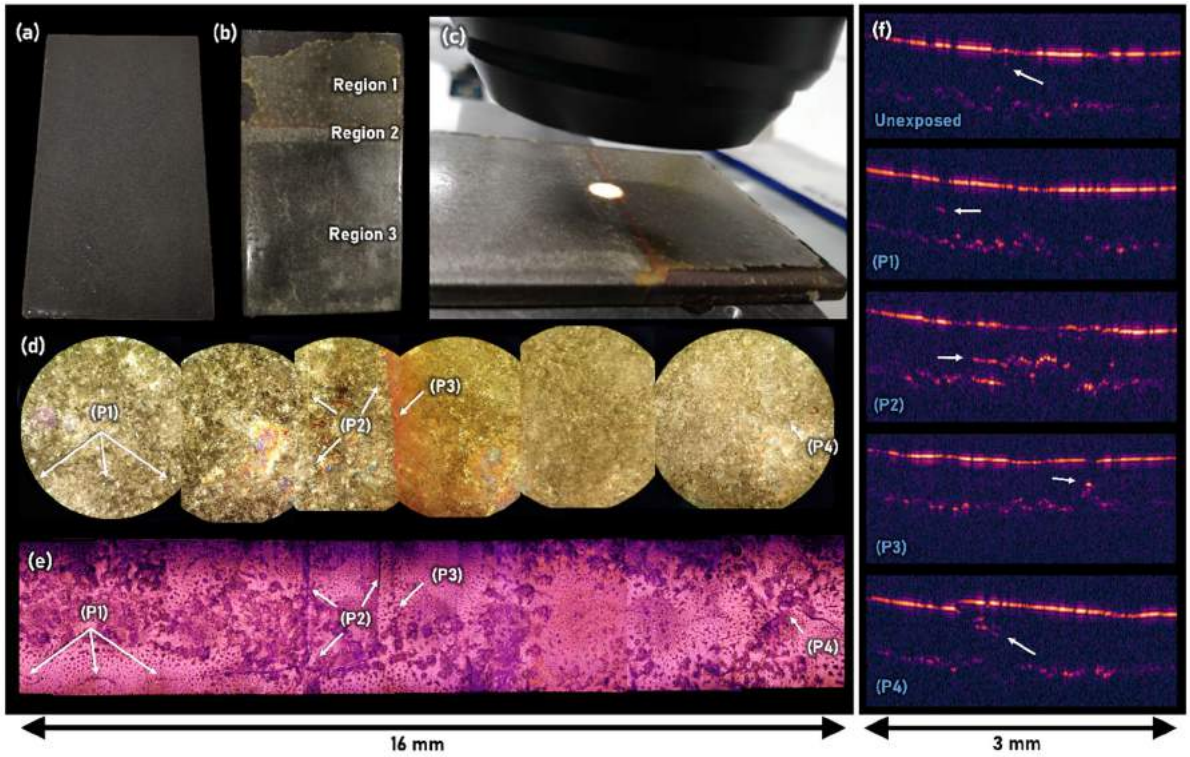

Figure 2. (a) Photograph of the coated steel sample. (b) Photograph of the coated sample after HPHT exposure. (c) Photograph showing the inspection region of the microscope. (d,e) Mosaic composite of microscope and OCT images, respectively, covering around a 3x16 mm area near the iron oxide line. (f) OCT cross-section images of unexposed and exposed samples near positions P1-P4.

Commercial coatings

Corrosion detection.

Figure 3 show a proof-of-concept demonstration of substrate corrosion detection using OCT. Figure 3(a) is a photo of the sample, where the commercial HG alkyd enamel was applied to a partially corroded aluminum plate. An OCT B-scan near the edge of the coated area is shown in Figure 3(b). Once cured, the coating was scribed with a scalpel at the interface between the corroded and non-corroded part of the plate, and a 3D scan was performed near the scratch. Figure 3(c) and 3(d) show a top-view projection of the scan at the coating surface, and at the coating-substrate interface, respectively. Corrosion is clearly

detected through the entire layer, which was estimated to be up to 369 µm thick [12]. Figure 3(e) is an ImageJ 3D visualization of the scan, applying a transparency of 40 and the GEM colormap. OCT therefore show promise as a method for early detection of corrosion onset at the coating-substrate interface.

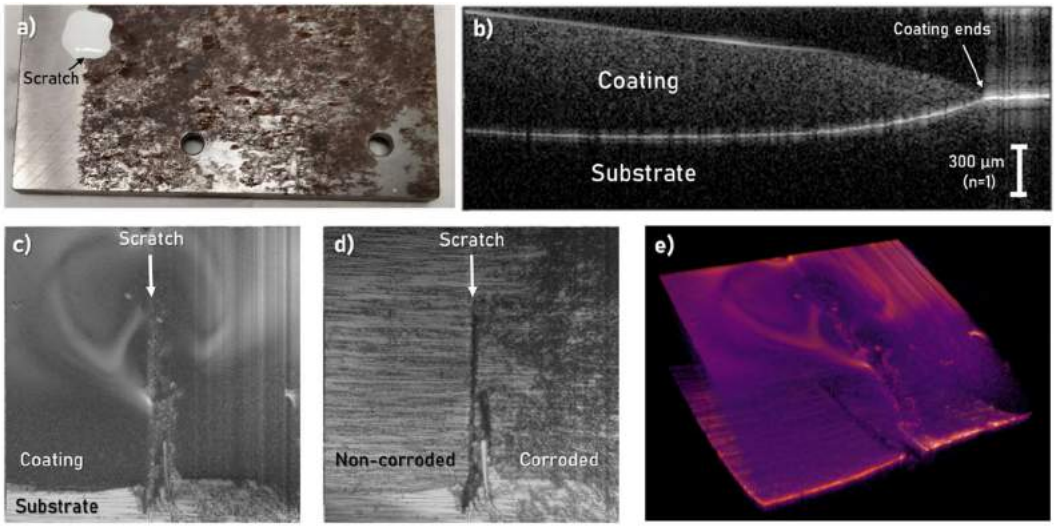

Figure 3. (a) Photograph of the HG coating applied to a partially corroded aluminum sample. (b) OCT B-scan near the edge of the coating. (c,d) Top-view projection of the scan at the coating surface, and coating-substrate interface, respectively. (e) ImageJ 3D visualization of the scan.

Detection of other defects.

Figure 4 shows a series of cases with OCT inspection of coatings. Figure 4(a) is a B-scan of the blue-pigmented AF coating containing Cu_2O particles, as seen in the microscope image of Fig. 4(b). Once cured, the surface of the coating is very rough, which combined with the many large Cu_2O-particles inhibits clear detection of the substrate. However, by averaging a number of adjacent scans it is possible to clearly see the coating-substrate interface to e.g. estimate the thickness or identify defects. Figure 4(c) show another case, where the HG coating is applied on top of a thinner layer of AF coating. In this case, OCT was able to detect a Cu_2O-particle that had diffused from the AF coating towards the surface. A similar case is shown in the microscope image of Fig. 4(d). Other interesting cases include detection of possible delamination (Fig. 4(e)), multiple HG-layer boundaries (Fig. 4(f)), and bubbles/voids (Fig. 4(g)).

Field operation.

As mentioned in the introduction, the OCT system was also tested under field conditions. To accommodate curved surfaces and larger reach, the galvanometric scanner was replaced with a robotic arm (Universal Robots UR5-e), and the interferometer was built into a probe that was mounted at the end of the arm, as shown in Figure 5(a). Operation of the system at a Copenhagen boat wharf is shown in Figure 5(b) and 5(c). The latter also show one of the issues encountered during testing, which is condensation and humidity. This is an issue because water absorbs light in the mid-infrared, reducing the depth from which a signal can be seen. Another issue is the poor coating surface quality of the tested hulls, as is evident from Figure 5(d). For instance, the hull showed signs of barnacles that had not been completely removed, and was thus visible through the coating. A B-scan of the coated barnacle surface is shown in Figure 5(e). B-scans from other parts of the hull also reveal multiple layers, and defects such as voids under the surface of the coating (see Figure 5(e,f)). This field test thus establishes that the technology can be brought out of the lab and into a marine environment to perform non-destructive inspection.

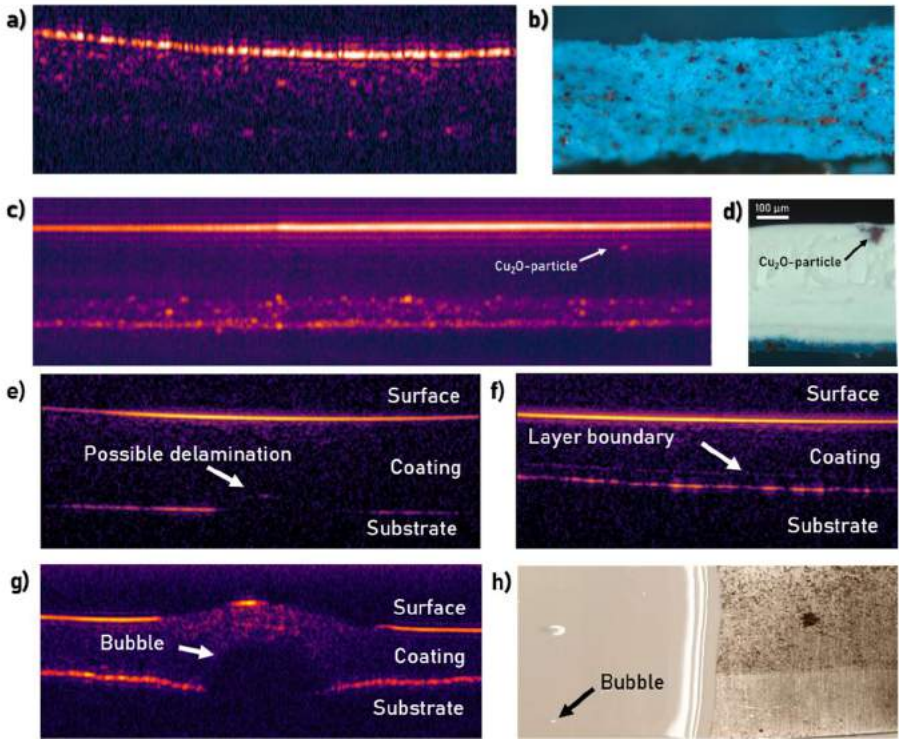

Figure 4. Various OCT images of structures, defects, and interfaces. (a,b) OCT B-scan and photograph of AF coating cross-section, respectively. (c,d) Detection of Cu_2O particle from the AF coating that has diffused into the HG coating. (e-f) OCT images of various defects in the HG coating. (h) Photograph of the HG coated sample, indicating the position of the bubble.

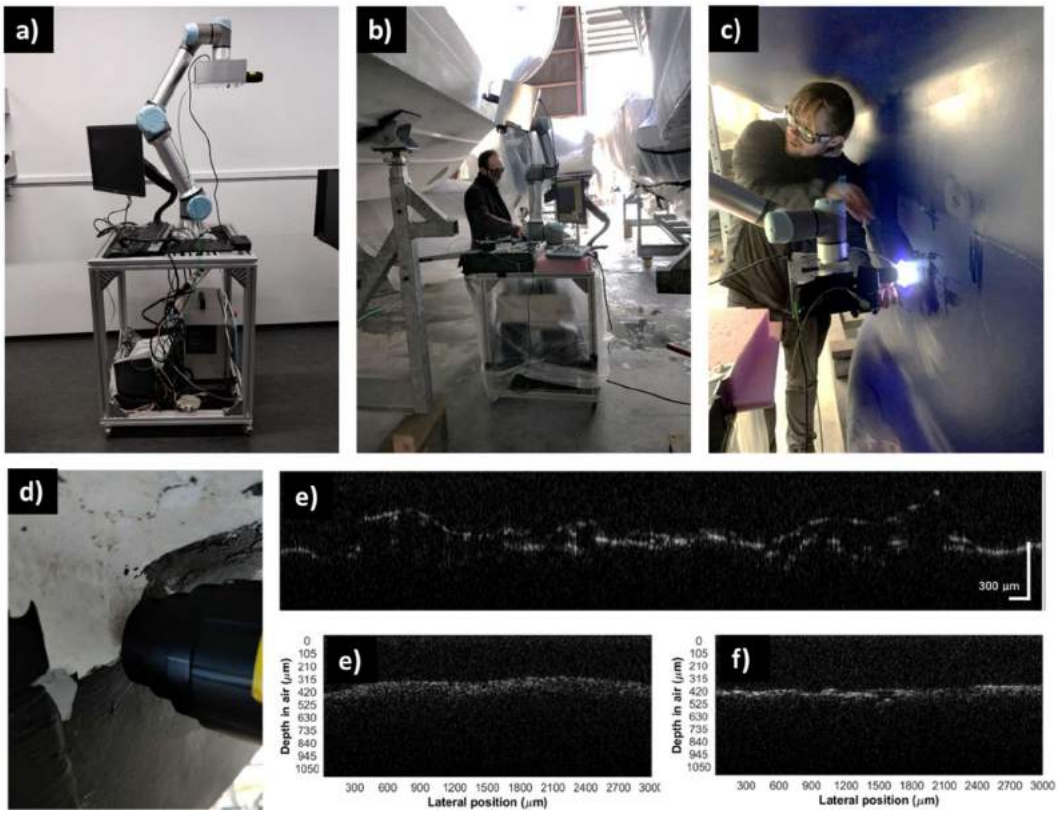

Figure 5. Field transportable OCT system. (a-c) Photographs of the system. (d) Photograph of a coated hull that showed signs of barnacle growth. (e-f) B-scans from the hull acquired using the field system.

CONCLUSIONS

In this paper, it was demonstrated how OCT based on mid-infrared supercontinuum light can be used for subsurface inspection of coatings. The technique was shown to be useful for imaging cracks and defects below the surface, including detection of substrate corrosion through 369 µm of HG coating. The penetration depth of OCT was found to be highly dependent on the surface roughness and particle size, limiting the useful imaging depth in highly scattering coatings, such as AF coating, to just a few hundred microns. The system was also tested at a boat wharf under field conditions, which revealed an issue with scanning in high humidity and condensation, as well as dirty and rough hull surfaces. With further development of the technology, OCT is believed to have great potential as a non-destructive imaging technique for industrial inspection of marine structures and vessels.

ACKNOWLEDGEMENTS

The authors acknowledge financial support by The Danish Maritime Fund in the project “SHIP-COAT” (project no. 2019-137).

REFERENCES

1. C. R. Petersen, U. Møller, I. Kubat, B. Zhou, S. Dupont, J. Ramsay, T. Benson, S. Sujecki, N. Abdel-Moneim, Z. Tang, D. Furniss, A. Seddon, and O. Bang, "Mid-infrared supercontinuum covering the 1.4–13.3 µm molecular fingerprint region using ultra-high NA chalcogenide step-index fibre," Nat. Photonics **8**(11), 830–834 (2014).
2. J. M. Dudley, G. Genty, and S. Coen, "Supercontinuum generation in photonic crystal fiber," Rev. Mod. Phys. **78**(4), 1135–1184 (2006).
3. C. S. Cheung, J. M. O. Daniel, M. Tokurakawa, W. A. Clarkson, and H. Liang, "Optical coherence tomography in the 2-µm wavelength regime for paint and other high opacity materials," Opt. Lett. **39**(22), 6509–6511 (2014).
4. M. Lenz, C. Mazzon, C. Dillmann, N. Gerhardt, H. Welp, M. Prange, and M. Hofmann, "Spectral Domain Optical Coherence Tomography for Non-Destructive Testing of Protection Coatings on Metal Substrates," Appl. Sci. **7**(4), 364 (2017).
5. P. Targowski and M. Iwanicka, "Optical Coherence Tomography: its role in the non-invasive structural examination and conservation of cultural heritage objects—a review," Appl. Phys. A **106**(2), 265–277 (2012).
6. Y. Dong, S. Lawman, Y. Zheng, D. Williams, J. Zhang, and Y.-C. Shen, "Nondestructive analysis of automotive paints with spectral domain optical coherence tomography," Appl. Opt. **55**(13), 3695–3700 (2016).
7. C. Wang, N. Zhang, Z. Sun, Z. Li, Z. Li, and X. Xu, "Recovering hidden sub-layers of repainted automotive paint by 3D optical coherence tomography," Aust. J. Forensic Sci. **51**(3), 331–339 (2019).
8. N. Zhang, C. Wang, Z. Sun, H. Mei, W. Huang, L. Xu, L. Xie, J. Guo, Y. Yan, Z. Li, X. Xu, P. Xue, and N. Liu, "Characterization of automotive paint by optical coherence tomography," Forensic Sci. Int. **266**, 239–244 (2016).
9. J. Zhang, B. M. Williams, S. Lawman, D. Atkinson, Z. Zhang, Y. Shen, and Y. Zheng, "Non-destructive analysis of flake properties in automotive paints with full-field optical coherence tomography and 3D segmentation," Opt. Express **25**(16), 18614–18626 (2017).
10. I. Zorin, P. Gattinger, M. Brandstetter, and B. Heise, "Dual-band infrared optical coherence tomography using a single supercontinuum source," Opt. Express **28**(6), 7858–7874 (2020).
11. N. M. Israelsen, C. R. Petersen, A. Barh, D. Jain, M. Jensen, G. Hannesschläger, P. Tidemand-Lichtenberg, C. Pedersen, A. Podoleanu, and O. Bang, "Real-time high-resolution mid-infrared optical coherence tomography," Light Sci. Appl. 8:11 (2019).
12. C. R. Petersen, N. Rajagopalan, C. Markos, N. M. Israelsen, P. J. Rodrigo, G. Woyessa, P. Tidemand-Lichtenberg, C. Pedersen, C. E. Weinell, S. Kiil, and O. Bang, "Non-Destructive Subsurface Inspection of Marine and Protective Coatings Using Near- and Mid-Infrared Optical Coherence Tomography," Coatings **11**(8), 877 (2021).
13. A. Barh, P. J. Rodrigo, L. Meng, C. Pedersen, and P. Tidemand-Lichtenberg, "Parametric upconversion imaging and its applications," Adv. Opt. Photonics **11**(4), 952–1018 (2019).
14. N. M. Israelsen, P. J. Rodrigo, C. R. Petersen, G. Woyessa, R. E. Hansen, P. Tidemand-Lichtenberg, C. Pedersen, and O. Bang, "High-resolution mid-infrared optical coherence tomography with kHz line rate," Opt. Lett. **46**(18), 4558–4561 (2021).
15. N. Rajagopalan, C. E. Weinell, K. Dam-Johansen, and S. Kiil, "Degradation mechanisms of amine-cured epoxy novolac and bisphenol F resins under conditions of high pressures and high temperatures," Prog. Org. Coat. **156**, 106268 (2021).

PROBABILISTIC ASSESSMENT ON THE EFFECTIVENESS OF MOMENTARY STATE-FEEDBACK CONTROL FOR BROACHING-TO PREVENTION IN REAL-TIME

Sreenath Maniyappan[1] and Naoya Umeda[1]

ABSTRACT

A momentary state-feedback control focusing on a saddle point of the dynamical system was proposed and its effectiveness for preventing ship broaching-to in waves was confirmed for a regular wave condition by the authors in recent research (Maniyappan and Umeda, 2021)*. In this paper, the momentary state-feedback control model (proposed model) is applied to a wide range of regular wave conditions of a fishing vessel in the following and quartering seas at the operational Froude number. A probabilistic approach is adopted to assess the effectiveness of this control approach in the irregular waves. The authors determine the occurrence probability of large heel due to broaching-to by the deterministic identification of broaching-to cases using a maneuvering numerical simulation model and the probabilistic theory of the local wave steepness and wavelength. By carrying out a comparison of the probability of large heel due to broaching-to under the conventional PD control and the proposed control model, the advantages and shortcomings of the proposed control model are identified.*

KEYWORDS

Critical wave method; Saddle point; Periodic motion; Surf-riding

NOMENCLATURE

A	Jacobian with respect to the state vector	s_j	Wave steepness
B	Jacobian with respect to the control vector	T_{01}	Mean wave period
C	Wave celerity	T_E	Steering gear time constant
g	Acceleration due to gravity	T_Z	Zero crossing period
H_s	Significant wave height	u	Surge velocity
$\boldsymbol{K}$	LQR Feedback gain	W	Weight matrix for vicinity parameter
K_P	Steering gear proportional gain	$\mathbf{x}$	State vector
K_d	Steering gear differential gain	$\mathbf{x}^*$	Fixed point
l_i	Wavelength to ship length ratio	χ	Heading angle
n	Propeller rps	δ	Rudder angle
n_{max}	Maximum propeller rps	ϵ	Control switching value of the vicinity parameter
p	Probability	η	Vicinity parameter
r	Yaw rate	ν	Spectrum bandwidth parameter
$\boldsymbol{s}$	Control vector	ϕ	Roll angle
$\boldsymbol{s}^*$	Constant value of control parameters	ξ_G	The relative position of the ship center of gravity on the wave with origin at wave trough.

INTRODUCTION

Broaching-to, for a very long time in the past was referred to as one of the most dreadful conditions that a ship could be subjected to (Spyrou, 2009). Researches in the latter half of the 20th century had provided distinct insights into the phenomenon with the help of model experiments and the nonlinear dynamical system approach (Umeda and .Hamamoto, 2000) This helped to draw guidelines for the ship master to tackle broaching-to with caution. To date, broaching-to

[1] Department of Naval Architecture and Ocean Engineering, Graduate School of Engineering, Osaka University, 2-1 Yamadaoka, Suita, Osaka 565-0971, Japan

prevention relies primarily on avoiding the dangerous heading and speed by following the operational guidance (IMO, 2007) by the International Maritime Organization (IMO). Such a passive approach is necessary because the present autopilot system is not developed to handle adverse weather scenarios happening in following and quartering seas. In modern days, where the autonomous nature of ship maneuvering is increasing, it would be desirable to have an active control method for adverse weather scenarios such as broaching-to.

The phenomenon of broaching-to starts with the ship leaving the periodic orbit and getting into the surf-riding equilibrium which being a saddle repels the ship with violent yaw and surge motion in the wave downslope. Hence, two factors that are key to actively prevent this phenomenon is controlling the surge speed to avoid surf-riding or help the ship enter into stable surf-riding and applying maximum steering effort to counter the large yaw moment. Research in the area of broaching-to prevention had started with devices such as sea anchor and seabrake (Renilson, 1986) which induce an additional drag and controls the surge velocity, but these are difficult to handle. Then control approaches like anti-broaching steering system (Umeda et al., 1999) using a high-performance steering gear, optimal control using SQP (Maki et al., 2008) and a much more powerful optimal control algorithm the covariance matrix adaptation evolution strategy (CMA-ES) (Maki et al., 2021) were attempted. The previous research by the authors (Maniyappan et al., 2020) investigated the optimal control using CMA-ES for avoiding broaching-to, but only for off-line control because of a huge computational time. By understanding the mechanism of broaching-to prevention by optimal control using CMA-ES, the authors (Maniyappan and Umeda, 2021) proposed a momentary state-feedback control near the saddle point for real-time broaching-to prevention in a particular regular wave condition. This is an extension of the Ott-Grebogi-Yorke (OGY) algorithm (Ott, Edward.Grebogi, Celso.Yorke, 1990) used in chaos control, but its effectiveness in irregular seaways has not yet been examined.

The knowledge of saddle point in the surge direction, i.e., the relative position of the ship on the waves and surge velocity is necessary for implementing the proposed control approach. However, in irregular waves, direct estimation of fixed points or the knowledge of the relative position of the ship on the waves is not possible. Alternatively, approximating the mean wave celerity as the equilibrium surge velocity and the measure of pitch angle to approximate the ship position on the waves could be used. It shall be noted here that the phenomenon of broaching-to associated with surf-riding normally occurs within one or two waves. Hence, before moving to the numerical simulation in irregular waves, the authors intend to evaluate the proposed control model over a wide range of regular wave conditions. Then the effectiveness of the proposed control model can be assessed using a deterministic broaching region obtained from regular wave cases and probability of wave encounter using stochastic wave theory. Ocean waves can be considered as a sequence of local sinusoidal waves defined between the zero-crossing or peak to peak of water elevation. Here each local wave is represented using a wave height and wavelength. In this framework proposed by Umeda (1990) the occurrence of broaching-to can be estimated from the probability of encountering the local wave leading to broaching-to. This concept combined with Longuet-Higgin (1983)'s theory forms the critical wave method mentioned in the IMO's level 2 vulnerability criteria (IMO, 2020) for probabilistic evaluation of broaching-to failure mode.

By applying the critical wave method, a probabilistic assessment of the effectiveness of the momentary state-feedback control for broaching-to prevention at sea could be done. Hence in this research, the authors define the scope of this real-time control approach quantitatively over the North Atlantic Sea states and draw practical conclusions for effectively utilizing this proposed control strategy.

CONTROL SYSTEM SCHEMATIC

Figure 1 shows the schematic representation of the closed-loop control system model. The proposed model consists of two loops: the conventional PD control realized in the upper one and the state feedback using the linear quadratic regulator (LQR) implemented in the lower loop. The linearized system used near the saddle point, the control vector, and the LQR state feedback are given by equations 1 to 3. The switch between the upper and the lower loop operates depending on the value of the vicinity parameter (η) given by equation 4. The vicinity parameter represents the proximity of the state of the system to the fixed points in the system, with a higher weightage given in the surge direction. When the system is near to the fixed point the control is switched to the lower loop i.e. the state feedback using LQR. The limits of the rudder gains are chosen as per Ohtsu and Hasegawa (1981) based on manufacturers' data used for commercial autopilots, n_d is the desired rps and n_{max} refers to the propeller rps at the surf-riding equilibrium limited by the maximum rps of engine. The type of feedback (equation 3) whether positive or negative varies with ship proximity to a wave crest equilibrium or a wave trough equilibrium respectively. A detailed explanation of the control model can be found in Maniyappan and Umeda (2021).

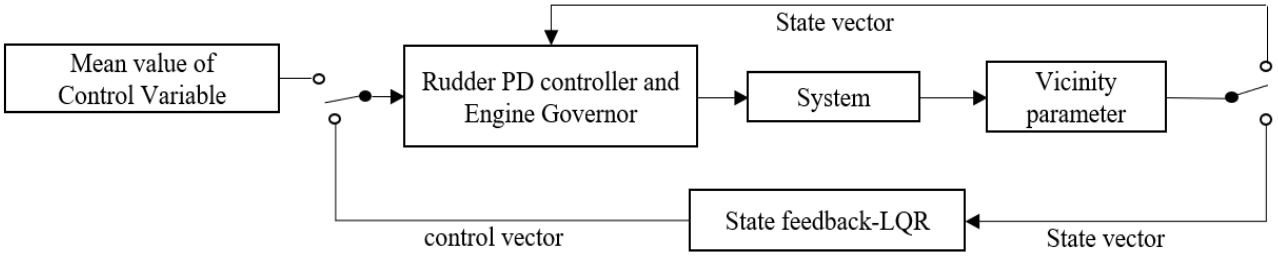

Figure 1: Schematic of the proposed control model

$$\dot{\mathbf{x}}_t - \dot{\mathbf{x}}^* = A(\mathbf{x}_t - \mathbf{x}^*) + B(\boldsymbol{s} - \boldsymbol{s}^*), \forall\, \eta \leq \epsilon \quad [1]$$

$$\boldsymbol{s} = [K_P\ K_d\ n_d], K_P \in [0,3], K_d \in [0,900\text{s}], n \in [0, n_{max}] \quad [2]$$

$$\delta\boldsymbol{s} = \boldsymbol{s} - \boldsymbol{s}^* = \pm K dx \quad [3]$$

$$\eta = d\mathbf{x} W d\mathbf{x} \quad [4]$$

PROBABILISTIC ANALYSIS

The probabilistic analysis for the effectiveness of the control model is based on the critical wave method and carried out at the operational Froude number of 0.35. The IMO's level 2 vulnerability criteria specify a wave steepness range of 0.03 to 0.15 at steps of 0.012 and a wavelength to ship length ratio varying from 1.0 to 3.0 at steps of 0.025 to be considered. Since surf-riding is a prerequisite for broaching, the surf-riding region is firstly determined in this range of regular wave conditions at nominal Froude number of 0.35. Maki et al. (2010) proposed an analytical approach to predict the surf-riding region using Melnikov's method (Holmes, 1980). In this method, a polynomial approximated surge equation is analytically solved to obtain the surf-riding and wave blocking thresholds of Froude number for a particular wave condition. An operational Froude number exceeding this threshold is likely to be subjected to surf-riding. Hence, the Melnikov analysis is carried out to identify the surf-riding wave conditions. Subsequently, the numerical simulation using the 4-DoF surge-sway-yaw-roll model (Umeda and Hashimoto, 2002) is carried out using the conventional PD control for the autopilot course from 0 to 45 degrees from the wave direction at steps of 0.1 degrees. Wave conditions leading to large roll due to broaching to are identified by following the criteria proposed by Umeda and Renilson (1992) and Umeda et al. (1999). A roll angle greater than 40 degrees is considered as a large heel relevant to the stability failure. Further, the proposed control model is applied to the broaching-to cases happening under the conventional PD control region to identify the broaching-to region under the proposed control model. This gives the set of local wave conditions leading to broaching-to under conventional PD control and under the proposed momentary state-feedback control.

After identifying the broaching-to region as pairs of wave steepness and wavelength to ship length ratio, the joint probability of encountering a particular local wave steepness and wavelength to ship length ratio can be calculated based on Longuet-Higgin's theory under the assumption of the narrow banded spectrum. Here, the Pierson-Moskowitz spectrum representing the North Atlantic is used. The joint probability density function for $l_i = \frac{\lambda}{L}$ and $s_i = \frac{H}{\lambda}$ at H_s, T_s for a narrow banded spectrum with bandwidth parameter, ν is given by equation 5. The broaching-to probability here is the same as the conditional probability when a ship meets a local wave of s_i and l_i, given by equation 6, where $C(l_i, s_j) = 1$ if broaching-to occurs and zero otherwise.

$$p^*(l_i, s_j) = 4\frac{\sqrt{g}}{\pi\nu}\frac{L^{5/2}T_{01}}{(H_s)^3}s_j^2 l_i^{3/2}\left(\frac{\sqrt{1+\nu^2}}{1+\sqrt{1+\nu^2}}\right)\cdot \exp\left[-2\left(\frac{L\cdot l_i \cdot s_j}{H_s}\right)^2\left\{1+\frac{1}{\nu^2}\left(1-\sqrt{\frac{gT_{01}^2}{2\pi l_i L}}\right)^2\right\}\right] \quad [5]$$

$$P = \Sigma_i \Sigma_j C(l_i, s_j) p^*(l_i, s_j)\,|_{H_s, T_Z} \quad [6]$$

MANEUVERING SIMULATION

The ITTC A2 ship a 34.5m purse seiner is used here for the study (ITTC, 2002). The ship was found vulnerable to broaching-to during the model experiments carried out by Umeda and Hamamoto (2000). Numerical simulation using the 4 DoF surge-sway-yaw-roll maneuvering model (Umeda and Hashimoto, 2002) is carried out for each of the surf-riding local waves obtained from Melnikov analysis. Simulation is carried out for autopilot course range 0 to 45 degrees from the wave direction at an interval of 0.1 degrees and the large heel due to broaching-to cases are identified according to equation 7. Firstly, broaching-to cases under the conventional PD control are identified. The conventional PD control here refers to a steering gear dynamic equation of the form shown in equation 8, where constant values of rudder gains are used. Further, the proposed momentary state-feedback control is applied to the broaching-to cases identified under conventional PD control to find the effective region of the proposed control for each autopilot course.

$$r > 0, \dot{r} > 0\ , \delta = -\delta_{max}\ \&\ |\phi| > 40\ degree \quad or \quad r < 0, \dot{r} < 0, \delta = \delta_{max}\ \&\ |\phi| > 40\ degree \tag{7}$$

$$\dot{\delta} = \{-\delta - \mathrm{K}_P(\chi - \chi_c) - K_d r\}/T_E, \left|\dot{\delta}\right| \leq 3.5\ degrees/s, |\delta| \leq 35\ degrees \tag{8}$$

The mechanism of broaching-to prevention by the proposed model is either by undergoing periodic motion or surf-riding as explained in the recent research (Maniyappan and Umeda, 2021). The mode of motion observed after evading broaching-to is categorized into periodic or surf-riding in this study as follows:

a) periodic motion is identified when a real value of τ exists which satisfied the relation $\cos(x_i(t)) = \cos(x_i(t+\tau))$ and $x_i(t) = x_i(t+\tau), i = 2, \dots, 9$

b) stable surf-riding is identified when each of the state vectors falls into an equilibrium value i.e. $\dot{x_\iota} = 0, \forall\ 1 \leq i \leq 9$

Realizing the surf-riding mechanism by applying a higher rps depends on the engine specification. Hence, it is important to identify the mechanism of broaching-to prevention to understand how effective the approach could be in real seas.

NUMERICAL RESULTS AND DISCUSSION

To begin with, the surf-riding domain is evaluated at a nominal Froude number of 0.35. Figure 2 shows the combination of wave steepness and wavelength to ship length ratio that could result in surf-riding. At a longer wavelength, the high wave celerity results in increase of surf-riding threshold and at higher wave steepness the increase in wave force reduces the surf-riding threshold. This results in a trend as shown in Figure 2.

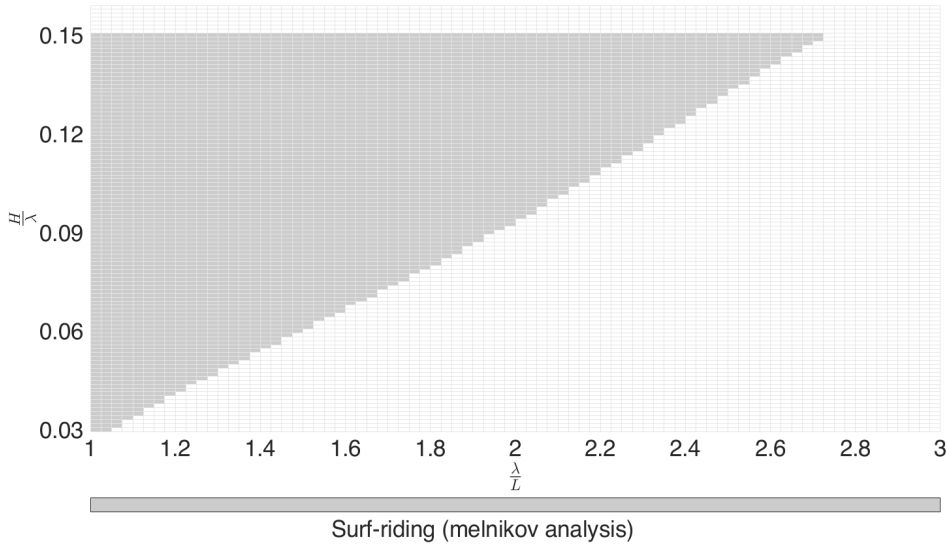

Figure 2: Surf-riding region at Fn=0.35 from Melnikov analysis

Numerical simulation using the maneuvering model is carried out at these wave conditions under the different heading angles as explained in the earlier section. The initial condition is chosen from a periodic motion case based on the sudden change concept (SCC) (Umeda, 2000) to avoid impractical initial conditions. The broaching-to prevention is achieved by the proposed model either by undergoing periodic motion or by surf-riding. Typical simulation results are presented here showing broaching-to prevention by periodic motion in Figure 4 and broaching-to prevention by surf-riding in Figure 5. Figure 3 shows the eigenvalues of the two typical cases discussed further in this section.

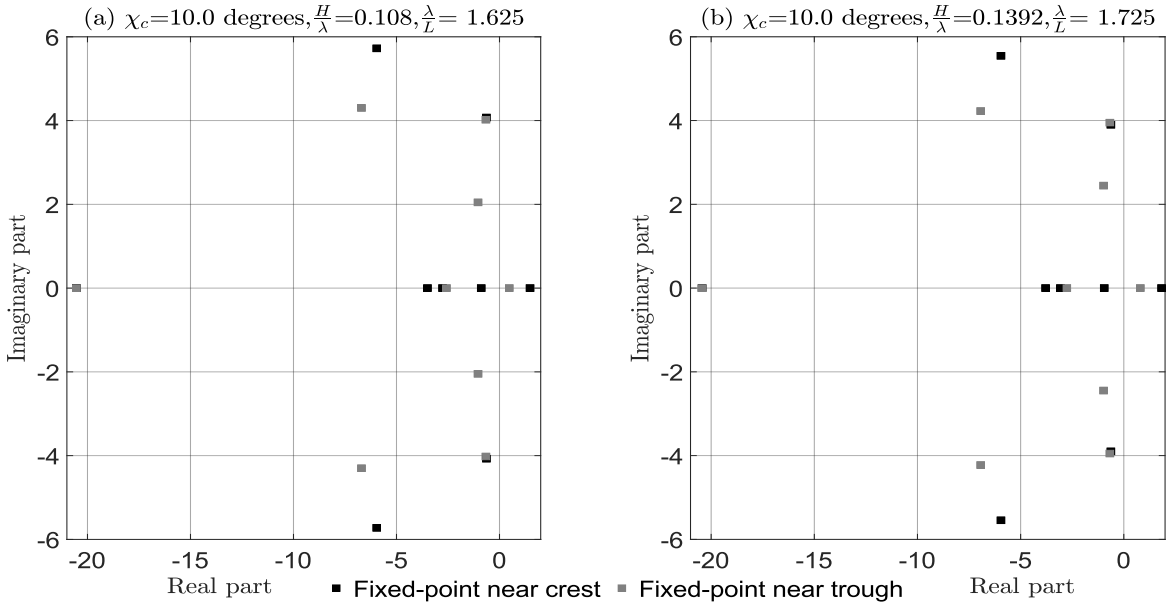

Figure 3 Eigenvalues of the fixed points for two typical cases discussed below (Fn=0.35)

Broaching-to Prevention Resulting in Periodic Motion

Figure 4 shows an example where the system settles into a periodic motion under proposed control. Under the conventional PD control (time 0s to 40s) the ship is subjected to violent surging at wave downslope (Figure 4 (a) & (c)) and large yawing (Figure 4 (d)) despite the rudder angle reaching its limit in the opposite direction (Figure 4 (f)) and this results in large roll due to the broaching-to (Figure 4 (b)). In the perspective of the nonlinear dynamics, the system is attracted towards the fixed point near a wave crest which is a saddle of index 1 (Figure 3 (a)) and its highly unstable nature causes the ship to be repelled away with a positive real part of the eigenvalue of the system. On applying the proposed momentary state-feedback control, when the system is near the saddle point the additional control action causes a drop in rps (Figure 4 (e)) and higher rudder angle (Figure 4 (f)) which slightly reduces the surge velocity and keeps the system away from the saddle and avoids violent surging downslope. This momentary control action pushes the system into a different trajectory and the control action continues periodically and the system settles into a periodic motion.

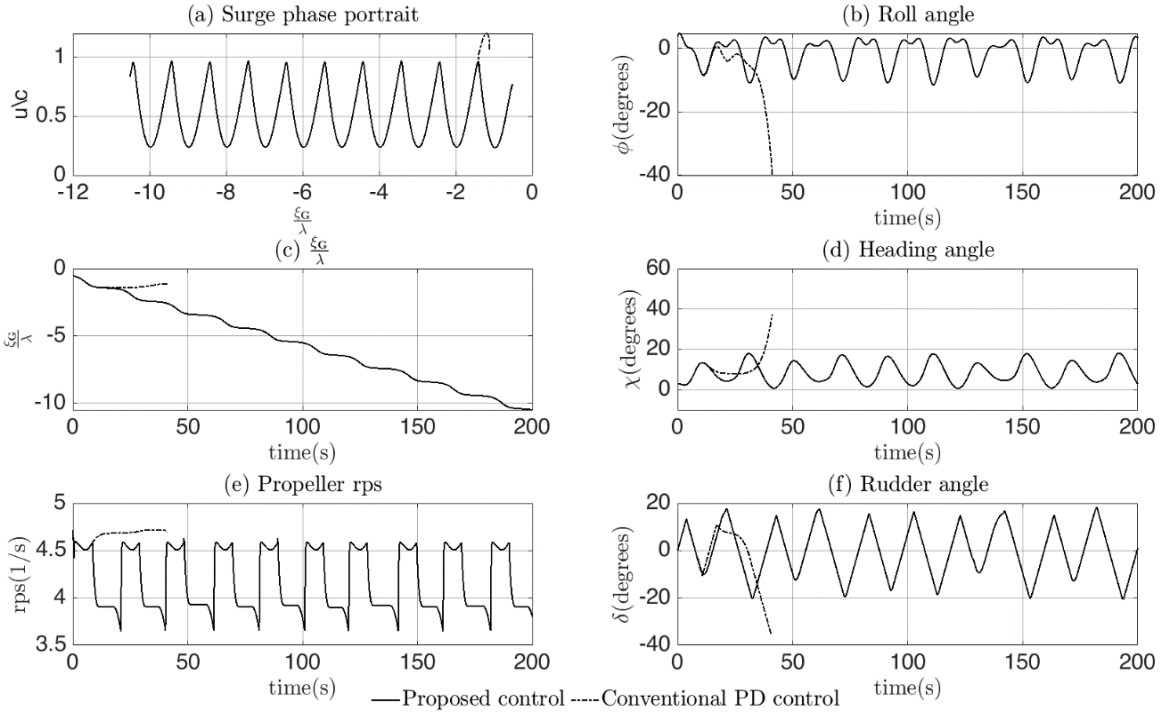

Figure 4: Surge phase portrait and time-series comparison at Fn=0.35 and $\chi_c = 10$ degrees for $\frac{H}{\lambda} = 0.108$ and $\frac{\lambda}{L} = 1.625$

Broaching-to Prevention Resulting in Surf-riding

Stable surf-riding is observed in some of the cases, especially when the wave steepness is high. Figure 5 shows an example where the system settles into stable surf-riding. Under the conventional PD control (time 0s to 40s) the ship is subjected to violent surging at the wave downslope (Figure 5 (a) & (b)) and large yawing (Figure 5 (d)) despite the maximum opposite rudder angle (Figure 5 (f)) and this results in large roll due to the broaching-to (Figure 5 (b)). On applying the proposed control, firstly positive feedback suceeds to keep the system away from the wave crest saddle (Figure 3 (b)) by dropping rps. However, the ship is captured by the next wave crest and repelled. Then the ship increases the propeller rps (Figure 5 (e)) to the surf-riding equilibrium rps resulting the increase in rudder force, so that the ship can undergo stable surf-riding. Since the system settles into fixed-point near the wave trough, the control effort stays on. However, applying a higher rps depends on the engine specifications.

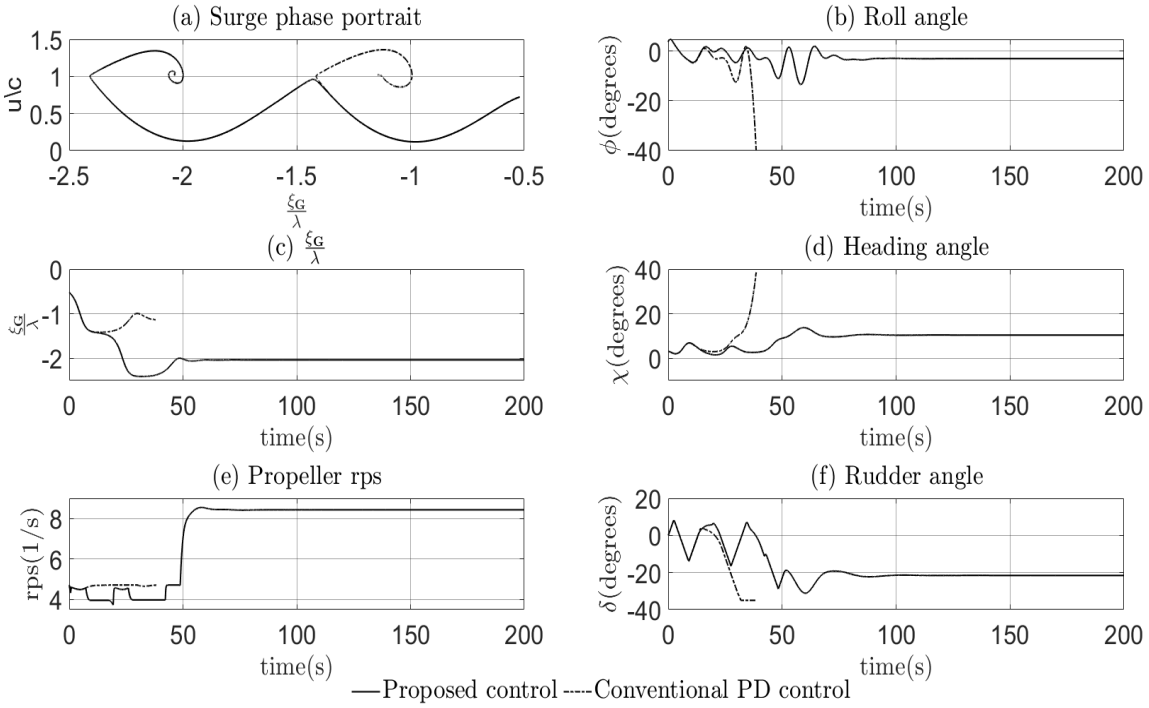

Figure 5: Surge phase portrait and time-series comparison at Fn=0.35 and $\chi_c = 3$ degrees for $\frac{H}{\lambda} = 0.1392$ and $\frac{\lambda}{L} = 1.725$

The mechanism of broaching-to prevention was observed to depend on the wave steepness or the wave forces acting on the ship. Figure 6 shows the classification of the two mechanisms i.e. periodic motion and surf-riding achieved by the proposed control model. Mostly periodic motion is achieved except for the very high wave steepness region because of the lower surf-riding threshold.

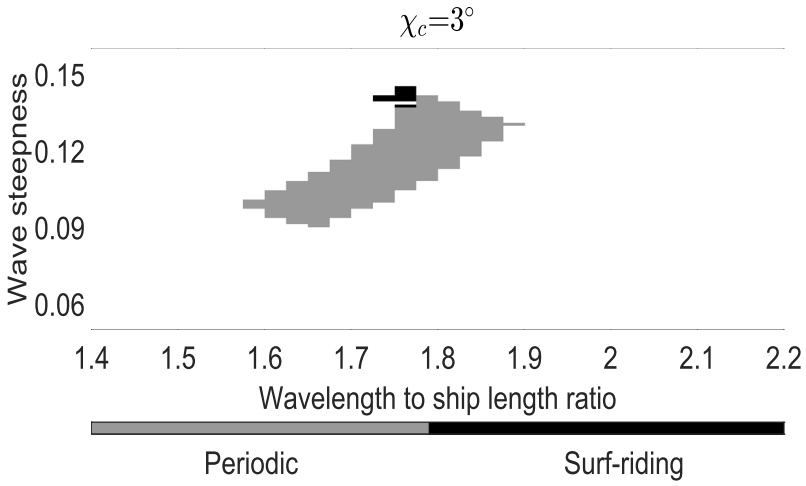

Figure 6: Mechanism of broaching-to prevention at Fn=0.35 and $\chi_c = 3.0$ degrees

Probability of Large Heel Due to Broaching-to

With the knowledge of local waves that result in broaching-to under conventional PD control and the proposed control model, the probability of broaching-to for a narrow-banded wave spectrum can be evaluated. Here, the probability of broaching-to over the North Atlantic is evaluated (equations 5 and 6) using the Pierson-Moskowitz wave spectrum and the wave scatter table for the North Atlantic. Figure 7 shows the comparison of the probability of large heel due to broaching-to at various autopilot courses in the following and quartering seas. It can be noted that at higher heading angles of above 23 degrees the phenomenon of broaching-to was not observed. The comparison shows that the proposed control model could significantly reduce the broaching-to cases at lower autopilot courses. However, at higher autopilot courses of over 12 degrees, there is no significant advantage with the proposed control model and further over 16 degrees the broaching-to cases decline in general, and both the control methods are subjected to broaching-to to the same extend. The ineffectiveness of the proposed control model in larger autopilot courses could be due to a limitation of the steering gear and rudder system to resist such large yaw force at higher heading angles. In nonlinear dynamical systems points of view, this could be attributed to the increased instability in yaw direction in higher heading angles.

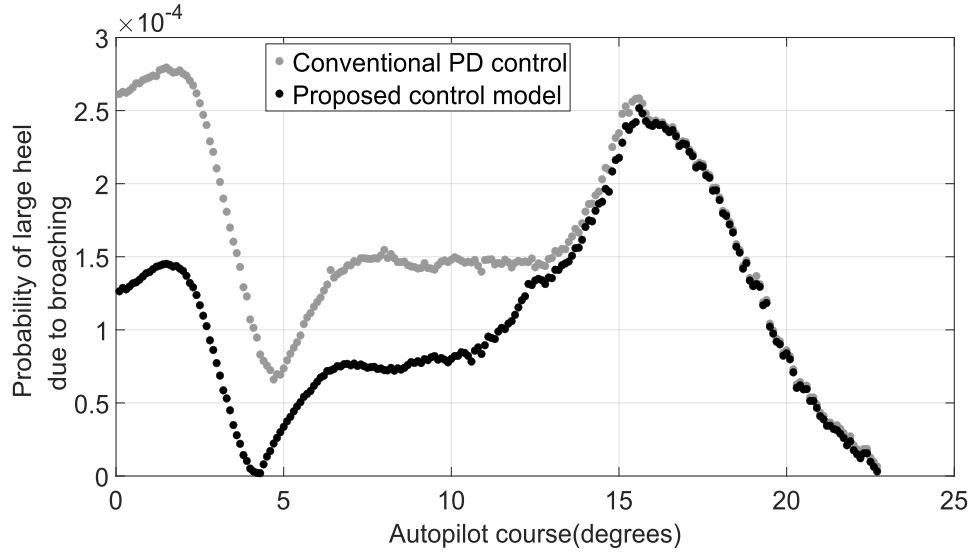

Figure 7: Probability of large heel due to broaching-to at Fn=0.35 in the North Atlantic

Figure 8 shows the comparison of the average probability of large heel due to broaching-to under the conventional PD control and proposed control model. Since the effectiveness of the proposed model is significant for an autopilot course range of 0 to 12 degrees. The averaging is also presented as two different regions, where the first region shows a significant reduction of 51.0% under the proposed control model and the higher autopilot course region shows only a slight reduction in broaching-to probability.

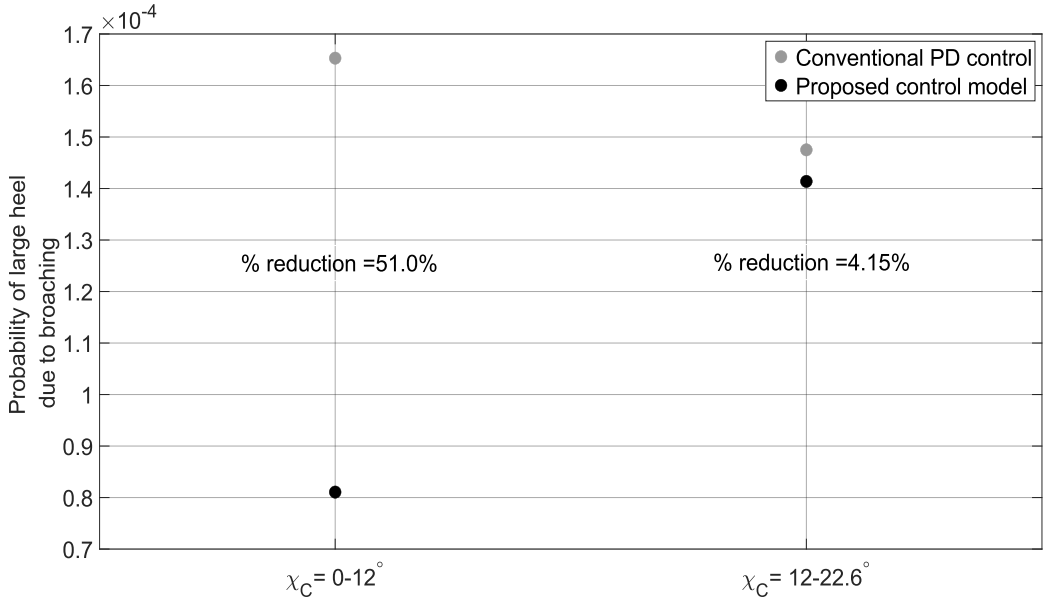

Figure 8: Average probability of large heel due to broaching-to at Fn=0.35 in the North Atlantic

CONCLUSIONS AND FUTURE WORK

The proposed momentary state feedback control is applied to different regular wave conditions and its effectiveness is assessed in real seas using a probabilistic approach for a nominal Froude number of 0.35. The comparison of the probability of large heel due to broaching-to in the North Atlantic is provided. The proposed model could significantly reduce the broaching-to probability in lower autopilot course from the wave direction. This implies that the occurrence of broaching-to could be significantly reduced by keeping the heading angle close to the following seas with the proposed control method. The broaching-to is mainly avoided by undergoing periodic motion with the additional control actions, except at very high wave steepness where it goes to stable surf-riding. However, at higher heading angles broaching-to occurrence could not be prevented by the proposed control model, so that design measures, such as rudder size increases, would be required.

The authors intend to extend the momentary control approach to irregular waves by direct numerical simulation using the proposed control model. Identifying the ship's proximity to the saddle point will require a measure of proxy variables such as pitch angle and mean wave celerity. Methods to counter the broaching-to in higher heading angle also needs to be investigated.

ACKNOWLEDGEMENTS

This work was supported by a Grant-in-Aid for Scientific Research from the Japan Society for Promotion of Science (JSPS KAKENHI Grant Number 19H02360).

REFERENCES

Holmes, Philip J. "1980 Averaging and Chaotic Motions in Forced Oscillations". *SIAM Journal on Applied Mathematics* , 38:1 (1980): 65–80. https://doi.org/10.1137/0138005.

IMO. "2007 Revised Guidance to the Master for Avoiding Dangerous Situations in Adverse Weather and Sea Conditions". *MSC.1/Circ. 1228* (2007).

———. "2020 Interim Guidelines on the Second Generation Intact Stability Criteria". *MSC/Circ. 1627* (2020), Section 2.6.3.

ITTC. "2002 The Specialist Committee on Prediction of Extreme Ship Motions and Capsizing". *Proceedings of the 23rd International Towing Tank Conference (ITTC)* (2002): 619–748.

M. S. Longuet-Higgins. "1983 On the Joint Distribution of Wave Periods and Amplitudes in a Random Wave Field". *Proceedings of the Royal Society of London. A. Mathematical and Physical Sciences* , 389:1797 (1983): 241–58. https://doi.org/10.1098/rspa.1983.0107.

Maki, Atsuo, Naoki Sakamoto, Youhei Akimoto, Yuki Banno, Sreenath Maniyappan, and Naoya Umeda. "2021 On Broaching-to Prevention Using Optimal Control Theory with Evolution Strategy (CMA-ES)". *Journal of Marine Science and Technology* , 26:1 (2021): 71–87. https://doi.org/10.1007/s00773-020-00722-9.

Maki, Atsuo, Naoya Umeda, Martin Renilson, and Tetsushi Ueta. "2010 Analytical Formulae for Predicting the Surf-Riding Threshold for a Ship in Following Seas". *Journal of Marine Science and Technology* , 15:3 (2010): 218–29.

https://doi.org/10.1007/s00773-010-0085-y.
Maki, Atsuo, Naoya Umeda, and Seiya Ueno. "2008 Investigation on Broaching-to Using Optimal Control Theory". *Journal of the Japan Society of Naval Architects and Ocean Engineers* (2008): 115–22. https://doi.org/10.2534/jjasnaoe.8.115.
Maniyappan, Sreenath, and Naoya Umeda. "2021 (Under Review) Broaching-to Prevention in Real-Time Using Momentary State Feedback Control Focusing on the Saddle Point in the System". *Journal of Marine Science and Technology* (2021).
Maniyappan, Sreenath, Naoya Umeda, Atsuo Maki, and Youhei Akimoto. "2020 Effectiveness and Mechanism of Broaching-to Prevention Using Global Optimal Control with Evolution Strategy (CMA-ES)". *Journal of Marine Science and Technology*, June (2020). https://doi.org/10.1007/s00773-020-00743-4.
Ohtsu, K, and K Hasegawa. "1981 Evaluation and Perspectives of Autopilot". In *Proceedings of the 3rd Symposium on Ship Maneuverability*, 243–79 (1981). Tokyo: The society of Naval Architects of Japan.
Ott, Edward.Grebogi, Celso.Yorke, James A. "1990 Controlling Chaos". *Physical Review Letters* , 64:11 (1990): 1196–99. https://doi.org/10.1103/PhysRevLett.64.1196.
Renilson, M.R. "1986 The Seabrake : A Device for Assisting in the Prevention of Broaching-To". In *Third International Conference on Stability of Ships and Ocean Vehicles*, 75–80 (1986).
Spyrou, K. J. "2009 Perceptions of Broaching-to: Discovering the Past". In *10th International Conference on Stability of Ships and Ocean Vehicles*, 357–68 (2009).
Umeda, Naoya. "1990 Probabilistic Study on Surf-Riding of a Ship in Irregular Following Seas". In *Fourth International Conference on Stability of Ships & Ocean Vehicles*, 336–43 (1990). Naples.
———. "2000 Application of Nonlinear Dynamical System Approach to Ship Capsize Due to Broaching in Following and Quartering Seas". In *Contemporary Ideas on Ship Stability*, 57–68 (2000). Elsevier Science Publications (Amsterdam).
Umeda, Naoya, and Masami Hamamoto. "2000 Capsize of Ship Models in Following/Quartering Waves: Physical Experiments and Nonlinear Dynamics". Edited by K. J. Spyrou and J. M. T. Thompson. *Philosophical Transactions of the Royal Society of London. Series A: Mathematical, Physical and Engineering Sciences* , 358:1771 (2000): 1883–1904. https://doi.org/10.1098/rsta.2000.0619.
Umeda, Naoya, and Hirotada Hashimoto. "2002 Qualitative Aspects of Nonlinear Ship Motions in Following and Quartering Seas with High Forward Velocity". *Journal of Marine Science and Technology* , 6:3 (2002): 111–21. https://doi.org/10.1007/s007730200000.
Umeda, Naoya, Akihiko Matsuda, and Matao Takagi. "1999 Model Experiment on Anti-Broaching Steering System". *Journal of the Society of Naval Architects of Japan* , 1999:185 (1999): 41–48. https://doi.org/10.2534/jjasnaoe1968.1999.41.
Umeda, Naoya, and M.R Renilson. "1992 Broaching- A Dynamic Analysis of Yaw Behaviour of a Vessel in a Following Sea". In *Manoeuvering and Control of Marine Craft*, edited by P A Wilson, 533–43 (1992). Computational Mechanics Publications, Southampton.

Project for Measuring Underwater Radiated Noise from Ships near Pacific Islands off Japan

Masahiro Sakai[1], Soma Oizumi[1], Kengo Yasumoto[1], Naoya Umeda[1]

ABSTRACT

In recent years, the relationship between the marine ecosystem and underwater noise caused by human activities has been attracting attention. The IMO started a review of the guidelines for the reduction of underwater radiated noise from ships and identification of the next step in the sub-committee on Ship Design and Construction in January 2022. Research related to underwater radiated noise by shipping have been conducted. ISO 17208-1:2016 is a method to accurately evaluate a source level of underwater radiated noise (URN) from a ship. However, this strict method is too laborious to evaluate the source levels of URN from many ships. As a simplified method, a long-time measurement by hydrophones installed near a shipping route is being attempted. This method allows to evaluate source levels of URN from several ships that pass near the hydrophones. However, since the population of the ships whose noise levels are observed is the ships going near the shipping route, the noise level model should be affected by the site of measurement. This study aims to know the underwater radiated noise levels of ships around Japan and to examine how to evaluate the noise by hydrophones installed underwater. Furthermore, the results are compared with preceding research. Several hydrophones will be installed underwater near the shipping route through the south of Izu-Oshima Island, Japan. When a ship passes enough near the hydrophones and there are no other ships around, the underwater radiated noise level can be evaluated by a sound propagation theory. The position of hydrophones and AIS data provide the distance between the hydrophones and ship. The measurement was conducted under the same condition as the ISO 17208-1 method as much as possible, so that three hydrophones were vertically installed at a point with a water depth of more than 300 meters. We measured the underwater sound from November 2020 to January 2021. We will report the underwater radiated noise levels from ships around Japan.

KEY WORDS

Underwater Radiated Noise from Ships; Marine Acoustics; Izu-Oshima.

INTRODUCTION

Shipping is a source of underwater noise, and the noise may be dominant near sea lanes (Wenz,1962). Ships unintentionally radiate noises underwater mainly due to propeller cavitation (Urick,1975; Ross,1976). In recent years, the relationship between the marine ecosystem and underwater noise caused by human activities has been attracting attention. The IMO started a review of the guidelines for the reduction of underwater radiated noise from ships and identification of the next step in the sub-committee on Ship Design and Construction in January 2022. Projects on underwater radiated noise (URN) from ships were carried out or are undergoing all over the world: e.g., SONIC (2012-2015), AQUO (2012-2015), ECHO Program (2014-), and SATURN (2021-2025). In Japan, a survey of URN from a coastal passenger liner was conducted in 2015-2017, and it was shown that it is possible to estimate the source sound pressure level by CFD (Sakamoto et al., 2018). ISO 17208-1:2016 (ISO,2016) is a widely known method to evaluate the source level of URN from a ship. However, it is not practical to apply the ISO method to many ships because the ship should go and return several times near hydrophones in a deep-water area. To resolve this difficulty, installing hydrophones near a shipping route and evaluating source levels of URN from ships passing near the hydrophones were examined. Simard et al. (2016) installed three hydrophones in the St. Lawrence Seaway setting up to comply as much as possible with ASA/ANSIS12.64 (ANSI,2009), estimated the source level using the transmission loss of underwater sound based on in situ measurements, and discussed the relationship between the source

[1]Osaka University

levels and ship type, age, length and speed. Karasalo et al. (2017) installed hydrophones at 3 m from the seafloor off the coast of Orlando Island (41 m depth), measured the URN from ships passing in the vicinity, and analyzed the trend of the source level for each type of ship. MacGillivray et al. (2019) installed three hydrophones, two in the slowdown zone in Haro Strait and one in the Strait of Georgia and examined the effect of noise reduction during slowdown operation. The Vancouver Fraser Port Authority asked ships navigating in the area to voluntarily slow down to 11 knots. The analysis of the sound source levels of a total of 1317 ships showed that the reduction of underwater sound levels by 11 knot slow steaming was about 10 dB for high-speed ships such as container ships and about 6 dB for low-speed ships such as tankers.
In this project, hydrophones were installed under the sea to continuously measure the underwater sound near Japan. The purpose of this project is to investigate the source level of the URN from ships passing near the hydrophones. Three hydrophones were installed near the shipping lane passing through the south of Izu-Oshima Island for about two months from November 19, 2020, to January 21, 2021.

METHODS

Measurement Site, Duration and Hydrophone System

The measurement site was determined based on the two points: target ships should pass near the measurement site, and the measurement method should be as close as possible to that of ISO 17208-1:2016. Since the URN from several vessels may be recorded simultaneously in a congested sea area, the number of ships for which the source level can be estimated may decrease due to the interference of their URN. As for the ISO method (ISO, 2016), it is required to install three hydrophones at different depths in a sea area where the water depth is 150 m or more than 1.5 times the ship length. In this project, the measurements were conducted in a sea area where a water depth of about 300 m. Considering the above conditions, the measurements were conducted south of Izu-Oshima Island as shown in Figure 1. The white lines indicate samples of ships' paths. The position of the hydrophones is the centre of the shipping route but the route is not so congested. In addition, the point where the hydrophones were installed was determined by avoiding fishing grounds and underwater cables. The measurement period, the sinker points for the hydrophone system, and the water depth are as follows.

- 1st period: from Nov. 19th, 2020, to Dec. 20th, 2020
  - Lat. 34° 36.423′ N, Lon. 139° 21.036′ E
  - Water depth: 328 m
- 2nd period: from Dec. 22nd, 2020, to Jan. 21st, 2021
  - Lat. 34° 36.444′ N, Lon. 139° 20.992′ E
  - Water depth: 329 m

The hydrophones were installed under the sea by using a buoyant material to raise the hydrophone system from a sinker installed on the seabed. The schematic view of the hydrophone system is shown in Figure 2. The depths for the 1st period are shown, and also the depths for the 2nd period are shown in the parentheses. In addition to the three hydrophones installed at different depths, a pressure gauge (depth meter) and a current meter were installed at the upper hydrophone location and a pressure gauge at the lower hydrophone location, respectively, to estimate the hydrophone position underwater. The water depths at the site and each hydrophone depth in the upright position are also shown in Figure 2. The disconnection device was activated to recover the upper part of the hydrophone system. The depths of the hydrophones were determined based on the ISO method (ISO,2016), in which the target ship passes near the hydrophones so that the horizontal distance at the closest point of approach (CPA distance) to the hydrophones is the same as the ship length. The water depths of the three hydrophones is determined so that the depression angles of 15, 30, and 45 deg. Since the effect on reflection on the seafloor is pronounced near the seafloor, this project uses the hydrophone depth when the CPA distance is 200 meters to design the hydrophone system. In other words, the hydrophone depths were designed as 53.6, 115.5, and 200 meters from the top. The hydrophone was installed at a depth of 327 m, which is approximately the same as the design depth. The measurement devices and their settings are as follows.

- Hydrophone: SoundTrap ST300 (Ocean Instruments Ltd.)
  - Minimum working frequency: 20 Hz
  - Sampling rate: 48 kHz
- Pressure gauge (depth meter): DEFI2-D50 (JFE Advantech Co., Ltd.)
  - Sampling rate: 0.2 Hz (once every 5 s)
- Current meter: DEFI2-D50 (JFE Advantech Co., Ltd.)
  - Sampling rate: 1/120 Hz (once every 5 min)

The setting is determined to sufficiently measure underwater sound for one month in consideration of the battery and storage of the devices. The frequency range of the hydrophone is enough to measure the URN from ships, whose frequency peaks around 100 Hz.

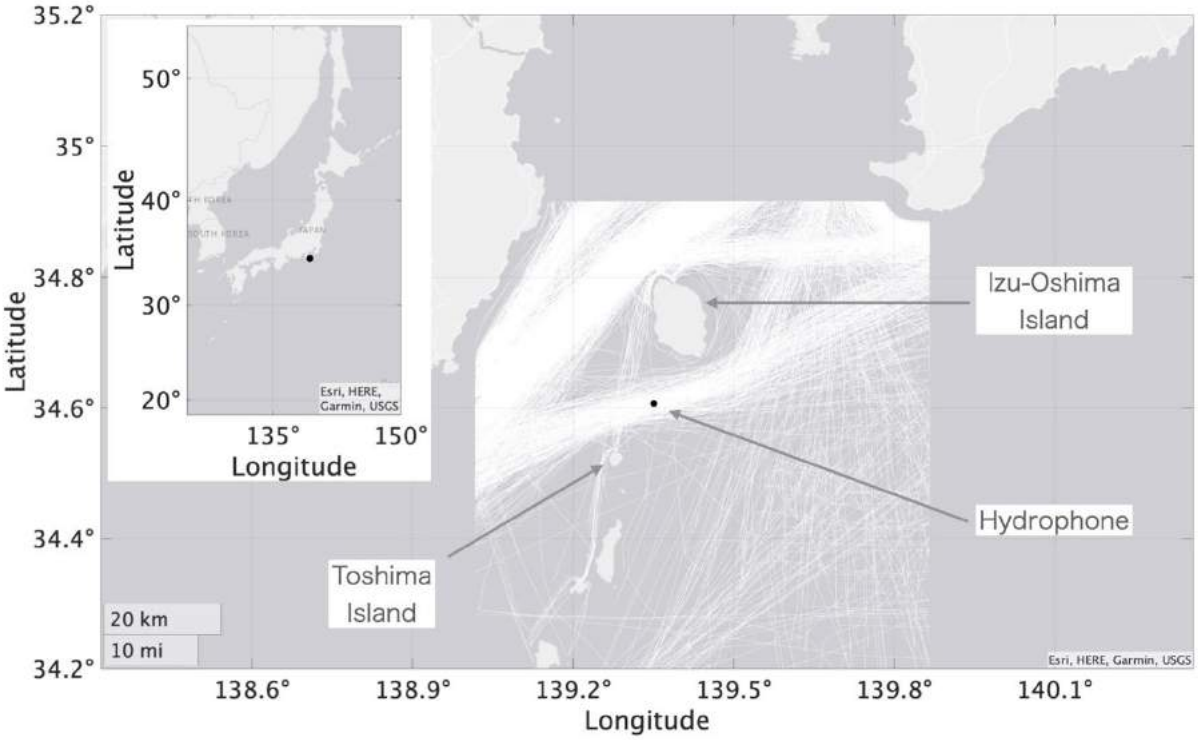

Figure 1: Measurement site with ships' paths (Basemap Sources: Esri, HERE, Garmin, USGS)

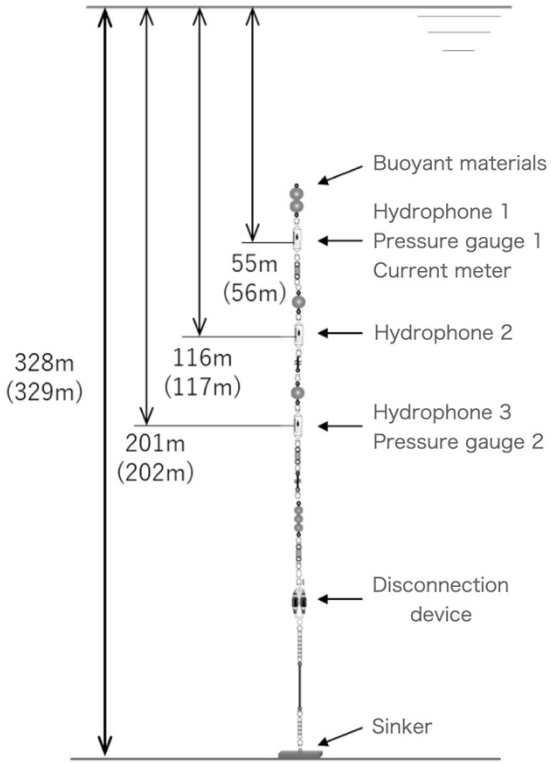

Figure 2: Set-up of the hydrophone system

Estimation of Source Level of URN from a Ship

The source level of the URN from a ship, *SL* [dB], is estimated by the receive level, *RL* [dB] and the transmission loss, *TL* [dB].

$$SL = RL + TL \quad [1]$$

In this research, TL is estimated based on spherical spreading.

$$TL = 20 \log_{10} r \quad [2]$$

Here, r [m] is the distance between the source of sound and the hydrophone, which is calculated by the depth of sound source, d_S (0.7 times the draught), the depth of the hydrophone, d_H, and CPA distance, CPA.

$$r = \sqrt{CPA^2 + \left(d_H - d_S\right)^2} \quad [3]$$

The receive level is obtained by calculating the power spectrum density (PSD) of the voltage using FFT from the voltage data of the hydrophones, converting the PSD to dB, and adding the calibration factor. The FFT was calculated every second, and the number of data was set to 2^15, which corresponds to data for about 0.683 s. In the process of FFT, the Hann window was applied to the voltage data. The time of the closest point of approach is distinguished by checking spectrogram (colour map that visualizes intensity of time-varying spectrum with time and frequency), at the same time, it is confirmed that the ship noise is dominant over the background noise.

In some cases, the URN from a ship cannot be distinguished from other noise even though the ship was passing very close to the hydrophones. Since it is impossible to simply estimate SL based on Equations 1 to 2, such data are excluded in this study. Figure 3 shows the receive level in spectrogram, summation of the receive level with frequencies, speed of the current, and the inclination angle for three days. The horizontal axis is the date and time. The top figure shows the receive level in spectrogram with the ships' passages (solid black lines). The bottom figure shows the speed of the current [cm/s] (black solid line) and the inclination angle of the hydrophone system [deg] (black broken line). When the receive level is high without ships' passages, both the speed of the current and the inclination angle of the hydrophone system are at their maximum. Also from the periodicity, the noise may be related to the tide or the ocean current.

The SL estimated by the above procedure is converted to a 1/3-octave band spectrum. The power spectrum of SL, S_{SL}, is expressed as

$$S_{SL}\left(f\right) = 10^{\frac{SL(f)}{10}} \quad [4]$$

In 1/3-octave band analysis, the centre frequency f_k and cut-off frequencies f_{k-} and f_{k+} are determined based on powers of two or powers of ten. In this study, powers of ten are used, but there is no significant difference between them.

$$f_k = 1000 \times 10^{\frac{k}{10}},\ f_{k-} = f_k \times 10^{-\frac{1}{20}},\ f_{k+} = f_k \times 10^{\frac{1}{20}} \quad [5]$$

The 1/3-octave band of SL, $SL_{1/3}$, is calculated as

$$SL_{1/3}\left(f_k\right) = 10 \log_{10}\left(\frac{1}{f_{k+} - f_{k-}} \int_{f_{k-}}^{f_{k+}} S_{SL}\left(f\right) df\right) \quad [6]$$

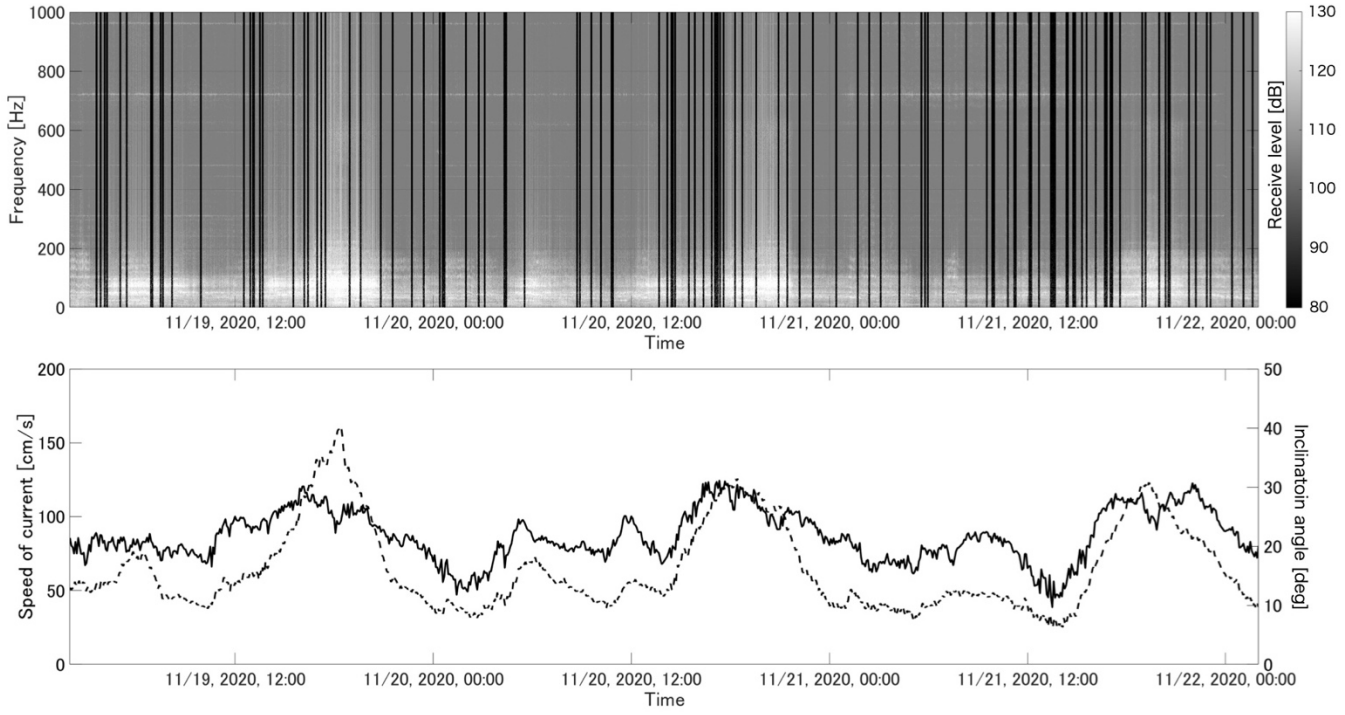

Figure 3: Noise on hydrophones, speed of the current, and inclination of the hydrophone system

RESULTS AND DISCUSSION

Validation of Spherical Spreading

In this study, the source level of the URN from ships is estimated by using the spherical spreading (Equation 2), which is derived by assuming that the underwater sound source is considered as a monopole source and that the sound energy radiates on a sphere. Therefore, if the hydrophone is too close or too far from the sound source, the estimation error will be non-negligible. The source level of ship A and B is estimated as shown in subsection "Estimation of Source Level of URN from a Ship", which passed near the hydrophone several times during the measurement period, and the source levels are shown in Figure 4 to 5 to examine the CPA distance at which the spherical spreading could be considered effective. The horizontal axis is the frequency [Hz] in logarithmic scale, and the vertical axis is the source levels [dB]. Black broken lines indicate the results of the top hydrophone (Hy1), black solid lines indicate the results of the middle hydrophone (Hy2), gray solid lines indicate the results of the bottom hydrophone (Hy3). The source levels of each ship show a certain amount of variation because it is impossible to match the sea conditions since this measurement is carried out in the real sea, and since the sailing conditions may be slightly different. The source levels estimated from Hy1 is larger than Hy2 and Hy3 in the frequency range up to 200 Hz. This may be because of low-frequency noise from the hydrophone system and sound wave characteristics including the reflection of the sea surface and bottom. At low frequencies, since tonal ship noise also appears, it is difficult to distinguish the noise source. Although the source level is estimated as a mean value of the three hydrophones in the ISO method, source levels were analyzed for the middle hydrophone (Hy2) because of the low-frequency noise. There is no significant difference in the source levels due to the CPA distance in Figures 4 to 5, in which the CPA distance ranges 10 to 850 [m]. In this study, the data with a CPA distance up to twice the water depth were analyzed a little more strictly.

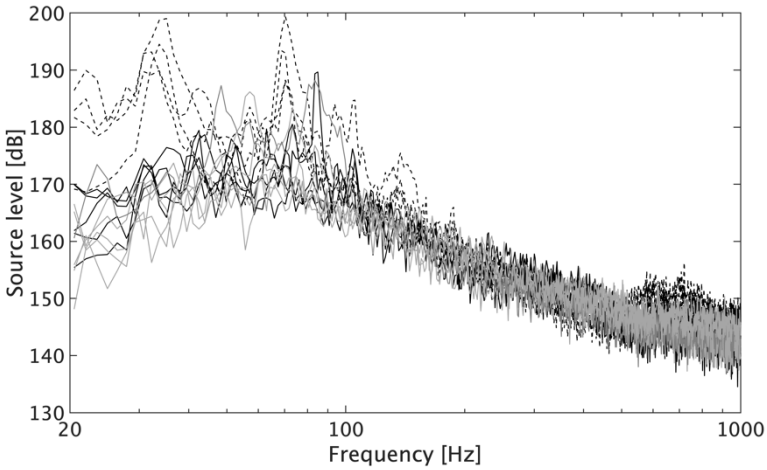

Figure 4: Source levels of ship A from several passages

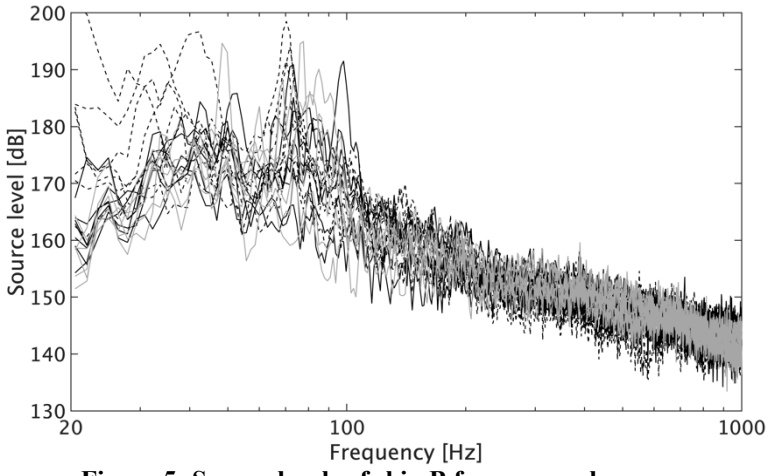

Figure 5: Source levels of ship B from several passages

Source Levels with Ship Types

In the measurement area, the number of container ships and car carriers' passages is larger than that of other ship types. Figure 6 shows box plots of the 1/3-octave band spectrum of source levels with ship types. The ship type and the number of ships are shown just above each figure. The source level peaks below 100 Hz and decreases linearly above a few hundred Hz, which is consistent with the general characteristics of the URN from ships. The source levels of container ships and pure car carriers seem to be slightly larger than that of other types of ships. In this subsection, the source levels trend is clarified by ship types. However, the analysis can be a combination of various factors, such as ship length and age. Therefore, in the following section, the trend is considered with ship length and age using container ships, whose number of passages was the largest.

Source Levels of Container Ships with Ship Length and Age

Figures 7 shows box plots of the 1/3-octave band spectrum of source levels of container ships, which pass near the hydrophones the most frequently, with ship length and age. The range of ship length and age are shown just above each figure. Figure 7 shows that larger ships and older ships are noisier. Particularly, the source level increases by almost 5 dB with a 100 m increase of ship length. The effect of age is less pronounced than that of length, but container ships built in recent years seem to be somewhat quieter. Compared to the URN from ships along St. Lawrence Seaway shown by Simard et al. (2016), the URN shown in Fig. 6-7 shows a little bit quieter in all frequency ranges. However, this cannot directly show the difference in noise levels between areas because of the difference in the estimation method of the transmission loss of underwater sound. Note that, in this study, the energy of the 1/3 octave band spectrum is divided by the frequency range as Equation 4, which is different from the usual octave band analysis, to adjust the level of the 1/3 octave band noise level to that of the narrowband spectrum. In the case of 100 Hz, 13.63 dB should be added to compare the results in this study with the results of Simard et al. (2016). On the other hand, the tendency of the URN source level variability with ship length of this research is similar to that of Simard et al. (2016).

CONCLUSIONS

Three hydrophones were installed near the shipping lane passing through the south of Izu-Oshima Island, Japan, for about two months. The source levels of URN from ships that pass near the hydrophones are estimated by using spherical spreading. In the measurement area, the number of container ships and car carriers' passages is larger than that of other ship types. The source levels of container ships and pure car carriers seem to be slightly larger than that of other types of ships. For container ships, the source level increases by almost 5 dB with a 100 m increase of ship length, and recent ships seem to be somewhat quieter. We are planning to perform Phase 2 URN measurements on the same site to analyze more data.

ACKNOWLEDGEMENTS

This work is supported by a research activity of Under Water Radiated Noise by Shipping Project of Japan Ship Technology Research Association in the fiscal years of 2020 funded by the Nippon Foundation. The authors would like to thank Drs. Akamatsu, T. and Tsuchiya, T. for their technical advice and useful discussions.

REFERENCES

ANSI. "American national standard quantities and procedures for description and measurement of underwater sound from ships – part 1: General requirements." 2009.
ISO "ISO 17208-1:2016 underwater acoustics — quantities and procedures for description and measurement of underwater sound from ships— part 1: Requirements for precision measurements in deep water used for comparison purposes." 2016.
KARASALO, I., ÖSTBERG, M., SIGRAY, P., JALKANEN, J.P., JOHANSSON, L., LIEFVENDAHL, M., BENSOW, R. "Estimates of source spectra of ships from long term recordings in the Baltic Sea." *Frontiers in Marine Science*, **4** (2017): 164.
MACGILLIVRAY, A.O., LI, Z., HANNAY, D.E., TROUNCE, K.B., ROBINSON, O.M. "Slowing deep-sea commercial vessels reduces underwater radiated noise." *J. Acoust. Soc. Am.*, **146** (2019): 340-351.
ROSS, D. "Mechanics of Underwater Noise." Pergamon Press Inc, 1976.
SAKAMOTO, N., KAMIIRISA, H. "Prediction of near field propeller cavitation noise by viscous CFD with semi-empirical approach and its validation in model and full scale." Ocean Engineering, **168** (2018): 41-59.

SIMARD, Y., ROY, N., GERVAISE, C., GIARD, S. “Analysis and modeling of 255 source levels of merchant ships from an acoustic observatory along St. Lawrence Seaway.” *J. Acoust. Soc. Am.*, **140** (2016): 2002-2018.
URICK, R.J., 1975. “Principles of underwater sound.” McGraw-Hill Book.
WENZ, G.M. “Acoustic ambient noise in the ocean: Spectra and sources.” *J. Acoust. Soc. Am.* 34 (1962): 1936–1956.

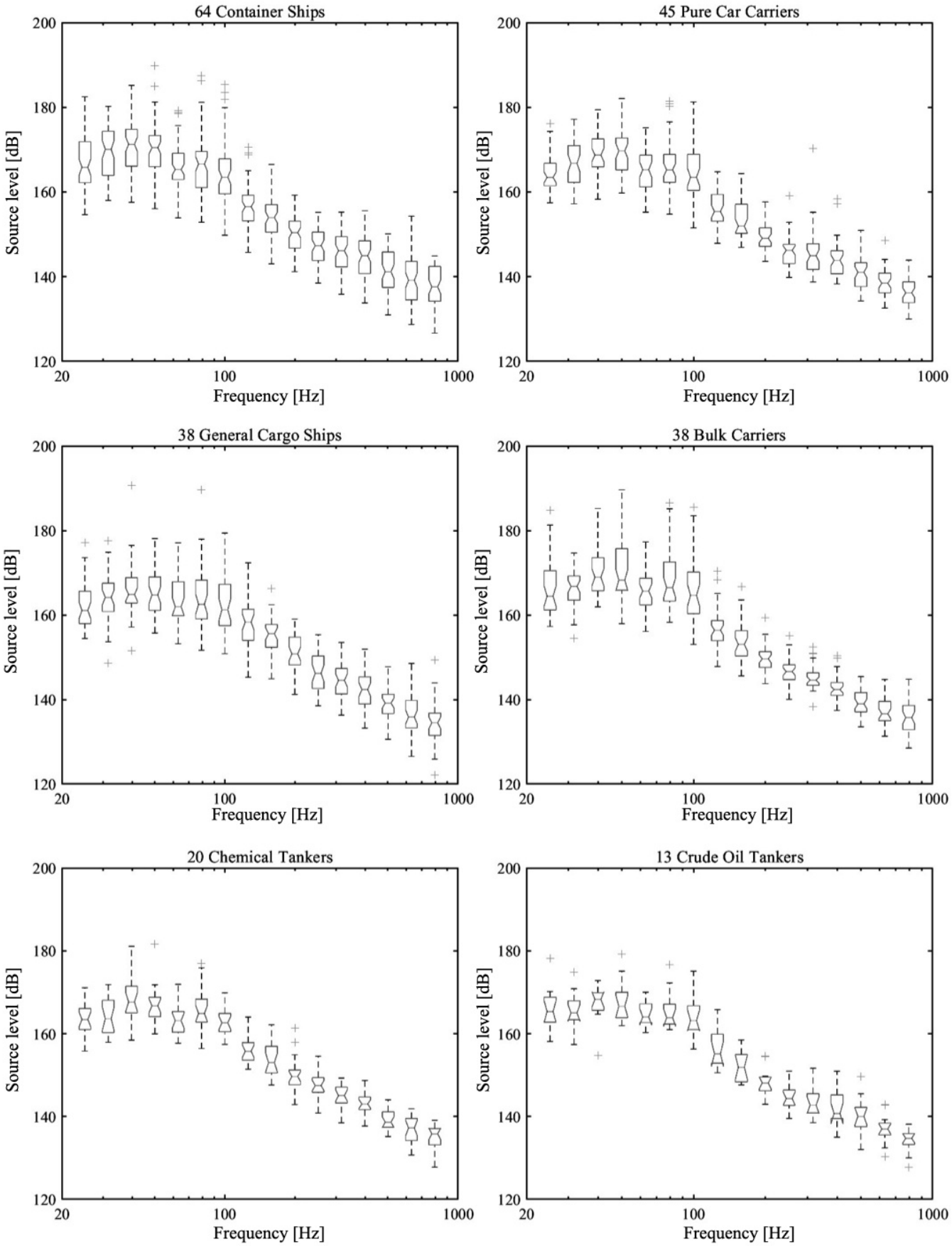

Figure 6: Box plots of 1/3-octave band spectrum of source levels with ship types (Hy2)

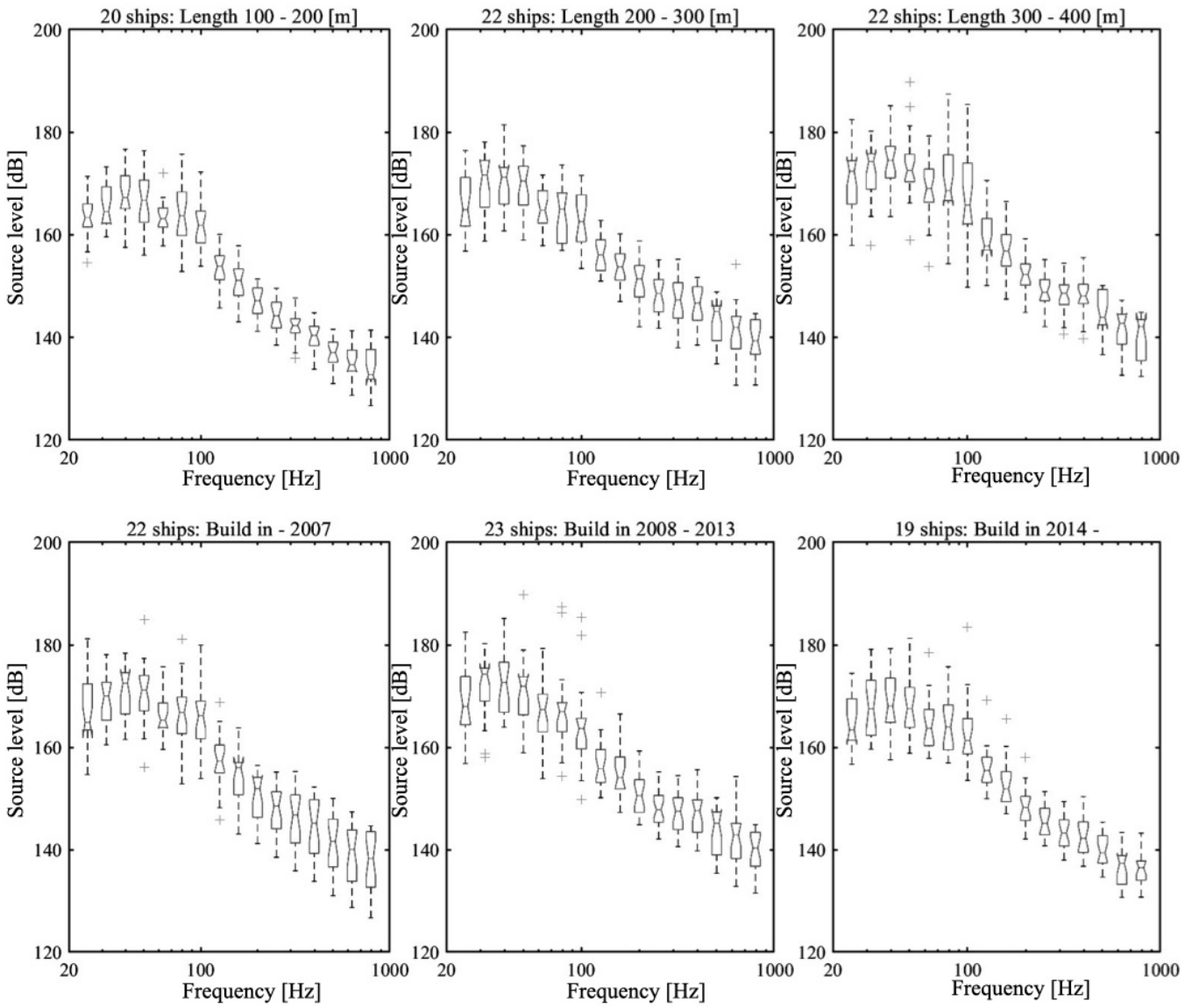

Figure 7: Box plots of 1/3-octave band spectrum of source level of container ships (Hy2)

EXPERIMENTAL INVESTIGATION ON FIRE SPREAD MECHANISMS BETWEEN SHIPPING CONTAINERS

Blanca Andres[1] and Konrad Wilkens Flecknoe-Brown[1]

ABSTRACT

Recent fire events have shown that fires in containerships can have devastating consequences. There are many aspects of containership fires needing further investigation in order to prevent their occurrence and minimise their consequences. This paper investigates the mechanisms of fire spread between a container that has caught on fire to adjacent containers. It presents an experimental analysis in which the hypothesis of fire spreading vertically due to ignition of plywood flooring, and fire spreading laterally due to radiation and passage of flames through the container door are investigated. For that purpose, a total of 41 cone calorimeter tests were performed on plywood samples to obtain their fire properties, such as Heat Release Rate, time to ignition and critical heat flux. Further, the hypothesis of vertical fire spread is also tested in a small-scale furnace test replicating the conditions of necessary heat flux to ignite the sample. Finally, a full-scale door fire test is performed to investigate the fire spread through the container door. Results have shown that both mechanisms are potential causes of fire spread between shipping containers.

KEY WORDS

Container Fire; Fire Spread; Fire Testing; Ignition; Plywood Floors; Small-Scale Fire Test; Furnace Fire Test.

INTRODUCTION

Fires aboard ships can have severe consequences in terms of human lives and economic losses. Limited evacuation options combined with limited possibilities for firefighting make fires on board container ships a complex scenario. Recent fires in container ships have highlighted this matter, and catastrophic events such as the MSC FLAMINIA (Robbins, 2019) and MAERSK HONAM (TISB Singapore, 2020), have brought further debate into the topic. Understanding the issue of containership fires requires understanding the sources of ignition, fire growth, and the mechanisms of fire spread between containers.

This work studies the plausible mechanisms of fire spread between containers in the cargo hold of a container ship. Six hypothesis were proposed: (1) vertical fire spread by ignition of the plywood floor in the container above, (2) fire spread through container door, (3) lateral fire spread by radiation to neighbouring containers, (4) fire spread through plastic vents in the containers, (5) fire spread through container structural collapse, (6) external fires. The hypothesis are either based on a literature research e.g. (Eberly, 1977; El Moctar, Povel, Shibunov, & Tide, 2015; Souer, 1973), on fire investigation reports of container fire incidents, or based on discussion with experts and staff members of the fire school at Helsingør. The investigation is undertaken by combination of experiments and numerical modelling. This article focuses on the experimental investigation of hypothesis 1 and 2. The work presented is part of the CONTAIN project, and the results of all the analysis can be found in the report (Hulin et al., 2021).

The likelihood of vertical fire spread between shipping containers by ignition of the plywood floor (hypothesis 1) was investigated at two different scales:

1. The fire properties of plywood floors were investigated at a material scale using the cone calorimeter.
2. Small-scale furnace tests were performed to confirm cone calorimeter findings in a more realistic testing scenario.

[1] The Danish Institute of Fire and Security Technology, DBI, Hvidovre, Denmark

The likelihood of lateral fire spread through the container door was investigated with a full-scale furnace test on a container door following the standard ISO 834 fire exposure (International Organisation for Standardisation, 1999).

EXPERIMENTAL PROGRAM

Hypothesis 1- Vertical fire spread by ignition of the plywood floor above.

Hypothesis 1 was analysed under two different experimental set-ups. The testing methodologies consisted of: Cone Calorimeter tests to obtain the fire properties of the plywood floors, and small-scale furnace test to identify the possibility of a hot steel plate to ignite the plywood above.

Materials

A seaworthy container was purchase for this study, and was cut up as required to provide samples for the various experiments. The plywood floor of the container was made of a patchwork of plywood sections, with different age, condition, material and surface treatment (bitumen waterproofing was on some section and not on others). Additionally, the plywood from different patches had different densities, varying between 600-900 kg/m^3. Figure 1 shows an image of the state of the container floor.

Figure 1: Image of the container floor.

Sections of the floor were then randomly sampled, and specimens of 100×100mm were cut from the different sections in preparation for the cone calorimeter testing. Figure 2 highlights some of the varied specimens obtained.

Figure 2: Examples of the plywood samples made for the Cone Calorimeter tests.

Cone Calorimeter Tests

The cone calorimeter (Lindholm, Brink, & Hupa, 2009) is a testing apparatus used to study the fire behaviour of small material samples. It consists of a conical shaped heater that emits a defined level of radiant heat to a specimen positioned 25 mm below. The heat exposure is designated at the start of the test and remains constant throughout its duration. A spark ignitor located above the sample ignites the flammable gases released by the sample when the concentration is sufficient, at which time of ignition is recorded. The post-combustion gases are measured in the hood and the energy released is calculated via oxygen consumption calorimetry (Beyler, Croce, Dubay, Johnson, & McNamee, 2017). Additionally, smoke production is measured using a laser and the mass loss is recorded using a load cell. Specimens of 100×100 mm were tested in a

horizontal orientation. A total of 41 tests were performed under four different radiant heat fluxes: 15, 25, 35, and 50 kW/m². The test program included piloted ignition, self-ignition (i.e. without using the spark ignitor), and damaged samples. Tests were performed according to ISO 5660 (International Organisation for Standardisation, 2002). Figure 3 shows a schematic representation of the cone calorimeter test set-up.

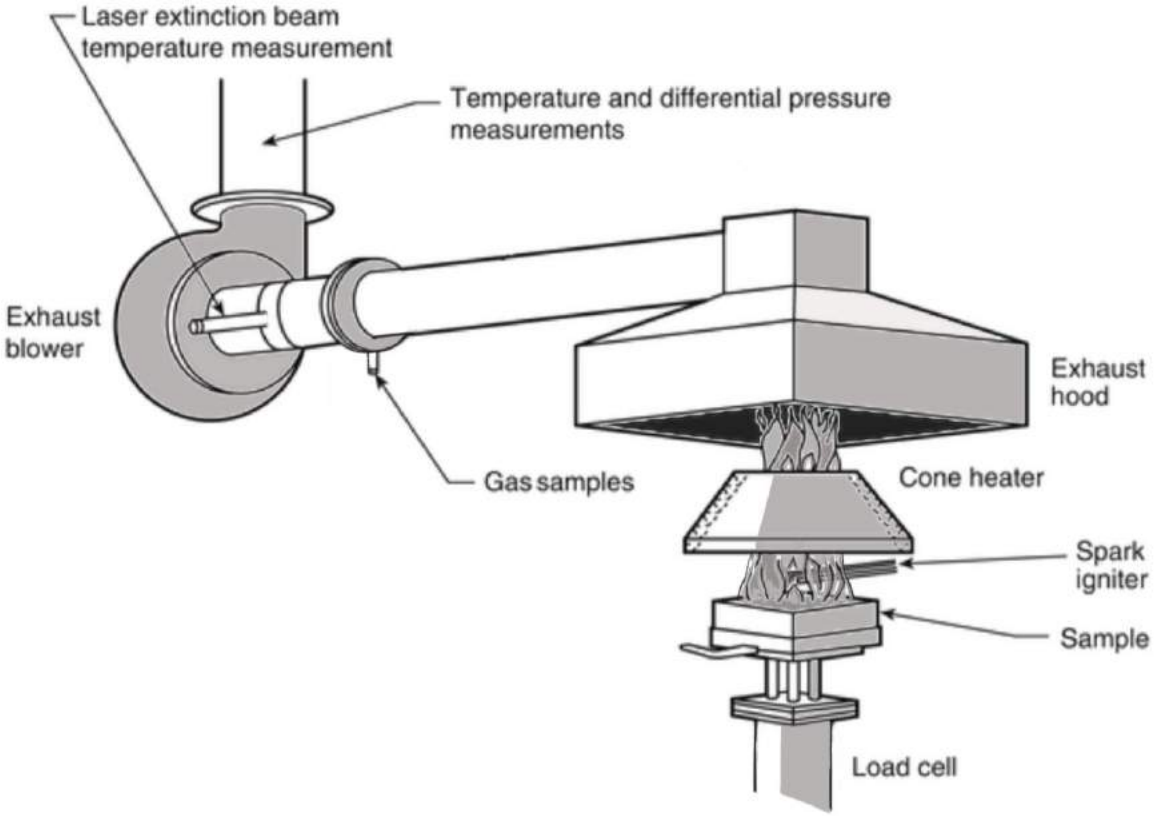

Figure 3: Schematic of Cone Calorimeter Apparatus (International Organisation for Standardisation, 2002)

Small-Scale Furnace Test

A small-scale furnace test was used to confirm the findings obtained from the cone calorimeter tests, in a more realistic setting. It was used to simulate the hot steel roof from a container fire and confirm if this could ignite the plywood floor of the container placed on top. The furnace used for that purpose, developed by DBI, is electrically heated, and allows testing samples of 500×500 mm. In container stacks, a 50 mm gap is allowed between the top of one container and the bottom structure of the container placed on top. The bottom flooring consists of a steel frame and steel cross-beams boarded with a 28 mm plywood plate. A section of the floor structure of the purchased container was cut to fit the opening of the furnace, and a steel plate was placed underneath to simulate the roof of the container below. Figure 4 shows an image of the small-scale furnace and the test sample setup. During the test the sides of the specimen were insulated with stone wool to avoid heat losses from the sides.

(a) (b)

Figure 4: (a) Small-Scale Furnace; (b) Test sample and configuration.

The heat exposure consisted of a steel plate, set to a temperature of 620 °C for 100 minutes with 20 minutes warm up time, controlled by three thermocouples welded to the steel plate. The temperature of the test specimen was recorded by eight Type K thermocouples: five thermocouples were attached to the unexposed side of the plywood, and three thermocouples measured the air temperature in the cavity between the steel plate and the plywood floor. Additionally, a thermal camera recorded the heat distribution on the unexposed side of the plywood floor.

Hypothesis 2- Lateral fire spread through the container door.

In order to test the likelihood of fire spread through a container door, the door was tested in a standard resistance-to-fire vertical furnace. This test aimed at simulating a fire event occurring inside the container and analysing the response of the container door. The full door of the container was placed in the 3×3 m² opening of the furnace, as shown in Figure 5b.

The tested specimen consisted of the door leaves and frame cut from the purchased 20 ft. seaworthy container, as shown in figure 5a. The specimen was placed in an aerated concrete frame, the gaps between the specimen and the frame were filled with mineral wool insulation.

(a) (b)

Figure 5: Tested door – (a) door and surrounding frame as cut from the container, (b) door mounted on the furnace

During the test, gas burners heat up the space inside the furnace, and the temperature exposure to the specimen was controlled by plate thermometers. The temperature-time curve used consisted on an ISO 834 standard fire curve (International Organisation for Standardisation, 1999) run for 90 minutes as shown in Figure 6.

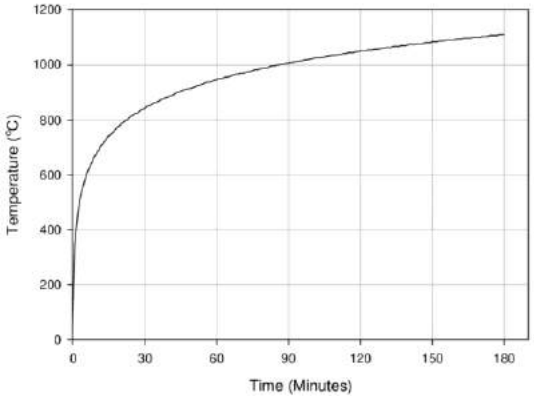

Figure 6: Standard ISO 834 Fire curve

During the test, temperatures and displacement of the steel door were measured at different locations. Additionally, the heat flux to the surrounding was also measured. The instrumentation is summarised as follows:

- Temperature measurements: A total of 31 type K thermocouples attached to various locations of the frame and door, similar to that in a standardised fire test, were split in 5 groups. Figure 7(a) shows the location of the thermocouples.
    - Group 1: Thermocouples on the panel of each door leaf
    - Group 2: Thermocouples on the structural door frame
    - Group A3: Thermocouples on the left door frame
    - Group B3: Thermocouples on the right door frame
    - Group 4: Thermocouples on the sides

- The deflection measurements aimed at measuring how much the door bends or warps during the test. This was measured by a specialised camera that measures the displacement of specifically designed nodes that were attached to the unexposed side of the door at the 18 locations shown in Figure 7(b).

- The heat flux at two locations were measured by two heat flux meters, which were located centrally at a distance of 1 m from the unexposed side of the door, positioned at heights of 102 and 185 cm from the container floor level.

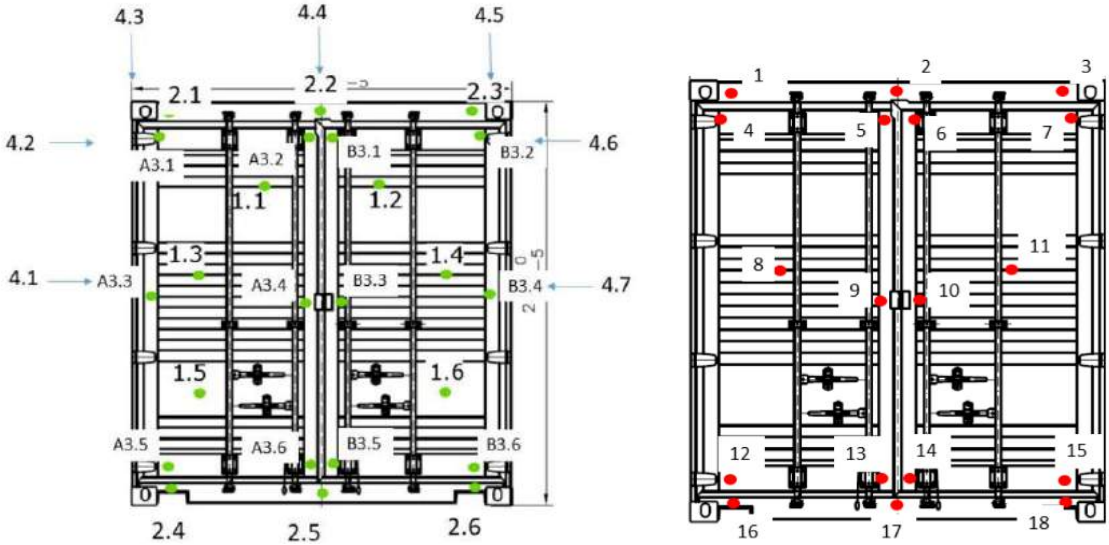

Figure 7: (a) Placement of the thermocouples on the door, (b) Deflection measurement points on the door.

RESULTS AND DISCUSSION

Cone Calorimeter Tests Results

Results from the cone calorimeter tests show two distinct burning phases. Once ignition has occurred, there is an initial peak of heat being released. Afterwards, a char layer forms protecting the sample and the heat release rate decreases significantly. Once the char layer reaches a certain thickness, there is a second phase with a relatively steady burning. Tests were terminated after 20-30 minutes; as it was expected that samples would have kept burning steadily until no material was left. Figure 8 exemplifies the results of the tests performed at 50 kW/m² illustrating the described burning behaviour.

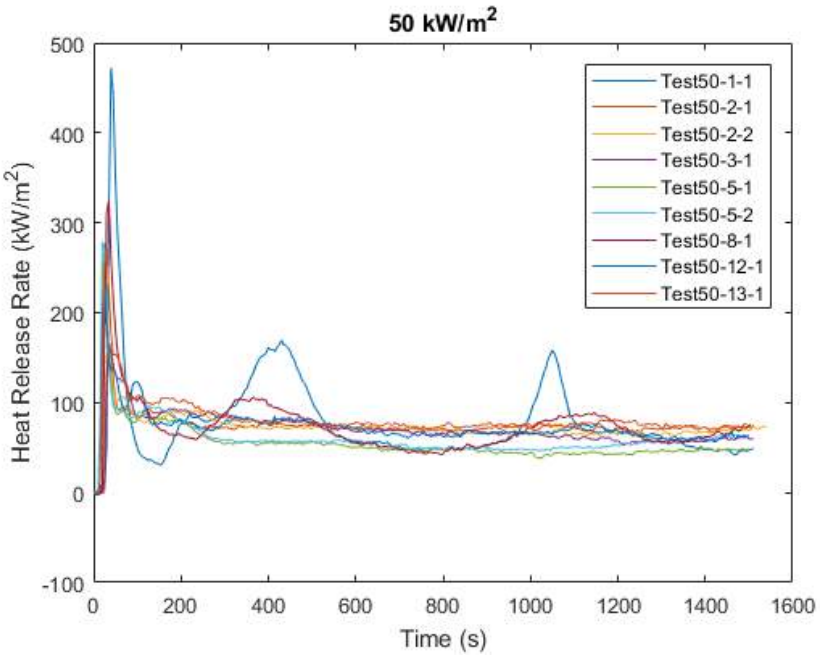

Figure 8: Heat Release Rate of samples tested at 50 kW/m² incident heat flux.

From the 41 tests performed it was observed that the material variation in the plywood floor resulted in a great variation of the fire properties. As an example, in tests performed at 50 kW/m² the peak Heat Released Rate (an important metric for quantifying fire performance) varied between 150 and 500 kW/m², this significant variation was also observed with the time to ignition results. Further, cone calorimeter test results produced the following findings:

- The newer plywood samples (taken from patches on the floor made to repair it) performed, in general, significantly worse than the older sections, both in time to ignition (i.e. it ignited faster) and in peak Heat Release Rate (i.e. it release energy more quickly).
- The samples with a bitumen waterproofing coating resulted in higher peak Heat Release Rate and shorter time to ignition
- Damaged samples did not show significantly different behaviour compared to undamaged samples.
- Self-ignition tests showed no ignition below 25 kW/m² incident radiant heat flux after 20-30mins. At 35 kW/m² only new samples ignited, and at 50 kW/m² all specimens tested self-ignited (i.e. no external ignition source was needed to initiate flaming combustion)
- Based on the cone calorimeter test data the critical heat flux was estimated to be 10-12 kW/m². The critical heat flux represents the minimum heat flux required for ignition of the plywood.

Small-Scale Furnace Test

In the small scale furnace tests (see figure 4 for the test set-up), the unexposed side temperature of the plywood floor and cavity temperature was recorded in 8 different locations. Figure 9 shows the thermocouple readings throughout the test period. Thermocouples T1-5 show the unexposed side temperatures and T6-8 the cavity temperature. The readings show that during the first 20 minutes there is a steady growth in temperature. At 23 minutes, ignition of the plywood occurred at which time a sharp increase in temperatures in the cavity is observed. Flames and smoke were observed in the cavity, and increased when the rubber seal melted. The unexposed side temperatures showed a steady increase in temperature reaching 200 °C, without complete burn-through at 100 minutes after the beginning of the test.

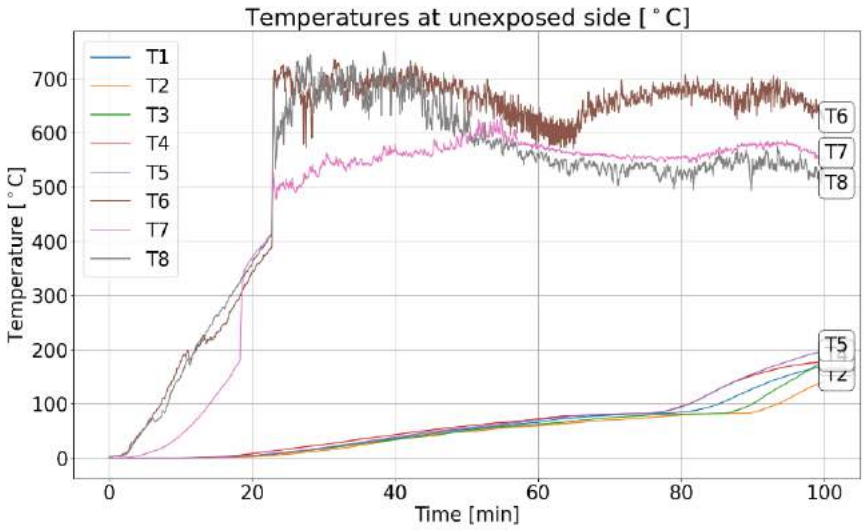

Figure 9: Unexposed side temperature readings in the small-scale furnace test to a floor section.

The small-scale furnace test was undertaken to confirm the results obtained from the cone calorimeter in a more realistic set-up. Given the distance between the plywood and the heated steel plate, using a basic radiation hand calculation, a temperature of 620 °C was selected for the steel plate exposure. This temperature was equivalent to approximately 20 kW/m², and was chosen as representing the cone calorimeter test with a heat flux above the critical heat flux. Furthermore, 620 °C is a realistic gas temperature for a fully developed fire inside a container. As foreseen, ignition occurred after 23 minutes within the test, validating the original hypothesis. In other words, these results show that the fire could spread from a hot steel roof to the plywood floor of the container located above.

Container Door Fire Test

During the container door fire test, the thermocouple readings on the unexposed side show a steady increase in temperature during the first 17 minutes of the test. At that time, the EPDM rubber door gasket ignited and continued burning for approx. 20 minutes. After all the rubber gasket had burned away, the temperatures continue to steadily increase until the end of the test (90 minutes), reaching temperatures between 550-680 °C. Figure 10 shows the maximum temperature readings for the 5 groups of thermocouples recording unexposed side temperature, and an image of the rubber gasket burning. Deflection measurements showed an inwards deflection towards the furnace from the beginning of the test but was considered insignificant. The heat flux measurements located 1m in front of the door showed a maximum radiant heat flux of 19.7 and 17.7 kW. After the test, the door showed no major deformations other than a 2 cm gap left from the burning of the gaskets. The door still functioned and could be opened and closed as prior to the fire.

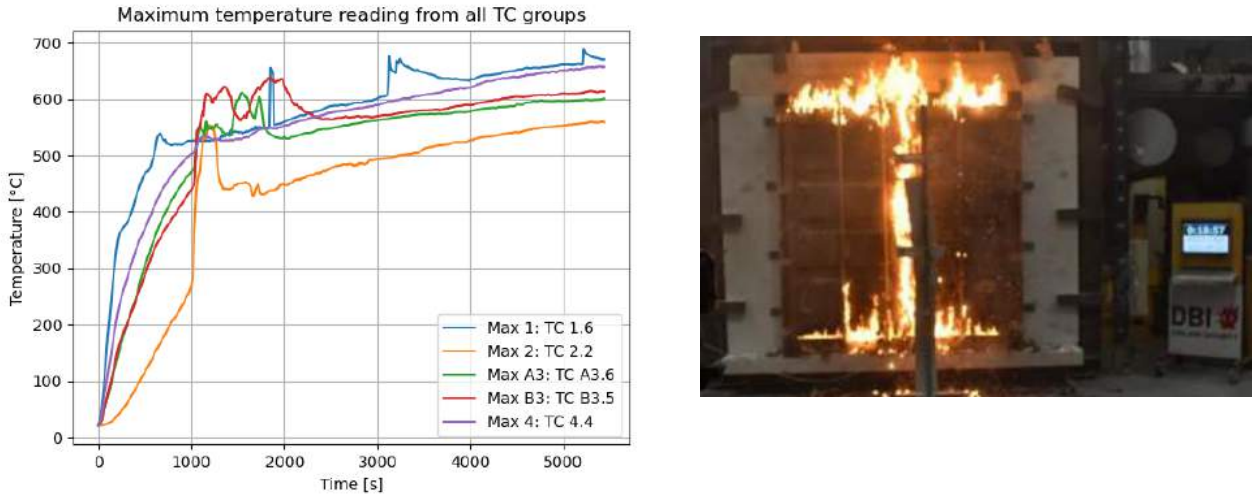

(a) (b)

Figure 10: (a) Maximum temperature recordings for the four groups of thermocouples; (b) burning of the EPMD rubber gasket.

The door furnace tests were performed to investigate hypothesis 2 - the possibility of fire spread through the door of a container. Multiple mechanisms were identified as plausible methods that may allow fire spread between containers or from the container to the exterior, these are surmised as follows:

- The radiation measured one metre away from the steel door reached almost 20 kW. This radiant heat flux would be enough to ignite other combustibles located in the vicinity of the container(LaRue, 2002).
- The rubber gaskets ignited 17 minutes after the start of the test and burned steadily for 20 minutes. The flames coming from the burning of the gasket constitute a loss of integrity and can lead to ignition of the plywood located on the container floor above, or any other combustible located close. Loss of the rubber gaskets will also allow higher air entrainment into the container, and may lead to a significant increase in burning behaviour of the materials located within due to more available oxygen.
- Flaming droplets were also observed falling from the burning rubber gaskets and/or from peeling of the container door paint. Flaming droplets could also lead to ignition of other combustibles located below the container.

The readers are referred to the project report for further detailed results and discussions (Hulin et al., 2021).

CONCLUSIONS

In this article an experimental investigation was presented investigating some of the potential mechanisms of fire spread between shipping containers. A number of hypotheses on the potential mechanisms of fire spread between containers were outlined, and experiments were performed to investigate hypothesis 1 - fire spread between containers, by ignition of the plywood flooring on the container above, and 2 - fire spread through the container door. The tests performed confirm that these hypotheses posed are plausible. The fire properties of the plywood flooring were obtained through Cone Calorimeter tests. The Cone Calorimeter test results combined with small-scale furnace tests, have shown that ignition of the plywood floor can occur even without a direct ignition source. Given the calculated critical heat flux, ignition of the plywood floor could occur if a fire located in a container below raised the container steel temperature above 500 °C, even without direct flame impingement. These temperatures could be even lower if hot air is trapped in the support structure due to poor ventilation between the containers. In the small-scale furnace tests, ignition occurred when the temperature in the cavity was between 350-400 °C. Further, the door fire test has shown that fire can also be spread to adjacent containers and surrounding combustibles, solely through radiation from the heated steel doors, by flame impingement from the combustion of the rubber seals, and/or through flaming droplets that could carry fire to other locations with the cargo areas. Finally, the results from these tests not only provide confirmation of potential spread mechanisms between container, they also provide valuable data that can be use further for modelling the consequences of container fires within cargo hold scenarios.

This investigation was part of a larger project (“CONTAIN”) undertaken by the Danish institute of fire and security technology (DBI) examining fire safety on board container ships, funded by the Danish Maritime Fund.

ACKNOWLEDGEMENTS

The authors would like to acknowledge The Danish Maritime Fund, who funded this project.

REFERENCES

Beyler, C., Croce, P., Dubay, C., Johnson, P., & McNamee, M. (2017). Oxygen consumption calorimetry, William Parker: 2016 DiNenno Prize. *Fire Science Reviews*, *6*(1), 1–7. https://doi.org/10.1186/s40038-016-0016-z

Eberly, R. (1977). *Fire performance of intermodal shipping containers*. Washington D.C.

El Moctar, O., Povel, D., Shibunov, V., & Tide, A. (2015). Fire Investigation in a Container. *Ship Technology Research*, 40–55. https://doi.org/10.1179/str.2010.57.1.004

Hulin, T., Wilkens, K., Ruge, A., Møller, C., Perovic, D., Koch, N. S., … Kleiman, A. B. (2021). *PILOT PROJECT "CONTAIN" - Exploring the Challenges of Containership Fires*. Hvidovre, Denmark.

International Organisation for Standardisation. (1999). ISO 834–1:1999: Fire Resistance Tests – Elements of Building Construction – Part 1: General Requirements.

International Organisation for Standardisation. (2002). ISO 5660-1&2 Reaction-to-fire tests-Heat release, smoke production and mass loss rate -Part 1&2 (cone calorimeter method).

LaRue, D. L. (2002). *FIRE INDICATORS*. Washington D.C.

Lindholm, J., Brink, A., & Hupa, M. (2009). Cone calorimeter – a tool for measuring heat release rate. *Finnish-Swedish Flame Days 2009*, (February 2014), 4B. https://doi.org/10.1002/fam

Robbins, D. (2019). MSC FLAMINIA- A brief account of an investigation. Retrieved from https://www.burgoynes.com/articles/2019/02/msc-flaminia-a-brief-account-of-an-investigation

Souer, H. J. (1973). *MARITIME TRANSPORTATION OF CONTAINERIZED CARGO PART III - Fire tests in closed containers*. Delft.

TISB Singapore. (2020). Fire on Board MAERSK HONAM at Arabian Sea on 6 March 2018, (October).

Simulation Code for Financial Evaluation of Investment in Sustainable Technology

Joannes Gullaksen[1]

ABSTRACT

Sustainable technology enables valuable use of natural resources and reduced ecological impact, whereas impact management is the ongoing practice of measuring, assessing and improving impacts on sustainability issues. The aims are to achieve the balance between economic, environmental and social impacts through the effective management of resources whilst maximizing organizational profitability. A financial evaluation helps an investor to take rational decision about an analyzed investment, whereas an economic analysis broadens this perspective to include effects of the investment imposed on other stakeholders and the environment. Changing technology landscapes, development risks and new opportunities are characterized by a need of innovative financing and investment models in order to adequately assess the uncertainty and risks. The aims are to achieve the balance between economic, environmental and social impacts through the effective management of resources whilst maximizing organizational profitability.

This paper looks at a method for financial evaluation of investments in clean energy and sustainability, where the objective is to measure and quantify uncertainty and risk with probabilistic distribution models that includes the stochastic processes that underly the discounted cash-flow from new technology and innovation. Traditional quantitative analysis calculates measures of risk and financial return for hypothetical investments based on some time series for the analysis, that also should account for market dynamics. The shortcomings with this approach could be a single constituent dominate a risk and return profile, where noise is a random variation, including any variation that is not predicted, except in terms of a statistical distribution function. Simulation, however, improves on this by looking at the impact of many variables changing at the same time. The simulation process consists of successively generating random numbers, used to select from the probability distribution of each uncertain input parameter. The process continues repeatedly to obtain a sufficient number of variable values for statistical analysis and a sufficient number of output parameters, where probability curves are used to determine the likelihood of the outcome and create a picture of risk.

Decision support require software tools that make it easier to evaluate project proposal at the critically important initial planning stage. There are a number of commercial packages that run Monte Carlo simulation; however, during this research a software tool has been developed to automate financial evaluation as part of a common platform for sustainability of new technology development & innovation, impact management and financial evaluation of clean energy projects. The result is a detailed statistical description for the probability of different outcomes, such as discounted cash-flow and/or NPV, including histograms, statistics and statistical interference, etc.

KEY WORDS

Sustainable Technology; Impact Management; Financial Evaluation; Economic Analysis; Uncertainty and Risk; Probability Distribution; Environmental Performance.

INTRODUCTION

Sustainability and sustainable development are fundamental to designing effective short- and long-term strategies, including sustainability problems related to climate change and United Nations sustainable development goals. Most of emissions causing climate change come from fossil fuels like coal and natural gas. Carbon dioxide (CO_2) is the most prevalent greenhouse gas, but other air pollutants, such as methane, also cause global warming. Different energy sources produce different amounts of these pollutants. Therefore, human activity is overloading our atmosphere with carbon dioxide and other global warming emissions. These gases act like a blanket, trapping heat. The result is a web of significant and harmful impacts, from stronger, more frequent storms, to drought, sea level rise, and extinction. In contrast, most renewable energy, or clean energy, sources produce little to no global warming emissions. UN Sustainable Development Goals encompasses 17 goals to transform our world, [1].

[1] JG Maritime Engineering Ltd

According to the IEA report [9], a cleaner and more resilient future energy system with net-zero emissions will require a wide range of technologies, some of which are still at an early stage of development. For these new technologies, innovation is an uncertain and competitive process, where many ideas fall by the wayside. The IEA report looks at how to manage uncertainty and expand the number of available and affordable clean energy technologies in support of net-zero emissions on a timetable compatible with international energy and climate goals. It also highlights that governments have a central and wide-ranging role to play that goes far beyond the provision of funds for R&D. They set overall national objectives and priorities and play a vital role in determining market expectations.

The IEA report [10] also highlights investments in renewables companies appear to increasingly make sense from a performance and economic perspective, especially as renewable energy markets continue to expand and mature. Shifting allocations towards renewables equities and away from fossil fuel stocks appears to also provide greater diversification given their lower correlation with the broader market, especially in down markets.

This paper is engaged in development of standalone small scale software applications, that also encompass a method for financial evaluation of investment in new technology and innovation for Clean Energy & Transport. It provides an overview of the status-, reason, benefits, and common characteristics of clean energy technology, including competitive landscape and future technology innovation. A brief introduction to a common platform for evaluation and development, including a method for financial evaluation of investment in clean energy. The process of financial evaluation may include uncertainty and significant risks to clean energy project viability or sustainability.

CLEAN ENERGY AND SUSTAINABLE TECHNOLOGIES

Sustainability is a broad term that describes managing resources without depleting them for future generations, whereas sustainable development describes the processes for improving long-term economic well-being and quality of life without compromising future generations' ability to meet their needs. This concept of sustainability goes beyond environmental sustainability only, which concerns earth's natural resources, to include economic and social sustainability, which relate to meeting people's current economic and social needs without compromising future generations. Thus, it encompasses a tribble support by economic, environmental, and social sustainability:

- ***Economic sustainability*** canters on the idea of an efficient and responsible use of resources that leads to long-term profitability by transitioning to a sustainable business to improve the chances of operating over the long term.
- ***Environmental sustainability*** means reducing carbon footprints, waste, and water usage while maximizing energy efficiency to provide both environmental and financial benefits, and show responsiveness to community opinion.
- ***Social sustainability*** focuses on the interrelationship of systems and processes that support the creation of healthy and liveable communities that can sustain themselves.

Sustainability can only be achieved when economic, environmental, and social sustainability are addressed together. The ***objective*** is to increase awareness about sustainable technologies and energy efficiency measures, including markets and typical applications. Clean energy can be ***defined*** in these broad categories:

- Energy Efficiency - Using less energy resources to meet the same energy needs
- Renewable Energy - Using non-depleting natural resources to meet energy needs

Clean Energy Technologies:

- Wind energy
- Hydroelectric energy
- Geothermal energy
- Solar-thermal energy
- Ocean-thermal energy
- Tidal, current and wave energy
- Biomass energy
- Hydrogen
- Etc.

Reason for Clean Energy Technologies:

- Environmental:
  - Climate change & Local pollution
- Economic:
  - *Life-cycle costs (including income => NPV)*
  - Fossil fuel depletion
- Social:
  - Employment generation
  - Reduced drain of local money
  - Growth in energy demand (x3 by 2050)

Relative to conventional technologies the following characteristics can be relevant using sustainable technologies:

- Typical higher initial costs
- General lower operating costs
- Environmentally cleaner
- Often cost effective on life-cycle cost basis

Visions of the future of renewable energy include clean energy technology that are being tested today, and some that are currently beyond the scope technologically - but could be within a reasonable time frame. Thus, some clean energy technologies have matured, many cost-effective applications exist and markets are growing rapidly. However, there is still a great deal of uncertainty surrounding renewable energy and green technology. In which case, global efforts going forward, have a huge responsibility to alleviate this uncertainty and put in place the infrastructure needed to embrace these technologies fully.

Commercial Sustainability

Commercial sustainability aims to achieve the balance between economic, environmental and social impacts through the effective management of resources whilst maximizing organizational profitability. Figure 1 is showing a stakeholder view of a common platform for sustainability of new technology development & innovation, impact management and financial evaluation of investment in sustainable new technology & innovation for clean energy & transport projects.

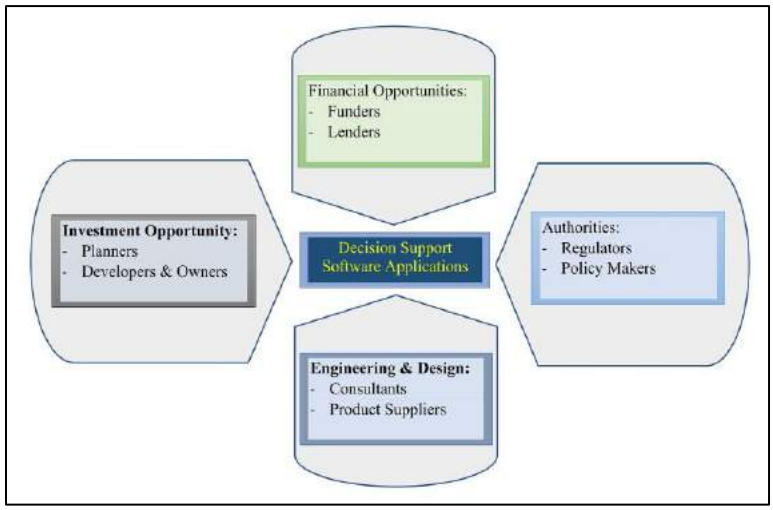

Figure 1: Common platform for sustainability of new technology development & innovation, impact management and financial evaluation of investment in sustainable new technology projects (Source: JG Maritime Engineering Ltd)

Decision support for sustainable technology development require software tools that make it easier for planners, decision-makers and industry to consider new technologies at the critically important initial planning stage.
This should include:

- Decision support tools that significantly reduce the cost of assessing possible projects.
- Provide these tools to users via the Internet.
- Training & technical support provided via network.
- Industry products & services accessible via an Internet Marketplace.
- Applications able to perform high-quality & low-cost preliminary feasibility studies.

Figure 2 is showing a stakeholder view of the financial evaluation of investment opportunities using the free-cash-flow through the company.

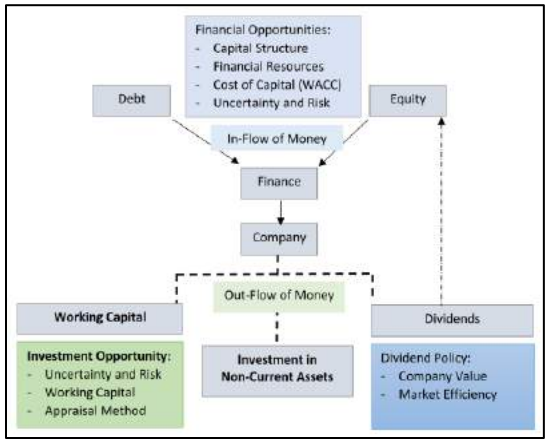

Figure 2: Cash-flow in financial evaluation of investment opportunities (Source: JG Maritime Engineering Ltd)

The New Paradigm & Uncertainty

Uncertainty refers to the state of information about a variable or parameter of interest, whereas variability refers to a parameter varying across a sample. *Risk* is defined as the uncertainty associated with a key value criterion.

Many industries are currently in the process of digital innovation where several digital initiatives are being driven simultaneously by several groupings within the industry, such as Blockchain, IoT, Big Data, artificial intelligence etc. Nevertheless, the largest threat to green energy might also be the greatest opportunity, namely the integration of artificial intelligence in the green energy industry by digitalization and machine learning. Digitalization is incorporation of digital technology into all aspects of everyday operation. Machine learning is a way for artificial intelligence to progressively improve performance on specific tasks based on the big data collected in the digitalized environment using cloud computing.

Regulations intended to influence technological design or business operation has largely taken the form of performance or design standards. Imagine a digitalized environment using cloud computing where everyone follows a set standards and stakeholders know what to expect. Stakeholders have to consider the cost associated with to falling behind. Here the objective would be to create a framework for standardizing data, message formats and interface specifications.

Investors and stockholders face changing landscapes, where risks and new opportunities are characterized by an increasingly complex decision-making space in need of innovative financing and investment models in order to adequately assess the uncertainty and risks. Many processes taking place in the operational life of new technology can optionally be described by different distributions that have been well-researched and analyzed. Extending this goes a long way towards being able to statistically model a range of cash-flow phenomena.

In this study an application is developed as a tool to automate evaluation of commercial sustainable technology as part of a common platform for financial evaluation, including investment in sustainability of new technology development & innovation and impact management. The objective is to measure and quantify uncertainty and risk and to build business models that includes the stochastic processes that underly the commercial sustainable measures from sustainable technology.

This will include a more extensive scope of descriptive statistics that describes data to provide information for future cash-flow; however, it will not allow for conclusions to be made based on the analysis but rather provide a description of the future cash-flow being analyzed. Therefore, the model is extended with inferential statistics that draws conclusions from data, and, thus, allow for conclusions to be made based on the analysis.

FINANCIAL EVALUATION & INVESTMENT APPRAISAL METHODS

Strategic cost management, value chain analysis and technology road mapping can be used as strategic investment evaluation method for public funding purposes. These methods are applying cost analysis concepts as well as taking into account the strategic aspects and the context for the investment opportunity. Value chain analysis is a tool to identify strategically important value-creating activities and to develop appropriate competitive strategies. However, technology road mapping is a process that contributes to the definition of technology strategy by displaying the interaction between products and technologies over time, by using charts and graphs to reveal the links between technology and business needs.

An investment can be evaluated with traditional payback period, or considering time value of money with discounted cash flow (DCF), net present value (NPV), internal rate of return (IRR) and profitability index (PI). However, common investment evaluation methods are the payback period, net present value and the internal rate of return. Because of the complexity of measuring energy efficiency future savings, simple payback decision-rules are common method for financial evaluation of energy efficiency investments.

By adding strategic investment appraisal methods to the investment process and using them in conjunction with the financial considerations is claimed to be the key for improving the quality of the investment decisions. The complex nature of sustainable technology, including clean energy and energy efficiency investments, makes it difficult to evaluate with traditional investment evaluation methods and thus can be rejected compared to traditional financial evaluation methods.

More comprehensive view of the energy efficiency investment's financial return and strategic compatibility could possibly be attained with more sophisticated and strategic investment appraisal methods, and thus more equal treatment among other kind of investment possibilities. Hence, it is intriguing to examine whether some investment appraisal methods are more common in the companies that implement energy efficiency investments and if so, why would this causal relation exist. Using more sophisticated financial evaluation methods, can maybe implement more energy efficiency investments than only using traditional methods.

In the traditional sensitivity analysis of cash-flow components, the effect of change in only one variable is considered at a time, where the method to measure risk is to determine several different scenarios for probable results of discounted cash flow (DCF) or net present value (NPV) to justify a realization of the project. In contrast a simulation method, however, improves on this by looking at the impact of many variables changing at the same time, where a probabilistic simulation model is using statistical distributions as input to incorporate uncertainty and risk. The simulation produces a distribution of the possible outcomes from the simulation, and then a detailed statistical description for the variables of interest and the probability of different outcomes in each scenario is achieved.

Please note, the financial evaluation method is only one aspect affecting the sustainable energy investment decisions. In the capital budgeting process, the investment process consists of complex aspects in the organizational setting. In the investment planning process, the capital budgeting projects become identified, developed, justified and finally approved.

MODELLING WITH PROBABILITY DISTRIBUTIONS AND RANDOM VARIABLES

Probability distributions are mathematical statistics functions used in data analysis that may be implemented to calculate probabilities of scenarios in cash-flow variables. Thus, many processes taking place in the operational life of an investment in sustainable technology can optionally be described by different distributions that have been well-researched and analyzed. Extending this application around these goes a long way towards being able to statistically model a range of cash-flow phenomena.

In a simulated capital budgeting problem, distributions are used to randomly generate and sample a large number of variable inputs for the following input variables:

- *Initial investment* - Distribution to describe the min to max capital distribution.
- *Discount rate* - Distribution to describe the variable discount rate.
- *Income/revenue* - Distribution to describe the variable energy income growth distribution.
- *Operating cost margin* - Distribution to describe the variable EBITDA margin cost distribution (for example as a fraction of income/revenue).
- *Net working capital* - Distribution to describe the variable NWC distribution (for example as a fraction of income/revenue).
- *Terminal value* - Distribution to describe the variable terminal value.

Random Distributed Variables

Random variables can be classified as discrete, which are variables that have specific values, or continuous, which are variables that can have any values within a continuous range as in this context. If a random variable X takes one values from a discrete set of numbers, it is called a discrete random variable. However, if this random variable X takes on any value out of a certain interval [a, b], it is called continuous. Function y = f(x) is called the probability density of X for $a \leq x \leq b$. However, the density f(x) must satisfy two conditions:

a) The density f(x) is positive, i.e., $f(x) > 0$
b) The integral of the density f(x) over the whole interval [a, b] is equal to 1, that is $\int_a^b f(x)dx = 1$.

Generating a value of random variable, X, distributed in the interval [a, b] with the density f(x), can be obtained from, $\int_a^X f(x)dx = \gamma$ where γ is a random number distributed on the interval [0, 1].

By using a simulation, the random distribution is used to randomly generate and sample a large number of variable inputs. Probability distributions are chosen for the following input variables,

- *Freight income* - The normal distribution is used to describe the freight income growth distribution.
- *Operating cost margin* - The normal distribution is used to describe the EBITDA margin cost distribution as a fraction of freight income.
- *Net working capital* - The normal distribution is used to describe the NWC distribution as a fraction of freight income.
- *Discount rate* - The normal distribution is used to describe the WACC distribution as weighted average cost of capital.

Simulation Method

The method can be summarized as follows,

Step 1 Creating a parametric model, $y = f(x_1, x_2, \cdots, x_n)$
Step 2 Generation of random input set of data, $x_{1,i}, x_{2,i}, \cdots, x_{n,i}$
Step 3 Calculations and memorizing results as y_i
Step 4 Repeating steps 2 and 3 for $i = 1\ to\ n$
Step 5 Analyzing the results using histograms, confidence intervals, other statistic indicators resulting from the simulation, etc.

The method provides an estimate of the expected value of a random variable and also predicts the estimation error, which is proportional to the number of iterations, given by $\varepsilon = \frac{3\sigma}{\sqrt{N}}$ where σ is the standard deviation of the random variable, and N is the number of iterations. The basis of the method is provided by the following relationship $P\left\{\left|\frac{1}{N}\sum_N x - \mu\right| < \frac{2\sigma}{\sqrt{N}}\right\} = 99\%$. The number of iterations required for an error of less than 1%, is given by $N = \left(\frac{2\sigma}{\varepsilon}\right)^2$. The model is then running by propagating a total of N times. Then the expected value of the random variable is the average of the total.

Simulation Code & Financial Evaluation

The discounted cash flow, DCF, is based upon a variety of cash flow and income streams.

$$DCF = \frac{FCF_1}{(1+k)^1} + \frac{FCF_2}{(1+k)^2} + \cdots + \frac{FCF_n}{(1+k)^n} \quad (1)$$

Weighted average cost of capital, WACC, is the cost of each capital component multiplied by its proportional weight and then summing,

$$WACC = \frac{E}{V} \times r_e + \frac{D}{V} \times r_d \times (1 - T_c) \quad (2)$$

where:

r_e	= cost of equity	V	= E + D
r_d	= cost of debt	E/V	= percentage of financing that is equity
E	= market value of equity	D/V	= percentage of financing that is debt
D	= market value of debt	Tc	= corporate tax rate

Figure 3 is a screenshot showing an input as normal distributed discount rate.

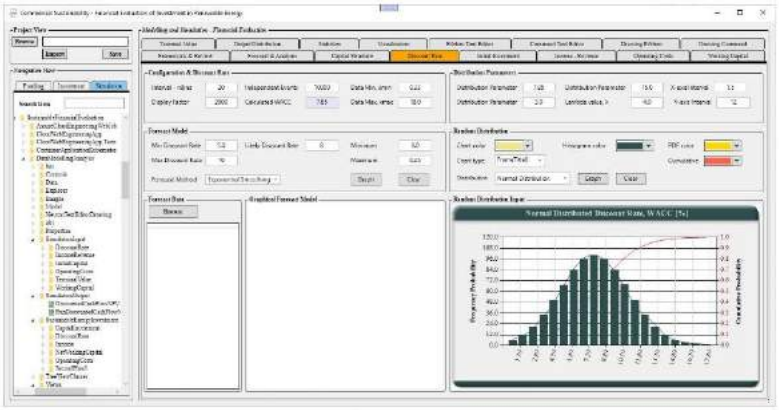

Figure 3: Normal Distributed Discount Rate (WACC).

A random probability distributed growth rate in each year during the time horizon is used to describe the cash-flow parameter growth rate.

$$Revenue_{Income}[y] = \sum_{i=0}^{Iterations} \sum_{y=1}^{Years} Revenue\_Income[y-1] \times (1 + Revenue\_Income\_Growth\_Distribution[0]) \quad (3)$$

$$EBITDA[year] = \sum_{i=0}^{Iterations} \sum_{y=1}^{Years} Revenue\_Income[y] \times EBITDA\_Margin\_Distribution[i] \quad (4)$$

$$Depreciation[y] = \sum_{y=1}^{Years} Revenue\_Income[y] \times Depreciation\_Percent[y] \quad (5)$$

$$EBIT[y] = \sum_{y=1}^{Years} EBITDA[y] - Depreciation[y] \quad (6)$$

$$Tax\_Payment[y] = \sum_{y=1}^{Years} -EBIT[y] \times Tax\_Rate \quad (7)$$

$$CAPEX[y] = \sum_{y=1}^{Years} -Revenue\_Income[y] \times CAPEX\_Percent \quad (8)$$

$$NWC[y] = \sum_{i=0}^{Iterations} \sum_{y=1}^{Years} Revenue\_Income[y] \times NWC\_Percent\_Distribution[i]) \quad (9)$$

$$Change\_in\_NWC[y] = \sum_{y=1}^{Years} NWC[y] - NWC[y-1] \quad (10)$$

The free cash flow can now be calculated for each year by summing over the cash flow components,

$$Free\_Cash\_Flow[y] = \sum_{y=1}^{Years} EBIT[y] + Depreciation[y] + Tax\_Payment[y] + CAPEX[y] + Change\_in\_NWC[y] \quad (11)$$

$$Terminal_{Value} = \sum_{y=1}^{Years} Free\_Cash\_Flow[y-1] * \frac{Termina\_Growth}{WACC - 0.02} \quad (12)$$

RESULTS AND DISCUSSION

The output probability distribution is a picture of risk, where the basic result from the outputs is a distribution function, or histogram, of the discounted cash flow.
Figure 4 is a screenshot showing the output distribution of discounted cash flow, DCF, together with some statistics.

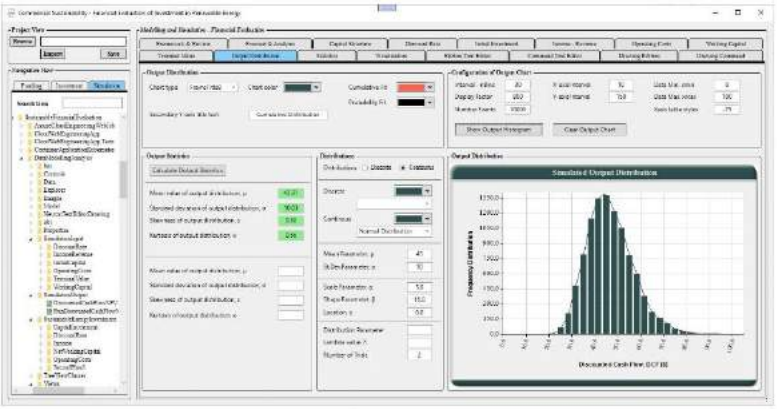

Figure 4 Discounted Cash-Flow (DCF) Output Distribution and Statistics

The output distribution shows that the discounted cash flow value is most frequent around 40-45 million US dollars with a standard deviation σ of 10.03.

Variance & Standard Deviation

The simulation method provides an estimate of the expected value of a random variable and also predicts the estimation error, which is proportional to the number of iterations, given by $\varepsilon = \frac{3\sigma}{\sqrt{N}}$ where σ is the standard deviation of the random variable, and N is the number of iterations.

The basis of the method is provided by the following relationship $P\left\{\left|\frac{1}{N}\sum_N x - \mu\right| < \frac{2\sigma}{\sqrt{N}}\right\} = 99\%$. The number of iterations required for an error of less than 1%, is given by $N = \left(\frac{2\sigma}{\varepsilon}\right)^2$. The model is then running by propagating a total of N times. Then the expected value of the random variable is the average of the total.

The expected value of a random variable is denoted by E[X]. The formula for expected value of a discrete random variable is,

$$E[X] = \sum_{all\ possible\ x} xP(X = x) \tag{13}$$

In other words, the expected value is the sum, over all possible values x, of x times its probability $P(X = x)$.

Variance & Standard Deviation – Risk Distribution

The variance is defined by $\sigma_X^2 = E[(X - \mu_X)^2]$. This is the expected value of the squared difference between X and its mean. An alternative expression for the variance, that is valid for both discrete and continuous random variables is,

$$\sigma_X^2 = E[(X^2)] - (\mu_X)^2 \tag{14}$$

This is the difference between the expected value of X^2 and the square of the mean of X. The standard deviation of a random variable is the square-root of its variance and is denoted by σ_X.

The standard deviation is a statistic that denotes the likelihood that the actual outcome being estimated will be something other than the most probable event or expected mean value. Generally speaking, the greater the standard deviation, the more spread-out the possible values of the random variable, representing higher risk.

From the distribution function it is possible to know other parameters as for example the mean value of the output indicator with the aid of the following model:

$$E(X) = \int_{-\infty}^{\infty} xf(x)dx, \ \ where\ f(x) = \frac{dF(x)}{dx} \tag{15}$$

The level of the method's error related to the calculations is proportional to the value $\sqrt{1/N}$, where N is the number of iterations.

Thus, the error in the simulation will be halved for each four times greater number of iterations. This error is due to the effect of the central limit theorem. For the estimation of the number of simulations it is necessary to know the probability effect that has to be intercepted. It can even occur at the lowest probability, p_{min}. The mean value of the estimation that the effect will occur at the lowest probability is:

$$\lambda = p_{min} \times n \tag{16}$$

where n is number of iterations, and λ is the mean value of the effects of the simulation.

Skewness and Kurtosis

Several statistical techniques and models assume that the underlying data is normally distributed with Skewness and Kurtosis of 0. Thus, Skewness and Kurtosis are moment-based measures and, they are central, standardized moments, and can be used as a statistical measure of degree to which data deviates from normality.

Skewness is a measure of asymmetry of the output distribution. The result shows a skewness of 0.58. This small positive value indicates that the tail of the output distribution extends towards the right. For a DCF sample of x in N values, the sample skewness is given by the formula,

$$Skewness = \frac{\frac{1}{N}\sum_{i=1}^{N}(x_i - \bar{x})^3}{\left(\frac{1}{N}\sum_{i=1}^{N}(x_i - \bar{x})^2\right)^{3/2}} \tag{17}$$

where N is the number of iterations, x_i is the iterated DCF value, and $\bar{x}$ is the mean value of the output distribution.

Kurtosis is a relative measure of the shape of the output distribution. The result shows a kurtosis of 0.56. This small value indicates that the distribution is approximated to somewhat flatter than a theoretical normal distribution. For a DCF sample of x in N values, the sample kurtosis is given by the formula,

$$Kurtosis = \frac{\frac{1}{N}\sum_{i=1}^{N}(x_i - \bar{x})^4}{\left(\frac{1}{N}\sum_{i=1}^{N}(x_i - \bar{x})^2\right)^{2}} - 3 \tag{18}$$

where N is the number of iterations, x_i is the iterated DCF value, and $\bar{x}$ is the mean value of the output distribution.

Covariance and Correlation

The covariance and correlation have not used in below model example. However, the application as a tool considers covariance and correlation as applicable together with other most common statistics.
The relationship, or dependency, between random variables is measured by covariance and correlation. The covariance between two random variables is,

$$Cov[X,Y] = E[(X-\mu_X)(Y-\mu_Y)] = E[XY] - \mu_X\mu_Y \quad (19)$$

If X tends to be large when Y is large, the covariance will be positive. If two random variables are independent, their covariance is zero. However, the opposite is not (quite) true, as two random variables can have zero covariance without being independent.

The correlation coefficient of X and Y is,

$$\rho_{XY} = Corr[X,Y] = \frac{Cov[X,Y]}{\sigma_X\sigma_Y} \quad (20)$$

the ratio of the covariance to the product of the standard deviations.

Statistical Interference

Hypothesis testing and confidence intervals are the applications of the statistical inference. The central tendency is used to create a statistical summary of the data.

Confidence intervals are a range of values so defined that there is a specified probability that the value of a parameter lies within it. Confidence level refers to the percentage of probability, or certainty, the confidence interval would contain the correct DCF or NPV when a distribution is drawn at random many times. Confidence interval formula $CI = \bar{x} \pm z\frac{\sigma}{\sqrt{n}}$, where x is the mean, z is the chosen z-value (1.96 for 95% CI), $\boldsymbol{\sigma}$ is the standard deviation (a measure of risk) and n is the sample size.
Critical values mean how many standard deviations away from the mean are needed in order to reach the desired confidence level for the confidence interval.
The alpha value is the probability threshold for statistical significance. If approximately normally distributed, the z-statistic is used.

Table 1: Confidence Level

Confidence Level	95%	99%
Alpha for one-tailed CI	0.050	0.010
Alpha for two-tailed CI	0.025	0.005
z-statistic	1.96	2.57

To calculate the 95% confidence interval for the mean value:

$$CI = 43.31 \pm 1.96 \times \frac{10.03}{\sqrt{10000}} = 43.31 \pm 1.96 \times 0.1003$$

$$= 43.31 \pm 0.1965$$

Reporting Result

Following screenshot is showing reporting opportunities integrated in the application to automate the result presentation.

CONCLUSION AND FUTURE PERSPECTIVES

This paper was looking at a method for financial evaluation of investments in sustainable technology, where the objective was to measure and quantify uncertainty and risk with probabilistic distribution models that includes the stochastic processes that underly the discounted cash-flow.

Clean energy investors face changing technology landscape, multiple developmental risks, and new opportunities characterized by an increasingly complex decision space with need for innovative financing and investment models to appropriately assess risk from uncertainty and profitability from new sustainable technology – a risks that will challenge the renewable industry as it grows and matures during the next few years.

The traditional method to measure risk is to determine several different scenarios for probable results of discounted cash flow (DCF) or net present value (NPV) to justify a realization of the project. However, a probabilistic simulation models incorporate uncertainty and risk by using statistical distributions as input, that includes the stochastic processes that underly the discounted cash-flow. Then a detailed statistical description and the probability of different outcomes in each scenario is achieved.

It can be concluded that a simulation can be a useful technique for risk analysis, however, there are number of shortcomings, including

- The variables are interrelated with each other and each variable depends on its value in the previous periods as well.
- The model helps in generating a probability distribution of the output, discounted cash-flow (DCF) or net present value (NPV); however, it does not indicate whether or not the project should be accepted.
- The simulation analysis considers the risk of any project in isolation of other projects, however, if a portfolio of projects is considered, the unsystematic risk can be diversified. A risky project may have a negative correlation with other projects, and accepting the project may reduce the overall risk.

Environmental impact involves reducing the direct and indirect impacts of technology on the environment, whereas economy is concerned with improving the economic efficiency of sustainable technology. There may be tension between objectives, such that proposals may contribute to the achievement of one objective, but work against the achievement of others. However, the evaluation method must allow determination of an appropriate balance between the objectives.

Future Work

In a future research perspective, uncertainty and probability distributions are fundamental to the field of machine learning. Simulation and machine learning have different sources to model generation. In the output the differences are a little subtle, as the uncertainty in the output has different sources.

The evaluation method should consider the environmental, engineering and economic advantages, disadvantages and constraints associated with defined objectives and scope. The factors to be taken into account in choosing alternative technology or innovation and the associated environmental, engineering and economic advantages and constraints, have to be identified, including the advantages and disadvantages, environmental, engineering and economic value of the preferred technology or innovation option. A particular requirement at this stage is an assessment of the significant environmental effects of the project in accordance with governmental regulations.

The future objectives and scope should be development of a tool to track, rank, and analyze uncertainty and risks in-depth, including a comprehensive risk management and risk analysis solution. Maintain a risk register and quantitatively analyze risks with simulation, including,

- Track and analyse risks in one place.
- Rank risks qualitatively to find the risks that are most important.
- Communicate risks to stakeholders, including reports and charts that focus on risk and not manipulation.
- Drill down into critical risks using simulation and avoid single point estimates to get a more realistic view of risk.
- Expert knowledge will not be needed.

Machine Learning

Machine learning is a way for artificial intelligence to progressively improve performance on specific tasks based on the big data collected in the digitalized environment using cloud computing. Artificial intelligence (AI) and machine learning (ML) has many potential applications in the renewable industry, and AI, including digitalization and machine learning, can be seen as keys to achieving a competitive advantage. These technologies are currently able to give an economic effect from the use, optimize and increase the efficiency.

In a machine learning, the model is unknown, and there is no way of determining the output value based on input values. Where

machine learning is based on dataset, inputs and the corresponding output are known, and a supervised learning can be used to train a machine learning model.

Supervised learning means to keep track of how well the machine learning model is predicting versus the known outputs. Each iteration of the learning process refines the model to improve prediction. After training of the machine learning model, a learned model is created that can be used to determine the predicted output having some uncertainty associated with the model. However, in prediction mode, known inputs can still be fed to the model.

However, in contrast, in a simulation the main source of uncertainty is in the input variables, whereas, in a machine learning process, the input variables are known, and the model is unknown prior to the model is learned, and the main source of uncertainty is in the model. Even when making a prediction, the model is often not 100% certain of the prediction.

MS Visual Studio and ML.NET

ML.NET is a .NET package to create and use Machine Learning models inside .NET. It can be used as an add-in to MS Visual Studio.
Loading in and preprocessing a data-set in ML.NET requires explicitly to state the structure of data, or state all the columns of the data-set, by creating a model input file inside the data model folder. Thus, a field is created for each of the columns inside the data-set. It is important that the right data type is specified together with the column index. Then the output also has to be modelled in a similar way.

The probabilistic forecast field will be Boolean, while the output will be some score or probability in percent. When the model is trained, the performance has to be checked by using, for example cross-validation. ML.Net offers cross-validation methods for different data-set. Making predictions on new data is straight forward in ML.NET. Using a prediction engine and another model made for inference, and calling the prediction method and passing it to model input object.
Infer.NET is an open-source library that can be used to create probabilistic programming systems, as for example to solve machine learning problems.

Digitalization

Digitalization is incorporation of digital technology into all aspects of everyday operation. Digitalization and new developments in the field of artificial intelligence, blockchain, IoT and automation are becoming increasingly relevant.

Despite the potential, opportunities and benefits offered by these technologies, they also entail risks and potential costs. This demand for the role of interoperability and global standards, and the need to ensure that digitalization works towards the sustainable technology development, including digital tools for optimizing energy resources.

REFERENCES

The following references provide an informative basis for development of sustainable technology and innovation:

[1] UN - United Nations. https://sdgs.un.org/goals
[2] UN - United Nations, "*SDG Good Practices*". https://sdgs.un.org/sdg-good-practices.
[3] UN - United Nations, "*Proposed global roadmap shows how universal access to sustainable energy can be achieved by 2030, transforming the lives of millions*". https://sdgs.un.org/news/proposed-global-roadmap-shows-how-universal-access-sustainable-energy-can-be-achieved-2030
[4] IMO - International Maritime Organization, https://www.imo.org/
[5] IMO - International Maritime Organization, "*IMO and the Sustainable Development Goals*". https://www.imo.org/en/MediaCentre/HotTopics/Pages/SustainableDevelopmentGoals.aspx
[6] The Paris Agreement | UNFCCC. https://unfccc.int/process-and-meetings/the-paris-agreement/the-paris-agreement/
[7] IRENA - International Renewable Energy Agency. https://www.irena.org/
[8] IEA - International Energy Agency's. https://www.iea.org/
[9] IEA, Energy Technology Perspectives 2020, Special Report on Clean Energy Innovation, Accelerating technology progress for a sustainable future.
[10] IEA, Clean Energy Investing: Global Comparison of Investment Returns. March 2021
[11] European Commission, official website: https://ec.europa.eu/info/index_en/
[12] Louis B. Sohn et al., "*Low of the Sea*", West 1984.
[13] M. Stopford: *Maritime Economics*, Routledge, London 2009.
[14] Jóannes Gullaksen - JG Maritime Engineering Ltd, "*A method for financial appraisal of investment in clean energy and transport projects*". IMarEST Annual Conference 2021, Presented at the Online Conference 28 June – 9 July, 2021.

Circular-adaptive designing, a design shift in sustainable fishing vessel design processes

Frans Veenstra[1]

ABSTRACT

Since the Paris Climate Conference (2015) new circular-sustainable system design knowledge is needed to comply with the current socio-political climate neutral transitions and climate ambitions. For this, transition-proof designing is urgently required anticipating the upcoming, stricter GHG emission reduction regulations (Green Deal 2030/2050). The design challenge, at the same time the PhD research question is how to design/launch a new fishing vessel, which can easily be upgraded to integrate evolving green technologies, to become more recyclable and to prevent (food)waste without the need for any costly, large scale retrofits in the vessels lifetime. Since 2000, fishers must increasingly adapt to stricter eco-requirements, nowadays even with the circular economy principles of re-use raw materials while the newest green shipping technologies aren't marine proven yet. To keep up with the rapid, green technological developments (energy transitions) and upcoming stricter climate- and food regulations (cyclical food chains), climate-smart design processes are necessary to accommodate innovative technologies. For this participatory designing and system design integration are becoming prerequisite design skills. Scientific design knowledge have to be combined with fishery/fishing vessel design practices, in particular regarding the energy-intensive, 24 – 40 m North Sea bottom trawlers. Based on the scientific Beamer-2000 research (safety integrated redesign, 1990) and the MDV-1 benchmark design process (sustainability integrated design, Ship of the Year,2016), circular design knowledge with circular-adaptive MDV-CE design concept has been developed in the PhD trajectory (Veenstra). To support fishery SMEs to become more future proof with short term, already proven green technology solutions and long term circular-adaptive design strategies. Additionally, a supportive designers tool, Circular Economy Design Index was developed, gradually achieving the long term transition design goals. Consequently, designers can integrate the new circular economy design drivers. Preferably, in the early design phases with limitations of current pieces of green technologies (fossil-free, re-use/recycling materials) and emerging robotic fish processing technologies (non-waste). Resulting in a new, circular-adaptive design methodology, a design shift to expand the already modular and flexible marine applied value chain ship design processes. Incorporating the circular-sustainable design aspects, from product designing in more vessel system designing. Derived from two Dutch fishing vessel cases (Beamer-2000, MDV-1, 2015), system design innovationpillars have been developed and generic, MDV (semi-)circular vessel design principles.

KEY WORDS

Future proof designing; sustainability integrated design processes; circular adaptive designing; energy-and climate neutral; Green Deals; Circular Economy; Cyclical food value chains

NOMENCLATURE

ARBO	Safety, health, working conditions (NL)
CC	Cyclical mode of food value Chains
CE	Circular Economy
CEDI	Circular Economy Design Index
D.E	Diesel-Electric
GHG	Green House Gas
MDV	Masterplan sustainable North Sea fisheries (NL)
SHE	Safety Health Environment
SME	Small-Medium sized Enterprises
ROI	Return Of Investments
Triple P	People, Planet, Profit
Triple ZERO	Zero emissions, Zero waste, Zero accidents

[1] Naval architect (1981-present), MDV fishery innovation manager (2013-present), Senior PhD student WUR-TU Delft

INTRODUCTION

Although the MDV-1 collaborative design approach and MDV-type follow-up vessels are ample green deal 2030 proven, this successful, economically and environmentally sustainable pilot vessel (Ship of the year, 2016) became within 5 years "a design with a promising past". The MDV-type fishing vessels can't cost-effective approach the current energy-, nature- and food transitions policy and goals. Besides, too many evolving green technologies aren't yet fully marine proven and/or have realistic return of investments.

The research question arose how to design a more mid-long term futureproof fishing vessel, keeping pace with the current green technology developments CE-CC business perspectives. Consequently, the designers must preserve future adaptive capacities in the fishing vessel design process, a design shift. Stimulated by MDV fishermen, prof. John Stoop and prof. Hans Hopman (TU Delft), it became my dissertation topic "Multi-sustainability and fishery design processes" (Veenstra, 2017-present), developing new scientific design knowledge with practical MDV circular solution directions.

Starting from the derivative Beamer-2000 proof of concepts (safety-evidence based, fig. 1) and the disruptive MDV-1 new ship design (2015;triple-P based, fig. 2), the next, more prospective MDV-CE design step has been taken (2020;valuetransition based, fig.3). Connecting designers thinking (past-present) to the urgent climate challenges of today toward 2050.with new, circular design drivers. For this, new triple-ZERO design targets have been determined: Zero accidents (SHE), Zero emissions (CSR), Zero waste (CE).The best way to predict the future is to (re)design it, controlled by naval architects with insight (users, culture), oversight (designing, system design processes) and foresight (legislation, future-proof business models).

fig. 1 Beamer-2000

fig. 2 MDV-1 2015

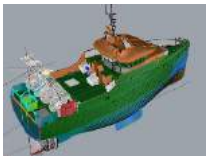

fig. 3 MDV-CE 2020

Traditionally, the shipping industry used to work with basic design concepts, modifying them as long as possible. Before outstretching these 'parent vessel into unacceptable grandparent vessels' with new operational- and safety risks, it is time for new design knowledge with design-transparent, multiple-sustainability targets (Veenstra,2018).

Taking into account upcoming IMO/ EU green regulatory frameworks and evolving climate smart technologies. The here concerning circular-adaptive design methodology integrates climate-, energy and post-corona transitions through "knowledge based and smart modular, flexible and circular-adaptive designing". Therefore, it is the reconsidered role of naval architect as system integrator through communicating and coordinating multiple-sustainable variables across their (maritime)boundaries.

SUSTAINABLE DESIGN DRIVERS AND GOALS

Since the 1970s the Dutch fishing vessel owners and researchers have been dealing with three major socio-political changes in North Sea sustainability transitions . First single-sustainability, focusing on decreasing the number of (fatal) accidents on board (Safety & Health Environment (SHE,80s, Stoop, 1990), second triple-P sustainability, focusing on the impact of fishery not only on income (Profit) but also on society (People) and the environment (Planet; Corporate Social Responsibility (CSR, Veenstra 1990,'92). Finally, since 2020 aiming for circular-sustainability with the focus on energy-, climate-neutral and circular economy fisheries. In the case of single-sustainability towards safer ships, for the first time human values had to be accounted for in the design spiral approach (fig.4). Personal safety and well-being aspects have explicitly been integrated in a safety system problem solving methodology. This created a design shift by integrating hard & vague requirements (Stoop, 1990). Becoming the benchmark design approach for multi-sustainable MDV-1 new design. However, since 2020 an increased demand for design knowledge was needed to find answers to the new socio-political realities and provide alignment with multi-actor combinations and general public/NGO perceptions. Since the Paris Climate Conference (2015), there is worldwide socio-political awareness to stop further global warming to well below 2 C. The latest IPCC report (6th , Aug.'21) scientifically emphasized that global warming is "manmade, linear to GHG emissions and has to be solved manmade".

These climate-control challenges can only be achieved in a participatory way. Increasingly, policymakers, critical stakeholders and fishers are willing that fisheries are becoming more nature-inclusive and operating in a more climate neutral way. This means, that centuries of linear economy approaches (production ↑/costs↓) have to be abolished and changed into circular economy approaches (recycling/renewables ↑). Through the multi-sustainability MDV design approach the Dutch fisheries have already successfully integrated the triple-P: People, Planet Profit design aspects in fishing vessel design practices (Veenstra, 2016).

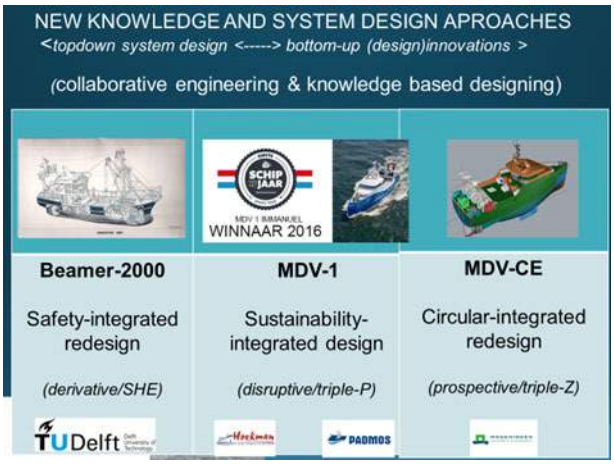

fig.4 Sustainability design principles/proof of concepts

The MDV type vessels already surpassing the Green deal 2030 CO2 requirements. However, aiming for the Green Deal 2050 requirements the triple-P design drivers had to be upgraded into triple ZERO design targets. Socio-politically driven by (inter)national climate-neutral strategies (EU Green Deals, Climate Agreements, IMO, 2018-2020). In addition, the Dutch ministry of LNV published the national vision "Cyclical food value Chain" (CC; 2019), by which the North sea fishery was also challenged to operate in a more climate neutral way by gradually implementing the cyclical mode of (sea) production (waste ↓). A lot of talking, but before designers/fishers can integrate these in CE- and CC design aspects, it must be translated in actual design drivers/-goals (table 1). In addition to CE/ CC, attention must be given to workers welfare and consumers health as well. Fifty years after the Club of Rome report "Limits to Growth" and nowadays increased irreversible consequences of climate changes (storms, floods, droughts, fires), climate smart design shifts in fishing vessel eco-designing and non-food waste operations should be actually dealt with.

Climate principles	Change drivers	Triple -P design drivers 2030	Triple-Zero design goals '50
Circular Economy Principles (CE) *"made to be---> made again"*	Recycling ↑	-recyclable raw materials -usage of renewable materials -re-use equipment/installations - good profits & happy people	-zero waste -zero emissions & -accidents
LNV vision: Cyclical mode of seafood production/value chains (CC) *" no food-waste"*	Seafood waste ↓	50 % waste ↓ -utilize raw materials/residual-finished products - product transparency -nature-, safety-,health inclusive	100 % waste ↓ -(re)use raw materials -retaining value -safety/healthy (sea)food
EU Green Deal/ NL Climate Agreement/ IMO *"decarbonization"*	Green House Gas emissions ↓	50 % - 55 % CO2 ↓ -low energy intensive	100 % CO2↓ -energy- & climate neutral

Table 1 Energy-, climate change and design-drivers/-goals

MDV-1 SUSTAINABLE DESIGPROCESS AND MDV DESIGN PRINCIPLES

By introduction of the Working Conditions law in the North Sea fisheries (SHE/Arbo, late 80s) the TH Delft Safety Science group started to collaborate with the RIVO fishery research designers and their fishers network. From designer perspective, the personal-safety aspects were integrated in the then usual iterative ship design spiral, weighing 'hard' design aspects (design & construction) with 'vague' design aspects (safety & wellbeing; fig. 4). This new participatory approach and safety problem solving methodology have been described in detail, both from scientific (Kindunos, Stoop, 1990) and practical point of view(Beamer-2000, Veenstra, 1990). Although the Beamer-2000 redesign solutions were personal-safety and operationally driven, impetus was given to integrate multi-sustainability design aspects (triple-P) as well, due to the emerging corporate social responsibilities in the late 90s and increasing socio-political interferences (Veenstra, 2002).

The Beamer-2000 collaborative design process was the good starting point when at the 2008 economic crisis, with an obsolete fleet and negative business models, the beam trawl fisheries were in need of out-of-the-box thinking for a proven economically and environmentally sustainable fleet. After the national fishery innovation plan (VIP, 2009) and a stakeholders sustainability-covenant were established, regional fishermen knowledge groups discussed various technical innovation themes, among which the SMART fishing group at Urk for sustainable business models and fleet renewal (good for the fishermen, good for shipbuilders and good for the environment). In this group, from/through/for skippers the idea originated for a proven sustainable North Sea fleet renewal with smaller fishing vessels (30-35 m), intrinsic safe/seaworthy with ambitious short- and midterm sustainable business- and design goals (80 % CO2 ↓, triple-P).

To achieve this fleet renewal the new design and delivery of a first proven sustainable pilot vessel was obvious and the foundation Masterplan sustainable fisheries (MDV) was established (2010). The lean and mean multidisciplinary MDV team developed feasibility studies and the MDV-1 business case for public-private co-financing. Knowledge transfer and stakeholder interactions took regularly place; on three levels, micro (crew), meso (sector) and macro (politics) and through (shipbuilding exhibition)meetings, lectures at fishery schools, publications in fishery/maritime magazines and making extensive use of social media (https://masterplanduurzamevisserij.nl/nl/kennisbank/english-documentation).

The delivery of the sustainableMDV-1 pilot vessel (triple-P) was the MDV major goal (Veenstra, 2016). Whereby for the first time fishing gears were subordinate and the Dutch fisheries dealt with a disruptive fishing vessel design process. The scientific design knowledge, Beamer-2000 based was introduced by the fishery innovation manager. Who was also responsible to suggest viable technical ship innovations and keeping the sustainable innovation triggers in play during the designing and building process. After the MDV-1 delivery, the new innovations were evaluated in collaboration with the crew, resulting in recommendations for the follow-up MDV type vessels and fleet renewal (2015- present ;10 parent-vessels with more or less MDV multi-sustainable innovations; table 3).

The difference between derivative (Beamer -2000) and disruptive designing (MDV-1) is mainly determined by form variations and specific fishery function allocations. Whereby manageable subproblems and partial solutions could be visualized by means of fishery system boundary approaches. In addition, to discuss disruptive layouts a convenient conceptual design tool was applied, the fishing vessel morphological plan (fig. 5). With which new combinations of main functions within the intended overall dimensions can be considered and new layout-concepts can be shown.

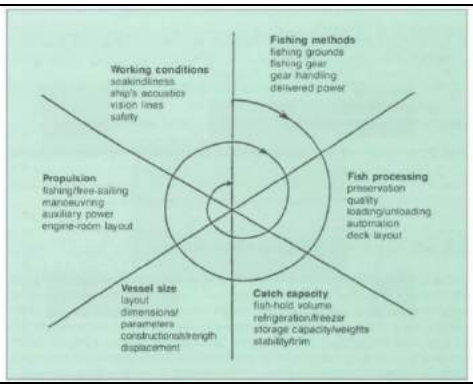

Fig. 4 Fishing vessel, iterative design spiral with technical & personal safety/well-being requirements (Veenstra, Stoop, 1990)

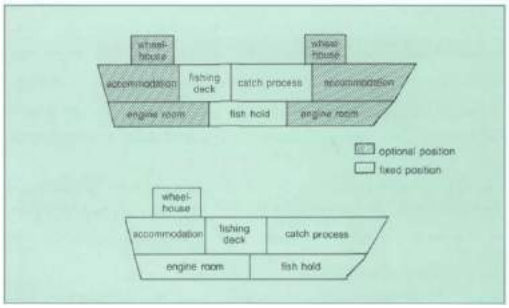

Fig. 5 Morphological plan Beamer-2000 layout options for personal safety/well-being improvements (Stoop, Veenstra,1990).

After feasibility studies and technical (ship)innovations performed by the MDV technical working group, the final MDV Masterplan came about and the MDV-1 specifications were drafted. Extensively discussed in the MDV-team with on a regular basis feedback to the sector and all stakeholders. Based on four preliminary design- and cost specifications and consultations with concerned Dutch beamtrawl shipbuilders (Hoekman/ Herman Jansen, Maaskant, Padmos), the ultimate MDV disruptive concept was chosen, namely the 3D printed study model (35-40 m stern trawler, Padmos 2012). In particular, the two MDV skippers, also co-owners opted for this appealing model. Best fitting the MDV goals and time schedule to finalize the MDV-1 specifications, public-private financing, to build and to operate the MDV-1 under the MDV umbrella for three years. In retrospect and for knowledge transfer, the MDV-1 design methodology and building process have been described in detail in the MDV report “From IDEA (2006) to Ship of the Year (2016), Veenstra, 2016” and has scientifically been elaborated in the doc thesis as generic MDV ship design principles (MDV practice to system-designing; table 2), then applied for a more circular-adaptive design approach towards 2050 (system-designing to climate neutral designing and practical, circular solutions, table 3).

MDV fishing vessels design principles	Key design issues	Key design approach and methodology
1. **Analysis**	Multi-sustainability challenges	Which legal multi-sustainable change drivers must be transferred into transparent design drivers, from triple-P toward triple ZERO.
2. **Identification**	Manageable sustainability problem areas	Which design drivers must be intertwined to manage the sustainable functional problem areas, from evidence-, business- toward value chain based
3. **Co-designing**	Design knowledge and fishery practice combined	Collaborative engineering, scientific design- and practice knowledge based; leading to system model choice & first set of vessel main specifications
4. **Dissection**	Decompose in design functional-innovation pillars	Innovation pillars: 1.Hullform and ship weight optimization (resistance ↓/seaworthiness↑) 2.Low energy propulsion installations, (near) future adaptive to zero emissions 3. Recyclable, hybrid construction materials/equipment 4.Onboard fish processing optimization (quality, price ↑) 5.Selective gears (bottom impact ↓)
5. **Innovation**	To generate innovative (partial) sustainable design solutions	Ad 1.Innovation pillar: CFD digital ship-model analysis and/or model tank testing Ad 2. Hybrid propulsion, power trains,- management systems; low energy equipment; waste heat recovery Ad 3. Composite or steel ship's hull with composite wheelhouse and/or components (doors, hatches) Ad 4. Automation/robotics; cyclical food chains Ad 5. Selective gears; next-to-non bottom impact/bycatch ↓
6. **Synthesis**	Holistic system integration	From green, safety-health and business perspectives; knowledge smart, modular/flexible & adaptive for new green technologies in medium and long run.
7. **Evaluation**	Sustainable innovations in practice	In concert with crew during multiple fishing trips, esp. in adverse weather to explore the limit state design conditions; leading to practical recommendations for follow-up vessels

Table 2 Generic MDV semi-circular fishing vessel design principles

MDV-CE CIRCULAR-ADAPTIVE DESIGN APPROACH

Before starting the MDV design processes, it is of utmost importance to set also long term design goals and formulate which fishery business models are (becoming) sustainable in the short-, medium- and long run as well. In addition, the (upcoming) legal climate transitions must be clarified from ship, crew and environment perspectives, beyond shipping inspectorate/class requirements and in concert with the current socio-political climate change realities. Because current edge green technologies aren't proven yet, knowledge-smart modular and flexible designing must be enhanced and expanded with the circular-adaptive approach, whereby the MDV generic design principles can be followed.

After extensive analyzing/identification of the multi-sustainability transitions/ fishery problems (CE, CC) and the long term goals were set (triple ZERO), in consultation (researchers/ fishers) the reference system model was chosen with the first set of design specifications (MDV-1 hybrid d.e., 32 m). In the next step the system model have been dissected in five functional innovation pillars. Per pillar viable green-recyclable technologies were generated, either proven and applied in the short run (pilot vessel) or delayed retrofitted in the mid and long run. All innovations were integrated in the system model from holistic perspectives, operational feedback-inclusive with MDV recommendations and evolving green shipping innovations (table 3). By the system integrator the technical and operational boundaries for the groundbreaking, eco- and crew friendly innovations could be clarified. Besides, for every subsystem and intended technical innovations the technical readiness level and lifespan should be established. The innovation introductions were accompanied with sound aftersales prospects as well as sound maintenance services in the fishing harbors. Thereafter, a retrofit plan and pragmatic time line was established with foreseeable additional investment costs and mid to long term SME business plan foresights.

A prerequisite in this design process is, that the shipyards involved are well-known with the iterative fishing vessel design spiral, human safety aspects inclusive (fig. 4), but also being familiar with modular designing and building. Modular designing & building means that the vessel is subdivided in functional modules. Which can separately be built and tested as

much as possible to easily be retrofitted in 10 to 20 years. For this retrofit design approach, tangible circular technology alternatives must be circular-adaptively considered, matching its MDV-CE operating (eco-)environments and substantial reduction of energy consumption-, emissions and operating costs towards MDV-CE/CC design goals. In particular beneficial for large scale cost-efficient retrofits and high recycling/re-use potentials and better end of life values (ship/installations). This means climate smart (re)designing is not only a new ship (re)designing CE-CC problem solving approach (safety,fish2dish, license2fish), but also reflects on input of multi-stakeholder commitments and upcoming climate neutral politics. Participatory system designing with input of explicit scientific design- & practical fishery knowledge, contribute to the circular design shifts in the Dutch North Sea fisheries towards 2050. With knowledge transfer in cross design domains as happened with the safety integrated Beamer-2000 redesign, MDV-1 new sustainable system-design methodology and proof of concepts (Veenstra, 2002, 2018).

CE/CC innovation pillars North sea fishing vessels 30 – 35 m	**MDV-1 technical/operational improvements 2015-2020**	**Green shipping innovations 2020-2030**	**MDV-CE/CC design goals 2030-2050**
1.Hullforms and ship weight	-CFD optimizations /ship model testing -Length/weight optimiza-tion (30 – 35 m) -optional antiroll- and trim tanks	-air-lubrication -renewable hull form kinetic energy	Hull resistance & weight reduction 30 % (> MDV-1) to 50 % ↓
2.Power trains and propulsion	-fore and aft engine room -bio-,synthetic, duel-fuel -battery packs -energy recovery -low energy equipment -solar-panel assisted	-Power management systems -hybrid hydrogen/am-monia/methanol d.e. -scrubbers -H2 fuel cells -remotely condition monitoring - Post corona HVAC ventilation	>50 % CO2 ↓ (= MDV-1) toward 100 % ↓ (= triple ZERO)
3. Hybrid construction materials	-composite wheelhouse consoles, inclusive on steel hull	- light weight, recyclable materials -fully composite -life cycle analysis	>30 % weight ↓ (= MDV-1) 50 - 100 % recyclable -higher end-of-life value -longer lifespan
4. Fish processing and handling	-fish processing amidship -further automation/ robotics to reduce dangerous operation and improving work-rest hours	-fish sorting, handling & cutting -fish4food -smart food value chain	-50 -100 % waste ↓ -higher fish-landing prices in cyclical food value chain
5. Selective fishing gears	-selective, less-discards, low bottom impact trawl gears	-polyvalent gears -alternative flatfish stimuli (led, noise, pheromones) - underwater drones	50 – 100 % selective/ next-to-non bottom impact & bycatches; higher safe gear handling

Table 3 Dutch fishery application of MDV design principles towards circular-adaptive MDV-CE/CC concepts

CONCLUSIONS AND RECOMMENDATIONS

Through the socio-political sustainability changes (SHE, CSR, CE) the Dutch, North Sea fishing vessel design processes have substantially been changed, collaborative design and engineering based. These design shifts have been system-methodologically analyzed in the PhD ship design trajectory (2017-present), resulting in MDV (semi-)circular design principles (table 1,2) and a pragmatic modular, flexible and circular-adaptive (re)designing, retrofitting process (table 3). The

proof of concepts regarding derivative-, disruptive and prospective (re)designing (fig.1) contribute to sustainable North sea fishery solutions to stop further global warming and improving crew well-being.

First, derivative designing was (safety)data driven, at which (hull)forms and layout are being kept as long as possible and innovative technologies can be refitted in the vessels life time, the so-called parent vessels with Beamer-2000 proof design modifications. Second, disruptive designing was (business)performance driven, at which main functions/subsystems have been changed, so that with the MDV proof of concept current sustainability regulations (CSR, triple-P) and sustainable business plans for the short- and mid-term could be foreseen. Third, prospective designing must be foreseen due to current and upcoming circular-economy/climate change regulations and emerging green technologies. The here PhD developed MDV-CE system-design methodology (table 3) is becoming a more futureproof design approach, in particular energy- and climate neutral and food-value chain driven. Giving full substance to the post MDV-1 CE/CC redesign challenges and to the PhD system-methodological research questions with in time pragmatic integration of evolving green shipping innovations. A design shift in circular-adaptive designing with fishery solutions towards Green Deal 2050.

By which ship designers and fishery SMEs can gradually integrate viable green technologies through modular, flexible & circular-adaptive designing by making use of the CEDI index multi-sustainable solution matrices (Veenstra, 2019, WMTC-2018). A design tool to help realizing the prevailing energy- and climate transitions. Furthermore, these MDV-CE fishing vessel concepts are also crucial as proven sustainable means of production in the upcoming cyclical modes of fish supply chains (fish4food). After the Circular Economy ship design objectives and substantial greenhouse gas emission reductions, the next fishery climate smart challenges are the cyclical modes of fish supply value chains with next-to-non waste of energy, raw materials and healthy food.

However, from a SME business point of view, Green House Gas reductions (GHG) aren't only a matter of applying low-carbon and non-fossil fuels, but also through substantially reducing the onboard energy consumption and making use of residual heat as well. In these design practices, on the cutting edge of theory and fishery practice, first the design and engineering focus are on optimized hull forms and low-energy propulsion and powertrains, second on low energy-intensive equipment, from engine room installations up to crew's coffee machines. The biggest energy/CO2 savings can be achieved through applying the newest, low-energy engines with hybrid power- and gearbox installations and renewable energy support, such as battery packs, wind and solar assistance and recharge facilities onboard/onshore; often not yet marine proven.

For ultimate circular-sustainable designing, the intended fishing vessel should be looked at from a system model perspective with the five innovation pillars and corresponding subsystems. Additionally, the technical and operational technical readiness levels must be clarified as well as the planned sustainability refits/retrofits in abt. 10 to 20 years' timeframe. Once the subsystems have been equipped with proven installations, then the design spaces must be 'flexibly & adaptively' reconsidered as well for later integration of potential new green technologies and alternative fuel propulsion systems. Because of the lower fuel oil energy densities, the original planned tank capacities must be enlarged. Although, diesel combustion engines will be in use for quite some decades, the quick emerging dual-fuel engines can be used in between, gradually achieving the IMO/Green Deal decarbonization targets 2030-2050. With automated work processes and introduction of smart fish processing/handling systems, the crew's working & living conditions and working-rest hours at sea can be/ have been onboard considerably improved (MDV-1/MDV-CE). Also reducing recessive workload and paperwork, cut fatigue and good fishermen can be retained & attracted, now and in the long run.

Furthermore, zero impact, climate-friendly fishing vessels and sustainable fishermen earnings can't be realized by individual actors only. Even more than before, scientific design knowledge should be combined with fishery-, ngo practices and technical solution providers with advanced cutting edge green technologies. Resulting in more futureproof fishing vessels, good ROI and more socio-political commitment. Only then, technical- and governmental-, business- and NGO barriers could be cost-efficiently tackled and integrated in the design. Nowadays, public-private commitment and knowledge transfer is absolutely required, in particular when EU/NL innovation-subsidies have been involved and preventing negative fisheries framing. To design and build a future proof fishing vessel in a cyclical fish supply chain, one must think globally, act locally with the new socio-political fishery foresights, advancing multiple-sustainability system-design insights and oversight in developing green, energy- and climate neutral technologies.

ACKNOWLEDGEMENTS

The author is thankful for the received constructive criticism of the WUR-TU Delft PhD promotor team and stimulating academic (notion)discussions in the context of multi-sustainable fishery design & engineering. Also thanks to the MDV-1/MDV-2 crew and fishing vessel shipyards for participatory designing and pragmatic circular-adaptive design solutions.

REFERENCES

STOOP J.A (1990). "Safety and the Design Process*"*, *TU Delft:* ISBN 90-9003301-7
VEENSTRA, F.A. and J.A Stoop."Beamer-2000, Safety integrated (re)designing", Royal Library The Hague: ISBN 90-74549-02-0.

VEENSTRA, Frans and R. Brinckman (1992) "*Sternrawler-2000, a new approach designing on points of integral sustainable aspects (working conditions, HACCP quality control, environment*". Holland Shipbuilding, HSB, VOL. 44 No1; pages 51- 54.
VEENSTRA, F.A (2002). "Dutch newbuilding's after the 2000 re-design requirements*"*. *Fishing News International, Good Gear Guide 2002-new vessels:* ISBN 0-9518579-9-1; pgs25-31
VEENSTRA, FRANS (2016)."*MDV-1,from innovative IDEA (2006) to Ship of the Year (2016), in Dutch".* Urk: https://masterplanduurzamevisserij.nl/nl/kennisbank/onderzoek/publicaties.
VEENSTRA, F.A.and J.J. Hopman, J.A. Stoop (2017). Multicriteria Fishing Vessel Design Methodology. *USA journal of fisheries and Aquaculture*: Volume, Issue Oct.2017- 06.
VEENSTRA, F.A. and J.A. Stoop, J.J. Hopman (2018). "Sustainability in fishing vessel design process". *Martech-congress, Progress in Maritime Engineering and Technology*: Taylor and Francis Group, London, ISBN 978-1-138585393-3, pgs 275-282.
VEENSTRA, F.A. and J.A Stoop, J.J Hopman, J.J (2018). "CEDI sustainability-ranking in fishing vessel design process" *WMTC18, f-180612-259:* World Maritime Technology Conference. Shanghai; Dec. 5-7
VEENSTRA,F.A and J.A. Stoop, J.J Hopman J.J (2019) *"*Cedi-Index Validation In circular Fishing Vessel Design Process": *International Journal of Current Advanced Research,(IJCAR)* 08(01), pp.16776-16782. DOI: http://dx.doi.org/10.24327/ijcar.2019.16782.31
VEENSTRA, F.A (2019). "Contemporary fisheries risks and SME resilience, Dutch fishing vessel (re)designing 1988-2018".*Proceedings 8th REA symposium on resilience engineering*, Sweden, Kalmar, 24-27 June 2019.
VEENSTRA, FRANS (2021). "THE MDV FISHERY CASE, circular sustainability and climate smart design processes". SWZ Maritime, Volume142, January 2021 www.swzmaritime.nl
VEENSTRA, FRANS (2021). "Bridging The Gap, from North Sea fishing vessel design to climate smart design processes". SWZ Maritime, Volume142, November 2021 www.swzmaritime.nl

MODELLING A MODULAR CONFIGURATION OF PEM FUEL CELL SYSTEM FOR VESSELS APPLICATIONS

Vincenzo Liso[1] , Peilin Xie[1] , Samuel S. Araya[1] , Josep M. Guerrero[1]

ABSTRACT

***Introduction**: Increasing restrictions on the vessel emissions both in the ports and at sea has opened to the possibility for the electrification of the vessels using batteries and hydrogen fuel cells thereby reducing the dependency on fossil fuel which emits CO_2, NO_x, SO_x, and other unwanted particle emissions.*
***Objectives**: The hybridization of modularized vessel power trains with fuel cells and batteries is still a novel concept, although it takes advantage of the experience developed in other heavy-duty applications such as cars, buses, forklifts, and trains.*
***Methods**: In this study, we focus on the operation of a modular fuel cell system. Three power allocating strategies across several fuel cell modules were considered: the equal distribution and the sequential distribution (also known as Daisy chain) and the independent distribution. The simulation was run in MATLAB-Simulink where the components models and optimization of the modules power distribution were developed. The system dynamic operation reflects the typical drive cycle and load profile of a ship in a short trip (approx. 30min). The system structure considers fuel cell modules with batteries and ultracapacitors. A real-time Power Management System (PMS) is integrated to decide the optimal fuel splitting between them with the aim of high fuel-efficiency operation. The PMS is developed based on Equivalence Consumption Minimization Strategy (ECMS), an effective energy management technique capable of determining the instantaneous equivalent fuel consumption of energy storage systems and determines the optimal power split with low computational burden and limited calibration of control parameters.*
***Results**: The results point to a modular power splitting strategy which increases the system energy efficiency and reduces the risk of failure. It is finally suggested that a combination of both the sequential and equal distribution of power among the fuel cell modules is in most cases desirable. We find that the sequential distribution provides a better efficiency at lower power demands while equalizing the distribution at higher power demands. The real time optimization suggest that the system can operate at a better efficiency during the load changes by increasing the power supplied by the batteries and ultracapacitors.*

KEY WORDS
PEM fuel cells; Modularity; Vessels electrification; Marine applications; Liquid Hydrogen; Energy System analysis.

NOMENCLATURE
BAT: Battery
BoP: Balance of plant
ECMS: Equivalence consumption minimization strategy
FC: Fuel cell
HESS: Hybrid energy storage system
LH2: Liquid Hydrogen
PMS: Power Management System
SOC: State of charge
UC: ultra-capacitor

INTRODUCTION

The electrification of vessels for the mitigation of emissions at sea and in the ports requires that new solutions are to be implemented to substitute the conventional ships power trains and fuels. Among different options, hybrid power trains for vessels which combine the utilization of fuel cells batteries and ultracapacitors have been proposed.

[1] Aalborg University, AAU Energy | Pontoppidanstræde 111, room 1-104 | 9220 Aalborg East

Hydrogen offers a carbon free alternative to conventional fuels such as diesel commonly used in the maritime sector and it can be consumed in fuel cell to produce electricity, where the only reaction product is water. Green hydrogen can be produced via water electrolysis using electricity from solar and wind farms. Hydrogen can be stored in the liquid phase and ensure long term energy storage which is required in the naval sector. In terms of volume liquid hydrogen has a volumetric energy density which is twice higher than gas hydrogen although it is yet four and a half times lower than a conventional fuel such as diesel (DOE)– for this reason liquid hydrogen has been considered for ferry boats employed in short haul trips. Liquid hydrogen has attracted attention in the recent period as it can be produced by off-shore wind energy generation, as wind stability is more favorable (Bonacina, Gaskare, and Valenti).

Different power train configurations for ships have been proposed. The combination of fuel cell batteries and ultracapacitors offers good response time even to the sudden load changes. In fact, while the fuel cell has a slow response time, the batteries and ultracapacitors can provide electrical output in fractions of seconds. In the scope of the LH2vessel project, ("Liquid Hydrogen Concept Validation for Large Efficient, Scaled and Stacked FC Electric Power Systems for Vessels"), we have studied the possibility to optimize the utilization of batteries and ultracapacitors to take advantage of the different response time.

In this paper we use an optimization algorithm based on the minimization of a cost function to identify a strategy to operates a modular fuel cell system assisted by ultracapacitors and batteries as shown in figure 1. The combination of the ultracapacitors and batteries is indicated as Hybrid Energy Storage System (HESS). A half an hour load profile was constructed to describe the typical short distance ferry boat trips. In the results, we will present how the different configuration of the modular fuel cell system will react to the load change and come with some concluding remarks.

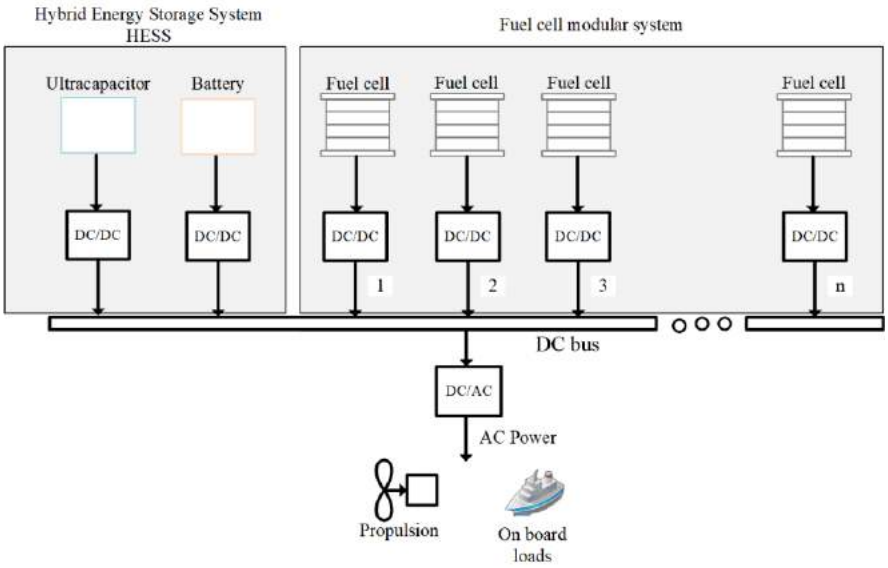

Figure 1: Ship power train based on a modular fuel cell hybrid system with battery and ultracapacitor

METHODS

In this section the methodology of the model is presented. The simulation was performed in Matlab Simulink. First, we present the model for the fuel cell module, the battery, and ultracapacitors, after the optimization algorithm which decides the power distribution among for the three different electrochemical energy conversion devices is presented.

Fuel cell module

To ensure a reasonably fast simulation computational time, the fuel cell performance was described in a lookup table, efficiency vs. power demand, instead of using a more accurate mechanistic model. The limitation of this approach is that the model is not able to describe the performance changes as a function of parameters such as temperature and cell degradation. Nevertheless, this approach enables us to provide reasonable answers to understand how the system would react to load changes.

A smaller portion of the overall fuel cell power output is used to support the fuel cell module balance-of-plant (BoP) i.e. the air compressor, valves, sensors, fans, and all the other components which maintain the operation of a fuel cell stack. This means

that the power output of the fuel cell modules, $P_{Mod,n}$ [kW] is the difference between the fuel cell power output, $P_{FC,n}$ [kW], and the power demanded by the balance of plant, $P_{BOP,n}$ [kW]. Generally, power demand of the BoP has a base load and a part which is depending on the fuel cell power output, $P_{FC,n}$. For instance, cooling and air compression require an amount of power which increases with the fuel cell load. A relationship can be summarized in the following equation:

$$P_{Mod,n} = P_{FC,n} - P_{BOP,n} \quad [1]$$

The efficiency of the *n-th* fuel cell module can be calculated by dividing the power delivered by the module with the hydrogen lower heating value, LHV times the hydrogen flow rate.

$$\eta_{FC,n} = \frac{P_{Mod,n}}{\dot{n}_{H2,n} \cdot LHV_{H2}} \quad [2]$$

The total efficiency of the modular system η_{FCsys} [kW], is a weighted average where each module efficiency is weighted considering the power that it delivers.

$$\eta_{FCsys} = \frac{\eta_{FC,1} \cdot P_{FC,1} + \eta_{FC,2} \cdot P_{FC,2} + \eta_{FC,3} \cdot P_{FC,3} \cdots \cdot \eta_{FC,n} \cdot P_{FC,n}}{P_{TOT}} \quad [3]$$

The fuel cell system efficiency map can change depending on how a fuel cell system is designed and engineered. In general, a fuel cell system shows lower efficiencies in the lower range of the power output and almost unchanged high values in the mid and high range. For this simulation, the efficiency map in figure 2 was utilized to describe the FC performance as a function of power. The profile was constructed based on what found is several references and it does not describe one specific fuel cell system.

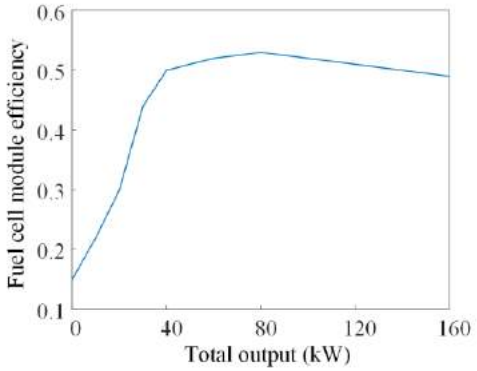

Figure 2: Fuel cell module power output

The slow dynamic of fuel cell modules can be approximated to a first-order system. The exists a relationship between the reference power ($u_{fc,n}$) and the actual output power ($P_{fc,n}$) is:

$$P_{fc,n} = \frac{1}{T_s s + 1} u_{fc,n} \quad [4]$$

In the equation, T_s is the time constant is set to 80 s, this is the time needed for the load step response to reach 63.2% of its final value. A similar approach was followed by (Wang, Nehrir, and Shaw). For FCs in independent distribution, there would be five control variables $u_{fc,1}, u_{fc,2}, \cdots, u_{fc,5}$. They are the reference power for each fuel cell module. While for those in equal distribution and sequential distribution, all the fuel cells are treated as a whole and one control variable (u_{fc}) would be enough, which stands for the total amount of FC reference power. The relationship between the overall reference variable (u_{fc}) and actual output power (P_{fc}) are the same:

$$\dot{P}_{fc} = -\frac{1}{T_s} P_{fc} + \frac{1}{T_s} u_{fc} \quad [5]$$

where $\dot{P}_{fc,n}$ is the power change in the time unit.

Fuel cell module power distribution

The power distribution among several fuel cell modules has previously been studied (Marx et al.). In this study we consider the three options listed below:

- *Equal distribution*. In this the power demand is equally allocated to each module.
- *Independent distribution*. The optimization algorithm decides how to allocate the power to each module
- *Sequential distribution*. The power demand is allocated to one module after another where one module is activated when the previous one has reached maximum power output. This configuration is also known as "daisy-chain" power distribution (Garcia et al.).

In figure 3, the three different module load distribution configurations are shown. Five modules were considered for this study. A power limiter between 0 and 160 kW was considered for each fuel cell module.

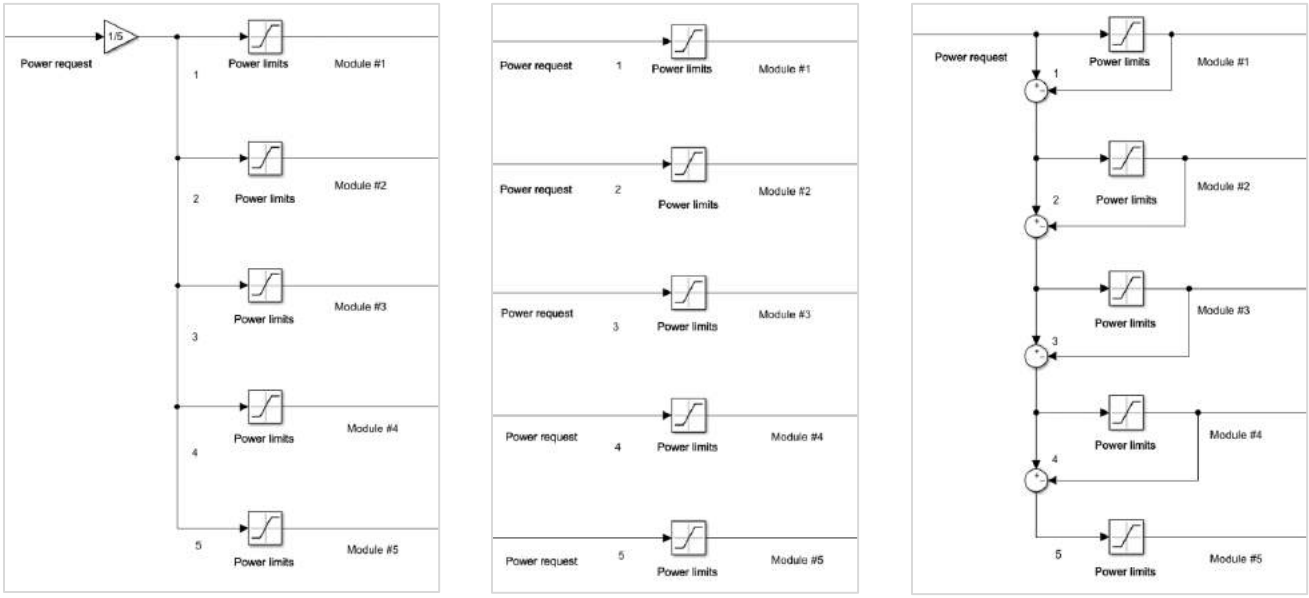

Figure 3: Equal distribution (left), sequential (center) and independent (right) distribution of power among five fuel cell modules

The efficiency profile for the equal distribution and the sequential distribution as a function of the load are presented in figure 4. For the sequential distribution an equivalent efficiency was derived. In the equal distribution low efficiency is delivered in the low range of the total power output. The undulations in the equivalent curve of the sequential distribution are attributed to the low efficiencies in the lower power range of each module activated one after another. Also, it appears that the sequential distribution has a lower efficiency in the middle and higher power range.

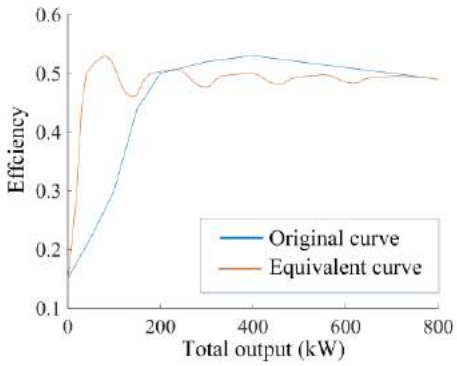

Figure 4: Comparison between the efficiency of the fuel cell in equal distribution and the equivalent efficiency of the sequential distribution

Hybrid Energy Storage System

Despite the advantages of high efficiency and zero emission, the slow dynamic nature of hydrogen fuel cells makes energy storage systems a necessity, especially considering of the changeable marine load condition. A hybrid energy storage system (HESS) consisting of batteries and ultra-capacitor (UC) is utilized here, with the batteries providing auxiliary to the FC system and the UC supporting sudden load changes. The HESS model can be presented as follows:

$$\begin{bmatrix} \dot{SOC}_{bat} \\ \dot{SOC}_{uc} \end{bmatrix} = \begin{bmatrix} -\frac{1}{3600}Q_B & 0 \\ 0 & -\frac{1}{V_{uc}}C_{uc} \end{bmatrix} \begin{bmatrix} I_{bat} \\ I_{uc} \end{bmatrix} \quad [6]$$

where SOC_{bat}, SOC_{uc} [kWh] stands for the SOC of battery and UC, respectively. Q_B is the battery capacity [Ah], V_{uc} is the maximum voltage of ultra-capacitor (UC), C_{uc} is the capacitance, I_{bat} and I_{uc} are their respective currents. Due to the existence of inner resistance, the terminal output powers of HESS (P_{bat} and P_{uc}) are determined by:

$$P_{bat} = V_{oc} I_{bat} - R_{bat} I_b^2 \quad [7]$$

$$P_{uc} = V_{uc} SOC_{uc} I_{uc} - R_{uc} I_{uc}^2 \quad [8]$$

Here V_{oc} is the open circuit voltage of battery and is assumed as equal to DC bus voltage. R_{bat} and R_{uc} are the resistance of battery and UC.

System Description and power management system problem Formulation

To ensure a stable and high-efficiency operation, a real-time power management system (PMS) is developed to make the optimal power splitting decision. The PMS is optimization-based and is developed based on equivalence consumption minimization strategy (ECMS), an effective energy management technique capable to calculate the instantaneous equivalent fuel consumption of energy storage systems and determines the optimal power split with low computational burden and limited calibration of control parameters (Xie et al.).

The objective is to minimize the total equivalent hydrogen consumption, which is the sum of actual hydrogen consumption from FC (C_{fc}) and the equivalent hydrogen consumption from HESS (C_{bat} and C_{uc}):

$$\begin{aligned} &\min && J = C_{fc} + C_{bat} + C_{uc} \\ &s.t. && \begin{cases} P_{fc} + P_{bat} + P_{uc} = P_{load} \\ P_{fc} \in [P_{fc(min)}, P_{fc(max)}] \\ I_{bat,uc} \in [I_{bat,uc(min)}, I_{bat,uc(max)}] \\ SOC_{bat,uc} \in [SOC_{bat,uc(min)}, SOC_{bat,uc(max)}] \\ \Delta u_{fc} \le \Delta u_{fc(max)} \\ \Delta I_{bat,uc} \le \Delta I_{bat,uc(max)} \end{cases} \end{aligned} \quad [9]$$

The optimization problem subjects to several constraints. The equality constraint stands for the power balance, ensuring that the load demand (P_{load}) is met at every sampling time by FC (P_{fc}), batteries (P_{bat}) and UCs (P_{uc}). The inequality constraints limit output power of FC, the currents of HESS ($I_{bat,uc}$), the SOC of HESS ($SOC_{bat,uc}$), and the changing rate of them, respectively. Subscript *min* and *max* refer to the lower and upper limit. $\Delta u_{fc} \le \Delta u_{fc(max)}$ is a constraint which is limiting the

change in the reference fuel cell module power in the time unit and $\Delta I_{bat,uc} \le \Delta I_{bat,uc(max)}$ is a constraint which is limiting the current of the battery and ultracapacitors in the time unit.

(1) The fuel cell hydrogen consumption: C_{fc}

The relationship between C_{fc} and P_{fc} can be expressed as:

$$C_{fc} = \sum_{n=1}^{N_{fc}} C_{fc,n} = \sum_{n=1}^{N_{fc}} \frac{P_{fc,n}}{\eta_{fc,n}} \quad [10]$$

where N_{fc} is the amount of fuel cell module, $P_{fc,n}$ is the output power of n^{th} fuel cell module. $\eta_{fc,n}$ is its corresponding efficiency value at that moment, and is calculated based on specific fuel cell efficiency curve as shown in Fig.4.

(2) Equivalent hydrogen consumption of HESS: C_{bat} and C_{uc}

The basic idea of ECMS is that HESS can be treated as a buffered energy source. It is assumed that the amount of energy that is discharged from HESS will be charged later. Thus, the hydrogen consumption required for the FC to charge the battery and ultracapacitor is equivalent to the hydrogen consumption of HESS.

The equivalent hydrogen consumption of battery can be calculated as:

$$C_{bat} = ef_{bat} \frac{P_{bat}}{\eta_{fc.av}} \quad [11]$$

where $\eta_{fc.av}$ is a constant middle value of the fuel cell efficiency, representing the average efficiency of the fuel cell. ef_{bat} is the equivalence factor, which stands for the conversion from electricity to hydrogen consumption and is calculated by the equations below in the cases the battery is discharging, $P_{bat} \ge 0$, or charging, $P_{bat} < 0$:

$$ef_{bat} = \begin{cases} \dfrac{k_{bat}}{\eta_{chg.av} \cdot \eta_{dis}} & P_{bat} \ge 0 \\ k_{bat} \cdot \eta_{dis.av} \cdot \eta_{chg} & P_{bat} < 0 \end{cases} \quad [12]$$

$\eta_{chg.av}$ and $\eta_{dis.av}$ are set to 0.95, denoting average charging and average discharging efficiency of battery, respectively. η_{cha} and η_{dis} are real-time battery charging and discharging efficiency, affected by the battery output power and current SOC, can be calculated based on (Hong et al.). Another key factor is the SOC penalty coefficient, k_{bat}. The point of it is to avoid over-charging and over-discharging, thus maintain the battery SOC varies around a healthy level. It is defined as:

$$k_{bat} = 1 - \mu_{bat} \frac{SOC_{bat} - SOC_{base}}{SOC_{base}} \quad [13]$$

Here μ_{bat} is a constant value, standing for the penalty of SOC when it violates the base line (SOC_{base}). k_{bat} varies with the changing of SOC and effects the equivalence factor directly. For example, if the battery SOC is greater than SOC_{mid}, the larger it is, the cheaper we consider the energy stored in battery, thus encouraging battery to be discharged. Conversely, if SOC_{bat} is smaller than SOC_{mid}, the less it is, the more expensive we consider discharging the battery. And FCs are encouraged to take on more power or charge the battery instead. In this way, a healthy level of battery SOC can be maintained.

As for the equivalent hydrogen consumption of UC (C_{uc}), similar equations are held as those for batteries. However, the penalty for UC (μ_{uc}) is much larger than that of battery μ_{bat}. The reason is that UC is backed up only for sudden load changes, thus expected to have zero output power when at normal load conditions.

RESULTS AND DISCUSSION

The hybrid power train model was simulated using a load profile of half an hour (i.e., 1800 seconds). The profile describes the ship power demand on a short trip where the pick demand is reached in the middle of the trip and fast load changes are experienced due to maneuvering and changes in the on-boards power demand. The three identified power distribution modes in the five fuel cell modules are presented in figure 5.

From the simulations, it appears that the power output of the ultracapacitor increases greatly when its SOC validates from the base value, which leads to the results that ultracapacitor is mainly used to cover for the power demand during the quick load changes. The battery, on the other hand, is mainly used when the fuel cell delivers power at low efficiency, namely during the low efficiency – this occurs mainly in the beginning of the trip. In the sequential distribution, the fuel cells modules reach the max power output in the middle of the trip, and towards the end of the trip are used to recharge the batteries. In the case of the independent and the equal distribution there is a higher use of the battery in the middle of the trip – this is because a pick in the efficiency profile of the fuel cell module is shown in the range of 400 kW and lower efficiency at max power output, therefore batteries tend to take some of the load to make the fuel cell to operate at high efficiency range.

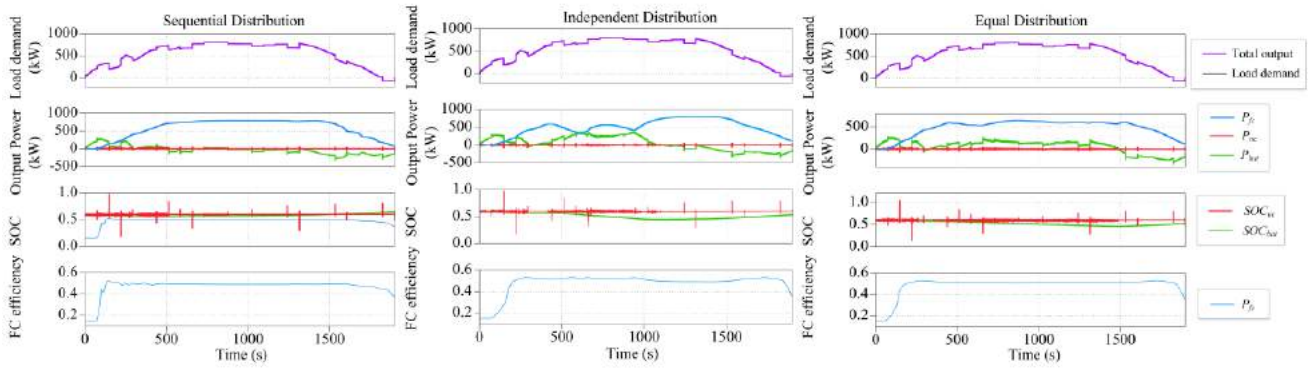

Figure 5: Comparison between power output, SOC [%] and total efficiency of the fuel cell modules for each of the three identified cases: sequential distribution (left), independent distribution (center) and equal distribution (right)

A comparison of the instantaneous equivalent hydrogen consumption between the three distribution is shown in figure 6. They represent the cost function which was used in the optimization objective function. It appears that the curves follow the same trends on the output power.

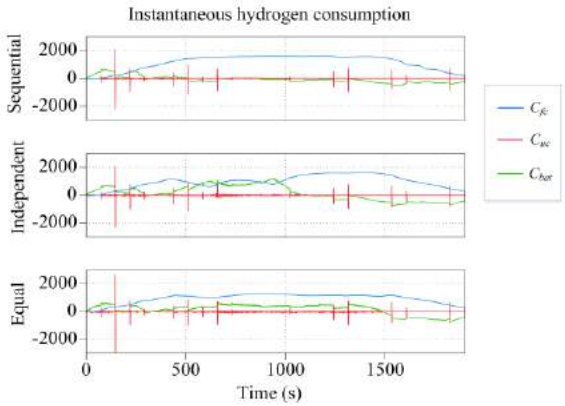

Figure 6: Comparison of the cost functions expressed as equivalent hydrogen consumption [kW] for fuel cell modules, ultracapacitors and batteries

In figure 7, a direct comparison between the power and the efficiency in each of the three fuel cell configurations is provided. Interestingly in the case of the independent distribution, the optimization algorithm decides that the fuel cell modules provide almost the same output during the trip. Two major drops are seen which can be attributed to the time limitation in the algorithm to produce the load changes.

In the sequential distribution the modules are activated one after another, therefore the drops in power are experienced by one module at the time.

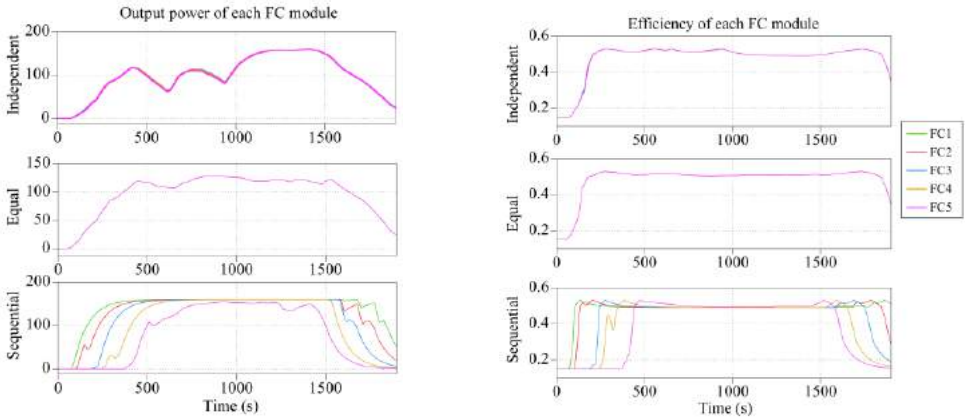

Figure 7: Break down of the power output [kW] (left) and efficiency [-] (right) of each of the five fuel cell modules

Figure 8 shows the comparison of the overall fuel cell modules efficiency η_{FCsys}, defined in the equation 3, in the 3 cases. It appears that the sequential distribution delivers power at a better efficiency in the beginning of the trip. This is consistent with what shown previously in figure 4 where it was discussed that the sequential distribution has a better efficiency in the low power range. On the contrary both the independent and the equal distribution show better efficiency in the middle of the trip when the power demand is higher.

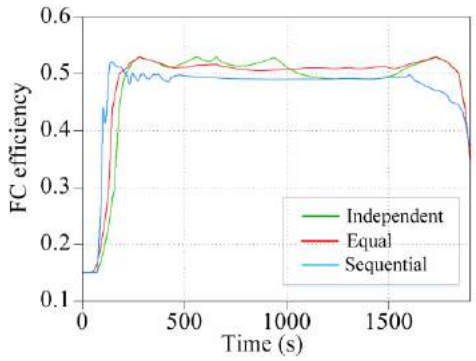

Figure 8: Comparison of the overall fuel cell module efficiency [-] in the three case-study: Independent, equal and sequential distribution

CONCLUSIONS

Due to the advantages in low emission, quiet operation, and high efficiency, fuel cells are drawing attention in marine application. The distribution way of fuel cell modules directly affects the overall operational efficiency and thus should show different characteristic under different load conditions. To maintain high efficiency operation, studies on fuel cell power distribution are necessary.

In this paper, a performance comparison of three different fuel cell power distributions in terms of hydrogen consumption and operation efficiency is presented. For ship under fluctuating load condition, a hybrid energy storage system consisting of ultracapacitor and battery is utilized. To decide the optimal power splitting between them, a real-time power management system is developed with the objective of minimizing the overall hydrogen consumption and maintaining a healthy SOC level of HESS.

Through the detailed analysis and simulation results, it is indicated that sequential distribution has a wider range of high hydrogen efficiency but smaller peak efficiency among all. Thus, sequential distribution would provide a better performance at low load condition while the other two at high load condition. In this study we have assumed no rotation across the modules, which means that on the long run the first module in the sequential distribution will be the most used and hence the most degraded. In the future work, we will include the possibility to rotate the modules based on the hours of operation and/or performance degradation.

Considering the advantages of each of the three configurations in terms of maximum efficiency, it is recommended that a combination between them according to the specific load demand is in most cases desirable. This paper provides a good foundation for future research, for example, the optimal fuel cell distribution selection, the real-time scheduling and switching, and the sizing of ultracapacitors, batteries and fuel cell modules based on the specific application.

ACKNOWLEDGMENT

We would like to acknowledge the project LH2Vessel (EUDP J.Nr. 64019-0023) for sponsoring this research.

REFERENCES

Bonacina, Camilla Nicol, Nima Bordbar Gaskare, and Gianluca Valenti. "Assessment of Offshore Liquid Hydrogen Production from Wind Power for Ship Refueling." *International Journal of Hydrogen Energy* (2021): n. pag. Web.

Chen, Yunru et al. "Parametric Analysis and Optimization for Exergoeconomic Performance of a Combined System Based on Solid Oxide Fuel Cell-Gas Turbine and Supercritical Carbon Dioxide Brayton Cycle." *Energy Conversion and Management* 186 (2019): 66–81. Web.

DOE. "Hydrogen Storage." N.p., n.d. Web.

Garcia, J E et al. "Power Sharing for Efficiency Optimisation into a Multi Fuel Cell System." *2014 IEEE 23rd International Symposium on Industrial Electronics (ISIE)*. N.p., 2014. 218–223. Web.

Hong, Zhihu et al. "An Energy Management Strategy Based on Dynamic Power Factor for Fuel Cell/Battery Hybrid Locomotive." *International Journal of Hydrogen Energy* 43.6 (2018): 3261–3272. Web.

"Liquid Hydrogen Concept Validation for Large Efficient, Scaled and Stacked FC Electric Power Systems for Vessels." N.p., n.d. Web.

Marx, N et al. "A Review of Multi-Stack and Modular Fuel Cell Systems: Interests, Application Areas and on-Going Research Activities." *International Journal of Hydrogen Energy* 39.23 (2014): 12101–12111. Web.

Wang, Caisheng, M H Nehrir, and S R Shaw. "Dynamic Models and Model Validation for PEM Fuel Cells Using Electrical Circuits." *IEEE Transactions on Energy Conversion* 20.2 (2005): 442–451. Web.

Xie, Peilin et al. "Optimization-Based Power and Energy Management System in Shipboard Microgrid: A Review." *I E E E Systems Journal* (2021): n. pag. Web.

AUTONOMOUS OPERATION AS AN ECONOMIC DRIVER FOR SMALLER MERCHANT SHIPS

Stig Eriksen[1]

ABSTRACT

If autonomous and/or unmanned operation of ships can be realised, reduced crew costs may offset the economy of scale effects of large ships and shift the favour towards the utilisation of smaller ships. This paper examines the impact of unmanned operation or reduced manning on the economy of scale effect on merchant ships. Data from different sizes of three types of ships: bulk carriers, tankers, and containerships, are analysed. A clear economy of scale effect is, as expected, found in the overall transport costs in general and in the manning costs in isolation. Larger ships can transport significantly more cargo over the same distance for the same expense in manning than smaller ships. Overall, however, the economy of scale effect of manning is greatly surpassed by the economy of scale effects of other costs, particularly fuel cost. Three cases of reduced manning or unmanned operation are analysed. Reduced manning or unmanned operation is found to reduce the overall economy of scale effect of larger ships, but overall, the economy of scale effect is still very significant across all cases. Despite reductions or the complete elimination of manning costs, it is still substantially cheaper to transport cargo on large than on small ships. The paper concludes that unmanned operation or reduced manning does not significantly alter the cost structure or economy of scale in favour of using small rather than large merchant ships

KEYWORDS

Autonomous ships; Unmanned ships; MASS; Economy of scale; Returns to scale; Fuel efficiency.

INTRODUCTION

Autonomous and unmanned ships have been the subject of considerable research and debate in the maritime community since the turn of the new millennium. Proposed benefits of autonomous and unmanned operation include reduced fuel consumption, larger cargo capacity, increased safety, and improved operational efficiency (Kobylinski, 2018). However, the primary economic benefit of autonomous operation is expected to come from reductions in crew costs (Hogg & Ghosh, 2016). The amount of cargo a ship can transport in proportion to the number of crewmembers required for their operation typically increases with ship size. As a result, the crew costs on small ships comprise a proportionally larger expense per unit of cargo transported than on large ships. With reductions in crew costs, autonomous operation of ships may offset this economy of scale effect and shift the favour from the super large ships of today towards smaller and more manageable ships in the future (Rødseth, 2018). However, the size of the crew is not the only economy of scale effect of larger ships. Fuel consumption and other operational parameters are also affected by ship size. This paper examines to which extent reductions in crew sizes by autonomous operation affect the economy of scale effect and shift the business case in favour of smaller ships.

Economy of scale has been investigated in relation to merchant ships by several authors. Lim (1998), Cullinane and Khanna (1999), and Wu and Lin (2015) examine economies of scale in container shipping. Glen and Reid (2010) explore cost elasticities in the tanker segment. The importance of economies of scale for reductions in greenhouse gas emissions from shipping is explored by Lindstad et al. (2012), and Bernacki (2021) assesses the link between vessel size and maritime supply chain sustainable performance. Methods for determining the optimal ship size in liner shipping, including, amongst other factors, economies of scale, are developed by Sys et al. (2008) and Lian et al. (2019). Manning costs are included in these analyses, but unmanned operation or reduced manning effects are not explicitly considered.

Some work has been done on assessing the business cases of autonomous and/or unmanned operation of ships. Kretschmann et al. (2015) conducts an economic analysis of the case of the autonomous bulk carrier as part of the Maritime Unmanned Navigation through Intelligence in Networks (MUNIN) project. Munim (2019) discusses potential business models from the perspective of the manufacturers of autonomous ships. Akbar et al. (2021) conduct an economic analysis of autonomous ships in a short-sea liner shipping network. However, none of these analyses considers the effect of unmanned or autonomous operation of ships on the economies of scale. Rødseth (2018) makes a qualitative assessment of the benefits and challenges related to unmanned ship operation in which the issue of economies of scale relating to unmanned operation is raised. The

[1] Svendborg International Maritime Academy (SIMAC)

analysis is, however, purely qualitative and no cases are evaluated, or numerical calculations made. No quantitative evaluations of this topic have been found in the existing literature.

Therefore, the objective of this paper is to explore the economy of scale effects of ships in relation to unmanned operation or reduced manning on ships. Cost structures of ships of different types and sizes are analysed. Case studies are used to explore the economy of scale effects of different operation elements. The paper examines the case of both unmanned operation and reduced crew sizes.

IMPORTANT CONCEPTS, METHODOLOGY, AND DATA

This section briefly describes the concepts of returns to scale and economy of scale around which this paper revolves. The data and the methodology used in the analyses is explained.

Returns to scale and economy of scale

Returns to scale are said to be increasing when the output of a process increases proportionally more than the increase in input (Salvatore, 2012). Economy of scale exists when the return to scale is increasing, as opposed to diseconomies of scale, which occurs when the output increases proportionally less than the input. Transport work, expressed for example, as tonnes, volume, or units of cargo transported over distance, typically in nautical miles (nm), is a typical measure of the output of shipping operations. Inputs are all those parameters required for the ship to deliver the output, such as fuel, manning, insurance and capital costs, and port fees. The total returns to scale are a product of many such input or cost categories which individual returns to scale can each follow different trajectories. Cost categories with increasing returns to scale for ships are typically crewing, fuel consumption, capital investments and interests, repairs and maintenance, etc. Diseconomies of scale for ships arise from, e.g. port operations, because large ship takes longer to load and discharge, which negatively affects the time in which they can perform transport work at sea (Bernacki, 2021). Typically, economy of scale is most prevalent at small levels of output where diseconomies of scale become more prevalent at higher levels of output (Salvatore, 2012). In the small ship segment, significant gains in output can be achieved by small increases in ship size, assuming no restrictions in cargo availability and other physical limitations. As the ships become bigger, the economy of scale will become increasingly marginal before reaching an inflexion point, after which the returns to scale will decrease.

Data

Data on the cost structures of different sizes of three types of ships are used for the analysis in the present paper, namely bulk carriers, tankers, and containerships. The data is taken from Delhaye et al. (2010), which built their cost structure models on the reports of Drewry Shipping Consultants (2021). The cost structure models are based on data from 2010 and earlier. More recent data would have been desirable, but sources of cost structures of commercial ships are typically not publicly and freely accessible. ~~, and n~~Newer sources of openly available data have not been found ~~available~~ for the analyses in the present paper. However, the lack of more recent data is not assessed to be significant to the findings of this paper.

Cases

This paper aims to explore the effects of unmanned operation or reduced manning on the economies of scale of merchant ships. No such ships are in operation today, and no direct comparisons can therefore be made. Instead, to investigate these effects, this paper proposes three cases. In case 1, it is assumed that the crew costs are reduced by 20 per cent. The assumption in case 1 is in line with the ~~assumptions used b~~findings of~~y~~ Schröder-Hinrichs et al. (2019) and Eriksen (2021) that the realistic potential for reductions in crew ~~crew l~~levels by increased automation in the near future is between ~~can be reduced by~~ 16 ~~to~~and 24 per cent ~~by 2040~~. In case 2, all the ships are assumed to be unmanned. In case 3, the smallest ship in the analysis is assumed to be unmanned, but the manning of the larger ships is not affected. Small ships are better suited for unmanned operation than large ships because of the distribution of onboard work required for their operation and their often limited and repetitive operation patterns (Eriksen, 2021; Jokioinen et al., 2016; Wariishi, 2019). It is, on the other hand, unlikely that the possible developments that will enable unmanned operation of small ships will not also enable reduced manning of large ships. Case 3 is not considered a realistic scenario but is included to illustrate the furthest hypothetical effect of unmanned operation on the economy of scale effects as examined in the present paper.

Case 1 describes a realistic scenario to the extent that it is based on existing literature, whereas cases 2 and 3 are considered more hypothetical scenarios. However, all cases are theoretical since it is assumed that reductions in manning costs follow the manning level 1:1 and that reducing the manning or making the operation unmanned is costless. The three analysed cases aim to investigate the theoretical effects of altering one single parameter, namely manning costs. All other costs are assumed to be unaffected. The analysis in the present paper focuses only on the sea voyage of the ships. It does not consider port

operations or time at anchor, nor does it consider cargo capacity utilisation or other factors decisive to the choice of optimal ship size.

RESULTS

This section presents the results of the analyses and case studies. First, the cost structures of the three different ship types are described. Secondly, the results of the calculations on the economy of scale are presented. Thirdly, the results of the case studies are presented, and lastly an additional analysis of energy consumption in relation to ship size is done.

Cost structure

The basis for understanding and assessing factors influencing economies of scale is the cost structures of each type of ship analysed in the present paper. Table 1 shows the cost of four typical sizes of oil/chemical tankers as taken from Delhaye et al. (2010). The corresponding cost structures of bulk carriers and containerships can be seen in Table A1 and A2 in the appendix. Figures in Table 1, A1, and A2 represent the daily costs for a typical vessel of the specific type and size during sea passage operating at normal operating speed. Figures in the three tables are shown in € per day and in per cent of total daily shipping costs for each category. For all three ship types and across all sizes, the highest cost is fuel accounting for between 36 and 54 per cent of the total cost, followed by capital repayments and interest on capital. Manning costs comprise the fourth or fifth most significant expense together with repairs and maintenance. As seen in Table 1, the crew costs decrease slightly with increasing ship size from 9 to 5 per cent. This trend is even more pronounced for containerships where the crew cost decreases from 10 to only 3 per cent. However, for bulk carriers, the crew costs are very stable at 6 to 7 per cent across all ship sizes.

Table 1 Tank: cost structure

Vessel size	**MR1**		**LR1**		**Suezmax**		**VLCC**	
Dwt (nominal)	25000-45000		45000-80000		120000-200000		200000-320000	
Costs (at sea, full steaming)	€/day	% of total	€/day	% of total	€/day	% of total	€/day	% of total
Manning	2369	9%	2369	8%	2600	6%	2808	5%
Insurance	554	2%	592	2%	1038	2%	1377	2%
Repairs and maintenance	1408	5%	2108	7%	2777	6%	3108	5%
Stores and lube oil	585	2%	654	2%	885	2%	1131	2%
Administration	1031	4%	1292	4%	1523	3%	1723	3%
Capital repayments	5748	22%	6684	22%	9358	21%	12368	21%
Interest	4725	18%	5495	18%	7692	17%	10989	18%
Fuel (€/day)	9242	36%	11154	37%	19122	42%	26480	44%
Total daily shipping cost (€/day)	**25662**		**30348**		**44995**		**59984**	

Overall, the cost structures across all three ship types are quite similar. Fuel costs account for a larger part of the total daily shipping costs of the smaller container ships than for the bulk and tank segment, presumably because of the higher operating speed of the former. The highest proportion of manning costs are also found in the smallest category of container ships, although it should be noted that the ships in this category are much smaller than the smallest categories of bulk carriers and tankers. The smallest proportion of manning costs are found amongst the largest container ships.

Economies of scale

When, instead of considering absolute costs, the cost of transport in relation to ship size is considered, the effects of economy of scale become clearly visible. Figure 1 shows the cost of transport in € per 1000 ton-mile (nautical miles) in relation to the cargo capacity in tons of the three ship types. The X-axis of Figure 1 has been cropped slightly, excluding the very largest of the tankers, to better visualise the remaining ship sizes. As Figure 1 shows, all three ship types follow the same general trend. The economy of scale is most pronounced for the smaller segment of ships and become less prevalent as the ships become

larger. The cost of transport in relation to ship size is almost identical for tankers and bulk carriers which is likely explained by the very similar constructions and type of operation of the two types of ships. Containerships carry more high volume/low weight products and generally operate at a higher speed than tankers and bulk carriers, which is likely the explanation for the higher cost of transport for this type of ship.

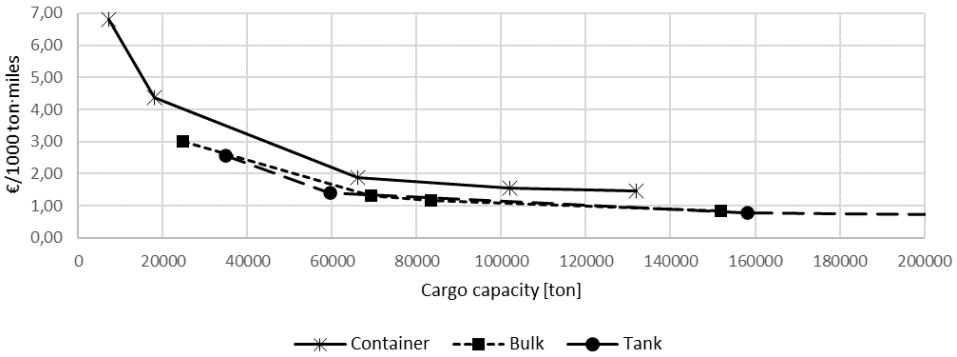

Figure 1 Cost of transport work vs. ship size for the three ship categories

However, the economy of scale is pronounced for all three ship types. For containerships, the cost of transporting 1000 tons of cargo over one nautical mile decreases from close to 7€ to just under 1.5€ from the smallest to the largest ship size, or by a factor of almost five. This factor is slightly smaller for bulk carriers and tankers at just under four, although it should be noted that a size segment corresponding to that of the smallest containerships is not included for these two ship types.

To examine how increases in ship size affects different aspects of the ships costs, the cost of transport work is further specified to each of the individual cost categories. Table 2 shows the cost of transport work specified by the individual cost category for the tankers. Table 2 also shows how much each cost category contributes to the total reduction in the cost of transport work compared to the smallest ship size. The per cent values in Table 2 are calculated as the difference between each category of each of the larger three ship sizes and the smallest ship category (MR1) divided in the difference in the total cost of transport work for the same two categories. For the Suezmax tankers, for example, manning costs 0.05 €/1000 ton-mile versus 0.24 €/1000 ton-mile for the MR1 size giving a difference of 0.19 €/1000 ton-mile. The total difference in the cost of transport work between the Suezmax and the MR1 is 1.77 €/1000 ton-mile. Manning, therefore, contributes with 11 per cent of the total saving in transport costs when the ship size increases from an MR1 type tanker to a Suezmax tanker. The cost of transport for each cost category for the container ships and the bulk carriers are shown in the appendix in tables A3 and A4.

Table 2 Tank: cost of transport work specified by individual cost category and contributions of each cost category to the economy of scale of the larger ships compared to the smallest ship

Vessel size	MR1		LR1		Suezmax		VLCC		
Cargo capacity [tons]	34763		59404		158078		256626		
Speed [knots]	12		15		15		15		
€/1000 ton·nm	€	%	€	%	€	%	€	%	**Avg.**
Manning	0.24	-	0.11	11%	0.05	11%	0.03	11%	**11%**
Insurance	0.06	-	0.03	2%	0.02	2%	0.01	2%	**2%**
Repairs and maintenance	0.14	-	0.10	4%	0.05	5%	0.03	6%	**5%**
Stores and lube oil	0.06	-	0.03	2%	0.02	2%	0.01	2%	**2%**
Administration	0.10	-	0.06	4%	0.03	4%	0.02	4%	**4%**
Capital repayments	0.57	-	0.31	23%	0.16	23%	0.13	23%	**23%**
Interest	0.47	-	0.26	19%	0.14	19%	0.12	18%	**19%**
Fuel	0.92	-	0.52	35%	0.34	33%	0.29	33%	**34%**

As seen in Table 2, the relative differences between the smallest ship type and each of the larger ship types are very consistent. It is also seen that the cost of manning, as is the focus of this paper, decreases dramatically with increasing ship size from 0.24 €/1000 ton-mile for the MR1 to only 0.03 €/1000 ton-mile for the VLCC, or by a factor of almost eight. A VLCC is, therefore, able to carry almost eight times more cargo over the same distance for the same manning cost as an MR1 tanker. For the bulk carriers, this development is slightly less dramatic with a decrease by a factor of about four, but for the containerships, it is even more pronounced with an increase by a factor of more than fifteen. The economy of scale effect in relation to manning costs is therefore strong for all ship types. However, overall manning costs only account for an average of 11 per cent of the total difference in the cost of transport work for the tankers, 7 per cent for the bulk carriers, and 13 per cent for the containerships. The cost of fuel accounts for by far the most significant part of the economy of scale effect at an average of 34 per cent for the tankers, 49 per cent for the bulk carriers, and 57 per cent for the container ships.

Cases

To investigate which effect reduced manning or unmanned operation will have on the economy of scale effect, the three cases, as previously described, is explored. Table 3 shows the results of the three cases for the tankers. The results for the bulk carriers and the containerships are shown in tables A5 and A6 in the appendix. Table 3 shows how much the cost of transport differs between the smallest vessel type, the MR1 class, and each of the larger vessel types. In the base case, which is the conventionally manned ships as seen in tables 1 and 2, the cost of transport in €/1000 ton-mile is for the VLCC, for example, 7~~5~~4.7 per cent smaller than for the MR1 class. For the three cases, Table 3 also shows the difference in transport costs between the specific case and the base case, i.e. the conventionally manned ships, within each vessel type class. When the manning is reduced by 20 per cent in case 1, for example, the overall cost of transport for the MR1 class is reduced by 1.8 per cent compared to the base case.
The results in Table 3 shows that the effect of reduced manning or unmanned operation on the transport costs become less pronounced as the ships become larger. A 20 per cent reduction in crew costs results in a 1.8 per cent decrease in transport costs for the MR1 class, but the corresponding reduction for the VLCC is only half as big at 0.9 per cent. This trend, of course, relates directly to the developments in the relative manning costs seen in tables 2, A3, and A4. For the bulk carriers, this trend is, therefore, less pronounced but still existing, whereas the trend is even more pronounced for the containerships.

Table 3 Tank: differences in cost of transport work in the three proposed cases

Vessel size	MR1	LR1	Suezmax	VLCC
Base case				
Diff. €/1000 ton·nm from MR1	-	-44.6%	-69.2%	-74.7%
Case 1 (-20% manning costs)				
Diff. €/1000 ton·nm from base case	-1.8%	-1.6%	-1.2%	-0.9%
Diff. €/1000 ton·nm from MR1	-	-44.5%	-68.9%	-74.4%
Case 2 (no manning costs)				
Diff. €/1000 ton·nm from base case	-9.2%	-7.8%	-5.8%	-4.7%
Diff. €/1000 ton·nm from MR1	-	-43.8%	-68.0%	-73.4%
Case 3 (no manning on MR1)				
Diff. €/1000 ton·nm from base case	-9.2%	0.0%	0.0%	0.0%
Diff. €/1000 ton·nm from MR1	-	-39.0%	-66.0%	-72.1%

More importantly, Table 3 shows that reducing the crew costs as in case ~~2~~1 or eliminating the costs as in case ~~3~~2 does affect the differences in the costs of transport between ship sizes. Where the difference in the cost of transport between the MR1 and the LR1 classes was 44.6 per cent in the base case, it is reduced to 44.5 per cent in case 1 and 43.8 per cent in case 2. What is also evident from the results in Table 3 is that the effects of reduced manning or unmanned operation on the economy of scale effects are relatively limited. Even in the most extreme scenario, case 3, where conventionally manned LR1, Suezmax, and VLCC tankers are compared to unmanned MR1 tankers, the economy of scale effect is still significant for the larger tankers. Instead of reducing the cost of transport by 44.6, 69.2, and 74.7 per cent, the cost of transport for the three larger ship type classes are in case 3 reduced to “only” 39.0, 66.0, and 72.1 per cent. The most significant effect of unmanned operation is found in the 1000-2000 TEU range of containerships in Table A6, where the differences in cost of transport are reduced by almost 1/5 from 35.7 per cent in the base case to 28.9 per cent in case 3. In cases 1 and 2, however, the differences are much more limited. Especially for in the bulk segment in Table A5, the effects of reduced manning in case 1 and unmanned operation in case 2 is almost undetectable with relative decreases in the economy of scale effect never exceeding half a per cent.

Energy consumption

As seen in Table 1, fuel consumption is by far the most significant single component of the total cost of transport. As seen in Table 2, fuel costs are also the most significant contributor to the economy of scale effect. Because of its importance, an additional analysis of the impact of ship size on fuel consumption is done here. Figure 2 shows the relation between fuel consumption in grams per ton-mile and cargo capacity in tons of the three ship types. The X-axis of Figure 2 has been cropped slightly, excluding the very largest of the tankers, to better visualise the remaining ship sizes. As Figure 2 shows, the fuel used to transport the same mass of cargo over the same distance decreases rapidly with increasing ship size. The development of the three curves in Figure 2 looks almost identical to those showing the development of the total transport cost in relation to ship size in Figure 1, as is perhaps not surprising considering that fuel comprises such a large part of those costs.
The largest reduction is seen amongst the containerships with a decrease by a factor of almost six from nearly 12 g/ton-mile for the smallest ship type to just over 2 g/ton-mile for the largest. The reductions for tankers and bulk carriers are less dramatic, but still very significant, at factors of about three and three and a half respectively.

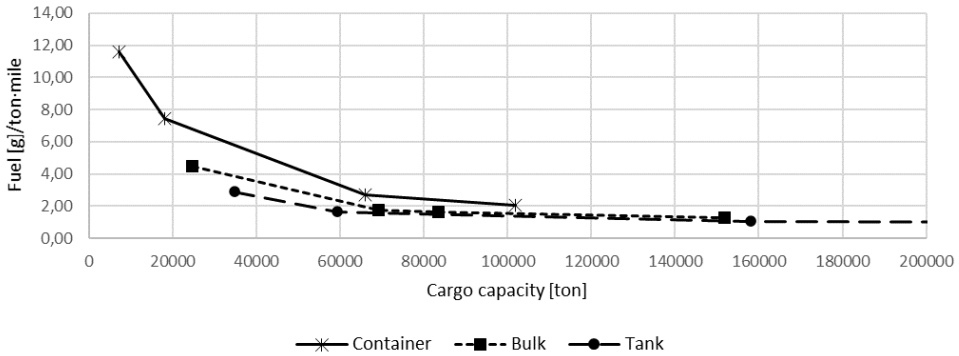

Figure 2 Fuel consumption vs. ship size for the three ship categories

The data shown in Figure 2 relate to the consumption of heavy fuel oil (HFO) or marine diesel/gas oil (MDO/MGO). These fuels are the dominant source of energy on most merchant ships today. However, that will likely change in the future with the more widespread implementation of alternative energy sources such as LNG, hydrogen, ammonia or other electro-fuels, or electricity stored in batteries. The economy of scale effect shown in Figure 2 will, however, apply regardless of which energy source is used. The relative proportions of the costs as shown in e.g. Table 1 may change with the introduction of new fuels, but larger ships will still be able to transport more cargo per unit of energy than small ships. With an increased focus on emissions and sustainability in maritime transport (Lindstad et al., 2012), the economy of scale effect on fuel/energy consumption may be a barrier towards the migration of cargo from large to small ships.

DISCUSSION

As the analysis in the present paper shows, there is clearly a pronounced economy of scale effect with regards to manning and manning costs. Large ships can transport more cargo over the same distance per € spent on manning than small ships. Considered in isolation, the large ships today have an advantage over the small ships regarding manning costs. If the manning costs were to be reduced, or perhaps even disappear completely, this advantage would be offset, and the favour would swing further towards smaller ships. However, as the analysis also shows, the crew costs are, in most cases, a relatively small part of the total shipping costs. Manning is found to comprise a maximum of 10 per cent of the total shipping costs and a minimum of as little as 3 per cent. The total achievable saving by reductions in manning costs, therefore, cannot, ceteris paribus, exceed these figures.

Furthermore, manning is far from the only cost which experiences economy of scale effects. The overall impact of manning costs on the economy of scale is overshadowed by, first and foremost, fuel costs but also capital repayments and interest in some cases. Therefore, the impact of reduced manning or unmanned operation on the economy of scale becomes very limited. In all the proposed cases, the larger ships can transport cargo significantly cheaper and with less fuel consumption than smaller ships. Reduced manning costs reduces the advantage that large ships have over small ships, but in most

scenarios, this reduction is very small. Small ships cannot compete with large ships in terms of cost of transport and energy efficiency, even in case 3, the most extreme case, where the manning costs are completely eliminated for the small ships.

Existing autonomous and/or unmanned ship projects such as the Yara Birkeland (Yara, 2020), the Asko project (Kongsberg, 2020), or the AUTOSHIP project (2021) focus on the small ship segment. There is likely more than one reason for focusing on the small ship segment: the cost of entry is smaller; the projects are more manageable; the operation of the ships is restricted and limited, and the manning costs are proportionally higher than for larger ships. It may be that the smaller autonomous and/or unmanned ships function just as a steppingstone going towards larger autonomous and/or unmanned ships. However, there is also the possibility that autonomy and unmanned operation do not easily scale up and that this form of operation is restricted to small inland vessels. If the latter turns out to be the case, it could present a significant problem for autonomous and/or unmanned ships. Small, unmanned ships may be able to compete with small, manned ships on routes or in trades that do not allow for larger vessels, either because of cargo availability or physical restrictions. However, in an unrestricted market and/or environment, they will not be able to compete with large, manned ships under the scenarios set out in the present paper. If autonomous and/or unmanned operation is restricted to small ships, the economy of scale effects of larger ships very quickly outweighs the economic benefits of reduced manning costs.

The analyses in the present paper are based on the scenario that manning costs is the only factor that changes. This choice is made deliberately to isolate the specific effect of reduced manning or unmanned operation on the cost of transport, but it is a rather crude assumption. Unmanned operation brings with it a whole range of other proposed benefits (Eriksen, 2019; Kobylinski, 2018), of which can be mentioned reduced energy consumption and reduced wind resistance due to a lack of an accommodation, although the latter presumably does not apply to containerships. In these respects, the analyses may be overly pessimistic towards unmanned operation. On the other hand, it is also wildly optimistic to imagine that the work required to operate a ship can be eliminated entirely by unmanned operation and that the unmanned and/or autonomous ships will not require additional systems and services that would add to the cost of operation. The scenarios proposed in the present paper should not be taken as examples of proposed cost structures of unmanned ships or ships with reduced crews. More in-depth economic analyses of autonomous and/or unmanned ships have been done as mentioned in the introduction, although all such analyses must also rely on multiple assumptions and approximations. The focus of the present has been specifically on the effect of unmanned operation or reduced manning on the economy of scale. For this purpose, the accuracy of the proposed scenarios is assessed to be sufficiently accurate.

CONCLUSION

This paper examines the impact of unmanned operation or reduced manning on the economy of scale effect on merchant ships. Data from different sizes of three types of ships: bulk carriers, tankers, and containerships, are analysed. The analysis finds that the largest part of the cost of transport originates from fuel costs, capital investments, and interest on loans, with manning costs on a fourth position tied with maintenance and repairs. Across all three ship types manning comprises between 3 and 10 per cent of the total transport cost. Manning costs make up more of the total costs on smaller ships and less on the larger ships. A clear economy of scale effect is, as expected, found in the transport costs in general and in the manning costs in isolation. Larger ships can transport significantly more cargo over the same distance for the same expense in manning than smaller ships. Overall, however, the economy of scale effect of manning is greatly surpassed by the economy of scale effects of other costs, in particular fuel cost.

The paper proposes three cases to explore the effect of reductions in manning costs on the economy of scale effects. In case 1, the manning is reduced by 20 per cent. In case 2, all the ships are unmanned, and the manning cost is completely eliminated. In case 3, the smallest ship type in the analysis is unmanned, whereas the larger of the ship types are conventionally manned. Reduced manning or unmanned operation diminishes the overall economy of scale effect of larger ships. In case 3, reductions in the economy of scale effect of close to 20 per cent are seen. The effects for cases 1 and 2 are limited to a few per cent and are, in some scenarios, barely detectable. Overall, the economy of scale effect is still very significant across all cases. Despite reductions or the complete elimination of manning costs, it is still substantially cheaper and energy efficient per unit of cargo to transport cargo on large than on small ships.

The paper concludes that reduced manning costs do have an impact on the economy of scale effect of merchant ships. However, it is also concluded that this impact does not, ceteris paribus, change the overall economy of scale effects arising from the use of larger ships. Large ships are still significantly cheaper and more energy-efficient per transported unit than small ships. Unmanned operation or reduced manning does not significantly alter cost structure or economy of scale in favour of using small rather than large merchant ships

References

Akbar, A., Aasen, A. K., Msakni, M. K., Fagerholt, K., Lindstad, E., & Meisel, F. (2021). An economic analysis of introducing autonomous ships in a short-sea liner shipping network. *International Transactions in Operational Research, 28*(4), 1740-1764.
AUTOSHIP. (2021). *AUTOSHIP Autonomous Shipping Initiative for European Waters*. Retrieved 29-07-2021 from https://www.autoship-project.eu/
Bernacki, D. (2021), (2021-07-27). Assessing the Link between Vessel Size and Maritime Supply Chain Sustainable Performance. *Energies, 14*(11), 2979. https://doi.org/http://dx.doi.org/10.3390/en14112979
Cullinane, K., & Khanna, M. (1999). Economies of Scale in Large Container Ships. *Journal of transport economics and policy, 33*(2), 185-207. https://go.exlibris.link/0lpTL2xW
Delhaye, E., Breemersch, T., Vanherle, K., Kehoe, J., Liddane, M., & Riordan, K. (2010). The competitiveness of European short-sea freight shipping compared with road and rail transport. *Final Report*.
Drewry Shipping Consultants. (2021). *Drewry Shipping Consultants - Maritime Research*. Retrieved 06-11-2021 from https://www.drewry.co.uk/maritime-research
Eriksen, S. (2019). *Autonomous Ships – Changing Perceptions and Expectations* 18th Conference on Computer and IT Applications in the Maritime Industries, Tullamore.
Eriksen, S. (2021). *Autonomous Ships from the Perspective of Operation and Maintenance* University of Southern Denmark.
Glen, D., & Reid, S. (2010). Tanker cost elasticities revisited. *Maritime policy and management, 37*(6), 585-600. https://doi.org/10.1080/03088839.2010.514956
Hogg, T., & Ghosh, S. (2016). Autonomous merchant vessels: examination of factors that impact the effective implementation of unmanned ships. *Australian Journal of Maritime & Ocean Affairs, 8*(3), 206-222. https://doi.org/https://doi.org/10.1080/18366503.2016.1229244
Jokioinen, E., Poikonen, J., Hyvönen, M., Kolu, A., Jokela, T., Tissari, J., Paasio, A., Ringbom, H., Collin, F., Viljanen, M., Jalonen, R., Tuominen, R., & Wahlström, M. (2016). *Remote and Autonomous Ships the next steps*. Rolls-Royce.
Kobylinski, L. (2018). Smart ships – autonomous or remote controlled. *Scientific Journals of the Maritime University of Szczecin, 53*(125), 28-34. https://doi.org/https://doi.org/10.17402/262
Kongsberg. (2020). *Kongsberg maritime and Massterly to equip and operate two zero-emission autonomous vessels for ASKO*. Retrieved 23-07-2021 from https://www.kongsberg.com/maritime/about-us/news-and-media/news-archive/2020/zero-emission-autonomous-vessels/
Kretschmann, L., Rødseth, Ø. J., Sage-Fuller, B., Noble, H., Horahan, J., & McDowell, H. (2015). *D9.3: Quantitative assessment*. MUNIN.
Lian, F., Jin, J., & Yang, Z. (2019). Optimal container ship size: a global cost minimization approach. *Maritime policy and management, 46*(7), 802-817. https://doi.org/10.1080/03088839.2019.1630760
Lim, S.-M. (1998). Economies of scale in container shipping. *Maritime policy and management, 25*(4), 361-373. https://doi.org/10.1080/03088839800000059
Lindstad, H., Asbjørnslett, B. E., & Strømman, A. H. (2012). The importance of economies of scale for reductions in greenhouse gas emissions from shipping. *Energy policy, 46*, 386-398. https://doi.org/10.1016/j.enpol.2012.03.077
Munim, Z. H. (2019). Autonomous ships: a review, innovative applications and future maritime business models. Supply Chain Forum: An International Journal,
Rødseth, Ø. J. (2018). Assessing business cases for autonomous and unmanned ships. In *Technology and Science for the Ships of the Future* (pp. 1033-1041). IOS Press.
Salvatore, D. (2012). *Managerial economics in a global economy* (7. ed.). Oxford University Press. https://go.exlibris.link/SpFbzlbN
Schröder-Hinrichs, J.-U., Song, D.-W., Fonseca, T., Lagdami, K., Shi, X., & Loer, K. (2019). *Transport 2040: Automation, technology, employment-The future of work* (World Maritime University, Transport, Issue.
Sys, C., Blauwens, G., Omey, E., Van De Voorde, E., & Witlox, F. (2008). In Search of the Link between Ship Size and Operations. *Transportation planning and technology, 31*(4), 435-463. https://doi.org/10.1080/03081060802335109
Wariishi, K. (2019). *MARITIME AUTONOMOUS SURFACE SHIPS : DEVELOPMENT TRENDS AND PROSPECTS — HOW DIGITALIZATION DRIVIES CHANGES IN MARITIME INDUSTRY—* (Mitsui & Co. Global Strategic Studies Institute Monthly Report September 2019, Issue.
Wu, W.-M., & Lin, J.-R. (2015). Productivity growth, scale economies, ship size economies and technical progress for the container shipping industry in Taiwan. *Transportation research. Part E, Logistics and transportation review, 73*, 1-16. https://doi.org/10.1016/j.tre.2014.10.011
Yara. (2020). *Yara Birkeland press kit*. Retrieved 23-07-2021 from https://www.yara.com/news-and-media/press-kits/yara-birkeland-press-kit/

formaterede: Finsk

Formateret: Ingen punkttegn eller nummerering

Appendix

Cost structures

Table A1 Bulk: cost structure

Vessel size	Handysize		Panamax		Post Panamax		Capesize	
DWT (nominal)	25000		70000		85000		155000	
Costs (at sea, full steaming)	€/day	% of total	€/day	% of total	€/day	% of total	€/day	% of total
Manning	1389	6%	1847	7%	1847	6%	2069	6%
Insurance	473	2%	702	2%	756	2%	817	2%
Repairs and maintenance	1107	5%	1458	5%	1656	5%	1824	5%
Stores and lube oil	374	2%	511	2%	557	2%	611	2%
Administration	947	4%	1099	4%	1160	4%	1237	3%
Capital repayments	3847	18%	5837	21%	6102	20%	6898	19%
Interest	3162	15%	4798	17%	5016	16%	5671	15%
Fuel (€/day)	10198	47%	12111	43%	13385	44%	17528	48%
Total daily shipping cost (€/day)	**21497**		**28363**		**30479**		**36655**	

Table A2 Container: cost structure

Vessel size (TEU range)	500-700		1000-2000		5000-6000		8000-9000		10000-12000	
DWT (nominal)	7308		18270		66991		103532		133982	
Costs (at sea, full steaming)	€/day	% of total	€/day	% of total	€/day	% of total	€/day	% of total	€/day	% of total
Manning	1588	10%	1588	6%	2176	4%	2313	3%	2466	3%
Insurance	313	2%	443	2%	931	2%	1168	2%	1336	2%
Repairs and maintenance	802	5%	977	4%	2603	5%	2786	4%	3092	4%
Stores and lube oil	351	2%	580	2%	1557	3%	1847	3%	2122	3%
Administration	504	3%	550	2%	931	2%	962	1%	1008	1%
Capital repayments	2189	13%	4378	17%	11276	21%	16848	24%	20430	24%
Interest	1799	11%	3599	14%	9269	17%	13850	20%	16794	20%
Fuel (€/day)	8924	54%	14341	54%	24540	46%	29002	42%	36969	44%
Total daily shipping cost (€/day)	**16470**		**26456**		**53283**		**68776**		**84217**	

Cost of transport work and contributions to economy of scale

Table A3 Bulk: cost of transport work specified by individual cost category and contributions of each cost category to the economy of scale of the larger ships compared to the smallest ship

Vessel size	Handysize		Panamax		Post Panamax		Capesize		
Cargo capacity [tons]	24739		69252		83448		151931		
Speed [knots]	12		13		13		12		
€/1000 ton·nm	€	%	€	%	€	%	€	%	**Avg.**
Manning	0.19	-	0.09	6%	0.07	7%	0.05	7%	**7%**
Insurance	0.07	-	0.03	2%	0.03	2%	0.02	2%	**2%**
Repairs and maintenance	0.16	-	0.07	5%	0.06	5%	0.04	5%	**5%**
Stores and lube oil	0.05	-	0.02	2%	0.02	2%	0.01	2%	**2%**
Administration	0.13	-	0.05	5%	0.04	5%	0.03	5%	**5%**
Capital repayments	0.54	-	0.27	16%	0.23	17%	0.16	18%	**17%**
Interest	0.44	-	0.22	13%	0.19	14%	0.13	14%	**14%**
Fuel	1.43	-	0.56	51%	0.51	50%	0.40	47%	**49%**

Table A4 Container: cost of transport work specified by individual cost category and contributions of each cost category to the economy of scale of the larger ships compared to the smallest ship

Vessel size (TEU range)	500-700		1000-2000		5000-6000		8000-9000		10000-12000		
Cargo capacity [tons]	7200		18000		66000		102000		132000		
Speed [knots]	14		14		18		18		18		
€/1000 ton·nm	€	%	€	%	€	%	€	%	€	%	**Avg.**
Manning	0.66	-	0.26	16%	0.08	12%	0.05	12%	0.04	12%	**13%**
Insurance	0.13	-	0.07	2%	0.03	2%	0.03	2%	0.02	2%	**2%**
Repairs and maintenance	0.33	-	0.16	7%	0.09	5%	0.06	5%	0.05	5%	**6%**
Stores and lube oil	0.15	-	0.10	2%	0.05	2%	0.04	2%	0.04	2%	**2%**
Administration	0.21	-	0.09	5%	0.03	4%	0.02	4%	0.02	4%	**4%**
Capital repayments	0.90	-	0.72	7%	0.40	10%	0.38	10%	0.36	10%	**9%**
Interest	0.74	-	0.60	6%	0.33	8%	0.31	8%	0.29	8%	**8%**
Fuel	3.69	-	2.37	54%	0.86	57%	0.66	58%	0.65	57%	**57%**

Differences in cost of transport work

Table A5 Bulk: differences in cost of transport work in the three proposed cases

Vessel size	Handysize	Panamax	Post Panamax	Capesize
Base case				
Diff. €/1000 ton·nm from Handysize	-	-56.5%	-61.2%	-72.2%
Case 1				
Diff. €/1000 ton·nm from base case	-1.3%	-1.3%	-1.2%	-1.1%
Diff. €/1000 ton·nm from Handysize	-	-56.5%	-61.2%	-72.2%
Case 2				
Diff. €/1000 ton·nm from base case	-6.5%	-6.5%	-6.1%	-5.6%
Diff. €/1000 ton·nm from Handysize	-	-56.5%	-61.0%	-72.0%
Case 3				
Diff. €/1000 ton·nm from base case	-6.5%	0.0%	0.0%	0.0%
Diff. €/1000 ton·nm from Handysize	-	-53.5%	-58.5%	-70.3%

Table A6 Container: differences in cost of transport work in the three proposed cases

Vessel size (TEU range)	500-700	1000-2000	5000-6000	8000-9000	10000-12000
Base case					
Diff. €/1000 ton·nm from 500-700 TEU size	-	-35.7%	-72.6%	-77.1%	-78.3%
Case 1					
Diff. €/1000 ton·nm from base case	-1.9%	-1.2%	-0.8%	-0.7%	-0.6%
Diff. €/1000 ton·nm from 500-700 TEU size	-	-35.3%	-72.2%	-76.8%	-78.0%
Case 2					
Diff. €/1000 ton·nm from base case	-9.6%	-6.0%	-4.1%	-3.4%	-2.9%
Diff. €/1000 ton·nm from 500-700 TEU size	-	-33.2%	-70.9%	-75.5%	-76.7%
Case 3					
Diff. €/1000 ton·nm from base case	-9.6%	0.0%	0.0%	0.0%	0.0%
Diff. €/1000 ton·nm from 500-700 TEU size	-	-28.9%	-69.6%	-74.6%	-76.0%

~~Eriksen, S. (2021). *Autonomous Ships from the Perspective of Operation and Maintenance* University of Southern Denmark]. University of Southern Denmark.~~

~~Eriksen, S. (2021). *Autonomous Ships from the Perspective of Operation and Maintenance* University of Southern Denmark]. University of Southern Denmark.~~

~~Jokioinen, E., Poikonen, J., Hyvönen, M., Kolu, A., Jokela, T., Tissari, J., Paasio, A., Ringbom, H., Collin, F., Viljanen, M., Jalonen, R., Tuominen, R., & Wahlström, M. (2016). *Remote and Autonomous Ships the next steps*. Rolls-Royce.~~

~~Wariishi, K. (2019). *MARITIME AUTONOMOUS SURFACE SHIPS : DEVELOPMENT TRENDS AND PROSPECTS — HOW DIGITALIZATION DRIVIES CHANGES IN MARITIME INDUSTRY* (Mitsui & Co. Global Strategic Studies Institute Monthly Report September 2019, Issue.~~

Proof Of Concept Model For Demonstrating Iot Based Vessel Control And Monitoring

Zia Ur Rahman
dept. of Naval Architecture and Ocean Engineering
Indian Maritime University
Visakhapatnam, India
ziacanyes@gmail.com

Anshul Kumar Rai
dept. of Naval Architecture and Ocean Engineering
Indian Maritime University
Visakhapatnam, India
raianshul1010@gmail.com

Late. U. S. Ramesh(Mentor)
chief manager MCRC
Indian Maritime University
Visakhapatnam, India
usramesh@imu.ac.in

***Abstract*— The internet of things has proved to be one of the most influential technologies affecting almost every other field, be it for remote control, monitoring or regulatory supervision. Similarly, maritime operation and management have the potential to be greatly influenced by IoT, making certain control and monitoring activities highly efficient and easy. This paper proposes a proof of concept design for controlling and monitoring the propulsion systems of an electric twin-screw vessel over the internet.**

The idea is to have Wi-Fi connectivity node modules at the control units to receive and send information about the states of the electro-mechanical units to be controlled or monitored. It is a prerequisite that the vessel should have reliable and persistent internet connectivity for the setup to efficiently function in coherence with the onboard machinery.

Wi-fi nodes receive data from the cloud using TCP/IP protocol and MQTT library function formats are used to push and pull the information, to and from cloud servers. The Wi-Fi modules are connected to a locally established network of programmable microcontrollers via I2C protocol connection. The embedded controller in the Wi-Fi node decides the action based on the received information and instructs the PMCs accordingly. At the delivery end, PMCs control actuators and relays based on the received instructions, resulting in the change of state of machinery.

Machinery attributes like motor RPM and thermal state can be detected and published to thingspeak in real time through http post requests using another connectivity module. Thingspeak is an IoT service from Mathworks to record, display, publish real time data from various IoT devices. Data can be exported to Matlab for tasks involving computations and the results can be sent back to devices through TalkBack service.

I. INTRODUCTION

A. Introduction to Internet of Things

Information and data have always been counted as valuable entities by humans since antiquity. But the type of data and methods of gathering it underwent a revolution after the invention of information technology during the latter half of the twentieth century. In today's scenario, a major part of the income for IT giants like Google and Facebook is generated from the ads they run on their electronic media platforms that are targeted based on the data collected from users. Data is collected by many corporations through various digital impressions of users like search queries, likes, comments, preferences, and purchases. Highly comprehensive analytical tools like artificial intelligence, machine learning, and deep learning are used to boost the significance of such data by generating valuable insights that assist analysts to decide on customer interests and marketing strategies. The fact that data can be collected only through digital impressions generated while using electronic gadgets like cell phones and computers limits many possibilities of extended applications. Humans interact with various physical entities daily, these interactions, if at all, are documented as digital data can help us to reveal marvelous insights about human-object interactions. Thus Page | 4 facilitating research, development, and optimization of current systems resulting in better products and services for mankind. IOT is one of the possible ways to collect data from daily life interactions. Since various electrical and non-electrical objects of regular use are connected to the internet as a result of the Internet of Things, they generate huge amounts of valuable data related to daily life activities.

B. A Brief Description of IoT Integration with Existing Products

Primarily the data to be gathered is categorized based on continuity, periodicity, and amplitude of the output signal. The device from which data will be collected is defined. The data formats are settled based on the requirements and abilities of the system in use. The basic need to accomplish this is the need to have a reliable and secure internet connection. Up next, an intermediate connectivity system is required to connect devices to the internet. Usually, this is accomplished by using connectivity modules like ESP8266, HC05 in combination with development boards from Arduino, raspberry pi, and Texas Instruments. These modules help us convert the data into digital formats and send it to the cloud servers via the internet. Further up, many systems support bidirectional communication, allowing us to control

and manage a number of things wirelessly, making things more interactive and user-friendly. All the data collected from the devices is stored on cloud platforms and can be made available for public use or kept personal. A lot of these cloud services facilitate cross-platform usage and provide computational services but at the cost of the privacy of data at most. Most of the IT companies now host IOT web services, which are mostly free for individual use and paid for corporate use, like Amazon Web Services, Things Speak, and Google Firebase to name a few. These technical leaps will entirely revolutionize the way people interact with their daily life commodities alongside while they gather huge amounts of useful data. This techno-economic real-life data gathering methodology can be very well implemented in the maritime industry. This will gather data generated by the operations of shipping vessels, utility systems, and port operations. Data can then be used to train machine learning models, AIs and will act as a provision for research analytics. Machinery maintenance is an important aspect to be sure about before vessels leave to score through the vast isolating blue oceans. IOT can effectively enhance the easy to condition-based maintenance to monitor the state of machines onboard and simultaneously contribute to real-time machine data content, which can help gain insightful results to improve the design and amend service methodology. Further, these results can assist regulatory authorities in drafting rules and setting standards. These applications promise a great deal of innovation and development in the near future but currently, the cons of this technology hold a seriously precarious reputation due to inappropriate security features.

C. Introduction to IoT in Shipping Industry

Just like any other industry, the maritime industry extensively uses information services to collectively carry out various operations involved in efficiently maintaining the balance of marine transport and off-shore services. Thus, it is an undeniable fact that the shipping industry has plenty of room for a revolutionary innovation like IOT. Page | 5 Introduction of IOT in ships will lead to the achievement of a certain level of automation in terms of the process control systems. Further, the shift of controls from the control room to the controller's mobile device will drastically reduce the space requirement for the control room while making the control interface easier and remotely accessible. Ships are relatively large floating structures that are in fact sometimes referred to as floating cities sailing in the vast blues. All the data that these ships would generate will be immense in quantitative as well as qualitative terms. This data can be used in many ways like training optimization models, building more autopilot systems and getting insights into the challenges involved in the practical implementation of complete autonomous vessels which in a broader sense has never been done before.

II. DESCRIPTION OF PROOF OF CONCEPT MODEL

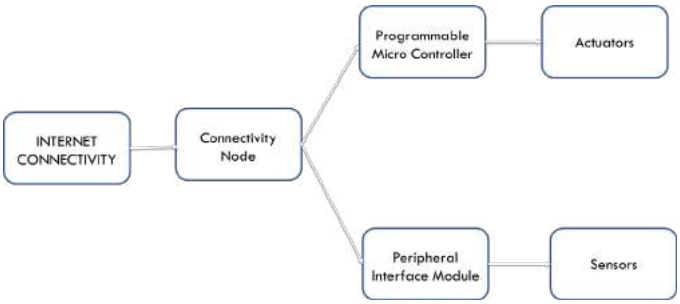

The model intends to prove the concept of implementing IoT in the remote and autonomous control of ships. It specifically focuses on propulsion control of a twin-screw vessel with the screws being rotated independently and in synchronization with each other. This setup allows the user to rotate the screws at variable rotations and directions as the need comes. The propeller action can be manually operated or set for automatic action based on predefined triggers in the Arduino script using any terminal connected to the internet with an adafruit.io compatible browser.

III. BRIEF ON MODEL HARDWARE AND SOFTWARE

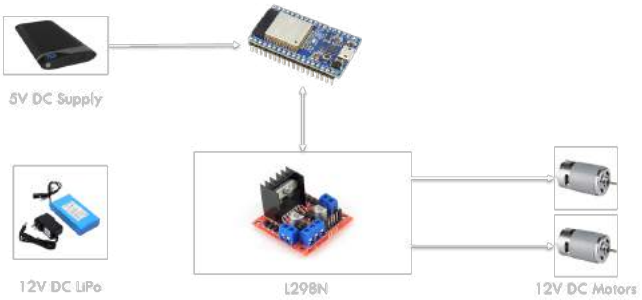

A. Propulsion and Powering

Propulsion consists of two fixed pitch propellers powered by two 12V DC motors and connected via a shaft of 6mm diameter and universal couplings. A starboard propeller is a right-hand screw and a port propeller is a left-hand screw. Power source for the propulsion consists of a 12v,2200mAh LiPo battery powering an L298N dc motor driver module. propulsion motors are connected to the PWM enabled bi-directional motor driver outputs.

B. Connectivity and Control Module

ESP32 system-on-chip (SOC) microcontroller with built-in Wi-Fi module is used for IoT connectivity module for obtaining internet connectivity over Wi-Fi and controlling the L298N for direction and speed control using pulse width modulation (PWM). ESP32 is powered by a 5v, 1.1amp, 10000mAh battery pack through a male-male USB to micro USB cable. The terminal here is an android device running android7 or above connected to the internet and has a browser installed which supports adafruit.io web application.

C. ESP32 Firmware and Software

ESP32 is flashed with Arduino firmware to run Arduino code. It runs an Arduino code to connect to Wi-Fi hotspot, subscribe to the MQTT server from adafruit and control L298N using GPIO pins. The complete code is given in the appendix.

D. The Code is Structured as Follows

- Include the required libraries
- Define the GPIO pins, state variables, WIFI credentials, MQTT credentials and MQTT connect function..
- Setup section consists of WIFI connect built-in function, assigning the in-out pins and subscribing data from the MQTT server.
- Void loop consists of converting the characters received from MQTT into integers and control loops are used to decide the pin state outputs.

IV. Web Application for Remote Control

Adafruit has a graphic user interface web application for publishing and subscribing data from terminals. The UI has a variety of customizable data publishing and subscribing tools like virtual monitors, virtual plotters, buttons, sliders etc. The data feeds can be connected to different display and control entities on the dashboard as it is convenient, depending on the purpose. Every user on adafruit is assigned a unique username and 32 bit authentication key. Device connects to the io.adafruit.com through port:1883 using the username and auth-key. The data is subscribed and published in character format.

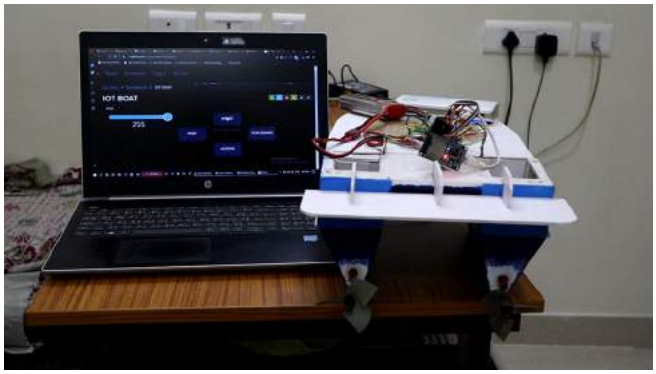

V. Voice Automation with Google Assistant

Trigger based publishing feature from adafruit is utilized to publish data using a third party cloud platform IFTTT which can receive data from google assistant for specific predefined voice commands and activate the corresponding triggers to publish the associated data on adafruit.io. For this to work all three platforms adafruit, IFTTT and google assistant must be using the same google account. IFTTT can be used to configure google assistant to respond accordingly to certain voice commands. We have set up four distinct commands for forward, reverse, port and starboard motion. Generally a delay of 1-2 seconds from giving the command to getting the response in the dc motors.

VI. Security Concerns

Anything hooked up to the internet, wired or wireless is at a potential risk of being hacked. But that doesn't stop us from using the technology.

A. Network security

Networks need to be secured from external penetration by employing firewalls to restrict, from and to communication passing through the network. Ports need to be actively monitored to limit unintended network intrusion. Potentially harmful web resource locations must be restricted from access. All data must be re-routed through a proxy network like socks5 proxy to hide the IP address so as not allow outsiders to digitally document network activity.

B. Software security

Firmware and programs on the IoT modules need to be updated regularly to keep it safe from vulnerabilities and bugs. Updates contain patches for codes, libraries and built-in functions diagnosed with vulnerabilities which can be exploited by hackers to partially or fully take over the system or network at stake. The update files need to be verified using digital signatures to confirm the originality of content and source. Further use of good antivirus software with up to date virus and malware repositories help to keep the system safe from trojans, viruses, malware and ransomware attacks. All data needs to have a reliable backup strategy in case of a possible attack or mishap leading to partial or complete loss of data.

C. Web security

The web-communication can be secured with SSL encryption, using a secure web browser, blocking malicious scripts and having it tested by penetration testers. Offensive

security techniques help in keeping the network, communication and system safe from external attacks.

VII. CURRENT SECURITY SCENARIO

A number of leaked documents and emails on WikiLeaks related to the secretive gatherings in Silicon Valley to discuss various issues regarding security of IoT-smart devices lead us to infer that improper security features of the IoT devices put forward some legitimate concerns that need to be met before implementing them on relatively larger scales. One of the newly emerged problems is that hackers can use the hacked IoT devices to send automated emails without the consent of the owner. This loophole can be exploited to imitate the situation of distributed denial of services and cause harm to large corporations by bringing down their stock rates and profits. There have been reports of government agencies and other corporations spying on commoners by hacking their cell phones and computers. Considering the vulnerability of IoT devices, one can easily predict the massive advantage these entities will have, to exploit the privacy of large masses without any noticeable offense. IoT is a multimillion dollar industry which has sought interests from big players of IT-industry like Google and Amazon. Thus it will definitely grow into a much larger business by the end of this decade, possessing a potential to impact humanity in an unpredictably substantial manner.

VIII. CONCLUSION

As intended initially we have successfully developed a twin screw vessel with IoT enabled propulsion control and tested its working in a well-connected space. The voice automation utility has also been successfully configured and tested with fairly satisfying results.

APPENDIX

Important terms

A. MQTT

MQTT is a machine-to-machine (M2M)/"Internet of Things" connectivity protocol. It was designed as an extremely lightweight publish/subscribe messaging transport. It is useful for connections with remote locations where a small code footprint is required and/or network bandwidth is at a premium. For example, it has been used in sensors communicating to a broker via satellite link, over occasional dial-up connections with healthcare providers, and in a range of home automation and small device scenarios.

B. Arduino

Arduino is an open-source electronics platform based on easy-to-use hardware and software. It's intended for anyone making interactive projects.

C. Adafruit IO

Adafruit IO is a platform designed (by us!) to display, respond, and interact with your project's data. We also keep your data private (data feeds are private by default) and secure (we will never sell or give this data away to another company) for you. It's the internet of things - for everyone!

D. IFTTT

IFTTT is the free way to get all your apps and devices talking to each other. Not everything on the internet plays nice, so we're on a mission to build a more connected world.

REFERENCES

[1] http://mqtt.org

[2] Io.adafruit.com

[3] https://www.arduino.cc

[4] https://www.espressif.com/sites/default/files/documentation/esp32_datasheet_en.pdf

[5] https://learn.adafruit.com/welcome-to-adafruit-io

[6] https://ifttt.com

[7] https://www.entrepreneur.com/article/332392

[8] https://theiotmagazine.com/iot-for-the-shipping-industry-41c8f85a654e

[9] https://www.rina.org.uk/The_Internet_of_Ships_a_new_design_for_Smart_Ships.html

[10] http://safety4sea.com/cm-maritime-ready-to-ride-on-internet-of-things/

[11] https://medium.com/harvard-business-school-digital-initiative/maersk-reinventing-the-shipping-industry-using-iot-and-blockchain-f84f74fe84f9

[12] https://www.networkworld.com/article/3432170/iot-enabled-shipping-containers-sail-the-high-seas-improving-global-supply-chains.html

[13] https://blog.roambee.com/supply-chain-technology/how-to-track-your-ocean-container-with-iot

[14] https://www.airfinder.com/blog/shipping-container-tracking

[15] https://www.scientific.net/AMR.756-759.4394

On Formal Methods for Design and Verification of Maritime Autonomous Surface Ships

Tobias R. Torben[1], Øyvind Smogeli[1,2], Ingrid B. Utne[1] and Asgeir J. Sørensen[1]

ABSTRACT

Maritime Autonomous Surface Ships (MASS) are approaching a reality, introducing a new level of complexity and criticality to maritime control systems. In this paper we investigate how Formal Methods (FMs) can be used to design and verify maritime control systems for safe and effective MASS. FMs are a family of mathematically based methods for specification and verification. We begin by giving a high-level introduction to FMs. We discuss the current practice for certification of maritime control systems and needs going towards autonomy. We give three specific examples on how FMs can be applied to meet these needs: Formal specification of COLREG, contract-based design and automation of simulation-based testing. Finally, some limitations of FMs are discussed. We conclude that FMs appear as a promising candidate to meet some of the needs going towards autonomy, and encourage further research into FMs for MASS.

KEY WORDS

Maritime Autonomous Surface Ships, Formal Methods, Verification, Specification, Assurance

INTRODUCTION

Maritime Autonomous Surface Ships (MASS) are approaching a reality, with numerous ongoing projects ranging from small research prototypes to full-scale industrial vessels. Although several degrees of autonomy exist, MASS are typically distinguished by being able to operate independently of a human operator in a non-trivial operation, requiring situational awareness and planning abilities. These characteristics have created a need for new design methodologies among MASS developers, as well as a need for new methods and processes for safety assurance among regulators (IMO 2021, NMD 2020) and classification societies (DNV 2018).

Formal Methods (FMs) are a family of mathematically based methods for specification and verification originating from theoretical computer science (Woodcock et al. 2009). FMs offer a high level of assurance and have therefore been used actively in the development and verification of critical systems in other industries, such as aerospace and railway, for several decades. With the advent of autonomous systems, FMs have been considered as a promising candidate to address some of the assurance challenges they introduce. This has resulted in active research on FMs applied to autonomous cars and aerial vehicles over the past decade (Luckcuck et al. 2019).

The maritime industry has not yet seen a significant adoption of FMs. This seems to be changing, however, as a few articles have been published during the last year. Shokri-Manninen et al. (2020) have created a formal automata-based model of single-vessel encounters and synthesized a correct-by-construction navigation strategy. Park and Kim (2020) have synthesized a correct-by-construction controller for automatic docking of marine vessels based on reachability analysis. Foster et al. (2020) present a controller for autonomous marine vessels in form of a hybrid dynamical system and use an automated theorem prover to verify some safety invariants.

This article aims to bring FMs to the attention of the maritime community by first giving a high-level introduction. Next, we review the current practice for design and verification of maritime control systems and discuss some needs going towards autonomy. We then motivate and demonstrate the use of FMs in three specific use cases to meet these needs. Finally, we discuss some of the limitations of FMs.

[1] Centre for Autonomous Marine Operations and Systems (AMOS), Department of Marine Technology, Norwegian University of Science and Technology
[2] Zeabuz AS

AN INTRODUCTION TO FORMAL METHODS

FMs are motivated by the common engineering expectation that mathematical analysis will improve the performance and reliability of a system. Early development of FMs dates to the 1960's, where they were first applied to the design of logic circuits and primitive computer programs.

Figure 1 shows the main steps and activities in a formal development process. We will use this figure to introduce the different FM tools and show where they fit in the development process. We also emphasize that taking on a full-fledged formal development process with all the steps in Figure 1 may be time-consuming and may not be appropriate in all cases. However, tools and methods from individual steps, such as only creating a formal specification, can still give great value to the development process. This is often referred to as *lightweight formal methods.*

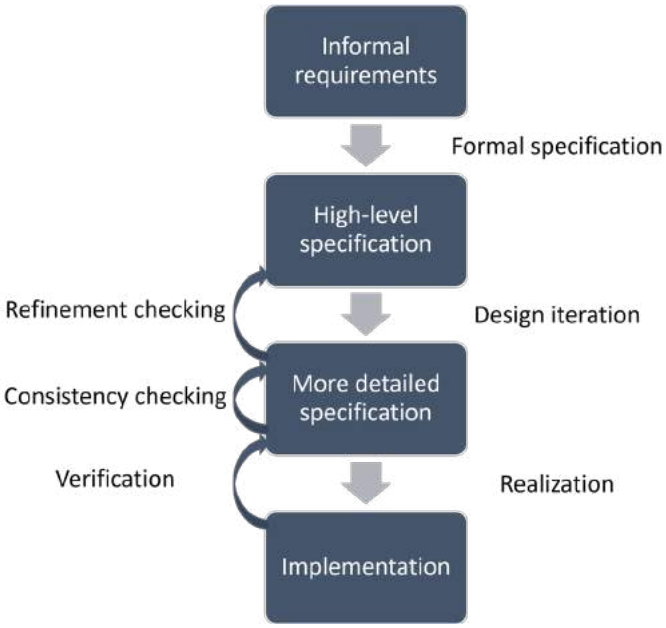

Figure 1: Steps and activities in a formal development process.

Formal specification

The first step in any development process is the requirements capture. This is often based on a text-based *concepts of operations* (CONOPS) document and produces an informal, text-based specification of high-level requirements. In a formal development process, the next step is to take the informal requirements and formulate them in a *formal specification language.*

Formal specification languages come in many forms, depending on what they are designed to describe. For instance, some are more suited for describing behaviour whereas others are better at describing structure. What they all have in common is that they have clearly defined syntax and semantics, that is, there are strict rules on valid statements, and it is clearly and unambiguously defined how the statements are to be interpreted. This not only means that they can be subject to mathematical analysis, but also that they are machine readable and, therefore, can be subject to automated reasoning by a computer.

A widely used class of specification languages are *temporal logics*, which are appropriate when specifying temporal behaviours, such as the ordering of events, timing, and avoidance of deadlocks. A temporal logic specification is written as a formula which combines logical operators, such as AND, OR, NOT and IMPLIES with temporal operators, such as ALWAYS, EVENTUALLY, NEXT and UNTIL. The original and simplest form of temporal logic is Linear Temporal Logic (LTL) (Pnueli 1977), which operates on Boolean signals in discrete time. An example of an LTL formula specifying correct behaviour of a traffic light is given below. In natural language, this formula specifies that always, if there is a red light, then it should eventually turn green after first being yellow.

*ALWAYS (**red** IMPLIES (EVENTUALLY **green** AND (NOT **green** UNTIL **yellow**)))* [1]

Signal Temporal Logic (STL) (Maler and Nickovic 2004) is another type of temporal logic which can be used to specify real-valued signals over continuous time, including timing constraints. It is therefore a popular choice for embedded and cyber-physical systems. STL also include *robustness semantics*, which instead of giving a true/false evaluation of whether a signal satisfies a temporal logic formula, gives a quantitative number on how robustly the formula is satisfied. Hence, STL offers both a syntax to specify behaviours and a metric for evaluating the compliance to the behaviour, which has proven to be a powerful combination.

Another class of specification languages are *set-based,* building on mathematical set-theory. A modern and prominent example of this is Event-B (Abrial 2011), which combined with the free software tool Rodin supports all the steps in Figure 1. Event-B is appropriate for specifying both structure and discrete-event behaviours. The predecessor of Event-B, called B Method, was used to formally specify, verify, and automatically generate 86 000 lines of code for the driverless metro in Paris, resulting in a system for which no bugs have been found (Lecomte et al. 1991).

A final important class of FMs is called *theorem provers.* Here, specifications are written as mathematical statements and there exists tools to generate mathematical proofs of the statements. Theorem provers can be divided into automatic provers, such as Z3 (de Moura and Bjørner 2008), and interactive provers, such as Isabelle (Paulson 1994), where the user interacts with a computer tool to build a proof.

Design iterations

Having created a high-level specification, the next step in a formal development process is to refine the specification in a series of design iterations. Each design iteration adds more detail to the specification and brings it closer to something which can be realized in hardware and software. An important activity for each design iteration is the *refinement checking*, which aims to verify that a refined specification still contains all the properties of the higher-level specification. In other words, if a system meets the refined specification, it should also meet the higher-level specification. Many FM tools include automated refinement checking.

Another important step in the design iterations is *consistency checking*. This involves checking a specification for contradictions. The most obvious form of a contradictory specification is the statement "(**a**) AND (NOT **a**)". In a complex specification however, contradictions can be subtle and hard to detect. A classic example is interface incompatibility. This can lead to expensive redesigns at a later stage in the development process. Many FM tools also support automated consistency checking.

Realization

The next step in a formal development process is to create an implementation in hardware or software based on the formal specification. In its most lightweight form, this can simply involve manual programming from the specification. Although this does not use the full potential of a formal development process, many find it easier to produce correct code when writing from a clear and unambiguous specification where fundamental design flaws have been removed at the design stages.

For some specification languages, there also exist tools which can automatically generate a *correct-by-construction* implementation from the specification. Examples of this include generation of computer code in various programming languages and synthesis of controllers which control a system to meet the specification.

Formal verification

The final step in the formal development process is the *verification.* Here, we define verification as checking that an implementation satisfies the lowest level specification. The most prominent formal verification technique is *model checking.* The input data to a model checking tool is the system to verify and a specification to verify against. The specification is usually in the form of a temporal logic formula. The model checker achieves an exhaustive verification by checking all possible executions of the system against the properties defined in the formal specification. The result is either a verification if no violating behaviour is found, or a falsification with a corresponding counter example if a violating behaviour is found. Some prominent model checkers are SPIN (Holzmann 1997), NuSMV (Cimatti et al. 2002) and UPPAAL (Larsen et al. 1997).

Automated theorem provers, as introduced earlier, can also be used to obtain a formal verification by for instance proving the correctness of an algorithm. Finally, *reachability analysis* (Asarin et al. 2007) is worth mentioning. This technique identifies the set of reachable states from any state in a system. By defining an unsafe set, this can be used to formally verify safety by showing that the unsafe set is not reachable from any state.

CURRENT PRACTICE IN THE MARITIME INDUSTRY AND NEEDS GOING TOWARDS AUTONOMY

Introducing novel and disruptive autonomous technology will alter the way ships are designed and operated. This has the potential to reduce some risks related to manned operations. At the same time, new risks emerge that need to be identified and mitigated to ensure safety. In this section the current practice for verification of maritime control systems is presented and some challenges and needs going towards autonomy are discussed.

To illustrate the current practice for verification of maritime control systems, we will use the certification process for dynamic positioning (DP) systems as an example. DP systems are complex automatic control systems involving both sensing, actuation, and computer systems (Sørensen 2011). The certification process for DP systems has been developed based on decades of experience. We therefore believe that DP systems represent a relevant example of state-of-the-art practice for verification of complex maritime control systems.

The international guidelines for DP systems are published by the International Maritime Organization (IMO) in IMO 1580 (IMO 2017). These guidelines provide the requirements for achieving a certification in form of a Dynamic Positioning Verification Acceptance Document (DPVAD). The guidelines specify both functional and operational documents in addition to requirements for verification activities. They are mostly concerned with the computer systems, power system, thrusters, and sensor systems. Classification societies publish class notations based on IMO 1580, which add more detailed and possibly additional requirements that strengthen safety and performance.

The overarching safety philosophy for IMO 1580 is heavily inspired by *functional safety.* This means that safety is promoted by identifying a set of *failure modes* and providing safety functions to ensure that no single failure can lead to a loss of position. The safety function is very often implemented by requiring redundancy, such as having two or three separate DP computers, three independent position reference sensors and two segregated power systems. The guidelines require that a *Failure Mode and Effect Analysis* (FMEA) should be carried out, which involves a systematic analysis of the DP system listing all failure modes and demonstrating the safe response. The survey and testing activities required by the guidelines involve a complete, physical survey of the DP system during commissioning and address primarily hardware components. This includes FMEA proving trials, where failure modes are simulated, and proper response by the DP system is verified. Furthermore, periodical testing at least every five years is required in addition to annual surveys. Proper testing and verification of software are not covered by FMEA testing alone. This may be characterized as a weakness with the existing mandatory regulations for software intensive systems such as DP (Johansen et al. 2007, Smogeli and Skogdalen 2011). Attempts at closing this gap includes both product assurance through e.g. Hardware-in-the-Loop testing (DNV 2013) and process assurance through SW development inspired standards such as ISDS (DNV 2017), but neither of these approaches have become mainstream in the assurance of maritime control systems.

Looking towards MASS, the need for new methodology for handling complex, software intensive systems is even more pressing. The challenges of the current, prescriptive classification regime are also acknowledged in the DNV class guideline for autonomous and remotely-operated ships (DNV 2018). A functional safety philosophy alone is not adequate when the level of autonomy increases. A key attribute of autonomous systems is that they interact with dynamic, unstructured, and uncertain environments. A consequence of this is that an autonomous vessel could exhibit unsafe behaviour without any equipment failure, for instance due to an unexpected environmental interaction or insufficient situational awareness. This challenge can be addressed by a complementary safety philosophy called *Safety Of The Intended Functionality* (SOTIF). Looking to the automotive industry, autonomous and advanced automation systems are now certified both for functional safety through ISO26262 (ISO 2011) and SOTIF through ISO21448 (ISO 2019), and it is likely that a similar development must take place for MASS.

Another consequence of interaction with dynamic, unstructured and uncertain environments is that the number of possible scenarios an autonomous system can encounter becomes enormous. Relying on testing alone, which even with massive scaling through parallelized simulators, only can analyse a limited number of scenarios, will therefore not be sufficient to ensure safety. Instead, there is a need for methodology to design systems with mathematically proven safety guarantees which reduce the span of possible scenarios.

Another gap in the current practice is the lack of focus on software failures. Autonomous vessels will be inherently software intensive, and their software will likely have significantly higher complexity than current systems. The current practice has a high focus on hardware failures, which have a different nature than software failures. The IEC 60050 standard defines a software failure as a manifestation of a dormant software fault, and a software fault is defined as a state of a software item that prevents it from performing as required. Software faults can for instance come in form of specification faults, design faults, programming faults, compiler-inserted faults, or faults introduced during software maintenance (IECTC 2002). A

software component may work perfectly for several years before a particular combination of input and internal state causes a software failure. Most of these types of failures are not possible to detect and remove by surveys and onboard FMEA testing only. Simulation-based testing through a Hardware-in-the-loop (HiL) setup has been practiced for DP systems for almost two decades as a voluntary additional service. In HiL testing, the DP software, running on the target hardware, is connected to a simulation model of the vessel (digital twin) and its environment through a HiL interface. This enables more targeted, detailed and extensive testing of the control software compared to onboard testing. It is possible to conduct a complete virtual sea trial before the targeted control system is installed on the ship. The experience from HiL testing of DP software has uncovered a large number of critical software bugs both in the core software and in configuration of particular DP vessels (Smogeli 2015). Large scale simulation-based testing is expected to be a key methodology for verification of MASS (Pedersen et al. 2020). This requires formalization and automation in the scenario generation and selection, simulation evaluation and coverage assessment (Torben et al. 2022). There is also a need for methodology to produce software which is correct-by-construction, which furthermore will result in reducing the test space.

Experience from DP vessels has also shown that system integration is difficult and error prone. Integration often receives little attention in the design stage, where changes are easy and cheap to make, and is instead delayed until commissioning and sea trials. This was the motivation for creating the Open Simulator Platform (OSP) which provides means for sharing simulation-models under a standardized interface while protecting vendor intellectual property (IP) (Smogeli et al. 2020). As the complexity and criticality increase further with MASS, there is clear a need for a structured and formalized integration processes.

Recent advances in Machine Learning (ML) are a key enabler for autonomy. The use of ML methods, which learn from data instead of being programmed from a specification, has enabled engineers to solve problems which are hard to specify completely. Computer vision is a classic example of this. However, ML based software also introduces major challenges for safety verification, as they have a strong black-box characteristic and lack of explainability. In addition, the input may be high-dimensional, such as all the pixels in an RGB image. This renders traditional input-output testing impractical to get sufficient test coverage. Clearly, there is a need for new methods for verification of ML-based software (DNV 2020).

Finally, we will mention the challenge due to lack of experience with autonomous vessels. Going autonomous represents a step change both in terms of the technology and the operations, which means that there is very limited experience, guidelines and best practices to build on. The automotive industry has approached this by releasing millions of cars driving autonomously under human supervision and continuously collecting data and building experience. As the number of MASS will be far less than the number of autonomous cars, combined with the tendency to use customized components and doing one-of-a-kind builds, we cannot expect to gain large-scale experience in this way. This necessitates increased efforts in the design and verification phases.

APPLICATIONS FOR FORMAL METHODS TO MASS DESIGN AND VERIFICATION

In this section we will demonstrate how FMs can be used to address some of the needs discussed in the previous section by presenting three specific use cases: Temporal logic specification of COLREG, contract-based design and automated simulation-based testing.

Temporal Logic Specification of COLREG

Safe interaction with other vessels is a challenging and critical aspect of MASS design and verification. Currently, this is regulated by the Convention on the International Regulations for Preventing Collisions at Sea – COLREG (IMO 1972), which specify a set of maritime traffic rules for collision avoidance. COLREG were designed for manned vessels and employ terms such as “due regard”, “appropriate distance” and “ample time”, and are therefore stated in a format that is not fit for computer parsing. To design collision avoidance algorithms and to enable automatic evaluation of COLREG compliance during verification, there is a need for machine readable COLREG. FMs stands out as a good candidate for formal specification of COLREG. An approach for this has been proposed in Torben et al. (2022) using STL, as shown in Figure 2. A similar approach, using the closely related Metric Temporal Logic (MTL) is proposed in Krasowski and Althoff (2021).

It may also be appropriate to develop a new collision avoidance protocol partially replacing COLREG, which is designed to be machine readable from the beginning. Using a formal language to specify the protocol also enables formal verification of safety properties. A similar development can be observed in the aviation industry, where the traditional TCAS protocol has been superseded by the ACAS X protocol, which has been formally specified and verified (Jeannin et al. 2017).

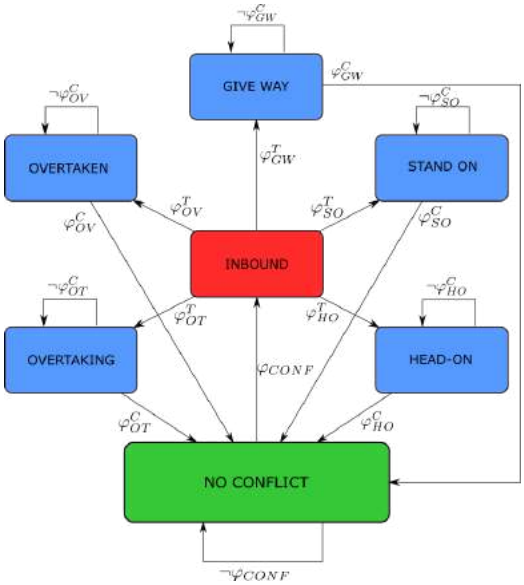

$$\varphi_{colreg} = \square\,(HO \rightarrow \varphi_{HO} \wedge GW \rightarrow \varphi_{GW} \wedge OT \rightarrow \varphi_{OT})$$
$$\varphi_{HO} = t_{CPA} \leq t_{CPA,turn} \rightarrow \beta_r \in [-170°, -10°]$$
$$\varphi_{GW} = t_{CPA} \leq t_{CPA,turn} \rightarrow d_{CPA} \geq d_{CPA,min}$$
$$\varphi_{OT} = t_{CPA} \leq t_{CPA,turn} \rightarrow d_{CPA} \geq d_{CPA,min}$$
$$\varphi^C_{OT} = \varphi^C_{OV} = \varphi^C_{GW} = \varphi^C_{SO} = \varphi^C_{HO} = t_{CPA} \leq 0$$
$$\varphi^C_{NC} = d_{CPA} \leq d_{CPA,min} \wedge t_{CPA} \leq t_{CPA,min}$$

Figure 2: Example of formal specification of COLREG using STL. The left figure shows a finite-state machine for selecting the COLREG situation (HO = Head-on, GW = Give way, SO = Stand-on, OT = Overtaking, OV = Overtaken). Each situation has a trigger condition based on the sectors for the heading and bearing of an incoming vessel. To the right, a set of STL formulas are given for the COLREG situations which require explicit action by own ship. The reader is referred to Torben et al. (2022) for more details.

Contract-based design

Modularity in design is a key success factor for managing complexity. This is motivated by the "divide and conquer" problem solving strategy, where a complex problem is broken up into a set of simpler subproblems, and the solutions of the subproblems are combined to solve the complex problem. Moreover, having a good framework for system integration of modular entities is a great benefit when interfacing with third-party systems and when integrating Commercial Off-The-Shelf (COTS) components. A challenge is to ensure that unsafe interactions across modules are sufficiently accounted for and mitigated.

Contract-based design is a formal approach for building modular systems (Sangiovanni-Vincetelli et al. 2012). Each modular unit is called a *component*, having a clearly defined interface in terms of inputs and outputs. Each component has a formal *contract* in assume-guarantee form. Verifying a single component involves producing evidence that the component satisfies a set of guarantees on its outputs, given that a set of assumptions on its inputs are satisfied. Contracts can be formulated in a formal specification language. When integrating a set of components, this reduces to checking the compatibility of the contracts. This activity is often termed *compositional reasoning.* The contract-based approach also supports design iterations, where a high-level abstract design is refined into more concrete and detailed designs, as illustrated in Figure 1.

Figure 3 shows an example of an autonomy system high-level component structure. The autonomy system component (grey) is intended to be connected to a DP system (not illustrated) which feeds the autonomy system with navigation data and controls the MASS to follow the motion reference given by the autonomy system. In addition, the autonomy system has environmental interactions in form of traffic, obstacles and weather. Looking inside the grey box, we can see that the abstract autonomy system component description is refined by three components, each with their own contract. To verify that this is a correct implementation, refinement checking is necessary. An informal description of refinement checking in assume-guarantee contracts is "assume no more, guarantee no less". This means that the combination of assumptions of the three subcomponents are less restrictive than the assumptions of the abstract autonomy system component, and that the combination of guarantees of the subcomponents are strong enough to enforce the guarantees of the abstract component. When integrating the three components, the compositional reasoning involves proving that the contracts of connected components are compatible. An example of a contract for the motion planning component, written in natural language could be:

Assuming that the tracks of other vessels are at accurate to 10m and that the navigation data are accurate to 1m, the motion reference is guaranteed to always have a distance of at least 50m to other vessels.

The compositional reasoning would then require verifying that the contract of the situational awareness component actually guarantees an accuracy of less than 10m on its tracks, and that the contract for the DP system guarantees navigation data with accuracy less than 1m. The refinement checking would involve verifying that the distance to other vessels guaranteed by the motion planning component is less than the distance guaranteed by the abstract autonomy system component. This shows how refinement with refinement checking can project high-level requirements onto lower-level components in a coherent way. If contracts are written in a formal specification language, both the refinement checking, and the compositional reasoning can be performed by an automated theorem prover.

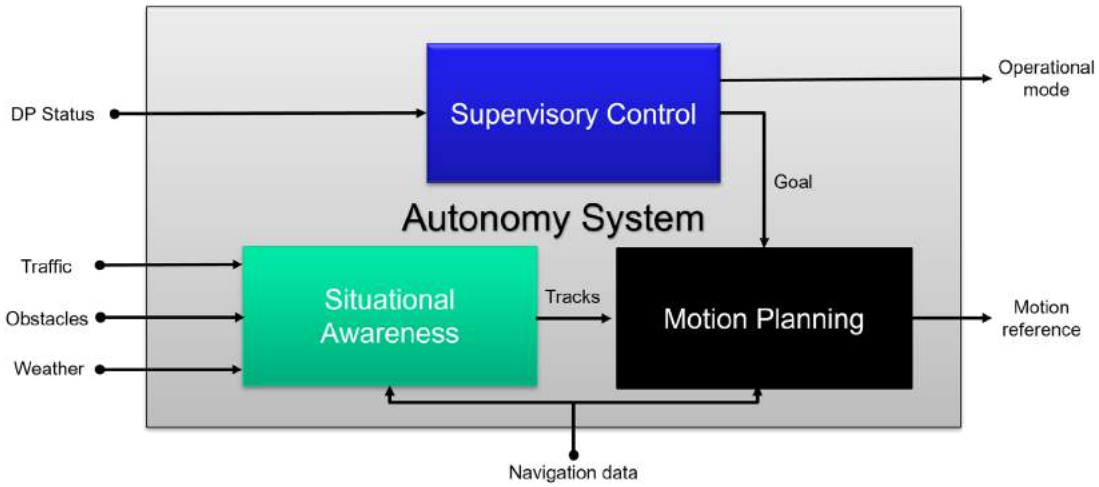

Figure 3: An example of a component structure for a high-level description of an autonomy system.

Automated simulation-based testing

In the final example we will show an example of how formal specification can be used to automate simulation-based testing. Evaluating the results of a simulation is often a non-trivial exercise which typically has been performed manually. If the testing scales to thousands of simulations, it is evident that manual evaluation is not practical, and for millions of simulations it is not practically possible. Torben et al. (2022) show how specifying requirements to test against in STL enables automatic evaluation of simulations using the STL robustness metric. The STL robustness metric gives a quantitative number on how robustly a simulation satisfies a requirement. If the robustness is greater than zero, the simulation satisfies the requirement, and if the robustness is less than zero, the simulation violates the requirement. The magnitude of the robustness is a measure of how much a signal can change without violating the requirement. Efficient algorithms exist for STL Monitors, which evaluate a signal against an STL formula (Fainekos et al. 2009).

The automatic testing methodology of Torben et al. (2022), shown in Figure 4, combines an STL monitor with a Gaussian Process (GP) model, which is used for smart scenario selection and coverage assessment. The user inputs an STL requirement and a test case. The test case is parametrized by a set of parameters which define the test space. The objective is to produce evidence that the system satisfies the STL formula to a desired probability level over the entire test space. The automatic testing algorithm selects a specific test case from the test space and runs this in the simulator. The STL monitor evaluates the simulation results against the STL requirement producing an STL robustness score. The GP model considers the STL robustness as an unknown function of the test case parameters and estimates the expected value and uncertainty of this function over the entire test space. The STL robustness score from a simulation is added to the GP model as an observation of this unknown function. This is shown to the right in Figure 4, where the GP estimate of the STL robustness is plotted in orange against the scenario parameters "*maneuver angle*" and "*obstacle speed*". The black dots show observations. The GP model is used to select the next test case to simulate in a smart way, where it favours cases which have low robustness or high uncertainty. This adaptive sampling is prominent in Figure 4, where the black dots are denser in areas with low robustness. After each simulation, two termination criteria are checked: If a simulation which falsifies the requirement is found, the algorithm terminates in a falsified state. This is the case in Figure 4, where falsifying scenario is identified at speed = 10m/s and maneuver angle = 27 degrees. If no falsifying scenario is found, the termination is determined by the desired level of confidence. If, for instance, 99% confidence that the system satisfied the requirement is desired, then the algorithm terminates in a verified state if the lower 99% confidence interval of the GP model is greater than zero over the entire test space. This shows that the simulation-based testing is completely automatic after the test case and requirement are defined.

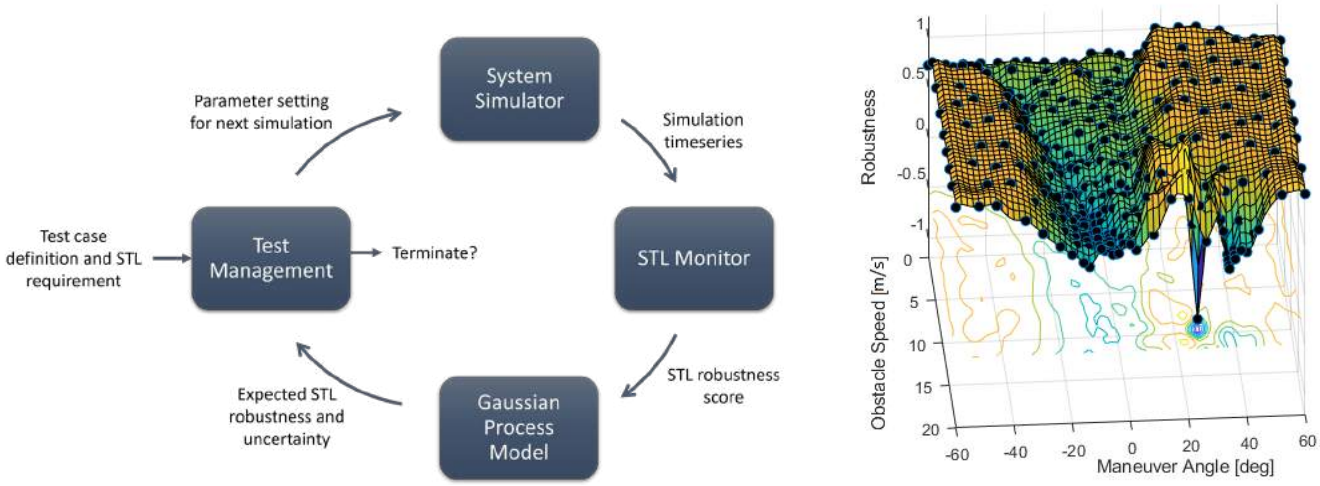

Figure 4: Left: Overview of the automatic test method of Torben et al. (2022). Right: Estimated STL robustness surface after a falsifying scenario is found.

LIMITATIONS OF FORMAL METHODS

The previous sections have shown some of the possibilities FMs have to offer. However, FMs not fit for all types of problems. In this section we will briefly discuss some limitations of FMs.

Scalability is a well-known limitation of FMs. Most FMs operate on discrete, finite-state models. As the number of variables in a model increases, the number of possible states increases exponentially. This is known as the *state space explosion* problem. Since a model checker exhaustively checks all possible executions, this limits the size of models which can be model checked. This has, however, been improved with recent innovations in model checking algorithms and the large increase in computational power.

FMs have traditionally also had limited support for systems with continuous dynamics, as they are often based on finite-state models. An approach to use FMs on continuous systems is to create a discrete approximation. However, this often ends up in huge state spaces which limits the size and accuracy of the discrete approximation. Several automated theorem provers have inherent support for continuous systems, by being able to use known theories on real-valued numbers in their reasoning.

Related to the two previous limitations is the *reality gap* problem. Formal verification is performed on a mathematical model of reality. In order for the verification of the mathematical model to have value as verification evidence, it needs to be an accurate representation of the real system. For some applications, such as logic circuits or software generated from a formal specification, the mathematical model is highly accurate. However, due to the scalability issues and limited support for continuous dynamics, some systems need to be simplified before they are subject to formal verification. Validating the fidelity of the simplified model is crucial in order to trust the results of a formal verification.

Finally, there is a long-standing challenge of limited uptake of FMs among professionals. We believe this is mainly caused by the perception that FMs are cumbersome, difficult and time-consuming. The majority of the background theory which FMs are built on originate from theoretical computer science and discrete mathematics, which is unfamiliar to many. This can make FMs seem intimidating to begin with. Also, taking on a formal development process often requires investing considerably more time in the design phase. However, this time is often returned in the verification and operational phases.

CONCLUSIONS

MASS are approaching reality, introducing a new level of complexity and criticality to maritime control systems. Given that the maritime industry already struggles with managing the complexity of current control systems, it is evident that new methods for development and verification are necessary to enable a safe and efficient introduction of autonomy. We have therefore proposed FMs as a candidate to aid the design and verification of safe MASS. We have discussed the needs the maritime industry faces and given three specific use cases demonstrating how FMs can be applied to meet these needs. Our conclusion is that FMs has the potential to meet many of the needs, despite some limitations. We therefore encourage further research into FMs for MASS.

ACKNOWLEDGEMENTS

The work is partly sponsored by the Research Council of Norway through the Centre of Excellence funding scheme, project number 223254, AMOS, and project ORCAS with project number 280655.

REFERENCES

Abrial, Jean Raymond. Modeling in Event-b: System and Software Engineering. Cambridge University Press, 2011.

Asarin, Eugene, et al. “Recent Progress in Continuous and Hybrid Reachability Analysis.” Proceedings of the 2006 IEEE Conference on Computer Aided Control Systems Design, CACSD, IEEE, 2007, pp. 1582–87.

Cimatti, Alessandro, et al. “NuSMV 2: An Opensource Tool for Symbolic Model Checking.” Lecture Notes in Computer Science, vol. 2404, 2002, pp. 359–64.

de Moura, Leonardo, and Nikolaj Bjørner. “Z3: An Efficient SMT Solver.” International Conference on Tools and Algorithms for the Construction and Analysis of Systems, Springer Berlin Heidelberg, 2008, pp. 337–40.

DNV. Rules for Classification of Ships Part 6 Chapter 22 - Enhanced System Verification. 2013.

DNV. Recommended Practice: Integrated Software Dependent Systems (ISDS). 2017.

DNV. Class Guideline: Autonomous and Remotely Operated Vehicles. 2018.

DNV. Recommended Practice DNVGL-RP-0510: Framework for Assurance of Data - Driven Algorithms and Models. 2020.

DNV. RULES FOR CLASSIFICATION Ships Part 6 Additional Class Notations Chapter 3 Navigation, Maneuvering and Position Keeping. 2021.

Fainekos, Georgios E., and George J. Pappas. “Robustness of Temporal Logic Specifications for Continuous-Time Signals.” Theoretical Computer Science, vol. 410, no. 42, Elsevier B.V., 2009, pp. 4262–91.

Foster, Simon, et al. “Towards Deductive Verification of Control Algorithms for Autonomous Marine Vehicles.” Proceedings of the IEEE International Conference on Engineering of Complex Computer Systems

Holzmann, G. J. “The Model Checker SPIN.” IEEE Transactions on Software Engineering, vol. 23, no. 5, 1997, pp. 279–95

IECTC. IEC 60050: International Electrotechnical Vocabulary. 2002.

IMO. COLREGs - International Regulations for Preventing Collisions at Sea. 1972.

IMO. Guidelines for Vessels and Units with Dynamic Positioning (DP) Systems. MSC.1/Circ.1580, 2017.

IMO. Outcome of the Regulatory Scoping Exercise For The Use Of Maritime Autonomous Surface Ships (MASS). 2021.

ISO. “Road Vehicles — Functional Safety.” ISO 26262, 2011.

ISO. “Road Vehicles - Safety of the Intended Functionality.” ISO 21448, 2019.

Jeannin, Jean-baptiste, et al. “Formal Verification of ACAS X, an Industrial Airborne Collision Avoidance System.” International Conference on Embedded Software, 2015, pp. 127–36.

Johansen, Tor A., et al. “Experiences from Hardware-in-the-Loop (HIL) Testing of Dynamic Positioning and Power Management Systems.” OSV Singapore, 2007, pp. 41–50.

Krasowski, Hanna, and Matthias Althoff. “Temporal Logic Formalization of Marine Traffic Rules.” IEEE Intelligent Vehicles Symposium (IV), 2021, pp. 186–92.

Larsen, Kim G., et al. “UPPAAL in a Nutshell.” International Journal on Software Tools for Technology Transfer, vol. 1, 1997, pp. 134–52.

Lecomte, Thierry, et al. “Formal Methods in Safety Critical Systems.” Safety and Reliability, vol. 11, no. 4, 1991, pp. 6–17.

Maler, Oded, and Dejan Nickovic. “Monitoring Temporal Properties of Continuous Signals.” Lecture Notes in Computer Science, vol. 3253, 2004, pp. 152-166.

NMD. Føringer i Forbindelse Med Bygging Eller Installering Av Automatisert Funksjonalitet, Med Hensikt å Kunne Utføre Ubemannet Eller Delvis Ubemannet Drift. 2020.

Park, Jinwook, and Jinwhan Kim. “Autonomous Docking of an Unmanned Surface Vehicle Based on Reachability Analysis.” International Conference on Control, Automation and Systems, 2020, pp. 962–66.

Paulson, Lawrence C. Isabelle: A Generic Theorem Prover. Vol. 828, Springer Science \& Business Media, 1994.

Pedersen, Tom Arne, et al. “Towards Simulation-Based Verification of Autonomous Navigation Systems.” Safety Science, vol. 129, no. December, Elsevier, 2020, p. 104799.

Pnueli, Amir. “The Temporal Logic of Programs.” Annual IEEE Symposium on Foundations of Computer Science, IEEE, 1977, pp. 46–57.

Sangiovanni-Vincentelli, Alberto, et al. “Taming Dr. Frankenstein: Contract-Based Design for Cyber-Physical Systems.” European Journal of Control, vol. 18, no. 3, Elsevier, 2012, pp. 217–38.

Shokri-Manninen, Fatima, et al. “Formal Verification of COLREG-Based Navigation of Maritime Autonomous Systems.” Lecture Notes in Computer Science, Software Engineering and Formal Methods, 2020

Smogeli, Øyvind. “Managing DP System Software - A Life-Cycle Perspective.” IFAC-PapersOnLine, vol. 48, no. 16, 2015, pp. 324–34.

Smogeli, Øyvind, et al. “Open Simulation Platform – An Open-Source Project for Maritime System Co-Simulation.” 19th Conference on Computer and IT Applications in the Maritime Industries, 2020, pp. 239–53.

Smogeli, Øyvind, and Jon Espen Skogdalen. “Third Party HIL Testing of Safety Critical Control System Software on Ships and Rigs.” Offshore Technology Conference, no. 2011, One Petro, 2011, pp. 839–45.

Sørensen, Asgeir J. “A Survey of Dynamic Positioning Control Systems.” Annual Reviews in Control, vol. 35, no. 1, 2011, pp. 123–36.

Torben, Tobias R., et al. “Automatic Simulation-Based Testing of Autonomous Ships Using Gaussian Processes and Temporal Logic.” Journal of Risk and Reliability, To be published, 2022.

Yan, Rongjie, et al. “Formal Collision Avoidance Analysis for Rigorous Building of Autonomous Marine Vehicles.” Embedded Systems Technology, edited by Yuanguo Bi et al., Springer Singapore, 2018, pp.

‘30 KNOTS FOR 30 YEARS’
how new-nuclear power can change the size and speed of containerships

Mikal Bøe, Giulio Gennaro, Tobi Menzies [1]

ABSTRACT

Container shipping has seen a constant trend of increasing ship dimensions. Today, containerships with a capacity in excess of 22,000 TEUs sail the seas, while vessels that were once considered large are considered little more than ‘feeders’. The ever-increasing size was fueled on one side by evident economies of scale, and on the other it was driven by the ever-diminishing margins in the “red ocean” of container shipping. There has been a dramatic reduction in both design and trading speeds. Until 2008 they were in excess of 25 and 20 knots respectively, while today design speed is generally around 23 knots, and average trading speed as low as 16 knots. Container shipping has as a result locked itself into managing extremely large vessels, which are largely inflexible with respect to trading patterns because of restrictions in port access and speed, and inefficient with respect to multi-port voyages and port operations. This paper shows how the advent of a new generation of advanced nuclear powered container ships can change all the above. Lower total life cycle costs could give competitive advantage back to the container ship industry, especially the operators who embrace new nuclear power. The decoupling between trading speed and operating cost could sweep slow steaming off the table, while the decoupling of trading speed from emissions could attract long term contracts from large-volume clients, who are also the ones more interested in certifying their supply chain as “zero emissions.” This could lead to a new generation of flexible, fast, mid-sized container ships which can operate more efficiently on point-to-point routes.

KEY WORDS

Nuclear, Decarbonization, Containerships, Emissions, Green House Gases, Propulsion, IMO2050

INTRODUCTION

Over the last 180 years, ship propulsion has progressed from sail to coal to oil power. Over the next two decades shipping must move away from fossil fuels and move toward new sustainable energy sources to reduce greenhouse gas (GHG) emissions, all while maintaining its competitiveness.

How significant is shipping’s contribution to global warming? The Fourth IMO GHG Study 2020 estimated that total shipping emitted 1,056 million tons of CO2 in 2018 which accounted for 2.9% of total global anthropogenic CO2 emissions. If treated as a country, this would make shipping the sixth largest emitter in the world, just above Germany. Left unchecked, the IMO has indicated that shipping emissions could increase from 2012 levels between 50% and 250% by 2050.

Given the urgency of reducing GHG to limit the effect of climate change the IMO has declared that GHG emissions must be reduced by 50% by 2050, and in 2023 it is expected the IMO could further revise this goal to a 100% reduction by 2050.

We must recognize that ocean transportation is a fiercely competitive business, and technological solutions that lead us towards sustainability must come with benefits to match the costs. Otherwise, adaptation of new climate technologies will fail.

There are several options for shipping to reduce its greenhouse gas emissions. Considering a full lifecycle of emissions, a well- to-wake approach, some of these solutions provide marginal environmental improvements, such as batteries, wind, and biofuels, whilst others offer a more substantial carbon and particulate matter emission reduction. These include electro fuels

[1] Core Power

(made with green hydrogen from electrolysis of water) like green hydrogen, green methanol, and green ammonia. Electro fuels cannot realistically scale to the volume needed of up to 340 million tons of HFO equivalent per year which would require over 800 million tons of electro fuels.

Gathering momentum among owners and charterers is also ‘new-nuclear’, a next generation of small and micro reactors that are built to operate very differently from the conventional nuclear technologies that exist today. New, advanced nuclear is the only one of the climate technology options available at scale which can provide a true-zero emission energy source to meet both the heavy power demands and competitive needs of large ships.

CONVENTIONAL MARINE REACTORS

Nuclear power is well suited to operate in the marine environment. On 17th January 1955 USS Nautilus SSN-571 put to sea for the first time and signaled "underway on nuclear power." The Nautilus was decommissioned in 1980 after 25 years of service, 2,500 dives, and a traveled distance of 513,000 miles. On 23rd March 1962 N/S Savannah the world first commercial nuclear ship set sails for her maiden voyage. She was laid up in 1971 after sailing almost half million miles, visiting 77 ports, and hosting almost 1.4 million visitors.

The U.S. and UK Navy nuclear propulsion programs, which have operated near faultlessly since the 1950s, and have become highly respected and specialized branches of their countriescountries’ militaries with their own highly specialized operating procedures. Their excellent safety records have led to growing calls that commercial marine industries could adopt a new generation of advanced reactor technologies coupled with a similar approach to marine safety and security as adopted by the nuclear navies.

Figure 1. N/S Savannah, launched on 23rd March 1962

We must recognize however, that modern naval Pressurized Water Reactors, PWR, are not suited for use in civilian applications. There are two key reasons for this. Firstly, they run on highly enriched uranium, HEU which is not possible in civilian applications, while running on low enriched uranium (LEU), would require vastly larger reactors, needing frequent refueling, which would pose a major challenge in managing both the supply of fresh fuel and the handling of spent fuels.

Secondly, pressurized reactors require the operator to maintain an Emergency Planning Zone which can extend several kilometres around the reactor. A PWR powered ship would therefore be responsible for managing emergency management in each port of call which would at time be larger than the port itself. This is a major obstacle for conventional nuclear-powered ships calling in commercial civilian ports.

Naval reactors are uniformly conventional pressurised water reactor (PWR) designs but differ from commercial power reactors. PWRs were originally designed to power propulsion for nuclear submarines and were used in the original design (1957) of the United States ’ first commercial power plant at Shippingport Atomic Power Station, which was also the world's first full-scale atomic electric power plant devoted exclusively to peaceful use.

Naval PWRs deliver enormous power from a very small volume and therefore most run on highly enriched uranium. Enrichment to 'weapons grade' fuel containing ~93% of the isotope Uranium-235 is standard for US submarines.

The PWR works by circulating its light water 'coolant' (as liquid, at ~300°C) through a pressurised 'primary loop' that passes through a steam generator, transferring heat to a 'secondary system' that produces steam to either produce electricity or drive a propeller shaft. The water enters through the bottom of the reactor's core at about 548 K (275°C; 527°F) and is heated as it flows upwards through the reactor core to a temperature of about 588K (315°C; 599°F). The water remains liquid despite the high temperature due to the high pressure in the primary coolant loop, usually around 155 bar.

Pressure in the primary circuit is maintained by a pressurizer, a separate vessel that is connected to the primary circuit and partially filled with water which is heated to the boiling point for the desired pressure using submerged electrical heaters. To achieve a pressure of 155 bars, the pressurizer temperature is maintained at 345°C (653°F), which causes a difference between the pressurizer temperature and the highest temperature in the reactor core of 30°C. 345°C is the boiling point of water at 155 bar and the liquid water is at the edge of a phase change.

Since the coolant water must be highly pressurized to remain liquid at high temperatures a PWR requires high strength piping and a heavy pressure vessel that increases construction costs. Additional high-pressure components such as reactor coolant pumps, pressurizer, and steam generators are also needed. The higher pressure can increase the consequences of a loss-of-coolant accident.

A submarine reactor is required to withstand the shock and vibration experienced by all warships in active service due to ocean turbulence and enemy action. The Russian, US, and British navies rely on steam turbine propulsion while French and Chinese submarines use their turbine to generate electricity for propulsion.

Nuclear power revolutionized by the Navy and the technology was shared with Britain. The US Navy has accumulated more than 5,400 reactor-years without incident. Special envoy John Kerry reflected on his career with nuclear propulsion at COP26 saying the US Navy had 'never had a spill, never lost a crew member.' Nuclear power at sea has proven to be one of the safest and most efficient ways to power large ships while coming with the benefit of true-zero emissions.

NEW NUCLEAR - ADVANCED MARINE REACTORS

With modern reactor advancements in fuel management, reactor safety, and manufacturing, advanced nuclear reactors are being designed that would be ideal for use in marine applications and applied to supply power to produce green electro-fuels.

Certain fundamental criteria exist in the marine environment and on floating platforms that nuclear reactors must meet to be considered feasible solutions. Three main evaluation criteria for the appropriate reactor technologies are the following:

- High-efficiency nuclear fuels that mitigate nuclear proliferation and reduce nuclear waste.
- Reactors that operate at ambient pressures and allow for small Emergency Planning Zones and simpler port calls.
- Economic viability.

The optimum solutions for advanced marine reactors are those which fulfil the three main criteria for success in the maritime industry.

Inherent safety

The safest place for nuclear fuel is in a reactor. Creating an acceptable security and risk profile for a maritime reactor would be based on excellent fuel efficiency and long fuel cycles where few or no refuelling of a reactor are required. With no fresh fuel going in and no spent fuel coming out during the life of a vessel, security, safeguarding, and proliferation risks are dramatically reduced.

Inherent safety is essential for maritime nuclear reactors to be implemented commercially. This means the implementation of passive safety systems and reactor designs that make operations, management, and emergency planning feasible for mobile reactors in ports.

Emergency Planning Zones

All nuclear plants, regardless of size and design, require an emergency planning zone (EPZ) around the reactor. As most reactors today are pressurized, the EPZ must consider the formation of a plume that would form if pressure was released from the reactor into the surrounding environment. As a result, EPZ requirements for PWRs are large. The Nuclear Regulatory Commission in the US requires two emergency planning zones around a nuclear plant.

The first is a 'Plume Exposure Pathway EPZ' extending about 15 km in radius around the reactor site. Protective action plans within this area are designed to avoid or reduce dose from potential exposures such as inhaling radioactive particles. The second is an 'Ingestion Exposure Pathway EPZ' extending about 80 km in radius around the reactor site. Protective action plans for this area are designed to avoid or reduce dose from eating or drinking radioactive materials.

Following the Three Mile Island accident in 1979, these two EPZs were included to establish standards upon which emergency plans are to be reviewed. As the size requirements for the two EPZs were derived from conservative analyses for large LWR plants, the 1980 rulemaking allowed that the size of the EPZs can be determined on a case-by-case basis for non-PWR reactor designs and for reactors with a power level less than 250 MW thermal. For these plants, smaller EPZs were permitted due to their reduced risk. Reactors operating at ambient pressure have the potential then to require very small EPZs as any expulsion of radioactive particles or potential plume formation would be significantly smaller than that of a PWR. Ships powered by PWRs require an EPZ that is usually larger than the dock of the port of call and sometimes larger than the port itself.

New-nuclear advanced reactors operating at ambient pressure have the potential to require Emergency Planning Zones (EPZs) that do not extend outside the boundary of the ship, making them far smaller than the EPZs required of conventional pressurized reactors. This would allow for simpler port calls, removing a major barrier to adoption.

Economic viability

Economic viability is the final key criteria. Due to their construction and arrangement, conventional reactor designs such as the pressurized water reactor and other land-based nuclear installations have benefited from economies of scale due to their large size. However, small, advanced reactors could be mass-assembled at the highest quality assurance levels, in dedicated facilities or specialist shipyards, making them affordable for maritime applications. This is a major departure from conventional nuclear building techniques and will be essential to allow future nuclear solutions a competitive chance against other alternative fuels for marine decarbonization.

It has been identified and is described below that two new reactor types can specifically meet these criteria and may offer the optimum solution for marine deployment. These are the Molten Salt Reactor (MSR) and the micro-Heat Pipe Reactor (HPR), the benefits of which can be seen in contrast to conventional marine nuclear reactors.

MOLTEN SALT REACTORS

Among the modern advanced reactor designs currently being developed taking advantage of improved fuel efficiency, fuel management, reactor safety, and manufacturing, Core Power has identified Molten Salt Reactors, MSRs, operating in the fast spectrum as the best suited for medium large scale marine applications, i.e not only for large ships but also for offshore installations for power generation, production of green electro fuels, water desalination…

MSRs were initially devised in the 1960s', in particular a 7.4 MW test reactor was operated at Oak Ridge National Laboratory from 1965 to 1969 under the so-called Molten Salt Reactor Experiment. The key feature in a Molten Salt Reactor is that both the fuel and the coolant are liquid salts, and with a very high boiling temperate (about 1400°C). This leads to huge advantages as contrary to operating at moderate temperature (about 315°C) and very high pressures (150 bar), as PWRs do, MSRs operate at high temperature (about 700°C) and ambient pressure.

The fuel salt contains the nuclear fuel and is therefore both the fuel that produces the heat and the coolant. As a result, MSRs are not prone to the same types of loss-of-coolant accidents that have been responsible for each of history's largest nuclear power accidents.

To generate electricity, the molten salt mixture transports heat to the power conversion system that can then be harnessed to produce power. MSRs operate at ambient pressure and therefore do not have the same amounts of contained force found in PWRs that during accidents have led to the expulsion of radio toxins into the environment. If an MSR stops and the fuel salt is cooled, it would solidify and be entombed in the reactor preventing fuel from leaking or escaping. This passive safety feature of the MSR is highly desirable for the marine environment in the possible case of non-reactor accidents such as a ship collision, grounding, or even sinking.

The lack of pressure in the reactor is beneficial for a ship or offshore structure where a small EPZ would be small and potentially not extend beyond the boundary of the hull, allowing for the ship or offshore structure to come into closer proximity to other ships or port infrastructure. With smaller EPZs, commercial nuclear ships could make port calls and transit narrow waterways without requiring extended safety zones around the ship.

MSRs consume their own long-lived transuranic elements, generating additional power, and transmute long-lived fission products into shorter-lived ones. These fission products generally decay to background levels of radioactivity in about 300 years, as opposed to over 200,000 years for spent fuel from conventional solid-fuel reactors.

MSRs design is focused on incorporating materials, salt chemistry, and components, in particular passive components, that have high technical readiness today, and that ensure high safety, reliability, availability, and efficiency. reducing total life cycle cost and, at the same time, decreasing the time needed for development and testing.

MSRs have the potential to revolutionize marine propulsion, in a similar way that steam revolutionized navigation when it took over from sailing ships almost 200 years ago.

'ATOMIC' CONTAINER SHIPPING

Container shipping, since its birth, has seen a constant trend in the increase of ship dimensions. Today, ships with a capacity in excess of 22,000 TEUs sail the seas, while vessels that were once reputed as large are consider little more than feeders. The ever-increasing size was fueled on one side by evident economies of scales, while on the other it was driven by the ever-diminishing margins in the "red ocean" of container shipping.

At the same time there has been a substantial reduction in both design and trading speeds: until 2008 they were in excess of 25 and 20 knots respectively, while today design speed is generally around 23 knots, and average trading speed can be as low as 16 knots. Container shipping has therefore locked itself up into managing extremely large vessels, quite inflexible in respect to trading patterns due to restriction in port access and speed, and quite inefficient in respect to multi-port voyages and port operations.

In this paper modern 22,000 a 14,000 and a 8,000 TEU Diesel powered ships, designed for 23 knots, are compared to a 22,000, a14,000 TEU and a 8,000 TEI 'Atomic ships', powered by new-nuclear reactor technology like the MSR, and designed for 23, 26 and 30 knots.

Table 1: modeled containerships

Capacity	Powering	Propulsion	Design Speed	Service Speed	Ship Life
22K TEU	Diesel Mechanic	Single Screw	23 knots	16 to 22 knots	20 years
22K TEU	Atomic Electric	Podded Multi Screw	23 to 30 knots	16 to 29 knots	30 years
14K TEU	Diesel Mechanic	Single Screw	23 knots	16 to 22 knots	20 years
14K TEU	Atomic Electric	Podded Multi Screw	23 to 30 knots	16 to 29 knots	30 years
8K TEU	Diesel Mechanic	Single Screw	23 knots	16 to 22 knots	20 years
8K TEU	Atomic Electric	Podded Multi Screw	23 to 30 knots	16 to 29 knots	30 years

In respect to the differences between the vessels it should be clarified that the Atomic Ships will be nuclear-electric, which we will call 'Atomic-electric' in this paper. This will in principle increase the propulsion power requirement, due to electric losses, however this will allow to use multi screw podded propulsion, which result a net decrease of the propulsion power requirement. The atomic ship will also benefit from increase cargo carrying capacity from the substitution of the main and auxiliary Diesel engines with the atomic power generation system, as well as from the removal of the fuel tanks and the funnel. Finally, the atomic ships will be designed for a longer operational life, of 30 years.

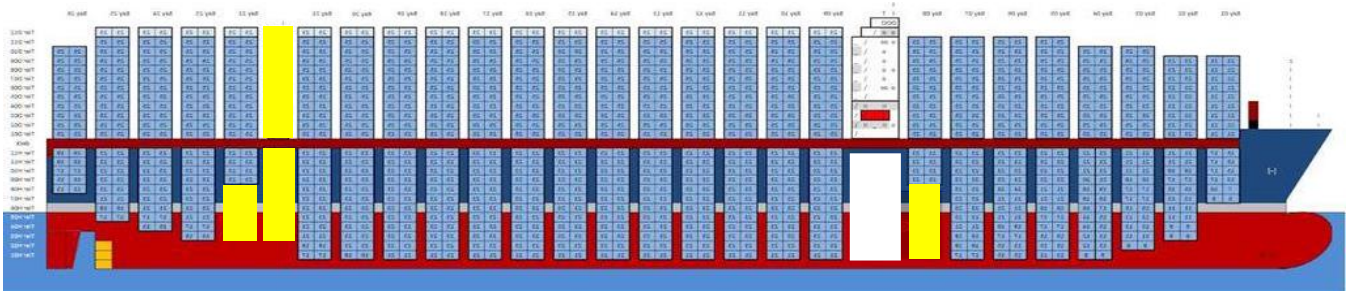

Figure 3. Increased cargo spaces, in yellow, for an atomic electric containership.

MODELLING

The methodology selected for comparing different alternatives is the Total Life Cycle Analysis divided by the number of container moved by the vessel over its life, resulting in specific margins and externalities (USD per TEU) and in specific emissions (tons of CO2 equivalent per TEU).

The model is high level / industry wide in nature, being based on the general characteristics of the propulsion / power plants of the vessels as found in literature with first principle optimization.

The best alternative, by definition, is the one providing the greatest value to the society as a whole. This value is calculated as a summation of the earnings (positive), the private and the external costs (negative). Since it has been assumed that the benefits generated by all alternatives of a given ship class are equal, the best alternative is the one generating the lowest Total Life Cycle Costs. These are considered to be the summation of both the private and the external cost referred to the total life of the powering system of the vessel. This is achieved by considering four distinct phases of the life of the asset:

- construction;
- operation;
- decommissioning;
- fuel supply chain.

It is extremely important to consider all these four phases since failure to do so will introduce large bias in the computation of emissions. The most obvious example is battery powered vehicles which are virtually emission free in the operation phase, but are far from emissions free since batteries have to be manufactured, disposed of, and charged, incurring quite substantial total life cycle emissions.

The model covers the following aspects:

- Ship life, interests, inflation;
- Capital expenses;
- Operational expenses (consumables, maintenance, crewing...)
- Operational profile (time spent underway, loading / unloading, idle);
- Carbon Taxation;
- Freight Rate and Loading Rate
- Health, Safety and Environmental, HSE, emissions and externalities;
- Climate Change, CC, emissions and externalities.

Emissions have been modeled combining several shipping related studies, most noticeably by IMO, LR-UMAS, KR, ICCT, Thinkstep. Externalities have been modelled on the basis of Markandya et al., 2011. This study presents a very detailed database of power generation emissions and externalities related to human health, loss of biodiversity, damage to crops, damage to materials, damages due to other pollutants, damages due to radionuclides, climate change. The database was adjusted to account for the differences between shipping and onshore power generation and for different technologies, emissions were adjusted considering shipping related studies.

In particular the following emissions have been considered:

- Health, Safety and Environmental relevant emissions: NH_3, NMVOC, NOx, PM, SOx, Cd, As, Ni, Pb, Hg, Cr, Formaldehyde, radionuclides;
- Climate Change relevant emissions: CO_2, CH_4, N_2O.

It should be noted that the modeled emissions and externalities are related to the power generation and the propulsion systems only. Emissions and externalities related the other components of the vessel, e.g. steel making and scrapping, are not yet considered and will be modelled in the future.

The Diesel powered vessels are considered operating on Very Low Sulphur Fuel Oil, priced at about 600 USD / ton. Tank to Wake GHG emissions are considered subject to a carbon tax of 100 USD for each ton of CO_2 equivalent. Total Life Cycle Well to Wake GHG emission are also calculated.

Table 2 presents a sample output of the model for a conventional and an atomic 22K TEU ULCS, both designed for 23 knots and operated at an average speed of 22 knots, trading between Far East and Europe and sailing through the Suez Canal.

Table 2: Sample Output for a Conventional and an Atomic 22K TEU ULCS

	22K TEU Conventional	22K TEU Atomic	
CAPEX	178.2	633.0	M USD
OPEX	47.2	6.8	M USD / year
Carbon Tax	22.5	0	M USD / year
Yearly revenues	172.9	176.8	M USD / year
Yearly capacity	237,600	243,000	TEU / year
Yearly externalities	17.6	0.4	USD / year
Yearly emissions	225,000	0	tons CO2eq / year
Specific margin	345	529	USD / TEU
Specific externalities	74.04	1.76	USD / TEU
Specific emissions	0.95	0.00	tons CO2eq / TEU

RESULTS

The investigation has considered operating the Diesel powered ships via the Suez Canal, while the Atomic ships are considered either transiting the Suez Canal or sailing around the Cape of Good Hope. It should be noted that, currently, nuclear powered ships are not allowed through the Suez Canal, however this has been nonetheless modelled for sake of comparison.

The results of the investigation and the different routes are presented in the following tables and picture.

Figure 4. Shanghai - Rotterdam route via Suez and around the Cape of Good Hope.

Table 3: Diesel and Atomic 22K TEU ULCS operated via the Suez Canal

Suez	22K TEU Diesel		22K TEU Atomic				
Design speed	23.0	23.0	23.0	23.0	26.0	30.0	knots
Service speed	16.0	22.0	16.0	22.0	25.0	29.0	knots
Specific emissions	1.04	1.30	0.02	0.03	0.04	0.05	tons CO2eq / TEU
Specific externalities	58	74	1	2	2	3	USD / TEU
Specific Profit	390	345	508	529	482	472	USD / TEU

Table 4: Diesel and Atomic 14K TEU ULCS operated via the Suez Canal

Suez	14K TEU Diesel		14K TEU Atomic				
Design speed	23.0	23.0	23.0	23.0	26.0	30.0	knots
Service speed	16.0	22.0	16.0	22.0	25.0	29.0	knots
Specific emissions	1.17	1.54	0.03	0.04	0.04	0.06	USD / TEU
Specific externalities	66.3	88.3	1.6	2.1	2.5	3.5	USD / TEU
Specific Profit	343	278	460	491	489	408	tons CO2eq / TEU

Table 5: Diesel and Atomic 8K TEU ULCS operated via the Suez Canal

Suez	8K TEU Diesel		8K TEU Atomic				
Design speed	23.0	23.0	23.0	23.0	26.0	30.0	knots
Service speed	16.0	22.0	16.0	22.0	25.0	29.0	knots
Specific emissions	2.05	2.69	0.05	0.05	0.06	0.08	USD / TEU
Specific externalities	115.9	154.4	2.8	2.6	3.2	4.6	USD / TEU
Specific Profit	264	93	342	390	391	370	tons CO2eq / TEU

Table 6: Atomic 22K TEU ULCS operated around the Cape of Good Hope

Cape Good Hope	22K TEU Atomic			
Design speed	23.0	26.0	30.0	knots
Service speed	22.0	25.0	30.0	knots
Specific emissions	0.04	0.05	0.06	USD / TEU
Specific externalities	2.3	2.7	3.7	USD / TEU
Specific Profit	550	493	481	tons CO2eq / TEU

Table 7: Atomic 14K TEU ULCS operated around the Cape of Good Hope

Cape Good Hope	14K TEU Atomic			
Design speed	23.0	26.0	30.0	knots
Service speed	22.0	25.0	30.0	knots
Specific emissions	0.05	0.06	0.08	USD / TEU
Specific externalities	2.8	3.3	4.6	USD / TEU
Specific Profit	495	495	396	tons CO2eq / TEU

Table 8: Atomic 8K TEU ULCS operated around the Cape of Good Hope

Cape Good Hope	8K TEU Atomic			
Design speed	23.0	26.0	30.0	knots
Service speed	22.0	25.0	30.0	knots
Specific emissions	0.06	0.07	0.11	USD / TEU
Specific externalities	3.5	4.3	6.1	USD / TEU
Specific Profit	383	385	361	tons CO2eq / TEU

In respect to specific margins, the results of the modelling, are consistent with the different CAPEX vs OPEX structure of Diesel powered and Atomic ships. In particular for a Diesel powered ship OPEX is more relevant than CAPEX, this is due to the relatively high cost incurred for fuel, which will be rendered more severe by the introduction of carbon taxation. The same conclusion is in principle true for green electro fuels, whose very high cost will favor super slow steaming.

For an Atomic vessel the scenario changes substantially. Slow and super slow steaming are now a liability rather than an asset, as a matter of fact all Atomic ships, with a design speed of 23 knots, generate larger profits when operated at 22 knots

than at 16 knots. Modelling suggests there could be occasions when going faster on a longer route might be superior to going slower on shorter route, this is clearly identified by the operating an atomic ship at 16 knots via Suez vs operating the same vessel at 22 knots around the Cape. As the Suez transit fees incurred by the former are high, while the former generates a larger container throughput while incurring in low added cost for nuclear fuel consumption.

For an Atomic ship, the economic speed is mainly coupled to the power rather than to the utilization of the reactor. Potentially the economic speed could be as high as permissible for that size of reactor, as a lower speed would generate marginal savings, while decreasing the container throughput, while a higher speed would require installing an additional reactor, thereby incurring a large additional CAPEX.

Therefore, for the same reactor size, larger atomic ships will be slower than smaller ones. This can be seen by the fact that the 22K TEU Atomic ship generates a higher specific profit at 22 rather than at 25 knots, while for the 14K TEU it is the opposite, the reason being that the 22K TEU Atomic ship would need an additional reactor to generate the power required to attain that speed. Finally the profits generated by the 8K atomic ship are fairly similar, regardless of the operating speed, making it extremely flexible, while for the convention vessel operations are 23 knots would result in a significant reduction in profits.

In respect to externalities and emissions the atomic ship would allow reductions in excess of 90%, in addition these would be concentrated in the construction, decommissioning and fuel supply chain, rather than during operations, meaning they would be easier to control and mitigate.

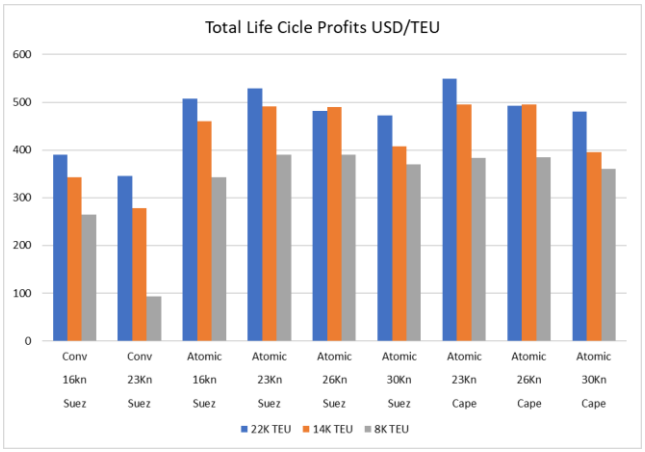

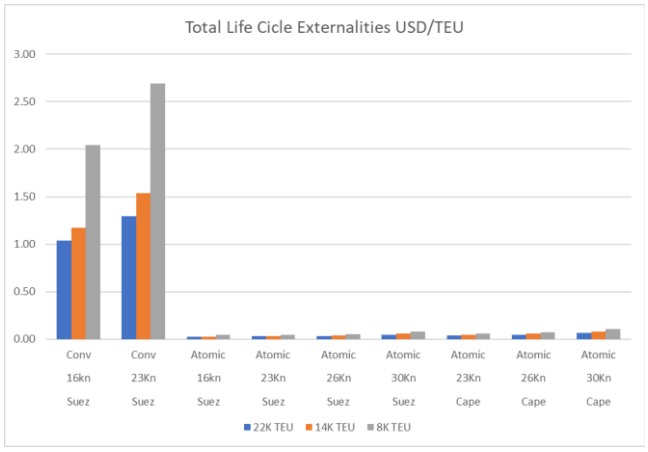

Figures 5 and 6. Total Life Cycle Profits (left) and Externalities (right), in USD / TEU, for all modelled ships, speed, routes.

CONCLUSIONS

Shipping has committed to decarbonization, however no clear path is present, unless atomic ships are considered. For this reason, Core Power has built and is constantly refining a comprehensive model providing qualitative and quantitative assessment of total life cycle costs, revenues, externalities and emissions of ships. The modelling considers vessels powered by different prime movers and running on different fuels. In the present research the model has been applied to Ultra Large Container Ships, trading between Far East and Europe, allowing the drawing of the following conclusions.

First and foremost. atomic ships appear as the only practical solution to decarbonize shipping, far beyond the scope of IMO2050, and in respect to both tank to wake and well to tank emissions. Atomic ships allow this to be done in a fully sustainable while increasing the margins for the operators. All other alternatives appear substandard, either due to allowing only a partial reduction of emissions, not being scalable to the size of the problem, or extremely high costs.

The second conclusion is that the operational profile of atomic ships will be different, atomic ships could in principle sail at higher speed, sweeping slow and super slow steaming off the table, and potentially making alternative routes attractive.

The third conclusion is that, also for atomic ships, economies of scale favor larger ships over smaller ones. However smaller ones are not as penalized as conventional ones.

The higher economic speed of smaller atomic ships in respect to larger atomic ships and to all conventional ships, will make them more flexible, and even if it will not be able to dislocate the economies of scale that favour large vessels, it will make smaller ships more attractive due to their combination of added flexibility, higher speed, and attractive margins.

In important also to note that the much higher CAPEX incurred by atomic ship require a long term lease scheme, similarly to what is already happening in civil aviation, whereby the maker of the reactor will be responsible for the lifetime management of the reactor, including decommissioning. This will mitigate the risk for the operators while sparing them from becoming licensed nuclear operators.

A final consideration is that not all atomic technologies are appropriate to be deployed at sea in commercial vessels. Core Power has vetted many different advanced reactor designs and has concluded that, for medium to large power applications, Molten Salt Reactors operating in the fast spectrum are the best suited and Core Power is actively investing and aiding the development of this technology.

REFERENCES

HAAS, B., “Strategies for the Success of Nuclear Powered Commercial Shipping.” 2014
KACKUR, J. “Shipping in the 2020 era – selection of fuel and propulsion machinery.” Wartsila. 2018
MARCANDYA et al. “The Social Cost of Electricity: Scenarios and Policy Implications - Private and external costs assessment, policy implication and scenarios for the EU and selected non-EU Countries.” FEEM. 2011.
SCHULLER et al. “Life Cycle GHG Emission Study on the Use of LNG as MarineFuel.” Nature Communications. 2018.
SOFIEV et al. “Cleaner fuels for ships provide public health benefits with climate tradeoffs.” Thinkstep. 2019.
IMO. MARPOL Annex VI regulation 14, including the 0.50% Sulfur limit from 1 January 2020
IMO. Amendments to MARPOL Annex VI (Prohibition on the carriage of non-compliant fuel oil for combustion purposes for propulsion or operation on board a ship), enter into force from 1 March 2020 (MEPC.305(73))
IMO. Note by the International Maritime Organization to the UNFCCC Talanoa Dialogue.
IMO. Fourth IMO Greenhouse Gas Study. 2018
IRENA. “Hydrogen: A renewable energy perspective. Report prepared for the 2nd Hydrogen Energy Ministerial Meeting in Tokyo, Japan.” 2019.
KOREAN REGISTER. “Forecasting the Alternative Marine Fuel Ammonia.” 2020
LLOYD REGISTER & UMAS. “Zero-Emission Vessels: Transition Pathways.” 2019, 2020
http://www.ssmaritime.com/NS-Savannah.htm

DATA-DRIVEN MODELS TO PREDICT THE EFFECT OF BIOFOULING ON SHIP PERFORMANCE

Haakon Christopher Bakka[1], Hanne Wist Rognebakke[2] and Erik Vanem[1,3]

ABSTRACT

Marine biofouling on a ship's hull and propeller increases the resistance of the ship moving through water and may seriously influence the propulsion efficiency of the ship. It may be removed by proper hull and propeller cleaning in order to maintain efficiency, but such cleaning is costly and time consuming. Moreover, cleaning may damage the anti-fouling system and hence accelerate further marine growth. Therefore, hull and propeller cleaning should only be performed when necessary and the optimal time to clean the hull is a trade-off between the cost of cleaning and the efficiency gain achieved. In order to make qualified decisions regarding this, there is a need for models to estimate the effect of biofouling on the ship resistance and propulsion efficiency, and to separate the effect of fouling from other factors such as ship speed, loading condition and weather conditions. This paper presents various data-driven models, based on operational data from ships in operation, combined with AIS data and weather data, for predicting the extent and effect of biofouling on a ship's hull. It describes the growth rate of biofouling as a function of variables related to the ship, its operation and weather conditions. In order to achieve this, sensor data measured on the ship will be synchronized with weather data and other data sources and used to train statistical models. In this paper, different models based on generalized additive models (GAM) and random forest will be explored. However, more important than the actual regression model is how the effect of biofouling, which is not observed, is modelled. The results indicate that estimates of the effect of biofouling can be obtained by carefully modelling the total shaft power of a ship in different conditions. The data-driven model is applied to data from a large container ship covering several years of operation.

KEY WORDS

Ship performance; Biofouling; hull resistance; data-driven models; Condition monitoring; Ship emission; Statistical modelling

INTRODUCTION

Marine growth and biofouling on a ship's hull and propeller increases the resistance of the ship moving through water and may seriously influence the propulsion efficiency of the ship (Schultz 2011). Previous studies have indicated that the efficiency loss due to biofouling could be in the order of 5% - 15% of total shaft power and fuel usage (Molland 2014), and that this contributes to up to 2.7% of the total anthropogenic emission of CO_2 (Coraddu 2019). Biofouling may be removed by proper hull and propeller cleaning in order to maintain efficiency, but such cleaning is costly and time consuming. Moreover, cleaning may damage the anti-fouling system and hence accelerate further marine growth. Therefore, hull and propeller cleaning should only be performed when necessary and the optimal time to clean the hull is a trade-off between the cost of cleaning and the efficiency gain achieved. In order to make qualified decisions regarding this, there is a need for models to estimate the effect of biofouling on the ship resistance and propulsion efficiency, and to separate the effect of fouling from other factors such as ship speed, loading condition and weather conditions. The effect of ship fouling on ship performance, fuel consumption and emissions from ships turns out to be a difficult problem. There are little data on coating performance and the hull roughness of ships in service is not well understood (Yeginbayeva 2018). Therefore, data-driven models based on sensor data from ships, combined with other data sources is an attractive approach to gain insight and estimate the effect of biofouling on a ship's performance.

[1] Department of Mathematics, University of Oslo, Oslo, Norway
[2] Norwegian Computing Center, Oslo, Norway
[3] DNV Group Research and Development, Høvik, Norway

Such insight and reliable estimation of the effect of biofouling are essential in order to address issues related to the efficiency loss due to biofouling, how this changes over time and with varying operating conditions and how it is affected by hull and propeller cleanings as well as the effectiveness of various anti-fouling systems. Moreover, reliable and accurate modelling of the effect of biofouling could also be used to evaluate the instantaneous and long-term effect of different cleaning techniques related to both the immediate efficiency gain and also possible damages to paint and antifouling systems that may yield faster increase of biofouling during a period after the cleaning. It will also be important input for cost-benefit assessment related to optimal cleaning intervals and optimal ship operation, and for assessing the effect of hull cleanings on ship emissions.

Data-driven methods have recently been used in several studies related to ship performance, and the increasing connectivity and availability of sensor data from ships are believed to make this approach even more attractive in the near future. Different regression models were used to predict the effect of environmental conditions on ship speed in (Brandsæter 2018) and data-driven approaches for predicting ship performance are also explored in e.g. (Karaginnidis 2021; Bui 2021; Dalheim 2021). Statistical models have also been used to evaluate structural stresses and fatigue rates for ships in actual seaway (Steinbakk 2020). In this paper, two different data-driven models will be presented, based on generalized additive models (GAM) and random forest, respectively. However, apart from representing different ways of regressing shaft power on a set of explanatory variables, the two modelling approaches differ by the way the effect of biofouling is modelled. Not being observed, the amount of biofouling cannot be used directly as a covariate in the models, and two different approaches are investigated in this study. With the first approach, the effect of biofouling is modelled as a piecewise function of time since last cleaning and with the second approach the effect of biofouling is estimated by comparing the observed shaft power to a reference value that should represent the shaft power without any biofouling. Hence, the increase in shaft power relative to this reference value is ascribed to biofouling. In the following, these two modelling approaches will be outlined, and the results will be presented.

DATA SOURCES AND DATA PRE-PROCESSING

This study utilizes data from different sources. The primary data source is operational sensor data from four different vessels that have been made available from a performance monitoring system on board. The data are supplemented by AIS (Automatic Identification System) data to track position, course and speed of the vessels. These locations are then mapped to weather data from the ERA5 reanalysis (Hersbach 2020) to obtain prevailing weather conditions. These data have different sampling frequencies and need to be synchronized. In addition to these time-series data, information about cleaning types and dates is available, distinguishing between hull and propeller cleanings and antifouling applications. In this paper, results from one of the ships will be presented, a large container vessel, covering a period from 2015 which include several hull cleanings.

Shaft power have been selected as the response variable, and several covariates are extracted from the combined datasets. These are: Ship speed, linear and angular ship accelerations, mean draft, draft trim, wave direction, wind speed, wind direction, wave period, significant wave height, cleaning period and time since last cleaning. Some filtering and subsetting of the data are performed prior to modelling to achieve more representative data. For example, in order to identify the effect of biofouling on shaft power, near steady state conditions are needed, and therefore data with ship speed < 5 knots, linear acceleration > 1 knot per 15 minutes and angular acceleration > 2.5 knots per 15 minutes have been removed. Furthermore, different subsampling of the remaining data has been explored in order to reduce the serial correlation in the data, resulting in different datasets used for modelling. Histograms of the response variable (shaft power) and ship speed, which is the most important covariate, are shown in Figure 1.

DATA-DRIVEN MODELS

Two types of data-driven models are used in this study, a piecewise spline on residual model based on GAM and a random forest model. These will be briefly described in the following.

Piecewise Spline Model

The piecewise spline model is a Bayesian generative model with a flexible prior model able to fit a variety of data structures. The prior model is trained on the observed data to produce a posterior model, which closely fits the structure found in the data. From the posterior model, any attribute of the data generating process can be computed as well as the uncertainty of that attribute.

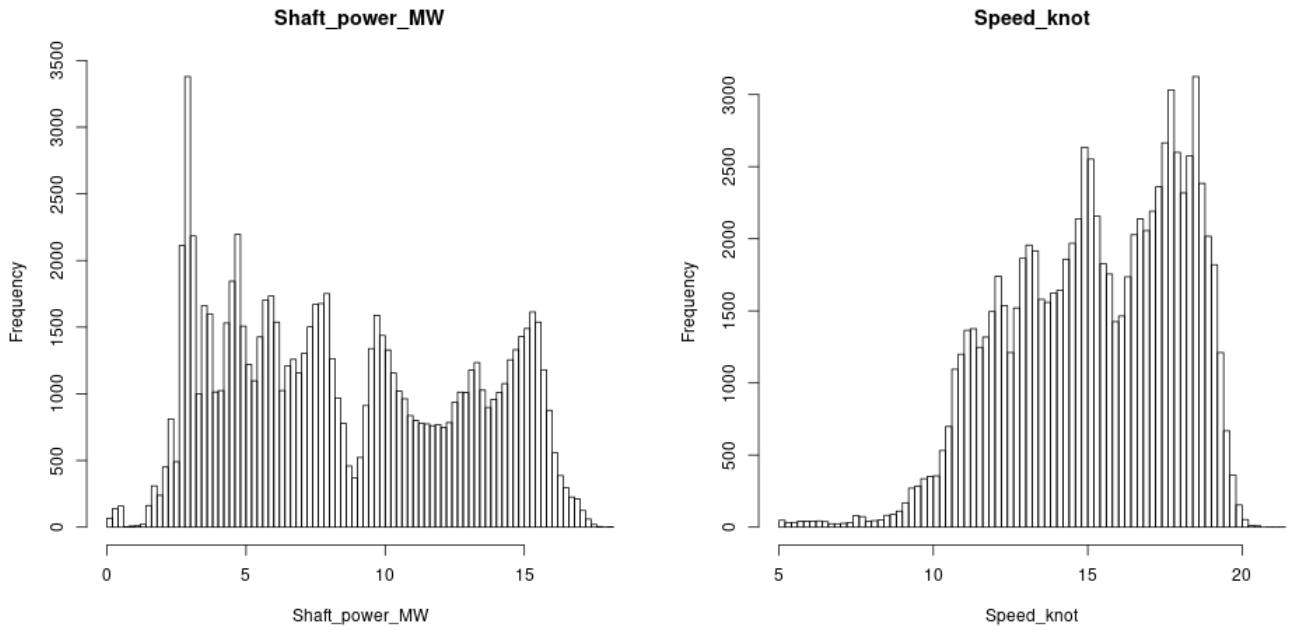

Figure 1: Histograms of Shaft Power (left) and Ship Speed (right)

The prior model is denoted $\pi(y,\ \theta)$, giving a joint distribution for model parameters θ and the response y. This prior model is built as $\pi(y,\ \theta)\ = \pi(y|\theta)\ \pi(\theta)$, where the first term is usually referred to as the observation likelihood, and the second as the prior. The posterior is

$$\pi(\theta|y)\ = \frac{\pi(y|\theta)}{\pi(y)} \quad [1]$$

After training the model on a set of data, the model can predict new observations by integrating over the parameters inferred by the old data

$$\pi(y_{new}|y_{old})\ = \int_{\theta}\ \pi(y_{new}|\theta)\pi(\theta|y_{old})d\theta \quad [2]$$

Inference with these models is based on INLA, short for Integrated Nested Laplace Approximations, which is based on quadratic approximations of the likelihood function and sparse matrix representations of Gaussian Markov Random Fields (Rue 2009).

The idea of this model is to create good contrasts by adjusting for all the covariates unrelated to fouling, and then to model the residual effect of biofouling on Shaft Power as a piecewise spline. These models, which we denote as PWSR (PieceWise Spline on Residuals), are Generalised Additive Models (GAMs) and can be written as

$$y\ =\ X\beta\ +\ f_1(v)\ +\ f_2(\varphi)\ +\ h(t)\ +\ \epsilon \quad [3]$$

where y is the observed Shaft Power in MW, ϵ is the residuals, and the other terms are referred to as model components. Linear relationships are assumed for the variables linear acceleration, angular acceleration, draft trim, mean draft, wind speed, significant wave height and wave period, and all the βs have approximately flat priors. The first non-linear function f_1 is a second order spline for the effect of ship speed (v), and the second non-linear function f_2 for wave direction (φ) is a two-parameter trigonometric function,$\alpha_1 \sin\varphi\ +\ \alpha_2 \cos\varphi$, with approximately flat priors for the two parameters. The residuals are modelled as iid (independent and identically distributed) Gaussian variables.

The biofouling effect $h(t)$ is a piecewise random function, with each piece corresponding to a cleaning interval. Two model alternatives are explored and the pieces of h are either linear in *time since the last cleaning event* (model PWSR-1), or linear in *time at rest since the last cleaning event* (model PWSR-2). Assume time t is in the k-th cleaning interval starting at time t_k, then

$$\mathrm{h(t)} = \alpha_k + b_k \int_{t_k}^{t} I(s)\, ds \quad [4]$$

where $I(s)$ is constant equal to 1 for PWSR-1, and an indicator for whether the ship was standing still or not for PWSR-2. The parameters α_k and b_k are given approximately uniform priors. Alternative models can also include interaction terms between the effect of fouling and other covariates. For example, an alternative model could assume that the effect of fouling increases with ship speed, and replace the fouling term in eq. [3] with a term on the form $v^p \mathrm{h(t)}$, where p is a polynomial exponent that could take values 1, 2, 3…. Typically, the so-called cubic rule would indicate that $p = 3$ is reasonable, but results would probably not be very sensitive to this in a rather narrow range of ship speeds. The models can be further extended by relaxing the iid assumption on the residuals, e.g. by modelling the residuals as an autoregressive process.

Random Forest Model

Random forest (Breiman 2001) is an ensemble learning method for regression, classification and other tasks by constructing a multitude of decision trees. After training the trees, the regression output is the mean prediction of the individual trees. Random forest searches for the best feature among a random subset of covariates. This results in a wide diversity that generally results in model with good predictability. Random forests correct for decision trees' habit of overfitting to their training set.

With this model, an alternative approach to predict the effect of fouling is investigated. The idea here is a two-step approach. First, a random forest is built for estimating the Shaft Power, $\mathrm{y_{RF}}$, based on the available covariates X, and can be written as

$$\mathrm{y_{RF}} = \mathrm{f(X)} + \varepsilon \quad [5]$$

where ε is the residuals. The model is trained on data from a period where the ship is assumed to have a clean hull. This represents a reference model and predicts the Shaft Power for a clean hull.

Second, this reference model is used to predict Shaft Power for the entire data period, denoted $\hat{\mathrm{y}}_{\mathrm{RF}}$. The difference between observed Shaft Power $\mathrm{y_{obs}}$ and predicted shaft power can then be ascribed to the effect of biofouling, h(t), e.g.

$$\mathrm{y_{obs}} = \hat{\mathrm{y}}_{\mathrm{RF}} + \mathrm{h(t)} + \varepsilon \quad [6]$$

The critical assumptions here are that the estimated model is valid when marine fouling is not present, and that the combination of covariate values in the training period is representative for the entire time period. That is, in the training period we need to observe the ship in many operational and environmental conditions, and these conditions must be representative for the entire time period. It is not clear how to define the training period in order to balance these two criteria, and for some cases this can be difficult to meet.

The estimates of biofouling $\hat{\mathrm{h}}(\mathrm{t})$ are then found from the calculated and observed Shaft Power over time using [6]. Again, different relationships could be assumed for the biofouling effect as a function of time in each cleaning interval, e.g. a linear relationship, $\hat{h}(t) = \alpha_k + b_k t$, or that it increases with ship speed as in $\hat{h}(t) = \alpha_k v^p + b_k t\, v^p$.

ANALYSIS AND RESULTS

In this section of the paper we highlight the main results from the analysis on data from a particular ship. Different out-of-sample tests can be applied to select the best model, and also the optimal data subset to use, based on predictive accuracy and measures such as root mean square error and mean absolute error. Details are not presented herein, and only main results from selected models will be presented. It is noted that larger subsets of the data generally yields narrower confidence bounds, whereas the point estimates may not be significantly influenced.

Estimated Effect of Biofouling from the Piecewise Spline Models

The estimated effect of biofouling on shaft power from the two main model alternatives PWSR-1 and PWSR-2 are shown in Figure 2. The estimated fouling effect is shown in black and residuals are added in red. Vertical lines correspond to cleaning events. These models are applied to data with no subsampling. Hence, the iid assumption is questionable and notable serial correlations can be observed in the residuals. Therefore, uncertainty bounds will tend to be unrealistically narrow and is not shown. However, when the same models are applied to a more heavily subsampled data-set, where the iid assumption is more realistic, a better estimation of the uncertainty can be obtained. Figure 3 shows results including uncertainty estimates from model PWSR-2 for data where subsampling down to one observation per day is performed. This yields much less data and

hence larger, but more realistic uncertainty estimates. It can be observed that the point estimates are not overly sensitive to this subsampling.

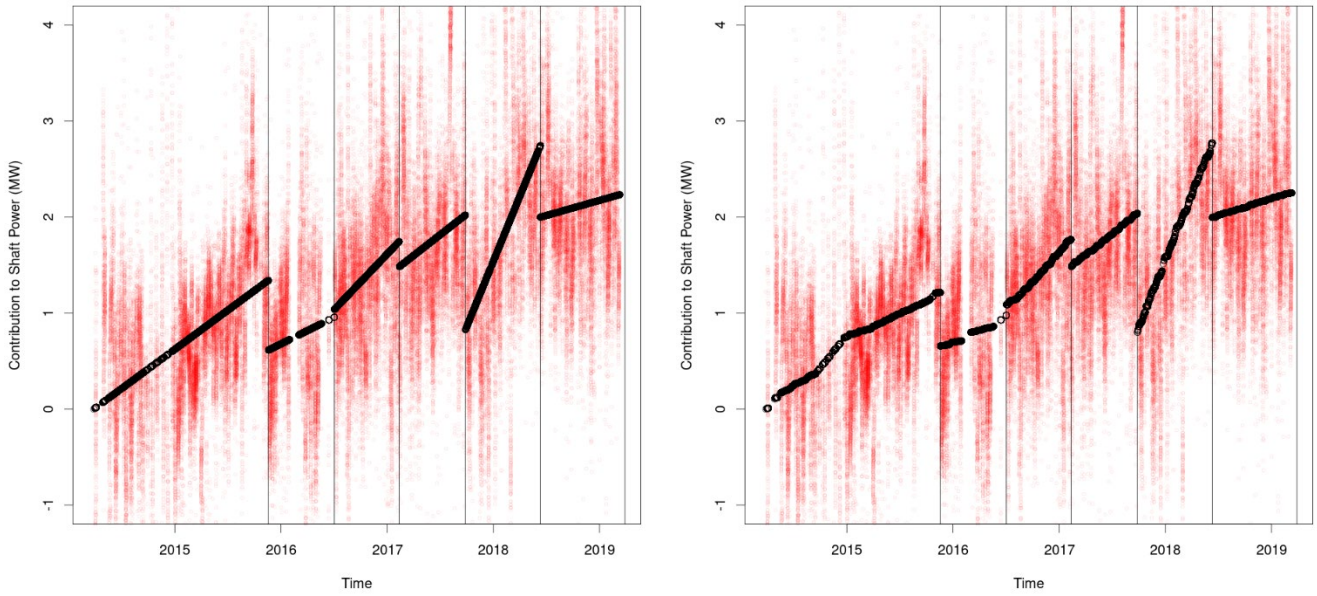

Figure 2: Estimated effect of fouling on shaft power from model PWSR-1 (left) and PWSR-2 (right)

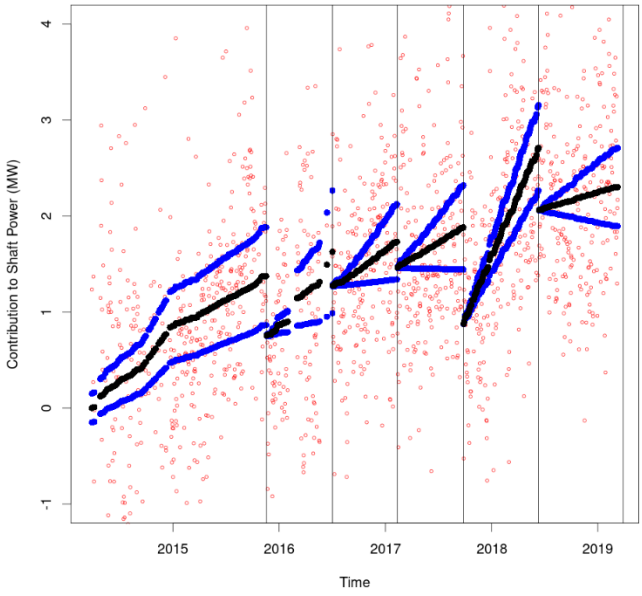

Figure 3: Estimated effect of fouling on shaft power, with uncertainty estimates, from model PWSR-2 applied to heavily subsampled data

One may also be interested in the estimated effect of ship speed, and this is shown in Figure 4, for results based on the initial and the subsampled dataset, respectively. Ideally, this should be a strictly increasing function, but this does not seem to be the case. Possibly, this could be due to problems with the data, especially at low speeds, or to inaccurate adjustments for other factors such as weather, accelerations and biofouling. Notwithstanding, the overall trend is that shaft power increases with speed, and the fact that the purely data-driven model picks this up can serve as a crude sanity check. A variance decomposition was performed for each model, by computing the empirical variance of each model component after the model was fitted to data. This decomposition indicated that ship speed is the variable responsible for explaining most of the variation in shaft power, followed by wind speed, and then biofouling as the third most important explanatory variable, where importance is understood as having a large variance.

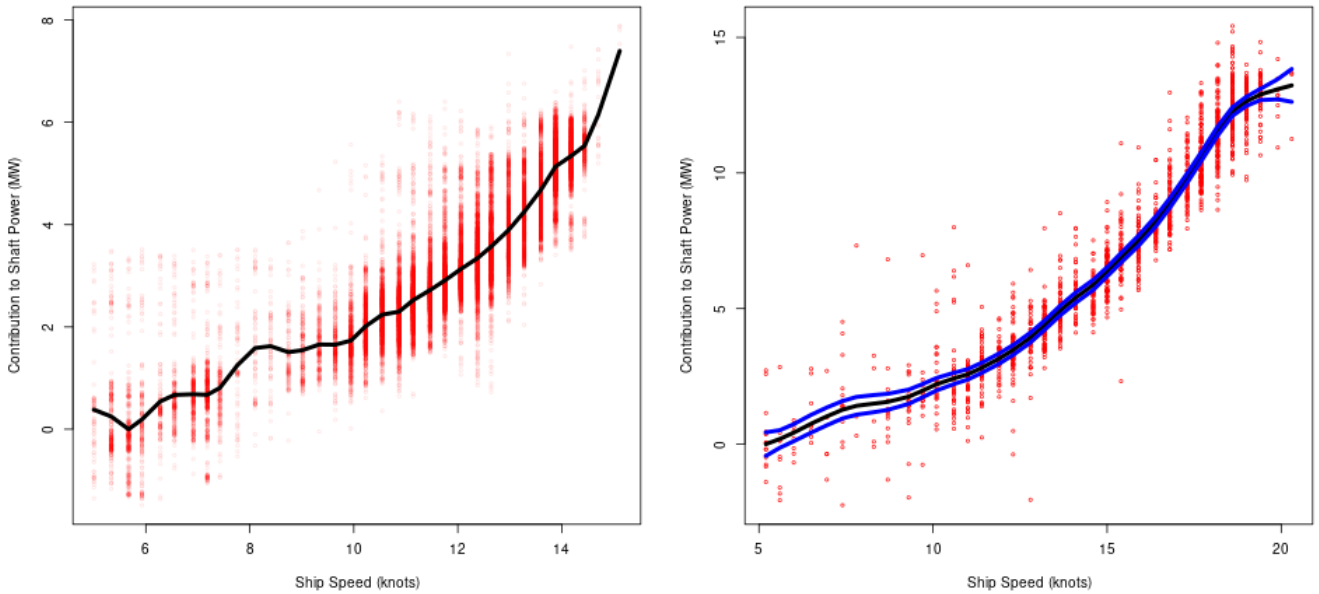

Figure 4: Estimated effect of ship speed on shaft power, from model PWSR-2 on initial dataset (left) and on heavily subsampled dataset (right)

Results from the Random Forest Models

This modelling approach requires a training data set from clean hull conditions, and for the purpose of this study, the whole first year of data are used as training data. This tacitly assumes that the effect of fouling is small in this period. Different combinations of the variables have been used in different alternative random forest models, and results presented here is from the model with best out-of-sample predictive performance. This includes all covariates except linear acceleration and wind direction. Figure 5 shows the estimated effect of biofouling on shaft power from this model, based on the initial dataset without subsampling. One attractive feature of random forest models is that they allow for an assessment of variable importance, i.e. which explanatory variables are most important in explaining the response. From the random forest models applied in this study, it is found that ship speed is the, by far, most important variable in explaining shaft power, followed by wind speed.

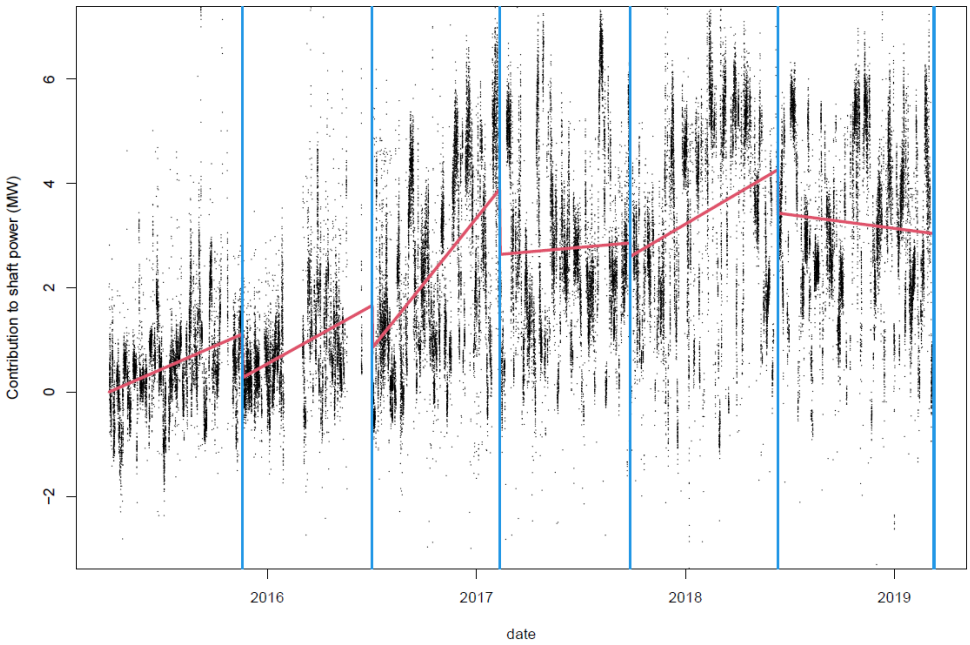

Figure 5: Estimated effect of biofouling on shaft power from a random forest model

Comparing Results from Piecewise Spline Models and Random Forest

Comparing the results from the piecewise spline models and the random forest models, some differences are apparent. In particular, the estimated fouling effect in some of the cleaning intervals are notably different. Especially in interval 3 the curve is much steeper and in interval 5 the curve is less steep than we would expect, compared to the PWSR models (compare Figures. 3 and 5; interval refers to the periods between the vertical lines in the figures). The estimated curve in the last interval has a negative slope, meaning that the contribution to shaft power decreases over time even though there has been no cleaning. This seems unlikely. In addition, the small decrease between interval 4 and interval 5 shows that the effect of cleaning has not been captured by this model. Hence, overall, the results from the random forest model are not exactly as expected. One possible explanation for this is that the conditions experienced by the ship have changed after the training period. Indeed, it can be observed in the data that the average ship speed is higher after the training period. Thus, the training data may not be fully representative for the subsequent data. Based on these observations, one may presume that the results from the piecewise spline models are more reliable than those obtained from the random forest models.

DISCUSSION

Some interesting observations can be made based on the results from the data-driven models (in particular, the piecewise spline models). The general trend is that the biofouling effect worsens over time, is reduced by cleaning, but that it hardly resets to the low effect of a new ship. Across the entire timeline, the total efficiency lost due to biofouling (including the gradual worsening) is 17% on average for this ship. As part of this total loss, there is the local worsening in each cleaning interval, corresponding to efficiency losses of 16%, 4.0%, 2.3%, 2.2%, 8.6%, and 1.2% in the six different cleaning intervals. These local deteriorations can be expected to be strongly influenced by any change in the cleaning times/events. However, the most important source of efficiency loss seems to be the gradual loss, i.e. that the ship never returns to its initial biofouling effect. This gradual worsening might be partly due to other factors than biofouling. If there are other age-related inefficiencies, e.g. small damages to the hull, or inefficiencies in the propeller, these will be accounted for in the models as global biofouling effect. If a cleaning event completely restores the hull to the conditions of a new ship, the estimated biofouling effect would still not revert to zero after the cleaning, due to these other inefficiencies.

The next-to-last cleaning seems to have caused additional biological growth on the ship, and should be further investigated. This could be due to a problem with this particular cleaning event, or the ship could have been operated under very different conditions in this period causing increased growth (e.g. warmer water or less movement).

The results from the models presented in this paper, may provide useful information when deciding on a cleaning schedule for a ship, or for general assessments of ship performance. The estimated added resistance from biofouling could also be used as an important input to models for calculating fuel consumption and ship emissions. It may also be used to gain further insight into factors that contribute to biofouling. Overall, the results from the data-driven models are reasonable and are able to predict increasing effect of biofouling over time. However, further improvements of the models are possible, and for example including more interaction effects between the covariates could improve the predictions.

SUMMARY AND CONCLUSIONS

This paper has presented data-driven models for estimating the effect of biofouling on ship performance. Different types of data-driven models have been investigated, and different ways of accounting for the effect of biofouling, which is not directly observed, have been tried. Some of these models achieved reasonable results and demonstrate that data-driven models are able to predict the effect of fouling, given that relevant performance data from the ships are available. This is believed to be useful in a range of different applications including optimized schedule for hull cleanings, improved operational performance of ships and in calculating fuel consumption and emissions to air from ships.

Overall, the data-driven models identify increasing effect of biofouling after a hull cleaning, with varying trends in different cleaning periods. Also, the effect of ship speed on shaft power are reasonably modelled by these purely data-driven models. Hence, such models are proposed for modelling the effect of biofouling on ship performance, a topic for which there are large knowledge gaps and lack of good physics-based models.

ACKNOWLEDGEMENTS

This research is funded by the Norwegian Research Council (NFR) research-based innovation center BigInsight, project no 237718, and is carried out in close collaboration with the VERDE project, funded by NFR, project no. 282293.

REFERENCES

BRANDSÆTER, A. and E. VANEM. “Ship speed prediction based on full scale sensor measurements of shaft thrust and environmental conditions”. *Ocean Engineering*, 162 (2018): 316-303

BREIMAN, L. “Random forests”. *Machine Learning*, 45 (2001): 5-32

BUI, K.Q. and PERERA, L.P. “Advanced data analytics for ship performance monitoring under localized operational conditions”. *Ocean Engineering*, 235 (2021): 109392

CORADDU, A., L. ONETO, F. BALDI, F. CIPOLLINI, M. ATLAR and S. SAVIO. “Data-driven ship digital twin for estimating the speed loss caused by marine fouling”. *Ocean Engineering*, 186 (2019): 106063

DALHEIM, Ø.Ø. and S. STEEN. “Uncertainty in the real-time estimation of ship speed through water”. *Ocean Engineering*, 235 (2021): 109423

HERSBACH H., B. BELL, P. BERRISFORD, S. HIRAHARA, A. HORÁNYI, J. MUÑOZ-SABATER, J. NICOLAS, C. PEUBEY, R. RADU, D. SCHEPERS, A. SIMMONS, C. SOCI, S. ABDALLA, X. ABELLAN, G: BALSAMO, P. BECHTOLD, G. BIVATI, J. BIDLOT, M. BONAVITA, G. DE CHIARA, P. DAHLGREN, D. DEE, M. DIAMANTAKIS, R. DRAGANI, J. FLEMMING, R. FORBES, M. FUENTES, A. GEER, L. HAIMBERGER, S. HEALY, R.J. HOGAN, E. HÓLM, M. JANISKOVÁ, S. KEELY, P. LALOYAUX, P. LOPEZ, C. LUPU, G. RADNOTI, P. de ROSNAY, I. ROZUM, F. VAMBORG, S. VILLAUME and J.-N. THÉPAUT. “The ERA5 global reanalysis”. *Quarterly Journal of the Royal Meteorological Society*, 146:730 (2020): 1999-2049

KARAGIANNIDIS, P. and N: THEMELIS. “Data-driven modelling of ship propulsion and the effect of data pre-processing on the prediction of ship fuel consumption and speed loss”. *Ocean Engineering*, 222 (2021):108616

MOLLAND, A., S. TURNOCK, D. HUDSON and I: UTAMA. “Reducing ship emission: a review of potential practical improvements in the propulsive efficiency of future ships”. *Transactions of the Royal Institution of Naval Architects Part A: International Journal of Maritime Engineering*, 156 (2014):175-188.

RUE, H., S. MARTINO and N. CHOPIN. “Approximate Bayesian inference for latent Gaussian models using integrated nested Laplace approximations (with discussions)”. *Journal of the Royal Statistical Society: Series B (Statistical Methodology)*, 71:2 (2009): 319-392

SHULTZ, M., J. BENDICK, E. HOLM and W. HERTEL. “Economic impact of biofouling on a naval surface ship”. *Biofouling*, 27:1 (2011): 87-98

STEINBAKK, G.H., L.H. AARSNES, M. ALDRIN, O.C. ASTRUP, O. HAUG, G. STORHAUG. and E. VANEM. “Statistical approximation to synthetic midship hull girder stress response”. *Journal of Ship Research*, 64:3 (2020): 266-277

YEGINBAYEVA, I.A. and M. ATLAR. “An experimental investigation into the roughness and hydrodynamic characteristics of marine coatings with mimicked hull roughness ranges”. *Biofouling*, 34:9 (2018): 1001-1019